Photoswitchable Molecular Systems for Supramolecular Assembly and Reversible Modulation of Catalysis

Surbhi Grewal

A thesis submitted for the partial fulfillment of the degree of Doctor of Philosophy

Department of Chemical Sciences

Indian Institute of Science Education and Research Mohali

Knowledge City, Sector 81, SAS Nagar, Manauli PO, Mohali 140306 Punjab, India

September 2022

Dedicated
To
My beloved parents
(Papa and Mummy)
and
Parents-in-law
(Aai and Anna)

Declaration

The work presented in this thesis has been carried out by me under the guidance of Dr. Sugumar Venkataramani at the Indian Institute of Science Education and Research Mohali. This work has not been submitted in part or in full for a degree, a diploma, or a fellowship to any other university or institute. Whenever contributions of others are involved, every effort is made to indicate this clearly, with due acknowledgement of collaborative research and discussions. This thesis is a bona fide record of original work done by me and all sources listed within have been detailed in the bibliography.

Surbhi Grewal

In my capacity as the supervisor of the candidate's thesis work, I certify that the above statements by the candidate are true to the best of my knowledge.

Dr. Sugumar Venkataramani

Acknowledgements

Without acquiring any help from others, nobody succeeds in any field. I hope with this completed PhD thesis, I am entering into Physical organic field to unravel the present challenges. It's obvious, similar to other researchers I received support to reach this level. Here, I would like to acknowledge all people, who directly or indirectly contributed to my research.

First and foremost, I would like to express my sincere gratitude to my thesis supervisor Dr. Sugumar Venkataramani for his constant support and encouragement throughout the period of my Ph.D. Though my experimental knowledge and communication skills were not up to the mark at my earlier stage, he never ever dismayed my communication and scientific calibre; rather he motivated me with his valuable suggestions to build up my skills. He has enriched me with his kind-heartedness, inventive ideas and passion towards science all through my research period, which helped me in enhancing my growth as a human and as a researcher. I enjoyed as a Ph.D. student in his laboratory during my doctoral study. It has been my privilege to work under his unconditional guidance, owing to which I have gained a positive attitude, diligence and problem solving capabilities.

I would especially like to thank my Doctoral Committee Members, Dr. Sanjay Singh and Dr. Sripada S. V. Rama Sastry for their valuable discussions and suggestions, and for evaluating my research improvement by yearly spending their valuable time.

I wish to thank our former Director, Professor N. Sathyamurthy, Director, Prof. Debi P. Sarkar and Prof. Jayaraman Gowrishankar for providing the world class infrastructure and facilities. I would like to thank our former Head of Department (HOD), Prof. K. S. Viswanathan and Dr. S. A. Babu and Head of Department (HOD), Dr. Sanjay Singh for valuable suggestions and providing the facilities at the department of chemical sciences. I am also thankful to IISER Mohali for NMR, HRMS, IR, departmental X-Ray facilities and other facilities. I wish to thank Dr. Santanu K. Pal and his PhD student Dr. Indu Bala for XRD studies which work I have included in my thesis and Dr. Sabyasachi Rakshit to provide his lab instrumentation facilities. I wish to thank Dr. Sharmistha Sinha and her PhD student Dr. Naimat K. Bari for ITC studies which work I have included in my thesis

I thank gratefully all the faculty members of the Department of Chemical Sciences for allowing me to use the departmental facilities. I must also acknowledge the IISER Mohali for my research fellowship during my doctoral study.

Furthermore, Special thanks to Manju Ma'am for her care and support during the

complete research journey.

I also owe this success to my brilliant labmates Dr. Sudha Devi, Dr. Saonli Roy, Dr. Mayank Saraswat, Dr. Chitranjan Sah, Ms. Anjali Srivastava, Ms. Debapriya Gupta, Ms. Sapna, Ms. Anjali Mahadevan, Ms. Sonam Suwasia, Mr. Pravesh Kumar, Mr. Himanshu Kumar, Mr. Ankit Gaur, Mr. Virender Singh, Mr. Sajal Nawaria, Mr. Roshan nasare, Mr. Hrishikesh, Mr. Piyush, Ms. Gayathri, Ms. Navneet Kaur, Ms. Ramanpreet Kaur for their valuable discussions, co-operation and for creating a healthy environment around me. I am grateful to Ms. Anjali and Ms. Sapna for assisting me in the synthesis and studies for the projects. I also acknowledge all the summer trainees who worked for a short time in our lab.

I am also thankful to Mr. Balbir and Mr. Triveni for their help in NMR and HRMS recordings. I would like to acknowledge the chemistry teaching lab assistants for their co-operation during my research period. I am also thankful to all my IISERM friends for their timely help.

Words are inadequate to explain my gratitude to all my beloved friends especially, Jyoti, Arushi, Preeti, Ritu, Indu, Anjali, Radha, Shaina. They stood with me during all my tough times and shared my sorrow and joy in many occasions. I would like to be grateful to Radha, Sapna and Anjali for their enjoyable and unforgettable negotiations (other than research) and chat during my journey.

I would like to express my heartfelt thanks to my better half Dr. Abhijeet S. Jadhav for his unconditional help, support and encouragement with lots of love. He stood always with me in both the good and bad phases of my life. I am fortunate to have my life-partner as Abhijeet, who has underpinned all my pitfalls.

Finally, I am very jubilant to mention my family members. Foremost, *Mummy* and *Papa* (mother and father) for their perseverance in making me an etiquette girl; their sacrifices and hard work yielded this degree. I can’t imagine this journey without their unconditional love and support. I am feeling blessed to have a brother like Ankit Grewal for standing with me in all the circumstances and always helping me throughout my studies. I would like to express my gratitude to my beloved Mother-in law (Aai) and Father-in law (Anna) who have always believed in me and supported me with unconditional love. Thank you to my sister-in-law Shailza and Sujata for their unconditional encouragement, support and care. The hard times during my Ph.D have been nullified by the exuberant atmosphere created by our home kids (Anuja,Yug, Nia, Uddu, Shreya, Rusi, Gattu, and Raj)

Publications

List of Publications (Thesis work)

† Equal contribution

- **S. Grewal**, S. Roy, H. Kumar, M. Saraswat, N. K. Bari, S. Sinha*, S. Venkataramani*, Temporal control in tritylation reactions through light-driven variation in chloride ion binding catalysis – A proof of concept, *Catal. Sci. Technol.* **2020**, *10*, 7027–7033.
- **S. Grewal**†, P. Kumar†, S. Roy, I. Bala, C. Sah, S. K. Pal*, S. Venkataramani*, Deciphering internal and external π-conjugation in *C*3-symmetric multiple azobenzene connected systems in self-assembly, *Chem. Eur. J.* **2022**, Just Accepted, DOI: 10.1002/chem.202104602.
- **S. Grewal**†, A. Srivastava†, S. Singh, S. Venkataramani*, Structure-property relationship in azobenzene photoswitches appended with picolinyl amides and their supramolecular assemblies, *manuscript under preparation.*

Publications from contributed projects

- S. Devi†, M. Saraswat†, **S. Grewal**†, S. Venkataramani*, Evaluation of Substituent Effect in *Z*-Isomer Stability of Arylazo-1H-3,5-dimethylpyrazoles – Interplay of Steric, Electronic Effects and Hydrogen Bonding, *J. Org. Chem.* **2018**, *83*, 4307–4322.
- A. Srivastava, **S. Grewal**, N. K Bari, M. Saraswat, S. Sinha,* S. Venkataramani*, Light controlled shape-changing azomacrocycles exhibiting reversible modulation of pyrene fluorescence emission, *Org. Biomol. Chem.* **2022**, *20*, 5284-5292.
- P. Kumar†, D. Gupta†, **S. Grewal**†, A. Srivastava†, A. K. Gaur†, S. Venkataramani*, Multiple Azoarenes Based Systems – Photoswitching, Supramolecular Chemistry and Application Prospects, *The Chemical Record*, **2022**.
- A. Srivastava, **S. Grewal**, S. Singh, S. Venkataramani*, Rhodamine tethered azobenzene- based photoswitchable probes as selective sensors for multiple metal ions, *manuscript under preparation.*

Book Chapter

S. Grewal†, D. Gupta†, A. K. Gaur†, M. Saraswat†, S. Venkataramani, "Azoheteroarene photoswitches – Synthesis, Photoswitching and Utility", *In Photoisomerization: Causes, Behavior and Effects*; Edited by D. Sampedro; Nova Publishers, **2019.**

Contents

List of Abbreviations

UV-Vis:	Ultraviolet-Visible
NMR:	Nuclear Magnetic Resonance
IR:	Infrared Spectroscopy
HRMS:	High-Resolution Mass Spectrometry
KBr:	Potassium bromide
$BaSO_4$:	Barium sulfate
PSS:	Photostationary State
FTIR:	Fourier Transform Infrared Spectroscopy
DFT:	Density Functional Theory
BTA:	Benzene-1,3,5-tricarboxamide
DMSO:	Dimethyl sulfoxide
E_a:	Activation Energy
$\Delta S^{\ddagger}$:	Entropy of Activation
$\Delta H^{\ddagger}$:	Enthalpy of Activation
$\Delta G^{\ddagger}$:	Gibbs Free Energy of Activation
SEM:	Scanning Electron Microscopy
POM:	Polarized Optical Microscopy
$[D_6]$DMSO:	Deuterated-Dimethyl sulfoxide
$CDCl_3$:	Deuterated-Chloroform
XRD:	X-ray Diffraction
AFM:	Atomic Force Microscopy
TEM:	Transmission Electron Microscopy
DMAP:	*N*,*N*-Dimethylpyridin-4-amine
$BzNH_2$:	Benzyl amine
DCM:	Dichloromethane
THF:	Tetrahydrofuran
ITC:	Isothermal Titration Calorimetry
TBAC:	Tetrabutylammonium chloride
DMAP-TrCl:	*N*,*N*-Dimethylpyridin-4-amine-trityl chloride Adduct

List of Figures

List of Tables

List of Schemes

Abstract

Photoresponsive materials refer to those materials that can reversibly toggle between two isomeric forms and can undergo physical and chemical changes upon irradiation at appropriate wavelengths of light. Therefore, various properties such as planarity, geometrical structure, absorption spectra, dipole moment, dielectric constant, color, solubility, chemical reactivity, conjugation, covalent bonding, non-covalent interaction, coordination properties, etc. can be modulated with the help of light. Among the various classes of photoswitchable molecules, azobenzenes are one of the robust molecules with excellent photoisomerization properties between *trans* (thermodynamically stable) and *cis*-isomers and are readily accessible, which makes them attractive candidates for functionalization. The resulting photoresponsive molecular materials have widespread applications in numerous fields that include molecular recognition, molecular machines, photopharmacology, supramolecular assembly, liquid crystals, catalysis, sensors, logic operations, data storage, optical memory devices, molecular devices, etc. For various applications, understanding the factors influencing the photoswitching behavior and *cis*-isomer stability of azoarenes is crucial.

In this regard, we have synthesized 18 photoresponsive molecular systems with variable connections and structural diversity in high yields through modular synthesis. We have also investigated the effect of structural modification on photoswitching characteristics and the thermal stability of the *Z*-isomers. Apart from that, the common amide functional group in all the derivatives has been explored for their aggregation and supramolecular behavior. The changes in the morphology of supramolecular assembly/microcrystals have been studied using polarized optical microscopy (POM), Scanning electron microscopy (SEM), and the effect of photoisomerization on their morphology has also been examined.

Next, we have designed and synthesized two novel C_3-symmetric tripodal trisazobenzene-based molecular systems with extended π-conjugation at internal and external positions. Here, we studied the effect of extended π-conjugation on photoswitching, thermal stability, and aggregation. We have investigated the impact of design on the supramolecular self-assembly, and also, demonstrated the morphological changes in the self-assembly behavior by atomic force microscopy (AFM), scanning electron microscope (SEM), transmission electron microscopy (TEM), and polarized optical microscopy (POM). X-ray diffraction studies (XRD) revealed that the external extended π-conjugation systems showed the columnar rectangular type of self-assembly and the internal one showed lamellar type

assembly.

In the last part of the thesis work, five *tris*-triazole-linked azo(hetero)arene-based molecular systems have been designed and synthesized that can act as photoswitchable catalysts. We envisioned that the catalytic activity can be light controlled by varying the anion-binding ability of the catalyst in its native and photoswitched states. Using these catalysts, temporal control of tritylation reaction rates of various nucleophiles has been achieved. Through HRMS data, NMR titrations, control experiments, and DFT computations, the mechanistic aspects, the mode of binding, and the importance of cooperative binding have been envisaged. Isothermal titration calorimetric (ITC) measurements revealed a two-fold difference in the dissociation constant between a chloride ion and the catalyst in its native (*EEE*) and photoswitched (*ZZZ*) states, which is very well corroborated with the differences in the isolated yields.

Chapter 1. General Introduction

1.1 Stimuli-Responsive Materials

Stimuli-Responsive materials, known as smart materials, are those systems capable of altering their physicochemical properties in response to the changes in the surrounding environment.[1] Such materials are extremely sensitive in nature that even a slight change in their environmental conditions can cause a significant effect on their respective properties. Stimuli-responsive materials are typically classified on the basis of their response to external stimuli, i.e., physical stimuli, chemical stimuli, and biochemical stimuli **(Figure 1.1)**.[2] The physical stimuli mainly include temperature, mechanical deformation, electric field, magnetic fields, ultrasound, and light. With regard to chemical stimuli, it mainly comprises pH, redox, solvent, and ionic strength, etc. Ligands, antigens, enzymes, or other biochemical agents are part of the biochemical stimuli.[2,3] The above types are classified based on single-stimuli responsive materials; however, multiple stimuli-responsive systems have also been realized.[4] Stimuli-responsive molecular systems possess a diverse range of applications such as used for controlled and triggered drug delivery,[5a-b] chemo-mechanical actuators,[5c-e] environmental remediation,[5f] in the fields of biology and medicine, and sensors,[5g] etc.[5a, 5i-j] Among all the above-mentioned external stimuli, light has attracted a great deal of attention due to its non-invasive nature, it is also convenient to use, can be directed into a specific area, and has easy availability. Therefore, those materials responding to light as an external stimulus are called light-responsive or photoresponsive materials.

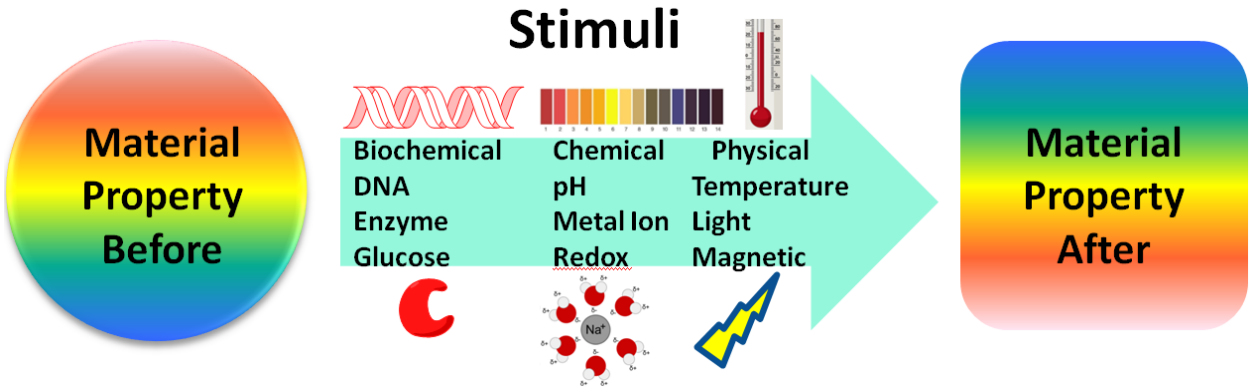

Figure 1.1 Stimuli-responsive materials.

1.2 Photoresponsive Materials and Photoswitches

Photoresponsive materials refer to those materials that can reversibly toggle between two isomeric forms and can undergo physical and chemical changes upon irradiation with light of appropriate wavelengths. Therefore, various properties such as planarity, geometrical structure, absorption spectra, dipole moment, dielectric constant, color, solubility, chemical reactivity, refractive index, magnetic properties, π- conjugation, fluorescence emission, covalent bonding, non-covalent interaction, electrochemical properties, electron conductivity, coordination properties, etc. can be modulated with the help of suitable light.[6] This phenomenon of reversible photoisomerization often exhibit color changes and shifts in the absorption profiles and it is known as photochromism, and the compounds exhibiting such properties are called photochromic compounds or photoswitches. Photoresponsive materials have widespread applications in numerous fields, for instance, molecular recognition, molecular machines, photopharmacological applications, supramolecular assembly, liquid crystals, catalysis, sensors, logic operations, data storage, optical memory devices, and molecular devices, etc.[6a,7] These materials can be prepared by incorporating photoresponsive chromophores and moieties such as azobenzenes, fulgides, stilbenes, spiropyrans, diarylethenes, chromenes, etc., in the framework. Contingent on the thermal stability of the photoisomers generated upon subjected to irradiation, photochromic materials can be classified into two types, i.e. (a) P-type (photochemically reversible type): These can be reversed photochemically but not thermally, e.g., diarylethenes and fulgides and; (b) T-type (thermally reversible type): These can be reversed thermally as well as photochemically, e.g., stilbenes, spiropyrans, chromenes, and azobenzenes, etc.[8] However, beyond these popular classes, few other chief organic photochromic scaffolds are also known, such as overcrowded alkenes, imines, donor-acceptor Stenhouse adducts (DASAs), acylhydrazones, norbornadienes/quadricyclanes (NBDs/QCs), and dihydroazulenes/vinylheptafulvenes (DHAs/VHFs), etc. and they have attracted widespread attention due to their emerging applications in photocontrol of biological systems and photoresponsive materials **(Table 1.1)**.[9]

Table 1.1 Various photochromic scaffolds and their photoisomerization process.

Photochromic Scaffolds	Photosiomerization process
Diarylethenes	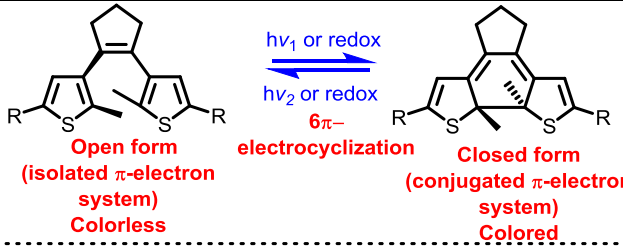
Fulgides	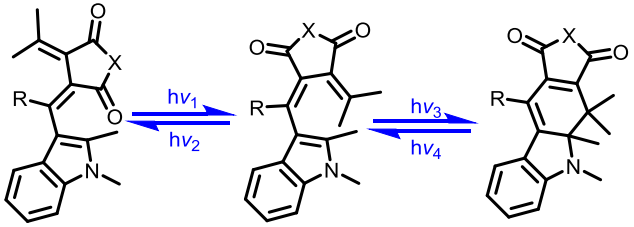
Stilbenes	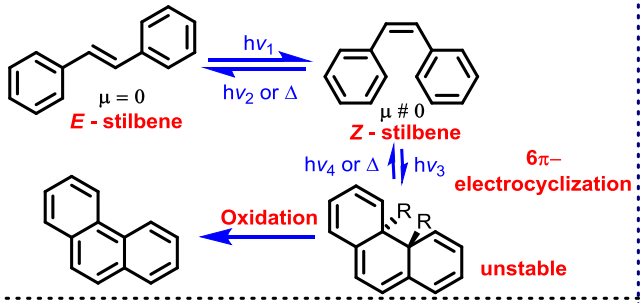
Spiropyrans	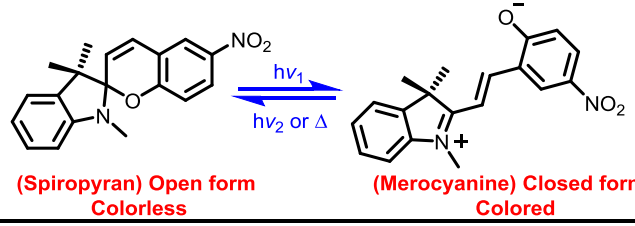

Photochromic Scaffolds	Photosiomerization process
Chromenes	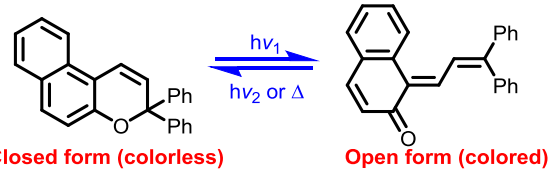
Azobenzenes	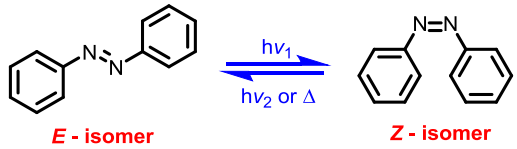
Acylhydrazone	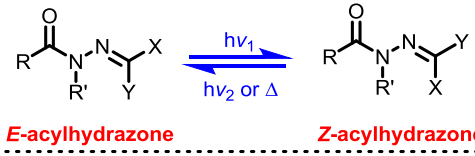
Norbornadiene /quadricyclane (NBDs/QCs)	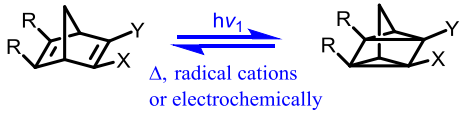
Dihydropyrene	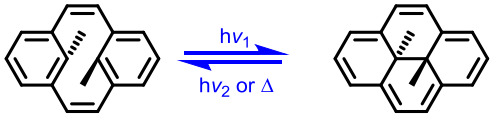
Donor-acceptor Stenhouse adducts (DASAs)	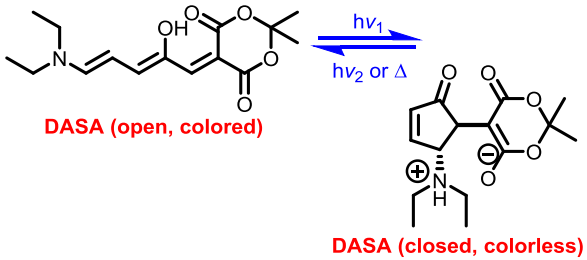

Among all the above-discussed photochromic scaffolds, azobenzenes are the most widely studied organic photochromic molecules, exhibiting extensive applications in diverse fields. Besides that, they have excellent salient features such as bidirectional photoswitching, tunable half-lives of the photoswitched state, ease of synthesis and functionalization, etc. Therefore, substituted azobenzenes analogs have been utilized throughout this investigation.

1.3 Azobenzenes

Azobenzene is an organic chromophore defined as a compound comprising two phenyl groups connected via a nitrogen-nitrogen double bond (diazene bonds). Azobenzene and its derivatives have an extensive history in synthetic chemistry and have been used in a plethora of applications.[10] Originally conceived as dyes,[11] used in molecular photoswitches,[12] molecular machines,[13] surfactants,[14] polymers,[15] guests in inclusion complexes,[16] linkers in biological macromolecules,[17] ligands,[18] liquid crystals,[19] and as multi-responsive triggers in degradable polymers,[20] artificial switchable catalysts,[21] supramolecular assembly and most recently azobenzene based solar thermal fuels,[22] etc. The synthesis of the distinct azobenzenes derivatives has been developed and known via various synthetic routes such as electrophilic aromatic substitution, reductive coupling of nitrobenzenes, oxidative coupling of anilines, nitrosobenzene-aniline condensation (Mills method), etc.[23]

The photochemistry of azobenzene has been a primary area of investigation. The use of ultraviolet (UV) light to excite these molecules allows exceptionally efficient and rapid isomerization from *trans* to *cis* state. The isomerization is usually completed with almost negligible side reactions and can be modulated to a wide range of wavelengths by introducing various functional groups. Furthermore, the photophysical and photochemical properties of *cis* azobenzene differ significantly from those of the *trans* isomer, which has led to the exploitation of this class of molecules. Stilbenes are structurally similar to azobenzenes and are isoelectronic with them; nonetheless, they cannot be isomerized reliably without side reactions.[24] Azobenzene is a relatively stable molecule, even when irradiated,[25] and as a result, it is frequently used in photochemistry due to its low potential for side reactions.

1.4 Photoisomerization in Azobenzene

The effect of light on the stereochemistry of azo bond was first introduced in 1937 by Hartley.[26] Owing to the azobenzene's rich photochemistry, understanding their photoisomerization behavior, characterization of photoisomers using various spectroscopic techniques, and the variation in properties during isomerization is crucial. Azobenzenes are archetypical molecules those exhibit fast, clean, reversible, and efficient photoisomerization. By absorbing light of a suitable wavelength, the thermodynamically stable, planar *trans* (*E*)

azobenzene isomer shows transition into the bent and non-planar *cis* (*Z*) isomer, whereas the *Z*-*E* isomerization can be achieved either thermally or photochemically **(Scheme 1.1)**. Generally, thermodynamically, the planar *trans* (*E*) form is more stable in comparison with the non-planar *cis* (*Z*) form, but in the case of constrained azobenzene systems (namely, diazocines) *Z*- isomeric stability is high due to ring strain.[27]

Theoretically the *E*-isomer of azobenzene is predicted to be around 10-12 kcal/mol, more stable than the *Z*-isomer, and the interconversion thermal barrier of *Z*- to *E*- isomer is approximately 18 kcal/mol. The photoswitching efficiency is affected by the substituents, temperature, viscosity, and polarity of the solvent in the solution phase; when embedded in polymers, the conformational change is affected by the polymer matrix. In solid-state, it is affected by molecular system packing or aggregation, and in the pure crystalline state, there is no conformational changes **(Figure 1.2)**.[27]

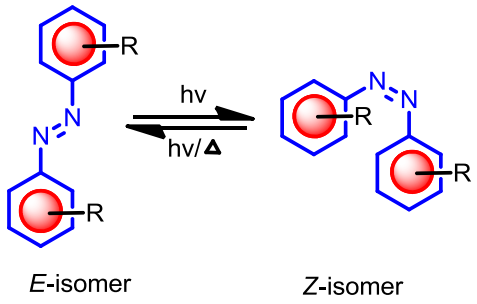

Scheme 1.1 Photoisomerization in azobenzene between *E*- and *Z*-isomers

In general, physical and spectroscopic properties change upon isomerization from the planar *trans* to the bent *cis* isomer. As photoisomerization results in distinct physical properties, therefore, *Z*-isomer possesses variation in size, absorption spectral features, dipole moment, planarity, melting point, solubility, π-conjugation, etc **(Table 1.2)**.[23,27] when compared to its *E*-isomer. These changes in physical properties make azobenzene chromophore a potential candidate for functional smart materials for light-harvesting, optical storage, long-term energy storage, catalysis, chemosensing, and liquid crystals.

For the investigation of changes in properties and both thermal and photochemical isomerization, different experimental techniques or theoretical methods have been utilized, such as computational methods, X-ray studies,[28] UV-Vis spectroscopy,[29] NMR spectroscopy,[30] IR spectroscopy,[31] Raman spectroscopy,[32] ion-mobility mass spectrometry (IMMS),[33] high-performance liquid chromatography (HPLC) can be combined with UV-Vis or Mass spectrometry (MS),[33c] cyclic voltammetry (CV),[33c] differential pulse voltammetry,[33c] terahertz time-domain spectroscopy (THz-TDS),[34a] etc. as per literature reports.[27]

Table 1.2 Changes in the properties during photoisomerization of simple azobenzene.

Property	*Trans* (*E*) isomer	*Cis* (*Z*) isomer
Structure	Planar	Bent or non-planar
Symmetry	C_{2h}	C_2
Dipole moment	0.5 D	3.1 D
Length	9.0 Å	5.5 Å
Melting point	Low	High
Solubility in polar solvents	Low	High
Molar extinction coefficient (Ɛ)	2–3 X 10^4 M^{-1} cm^{-1}	7–10 X 10^3 M^{-1} cm^{-1}
Stability	Stable	Unstable (Except cyclic)
Polarity	Non-polar	Polar

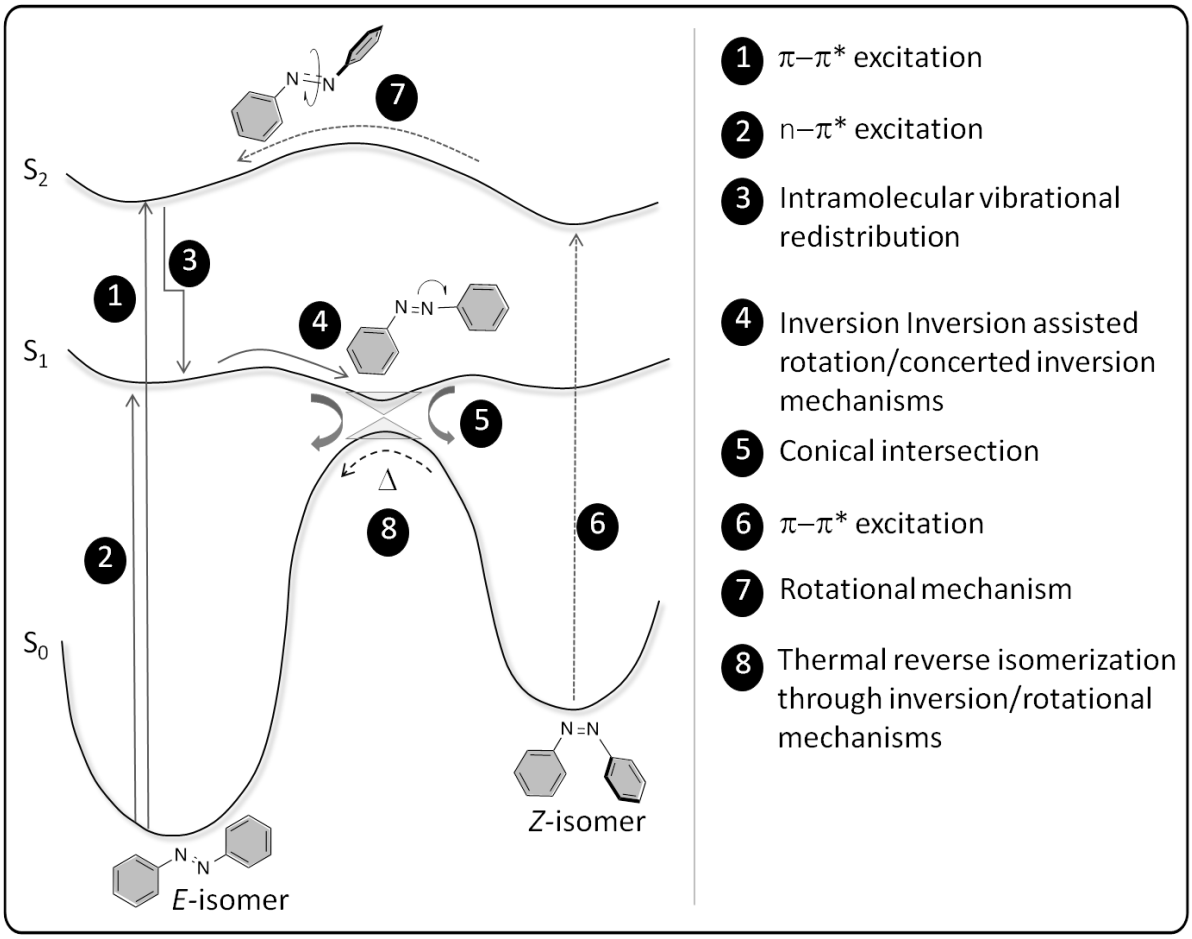

Figure 1.2 Photoisomerization mechanism of azobenzene.[23a]

1.5 Techniques and Methods for Investigation of Photoisomerization

1.5.1 UV-Vis Spectroscopy of Azobenzenes[29]

UV-vis absorption spectroscopy has been widely used as qualitative and quantitative tool for identification / characterization and estimation of *E*/*Z* photo-isomeric product ratios in one or more azobenzene containing systems. Azobenzenes usually show two well-separated bands corresponding to n-π* and π–π* electronic transitions in their absorption spectrum, and upon isomerization, they exhibit different absorption properties for *E*- and *Z*-isomers, particularly in the n-π* and π–π* absorptions **(Figure 1.3a)**. Typically, in *E*-azobenzene an intense π-π* (in UV region) and a weak n-π* (in visible region) absorption bands are observed, whereas the *Z*-isomer shows a blue-shifted (hypsochromic effect) and relatively lower intense π-π* and strong n-π* bands (hyperchromic effect). For instance, in *E*-isomer, a strong UV band (λ_{max}-320 nm; ε ~ 22000 L mol^{-1} cm^{-1}) arises due to a symmetry allowed π–π* transition, whereas a weaker band (λ_{max}-450 nm; ε ~ 400 L mol^{-1} cm^{-1}) due to a forbidden n-π* transition in the visible region. Contrary to this, in *Z*-isomer, the π–π* band (λ_{max}-270 nm; ε ~ 5000 L mol^{-1} cm^{-1}) is weaker than in *E*-isomer, while, the n-π* transition observed (λ_{max}-450 nm; ε ~ 1500 L mol^{-1} cm^{-1}) in the visible region that is stronger than in *E*-isomer. In general, *E*-azobenzene will lead to the forward (*E*-*Z*) isomerization with irradiation at a suitable wavelength of light corresponding to π-π* absorption, in contrast, the reverse reaction can be achieved either under irradiation conditions (photochemically) with a wavelength corresponding to n-π* absorption of the *Z*-isomer or under thermal conditions. For kinetic studies of the thermal isomerization of (*Z*- to *E*-) isomer, UV-vis absorption spectroscopy is one of the most preferred techniques. The n–π* and π–π* transitions stimulate azobenzene from S_0 (ground state) to S_1 (n–π*) and S_2 (π–π*) excited states after irradiation. When the π–π* band is excited, azobenzenes have a high molar extinction coefficient and a moderate photoisomerization quantum yield, therefore, low-intensity light can initiate their photoisomerization.[23b, 27] Besides solution phase, the isomerization can also be analysed in solid-state or in thin films using diffused reflectance assembly in some medium such as KBr, $BaSO_4$, etc. Although UV-Vis spectroscopy can be utilized to examine mono-photochromic systems effectively, the investigations on multi-state photoisomers, discrimination between photoisomers and their population analysis are not possible due to the broadness and overlapping signals. In this context, the NMR spectroscopic technique has proven to be one of the most effective and useful methods for quantifying such photoisomers in mono as well as in multi-photochromic systems.[30a]

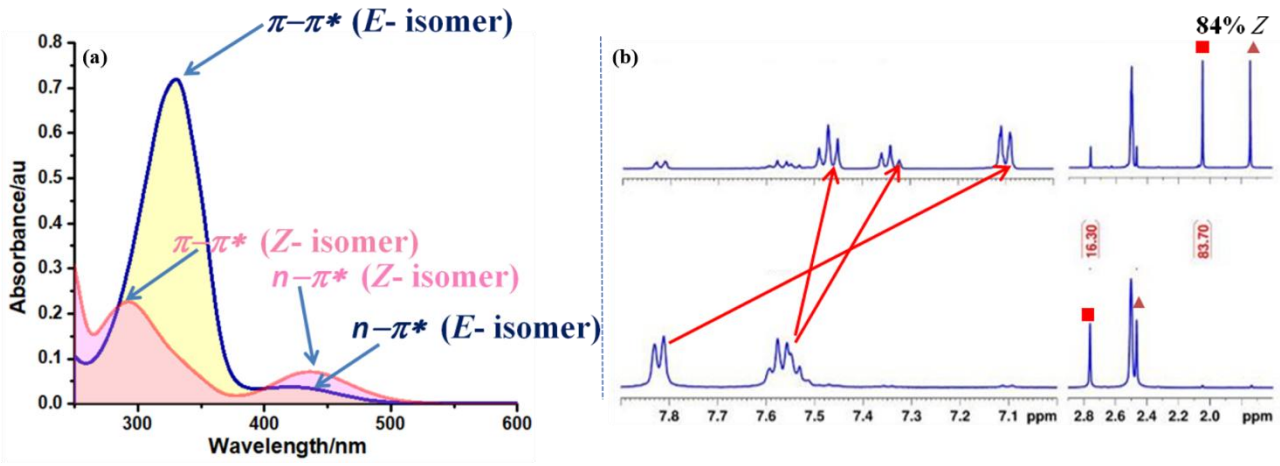

Figure 1.3 (a) Representative UV-Vis spectra corresponding to *E*-(blue line) and *Z*-isomers (pink line) of azobenzene; (b) Representative NMR spectra corresponding to *E*-(bottom) and *Z*-isomers (top) of azobenzene. (PSS composition quantification).

The % conversion of *E*-isomer at PSS for forward and reverse isomerization steps using UV-vis spectroscopy can be estimated using the formula:

PSS in Solution phase**:** % conversion of *E* isomer $= 1 - \frac{\text{absorption after irradiation at 365 nm}}{\text{absorption before irradiation}} * 100$

PSS in Solid phase: % conversion of *E* isomer $= 1 - \frac{\text{absorption before irradiation}}{\text{absorption after irradiation at 365 nm}} * 100$

1.5.2 NMR Spectroscopy[30]

The photoisomerization and thermal reverse isomerization of azobenzene can also be studied using NMR spectroscopy. Azobenzenes have distinct NMR spectra for the *E*- and *Z*-isomers. Upon UV irradiation at an appropriate wavelength, the ^{1}H NMR signals of the *E*-isomer drop in intensity, and the new signals corresponding to the *Z*-isomer typically appear in the shielded region **(Figure 1.3b)**.

The shielding effects of the two phenyl rings of an azobenzene moiety cause such upfield shifts for *Z*-isomer. For quantification and to follow the kinetics, the normalized integral ratios of any particular proton signals (non-overlapping) which are corresponding to *E*- and *Z*- isomers of azobenzene are used. The figure 1.3b demonstrates the ^{1}H-NMR spectral data of mono-azobenzene containing photochromic system, and the estimation of percentage conversion during the photoisomerization at PSS. However, in the case of more than one azobenzene-containing molecular systems, it becomes more complex.[29b] As the entire thesis includes both types of model compounds (mono and tris- azo containing), therefore, it is intriguing to discuss about those aspects. In 2016, Thiele and co-workers have thoroughly investigated the photoinduced forward and thermal reverse isomerization

processes in C_3-symmetric compound using *in situ* irradiation ^{1}H-NMR spectroscopy **(Figure 1.4)**.[30a]

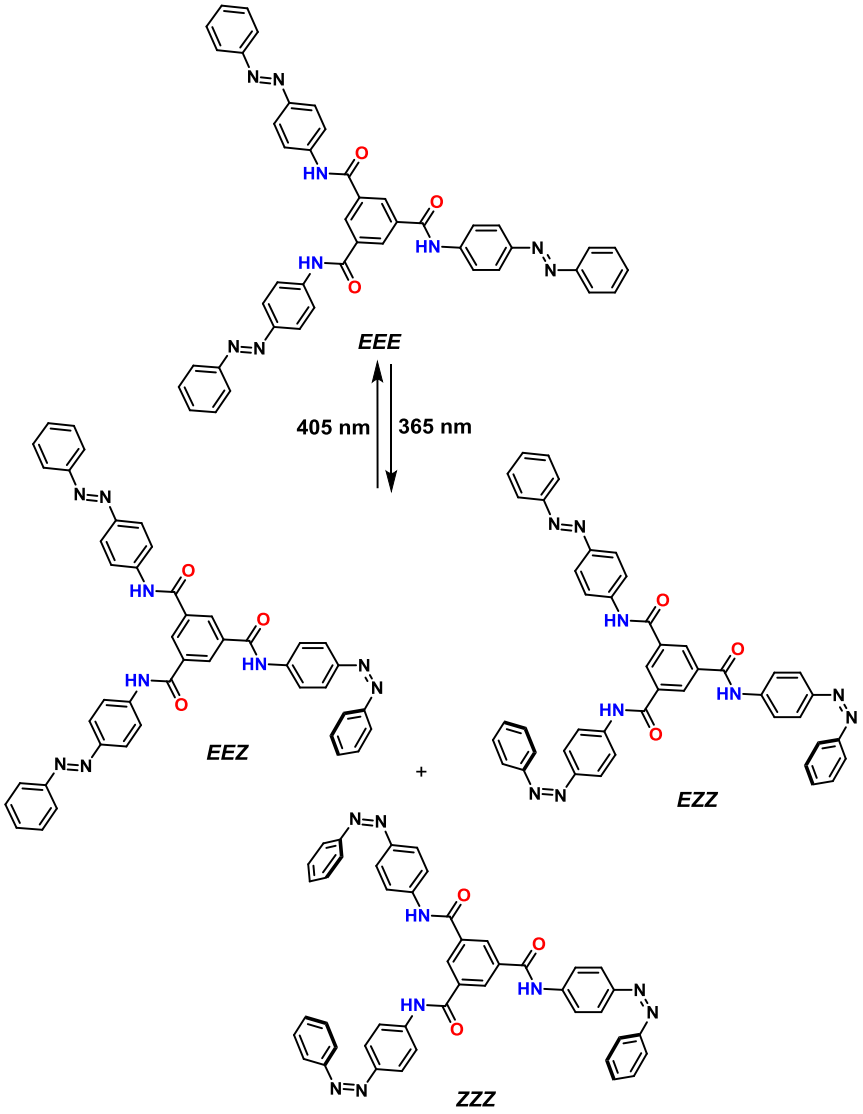

Figure 1.4 Photoisomerization in C_3-symmetric systems with three azobenzenes.

In the tripodal multiphotochromic systems, four photoisomers are expected, i.e., *EEE* (all-*trans*), *EEZ* (*trans*-*trans*-*cis*), *EZZ* (*trans*-*cis*-*cis*), and *ZZZ* (all *cis*). In thermal equilibrium, *EEE* should be the major component, and after being subjected to irradiation with a suitable wavelength of light, the *cis* containing photoisomers (*EEZ*, *EZZ*, *ZZZ*) will increase. In between the two proton signals due to *EEE* and *ZZZ*-isomers, two sets of signals at an intensity ratio of 2:1 appear that can be rationalized as *EEZ* and *EZZ* isomers. Using the integral ratios of the non-overlapping protons, we can identify the PSS composition at both forward as well as reverse switching. For instance, Figure 1.5 depicting the spectra for identification of percentage composition of each individual four photoisomers.[30b]

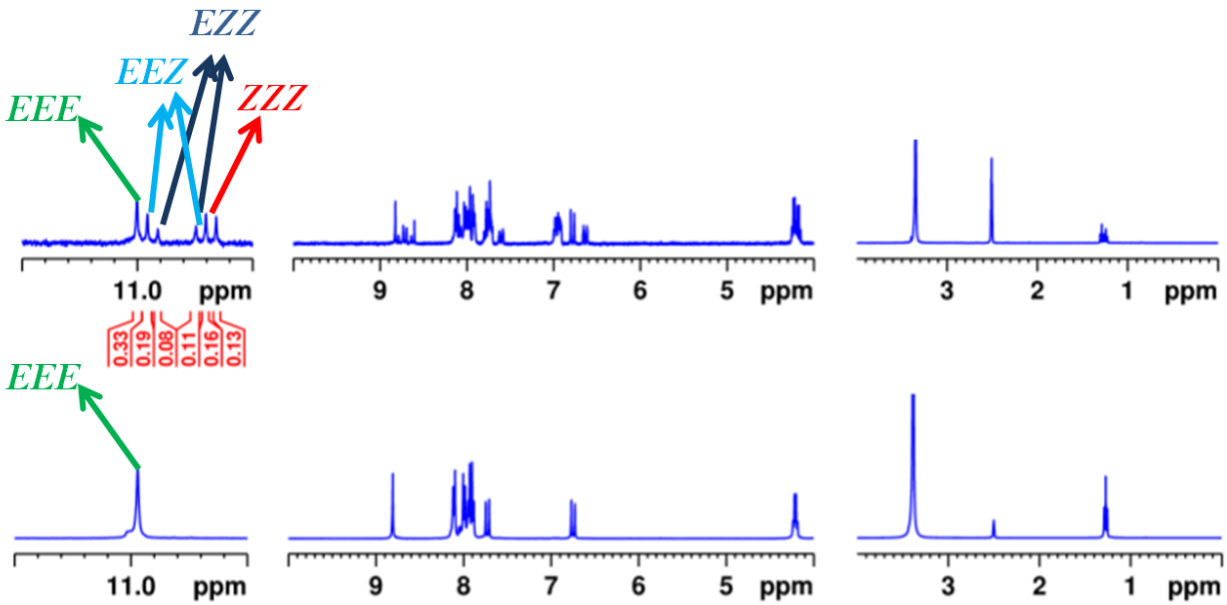

Figure 1.5 Representative ^{1}H-NMR spectra corresponding for before irradiation(bottom) and after irradiation with UV (top) of C_3-symmetric tripodal azobenzene molecular system. (All the photoisomers are identified based on the signal pattern and shifts, and the PSS composition has been quantified using the normalized integral values).

Apart from these commonly used methods for photoisomerization investigation, there are a few other techniques have also been exploited.

1.5.3 Fourier Transform Infrared Spectroscopy (FTIR)

FTIR spectroscopy has also been employed to observe the changes that occur when *E*- to *Z*- isomers are converted and *vice versa*. Shifts in IR signals and/or peak splitting in IR spectra resulted from the changes in geometry and symmetry, which can aid in understanding the photoisomerization process. Based on FTIR data, Heinke and co-workers have calculated the *Z* to *E* thermal reverse isomerization barrier in azobenzene, which was highly correlated with the theoretically calculated barrier.[31]

1.5.4 X-ray Emission Spectroscopy

The X-ray spectroscopy provides an understanding of the azobenzenes photo-isomers geometry because they are entirely different and spectral features are strongly geometry dominated. An elemental sensitive method, X-ray spectroscopy allows to study photo-isomerization around the reaction center via nitrogen K-edge emission. The tracking of isomerization using this spectroscopic technique involves the electronic effects without considering the vibrational effects. X-ray studies revealed that *E*-azobenzene has a planar structure with C_{2h} symmetry, whereas *Z*-azobenzene adopts a bent or nonplanar geometry having a C_2 symmetric structure.[28]

1.5.5 High-performance Liquid Chromatography (HPLC) and Ion-mobility Mass Spectrometry (IMMS)

To acquire a full understanding, UV-Vis spectroscopy has been combined with HPLC and ion-mobility mass spectrometry (IMMS) for extensive analyses of photophysical characteristics and photoisomerization quantum yields to bestow information onto photogenerated isomer mixtures. HPLC as well as IMMS, can be used to separate the four possible (*EEE*), (*EEZ*), (*EZZ*), and (*ZZZ*) isomers upon UV light irradiation. By examining the temporal evolution of the isomer mixture, the composition of the photostationary states (PSS) and the *Z*-*E* thermal isomerization kinetics have been quantified using HPLC-MS.[33] Moreover, IMMS provided clear evidence for the huge difference in the shape of the previously mentioned isomers. Single isomer absorption spectra produced by HPLC are also found to be well corroborated with spectra generated at the TD-DFT level. The relative isomeric ratio can be measured after integrating the peaks obtained for the four isomers at the PSS. The IMMS data is only extracted for singly deprotonated ions, whereas HPLC-MS quantification is done for all charge states and potential adducts.

1.6 Photoisomerization Mechanism

Since the isolation of *cis*-azobenzene, the mechanism of azobenzene isomerization has been the subject of research and debate. The isomerization mechanism and quantum yield are affected by the isomeric form (*cis* vs. *trans*), irradiation wavelength, substituents on phenyl rings, excitation technique (thermal vs. radiation), solvent properties, temperature, and pressure.[27]

As previously discussed, the *E* to *Z* forward isomerization of azobenzene can be achieved by irradiation of appropriate wavelength of light, whereas *Z* to *E* reverse isomerization can occur either thermally or photochemically. S_0 is the singlet ground state of *E*-azobenzene, while S_1 and S_2 are the first and second singlet excited states, respectively. Azobenzenes undergo *E*–*Z* photoisomerization via both $S_0 \rightarrow S_1$ ($n-\pi^*$) and $S_0 \rightarrow S_2$ ($\pi-\pi^*$) excited states, respectively, albeit the photochemical *Z* to *E* reverse isomerization in azobenzene, can be achieved by exciting into either S_1 or S_2 state. The wavelength-dependent photochemistry of azobenzenes (the quantum yield achieved by S_2 excitation is lower than that obtained by S_1 excitation, thus violating Kasha's rule) is now widely regarded as the outcome of distinct isomerization pathways following $n-\pi^*$ or $\pi-\pi^*$ excitation. Several explanations have been given for the wavelength dependence of quantum yield of photoisomerization and the violation of Kasha's rule (S_2 decay to ground state bypassing the

Franck Condon region of S_1 state). In earlier studies, isomerization on S_1 and S_2 states was assigned to inversion and torsion respectively.[34b] Later on, isomerization was proposed to occur for both states through inversion.[34c] Recently, to study the ultrafast photodynamics of azobenzene, sub20 femtosecond resolution transient absorption spectroscopy and computations have been utilized. Not only the π-π* life time has been estimated to be 50 fs, but it was also correlated with the buildup of n-π*, which was responsible for the observed Kasha's rule violation in UV excitation through CNN bending. The in plane CNNC bending in ππ* state leading to nπ*/ground state conical intersection which is otherwise not accessible when nπ* state is excited under UV. Through this, the reasons for the lowering of quantum yields at shorter wavelengths, and the ps time scale intramolecular vibrational redistribution from bending into the torsion in attaining *E*-isomer has been confirmed.[34d]

Typically, azobenzene absorbs radiation of the same wavelength or frequency, leading to the establishment of an equilibrium state between the *E* and *Z*-isomer, known as the photostationary state (PSS). Also, the quantum yield depends on solvent polarity, viscosity, and temperature **(Figure 1.2)**.[23b]

The absorption of photons, which dictates electronic transitions, drives the isomerization process. As a result, the transition from the flat *trans* form to the folded *cis* form involves changes in electrical and optical characteristics. Isomerization can be described in two ways: rotation and inversion, as well as a combination of the two mechanisms and transient states. The subject has been studied over time, models have been proposed, and new data from experiments and computations have been added on a regular basis **(Figure 1.6)**.[35-40] The Figure 1.6 schematizes the model that describes isomerization mechanism. The N=N double bond must be broken for the two N atoms to spin relative to each other during rotation along the azo moiety axis. This pathway ends with a change in the C–N–N–C dihedral angle while keeping the N–N–C angle at ~120 degrees. One "arm" of the azobenzene travels relative to the other in the inversion path: one N=N–C angle widens to 180°, while the C–N=N–C dihedral remains at 0°. As stated at the outset, two more complex pathways are possible, namely, the concerted rotation, which begins when both N=N–C angles broaden to 180 degrees, when the molecule turns linear and continues by bringing the two arms together, culminating in the final *cis* conformation. The other mix course entails an inversion assisted rotation, which is defined by a simultaneous change in the C–N=N–C dihedral angle and a lesser change in the N=N–C angles. It's worth noting that the azobenzenes transient states when they transition from *trans* to *cis* (or vice versa) are all polar, with the exception of the

linear conformation that occurs during the concerted inversion. As a result, the isomerization phenomena produce a change in the dipole moment in addition to the geometrical change.[27]

The mechanisms postulated for thermal *cis* → *trans* isomerization are rotation and inversion. The phenomenon's activation barrier is lower in solution than in melt, and the *cis* isomer's half-life in solution at room temperature is 2 days.[27]

1.7 Thermal Stability of *Z*-isomer

Azobenzenes with metastable *Z* isomers and extended half-lives have been used in the fabrication of information data storage devices and as photobiological probes. However, azobenzenes that undergo rapid thermal relaxation are preferred for applications such as optical data transmission and processing, as well as artificial muscles. Thermal isomerization is a first-order reaction that occurs by a unimolecular process. Various factors such as the polarity of the solvent, temperature, type and position of substituents, acids, hydrogen bonding, etc., influence the rate of the thermal reverse isomerization.

Solvent effect:[41-43] As per literature reports, when the polarity of the solvent increases, the rate of thermal isomerization (*Z*- to *E*-isomer) increases while the activation energy decreases. The isomerization mechanism of azobenzene is also influenced by solvent viscosity and polarity. The inversion mechanism is preferred by viscous non-polar solvents, whereas the rotation mechanism is preferred by non-viscous polar liquids.

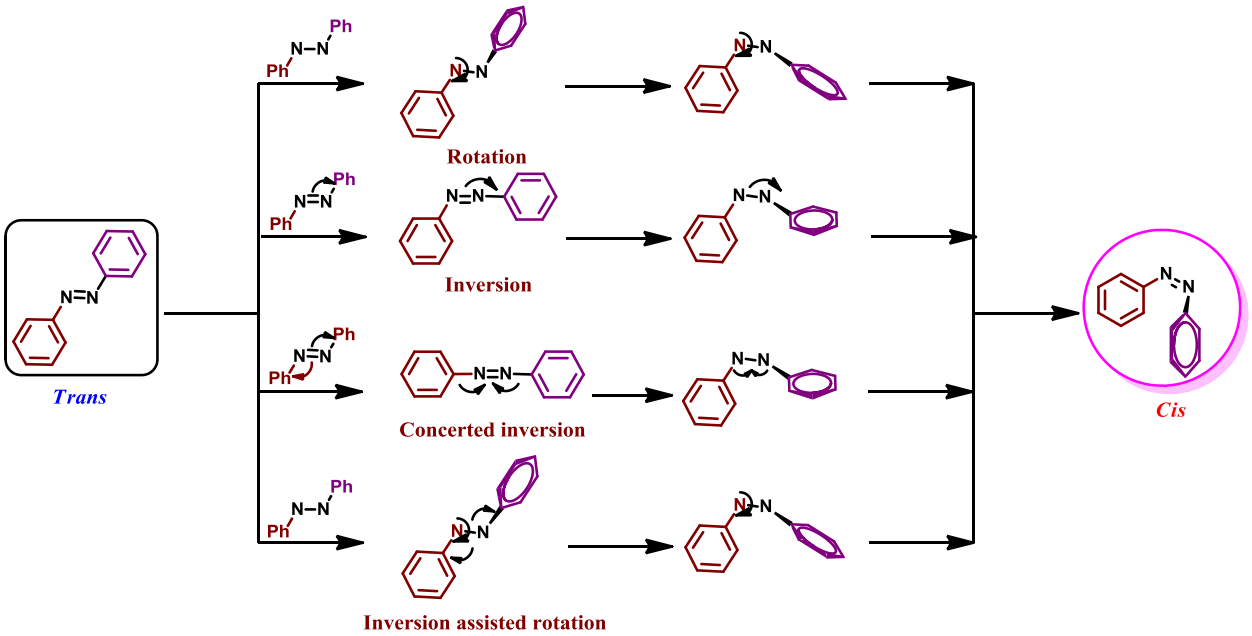

Figure 1.6 Proposed Mechanisms for *Trans*-*Cis* Isomerization.

Catalytic effects of acids:[44] The thermal isomerization of *Z*-azobenzene is accelerated by acids. The H^+ was absorbed by the N=N bond and formed its conjugate acid, lowering the *Z*

to *E* isomerization activation barrier.

Temperature:[29b] Since the rate of isomerization increases with increasing temperature, the *Z*–*E* thermal isomerization increases dramatically with increasing temperature.

Substituents effects:[23,27] The substituents on azobenzene's aryl rings have a significant impact on the absorption, emission, and photochemical properties of the compound. Based on their electronic states π–π*and n–π* absorption bands, Bandara et al have classified azobenzenes into three classes:

(a) **Azobenzene type:** These compounds have a well-defined π–π* and n–π* bands, with the π–π* band being quite intense and the n–π* band is weak.

(b) **Aminoazobenzene type:** In the UV-vis spectrum, these compounds have overlapping π–π* and n–π* bands. Electron donor substituents in the *ortho* or *para* positions of the azo bond are present in these compounds.

(c) **Pseudostilbene type:** These molecules have nearly degenerate π–π* and n–π* bands, with the π–π* absorption band experiences a bathochromic shift in comparison to the n–π* band. At the 4 and 4' positions of the phenyl rings, these compounds have electron-donating and electron-withdrawing groups. These compounds, in general, undergo rapid reverse switching.

Azobenzene-type derivatives have higher thermal stability than aminoazobenzenes and pseudo-stilbenes, with relaxation durations ranging from hours to days at ambient temperature. Inversion is the most common mechanism of their thermal relaxation. At normal temperature, aminoazobenzenes have a half-life ($t_{1/2}$) of seconds to minutes, but pseudo-stilbenes have a $t_{1/2}$ of microseconds to milliseconds, and their thermal relaxation occurs via rotation.

The photoswitching features are influenced by the action of aryl substituents at *ortho, meta*, and *para* positions relative to the azo group. When electron-rich substituents are inserted in all four locations of *ortho* to the N=N group, the π–π* band undergoes a modest bathochromic and hypochromic shift, whereas the n–π* band undergoes bathochromic and hyperchromic shifts. A redshift in the n–π* band and a blue shift in the first π–π* band are expected if steric bulkiness of *ortho* substituents are increased. The repulsive interaction between the *ortho* substituents and the lone pair on the more distant nitrogen to the azo group causes the redshift. These *ortho* substituents lower the n-π* excitation energy while raising the energy of the nonbonding orbital on nitrogen. The blue shift is caused by a decrease in azobenzene molecule conjugation. The result is due to phenyl ring twisting, an effect caused by bulky groups in the *ortho* position, which lowers the energy of the uppermost filled orbital

and/or raises the energy of the lowest empty π* orbital, thus increasing the proximal steric effects from *ortho*-substituents. Apart from these shifts, substituents also enhance the π–π* and n–π* separation at *ortho* locations. Bulky substituents at *ortho* locations, on the other hand, improve the rate of thermal isomerization from *Z* to *E* isomer. The isomerization of azobenzene can be successfully induced by visible light when all four *ortho* positions are replaced with bulky electron-rich substituents.[23b] In general, in comparison with *ortho* and *para* substitution, *meta* substituted azobenzenes exhibit high *Z*-thermal stability. Therefore, the observed trend for the thermal reverse isomerization is *meta*>*ortho*>*para*.[30b] The redshift of the π–π* transition band is caused by the LUMO (π*) energy level dropping when an amino or hydroxyl group is present in the *ortho* or *para* position. As a result, the *cis* isomers half-life is shorter than that of the unsubstituted azobenzene. Azobenzenes with alkyl or amide moieties, on the other hand, have long *cis* to *trans* conversion time.[45]

Hydrogen-bonding effects:[29a, 23a] Both the *E*-*Z* and *Z*-*E* isomerization steps are influenced by hydrogen bonding. In general, there are two types of hydrogen bonding effects, i.e., intramolecular and intermolecular. Intramolecular and intermolecular hydrogen bonding can lead to tautomeric equilibria resulting in fast photoswitching. However, certain functional groups, which are capable of forming hydrogen bonding are present, they can fold and lock the *Z*-isomer, which in turn, resulting in a stable *Z*-isomer.

1.8 Multi-state Photoresponsive Molecular Systems[46, 47]

In recent decades, synthesis, spectroscopic characterization, kinetics studies, and modeling of a wide range of multiphotochromic systems have been made in a field that is quickly establishing itself as a separate branch of photochemistry. Integration of more than one photochromic unit gives rise to multi-photochromic molecular systems, and the property they exhibit is multi-state photochromism. The chemistry of such systems was investigated from a variety of angles, including a primary understanding of multiple photoswitches, supramolecular chemistry, and many more possible applications. Few major breakthrough advances in this discipline are their diverse range of applications, such as light modulation of catalysis via cooperative switching, sensors based on supramolecular host-guest interactions, materials such as organic gels or hydrogels, liquid crystals, gratings, actuators, and data storage using multistate or orthogonal photoswitches and many more. Indeed, although a photochromic compound is predicted to offer two states, which can be considered as "on/off" states or binary "0/1" information, multiphotochromic compounds have the potential to produce up to 2^n different states (with n the number of photochromes). Combining many photochromic units in a single compound has the potential to escalate the quantity of data it

can retain while also allowing access to more complex phenomena.Light modulation of multiphotochromic compounds has proven to be a difficult task thus far.

However, the fusion of multi-photochromic units in a single modular system has its own advantages and disadvantages. In general, the photoisomerization efficiency as well as the thermal stability of the photoswitched states are susceptible to subtle molecular alterations and govern their application prospects. Electronic coupling between azo chromophores, competition between cooperative and multistate photoswitching, the possibilities and influence of aggregation due to molecular motifs, and isomerization independency to achieve orthogonal photoswitching are all crucial factors in the efficiency of such systems. The general design, the choice of azobenzene units, connectors, linkers or spacers between them, core units, functionalization prospects, and other considerations all influence these characteristics. As a result, when designing multiple azobenzene-containing systems, a lot of attention must be paid to the architectural features. So far, an extensive range of molecular systems with various applications has been reported. Such research can help researchers to learn more about the overall impact of structural factors on photophysical and photochemical capabilities, thermal stability of photoswitched states, self-assembly, and future applications. The thesis research focuses on both mono- as well as three photoresponsive azobenzene units containing C_3-symmetric tripodal molecular systems and their applications in supramolecular chemistry and anion binding photoswitchable catalysis. In this regard, a brief introduction to the above-mentioned applications is discussed in the forthcoming sections.

1.8.1 C_3-Symmetric Tripodal Systems: Properties and their Applications

The use of several azobenzene units on a rigid molecular scaffold allows for the amplification of structural changes caused by azobenzene switching.[48] However, the scaffold structure and the location where the switchable units are introduced must be considered for photoisomerization efficiency.

The substitution at *para* position on a benzene ring increases the electronic conjugation and thus decreases the photoreactivity of azobenzene whereas the substitution in the *meta* position reduces the electronic coupling between the switchable arms and improves the photoswitching efficiency. Electronic decoupling within the structure is fundamental to preserve the photochromism of the system.[49] Therefore, in this regard, C_3-symmetric tripodal systems with substitution at 1,3,5-positions or star-shaped designs become a potential candidate and are enormously popular. Typically, these systems comprise three azo units, coupled to the core units either directly or via a spacer **(Scheme 1.2)**.

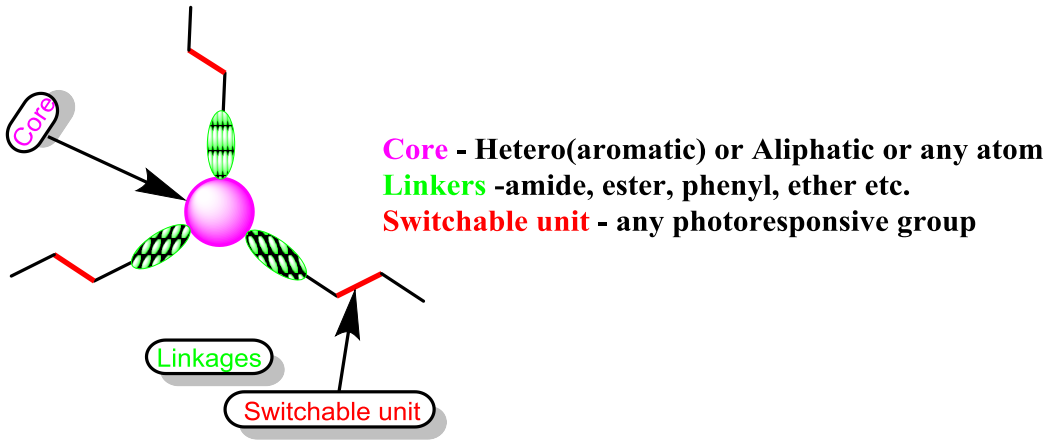

Scheme 1.2 Schematic representation of the target designs with multiple azobenzene-connected systems.

1.8.2 Supramolecular Properties

In recent times, C_3-symmetric tripodal systems have received a great deal of attention due to their utility in prominent applications such as supramolecular chemistry, photoswitchable catalysis, photoswitchable polymer, liquid crystals, rewritable actuators, rewritable imaging and erasing, etc. The design, synthesis, characterization, properties, and applications of a series of star-shaped azobenzenes featuring three photoswitchable "molecular arms" mounted on a stiff benzene core is the subject of two chapters in this thesis. Among all reported C_3-symmetric molecular systems, the azobenzene based 1,3,5-benzene tricaboxamide (BTA) core is one of the most common and versatile C_3-symmetric tripodal systems, which has been exploited for a diverse range of applications, for instance, exhibited excellent supramolecular properties, used as surface relief grating, for fabrication of remote controllable actuators, as anion-binder, etc.[50] Apart from the central phenyl ring in reinforcing π-π stacking, the preference for BTA core is owing to its intrinsic inclination to form H-bonds through the cooperative proton donating and receiving capacities of the three carboxamide groups. Hence, BTA derivatives functionalized with azoarenes can not only impart photoswitching properties but also aid in self-assembly formation. The latter is mainly caused by intermolecular non-covalent interactions between molecules driven by π-π stacking of planar, flat, and rigid azochromophores. The supramolecular self-assemblies that occur from such tripodal azo-based BTA derivatives can lead to intriguing molecular-based materials like liquid crystals, organogels, hydrogels, and strong self-assembly. One of the main goals of such designs is to use light to reversibly control supramolecular self-assembly, resulting in photoresponsive functional materials.[30b,50a] A novel class of self-assembled

stimuli-responsive soft materials, i.e., gels have received considerable attention in recent years due to their robust application in many areas, from food industries to electronics. Other than BTA-based tripods, incorporating *tris*-azobenzene on benzene core with ester linkage is also reported and found applications in the fabrication of stable holographic gratings.[51] Also, the direct connections of the azo moiety to the core exhibited aggregation-induced emission behavior and have drawn much attention due to their applications in information storage, sensors, optoelectronic devices, and actuators.[52] In conclusion, the properties demonstrated by the model compounds varied depending on the design changes (e.g., by modifying linkers, spacers, etc.).[30b]

1.9 Anion Binding Catalysis

In nature, hydrogen bonds are essential interactions which build cooperative non-covalent networks that facilitate very efficient chemical transformations. These non-covalent interactions are responsible for enzyme catalysis's strong substrate selectivity, activation, and stereocontrol. Anions are ubiquitous in biological systems, and molecular recognition,[53] which relies on specialized binding sites, is thus vital in life processes. Indeed, the majority of cofactors and enzyme substrates (>70%) are anionic species, making anions identification and binding essential.[54] Therefore, and inspired by nature, the creation of man-made tiny organic compounds as anion sensors and catalysts has received much attention. These synthetic anion receptors are frequently based on neutral[55] bi- or multi-H-bond donor compounds, such as (thio)ureas,[56] squarimides,[57] (macrocyclic)amides,[58] calixarenes,[59] and triazoles,[60] which can host important classes of anions such as phosphates, sulfates, carboxylates, cyanide, or halide anions via H-bonding. Depending on the nature and geometry of the H-bond donor and the anion, they can bind in a mono-, bi-, or multidentate way. In general, anion-binding catalysis consists of the concept of ion pairs, which was described by Anslyn and Dougherty: “An ion pair is defined to exist when a cation and anion are close enough in space that the energy associated with their electrostatic attraction is larger than the thermal energy (RT) available to separate them. This means that the ions stay associated longer than the time required for Brownian motion to separate non-interacting species.”[61] Anion acceptor organocatalysis did not emerge as a result of a well-crafted novel catalysis strategy. Indeed, Jacobsen and co-workers aim to understand the mechanism and functional requirements of hydrogen bonding catalysts in acyliminium species processes hinted that thiourea species could behave as anion acceptor catalysts.[62] These early efforts resulted in a novel paradigm that permitted new organocatalyzed reactions. In this context, E. N. Jacobsen and co-workers reported the effective enantioselective synthesis of α-amino

esters from α-chloroglycine ester and active methylene compounds via anion binding catalysis. This reaction proceeds through the formation of iminium ion by chloride ion abstraction of *α*-chloroglycine ester from bifunctional chiral thiourea catalyst followed by addition of 1,3-diketones or *β*-ketoesters to the *in situ* generated imine. Generally, these types of protocols require multi-pot operations and an excess amount of base, but these problems were overcome by using a bifunctional thiourea catalyst, which is capable of generating imine and inducing enantioselective addition of the enolate in a single pot.[63] Furthermore, a novel pyrrole-based catalyst has been developed by Maeda and co-workers for examining the catalytic ability of dipyrrolyldiketone boron complexes as hydrogen-bonding catalysts. They initially looked at the catalytic properties of *N*-acyl heteroarenium chlorides formed *in situ* from heteroarenes and 2,2,2-trichloroethyl chloroformate (TrocCl) in the Mannich-type reaction with ketene silyl acetals. Through the dissociation of Cl^{-}, dipyrrolyldiketone boron complexes bind Cl^{-} to activate the *N*-acyl heteroarenium cations, which serve as ionic electrophiles.

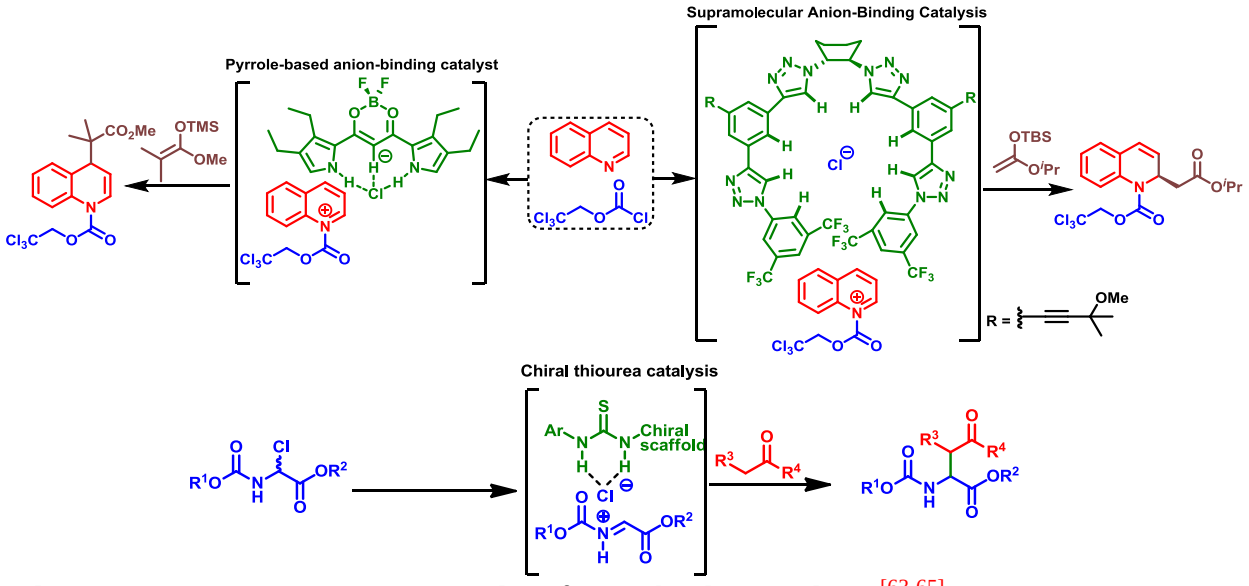

Scheme 1.3 Few representative examples of anion binding catalysis.[63-65]

The ketene silyl acetals then attack ionic electrophiles, resulting in dearomatization products. Using several types of dipyrrolyldiketone boron complexes in THF as the solvent at –78 °C, the Mannich-type synthesis of *N*-acyl quinolinium chloride, generated from quinoline and 1-methoxy-2-methyl-1-trimethylsiloxy-1-propene, was explored.[64] Afterwards, Mancheño and co-workers have presented insight into the cooperative nature, anion binding strength, and folding mechanism of a model chiral triazole catalyst for the above-mentioned reaction. They have combined experimental as well as computational studies and proved that multi-interaction catalysts exhibit low binding energies and can

effectively recognize ionic substrates by inducing chirality with strong temperature and solvent dependency. The chiral TetrakisTriazole catalyst is one of the known catalysts that showed lowest catalyst loading in this field (down to 0.05 mol %) **(Scheme 1.3)**.[65] Herein, only a few prominent model compounds are shown, whereas many more other examples are known besides all these.[66]

1.10 Photoswitchable Catalysis

Control of catalytic systems by using light as external stimuli is a highly challenging and still developing field of modern organic chemistry. Many advantages come from the use of light as a clean, non-invasive stimulus in the search for responsive catalytic systems, where a judicious choice of irradiation wavelength may allow precise control over catalyst function, activity, and selectivity. Over the last decade, a variety of photoresponsive catalysts have been developed based on the well-known switching characteristics of azobenzenes, diarylethenes, and overcrowded alkenes.[67] Different ways to exploit cooperative,[68] steric,[69] and electronic effects[70] of photo-accessible isomers have yielded promising findings in photochemical control of catalyst's activity or selectivity.

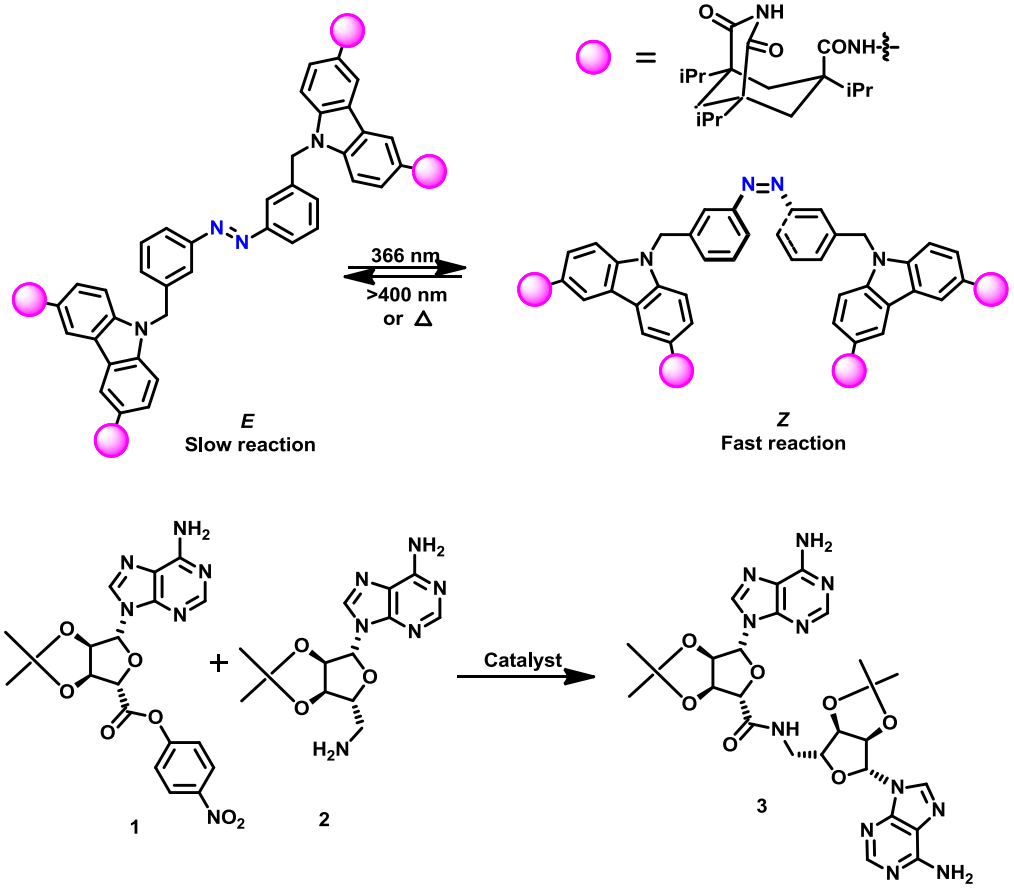

Scheme 1.4 Photocontrol over amide bond formation.[71]

The photoisomerization of azobenzenes causes a substantial geometrical change in the

molecule, which can be used to modulate the activity of catalytically active species. In 1995, Würthner and Rebek presented the first photoswitchable template for cooperative bifunctional catalysis, using two carbazole-based adenine receptors coupled by an azobenzene scaffold to modulate the rate of amide bond formation to give **3 (Scheme 1.4)**.[71] The *E*-form separates the adenine-containing substrates **1** and **2** after the recognition, resulting in a slow amide bond formation reaction rate. Whereas, Z-form, on the other hand, drives the two responding partners closer together, facilitating the coupling process, as evidenced by a substantial increase in the reaction rate following UV light irradiation. The usage of the 50:50 mixture of *E* and *Z* that resulted from irradiation with 366 nm light increased the coupling rate about nine-fold. Despite this, product **3** remains linked to the catalyst after the amide bond is formed, preventing its turnover and hence its function as a photoswitchable catalyst.[71] The first effective use of a photoswitchable cooperative effect in catalysis was successfully reported by Cacciapaglia *et al*. in 2003.[72] An azobis(benzo-18-crown-6) ether was utilized to catalyze a basic ethanolysis of tertiary anilides using a bis-barium complex (**Scheme 1.5**). The catalytic activity of the azobenzene spacer might be regulated via reversible *trans*→*cis* isomerization. *Trans* state, which is more thermodynamically stable, has a modest catalytic activity. In contrast, the geometry of the bis-barium complex is changed to a more favourable concave conformation in which the two barium centres are near to each other when the azobenzene moiety is switched to the *cis*-form and becomes a more active catalyst. One barium centre in the catalytically active complex binds a carboxylate anchoring group on the anilide substrate, while the second barium centre binds a nucleophilic ethoxide ion.[72]

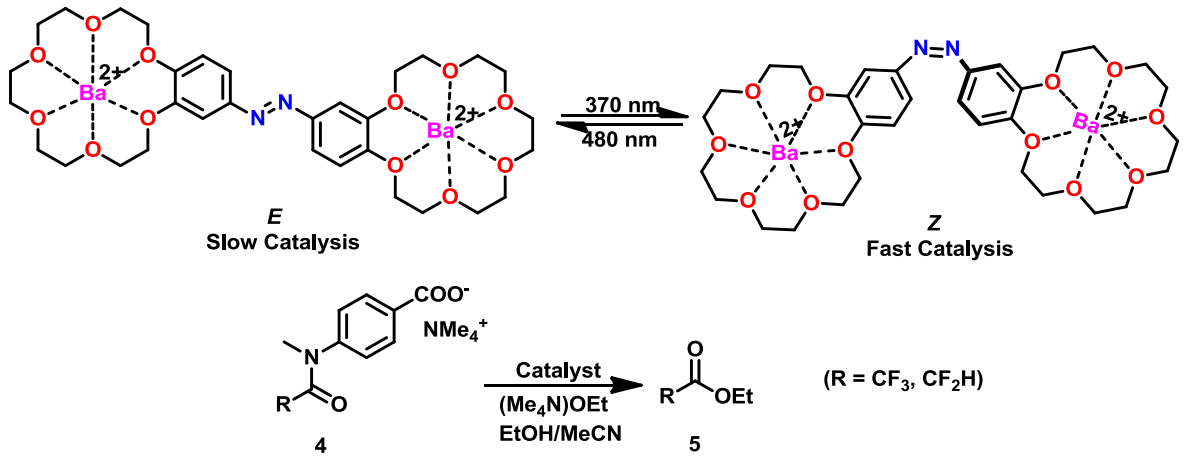

Scheme 1.5 Photoswitchable catalyst for the ethanolysis.[72]

In a similar fashion, cooperative effects have been employed to photoreversibly modulate the Morita Baylis-Hillman reaction of 3-phenylpropanal and 2-cyclopenten-1-one.

Imahori and co-workers functionalized a bifunctional cooperative acid catalyst with an azobenzene moiety to activate or deactivate the cooperative effect, resulting in reversible reaction rate control.[73]

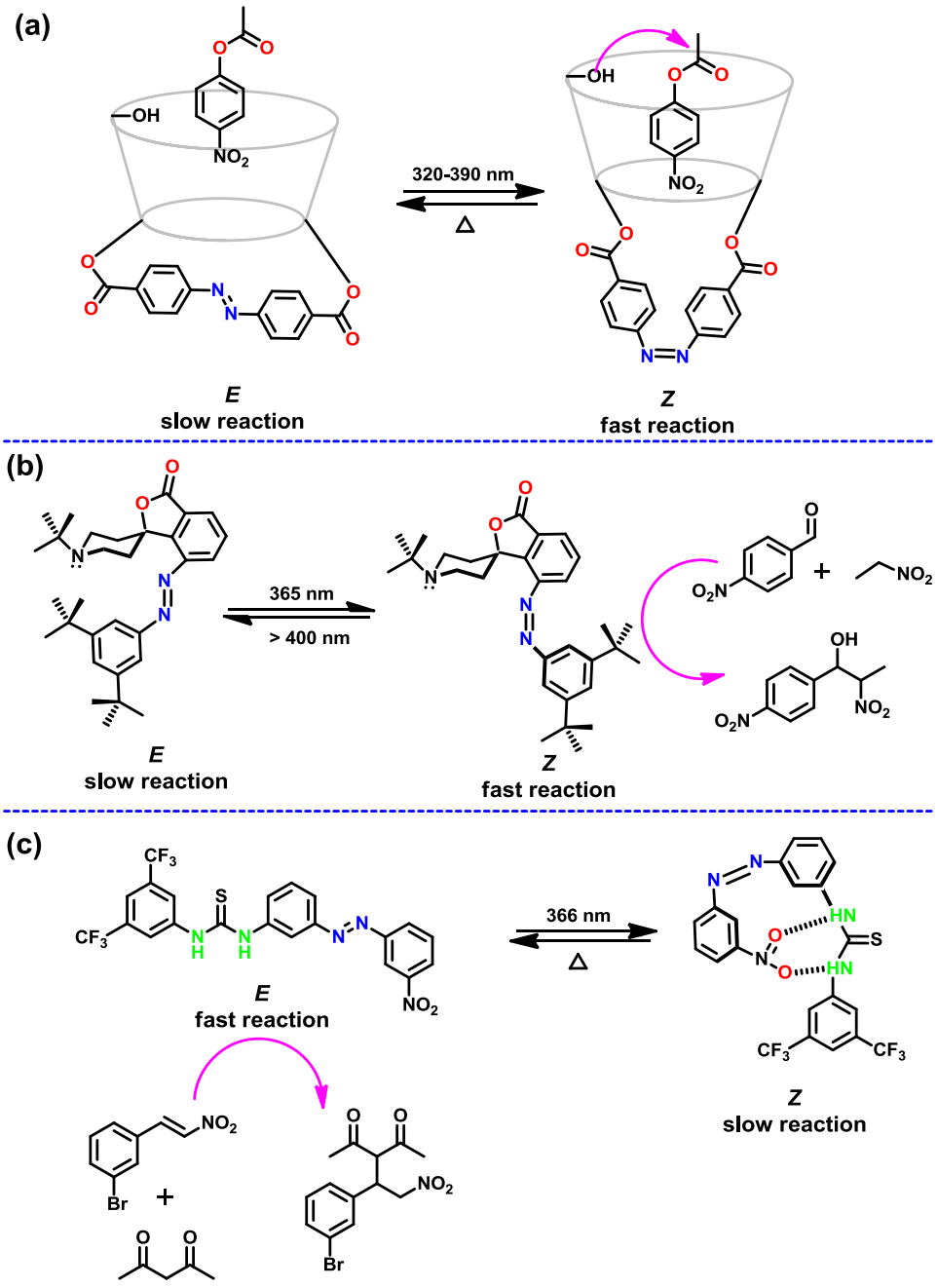

Scheme 1.6 Few representative examples of photoswitchable catalysts- (a) Photocontrol over ester hydrolysis; (b) Photoswitchable base; (c) Thiourea based photoswitchable catalysts.

Altering the steric bulk around a catalyst's reaction site is an alternative technique for controlling its activity and selectivity. In 1981, a pioneering example was reported for the photoswitchable hydrolysis of *p*-nitrophenylbenzoate catalyzed by *β*-cyclodextrin with a 4,4′-*bis*-(carboxy)azobenzene coupled as a capping unit.[74]

Upon irradiation changes the geometry of the azobenzene molecule, which changes the depth of the hydrophobic pocket of the *β*-cyclodextrin, where the substrate must bind before hydrolysis. The formation of the *Z*-isomer upon irradiation with 365 nm light resulted in up to a 5-fold increase in the hydrolysis reaction rate when 38 percent of the Z isomer was present, whereas the *E*-isomer effectively blocks the ester substrate from binding in the cavity, preventing its hydrolysis **(Scheme 1.6a)**.[74] Another approach introduced by Hecht and co-workers, where the combination of a bulky azobenzene fragment with a conformationally constrained *N*-alkylated piperidine that allowed light-gated modulation of the Brønsted basicity.

Herein, *trans*→*cis* -isomerization of a rigidly linked azobenzene "wiper" can reversibly protect the lone pair of the *N*-alkylated piperidine base. Titration tests revealed that the piperidine base has less basicity in the *trans*-form resting state. The piperidine electron lone-pair is exposed when the azobenzene molecule is switched into the *cis*-conformation, resulting in an increase in basicity. The photocontrol of a base-catalyzed nitroaldol (Henry) reaction was achieved by using varying basicities.[69] **(Scheme 1.6b)**

The catalyst was immobilized on silica gel particles, allowing the system to be employed as a heterogeneous switchable catalyst.[69] In 2014, Pericás and co-workers introduced photoswitchable thiourea-based organocatalyst to control Michael addition reactions via hydrogen bond shielding of the catalytic moiety. The catalyst consists of a blocking unit (a nitro group) and a hydrogen bond donor (the thiourea moiety) present on either side of the azobenzene core. The Michael addition of acetylacetone to *m*-bromonitrostyrene is effectively catalyzed by the thermodynamically stable *E*-isomer, whereas UV irradiation causes the nitro group to attach to the thiourea, resulting in substantially slower catalysis **(Scheme 1.6c)**.[69g]

1.11 Objectives and Scope of the Thesis

Azobenzenes are well-known as one of the robust photoswitches exhibiting a diverse range of applications and properties. Although, a lot of studies have been carried out on the azobenzenes containing molecular systems and a variety of applications are also explored for the systems, however, there are still open challenges remaining in this field. For several applications, the photoswitching ability of the azobenzenes and their *cis*-isomer stability are two of the important controlling factors. The questions, such as what are the factors influencing them, and how to tune them are quintessential, and understanding them are open challenges in the field. As azobenzenes can be easily functionalized and the introduction of

proper functional groups can lead to supramolecular architecture, additional challenges like the influence of supramolecular aggregation on the photoswitching ability and *cis*-isomeric stability are equally important to address. In this regard, we planned to have a systematic approach with the following three objectives that constitute this thesis:

1) How various functionalization in azobenzene molecule can impact the photoswitching ability and *cis*-isomeric stability, and derive a structure-property relationship?

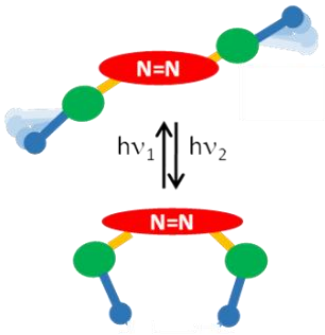

2) Impact of extended π-conjugation in tripodal C_3-symmetric azobenzene derivatives on supramolecular properties and their photophysical properties

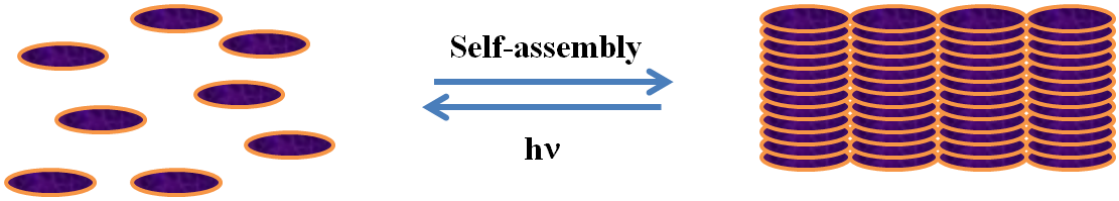

3) Whether *tripodal* C_3-symmetric azo(hetero)arene-based systems can be utilized for certain non-covalent interactions and cooperative binding? Also, whether such systems can be modulated in binding through photoisomerization of the azo(hetero)arene units, if so, can we utilize them in catalysis, particularly in controlling the rate of the reaction.

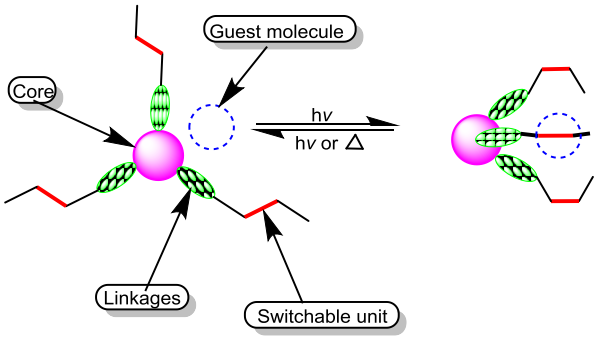

All these questions were set as the main research objectives, and we started working on them to address the above-mentioned goals.

1.12 References

[1] a) A. Bratek-Skicki, *Applied Surface Science Advances* **2021**, *4*, 100068; b) D. Roy, J. N. Cambre, B. S. Sumerlin, *Progress in Polymer Science* **2010**, *35*, 278–301.

[2] X. Sun, S. Agate, K. S. Salem, L. Lucia, L. Pal, *ACS Appl. Bio Mater.* **2021**, *4*, 140−162.

[3] a) E. Cabane, X. Zhang, K. Langowska, C. G. Palivan, W. Meier, *Biointerphases* **2012**, *7*, 9; b) F. D. Jochum, P. Theato, *Chem. Soc. Rev.* **2013**, ***42***, 7468-7483.

[4] a) S. Guragain, B. P. Bastakoti,V. Malgras, K. Nakashima, Y. Yamauchi, *Chem. Eur. J.* **2015**, *21*, 13164–13174; b) J. Zhuang, M. R. Gordon, J. Ventura, L. Li, S. Thayumanavan, ***Chem. Soc. Rev.*** **2013**, *42*, 7421-7435.

[5] a) M. Mrinalini, S. Prasanthkumar, *ChemPlusChem* **2019**, *84*, 1103-1121; b) A. Bajpai, S. K. Shukla, S. Bhanu, S. Kankane, *Prog. Polym. Sci.* **2008**, *33*, 1088–1118; c) M. Ma, L. Guo, D. G. Anderson, R. Langer, *Science* **2013**, *339*, 186–189; d) Q. Zhao, J. W. Dunlop, X. Qiu, F. Huang, Z. Zhang, J. Heyda, J. Dzubiella, M. Antonietti, J. Yuan, *Nat. Commun.* **2014**, *5*, 4293; e) Z. Hu, X. Zhang, Y. Li, *Science* **1995**, *269*, 525; f) D. Parasuraman, M. J. Serpe, *ACS Appl. Mater. Interfaces* **2011**, *3*, 2732–2737; g) J. Hu, S. Liu, *Macromolecules* **2010**, *43*, 8315–8330; h) H. Koerner, G. Price, N. A. Pearce, M. Alexander, R. A. Vaia, *Nat. Mater.* **2004**, *3*, 115–120; i) F. Wang, Y.-H. Lai, M.-Y. Han, *Macromolecules* **2004**, *37*, 3222–3230; j) F. Seker, P. R. Malenfant, M. Larsen, A. Alizadeh, K. Conway, A. M. Kulkarni, G. Goddard, R. Garaas, *Adv. Mater.* **2005**, *17*, 1941–1945.

[6] a) Y. Ru, Z. Shi, J. Zhang, J. Wang, B. Chen, R. Huang, G. Liu, T. Yu, *Mater. Chem. Front.* **2021**, *5*, 7737–7758; b) J. Cui, A. D. Campo, *Photoresponsive polymers: properties, synthesis and applications*. In Smart Polymers and Their Applications, *Elsevier*, **2014**, pp. 93–13; c) H. Tian, S. Yang, *Chem. Soc. Rev.* **2004**, *33*, 85–97; d) Szacilowski, K. *Chem. Rev.* **2008**, *108*, 3481-3548.

[7] a) J. Zhang, Q. Zou, H. Tian, *Adv. Mater.* **2013**, *25*, 378–399; b) A. Goulet-Hanssens, F. Eisenreich, S. Hecht, *Adv. Mater.* **2020**, *32*, 1905966; c) Y. Wakayama, R. Hayakawa, K. Higashiguchi, K. Matsuda, *J. Mater. Chem. C* **2020**, *8*, 10956-10974; d) I. M. Welleman, M. W. H. Hoorens, B. L. Feringa, H. H. Boersma, W. Szymański, *Chem. Sci.* **2020**, *11*, 11672–11691; e) X. Huang, T. Li, *J. Mater. Chem. C* **2020**, *8*, 821-848; f) H.-B. Cheng, S. Zhang, J. Qi, X.-J. Liang, J. Yoon, *Adv. Mater.* **2021**, *33*, 2007290; g) Z. Yang, Z. Liu, L. Yuan, *Asian J. Org. Chem.* 2021, *10*, 74– 90.

[8] J. Garcia–Amoros, D. Velasco, *Beilstein J. Org. Chem.* **2012**, *8*, 1003–1017.

[9] a) H. Nie, J. L. Self, A. S. Kuenstler, R. C. Hayward, J. R. d. Alaniz, *Adv. Optical Mater.*

2019, *7*, 1900224; b) Z. L. Pianowski, *Chem. Eur. J.* **2019**, *25*, 5128 – 5144.

[10] Y. Zhao, *Azobenzene-Containing Block Copolymer Micelles: Toward Light-Controllable Nanocarriers.* In Smart Light Responsive Materials - Azobenzene-containing Polymers and Liquid Crystals, Y. Zhao, T. Ikeda, Eds. John Wiley & Sons: Hoboken, NJ, **2009**; 215-242.

[11] K. Hunger, P. Mischke, W. Rieper, *Azo Dyes*. In Ullmann's Encyclopedia of Industrial Chemistry, Verlag GmbH & Co.: Weinheim, **2011**.

[12] A. A. Beharry, O. Sadovski, G. A. Woolley, *J. Am. Chem. Soc.* **2011,** *133*, 19684-19687.

[13] V. Balzani, M. Venturi, A. Credi, in *Molecular Devices and Machines A Journey Into the Nanoworld*, Wiley-VCH, Weinheim, Germany, **2006**.

[14] Y. Huang, D. H. Kim, *Nanoscale* **2012,** *4*, 6312-6317.

[15] G. Wang, X. Tong, Y. Zhao, *Macromolecules* **2004,** *37*, 8911-8917.

[16] W. -X. Gu, Q. -L. Li, H. Lu, L. Fang, Q. Chen, Y. -W. Yang, H. Gao, *Chem. Commun.* **2015,** *51*, 4715-4718.

[17] A. A. Beharry, O. Sadovski, G. A. Woolley, *Org. Biomol. Chem.* **2008,** *6*, 4323-4332.

[18] M. Juribasic, M. Curic, K. Molcanov, D. Matkovic-Calogovic, D. Babic, *Dalton Trans.* **2010,** *39*, 8769-8778.

[19] S. Fu, Y. Zhao, *Macromolecules* **2015,** *48*, 5088-5098.

[20] A. D. Wong, T. M. Güngör, E. R. Gillies, *ACS Macro Lett.* **2014,** *3*, 1191-1195.

[21] a) V. Blanco, D. A. Leigh, V. Marcos, *Chem. Soc. Rev.* **2015**, *44*, 5341–5370; b) R. Dorel, B. L. Feringa, *Chem. Commun.* **2019**, *55*, 6477-6486.

[22] L. Dong, Y. Feng, L. Wang, W. Feng, ***Chem. Soc. Rev.*** **2018**, **47**, 7339-7368.

[23] a) S. Grewal, D. Gupta, A. K. Gaur, M. Saraswat, S. Venkataramani, *Azoheteroarene photoswitches – Synthesis, Photoswitching and Utility*. In Photoisomerization: Causes, Behavior and Effects; Sampedro, D., Ed.; Nova Publishers, USA, **2019**; pp 111-188; b) F. A. Jerca, V. V. Jerca, R. Hoogenboom, *Nat. Rev. Chem.* **2022**, *6,* 51–69.

[24] K. B. Jorgensen, *Molecules* **2010,** *15*, 4334-4358.

[25] H. Rau, *Angew. Chem. Int. Ed. Engl.* **1973,** *12*, 224-235.

[26] G. S. Hartley, *Nature* **1937**, *140*, 281-281.

[27] H. M. D. Bandara, Shawn C. Burdette, *Chem. Soc. Rev.* **2012**, *41*, 1809-1825.

[28] H. Ebadi, *J. Phys. Chem. A* **2014**, *118*, 36, 7832-7837.

[29] a) S. Devi, M. Saraswat, S. Grewal, S. Venkataramani, *J. Org. Chem.* 2018, *83*, 4307–4322; b) P. Kumar, A. Srivastava, C. Sah, S. Devi, S. Venkataramani, *Chem. Eur. J.* **2019**, *25*, 11924– 11932; c) I. K. Lednev, T.-Q. Ye, P. Matousek, M. Towrie, P. Foggi,

F. V. R. Neuwahl, S. Umapathy, R. E. Hester, J. N. Moore, *Chemical Physics Letters* **1998,** *290*, 68-74.

[30] a) J. Kind, L. Kaltschnee, M. Leyendecker, C. M. Thiele, *Chem*. *Commun*. **2016**, *52*, 12506–12509; b) D. Gupta, A. K. Gaur, P. Kumar, H. Kumar, A. Mahadevan, S. Devi, S. Roy, S. Venkataramani, *Chem*. *Eur*. *J*. **2021**, *27*, 3463-3472.

[31] a) X. Yu, Z. Wang, M. Buchholz, N. Füllgrabe, S. Grosjean, F. Bebensee, S. Bräse, C. Wöll, L. Heinke, *Phys. Chem. Chem. Phys.* **2015**, *17*, 22721-22725; b) L. Duarte, R. Fausto, I. Reva, *Phys. Chem. Chem. Phys.* **2014**, *16*, 16919-16930.

[32] a) C. M. Stuart, R. R. Frontiera, R. A. Mathies, *J. Phys. Chem. A* **2007**, *111*, 12072-12080; b) M. Quick, A. L. Dobryakov, M. Gerecke, C. Richter, F. Berndt, I. N. Ioffe, A. A. Granovsky, R. Mahrwald, N. P. Ernsting, S. A. Kovalenko, *J. Phys. Chem. B* **2014**, *118*, 8756-8771.

[33] a) L. H. Urner, B. N. S. Thota, O. Nachtigall, S. Warnke, G. v. Helden, R. Haag, K. Pagel, *Chem. Commun.* **2015**, *51*, 8801-8804; b) J. N. Bull, M. S. Scholz, N. J. A. Coughlan and E. J. Bieske, *Phys. Chem. Chem. Phys.* **2017**, *19*, 12776-12783; c) A. Galanti, J. Santoro, R. Mannancherry, Q. Duez, V. Diez-Cabanes, M. Valášek, J. D Winter, J. Cornil, P. Gerbaux, M. Mayor, P. Samorì, *J*. *Am*. *Chem*. *Soc*. **2019**, *141*, 9273–9283.

[34] a) L. Zhou, L. Chen, G. Ren, Z. Zhu, H. Zhao, H. Wang, W. Zhang, J. Han, *Phys. Chem. Chem. Phys.* **2018**, *20*, 27205-27213; b) A. Cembran, F. Bernardi, M. Garavelli, L. Gagliardi, G. Orlandi, *J. Am. Chem. Soc.* **2004**, *126*, 10, 3234–3243; c) T. Fujino, S. Yu. Arzhantsev, T. Tahara, *J. Phys. Chem. A* **2001**, *105*, 8123-8129; d) A. Nenov, R. Borrego-Varillas, A. Oriana, L. Ganzer, F. Segatta, I. Conti, J. Segarra-Marti, J. Omachi, M. Dapor, S. Taioli, C. Manzoni, S. Mukamel, G. Cerullo, M. Garavelli, *J. Phys. Chem. Lett.* **2018**, *9*, 1534−1541.

[35] P. Cattaneo, M. Persico, *Phys. Chem. Chem. Phys.* **1999**, *1*, 4739-4743.

[36] T. Kobayashi, T. Saito, S. Adachi, *Journal of Luminescence* **2003**, *102–103*, 722–726.

[37] T. Schultz, J. Quenneville, B. Levine, A. Toniolo, T. J. MartÍnez, S. Lochbrunner, M. Schmitt, J. P. Shaffer, M. Z. Zgierski, A. Stolow, *J. Am. Chem. Soc.* **2003**, *125*, 8098-8099.

[38] A. Cembran, F. Bernardi, M. Garavelli, L. Gagliardi, G. Orlandi, *J. Am. Chem. Soc.* **2004**, *126*, 10, 3234–3243.

[39] Y. Ootani, K. Satoh, A. Nakayama, T. Noro, T. Taketsugu, *J. Chem. Phys.* **2009**, *131*, 194306.

[40] C. Xu, L. Yu, F. L. Gu, C. Zhu, *Phys. Chem. Chem. Phys.* **2018**, ***20***, 23885-23897.

[41] (a) A. S. Lubbe, J. C. M. Kistemaker, E. J. Smits, B. L. Feringa, *Phys. Chem. Chem. Phys.* **2016**, *18*, 26725-26735; (b) Serra, F.; Terentjev, E. M. Macromolecules 2008, 41, 981-986.

[42] J. Dokić, M. Gothe, J. Wirth, M. V. Peters, J. Schwarz, S. Hecht, P. Saalfrank, *J. Phys. Chem. A* **2009**, *113*, 6763–6773.

[43] C. Reichardt, T. Welton, *Solvents and Solvent Effects in Organic Chemistry*; 4th Ed.; Wiley-VCH: Weinheim, **2011**.

[44] a) L. Kortekaas, J. Simke, N. B. Arndt, M. Böckmann, N. L. Doltsinis, B. J. Ravoo, *Chem. Sci.* **2021**, *12*, 11338–11346; b) S. Ciccone, J. Halpern, *Can. J. Chem.* **1959**, 37, 1903– 1910; c) R. Lovrien, J. C. B. Waddington, *J. Am. Chem. Soc.* **1964**, *86*, 2315–2322; d) G. Wettermark, M. E. Langmuir, D. G. Anderson, *J. Am. Chem. Soc.* **1965**, *87*, 476–481; e) N. J. Dunn, W. H. Humphries, A. R. Offenbacher, T. L. King, J. A. Gray, *J. Phys. Chem. A* **2009**, 113, 13144–13151.

[45] N. Łukasik, K. Hemine, I. Anusiewicz, P. Skurski, E. Paluszkiewicz, *Materials* **2021**, *14*, 3995.

[46] A. Fihey, A. Perrier, W. R. Browne, D. Jacquemin, *Chem. Soc. Rev.* **2015**, *44*, 3719-3759.

[47] P. Kumar, D. Gupta, S. Grewal, A. Srivastava, A. K. Gaur, S. Venkataramani, *Chem. Rec.***2022.**

[48] a) D. Bléger, Z. Yu, S. Hecht, *Chem. Commun.* **2011**, *47*, 12260–12266; b) D. Bléger, T. Liebig, R. Thiermann, M. Maskos, J. P. Rabe, S. Hecht, *Angew. Chem. Int. Ed.* **2011**, *50*, 12559–12563.

[49] a) F. Cisnetti, R. Ballardini, A. Credi, M. T. Gandolfi, S. Masiero, F. Negri, S. Pieraccini, G. P. Spada, *Chem. Eur. J.* **2004**, *10*, 2011–2021; b) D. Bléger, J. Dokić, M. V. Peters, L. Grubert, P. Saalfrank, S. Hecht, *J. Phys. Chem. B* **2011**, *115*, 9930–9940.

[50] a) S. Lee, S. Oh, J. Lee, Y. Malpani, Y.-S. Jung, B. Kang, J. Y. Lee, K. Ozasa, T. Isoshima, S. Y. Lee, M. Hara, D. Hashizume, J. M. Kim, *Langmuir* **2013**, *29*, 5869–5877; b) L. M. Goldenberg, L. Kulikovsky, O. Kulikovska, J. Tomczyk, J. Stumpe, *Langmuir* **2010**, *26*, 2214 – 2217; c) Y.-J. Choi, D.-Y. Kim, M. Park, W.-J. Yoon, Y. Lee, J.-K. Hwang, Y.-W. Chiang, S.-W. Kuo, C-H. Hsu, K.-U. Jeong, *ACS Appl. Mater. Interfaces* **2016**, *8*, 9490–9498; d) N. Łukasik, E. Wagner-Wysiecka, *Photochem. Photobiol. Sci.* **2017**, *16*, 1570-1579.

[51] K. Kreger, P. Wolfer, H. Audorff, L. Kador, N. Stingelin-Stutzmann, P. Smith, H.-W. Schmidt, *J. Am. Chem. Soc.* **2010**, *132*, 509–516.

[52] a) M. Han, S. J. Cho, Y. Norikane, M. Shimizu, A. Kimura, T. Tamagawa, T. Seki, *Chem. Commun.* **2014**, *50*, 15815–15818; b) M. Han, Y. Takeoka, T. Seki, *J. Mater. Chem. C* **2015**, *3*, 4093-4098; c) M. Han, H. Nakanishi, *J. Photopolym. Sci. Technol.* **2018**, *31*, 527-531; d) I. Abe, M. Hara, T. Seki, S. J.Cho, M. Shimizu, K. Matsuura, H.-K. Cheong, J. Y. Kim, J. Oh, J. Jung, M. Han, *J. Mater. Chem. C* **2019**, *7*, 2276-2282; e) I. Abe, M. Han, *New J. Chem.* **2019**, *43*, 19014-19019.

[53] S. H. Gellman, *Chem. Rev.***1997**, *97*, 1231–1734.

[54] A. Bianchi, K. Bowman-James, E. García-España, *Supramolecular Chemistry of Anions*, Wiley-VCH, Weinheim, **1997**.

[55] M. P. Coles, *Chem. Commun.***2009**, 3659–3676.

[56] a) Y. Takemoto, *Org. Biomol. Chem.* **2005**, *3*, 4299–4306; b) Z. Zhang, P. R. Schreiner, *Chem. Soc. Rev.* **2009**, *38*, 1187–1198.

[57] J. Alemán, A. Parra, H. Jiang, K. A. Jørgensen, *Chem. Eur. J.* **2011**, *17*, 6890–6899.

[58] R. A. Pascal, J. Spergel, D. V. Engsbersen, *Tetrahedron Lett.* **1986**, *27*, 4099–4102.

[59] a) J. Scheerder, M. Fochi, J. F. J. Engbersen, D. N. Reinhoudt, *J. Org. Chem.***1994**, *59*, 7815–7820; b) S. E. Matthews, P. D. Beer in Calixarenes; Eds.: Z. Asfari,V. Böhmer, J. Harrowfield, J. Vicens, M. Saadioui, Kluwer Academic Publishers, Dordrecht, **2001**, pp. 421–439.

[60] M. Zurro, O. G. Mancheño, *Chem. Rec.* **2017**, *17*, 485–498.

[61] K. Brak, E. N. Jacobsen, *Angew. Chem. Int. Ed.* **2013**, *52*, 534 – 561.

[62] a) M. S. Taylor, E. N. Jacobsen, *J. Am. Chem. Soc.* **2004**, *126*, 10558–10559; b) M. S. Taylor, N. Tokunaga, E. N. Jacobsen, *Angew. Chem. Int. Ed.* **2005**, *44*, 6700–6704; c) I. T. Raheem, P. S. Thiara, E. A. Peterson, E. N. Jacobsen, *J. Am. Chem. Soc.* **2007**, *129*, 44, 13404–13405.

[63] M. Wasa, R. Y. Liu, S. P. Roche, E. N. Jacobsen, *J. Am. Chem. Soc.* **2014**, *136*, 12872−12875.

[64] G. Hirata, H. Maeda, *Org. Lett.* **2018**, *20*, 2853−2856.

[65] D. G. Piekarski, P. Steinforth, M. Gómez-Martínez, J. Bamberger, F. Ostler, M. Schönhoff, O. G. Mancheño, *Chem. Eur. J.* **2020**, *26*, 17598–17603.

[66] a) S. Beckendorf, S. Asmus, O. G. Mancheño, *ChemCatChem* **2012**, *4*, 926 – 936; b) O. G. Mancheño, *Anion binding catalysis*, Wiley-VCH, Weinheim, **2021.**

[67] a) R. S. Stoll, S. Hecht, *Angew. Chem. Int. Ed.* **2010**, *49*, 5054–5075; b) R. Göstl, A. Senf, S. Hecht, *Chem. Soc. Rev.* **2014**, *43*, 1982–1996; c) T. Imahori, S. Kurihara, *Chem. Lett.* **2014**, *43*, 1524–1531; d) V. Blanco, D. A. Leigh, V. Marcos, *Chem. Soc. Rev.* **2015**,

44, 5341–5370; e) M. Vlatković, B. S. L. Collins, B. L. Feringa, *Chem. Eur. J.* **2016**, *22*, 17080–17111.

[68] a) F. Würthner, J. Rebek, *Angew. Chem. Int. Ed.* **1995**, *34*, 446–448; b) R. Cacciapaglia, S. D. Stefano, L. Mandolini, *J. Am. Chem. Soc.* **2003**, *125*, 2224–2227; c) D. Sud, T. B. Norsten, N. R. Branda, *Angew. Chem. Int. Ed.* **2005**, *44*, 2019–2021; d) J. Wang, B. L. Feringa, *Science* **2011**, *331*, 1429–1432; e) T. Imahori, R. Yamaguchi, S. Kurihara, *Chem. Eur. J.* **2012**, *18*, 10802–10807; f) M. Samanta, V. S. R. Krishna, S. Bandyopadhyay, *Chem. Commun.* **2014**, *50*, 10577–10579; g) M. Vlatković, L. Bernardi, E. Otten, B. L. Feringa, *Chem. Commun.* **2014**, *50*, 7773–7775.

[69] a) W.-S. Lee, A. Ueno, *Macromol. Rapid Commun.* **2001**, *22*, 448–450; b) H. Sugimoto, T. Kimura, S. Inoue, *J. Am. Chem. Soc.* **1999**, *121*, 2325–2326; c) M. V. Peters, R. S. Stoll, A. Kühn, S. Hecht, *Angew. Chem. Int. Ed.* **2008**, *47*, 5968–5972; d) O. B. Berryman, A. C. Sather, A. Lledó, J. Rebek, *Angew. Chem. Int. Ed.* **2011**, *50*, 9400–9403; e) R. S. Stoll, M. V. Peters, A. Kuhn, S. Heiles, R. Goddard, M. Bühl, C. M. Thiele, S. Hecht, *J. Am. Chem. Soc.* **2009**, *131*, 357–367; f) R. S. Stoll, S. Hecht, *Org. Lett.* **2009**, *11*, 4790–4793; g) L. Osorio-Planes, C. Rodríguez-Escrich, M. A. Pericàs, *Org. Lett.* **2014**, *16*, 1704–1707.

[70] a) T. Niazov, B. Shlyahovsky, I. Willner, *J. Am. Chem. Soc.* **2007**, *129*, 6374–6375; b) D. Wilson, N. R. Branda, *Angew. Chem. Int. Ed.* **2012**, *51*, 5431–5434; c) B. M. Neilson, C. W. Bielawski, *J. Am. Chem. Soc.* **2012**, *134*, 12693–12699; d) B. M. Neilson, C. W. Bielawski, *Chem. Commun.* **2013**, *49*, 5453–5455; e) B. M. Neilson, C. W. Bielawski, *Organometallics* **2013**, *32*, 3121–3128.

[71] F. Würthner, J. Rebek, *Angew. Chem., Int. Ed. Engl.* **1995**, *34*, 446.

[72] R. Cacciapaglia, S. D. Stefano, L. Mandolini, *J. Am. Chem. Soc.* **2003**, *125*, 2224-2227.

[73] T. Imahori, R. Yamaguchi, S. Kurihara, *Chem. Eur. J.* **2012**, *18*, 10802-10807.

[74] A. Ueno, K. Takahashi, T. Osa, *J. Chem. Soc., Chem. Commun.* **1981**, *47*, 94–96.

Chapter 2. Structure-property Relationship in Azobenzene Photoswitches Appended with Picolinyl Amides and their Supramolecular Assemblies

2.1 Introduction

The photoswitching ability and the thermal stability of the photoswitches state (otherwise *Z*-*E* thermal relaxation) of azobenzenes are well established.[1] Various substitutions and their positions can influence both these properties through electronic effects, steric effects, hydrogen bonding and other non-covalent interactions, etc. Apart from that, the solvents can also play a crucial role in this regard. Such plethora of effects can influence the utility of azobenzene photoswitches towards various applications.[2] Many of these behaviour can be predicted to some extent based on their absorption features, in particular, the separation between the π–π* and n–π* bands of the azo chromophore.[3] For instance, the azobenzene containing alkyl, ester groups, etc. were found to have half-lives in the range from hours to days, whereas those with electron-donating substituents or push-pull type systems are found to exhibit fast thermal reverse isomerisation in minutes to ns time scales.[1-3] Also, several other factors such as presence of acids, temperature, hydrogen bonding with azo nitrogen, etc can also affect the rate of thermal reverse isomerization.[1,4] For many applications like catalysis, host-guest binding, data storage, drug delivery, etc., the demand for longer *cis*-stability is crucial.[5] Another growing interest in azobenzene derivatives is their role in supramolecular chemistry. In this domain, several studies have been reported, however, a systematic approach is still necessary.

In 2015, Wegner and co-workers have prepared tetrasubstituted azobenzenes with different substitutions, and their impact on *Z*-isomeric stability was investigated.[6] Here, they have introduced a variety of groups at all *meta* positions of the azobenzene moiety and they found that upon increasing the bulkiness, the *Z*-isomeric stability was found to be increasing. They attributed such effect to weak interactions such as London dispersion forces. Another report, by Jurczak *et.al.* have designed a molecular system with tetra-amide substitutions at 3,3′,5,5′ positions was prepared and revealed that Z-isomer of it was more stable than simple azobenzene, and their half-life was further increased with the help of complexation with different anions.[7] The intramolecular hydrogen bonding was responsible for higher stability, which got enhanced due to the chelation effect of the anions with the amide groups.

Another salient feature of amide groups can be their role in supramolecular assembly due to their higher propensity towards hydrogen-bond forming ability. Since the azobenzenes are decorated with carboxamide groups, their supramolecular assembly can light controlled.[8] However, a systematic study is needed to envisage structure-property relationships and light controlled supramolecular assembly and disassembly. In this regard, we combined the factors such as hydrogen bonding derived from 2^o carboxamides and steric factors through 3^o carboxamide derivatives to understand the structure-property relationships in the photoswitching and thermal stability of the *Z*-isomers. Herein, we present the investigations on the 18 molecular systems with variation in the designs on their photophysical studies and supramolecular aspects.

2.2 Design and Synthesis

In this context, we intended to design our target photoswitchable molecular systems by functionalization of azobenzene moiety, and utilize them towards light-driven reversible supramolecular assembly. Primarily, the impact of design on the light induced *E*-*Z* photoisomerization and the thermal stability of the *Z*-isomer were evaluated. For the design of the target systems, we considered the following:

(a) To enable photoswitching and photoswitchable supramolecular properties, azobenzene as core has been considered.

(b) To follow the effect of substitution and its position spectroscopically, we have decided to use symmetrical substitution.

(c) To induce supramolecular assembly, we considered the hydrogen bonding using carboxamide groups and π-stacking of aryl groups.

(d) To influence the *Z*-isomer stability, both hydrogen bonding through 2^o carboxamides and steric factors through 3^o carboxamide have been considered.

(e) To tune these properties and control them, the position of carboxamide groups has been varied. In this regard, 4,4′-, 3,3′- and 3,3′,5,5′- substituted derivatives have been designed.

(f) To utilize such systems for coordination with metal ions, we considered picolinyl groups, which differed by the position of nitrogen atom.

Based on these design principles, we have considered 18 different targets. In this regard, we mainly adopted a strategy towards designing the target molecules **(Figure 2.1)**:

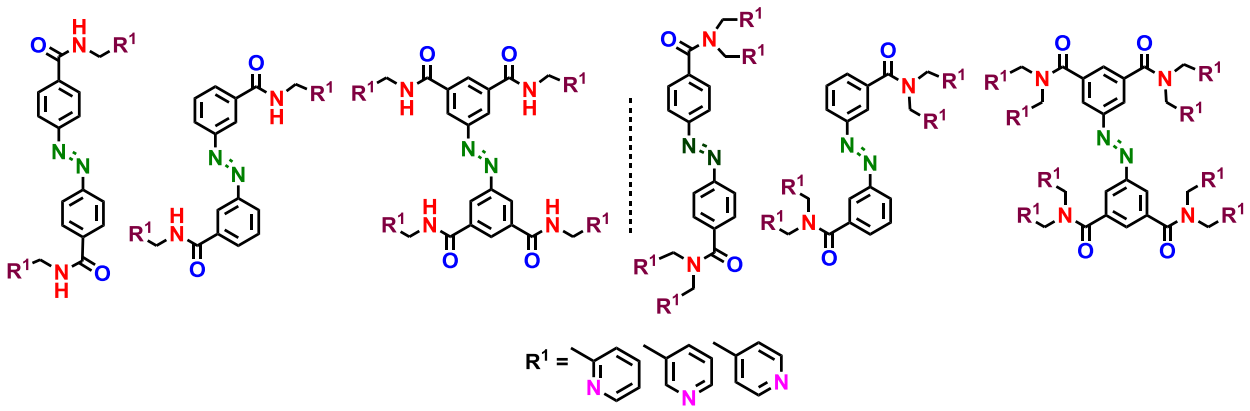

Figure 2.1 Target design for photoswitchable molecular systems.

Classification: Based on the substitution patterns, we have classified all the 18 targets into three different classes of photoswitchable molecular systems, namely,

(a) Type A – *para*- di substituted azobenzenes

(b) Type B – *meta*- di substituted azobenzenes

(c) Type C – *meta*- tetra substituted azobenzenes

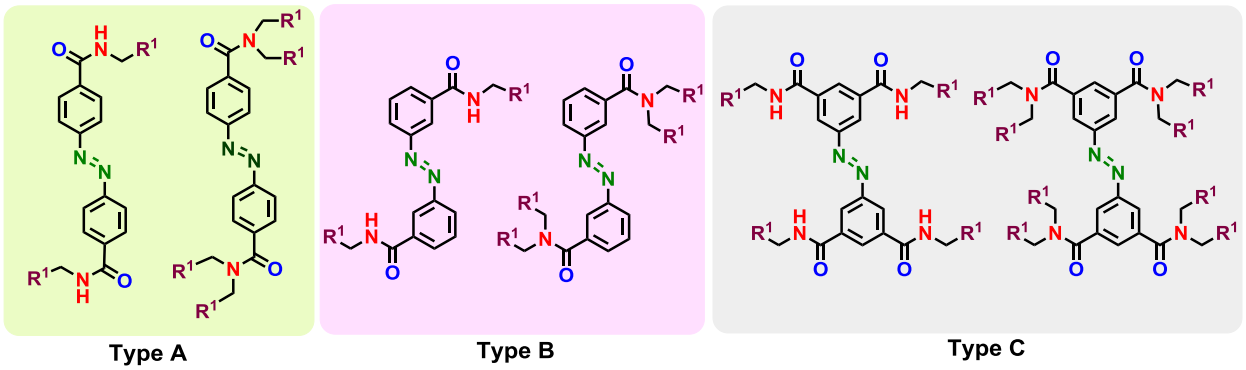

Figure 2.2 Classification of the target photoswitchable molecular systems.

Next, we targeted to synthesize the 18 designed molecules. To achieve this, the necessary condition is to synthesize azobenzenes as a core moiety with carboxylic groups that can be connected with different amines to obtain the desired targets. In this regard, we have synthesized 4,4'-, 3,3'-azobenzene di-carboxylic acid and 3,3',5,5'-azobenzene tetra-carboxylic acid as our photoswitchable core unit via reductive coupling of their respective nitrobenzoic acids in the presence of glucose and sodium hydroxide. Further, using a modular acid amine coupling strategy, all the desired targets have been successfully achieved in moderate to good yields **(Scheme 2.1)**.

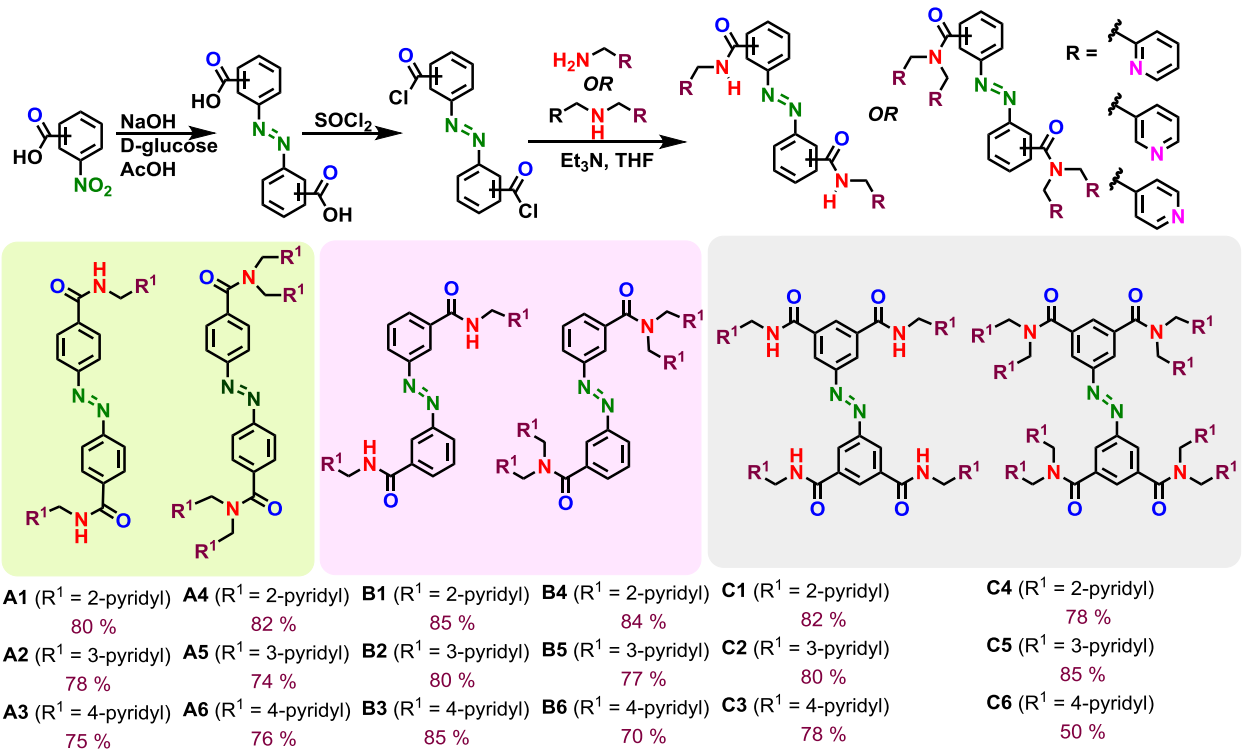

A1 (R^1 = 2-pyridyl) 80 %
A2 (R^1 = 3-pyridyl) 78 %
A3 (R^1 = 4-pyridyl) 75 %
A4 (R^1 = 2-pyridyl) 82 %
A5 (R^1 = 3-pyridyl) 74 %
A6 (R^1 = 4-pyridyl) 76 %
B1 (R^1 = 2-pyridyl) 85 %
B2 (R^1 = 3-pyridyl) 80 %
B3 (R^1 = 4-pyridyl) 85 %
B4 (R^1 = 2-pyridyl) 84 %
B5 (R^1 = 3-pyridyl) 77 %
B6 (R^1 = 4-pyridyl) 70 %
C1 (R^1 = 2-pyridyl) 82 %
C2 (R^1 = 3-pyridyl) 80 %
C3 (R^1 = 4-pyridyl) 78 %
C4 (R^1 = 2-pyridyl) 78 %
C5 (R^1 = 3-pyridyl) 85 %
C6 (R^1 = 4-pyridyl) 50 %

Scheme 2.1 Synthesis of photoswitchable molecular systems.

2.3 Photoswitching Studies

After the synthesis of all the targets, they were subjected to photoswitching studies and monitored by using UV-Vis spectroscopy. The studies of all 18 derivatives have been carried out in DMSO as a solvent. Firstly, we have performed the photoswitching studies where the analysis of the *E*-*Z* and *Z*-*E* photoisomerization steps have been followed by using UV-Vis spectroscopy. For forward photoisomerization, a light of 365 nm has been utilized, whereas for the reverse photoisomerization 405 nm light was used. Through this, the wavelengths for the forward and reverse photoisomerization steps, and their photoswitching efficiency of all the compounds have been scrutinized.

To explore the effect of functionalization on the absorption spectral features, we closely inspected the trends and effects of substituents on it **(Figure 2.3 and Table 2.1)**. In terms of spectral changes in the absorption spectra, it was found that the λ_{max} values of $\pi-\pi^*$ band of all the molecules ranges between 324 and 336 nm in their native state (*E*-isomeric form) of compounds. The maximum bathochromic shift of 12 nm was observed for type A compounds and the trend is type A (i.e. 334-336 nm) > type C (i.e. 327-329 nm) > type B (i.e. 324-325 nm). For *E*-isomer, $n-\pi^*$ ranges between 442 and 454 nm, whereas a blue shift is observed in $n-\pi^*$ upon isomerization that ranges between 427 and 438 nm **(Figure 2.4)**. To understand the photoswitching stability of all the derivatives, we subjected

them to reversible irradiation sequences in the forward and reverse directions over five / six cycles. All the compounds showed consistency in reversible photoswitching without any sign of fatigue. Also, the π–π* bands molar absorption coefficients (ε) of all the compounds were estimated and found to be ranging from 36535 $M^{-1}cm^{-1}$ to 12135 $M^{-1}cm^{-1}$ **(Appendix 2A)**.

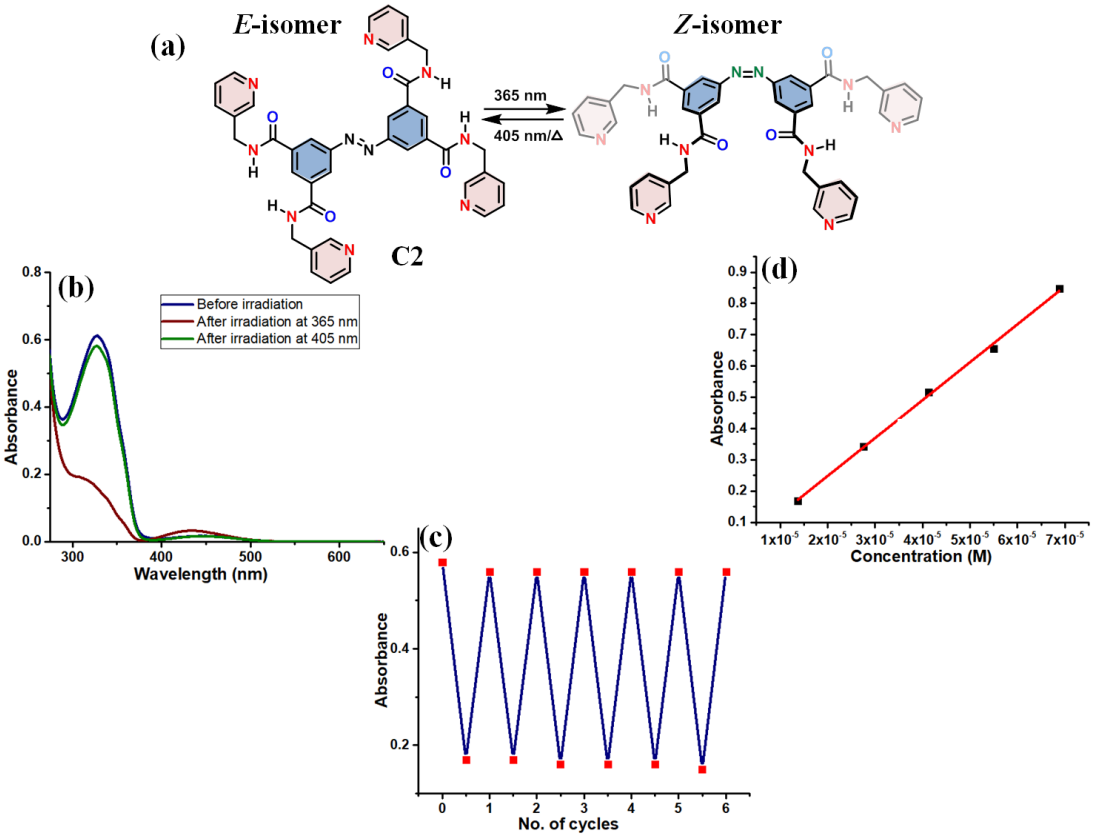

Figure 2.3 (a) Illustration of photoisomerization of selected derivative (**C2**), (b) UV-Vis spectroscopic data (DMSO) portraying photoisomerization, (c) Photoswitching stability over six cycles (Forward: 365 nm, reverse: 405 nm) with the monitoring of λ_{max} corresponding to the π–π* absorption of (*E*)-**C2**. and (d) Estimation of the epsilon (Concentration-60 μM).

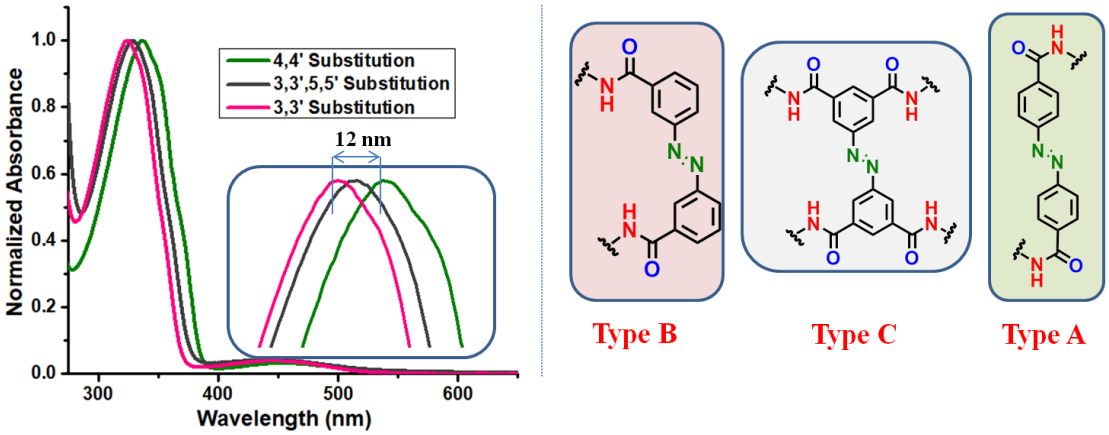

Figure 2.4 Comparison of absorption spectral shifts observed in λ_{max} values of π–π* band in native state.

Table 2.1 UV-Vis absorption spectral data of *E*-/*Z*-isomers and estimation of epsilon

Sr. No.	Target	UV-Vis spectroscopic data				ε ($M^{-1}cm^{-1}$)	Conc (μM)
		E-isomer		*Z*-isomer			
		π-π* (nm)	n–π* (nm)	π-π* (nm)	n–π* (nm)		
1	**A1**	336	454	-	438	29803 ± 753	23.8
2	**A2**	336	454	-	437	36535 ± 398	19.2
3	**A3**	336	454	-	435	29891 ± 919	24.4
4	**A4**	334	449	-	436	16561 ± 327	42.5
5	**A5**	335	452	-	438	16293 ± 230	44.2
6	**A6**	334	449	-	434	15796 ± 399	46.2
7	**B1**	324	442	-	431	17929 ± 74	42.4
8	**B2**	324	442	-	436	20150 ± 140	36.7
9	**B3**	324	442	-	431	19584 ± 148	40.8
10	**B4**	325	448	-	430	16789 ± 259	40.5
11	**B5**	324	446	-	430	16027 ± 342	44.9
12	**B6**	325	449	-	430	18310 ± 212	35.0
13	**C1**	327	447	-	430	22560 ± 468	32.4
14	**C2**	328	450	-	431	12135 ± 306	59.3
15	**C3**	327	447	-	440	13908 ± 305	51.8
16	**C4**	329	445	-	431	20581 ± 299	36.9
17	**C5**	328	449	-	427	24224 ± 450	28.9
18	**C6**	327	449	-	427	21278 ± 582	30.1

2.4 PSS Composition in the Forward and Reverse Isomerization Steps

For quantification of individual isomers at PSS, we have utilized NMR spectroscopy. In order to evaluate the photoswitching ability, we have estimated the percentage of *E*- and *Z*-isomers in the forward, and reverse photoisomerization steps. All derivatives showed moderate to good forward (60-86%) and excellent reverse photoisomerization (84-94%) conversions. The photostationary state (PSS) composition of the targets have been obtained by subjecting them to irradiation at appropriate wavelengths of light in [D_6]DMSO [at mM concentrations]. For each system, the signals of the CH_2 protons connected to the amide group were chosen for evaluating the conversion from *E* to *Z* state, because majority of the other signals in the aromatic region were found to be merging **(Figure 2.5)**. For type A molecules, forward isomerization found to have conversion ranging between 66-75% and the reverse isomerization percentage lies between 91-94%. For type B molecules, forward isomerization observed to have a conversion ranging between 74-86% and the reverse isomerization percentage lies between 84-88% **(Appendix 2B)**.

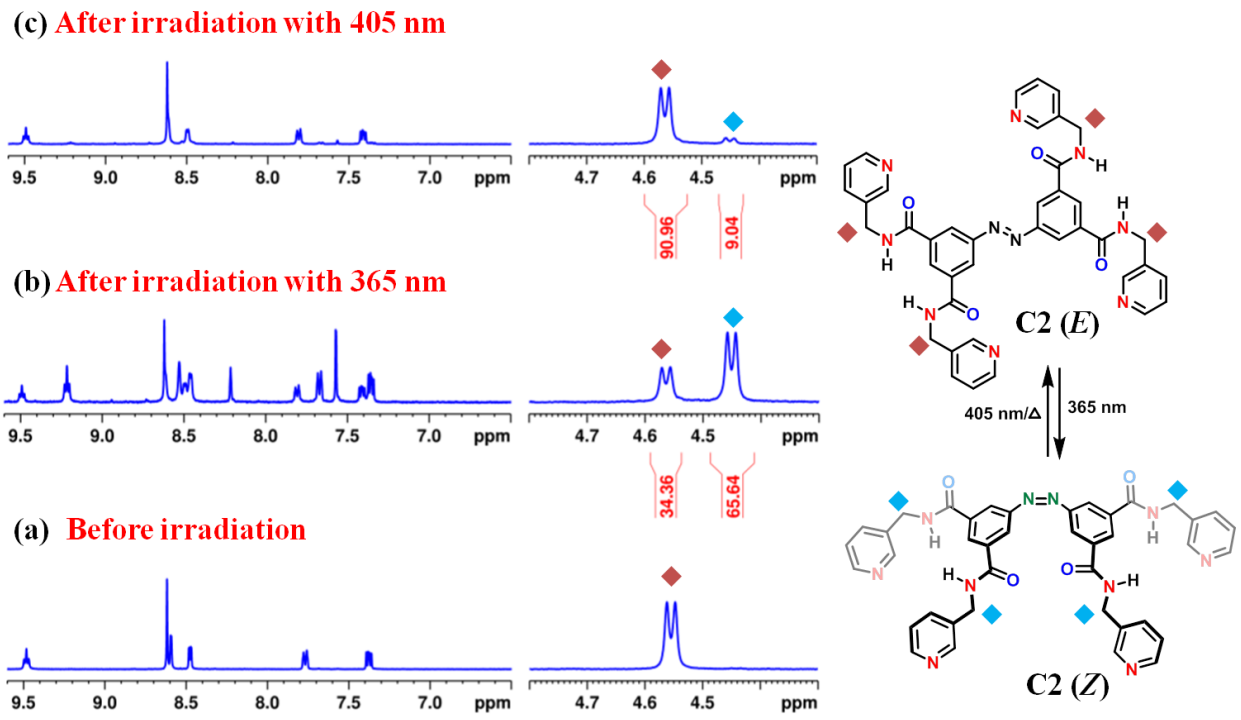

Figure 2.5 Estimation of PSS composition using ^{1}H-NMR spectroscopy of **C2** ([D_6]DMSO, 11.2 mM) (a) before irradiation; (b) after irradiation at 365 nm; (c) after irradiation at 405 nm (Normalized integral values of selected protons are indicated for *E*- and *Z*- isomers).

For type C molecules, forward isomerization observed to have conversion ranging between 60-72%, whereas the reverse isomerisation percentage lies between 88 and 91%. Overall, the following trend was observed when the forward isomerisation efficiency was compared: Type B > Type A > Type C. For type B molecules, reverse isomerisation was found to be least in comparison to type A and C systems **(Figure 2.6 and Table 2.2)**.

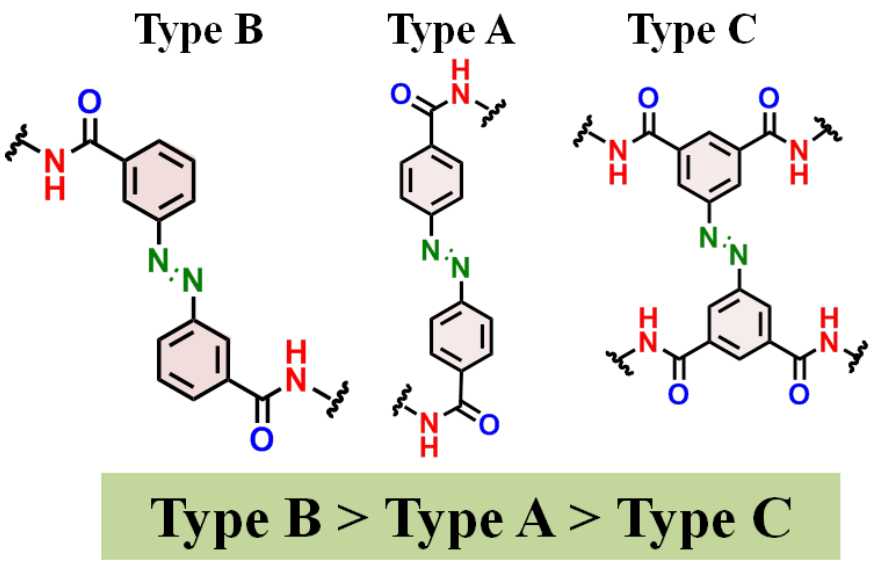

Figure 2.6 Illustration of trend for forward photoisomerization efficiency.

Table 2.2 Estimation of PSS composition at photoisomerization steps using ^{1}H-NMR spectroscopy.

Target	Forward (% *Z*)	Reverse (% *E*)	Conc. (mM)	Target	Forward (% *Z*)	Reverse (% *E*)	Conc. (mM)
A1	72	95	7.1	**B4**	86	86	5.1
A2	67	95	7.5	**B5**	81	87	6.3
A3	72	90	8.0	**B6**	74	89	3.8
A4	77	93	7.0	**C1**	60	91	4.8
A5	68	92	6.3	**C2**	66	91	4.2
A6	72	94	6.3	**C3**	64	89	4.2
B1	75	85	6.2	**C4**	72	86	3.7
B2	83	87	5.8	**C5**	70	91	3.7
B3	81	85	5.8	**C6**	51	95	3.5

2.5 Thermal Reverse Isomerization Kinetics

One of our motivations of this work was to understand the impact of design and substitution pattern on *Z*-isomeric stability. In general, the *Z*-isomers are thermally activated and by virtue of the thermal energy in the medium or its own, it can isomerize back to the *E*-isomeric state. One way of understanding the stability of *Z*-isomer is to compare the rate of isomerization or the half-life of it. In this regard, we performed the thermal reverse isomerization kinetics from *Z*-isomer to *E*-isomer was followed at constant temperature. For comparison, we have used DMSO as the common solvent. We have utilized UV-vis spectroscopy to follow the exponential growth of *E*-isomers **(Figure 2.7)**. By using the exponential fit for the first order growth curve, the rate constants have been obtained using the following equation:

$$[A] = [A]_o e^{-kt} \quad \text{.....(eqn 2.1)}$$

Further, the half-life of the Z-isomer has been estimated from the rate constant using the following expression:

$$t_{1/2} = \frac{0.693}{k} \quad \text{.....(eqn 2.2)}$$

Also, kinetics studies have been carried out at variable temperatures for each system in order to obtain the activation parameters. In this regard, the Arrhenius (eqn 2.3) and Eyring (eqn

2.4) equations were considered.

$$k = A\, e^{-E_a/RT} \quad \text{.....(eqn 2.3)}$$

$$k = \frac{k_B T}{H}\, e^{-\Delta G^{\neq}/RT} \quad \text{.....(eqn 2.4)}$$

By plotting the lnk vs 1/T (Arrhenius plot) and ln(k/T) vs 1/T (Eyring plot), the activation parameters such as E_a, $\Delta G^{\ddagger}$, $\Delta H^{\ddagger}$, and $\Delta S^{\ddagger}$ have been obtained.

The reverse thermal isomerization kinetics experiments of **A1**-**A3**, **B2**-**B6** and **C1** were carried out at four different temperatures (60, 70, 80 and 90 °C). On the other hand, **C3**, **C4** and **A4**-**A6** have been monitored at 60, 70, and 80 °C. Whereas for **B1**, **C2**, **C6**, **C5**, such experiments have been carried out at slightly elevated temperatures 70, 80, and 90 °C.

For all the cases, the formation rate constants and half-lives have been estimated for the *E*-isomer **(Table 2.3 and Table 2.4)**. Based on the data, we have noticed a remarkable difference in the rate constants and half-lives depending of design. In order to estimate the rate constant and *Z*-isomeric stability at room temperature, Arrhenius plot was extrapolated. Based on the Arrhenius plot, the room temperature estimates of the rate constants and the predicted half-lives were compared for understanding the impact of design. This revealed that the Z-isomeric stability follow certain trends.

Among the 2-picolinyl group containing systems, when we change the connections from 4,4'-disubstituted to 3,3'-disubstituted amides, there is an increase in *Z*-isomeric thermal stability, and which increased upon 3,3',5,5'- tetra substitution, For instance, the compound **A1** has a half-life 5.7 d, whereas the corresponding 3, 3'-derivative **B1** exhibited a half-life of 12.6 d. This further increased to 13.4 d in **C1**. A similar trend was also observed for the corresponding tertiary amides **A4**, **B4**, and **C4**. However, if we compare the effect of 3^o amides with that of 2^o amides, we realized a slight increase in the case of 4,4'-disubstituted systems. For instance, the compound **A1** has a half-life of 5.7 d, which becomes 6.5 d in **A4**. On contrast, both 3,3'-disubstituted amides and 3,3',5,5'- tetra substituted systems showed a drop in the half-lives upon introducing the tertiary amides. This can be observed in **B1** (12.6 d) changes to **B4** (11.2 d) and **C1** (13.4 d) becomes **C4** (11.9 d) **(Figure 2.8)**.

Similarly, when the half-lives are compared for 3-picolinyl group containing systems, there is an increase in *Z*- isomeric thermal stability upon changing the connections from 4,4'-disubstituted to 3,3'-disubstituted amides, which slightly decreases upon tetra-substitution.

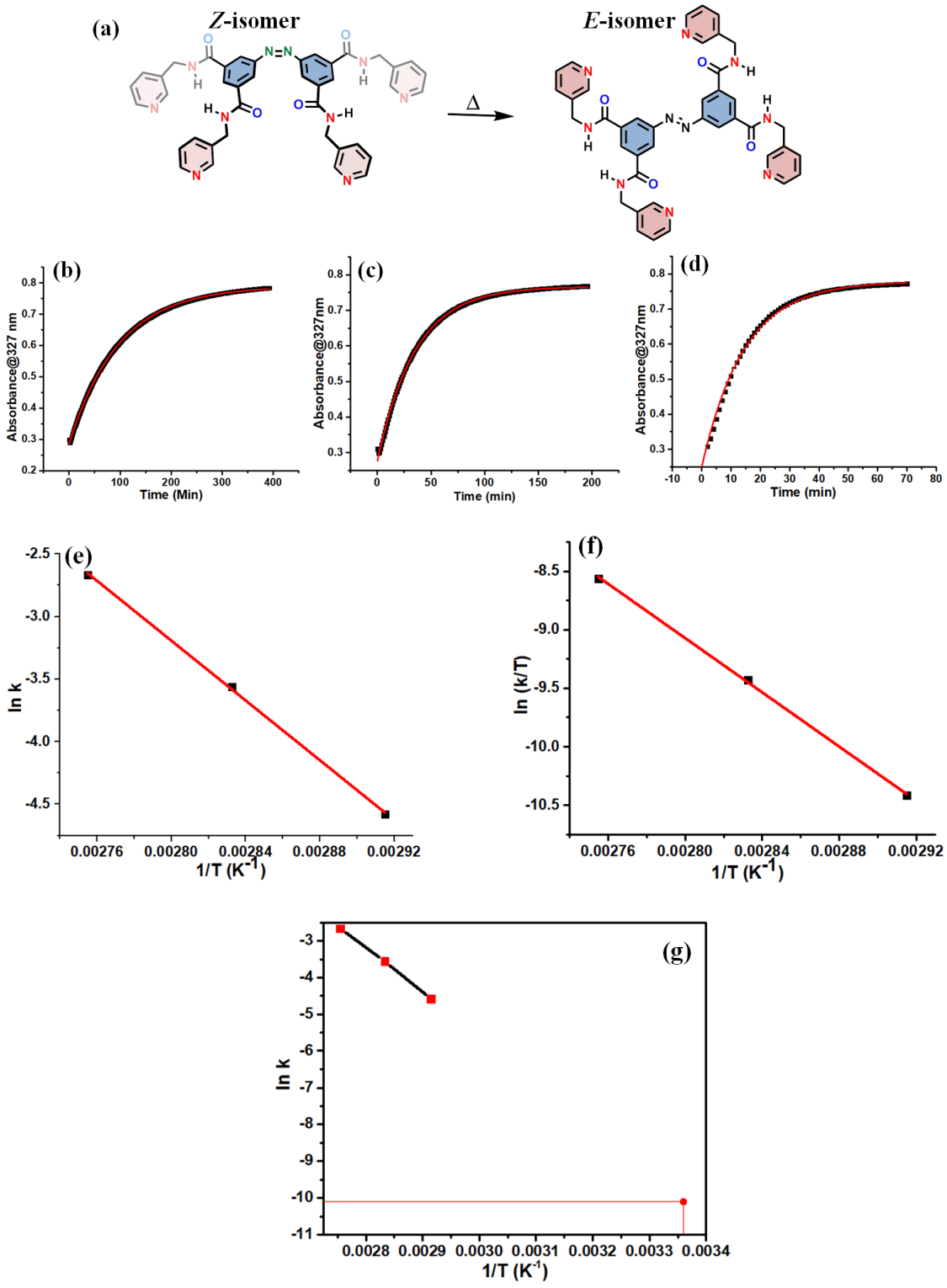

Figure 2.7 (a) Representation of thermal reverse *Z*-*E* isomerization step of **C2**; Variable temperature thermal reverse isomerization kinetics plots at (b) 70 °C, (c) 80 °C, and (d) 90 °C (Each solution had a concentration of 60 μM in DMSO, and the kinetics was followed at 324 nm); (e) Arrhenius plot, and (f) Eyring plot for corresponding to the thermal reverse isomerization; (g) Arrhenius plot for deducing the rate constant at 25 ^{o}C by extrapolation.

Table 2.3 Thermal reverse isomerization kinetics data of type A and B (in DMSO)

Target	Temp. (^{o} C)	Rate Constant (min^{-1})	Half life (min)	Conc. (μM)
A1	60	$9.03 \times 10^{-3} \pm 1.62 \times 10^{-5}$	77	24
	70	$2.85 \times 10^{-2} \pm 1.33 \times 10^{-4}$	24	
	80	$7.17 \times 10^{-2} \pm 1.34 \times 10^{-3}$	10	
	90	$1.82 \times 10^{-1} \pm 3.01 \times 10^{-3}$	4	
	25[a]	8.32×10^{-5}	8328	
A2	60	$9.16 \times 10^{-3} \pm 1.53 \times 10^{-5}$	76	19
	70	$2.76 \times 10^{-2} \pm 1.08 \times 10^{-4}$	25	
	80	$7.56 \times 10^{-2} \pm 2.92 \times 10^{-4}$	9	
	90	$1.80 \times 10^{-1} \pm 2.45 \times 10^{-3}$	4	
	25[a]	1.02×10^{-4}	6794	
A3	60	$8.86 \times 10^{-3} \pm 1.81 \times 10^{-5}$	78	24
	70	$2.81 \times 10^{-2} \pm 8.01 \times 10^{-5}$	25	
	80	$7.24 \times 10^{-2} \pm 1.03 \times 10^{-3}$	10	
	90	$1.82 \times 10^{-1} \pm 2.44 \times 10^{-3}$	4	
	25[a]	8.86×10^{-5}	7824	
A4	60	$8.25 \times 10^{-3} \pm 2.18 \times 10^{-5}$	84	43
	70	$2.62 \times 10^{-2} \pm 7.30 \times 10^{-5}$	26	
	80	$7.34 \times 10^{-2} \pm 5.69 \times 10^{-4}$	9	
	25[a]	7.46×10^{-5}	9287	
A5	60	$8.32 \times 10^{-3} \pm 7.63 \times 10^{-6}$	83	44
	70	$2.46 \times 10^{-3} \pm 7.04 \times 10^{-5}$	28	
	80	$6.58 \times 10^{-3} \pm 4.16 \times 10^{-4}$	11	
	25[a]	9.97×10^{-5}	6948	
A6	60	$7.71 \times 10^{-3} \pm 1.39 \times 10^{-5}$	90	46
	70	$2.29 \times 10^{-2} \pm 9.64 \times 10^{-5}$	30	
	80	$6.62 \times 10^{-2} \pm 4.12 \times 10^{-4}$	10	
	25[a]	9.06×10^{-5}	7652	
B1	70	$1.01 \times 10^{-2} \pm 2.54 \times 10^{-5}$	69	42
	80	$2.81 \times 10^{-2} \pm 1.07 \times 10^{-4}$	25	
	90	$6.92 \times 10^{-2} \pm 1.47 \times 10^{-3}$	10	
	25[a]	3.81×10^{-5}	18206	
B2	60	$3.66 \times 10^{-3} \pm 3.97 \times 10^{-6}$	189	37
	70	$1.11 \times 10^{-2} \pm 2.23 \times 10^{-5}$	62	
	80	$3.01 \times 10^{-2} \pm 1.32 \times 10^{-4}$	23	
	90	$7.40 \times 10^{-2} \pm 1.17 \times 10^{-3}$	9	
	25[a]	3.91×10^{-5}	17720	
B3	60	$3.34 \times 10^{-3} \pm 2.39 \times 10^{-6}$	208	41
	70	$1.00 \times 10^{-2} \pm 1.71 \times 10^{-5}$	69	
	80	$2.94 \times 10^{-2} \pm 1.27 \times 10^{-4}$	24	
	90	$7.13 \times 10^{-2} \pm 1.38 \times 10^{-3}$	10	
	25[a]	3.78×10^{-5}	18310	
B4	60	$3.34 \times 10^{-3} \pm 3.28 \times 10^{-6}$	208	41
	70	$9.72 \times 10^{-3} \pm 2.78 \times 10^{-5}$	71	
	80	$2.90 \times 10^{-2} \pm 8.95 \times 10^{-5}$	24	
	90	$7.13 \times 10^{-2} \pm 1.38 \times 10^{-3}$	10	
	25[a]	4.29×10^{-5}	16169	
B5	60	$2.27 \times 10^{-3} \pm 2.45 \times 10^{-6}$	306	45
	70	$6.90 \times 10^{-3} \pm 8.01 \times 10^{-6}$	101	
	80	$1.97 \times 10^{-2} \pm 4.19 \times 10^{-5}$	35	
	90	$5.15 \times 10^{-2} \pm 4.31 \times 10^{-4}$	13	
	25[a]	2.44×10^{-5}	28419	

Table 2.4 Thermal reverse isomerization kinetics data of type C (in DMSO)

Compound	Temperature (^{o} C)	Rate Constant (min^{-1}) [a]	Half life[a] (min)	Conc. (μM)
B6	60	$2.34 \times 10^{-3} \pm 1.65 \times 10^{-6}$	296	38
	70	$7.03 \times 10^{-3} \pm 8.71 \times 10^{-6}$	99	
	80	$2.05 \times 10^{-2} \pm 4.76 \times 10^{-6}$	34	
	90	$5.32 \times 10^{-2} \pm 7.67 \times 10^{-4}$	13	
	25[a]	2.64×10^{-5}	26284	
C1	60	$3.36 \times 10^{-3} \pm 4.05 \times 10^{-6}$	206	32
	70	$1.02 \times 10^{-2} \pm 1.66 \times 10^{-5}$	68	
	80	$2.89 \times 10^{-2} \pm 1.32 \times 10^{-4}$	24	
	90	$7.10 \times 10^{-2} \pm 7.74 \times 10^{-4}$	10	
	25[a]	3.60×10^{-5}	19246	
C2	70	$1.03 \times 10^{-2} \pm 2.03 \times 10^{-5}$	68	59
	80	$2.84 \times 10^{-2} \pm 1.23 \times 10^{-4}$	24	
	90	$6.95 \times 10^{-2} \pm 1.39 \times 10^{-3}$	10	
	25[a]	4.08×10^{-5}	16973	
C3	60	$3.21 \times 10^{-3} \pm 2.63 \times 10^{-6}$	216	52
	70	$9.43 \times 10^{-3} \pm 1.13 \times 10^{-5}$	73	
	80	$2.73 \times 10^{-2} \pm 1.21 \times 10^{-4}$	25	
	25[a]	3.96×10^{-5}	17481	
C4	60	$4.13 \times 10^{-3} \pm 4.25 \times 10^{-6}$	168	37
	70	$1.29 \times 10^{-2} \pm 1.33 \times 10^{-5}$	54	
	80	$3.71 \times 10^{-2} \pm 1.67 \times 10^{-4}$	19	
	25[a]	4.03×10^{-5}	17203	
C5	70	$5.05 \times 10^{-3} \pm 8.61 \times 10^{-6}$	137	29
	80	$1.50 \times 10^{-2} \pm 3.56 \times 10^{-5}$	46	
	90	$3.86 \times 10^{-2} \pm 1.71 \times 10^{-4}$	18	
	25[a]	1.43×10^{-5}	48623	
C6	70	$5.62 \times 10^{-3} \pm 2.81 \times 10^{-5}$	123	30
	80	$1.66 \times 10^{-2} \pm 1.19 \times 10^{-4}$	42	
	90	$4.98 \times 10^{-2} \pm 3.73 \times 10^{-4}$	14	
	25[a]	1.68×10^{-5}	41212	

[a] Extrapolated using Arrhenius plot to determine the rate constant and half-life at 25^{o}C

For example, in **A2** the half-life is found to be 4.7 days, which increases to 12.3 days for the compound **B2**. However, from **B2** to **C2** the half-life decreases to 11.8 days. When the bulkiness is increased through the incorporation of 3^{o} amides to the azobenzene moiety, the half-life for 4,4'-disubstitution is almost comparable to that of secondary amide derivative. Interestingly, the both 3,3'-disubstituted and 3,3',5,5'- tetrasubstituted systems showed approximately four-fold and seven-fold increase in the half-lifes, respectively. For instance, the target **A5** exhibited a half-life of 4.8 days, which increases upto 19.8 days in **B5**, and 33.8 days in 3,3',5,5'-tetrasubstituted **C5 (Figure 2.9 and Appendix 2C)**.

Likewise, a comparison of 4-picolinyl group containing systems also showed a similar trend as observed in the case of 3-picolinyl group containing targets. For example, upon moving from 4,4'-disubstituted **A3** (half-life = 5.4 days) to 3,3'-disubstituted **B3** (half-life = 12.7 days), there is an increase in *Z*- isomeric thermal stability, however, a slight decrease is observed upon 3,3',5,5'-tetrasubstitution (the estimated half-life of **C3** is 12.2 days).

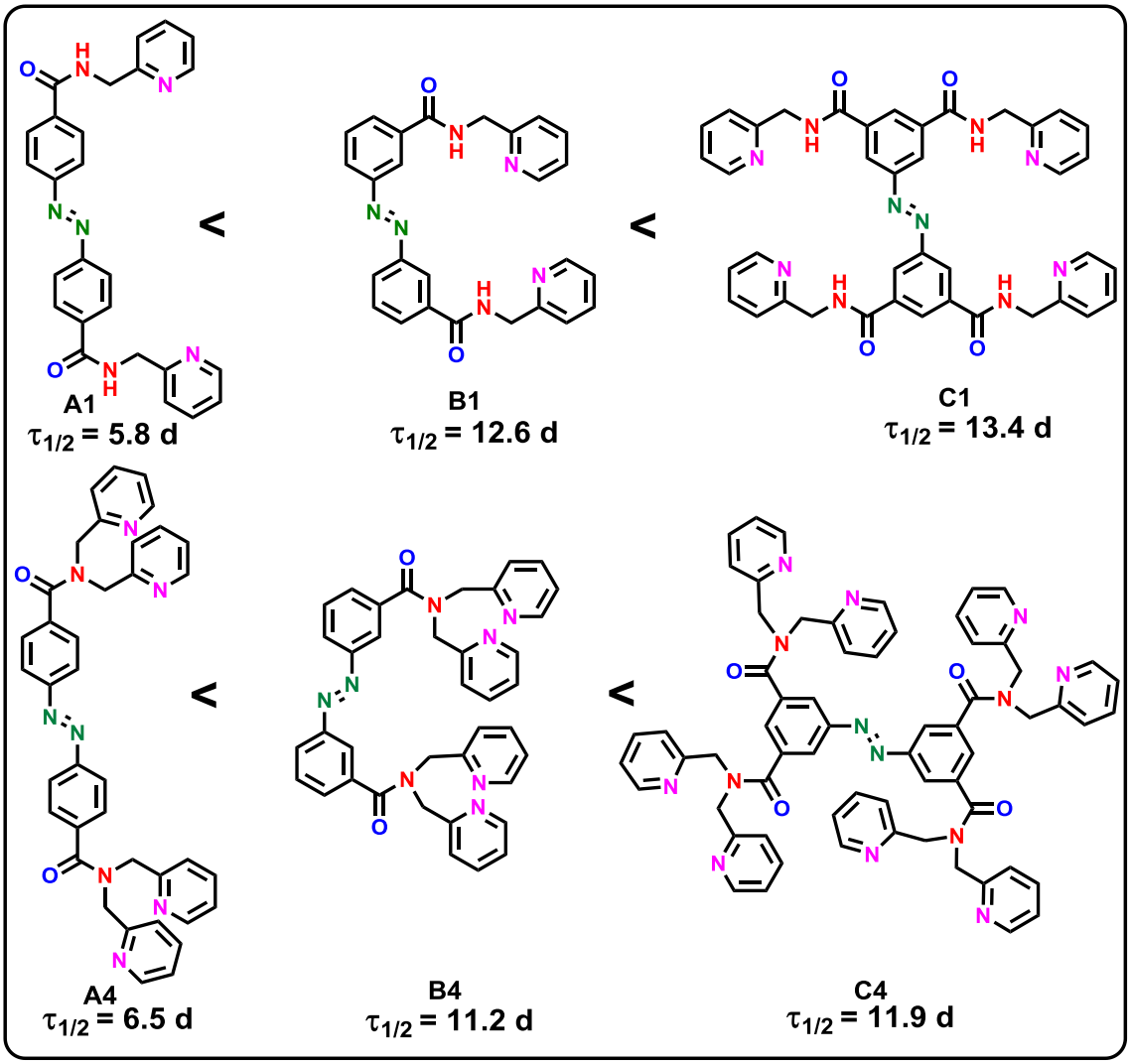

Figure 2.8 Comparison of half-lives of *Z*-isomer with 2-picolinyl group substitution.

Once again, the incorporation of tertiary amides in the azobenzenes showed a similar half-life as in the case of 4,4'-disubstituted system, however, it further increase in 3,3'-disubstituted and exhibits a maximum half-life in 3,3',5,5'- tetrasubstituted systems.(**Figure 2.10**). This can be understood from the half-lives of **A6** (5.3 days) that shows an increase upto 18.3 days in **B6**, which upon tetrasubstitution i.e. **C6** increases further (half-life = 28.6 days). Till now, we have compared the half-lives based on the connectivity of 2^{o} and 3^{o} amides to the azobenzene units. For getting further insights, we also compared the impact of 2-, 3- and 4-picolynyl groups on their respective classes A, B and C, respectively. In this regard, the comparison of all secondary amides for the three classes A, B and C were compared. Indeed, the effect of 2-, 3-, and 4-picolynyl groups exhibit

a marginal variation in the half-lives. For instance, among the Type-A systems, 2-, 3-, and 4-picolinyl groups exhibit a half-life 5.8, 4.7 and 5.4 days, respectively. In Type-B, it is 12.6, 12.3 and 12.7 days, respectively. In Type-C, the trends become 13.4, 11.8 and 12.2 days, respectively.

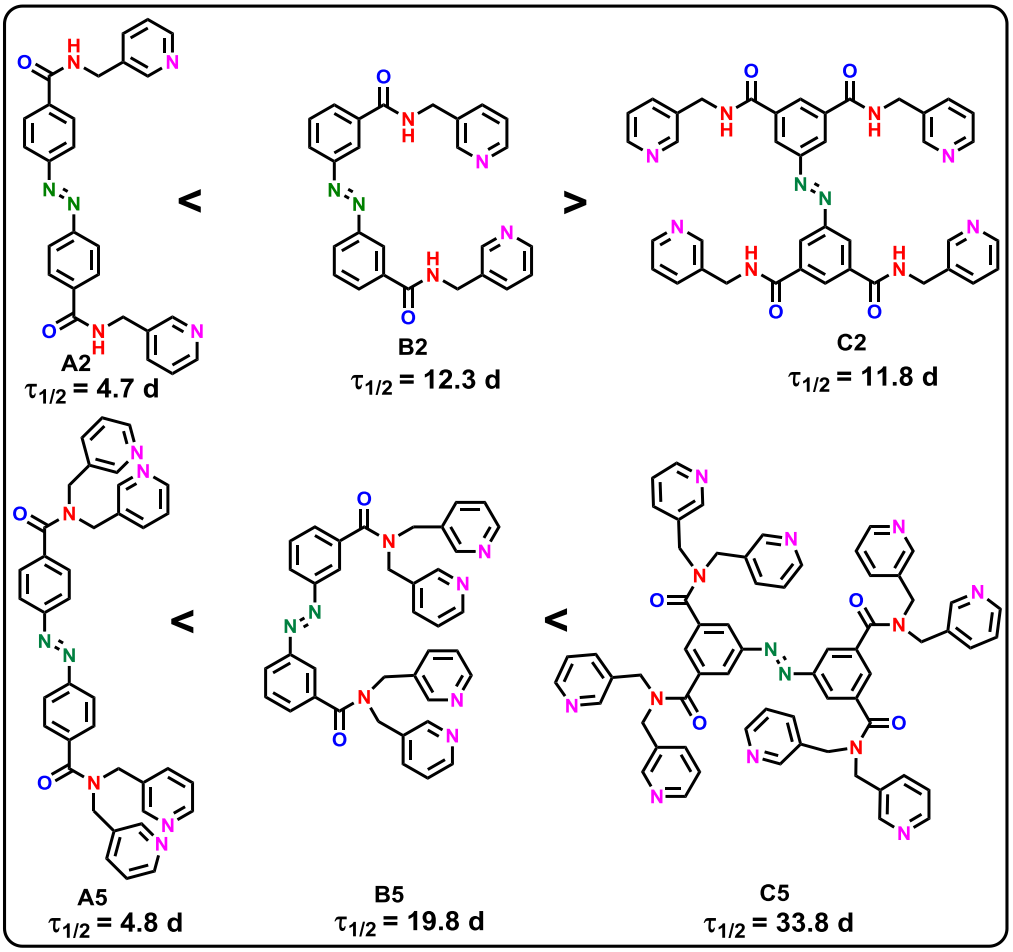

Figure 2.9 Comparison of half-lives of Z-isomer with 3- picolinyl group substitution.

Although the impact of the picolinyl groups are very small, the half-lives are still follow the following order: 2-picolinyl ≥ 4-picolinyl > 3-picolinyl connections. However, when the systems are incorporated with tertiary amide it is found that presence of different pyridyl group creates remarkable difference in *Z*-isomeric stability. For type A systems, it is found to be following an opposite trend than that of observed for type B and C. Herein, the half-life is found to be maximum for 2-picolinyl system (6.5 days – **A4**) and least for 3-picolinyl systems (4.8 days – **A5**); whereas for 4-picolinyl system it lies between the two i.e. half-life is 5.3 days for the target **A6**. On contrary, for tertiary amides of type B and C showed nearly the same trends, i.e. 3-picolinyl > 4-picolinyl > 2-picolinyl systems. For instance, in type B systems, it is 11.2 days for **B4**, 18.3 days for **B6** and a maximum half-life of 19.8 days for **B5**. Again, for type C systems, the half-lives are 11.9, 28.6 and 33.8 days for **C4**, **C6** and **C5**, respectively **(Figure 2.11 and 2.12)**.

Reason for the observed trends in the reverse thermal isomerization kinetics and half-lives:

Based on the trends, it is evident that the 3° amides are more stable in *Z*-isomeric form than their corresponding 2° amides in all the three classes A, B and C. One of the possible reasons for the stabilization of *Z*-isomers with the secondary amide scaffolds is the possible hydrogen bonding between the carbonyl of one phenyl ring and amide N-H of another phenyl ring across the azo bridge **(Figure 2.13)**. Such intramolecular hydrogen bonding is feasible only in the *Z*-isomeric form. Indeed, such hydrogen bonding motif has already been proposed by Jurczak and co-workers using computations.

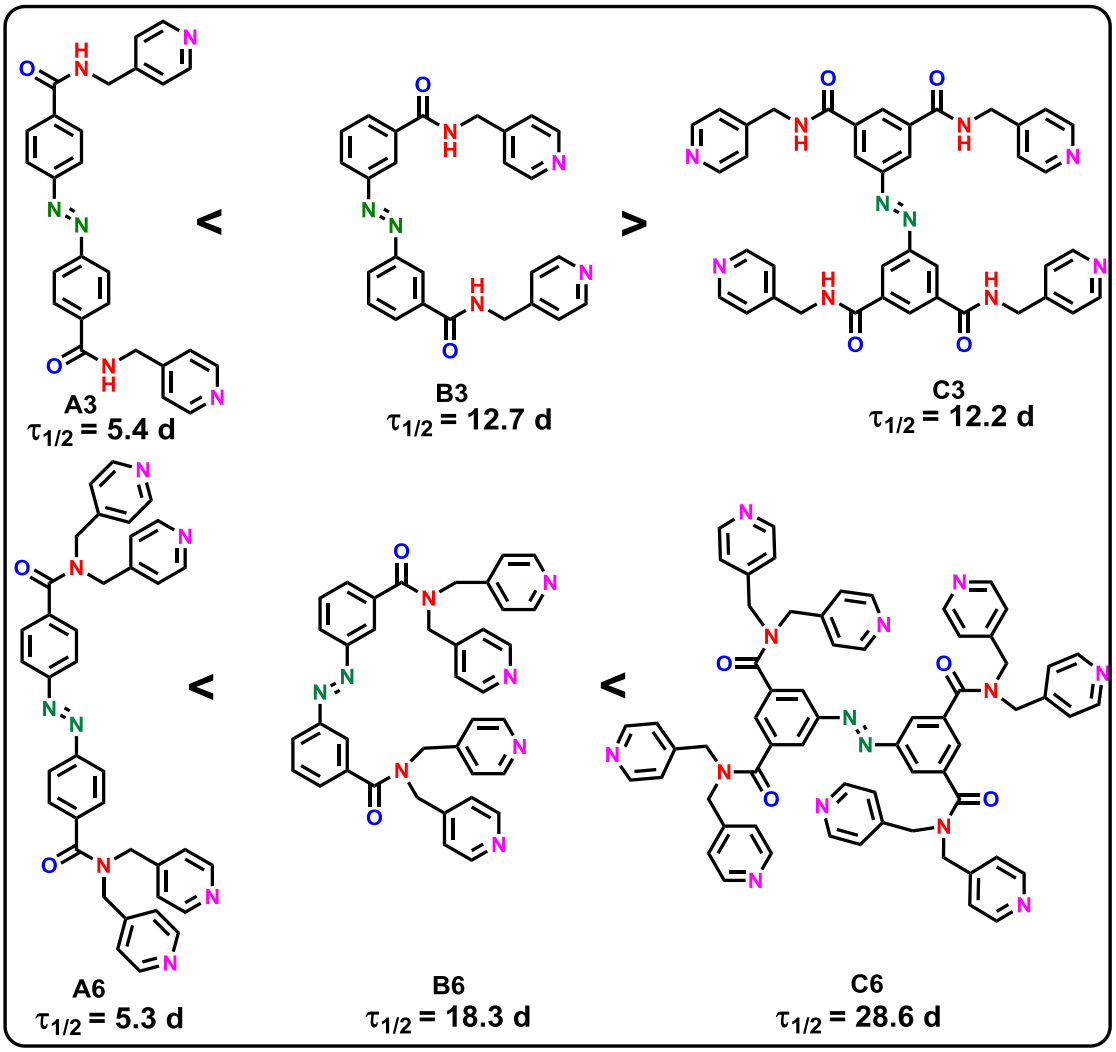

Figure 2.10 Comparison of half-lives of *Z*-isomer with 4- picolinyl group substitution.

Moreover, the observed trends in the half-lives have also been supportive of this model. Evidently, the 3,3'-disubstituted and 3,3',5,5'- tetrasubstituted have higher half-lives compared to that of 4,4'-disubstituted systems. Counterintuitively, the geometrical constraints and the conformational preferences of the phenyl rings may not allow higher propensity for hydrogen bonding in 3,3',5,5'- tetrasubstituted systems; in other words, dual hydrogen bonding is unfavourable due to the tilting of the phenyl rings to form H-bonding in one side. As a result, their *Z*-isomeric stability is comparable to that of 3,3'-disubstituted system only. On the other hand, the

distance between the carbonyl of one phenyl ring and N-H of the other ring increases, which slightly reduces the H-bonding propensity that dictates the lowering of half-lives.

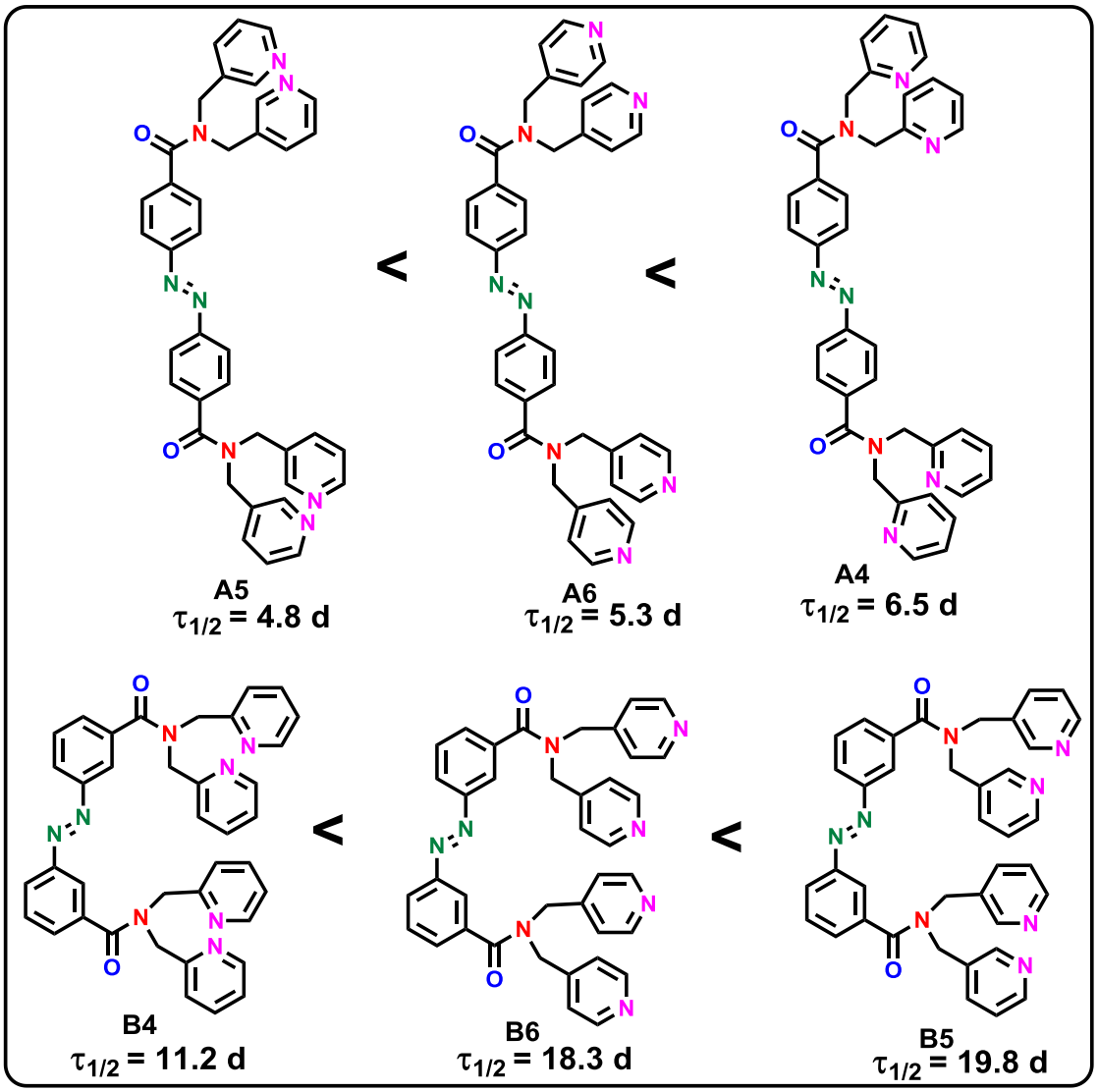

Figure 2.11 Comparison of half-lives of *Z*-isomer in tertiary amide substitution.

On the other hand, the systems with tertiary amides have showed a prominent enhancement in the *Z*-isomeric stability. With the loss of H-bonding and the steric factors due to more crowding, in principle, such derivatives can increase the rate of thermal reverse isomerization and decrease their half-lives. At this juncture, we assume electronic and/or other non-covalent interactions could be responsible for such extra stabilization and the surprising enhancement in the half-lives. According to a recent study by Wegner and co-workers, non-covalent interactions such as London dispersion and van der Waals forces have been proposed for the stabilization of *Z*-isomeric states of the azobenzenes with bulky substitutions. Taking cue from this work, such non-covalent interactions including π-π interactions and dipole-dipole interactions could assist in stabilizing the *Z*-isomers **(Figure 2.14)**. Particularly, the presence of picolinyl groups having aromatic π-cloud and large dipoles can be supportive of this assumption. In addition, by changing the connectivity of

picolinyl group, the stability of the *Z*-isomeric states exhibits modulation. Presumably, the presence of more picolinyl groups (eight units) could cause more steric repulsion in the transition state rather than in the *Z*-isomeric form, which leads to increase in the barrier. Again, such destabilization of the transition states has been reported for adamantly groups connected azobezenes.[6]

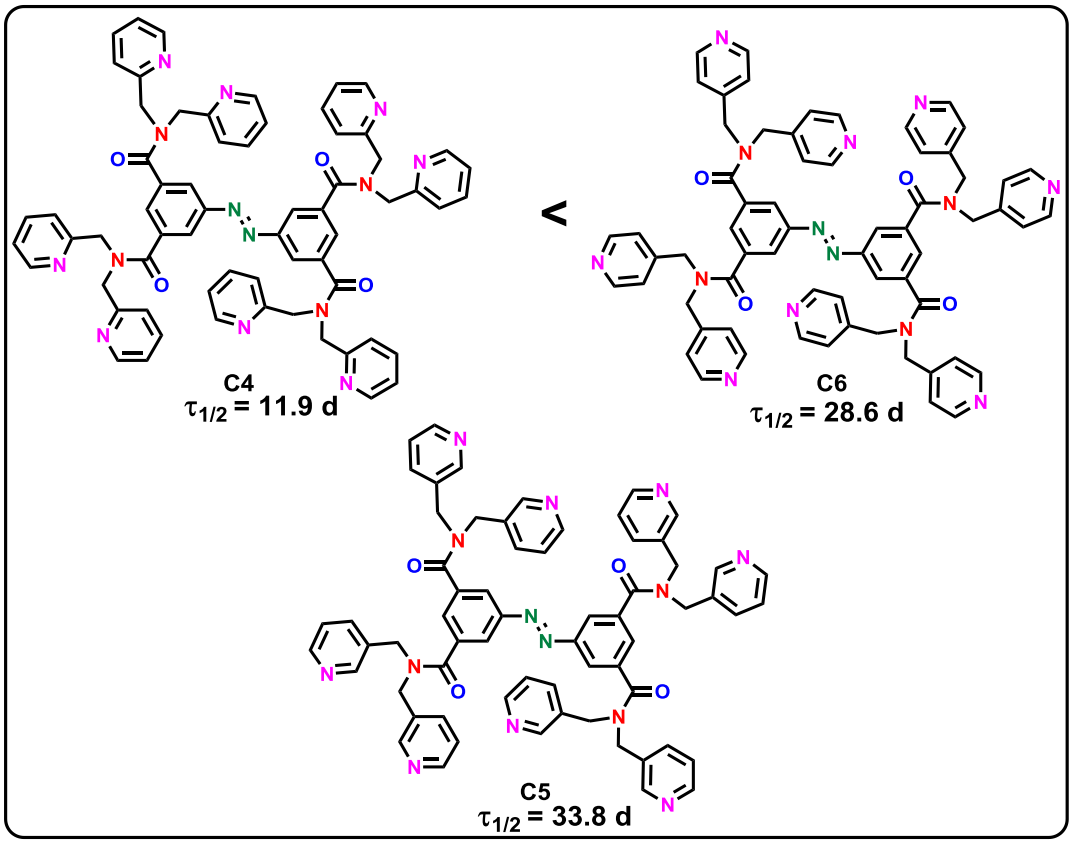

Figure 2.12 Comparison of half-lives of *Z*-isomer in tertiary amide substitution.

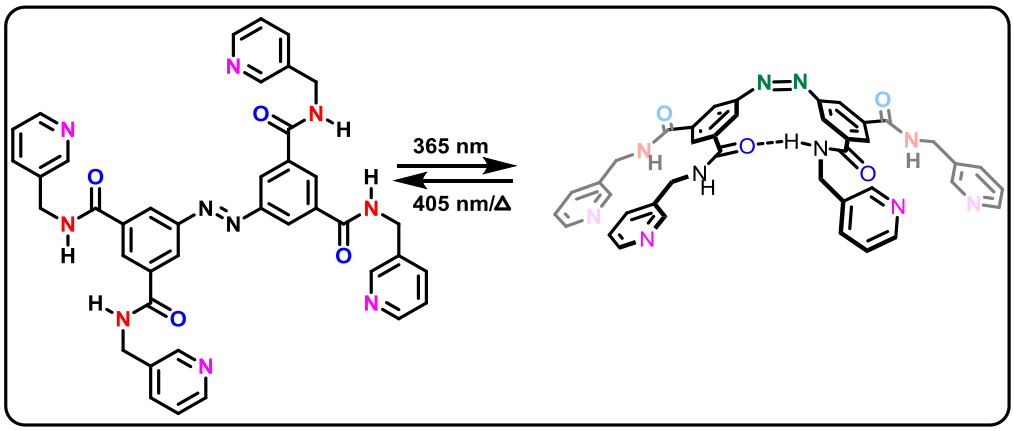

Figure 2.13 Intramolecular H-bonding Stabilization.

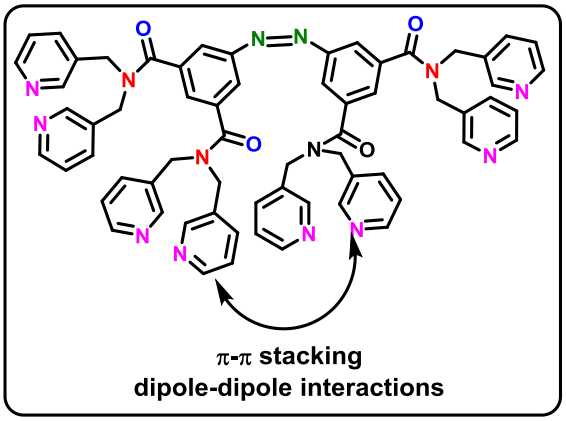

Figure 2.14 Weak interactions based Stabilization.

Table 2.5 Activation parameters associated with the thermal reverse isomerization step (in DMSO).

Compound	E_a	$\Delta G^{\ddagger}$	$\Delta H^{\ddagger}$	$\Delta S^{\ddagger}$
A1	99.9 ± 2.3[a]	95.0 ± 3.0[a]	97.0 ± 2.3[a]	6.7 ± 6.7[b]
A2	100.0 ± 2.0[a]	95.0 ± 2.6[a]	97.1 ± 2.0[a]	6.9 ± 5.7[b]
A3	100.7 ± 2.2[a]	95.1 ± 3.0[a]	97.8 ± 2.3[a]	9.0 ± 6.5[b]
A4	106.8 ± 1.7[a]	96.0 ± 2.3[a]	104.0 ± 1.7[a]	26.6 ± 5.0[b]
A5	101.1 ± 1.2[a]	95.4 ± 1.6[a]	98.2 ± 1.2[a]	9.4 ± 3.5[b]
A6	105.0 ± 0.9 [a]	94.5 ± 0.9[a]	86.9 ± 0.7[a]	-25.5 ± 2.0[b]
B1	100.1 ± 2.4[a]	97.5 ± 3.2[a]	97.2 ± 2.4[a]	-0.9 ± 6.9[b]
B2	100.7 ± 1.6[a]	97.4 ± 2.1[a]	97.8 ± 1.6[a]	1.5 ± 4.6[b]
B3	103.2 ± 2.0[a]	97.9 ± 2.6[a]	100.3 ± 2.0[a]	8.1 ± 5.7[b]
B4	103.3 ± 1.8[a]	97.9 ± 2.3[a]	100.4 ± 1.76[a]	8.3 ± 5.1[b]
B5	104.8 ± 0.5[a]	99.0 ± 0.7[a]	101.9 ± 0.6[a]	9.5 ± 1.6[b]
B6	105.0 ± 0.8[a]	99.0 ± 1.0[a]	102.1 ± 0.8[a]	10.3 ± 2.2[b]
C1	102.5 ± 1.6[a]	97.8 ± 2.2[a]	99.6 ± 1.7[a]	6.11 ± 4.8[b]
C2	99.3 ± 2.2[a]	97.3 ± 2.9[a]	96.3 ± 2.2[a]	-3.2 ± 6.2[b]
C3	104.4 ± 1.3[a]	98.2 ± 1.6[a]	101.6 ± 1.2[a]	11.4 ± 3.6[b]
C4	107.2 ± 0.4[a]	97.8 ± 0.6[a]	104.3 ± 0.4[a]	21.8 ± 1.3[b]
C5	105.3 ± 2.7[a]	99.8 ± 3.5[a]	102.4 ± 2.7[a]	8.6 ± 7.7[b]
C6	112.8 ± 2.4[a]	100.7 ± 3.5[a]	110.2 ± 2.7[a]	32.0 ± 7.6[b]

[a]kJ mol^{-1}; [b]J K^{-1}.

Furthermore, using the variable temperature kinetics measurements, and utilizing Arrhenius and Eyring plots, the activation parameters (E_a, $\Delta H^{\ddagger}$, $\Delta S^{\ddagger}$, and $\Delta G^{\ddagger}$) were estimated. On comparing the derivatives of secondary carboxamides, it is evident that activation energy (*E*a), Gibbs free energy ($\Delta G^{\ddagger}$) and enthalpy ($\Delta H^{\ddagger}$) showed an increase upon varying the substitution pattern from type A to type B; however, type B systems have almost similar values as that of type C, which is well corroborating with our thermal reverse isomerisation trends **(Table 2.5 and Appendix 2D)**.

Except **A3** and **A6** pair, the comparison of entropy of activation for the rest of the pairs of secondary and tertiary amides indicates a strong destabilization of transition states by bringing tertiary amides. The same trend is also observed in the enthalpy of activation. Since the non-covalent interactions are weak in nature, rather than stabilization of *Z*-isomers, the destabilization factor of the transition state could be responsible for the higher half-lives for the *Z*-isomers in the tertiary amides. In the case 2-, 3-, and 4-picolinyl substitutions, both the enthalpy and entropy factors do not follow any trend across different classes. Presumably, in such cases, the difference in the strength of weak interactions lead to such observed variations in the rate constants and the half-lives.

2.6 Supramolecular Studies

Since one of the important objectives is to understand the propensity of each target molecule for the formation of photoswitchable supramolecular assemblies. Particularly, all the targets appended with amide functional groups, which are well known for supramolecular assembly formation. To unravel this, experiment with incremental addition of water was performed and followed using UV-vis spectroscopy for a selected compounds **A1** and **C5 (Figure 2.15)**.

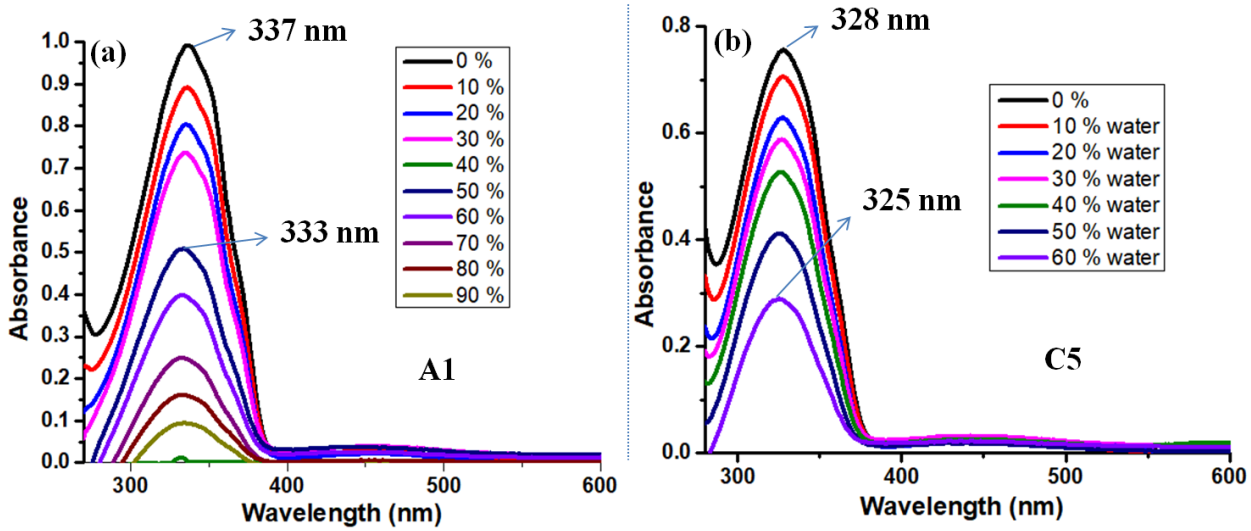

Figure 2.15 Aggregation experiment with incremental addition of water in DMSO solutions of (a) **A1** (32 μM) and (b) **C5** (29 μM) using UV-vis Spectroscopy.

Here, we observed a slight blue shift for both the samples upon addition of water. For **A1**, it shifts from 337 to 333 nm, whereas for **C5**, it shows a shift from 328 to 325 nm. Despite small shifts, a significant drop in the intensity in π–π* band indicating aggregation in both the targets. Interestingly, if the concentration is increased from micromolar to millimolar, under similar conditions, we observed the formation of tiny microcrystals. Indeed, such microcrystal formation in DMSO/H_2O solution was observed in three different classes of compounds **A1**, **B5**, and **C5**. After careful filtration of the microcrystals, they were subjected to microscopic studies using SEM and POM **(Figure 2.16-2.18)**. The inspection of SEM images revealed an aggregation with irregular shapes in all the three compounds, however, with systematic layered arrangement.

Surprisingly, the microcrystals of all the three compounds exhibited birefringence in the POM indicating their crystalline nature. However, upon subjecting them to irradiation with 365 nm of light, the microcrystals started disappearance of birefringence. More importantly, the extent of disappearance was little in **A1**, partial in **B5**, whereas it was completely disappeared in the case of **C5**. These clearly confirm the influence of light in disassembly in these targets. Due to the trapped solvent molecules during the microcrystal formation, the irradiation at 365 nm led to phase transition to isotropic phase in unequal extent in **A1**, **B5**, and **C5**.

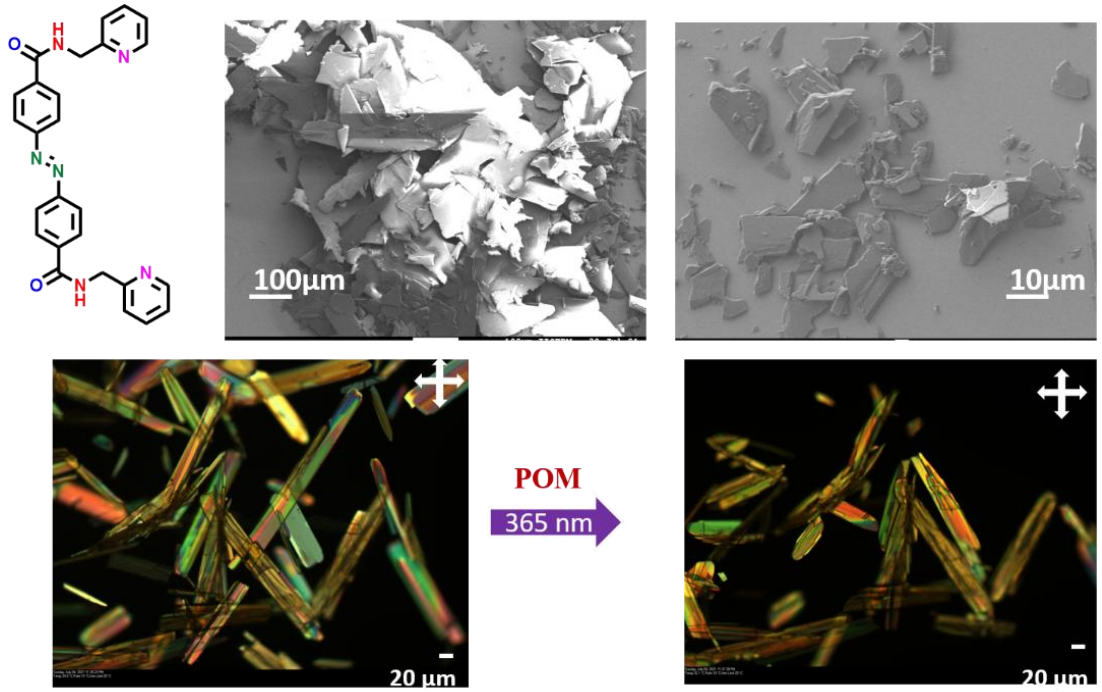

Figure 2.16 SEM and POM images of microcrystals of **A1** and the POM monitoring of partial disappearance of birefringence due to the microcrystals.

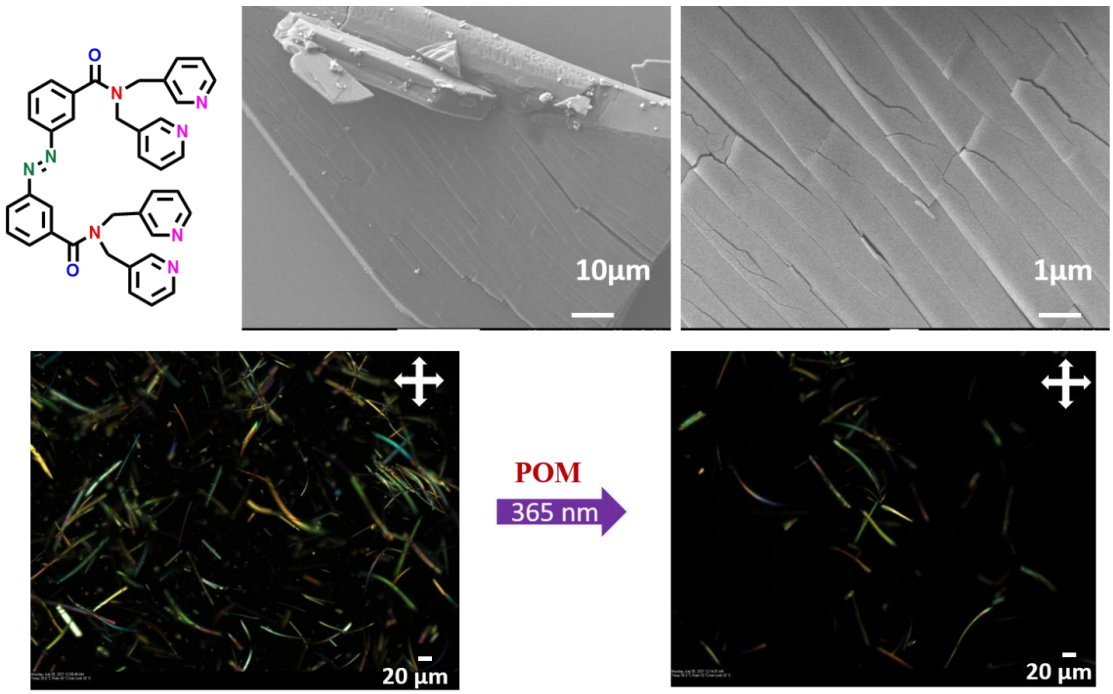

Figure 2.17 SEM and POM images of microcrystals of **B5** and the POM monitoring of partial disappearance of birefringence due to the microcrystals.

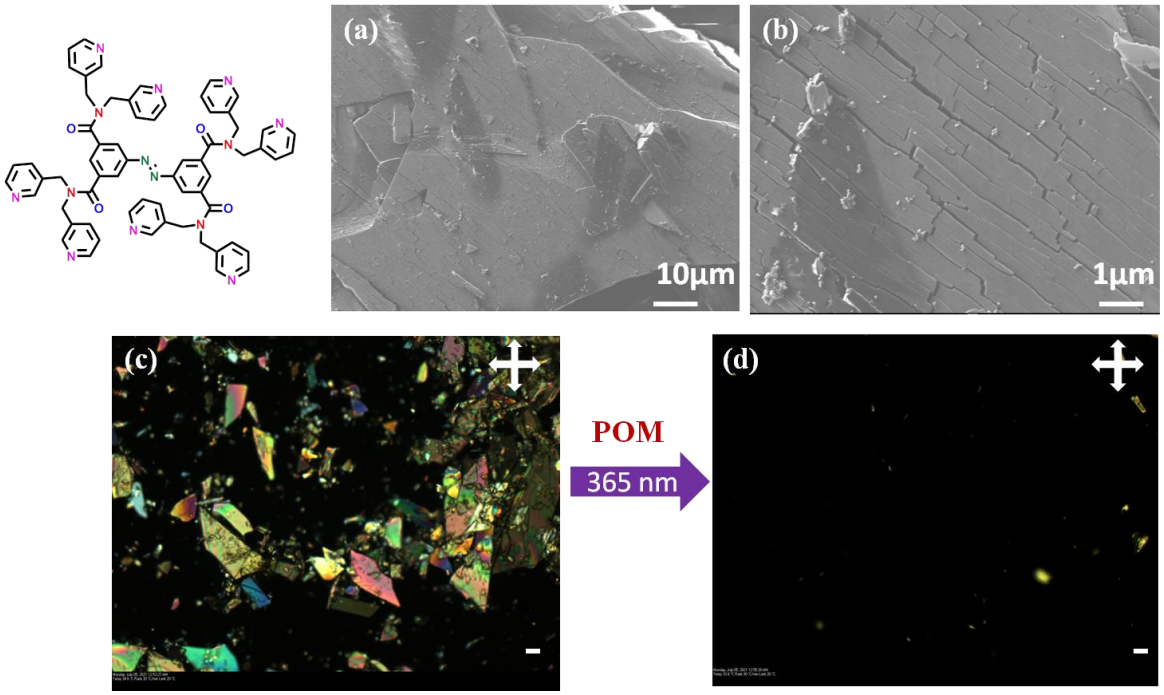

Figure 2.18 SEM and POM images of microcrystals of **C5** and the POM monitoring of partial disappearance of birefringence due to the microcrystals.

2.7 Summary

Herein, we have synthesized 18 photoresponsive molecular systems in moderate to high yields through a modular synthesis, having amide linkages for envisaging their aggregation and supramolecular behavior. All the designed targets have subtle variation at the connections to the

azobenzene core unit, position and orientations of picolinyl groups and the incorporation of 2^o vs 3^o amide groups. Through systematic variations in the designs, we have evaluated the structure-property relationships primarily on the photoswitching process. Furthermore, we have also investigated the effect of structural modifications on the *Z*-isomeric thermal stability. Among the 4,4′ and 3,3′ substitutions on the azobenzene, the former derivatives exhibit fast thermal relaxation in all the cases irrespective of the 2^o and 3^o amide connections compared to the latter. However, when the substitution is extended to 3,3′,5,5′, then the half-life is increased in the case of 3^o amides, whereas minimal increment was observed in the case of 2^o amides. Further, the formation of microcrystals was observed in few derivatives, revealed their tendency to form aggregation. The changes in the morphology of supramolecular assembly/microcrystals have been studied using polarized optical microscopy (POM), and scanning electron microscopy (SEM), and the effect of photoisomerization on their morphology revealed a photoswitchable supramolecular assembly in these systems.

2.8 Experimental Section

Synthesis of Azobenzene-4,4'-dicarboxylic acid and Azobenzene-3,3'-dicarboxylic acid :

4-Nitrobenzoic acid or 3- Nitrobenzoic acid (5.00 g, 30 mmol) and sodium hydroxide (17 g) were mixed in water (75 mL) and heated until the solid dissolved. A hot aqueous solution of glucose (30 g in 50 mL water) was added dropwise into the above solution at 50 ^oC. The solution was left to react at room temperature for 8 hours and the produced brown precipitates were filtered and washed with saturated NaCl solution. The precipitates were then dissolved in water and carefully acidified by acetic acid (20 mL) to produce pink precipitates. The final product was filtered, washed with water and dried in vacuum to yield Azobenzene-4,4'-dicarboxylic acid or Azobenzene-3,3'-dicarboxylic acid.

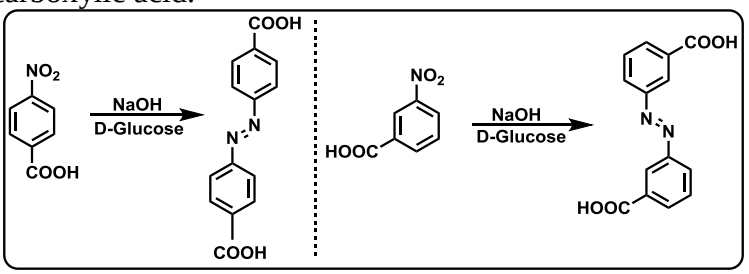

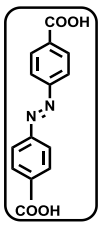

(*E*)-4,4'-(diazene-1,2-diyl)dibenzoic acid

Pink colored solid, 50% yield. ^1H NMR (400 MHz, [D_6]DMSO): δ (ppm) 13.28 (br, 2H), 8.16 (d, J = 8.4 Hz, 4H), 8.01 (d, J = 8.4 Hz, 4H); ^{13}C NMR (100 MHz, [D_6]DMSO): δ (ppm) 167.2, 154.5, 134.0, 131.1, 123.2.

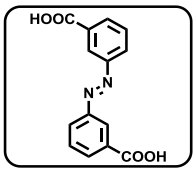

(*E*)-3,3'-(diazene-1,2-diyl)dibenzoic acid

Mud colored solid, 55% yield. ^{1}H NMR (400 MHz, [D_6]DMSO): δ (ppm) 13.36 (br, 2H), 8.40 (s, 2H), 8.18-8.12 (m, 4H), 7.74 (t, J = 7.8 Hz, 2H); ^{13}C NMR (100 MHz, [D_6]DMSO): δ (ppm) 167.1, 152.2, 132.7, 132.6, 130.4, 128.0, 122.8.

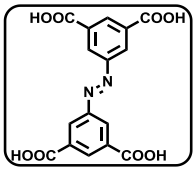

(*E*)-5,5'-(diazene-1,2-diyl)diisophthalic acid

Orange colored solid, 53% yield. ^{1}H NMR (400 MHz, [D_6]DMSO): δ (ppm) 13.57 (br, 4H), 8.57-8.52 (m, 6H); ^{13}C NMR (100 MHz, [D_6]DMSO): δ (ppm) 166.3, 152.0, 133.2, 132.9, 127.4.

Synthesis of (*E*)-5,5'-(diazene-1,2-diyl)diisophthalic acid:

5-nitroisophtalic acid (19 g) and sodium hydroxide (50 g) were suspended in 250 mL of Milli-Q water and reacted at 60 °C with continuous stirring for 1 hour. Then, in another flask, glucose (100 g) was dissolved in 100 mL of warm water which was added dropwise to the slurry. After addition, the mixture was kept to cool down for 30 minutes followed by exposure to an air stream for 16 hours with continuous stirring at room temperature. The crude product was isolated by filtration under vacuum. The solid portion was dissolved in 250 mL of water and was acidified with 37% HCl. Final product was filtered, washed with water and dried in an oven.

Synthesis of (A1), (A2), (A3) -

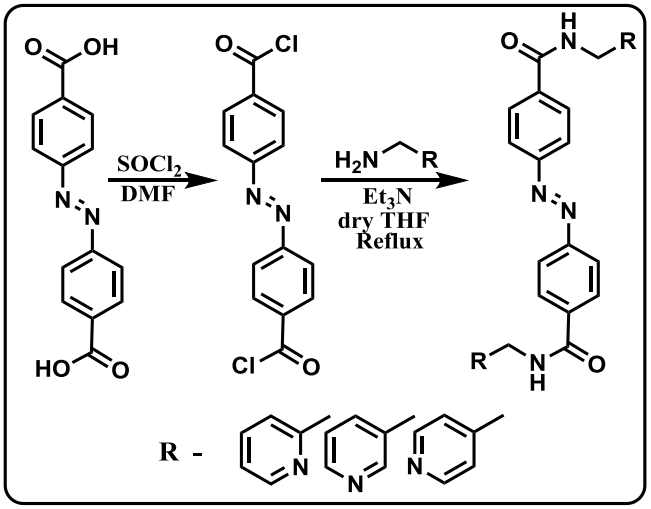

In a round bottom flask, azobenzene-4,4-dicarboxylic acid (500 mg, 1.9 mmol) was dissolved in 5 mL of thionyl chloride, then the mixture was refluxed at 70 °C for 5 h, yielding a clear red solution. Excess thionyl chloride was removed by distillation, and approximately 450 mg of crude 4,4-bis(chlorocarbonyl) azobenzene as a red solid was obtained. The obtained product was used directly for the next step without further purification. After this, in another two necked round bottom flask, respective aminomethylpyridine (475 mg, 4.4 mmol) was dissolved in 20.0 mL dry THF and

triethylamine (741 mg, 7.3 mmol) was slowly added to it. Azobenzene 4,4′-dicarbonyl chloride (450 mg, 1.5 mmol) dissolved in 15 mL dry THF was added dropwise to resulting solution. The reaction mixture was then stirred at 60 ^{O}C for 24 h. The yellow precipitate obtained was filtered and dried.

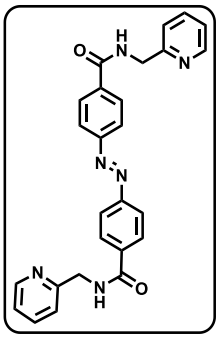

(*E*)-4,4'-(diazene-1,2-diyl)bis(N-(pyridin-2-ylmethyl)benzamide)

(A1): Orange solid, mp= 230-235 °C, 80% yield. ^{1}H NMR (400 MHz, $CDCl_3$): δ (ppm) 8.60-8.59 (m, 2H), 8.06-8.00 (m, 8H), 7.77-7.69 (m, 4H), 7.35 (d, J = 7.8 Hz, 2H), 7.26-7.23 (m, 2H), 4.80 (d, J = 4.7 Hz, 4H); ^{13}C NMR (100 MHz, $CDCl_3$): δ(ppm) 166.7, 156.1, 154.2, 148.9, 137.4, 136.6, 128.3, 123.3, 122.83, 122.82, 44.8; IR (ATR): 3294, 3066, 2930, 1629, 1539, 1460, 1296, 855, 766, 680 cm^{-1}; HRMS (ESI-TOF): *m/z* calcd. for $C_{26}H_{22}N_6O_2$ $[M+H]^+$: 451.1882; found : 451.1862.

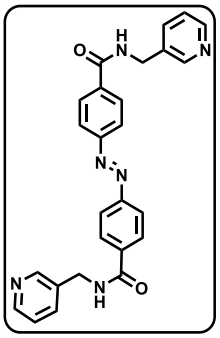

(*E*)-4,4'-(diazene-1,2-diyl)bis(N-(pyridin-3-ylmethyl)benzamide)

(A2): Orange solid, mp= 195-200 °C, 78% yield. ^{1}H NMR (400 MHz, $[D_6]$DMSO): δ (ppm) 9.31 (brs, 2H), 8.59-8.48 (m, 4H), 8.13-8.00 (m, 8H), 7.76 (d, J = 6.5 Hz, 2H), 7.37 (s, 2H), 4.54 (s, 4H); ^{13}C NMR (100 MHz, $[D_6]$DMSO): δ(ppm) 165.6, 153.3, 148.9, 148.2, 136.7, 135.2, 134.9, 128.7, 123.5, 122.7, 40.6; IR (ATR): 3286, 3042, 2933, 1628, 1534, 1423, 1285, 857, 790, 697 cm^{-1}; HRMS (ESI-TOF): *m/z* calcd. for $C_{26}H_{22}N_6O_2$ $[M+H]^+$: 451.1882; found : 451.1896.

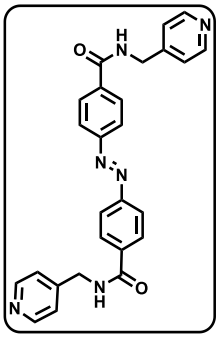

(E)-4,4'-(diazene-1,2-diyl)bis(N-(pyridin-4-ylmethyl)benzamide)

(A3): Orange solid, mp= 238-242 °C, 75% yield. ^{1}H NMR (400 MHz, $[D_6]$DMSO): δ (ppm) 9.36 (t, J = 5.8 Hz, 2H), 8.53-8.51 (m, 4H), 8.14 (d, J = 8.6 Hz, 4H), 8.03 (d, J = 8.6 Hz, 4H), 7.34 (d, J = 5.9 Hz, 4H), 4.54 (d, J = 5.9 Hz, 4H); ^{13}C NMR (100 MHz, $[D_6]$DMSO): δ(ppm) 165.7, 153.3, 149.5, 148.4, 136.5, 128.7, 122.7, 122.3, 41.9; IR (ATR): 3345, 3049, 2924, 1645, 1542, 1420, 1276, 865, 792, 701 cm^{-1}; HRMS (ESI-TOF): *m/z* calcd. for $C_{26}H_{22}N_6O_2$ $[M+H]^+$: 451.1882; found : 451.1901.

Synthesis of (B1), (B2), (B3) –

In a round bottom flask, azobenzene-3,3-dicarboxylic acid (500 mg, 1.9 mmol) was dissolved in 5 mL of thionyl chloride, then the mixture was refluxed at 70 °C for 5 h, yielding a clear red solution. Excess thionyl chloride was removed by distillation, and approximately 450 mg of crude 3,3-bis(chlorocarbonyl) azobenzene as a red solid was obtained. The obtained product was used directly for the next step without further purification. After this, in another two necked round

bottom flask, respective aminomethylpyridine (475 mg, 4.4 mmol) was dissolved in 20.0 mL dry THF and triethylamine (741 mg, 7.3 mmol) was slowly added to it. Azobenzene 3,3′-dicarbonyl chloride (450 mg, 1.5 mmol) dissolved in 15 mL dry THF was added dropwise to resulting solution. The reaction mixture was then stirred at 60 ^{O}C for 24 h. The yellow precipitate obtained was filtered and dried.

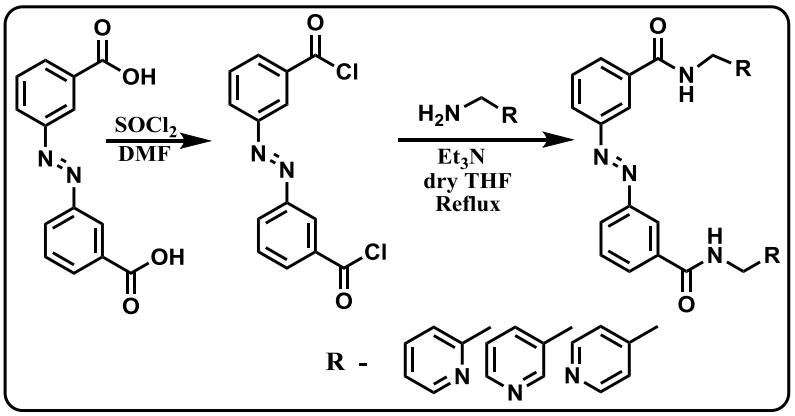

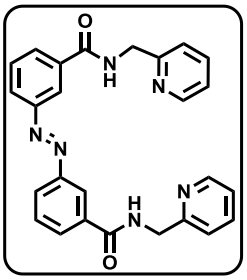

(*E*)-3,3'-(diazene-1,2-diyl)bis(N-(pyridin-2-ylmethyl)benzamide)

(B1): Orange solid, mp= 180-185 °C, 85% yield. ^{1}H NMR (400 MHz, [D$_6$]DMSO): δ (ppm) 9.40 (t, J = 5.8 Hz, 2H), 8.52 (d, J = 4.6 Hz, 2H), 8.48 (s, 2H), 8.15-8.10 (m, 4H), 7.79-7.73 (m, 4H), 7.36 (d, J = 7.8 Hz, 2H), 7.27 (dd, J = 5.3, 7.1 Hz, 2H), 4.62 (d, J = 5.8 Hz, 4H); ^{13}C NMR (100 MHz, [D$_6$]DMSO): δ(ppm) 165.6, 158.6, 151.8, 148.9, 136.8, 135.6, 130.5, 129.8, 125.5, 122.2, 121.4, 121.1, 41.9; IR (ATR): 3299, 3066, 2929, 1651, 1542, 1308, 914, 751, 700 cm^{-1}; HRMS (ESI-TOF): *m/z* calcd. for $C_{26}H_{22}N_6O_2$ $[M+H]^+$: 451.1882; found : 451.1892.

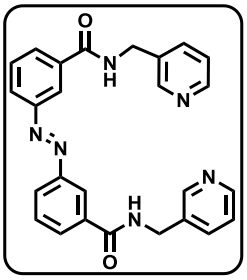

(E)-3,3'-(diazene-1,2-diyl)bis(N-(pyridin-3-ylmethyl)benzamide)

(B2): Orange solid, mp= 220-225 °C, 80% yield. ^{1}H NMR (400 MHz, [D$_6$]DMSO): δ (ppm) 9.36 (t, J = 5.7 Hz, 2H), 8.59 (d, J = 1.6 Hz, 2H), 8.47 (dd, J = 1.2, 4.7 Hz, 2H), 8.44 (brs, 2H), 8.11-8.09 (m, 4H), 7.77-7.72 (m, 4H), 7.37 (dd, J = 4.8, 7.8 Hz, 2H), 4.54 (d, J = 5.8 Hz, 4H); ^{13}C NMR (100 MHz, [D$_6$]DMSO): δ(ppm) 165.5, 151.8, 148.9, 148.2, 135.5, 135.3, 134.9, 130.4, 129.8, 125.4, 123.6, 121.4, 40.6; IR (ATR): 3253, 3042, 2934, 1644, 1422, 1282, 1206, 941, 809, 748 cm^{-1}; HRMS (ESI-TOF): *m/z* calcd. for $C_{26}H_{22}N_6O_2$ $[M+H]^+$: 451.1882; found : 451.1888.

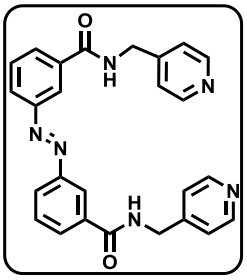

(E)-3,3'-(diazene-1,2-diyl)bis(N-(pyridin-2-ylmethyl)benzamide) (B3): Orange solid, mp= 215-220 °C, 85% yield. ^{1}H NMR (400 MHz, [D$_6$]DMSO): δ (ppm) 9.40 (t, J = 5.8 Hz, 2H), 8.52 (d, J = 5.6 Hz, 4H), 8.47 (brs, 2H), 8.14-8.11 (m, 4H), 7.76 (t, J = 7.8 Hz, 2H), 7.34 (d, J = 5.6 Hz, 4H), 4.55 (d, J = 5.8 Hz, 4H); ^{13}C NMR (100 MHz, [D$_6$]DMSO): δ(ppm) 165.7, 151.8, 149.6, 148.4, 135.4, 130.5, 129.9, 125.6, 122.2, 121.4, 41.9; IR (ATR): 3266, 3077, 2934, 1651, 1545, 1421, 1305, 1221, 989, 816, 695 cm^{-1}; HRMS (ESI-TOF): *m/z* calcd. for $C_{26}H_{22}N_6O_2$ $[M+H]^+$: 451.1882; found : 451.1876.

Synthesis of (C1), (C2), C3) –

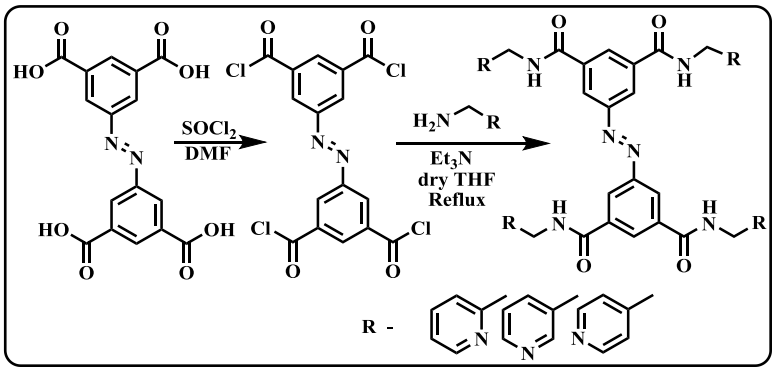

In a round bottom flask, azobenzene-3,3’,5,5’-tetracarboxylic acid (500 mg, 1.4 mmol) was dissolved in 5 mL of thionyl chloride, then the mixture was refluxed at 70 °C for 5 h, yielding a clear red solution. Excess thionyl chloride was removed by distillation, and approximately 450 mg of crude 3,3’,5,5’-tetra(chlorocarbonyl) azobenzene as a red solid was obtained. The obtained product was used directly for the next step without further purification. After this, in another two necked round bottom flask, respective aminomethylpyridine (563 mg, 5.2 mmol) was dissolved in 20.0 mL dry THF and triethylamine (738 mg, 7.3 mmol) was slowly added to it. Azobenzene 3,3′,5,5’-tetracarbonyl chloride (450 mg, 1.0 mmol) dissolved in 15 mL dry THF was added dropwise to resulting solution. The reaction mixture was then stirred at 60 ^{o}C for 24 h. The yellow precipitate obtained was filtered and dried.

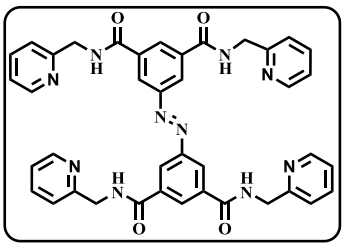

(*E*)-5,5'-(diazene-1,2-diyl)bis(N1,N3-bis(pyridin-2-ylmethyl)isophthalamide) (C1): Yellow solid, mp= 265-270 °C, 82% yield. ^{1}H NMR (400 MHz, [D$_6$]DMSO): δ (ppm) 9.52 (t, *J* = 5.8 Hz, 4H), 8.70-8.68 (m, 6H), 8.53-8.52 (m, 4H), 7.78 (td, *J* = 1.7, 7.7 Hz, 4H),7.38 (d, *J* = 7.8 Hz, 4H), 7.28 (dd, *J* = 5.1, 7.0 Hz, 4H), 4.64 (d, *J* = 5.8 Hz, 8H); ^{13}C-NMR (100 MHz, [D$_6$]DMSO): δ (ppm) 165.1, 158.5, 151.7, 148.9, 136.8, 135.9, 129.5, 124.0, 122.2, 121.1, 45.0; IR (ATR): 3276, 3073, 2935, 2348, 1643, 1543, 1426, 1288, 1224, 1018, 904, 699 cm^{-1}; HRMS (ESI): *m/z* calcd. for $C_{40}H_{34}N_{10}O_4$ $[M+H]^+$: 719.2843; found: 719.2878.

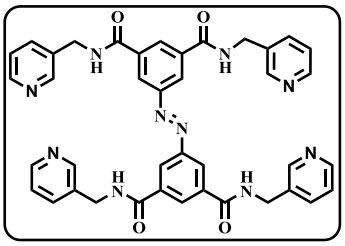

(*E*)-5,5'-(diazene-1,2-diyl)bis(N1,N3-bis(pyridin-3-ylmethyl)isophthalamide) (C2): Yellow solid, mp= 260-265 °C, 80% yield. ^{1}H NMR (400 MHz, [D$_6$]DMSO): δ (ppm) 9.50 (t, *J* = 5.6 Hz, 4H), 8.63-8.61 (m, 10H), 8.48 (d, *J* = 4.0 Hz, 4H), 7.79-7.77 (m, 4H), 7.38 (dd, *J* = 4.8, 7.6 Hz, 4H), 4.57 (d, *J* = 5.6 Hz, 8H); ^{13}C-NMR (100 MHz, [D$_6$]DMSO): δ (ppm) 165.1, 151.7, 149.0, 148.2, 135.9, 135.4, 134.8, 129.5, 124.0, 123.6, 40.8; IR (ATR): 3268, 3111, 3042, 2348, 1645, 1532, 1424, 1278, 1033, 914, 811, 700 cm^{-1}; HRMS (ESI): *m/z* calcd. for $C_{40}H_{34}N_{10}O_4$ $[M+H]^+$: 719.2843; found: 719.2841.

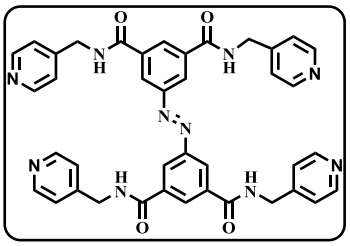

(*E*)-5,5'-(diazene-1,2-diyl)bis(N1,N3-bis(pyridin-4-ylmethyl)isophthalamide) (C3): Yellow solid, mp= 265-270 °C, 78% yield. ^{1}H NMR (400 MHz, [D$_6$]DMSO): δ (ppm) 9.55 (t, *J* = 5.8 Hz, 4H), 8.681-8.677 (m, 6H), 8.53-8.52 (m, 8H), 7.36-7.35 (m, 8H), 4.56 (d, *J* = 5.8 Hz, 8H); ^{13}C-NMR (100 MHz, [D$_6$]DMSO): δ (ppm) 165.2, 151.7, 149.6, 148.3, 135.8, 129.5, 124.1, 122.3, 42.0; IR (ATR): 3270, 3055, 2935, 2353, 1655, 1538, 1422, 1280, 1016, 910, 800, 687 cm^{-1}; HRMS (ESI): *m/z* calcd. for $C_{40}H_{34}N_{10}O_4$ $[M+H]^+$: 719.2843; found: 719.2842.

Synthesis of (A4), (A5), (A6) –

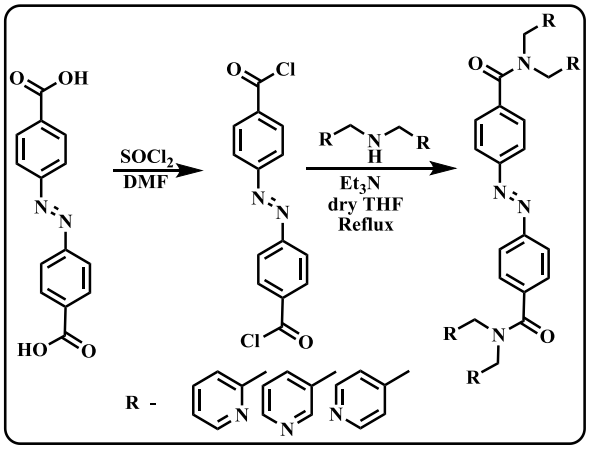

In a round bottom flask, azobenzene-4,4-dicarboxylic acid (500 mg, 1.9 mmol) was dissolved in 5 mL of thionyl chloride, then the mixture was refluxed at 70 °C for 5 h, yielding a clear red solution. Excess thionyl chloride was removed by distillation, and approximately 450 mg of crude 4,4-bis(chlorocarbonyl) azobenzene as a red solid was obtained. The obtained product was used directly for the next step without further purification. After this, in another two necked round bottom flask, respective bis-picolylamine (876 mg, 4.4 mmol) was dissolved in 20.0 mL dry THF and triethylamine (741 mg, 7.3 mmol) was slowly added to it. Azobenzene 4,4′-dicarbonyl chloride (450 mg, 1.5 mmol) dissolved in 15 mL dry THF was added dropwise to resulting solution. The reaction mixture was then stirred at 60 ^{O}C for 24 h. The yellow precipitate obtained was filtered and dried.

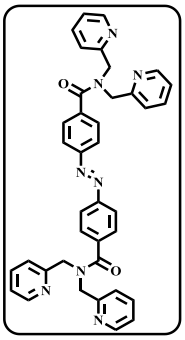

(*E*)-4,4'-(diazene-1,2-diyl)bis(N,N-bis(pyridin-2-ylmethyl)benzamide) (A4): Yellow solid, mp= 178-185 °C, 82% yield. ^{1}H NMR (400 MHz, [D$_6$]DMSO): δ (ppm) 8.59-8.53 (m, 4H), 7.90 (d, *J* = 8.4 Hz, 4H), 7.82-7.76 (m, 4H), 7.73 (d, *J* = 8.4 Hz, 4H), 7.42 (d, *J* = 7.7 Hz, 2H), 7.32-7.29 (m, 4H), 7.25 (d, *J* = 7.8 Hz, 2H), 4.73 (s, 4H), 4.64 (s, 4H) ; ^{13}C-NMR (100 MHz, $CDCl_3$): δ (ppm) 171.9, 157.0, 156.4, 153.0, 150.1, 149.5, 138.7, 136.9, 128.2, 123.1, 122.8, 122.7, 122.6, 121.7, 54.5, 50.6; IR (ATR): 3059, 2934, 1639, 1433, 1280, 1157, 997, 857, 757 cm^{-1}; HRMS (ESI): *m/z* calcd. for $C_{38}H_{32}N_8O_2$ $[M+H]^+$: 633.2726; found: 633.2736.

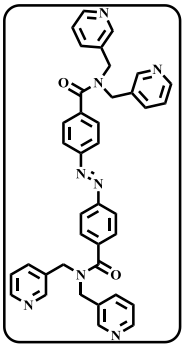

(E)-4,4'-(diazene-1,2-diyl)bis(N,N-bis(pyridin-3-ylmethyl)benzamide) (A5): Yellow solid, mp= 220-225 °C, 74% yield. ^{1}H NMR (400 MHz, [D$_6$]DMSO): δ (ppm) 8.53-8.48 (m, 6H), 8.34 (s, 2H), 7.94 (d, J = 8.4 Hz, 4H), 7.78-7.59 (m, 8H), 7.40-7.32 (m, 4H), 4.69 (s, 4H), 4.57 (s, 4H); ^{13}C-NMR (100 MHz, [D$_6$]DMSO): δ (ppm) 170.8, 152.1, 149.2, 148.8, 148.6, 138.8, 135.7, 135.68, 135.1, 135.0, 132.9, 132.2, 128.0, 123.8, 123.0, 50.2, 46.0; IR (ATR): 3018, 2930, 1633, 1424, 1267, 1000, 853, 798, 721 cm^{-1}; HRMS (ESI): *m/z* calcd. for $C_{38}H_{32}N_8O_2$ $[M+H]^+$: 633.2726; found: 633.2734.

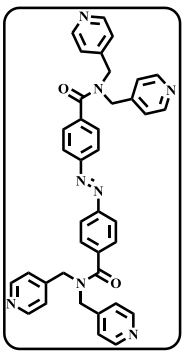

(E)-4,4'-(diazene-1,2-diyl)bis(N,N-bis(pyridin-3-ylmethyl)benzamide) (A6): Yellow solid, mp= 225-230 °C, 76% yield. ^{1}H NMR (400 MHz, [D$_6$]DMSO): δ (ppm) 8.55-8.52 (m, 8H), 7.91 (d, J = 7.6 Hz, 4H), 7.71 (d, J = 7.3 Hz, 4H), 7.36-7.23 (m, 8H), 4.70 (s, 4H), 4.57 (s, 4H); ^{13}C-NMR (100 MHz, [D$_6$]DMSO): δ (ppm) 170.8, 152.1, 149.9, 149.8, 146.1, 145.8, 138.5, 127.8, 122.9, 122.4, 121.9, 51.6, 47.5; IR (ATR): 3045, 2926, 1624, 1420, 1263, 1150, 989, 860, 793, 719 cm^{-1}; HRMS (ESI): *m/z* calcd. for $C_{38}H_{32}N_8O_2$ $[M+H]^+$: 633.2726; found: 633.2728.

Synthesis of (B4), (B5), (B6) –

In a round bottom flask, azobenzene-3,3-dicarboxylic acid (500 mg, 1.9 mmol) was dissolved in 5 mL of thionyl chloride, then the mixture was refluxed at 70 °C for 5 h, yielding a clear red solution. Excess thionyl chloride was removed by distillation, and approximately 450 mg of crude 3,3-bis(chlorocarbonyl) azobenzene as a red solid was obtained. The obtained product was used directly for the next step without further purification. After this, in another two necked round bottom flask, respective bis-picolylamine (876 mg, 4.4 mmol) was dissolved in 20.0 mL dry THF and triethylamine (741 mg, 7.3 mmol) was slowly added to it. Azobenzene 3,3′-dicarbonyl chloride (450 mg, 1.5 mmol) dissolved in 15 mL dry THF was added dropwise to resulting solution. The reaction mixture was then stirred at 60 ^{o}C for 24 h. The yellow precipitate obtained was filtered and dried.

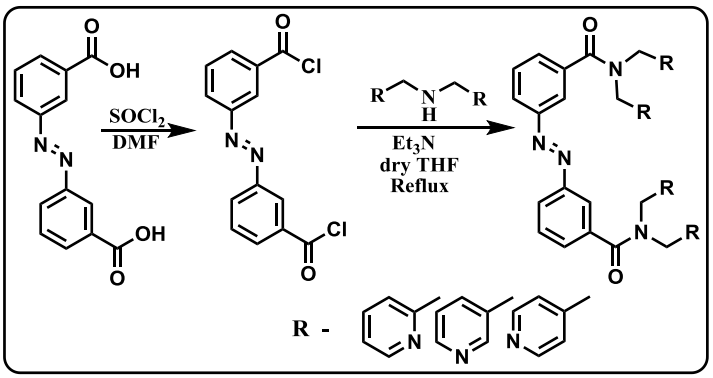

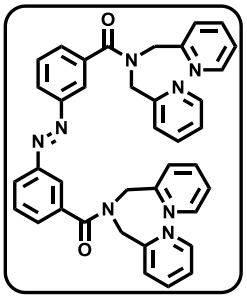

(*E*)-3,3'-(diazene-1,2-diyl)bis(N,N-bis(pyridin-2-ylmethyl)benzamide) (B4): Yellow solid, mp= 120-125 °C, 84% yield. ^{1}H NMR (400 MHz, [D$_6$]DMSO): δ (ppm) 8.60-8.54 (m, 4H), 7.94-7.92 (m, 4H), 7.84-7.72 (m, 6H), 7.67-7.63 (m, 2H), 7.44 (d, *J* = 7.6 Hz, 2H), 7.33-7.25 (m, 6H), 4.75 (s, 4H), 4.66 (s, 4H) ; ^{13}C-NMR (100 MHz, [D$_6$]DMSO): δ (ppm) 170.5, 156.8, 156.1, 151.4, 149.5, 149.2, 137.4, 137.04, 137.0, 130.0, 129.8, 124.7, 122.8, 122.4, 122.1, 121.8, 120.0, 54.1, 50.4; IR (ATR): 3062, 2936, 1638, 1427, 1284, 1178, 998, 937, 751 cm^{-1}; HRMS (ESI): *m/z* calcd. for $C_{38}H_{32}N_8O_2$ $[M+H]^+$: 633.2726; found: 633.2723.

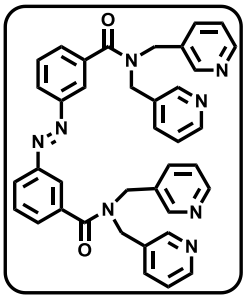

(*E*)-3,3'-(diazene-1,2-diyl)bis(N,N-bis(pyridin-3-ylmethyl)benzamide) (B5): Yellow solid, mp= 155-160 °C, 77% yield. ^{1}H NMR (400 MHz, [D$_6$]DMSO): δ (ppm) 8.53-8.33 (m, 8H), 7.94-7.88 (m, 4H), 7.77-7.60 (m, 8H), 7.36-7.34 (m, 4H), 4.70 (s, 4H), 4.58 (s, 4H); ^{13}C-NMR (100 MHz, [D$_6$]DMSO): δ (ppm) 170.5, 151.5, 149.2, 148.7, 148.6, 148.5, 137.0, 135.6, 134.8, 132.8, 132.2, 130.0, 129.7, 124.3, 123.7 (2C), 120.2, 50.2, 46.0; IR (ATR): 3040, 2933, 1637, 1424, 1277, 1184, 921, 807, 717 cm^{-1}; HRMS (ESI): *m/z* calcd. for $C_{38}H_{32}N_8O_2$ $[M+H]^+$: 633.2726; found: 633.2732.

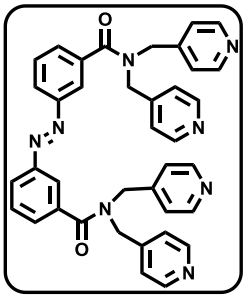

(*E*)-3,3'-(diazene-1,2-diyl)bis(N,N-bis(pyridin-4-ylmethyl)benzamide) (B6): Yellow solid, mp= 217-223 °C, 70% yield. ^{1}H NMR (400 MHz, [D$_6$]DMSO): δ (ppm) 8.57-8.54 (m, 8H), 7.93 (d, *J* = 7.0 Hz, 2H), 7.87 (s, 4H), 7.71-7.64 (m, 4H), 7.38 (s, 4H), 7.25 (s, 4H), 4.73 (s, 4H), 4.60 (s, 4H); ^{13}C-NMR (100 MHz, [D$_6$]DMSO): δ (ppm) 170.8, 151.4, 149.98, 149.88, 146.14, 146.10, 136.7, 130.2, 129.8, 124.6, 122.5, 122.0, 120.1, 51.8, 47.8; IR (ATR): 3043, 2933, 1629, 1421, 1281, 1206, 939, 808, 725 cm^{-1}; HRMS

(ESI): *m/z* calcd. for $C_{38}H_{32}N_8O_2$ $[M+H]^+$: 633.2726; found: 633.2727.

Synthesis of (C4), (C5), C6) –

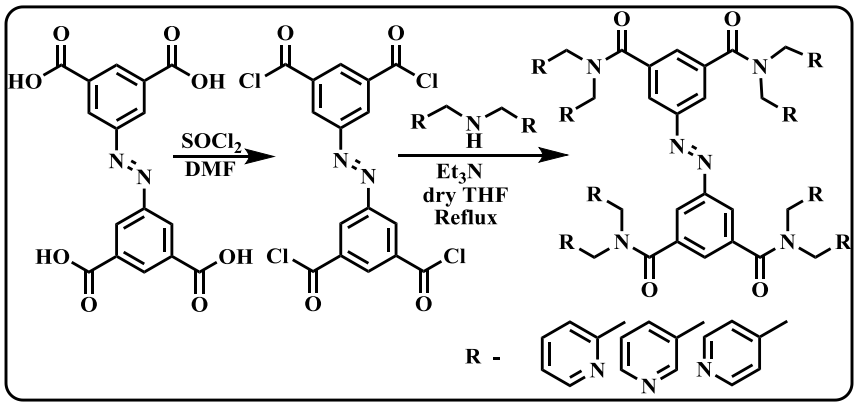

In a round bottom flask, azobenzene-3,3',5,5'-tetracarboxylic acid (500 mg, 1.4 mmol) was dissolved in 5 mL of thionyl chloride, then the mixture was refluxed at 70 °C for 5 h, yielding a clear red solution. Excess thionyl chloride was removed by distillation, and approximately 450 mg of crude 3,3',5,5'-tetra(chlorocarbonyl) azobenzene as a red solid was obtained. The obtained product was used directly for the next step without further purification. After this, in another two necked round bottom flask, respective bis-picolylamine (1453 mg, 7.3 mmol) was dissolved in 20.0 mL dry THF and triethylamine (1052 mg, 10.4 mmol) was slowly added to it. Azobenzene 3,3',5,5'-tetracarbonyl chloride (450 mg, 1.0 mmol) dissolved in 15 mL dry THF was added dropwise to resulting solution. The reaction mixture was then stirred at 60 ^{O}C for 24 h. The yellow precipitate obtained was filtered and dried.

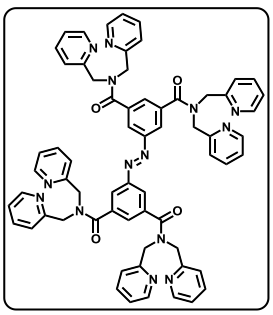

(*E*)-3,3'-(diazene-1,2-diyl)bis(N,N-bis(pyridin-2-ylmethyl)benzamide) (C4): Yellow solid, mp= 185-190 °C, 78% yield. ^{1}H NMR (400 MHz, [D_6]DMSO): δ (ppm) 8.56-8.52 (m, 8H), 7.96 (d, J = 1.4 Hz, 4H), 7.89 (t, J = 1.4 Hz, 2H), 7.84 (td, J = 1.6, 7.7 Hz, 4H), 7.70 (td, J = 1.5, 7.6 Hz, 4H), 7.41 (d, J = 7.8 Hz, 4H), 7.34 (dd, J = 5.2, 7.2 Hz, 4H), 7.24-7.20 (m, 8H), 4.72 (s, 8H), 4.56 (s, 8H); ^{13}C-NMR (100 MHz, [D_6]DMSO): δ (ppm) 169.7, 156.7, 156.0, 151.0, 149.4, 149.1, 137.6, 136.9 (2C), 128.2, 122.7, 122.4, 122.2, 121.9, 121.7, 53.9, 50.4; IR (ATR): 3062, 2936, 1640, 1426, 1216, 942, 835, 752 cm^{-1}; HRMS (ESI): *m/z* calcd. for $C_{64}H_{54}N_{14}O_4$ $[M+H]^+$: 1083.4531; found: 1083.4574.

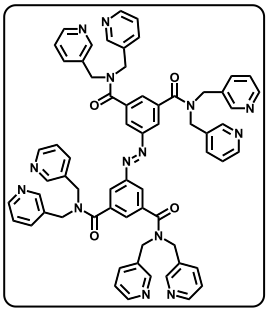

(E)-3,3'-(diazene-1,2-diyl)bis(N,N-bis(pyridin-3-ylmethyl)benzamide) (C5): Yellow solid, mp= 165-170 °C, 85% yield. ^{1}H NMR (400 MHz, [D$_6$]DMSO): δ (ppm) 8.53 (brs, 8H), 8.38-8.31 (m, 8H), 8.02-7.97 (m, 4H), 7.82 (s, 2H), 7.76-7.58 (m, 8H), 7.41-7.28 (m, 8H), 4.69 (s, 8H), 4.48 (s, 8H); ^{13}C-NMR (100 MHz, [D$_6$]DMSO): δ (ppm) 169.6, 151.3, 149.3, 148.7, 148.6, 137.5, 135.684, 135.678, 134.8, 132.7, 132.1, 127.7, 123.7 (2C), 121.9, 50.0, 46.1; IR (ATR): 3045, 2935, 1641, 1423, 1242, 1030, 918, 799, 718 cm^{-1}; HRMS (ESI): *m/z* calcd. for $C_{64}H_{54}N_{14}O_4[M+H]^+$: 1083.4531; found: 1083.4576.

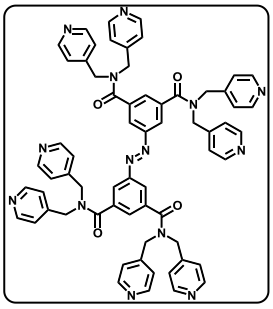

(E)-3,3'-(diazene-1,2-diyl)bis(N,N-bis(pyridin-4-ylmethyl)benzamide) (C6): Yellow solid, mp= 160-165 °C, 60% yield. ^{1}H NMR (400 MHz, [D$_6$]DMSO): δ (ppm) 8.58-8.51 (m, 16H), 7.92 (s, 4H), 7.81 (s, 4H), 7.35-7.21 (m, 16H), 4.71 (s, 8H), 4.44 (s, 8H); IR (ATR): 3043, 2928, 1632, 1415, 1228, 942, 805, 729 cm^{-1}; HRMS (ESI): *m/z* calcd. for $C_{64}H_{54}N_{14}O_4[M+H]^+$: 1083.4531; found: 1083.4539.

2.9 References

[1] H. M. D. Bandara, Shawn C. Burdette, *Chem. Soc. Rev.* **2012**, *41*, 1809-1825.

[2] a) F. A. Jerca, V. V. Jerca, R. Hoogenboom, *Nat. Rev. Chem.* **2022**, *6***,** 51–69; b) S. Grewal, D. Gupta, A. K. Gaur, M. Saraswat, S. Venkataramani, *Azoheteroarene photoswitches – Synthesis, Photoswitching and Utility*. In Photoisomerization: Causes, Behavior and Effects; Sampedro, D., Ed.; Nova Publishers, USA, **2019**; pp 111-188.

[3] J. Garcia–Amoros, D. Velasco, *Beilstein J. Org. Chem.* **2012**, *8*, 1003–1017.

[4] a) L. Kortekaas, J. Simke, N. B. Arndt, M. Böckmann, N. L. Doltsinis, B. J. Ravoo, *Chem. Sci.* **2021**, *12*, 11338–11346; b) S. Devi, M. Saraswat, S. Grewal, S. Venkataramani, *J. Org. Chem.* **2018**, *83*, 4307– 4322.

[5] a) D. Bléger, J. Schwarz, A. M. Brouwer, S. Hecht, *J. Am. Chem. Soc.* **2012**, *134*, 20597−20600; b) C. E. Weston, R. D. Richardson, P. R. Haycock, A. J. P. White, M. J. Fuchter, *J. Am. Chem. Soc.* **2014**, *136*, 11878−11881.

[6] L. Schweighauser, M. A. Strauss, S. Bellotto, H. A. Wegner, *Angew. Chem. Int. Ed.* **2015**, *54*, 13436 –13439.

[7] K. Dąbrowa, J. Jurczak, *Org. Lett.* **2017**, *19*, 1378−1381.

[8] a) G. Palui, A. Banerjee, *J. Phys. Chem. B* **2008**, *112*, 10107–10115; b) A. Panja, K. Ghosh, *New J. Chem.* **2019**, *43*, 934-945; c) J. Bachl , J. Mayr, F. J. Sayago, C. Cativiela, D. D. Díaz, *Chem. Commun.* **2015**, *51*, 5294-5297.

Appendix 2A

Photoswitching studies of the target molecules

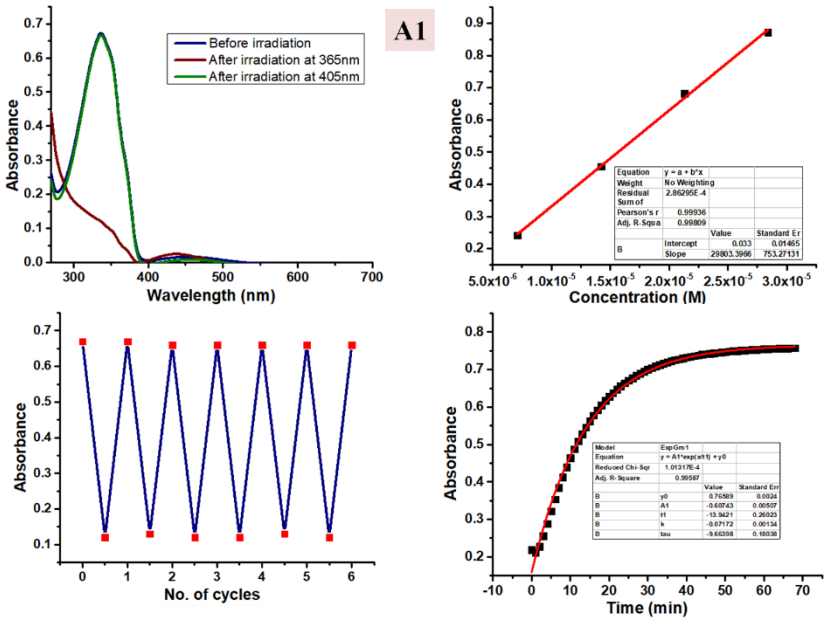

Figure 2A.1 UV-Vis spectroscopic data of **A1**: (a) Photoswitching studies performed in DMSO (24 μM); (b) Estimation of the molar absorption coefficient for π–π* absorption maxima; (c) Photoswitching stability test upto six cycles in DMSO (forward isomerization step: 365 nm; reverse isomerization step: 405 nm) and (d) first order thermal reverse isomerization kinetics plot and exponential fit at 80 ^{o}C.

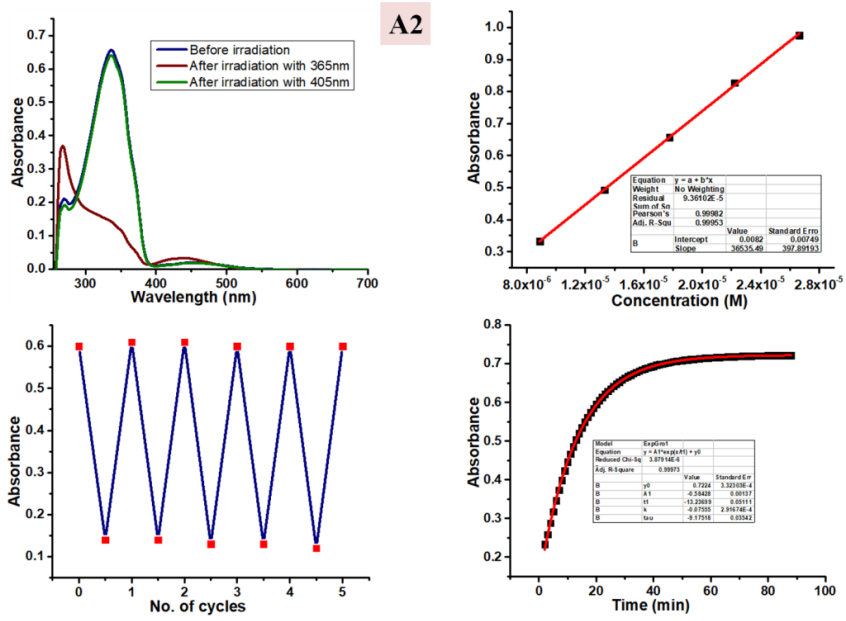

Figure 2A.2 UV-Vis spectroscopic data of **A2**: (a) Photoswitching studies performed in DMSO (19 μM); (b) Estimation of the molar absorption coefficient for π–π* absorption maxima; (c) Photoswitching stability test upto five cycles in DMSO (forward isomerization step: 365 nm; reverse isomerization step: 405 nm) and (d) First order thermal reverse isomerization kinetics plot and exponential fit at 80 ^{o}C.

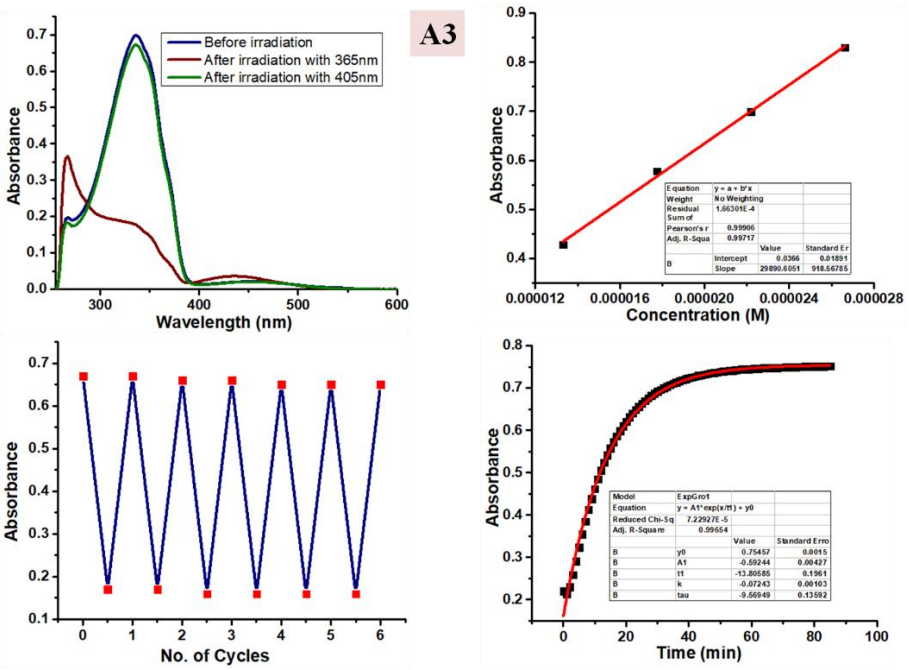

Figure 2A.3 UV-Vis spectroscopic data of **A3**: (a) Photoswitching studies performed in DMSO (24 μM); (b) Estimation of the molar absorption coefficient for π–π* absorption maxima; (c) Photoswitching stability test upto five cycles in DMSO (forward isomerization step: 365 nm; reverse isomerization step: 405 nm) and (d) First order thermal reverse isomerization kinetics plot and exponential fit at 80 ^{o}C.

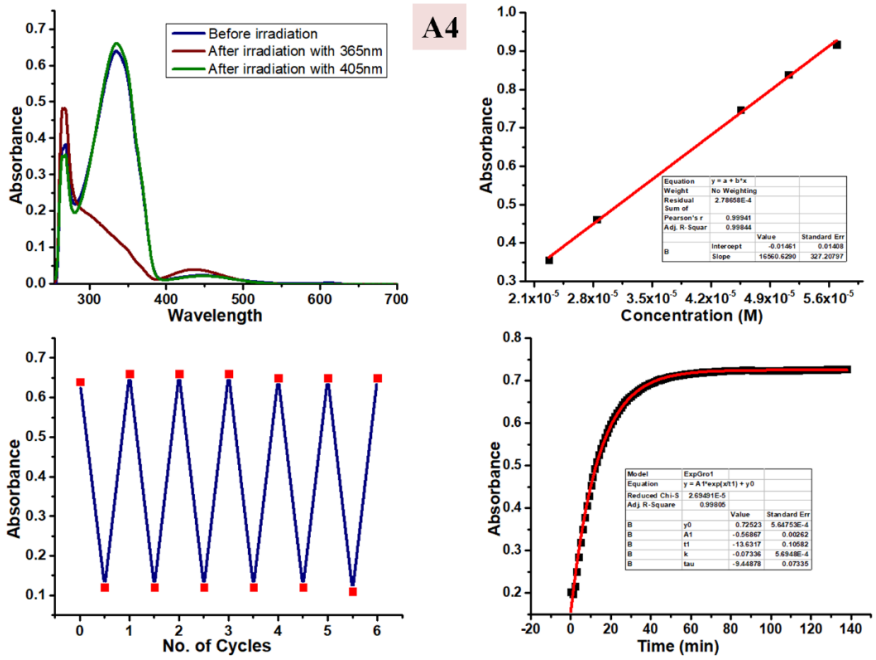

Figure 2A.4 UV-Vis spectroscopic data of **A4**: (a) Photoswitching studies performed in DMSO (42 μM); (b) Estimation of the molar absorption coefficient for π–π* absorption maxima; (c) Photoswitching stability test upto six cycles in DMSO (forward isomerization step: 365 nm; reverse isomerization step: 405 nm) and (d) First order thermal reverse isomerization kinetics plot and exponential fit at 80 ^{o}C.

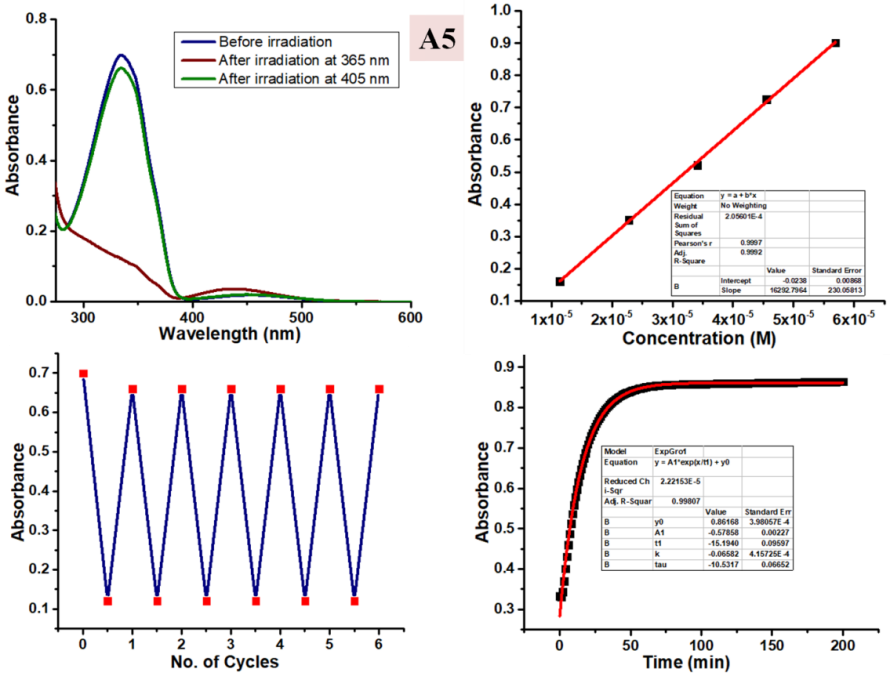

Figure 2A.5 UV-Vis spectroscopic data of **A5**: (a) Photoswitching studies performed in DMSO (44 μM); (b) Estimation of the molar absorption coefficient for π–π* absorption maxima; (c) Photoswitching stability test upto six cycles in DMSO (forward isomerization step: 365 nm; reverse isomerization step: 405 nm) and (d) First order thermal reverse isomerization kinetics plot and exponential fit at 80 ^{o}C.

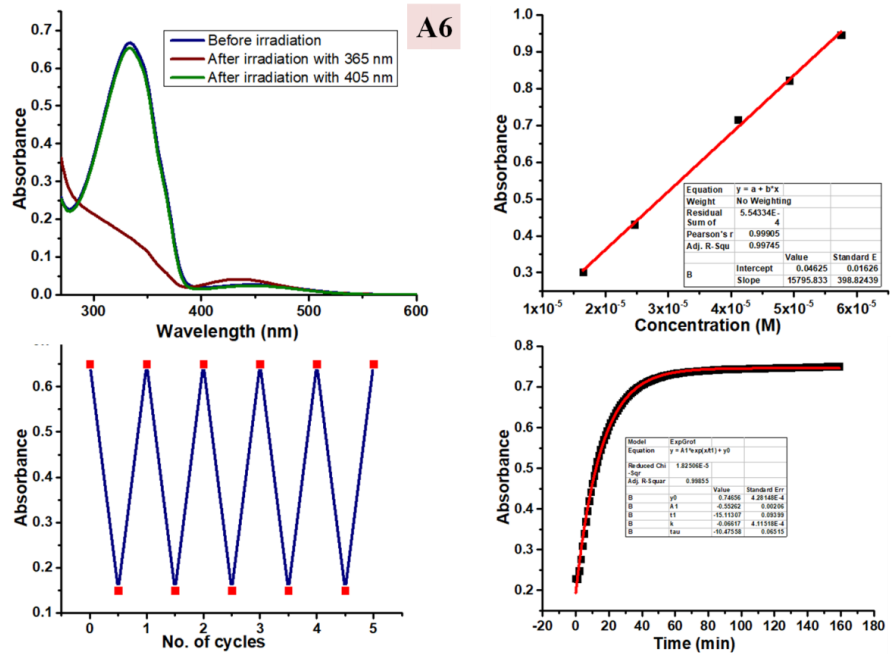

Figure 2A.6 UV-Vis spectroscopic data of **A6**: (a) Photoswitching studies performed in DMSO (46 μM); (b) Estimation of the molar absorption coefficient for π–π* absorption maxima; (c) Photoswitching stability test upto six cycles in DMSO (forward isomerization step: 365 nm; reverse isomerization step: 405 nm) and (d) First order thermal reverse isomerization kinetics plot and exponential fit at 80 ^{o}C.

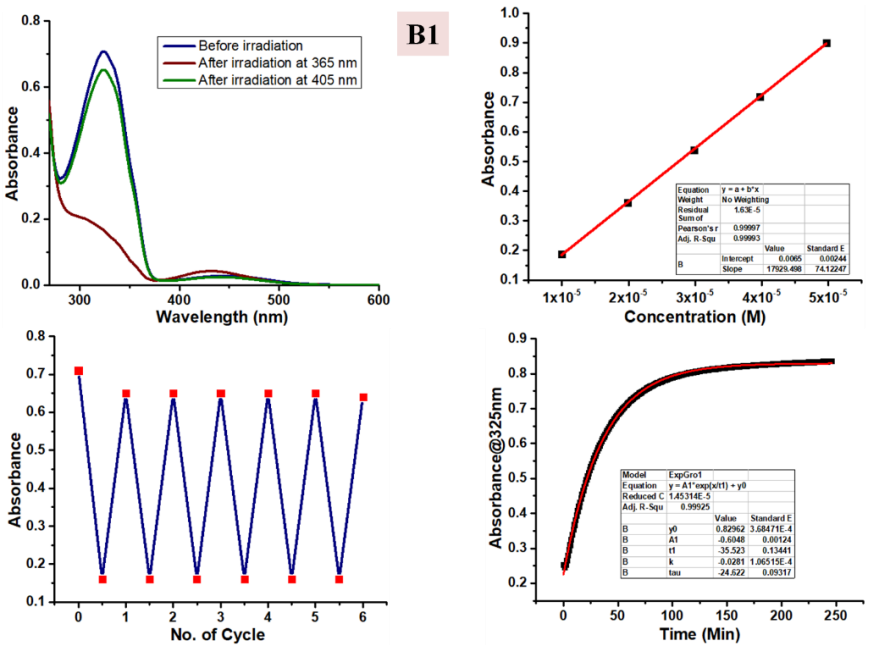

Figure 2A.7 UV-Vis spectroscopic data of **B1**: (a) Photoswitching studies performed in DMSO (42 μM); (b) Estimation of the molar absorption coefficient for π–π* absorption maxima; (c) Photoswitching stability test upto six cycles in DMSO (forward isomerization step: 365 nm; reverse isomerization step: 405 nm) and (d) First order thermal reverse isomerization kinetics plot and exponential fit at 80 ^{o}C.

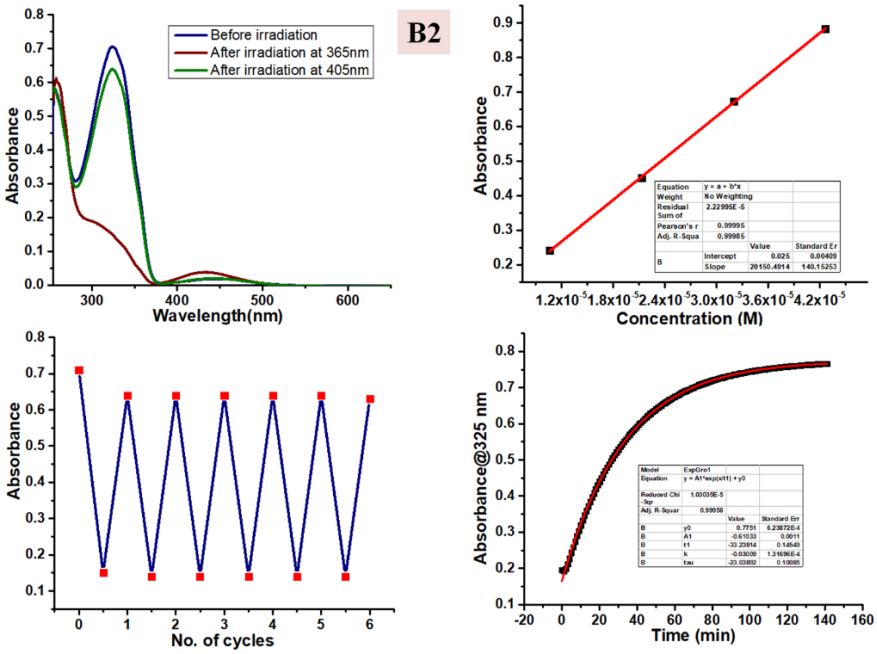

Figure 2A.8 UV-Vis spectroscopic data of **B2**: (a) Photoswitching studies performed in DMSO (37 μM); (b) Estimation of the molar absorption coefficient for π–π* absorption maxima; (c) Photoswitching stability test upto six cycles in DMSO (forward isomerization step: 365 nm; reverse isomerization step: 405 nm) and (d) First order thermal reverse isomerization kinetics plot and exponential fit at 80 ^{o}C.

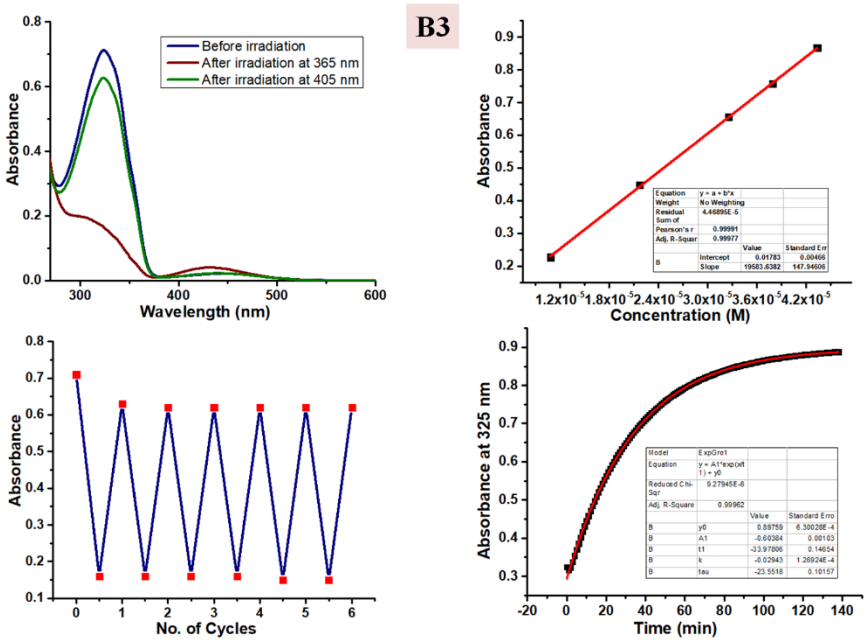

Figure 2A.9 UV-Vis spectroscopic data of **B3**: (a) Photoswitching studies performed in DMSO (41 μM); (b) Estimation of the molar absorption coefficient for π–π* absorption maxima; (c) Photoswitching stability test upto six cycles in DMSO (forward isomerization step: 365 nm; reverse isomerization step: 405 nm) and (d) First order thermal reverse isomerization kinetics plot and exponential fit at 80 ^{o}C.

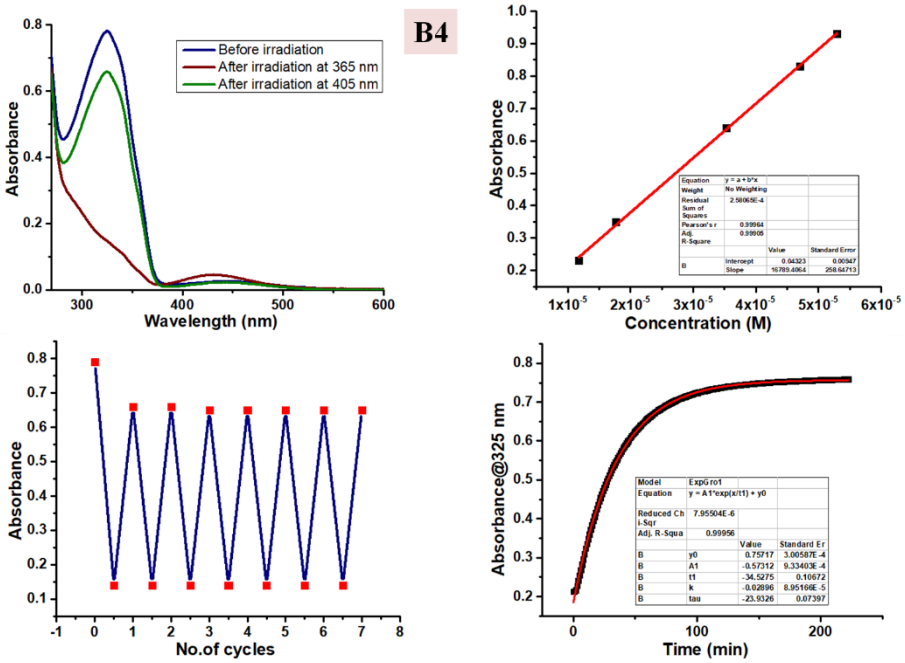

Figure 2A.10 UV-Vis spectroscopic data of **B4**: (a) Photoswitching studies performed in DMSO (41 μM); (b) Estimation of the molar absorption coefficient for π–π* absorption maxima; (c) Photoswitching stability test upto six cycles in DMSO (forward isomerization step: 365 nm; reverse isomerization step: 405 nm) and (d) First order thermal reverse isomerization kinetics plot and exponential fit at 80 ^{o}C.

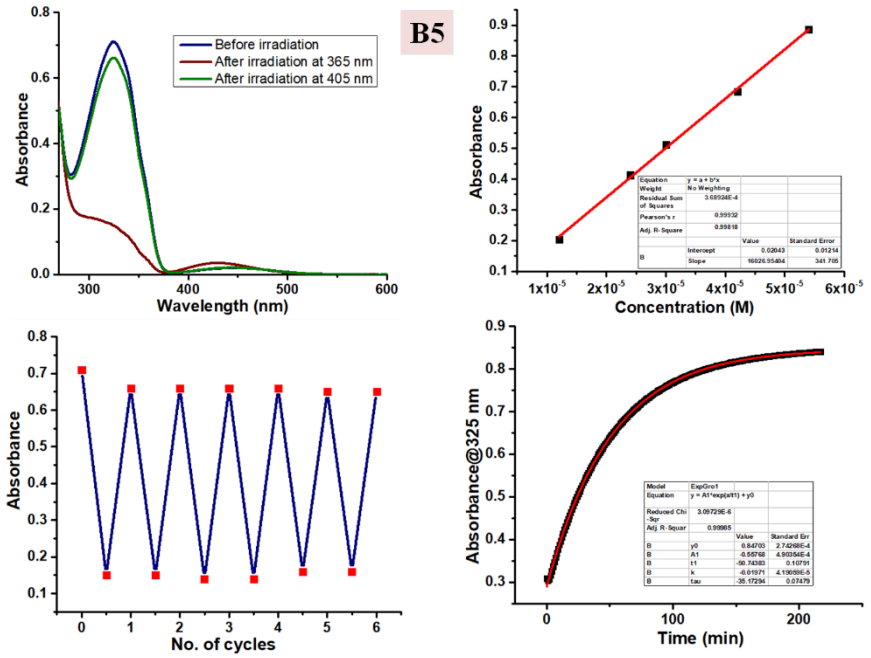

Figure 2A.11 UV-Vis spectroscopic data of **B5**: (a) Photoswitching studies performed in DMSO (45 μM); (b) Estimation of the molar absorption coefficient for π–π* absorption maxima; (c) Photoswitching stability test upto six cycles in DMSO (forward isomerization step: 365 nm; reverse isomerization step: 405 nm) and (d) First order thermal reverse isomerization kinetics plot and exponential fit at 80 ^{o}C.

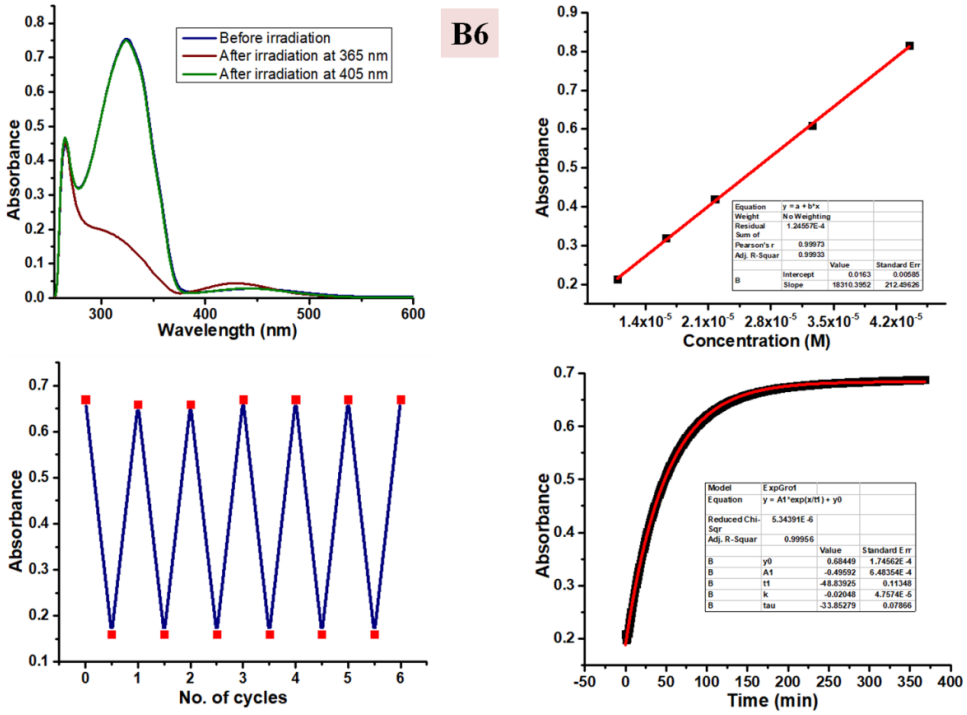

Figure 2A.12 UV-Vis spectroscopic data of **B6**: (a) Photoswitching studies performed in DMSO (35 μM); (b) Estimation of the molar absorption coefficient for π–π* absorption maxima; (c) Photoswitching stability test upto six cycles in DMSO (forward isomerization step: 365 nm; reverse isomerization step: 405 nm) and (d) First order thermal reverse isomerization kinetics plot and exponential fit at 80 ^{o}C.

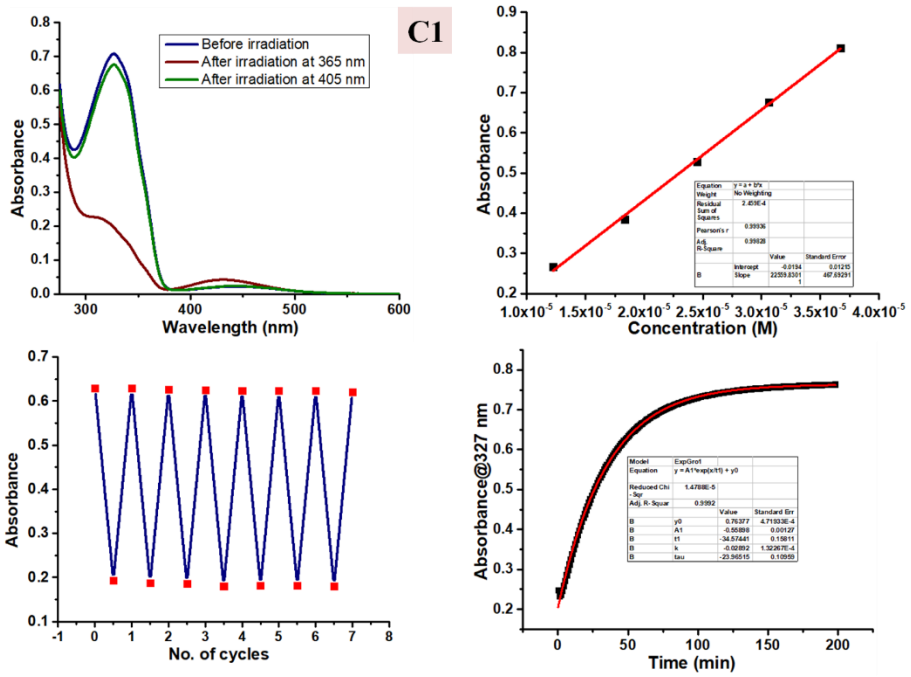

Figure 2A.13 UV-Vis spectroscopic data of **C1**: (a) Photoswitching studies performed in DMSO (32 μM); (b) Estimation of the molar absorption coefficient for π–π* absorption maxima; (c) Photoswitching stability test upto six cycles in DMSO (forward isomerization step: 365 nm; reverse isomerization step: 405 nm) and (d) First order thermal reverse isomerization kinetics plot and exponential fit at 80 ^{o}C.

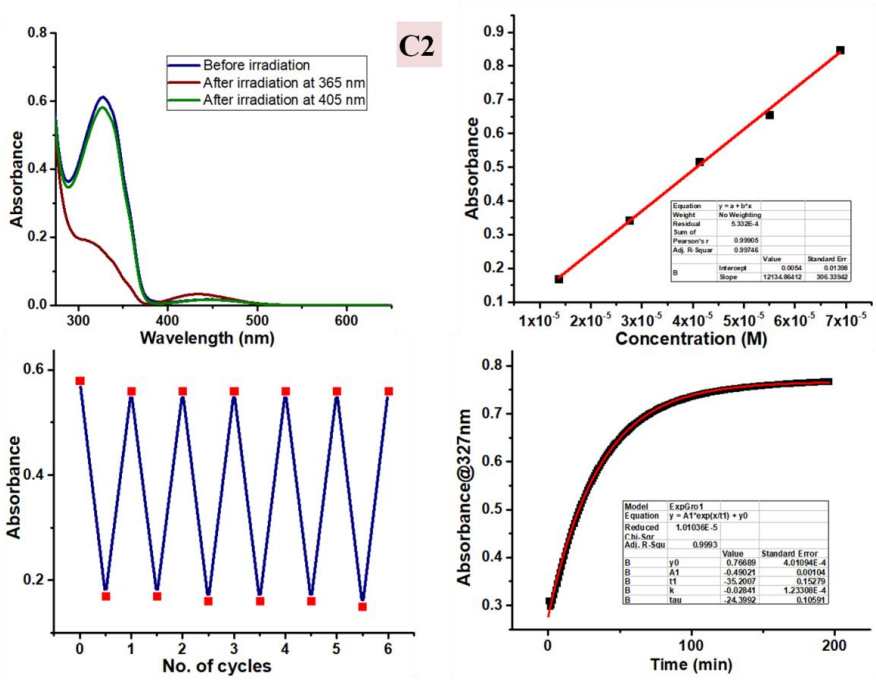

Figure 2A.14 UV-Vis spectroscopic data of **C2**: (a) Photoswitching studies performed in DMSO (59 μM); (b) Estimation of the molar absorption coefficient for π–π* absorption maxima; (c) Photoswitching stability test upto six cycles in DMSO (forward isomerization step: 365 nm; reverse isomerization step: 405 nm) and (d) First order thermal reverse isomerization kinetics plot and exponential fit at 80 ^{o}C.

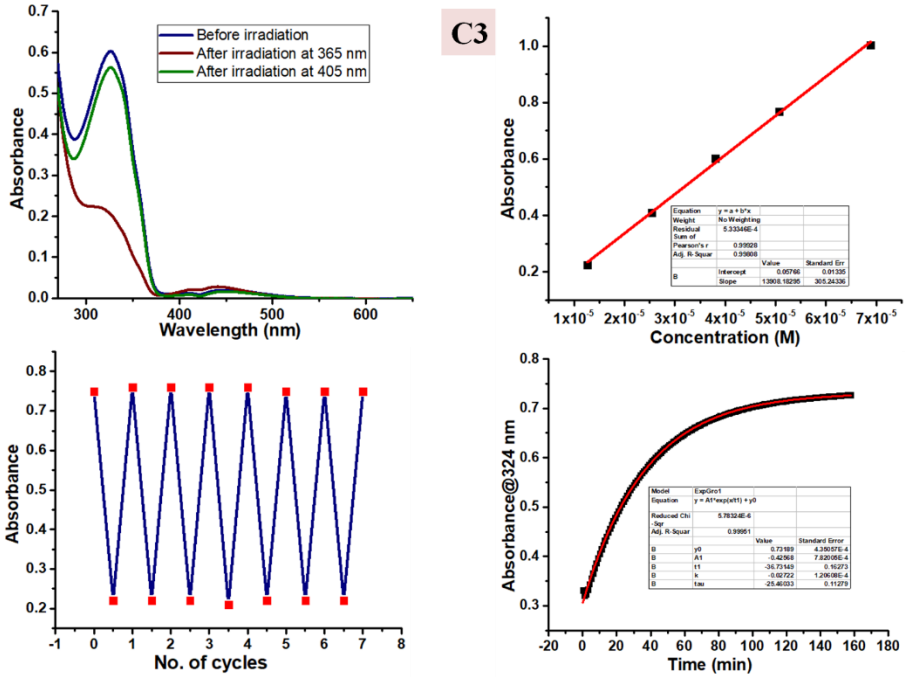

Figure 2A.15 UV-Vis spectroscopic data of **C3**: (a) Photoswitching studies performed in DMSO (52 μM); (b) Estimation of the molar absorption coefficient for π–π* absorption maxima; (c) Photoswitching stability test upto six cycles in DMSO (forward isomerization step: 365 nm; reverse isomerization step: 405 nm) and (d) First order thermal reverse isomerization kinetics plot and exponential fit at 80 ^{o}C.

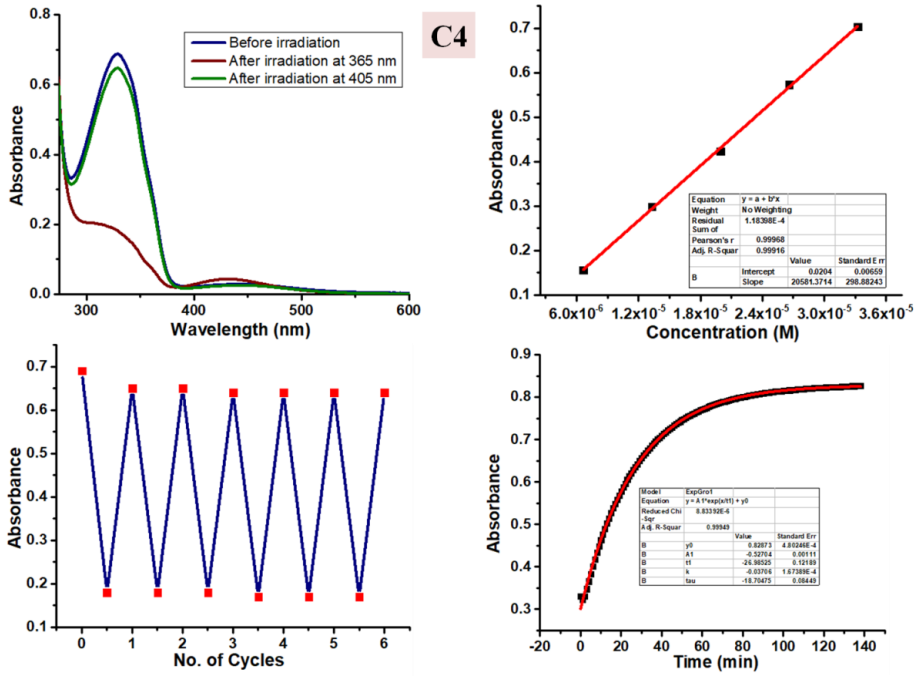

Figure 2A.16 UV-Vis spectroscopic data of **C4**: (a) Photoswitching studies performed in DMSO (37 μM); (b) Estimation of the molar absorption coefficient for π–π* absorption maxima; (c) Photoswitching stability test upto six cycles in DMSO (forward isomerization step: 365 nm; reverse isomerization step: 405 nm) and (d) First order thermal reverse isomerization kinetics plot and exponential fit at 80 ^{o}C.

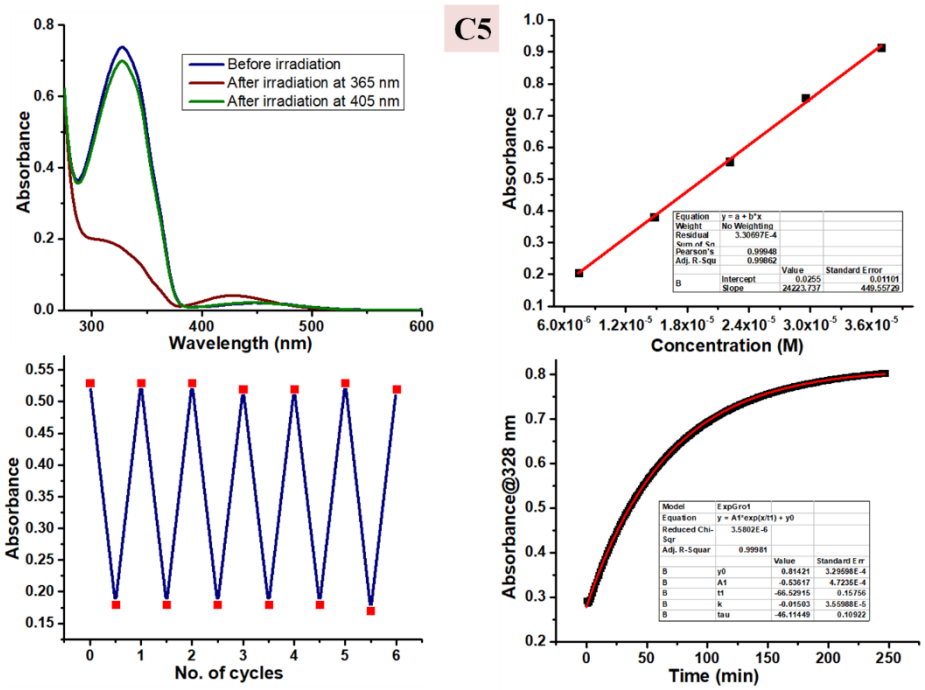

Figure 2A.17 UV-Vis spectroscopic data of **C5**: (a) Photoswitching studies performed in DMSO (29 μM); (b) Estimation of the molar absorption coefficient for π–π* absorption maxima; (c) Photoswitching stability test upto six cycles in DMSO (forward isomerization step: 365 nm; reverse isomerization step: 405 nm) and (d) First order thermal reverse isomerization kinetics plot and exponential fit at 80 ^{o}C.

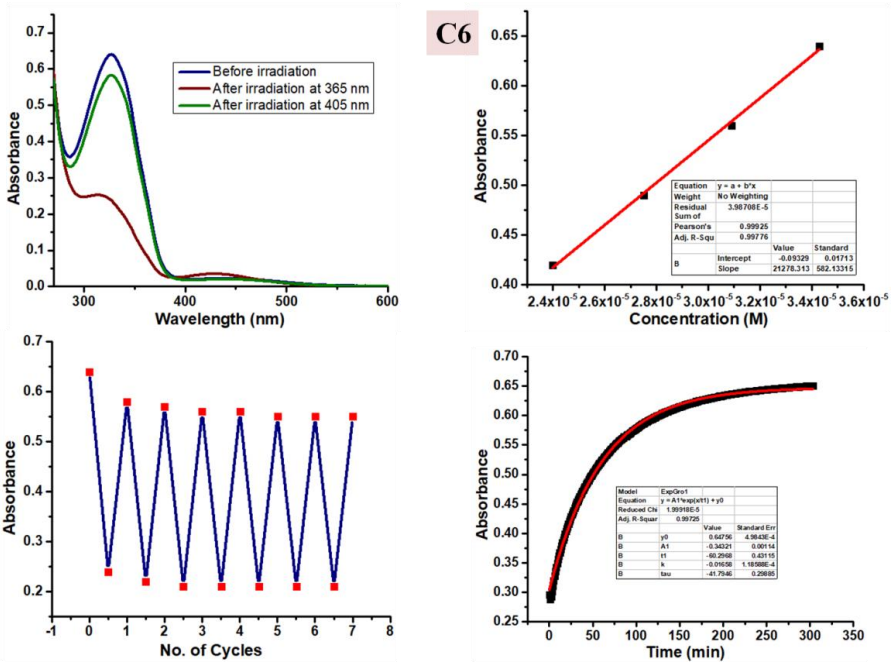

Figure 2A.18 UV-Vis spectroscopic data of **C6**: (a) Photoswitching studies performed in DMSO (30 μM); (b) Estimation of the molar absorption coefficient for π–π* absorption maxima; (c) Photoswitching stability test upto six cycles in DMSO (forward isomerization step: 365 nm; reverse isomerization step: 405 nm) and (d) First order thermal reverse isomerization kinetics plot and exponential fit at 80 ^{o}C.

Appendix 2B

Quantification of photoisomers by using 1H-NMR spectroscopy:

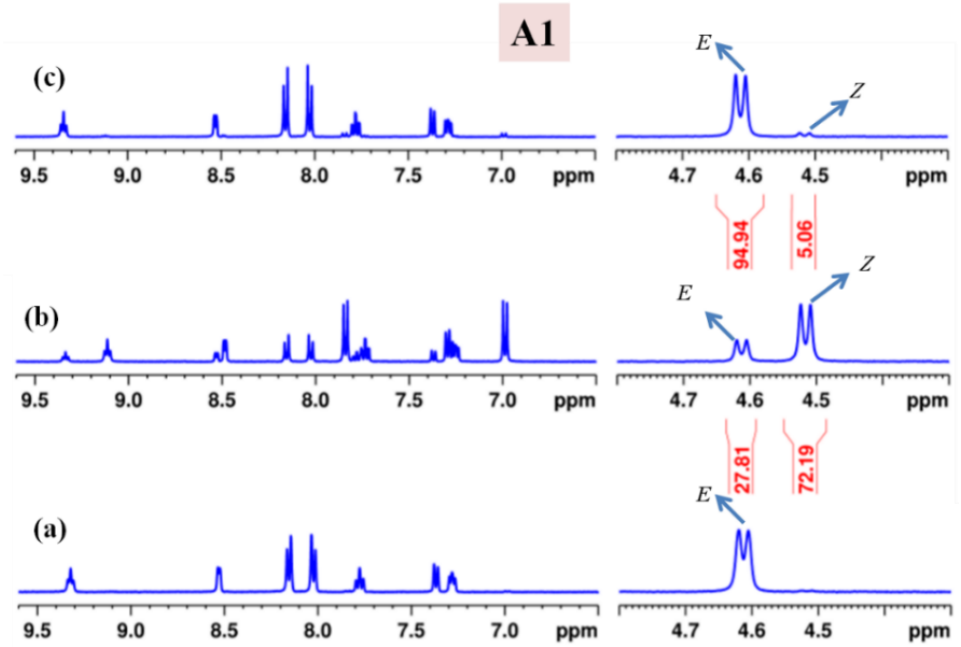

Figure 2B.1 Analysis of photoswitching for the target **A1** by using ^{1}H-NMR spectroscopy (7.1 mM) in [D_6]DMSO): (a) Before irradiation; (b) after irradiation at 365 nm, and (c) after irradiation at 405 nm. (The normalized integral values due to the signals corresponding to methylene C-H proton are indicated).

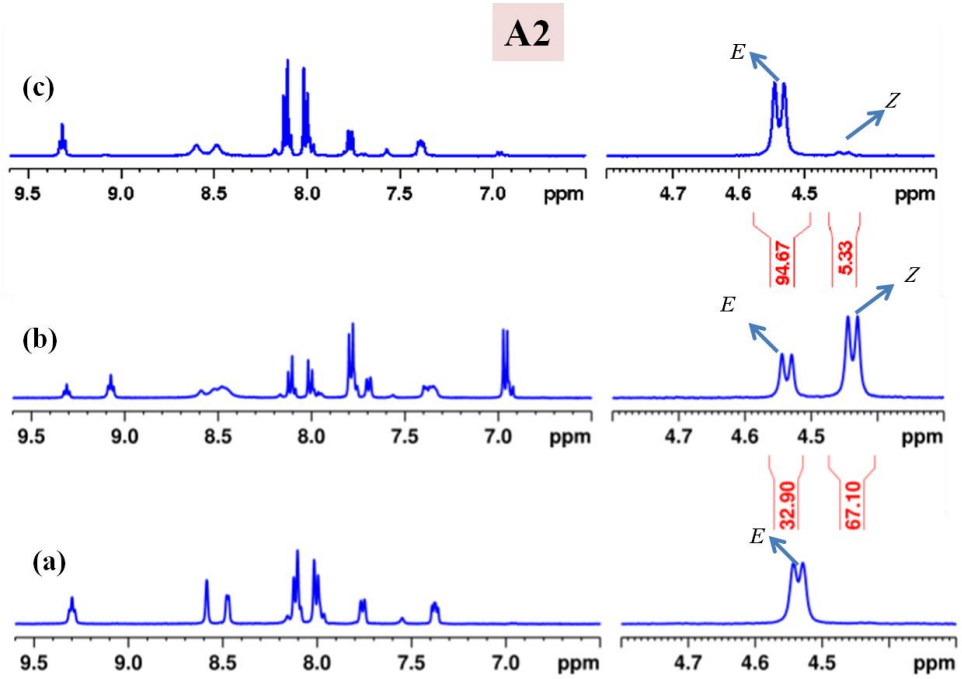

Figure 2B.2 Analysis of photoswitching for the target **A2** by using ^{1}H-NMR spectroscopy (7.5 mM) in [D_6]DMSO): (a) Before irradiation; (b) after irradiation at 365 nm, and (c) after irradiation at 405 nm. (The normalized integral values due to the signals corresponding to methylene C-H proton are indicated).

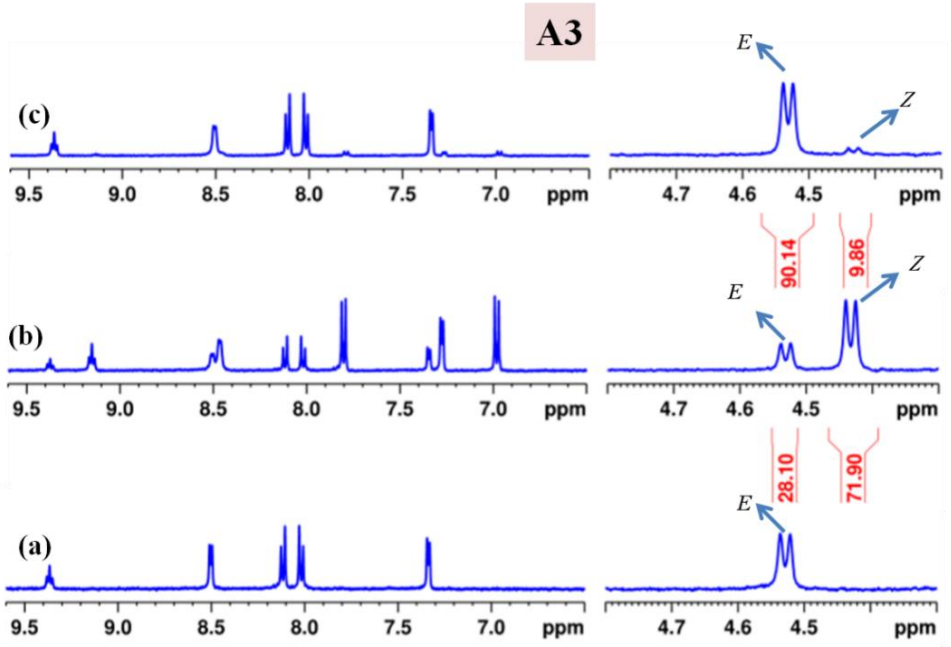

Figure 2B.3 Analysis of photoswitching for the target **A3** by using ^{1}H-NMR spectroscopy (8.0 mM) in [D_6]DMSO): (a) Before irradiation; (b) after irradiation at 365 nm, and (c) after irradiation at 405 nm. (The normalized integral values due to the signals corresponding to methylene C-H proton are indicated).

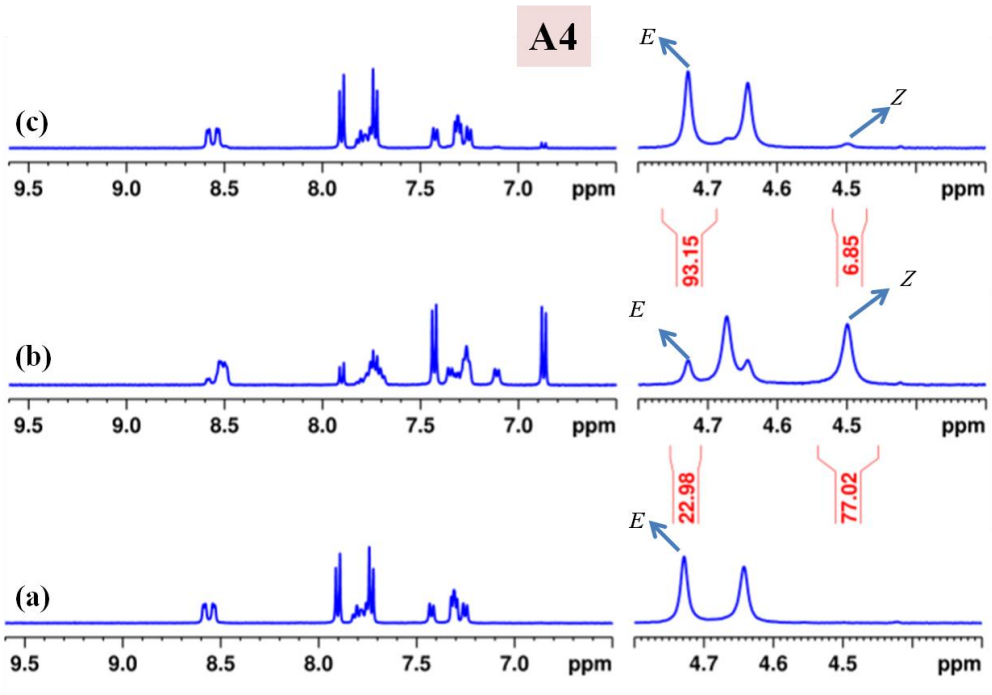

Figure 2B.4 Analysis of photoswitching for the target **A4** by using ^{1}H-NMR spectroscopy (7.0 mM) in [D_6]DMSO): (a) Before irradiation; (b) after irradiation at 365 nm, and (c) after irradiation at 405 nm. (The normalized integral values due to the signals corresponding to methylene C-H proton are indicated).

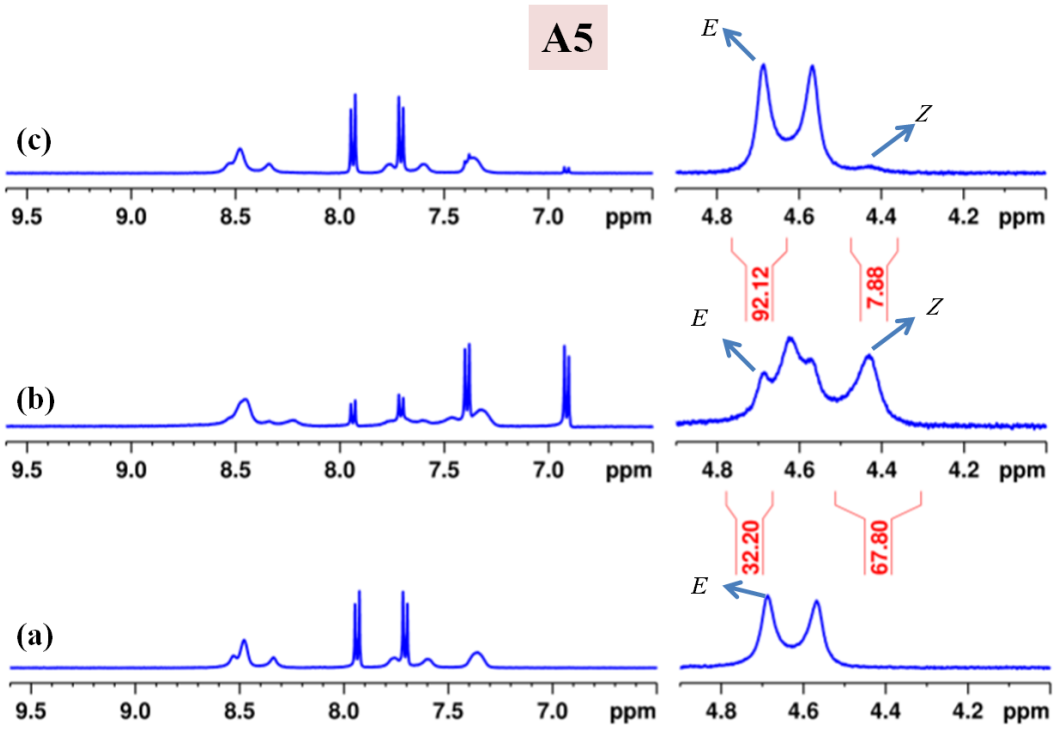

Figure 2B.5 Analysis of photoswitching for the target **A5** by using ^{1}H-NMR spectroscopy (6.3 mM) in [D_6]DMSO): (a) Before irradiation; (b) after irradiation at 365 nm, and (c) after irradiation at 405 nm. (The normalized integral values due to the signals corresponding to methylene C-H proton are indicated).

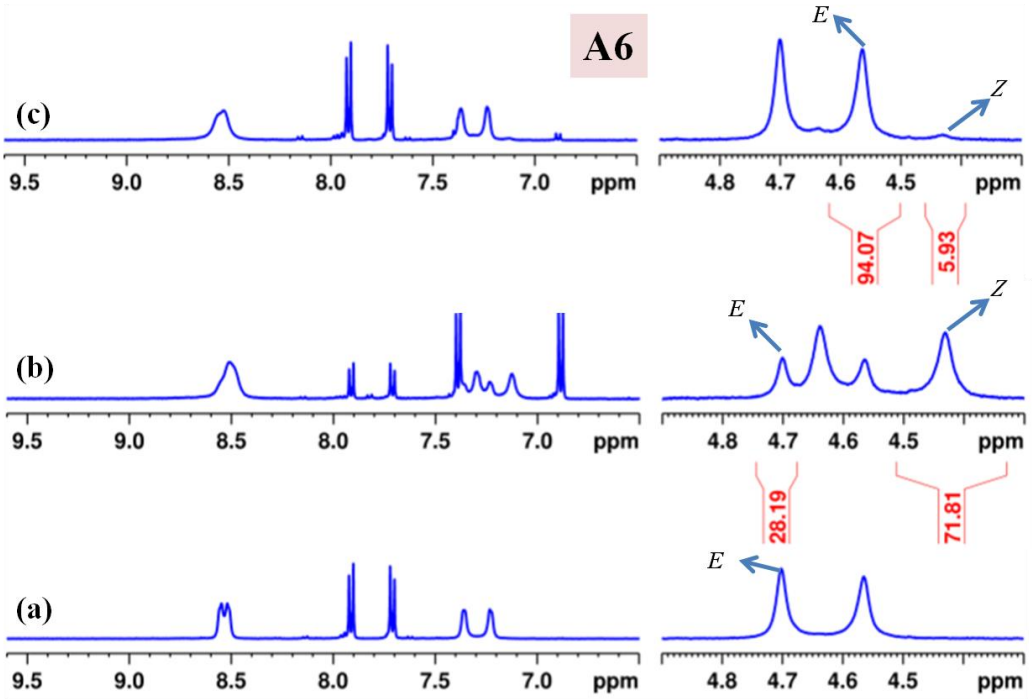

Figure 2B.6 Analysis of photoswitching for the target **A6** by using ^{1}H-NMR spectroscopy (6.3 mM) in [D_6]DMSO): (a) Before irradiation; (b) after irradiation at 365 nm, and (c) after irradiation at 405 nm. (The normalized integral values due to the signals corresponding to methylene C-H proton are indicated).

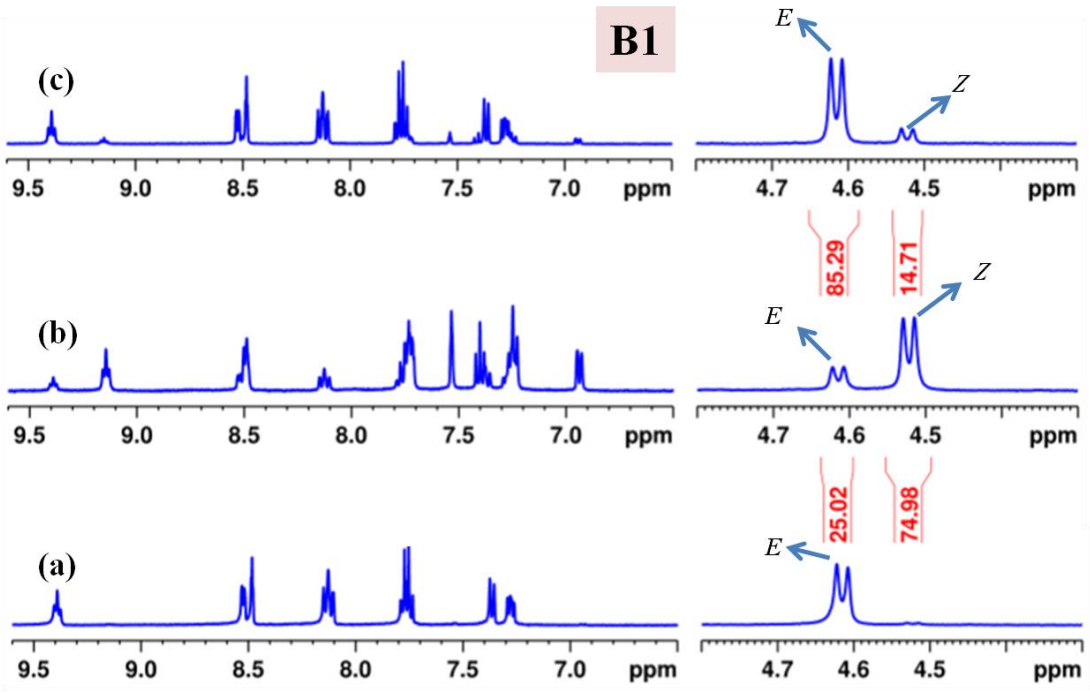

Figure 2B.7 Analysis of photoswitching for the target **B1** by using ^{1}H-NMR spectroscopy (6.2 mM) in [D_6]DMSO): (a) Before irradiation; (b) after irradiation at 365 nm, and (c) after irradiation at 405 nm. (The normalized integral values due to the signals corresponding to methylene C-H proton are indicated).

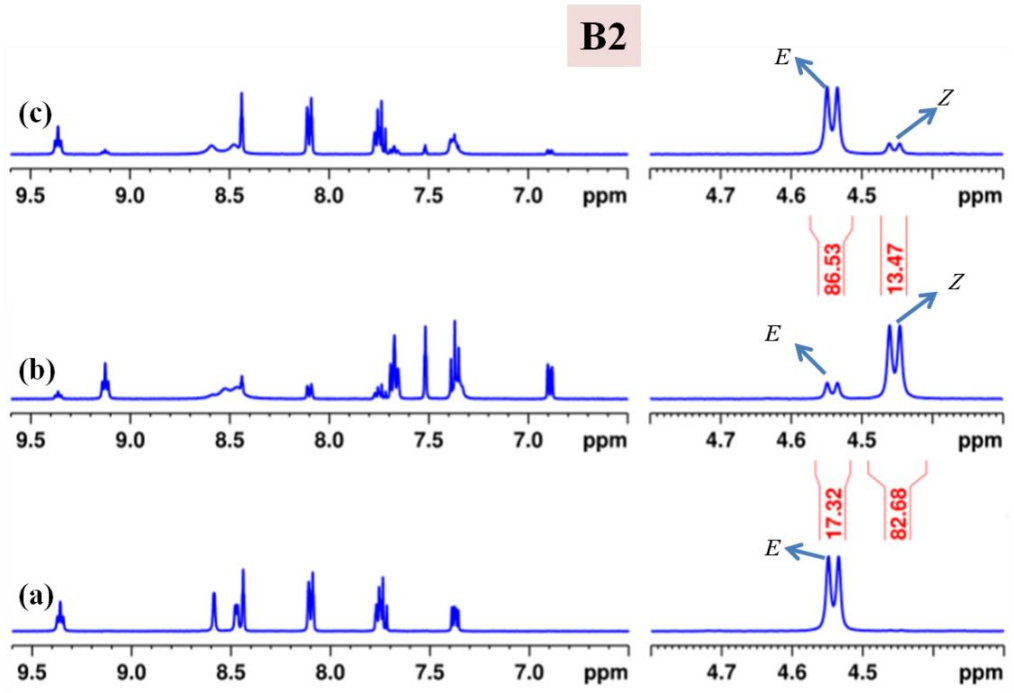

Figure 2B.8 Analysis of photoswitching for the target **B2** by using ^{1}H-NMR spectroscopy (5.8 mM) in [D_6]DMSO): (a) Before irradiation; (b) after irradiation at 365 nm, and (c) after irradiation at 405 nm. (The normalized integral values due to the signals corresponding to methylene C-H proton are indicated).

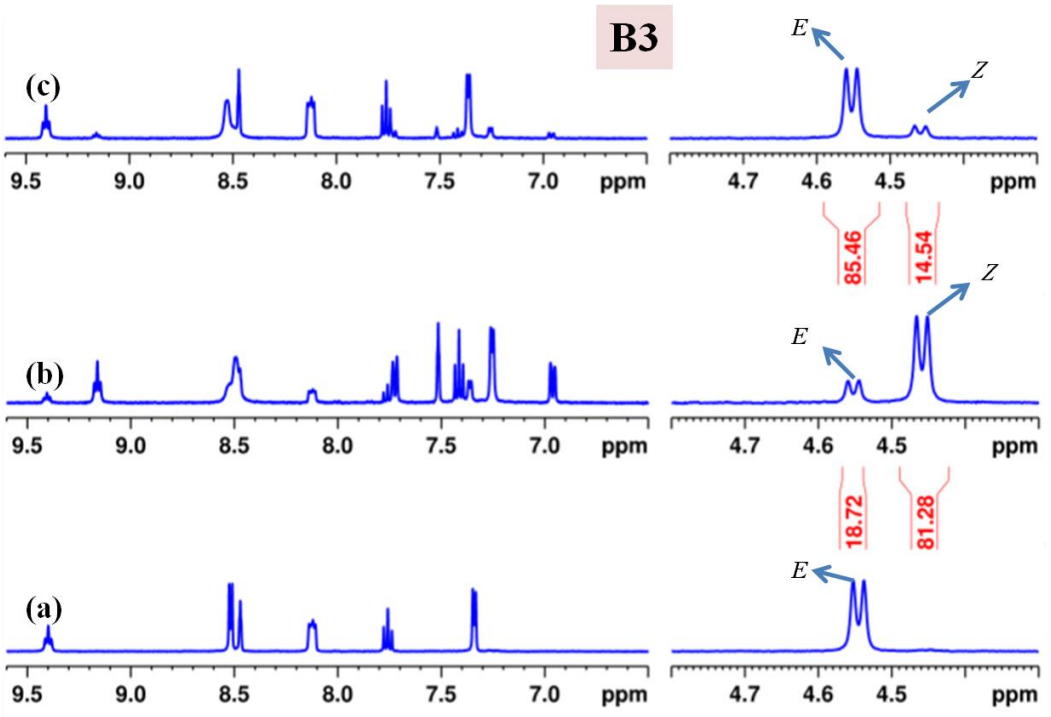

Figure 2B.9 Analysis of photoswitching for the target **B3** by using ^{1}H-NMR spectroscopy (5.8 mM) in [D_6]DMSO): (a) Before irradiation; (b) after irradiation at 365 nm, and (c) after irradiation at 405 nm. (The normalized integral values due to the signals corresponding to methylene C-H proton are indicated).

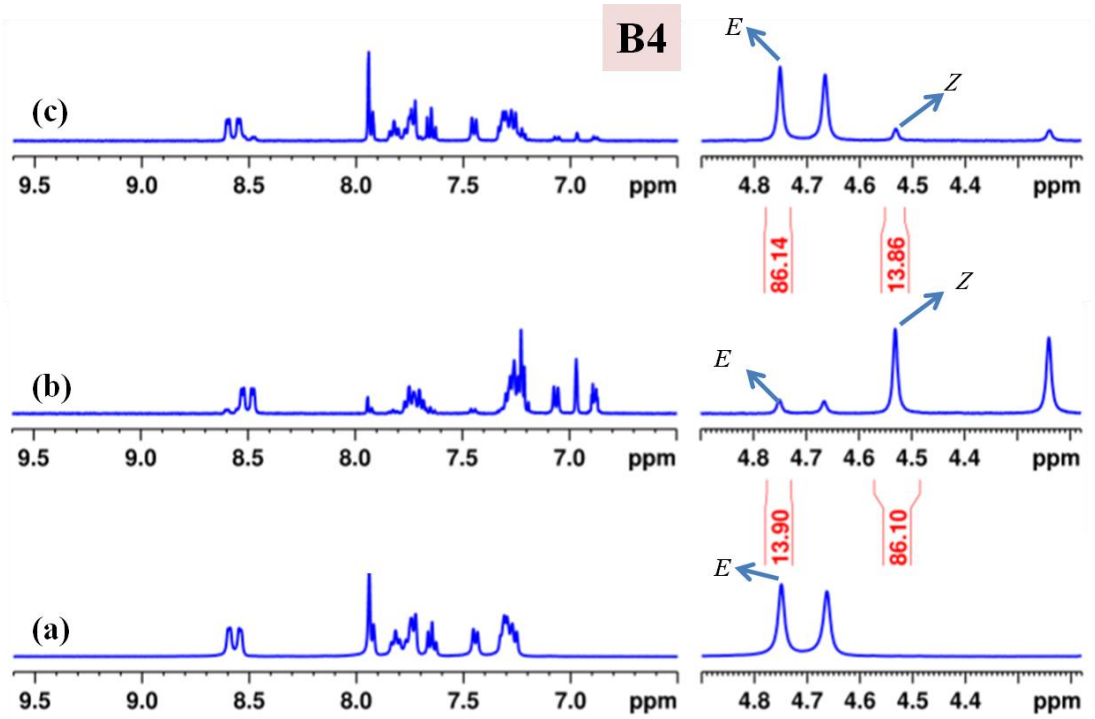

Figure 2B.10 Analysis of photoswitching for the target **B4** by using ^{1}H-NMR spectroscopy (5.1 mM) in [D_6]DMSO): (a) Before irradiation; (b) after irradiation at 365 nm, and (c) after irradiation at 405 nm. (The normalized integral values due to the signals corresponding to methylene C-H proton are indicated).

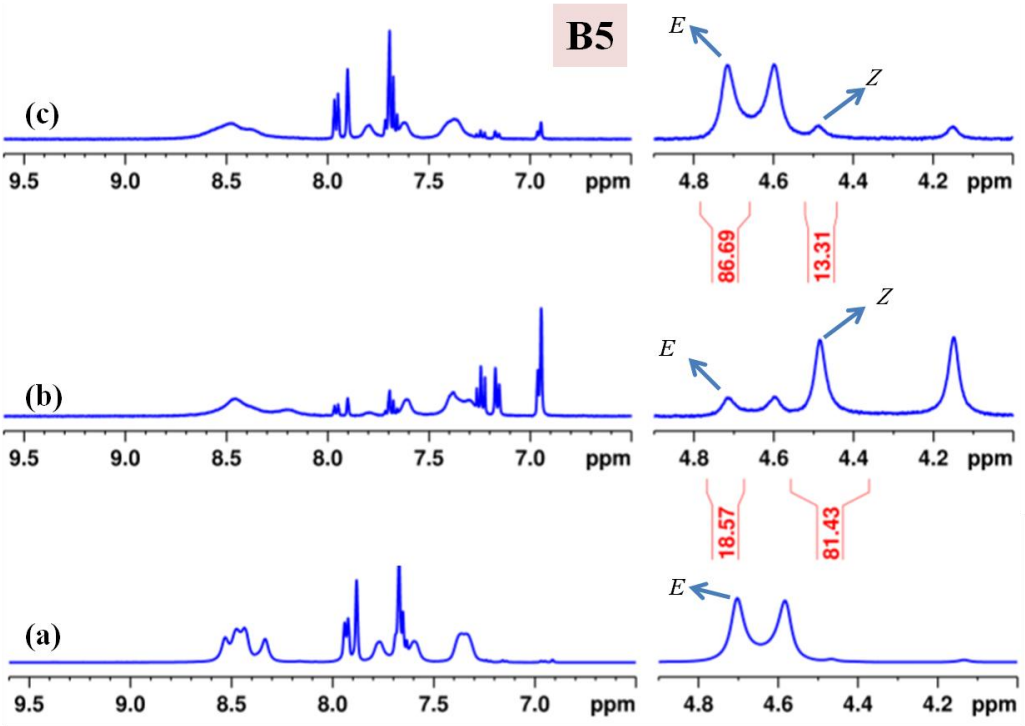

Figure 2B.11 Analysis of photoswitching for the target **B5** by using ^{1}H-NMR spectroscopy (6.3 mM) in [D_6]DMSO): (a) Before irradiation; (b) after irradiation at 365 nm, and (c) after irradiation at 405 nm. (The normalized integral values due to the signals corresponding to methylene C-H proton are indicated).

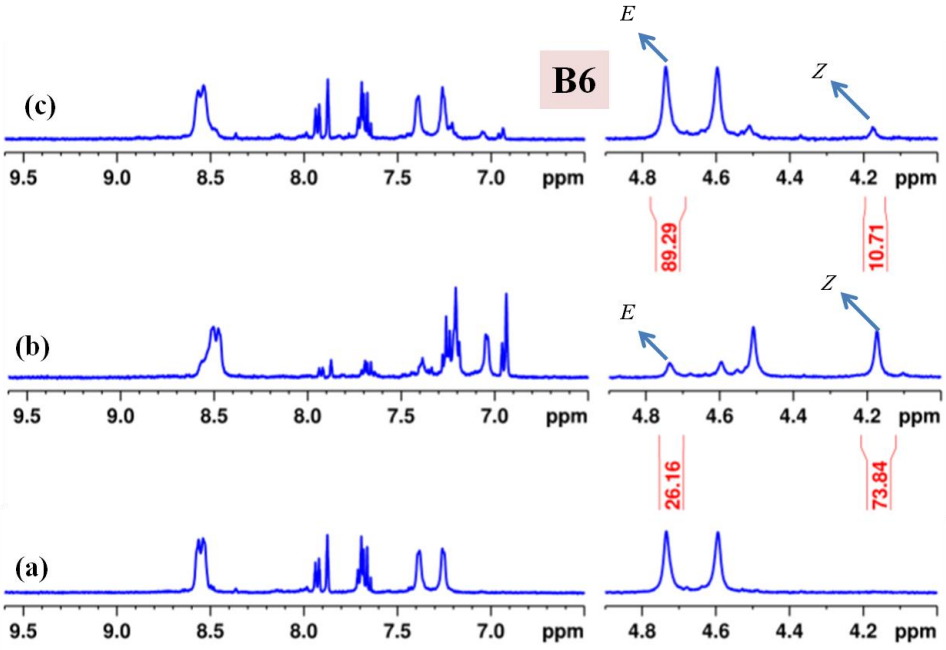

Figure 2B.12 Analysis of photoswitching for the target **B6** by using ^{1}H-NMR spectroscopy (3.8 mM) in [D_6]DMSO): (a) Before irradiation; (b) after irradiation at 365 nm, and (c) after irradiation at 405 nm. (The normalized integral values due to the signals corresponding to methylene C-H proton are indicated).

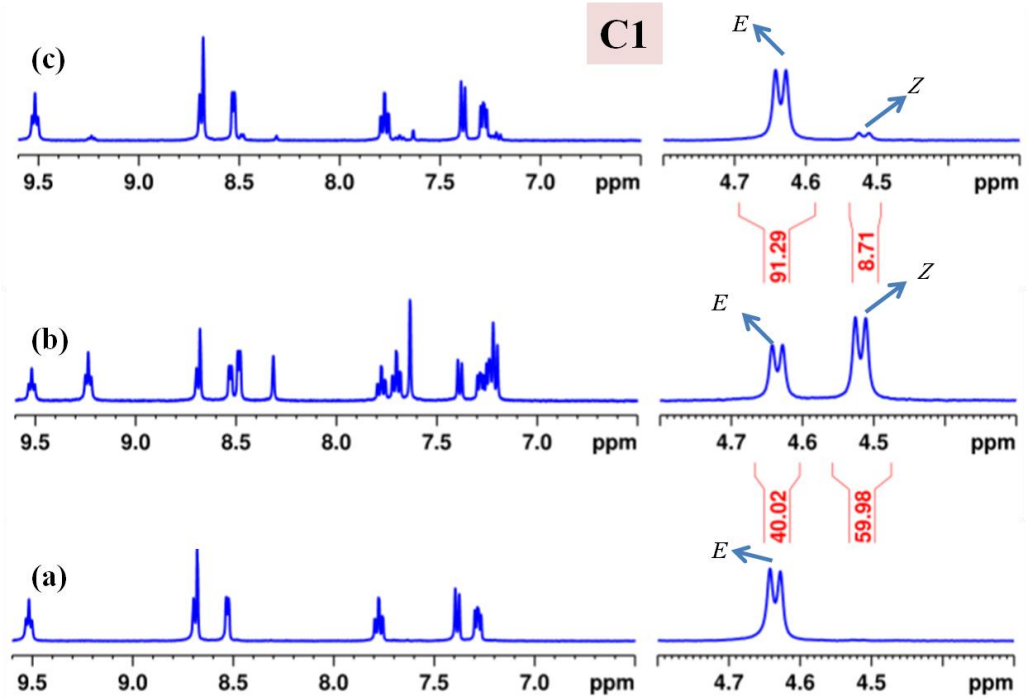

Figure 2B.13 Analysis of photoswitching for the target **C1** by using ^{1}H-NMR spectroscopy (4.8 mM) in [D_6]DMSO): (a) Before irradiation; (b) after irradiation at 365 nm, and (c) after irradiation at 405 nm. (The normalized integral values due to the signals corresponding to methylene C-H proton are indicated).

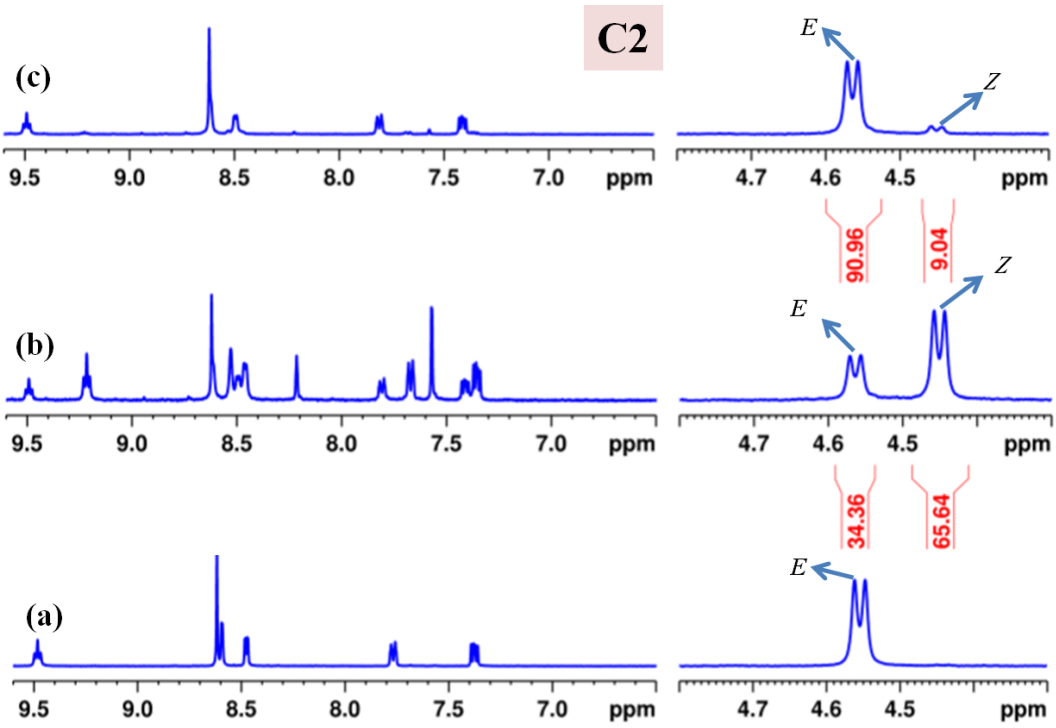

Figure 2B.14 Analysis of photoswitching for the target **C2** by using ^{1}H-NMR spectroscopy (4.2 mM) in [D_6]DMSO): (a) Before irradiation; (b) after irradiation at 365 nm, and (c) after irradiation at 405 nm. (The normalized integral values due to the signals corresponding to methylene C-H proton are indicated).

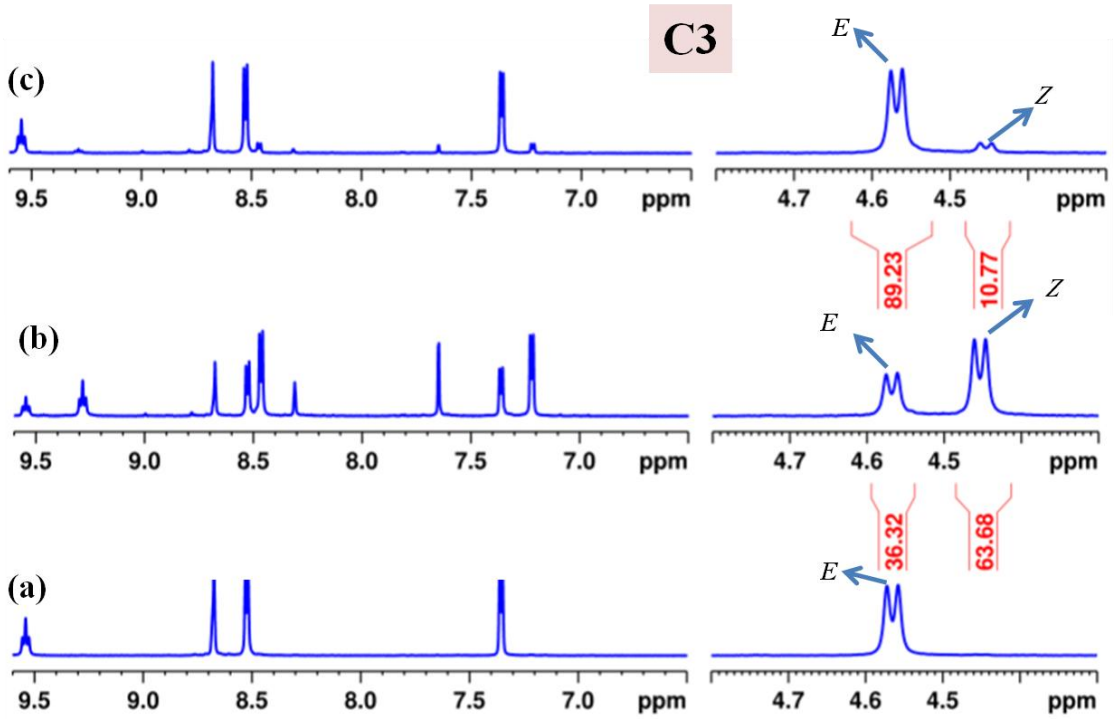

Figure 2B.15 Analysis of photoswitching for the target **C3** by using ^{1}H-NMR spectroscopy (4.2 mM) in [D_6]DMSO): (a) Before irradiation; (b) after irradiation at 365 nm, and (c) after irradiation at 405 nm. (The normalized integral values due to the signals corresponding to methylene C-H proton are indicated).

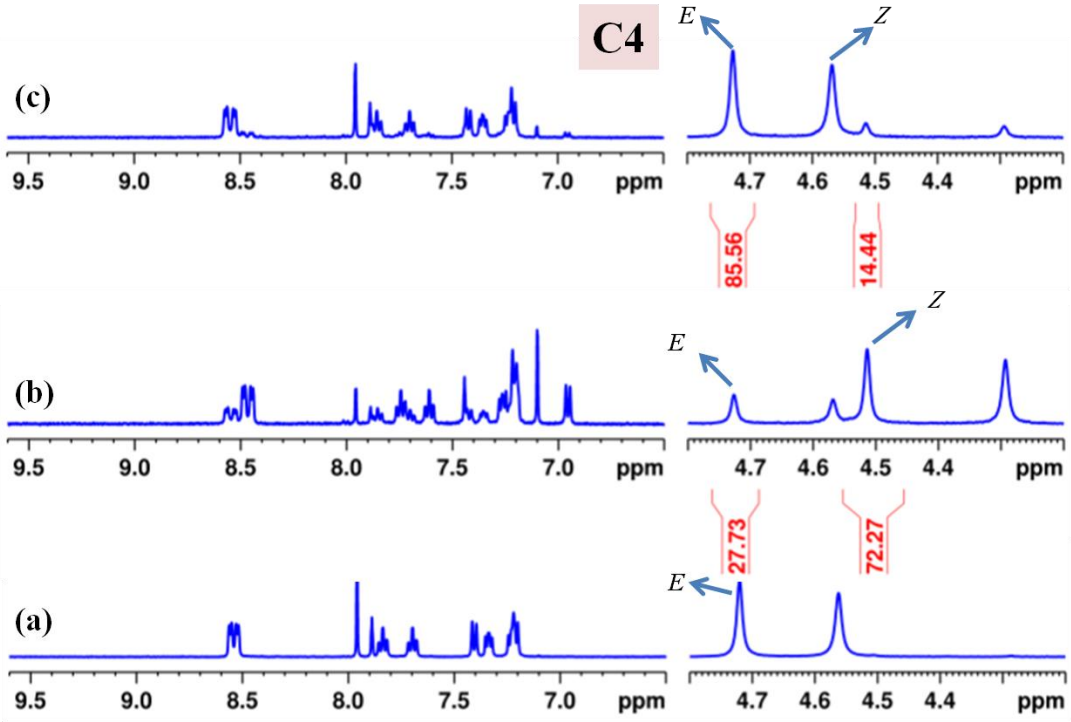

Figure 2B.16 Analysis of photoswitching for the target **C4** by using ^{1}H-NMR spectroscopy (3.7 mM) in [D_6]DMSO): (a) Before irradiation; (b) after irradiation at 365 nm, and (c) after irradiation at 405 nm. (The normalized integral values due to the signals corresponding to methylene C-H proton are indicated).

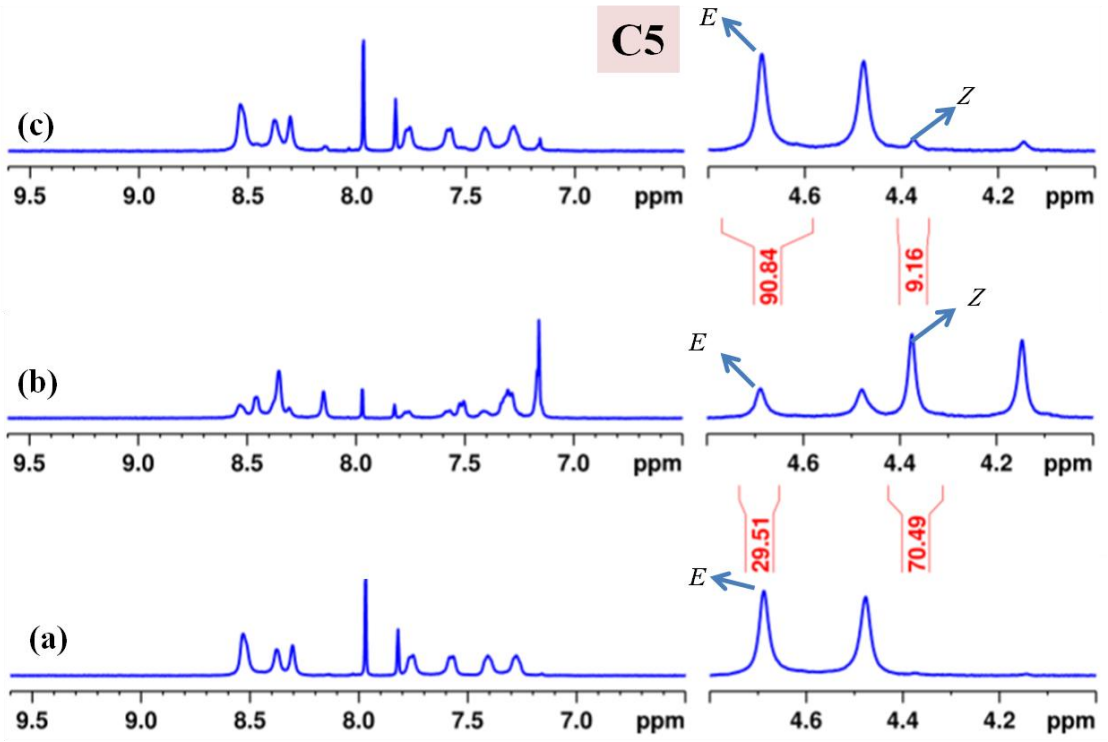

Figure 2B.17 Analysis of photoswitching for the target **C5** by using ^{1}H-NMR spectroscopy (3.7 mM) in [D_6]DMSO): (a) Before irradiation; (b) after irradiation at 365 nm, and (c) after irradiation at 405 nm. (The normalized integral values due to the signals corresponding to methylene C-H proton are indicated).

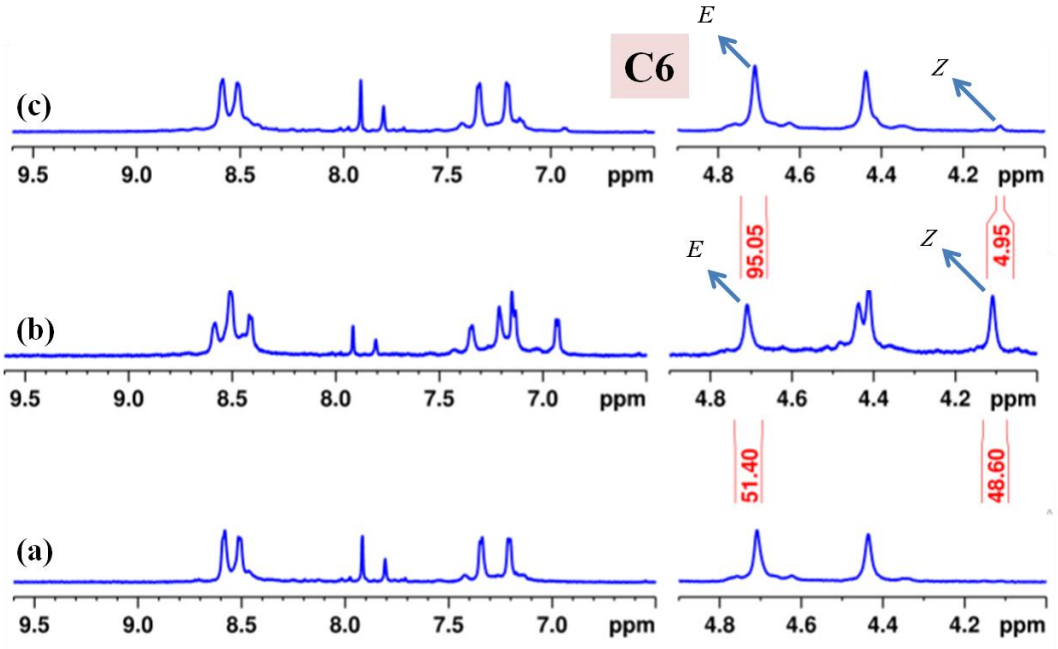

Figure 2B.18 Analysis of photoswitching for the target **C6** by using ^{1}H-NMR spectroscopy (3.5 mM) in [D_6]DMSO): (a) Before irradiation; (b) after irradiation at 365 nm, and (c) after irradiation at 405 nm. (The normalized integral values due to the signals corresponding to methylene C-H proton are indicated).

Appendix 2C

Thermal reverse isomerization

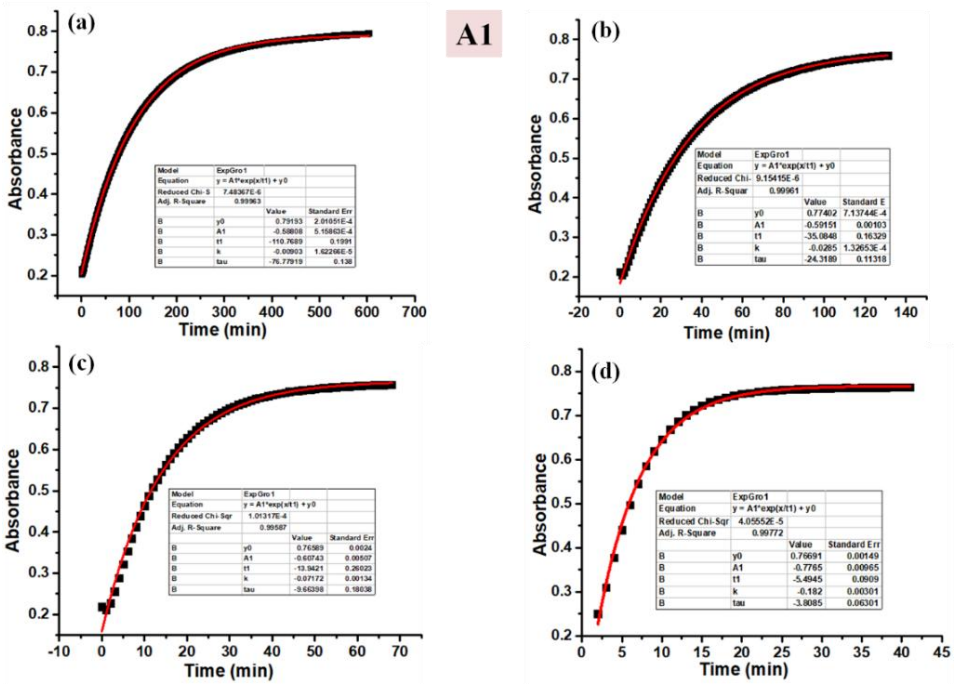

Figure 2C.1 Thermal reverse isomerization kinetics plots of **A1** in DMSO at (a) 60 ^{o}C; (b) 70 ^{o}C; (c) 80 ^{o}C; (d) 90 ^{o}C using UV-Vis Spectroscopy.

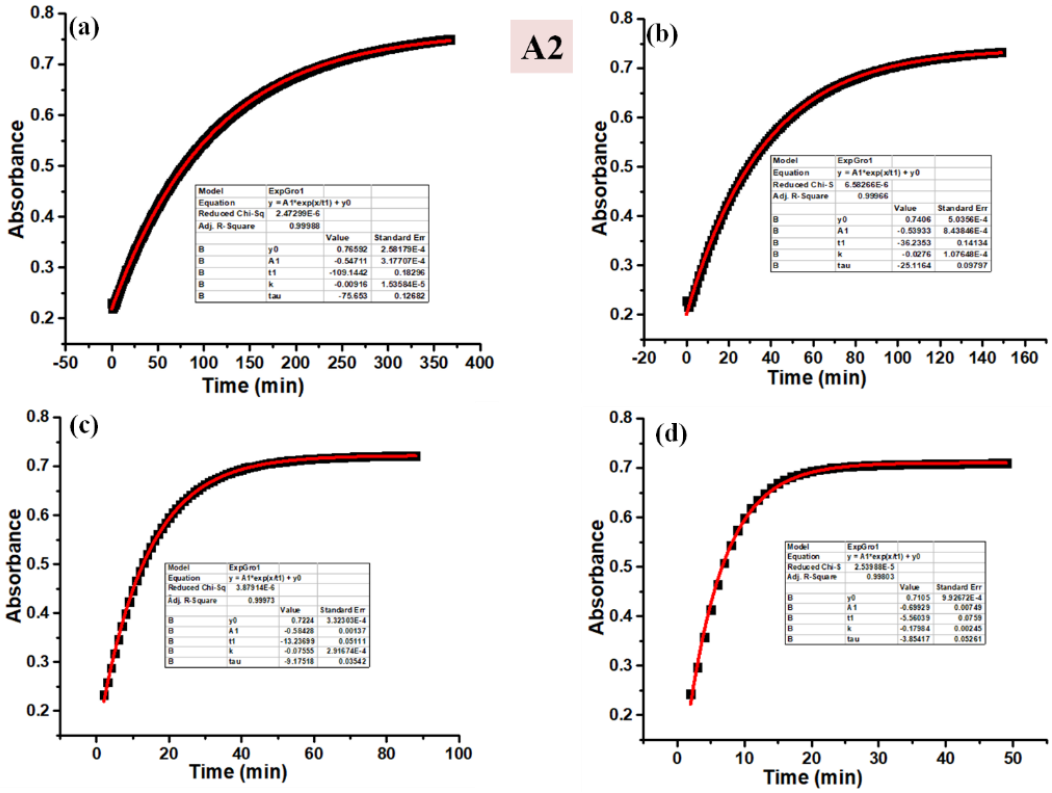

Figure 2C.2 Thermal reverse isomerization kinetics plots of **A2** in DMSO at (a) 60 ^{o}C; (b) 70 ^{o}C; (c) 80 ^{o}C; (d) 90 ^{o}C using UV-Vis Spectroscopy.

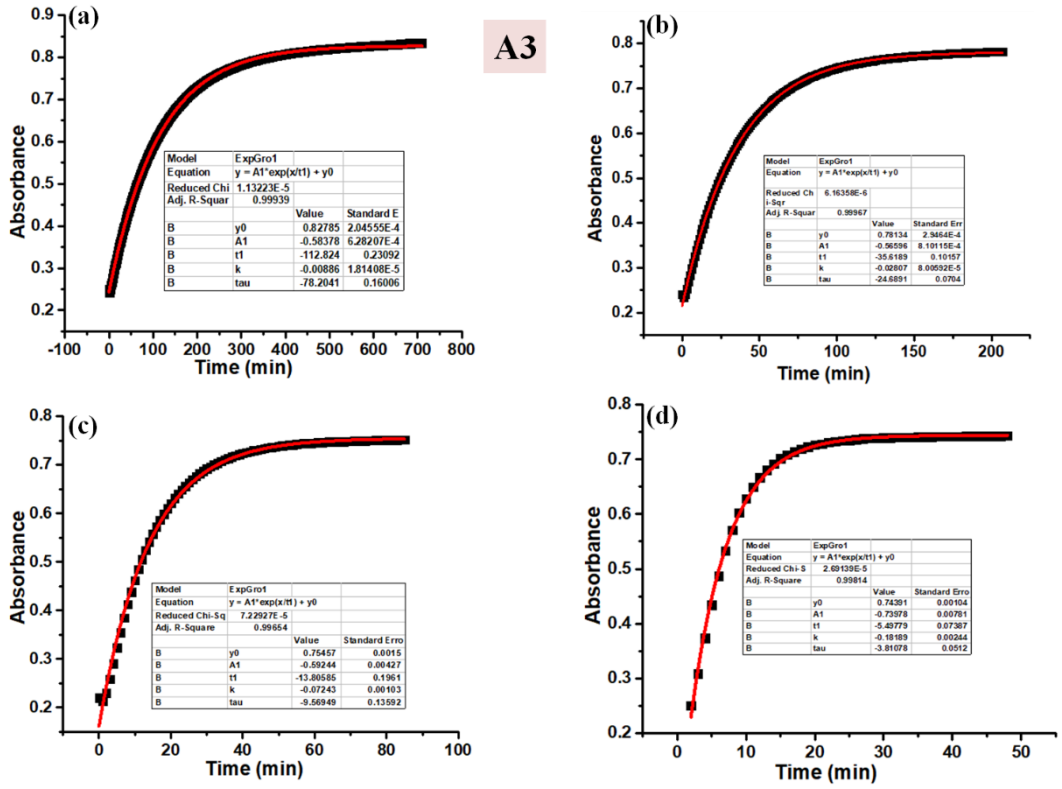

Figure 2C.3 Thermal reverse isomerization kinetics plots of **A3** in DMSO at (a) 60 ^{o}C; (b) 70 ^{o}C; (c) 80 ^{o}C; (d) 90 ^{o}C using UV-Vis Spectroscopy.

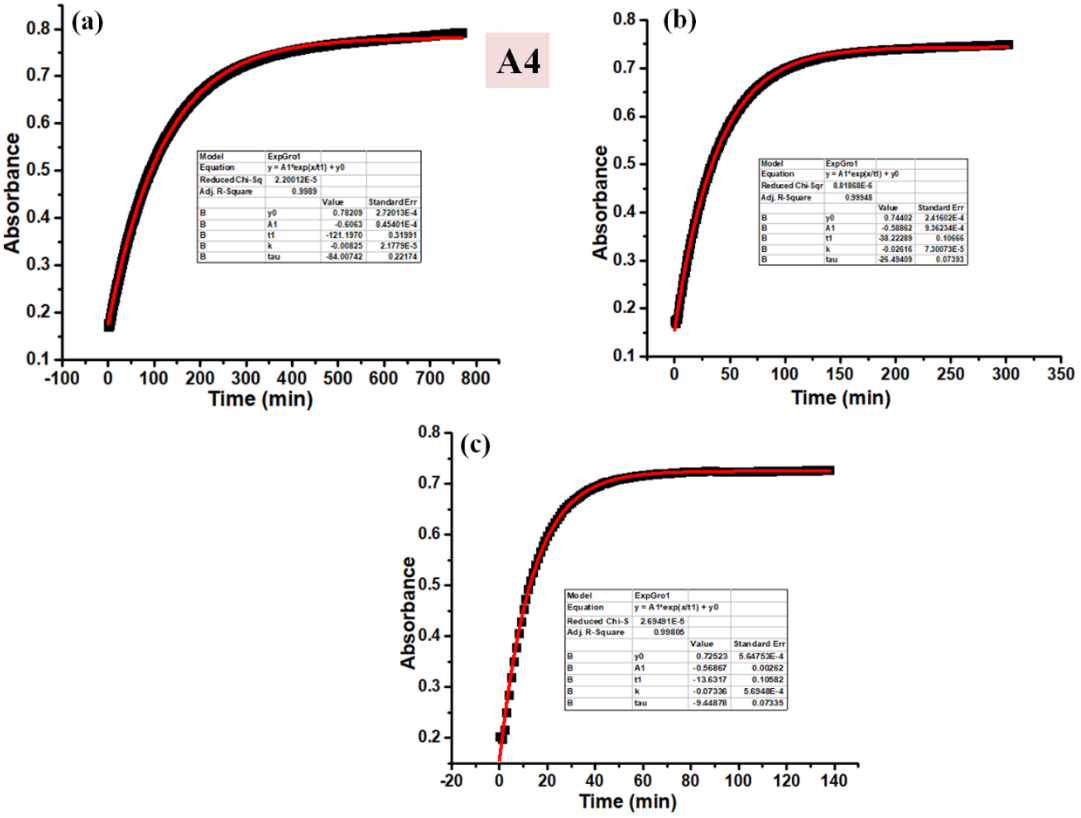

Figure 2C.4 Thermal reverse isomerization kinetics plots of **A4** in DMSO at (a) 60 ^{o}C; (b) 70 ^{o}C; (c) 80 ^{o}C using UV-Vis Spectroscopy

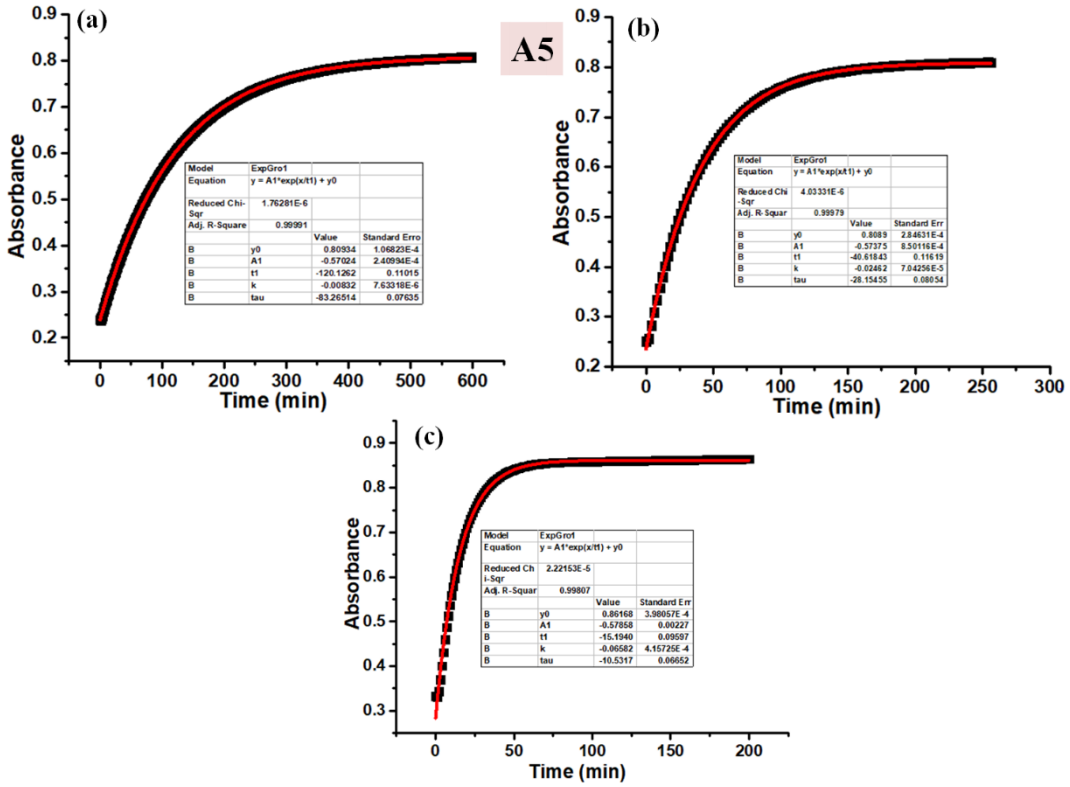

Figure 2C.5 Thermal reverse isomerization kinetics plots of **A5** in DMSO at (a) 60 ^{o}C; (b) 70 ^{o}C; (c) 80 ^{o}C using UV-Vis Spectroscopy

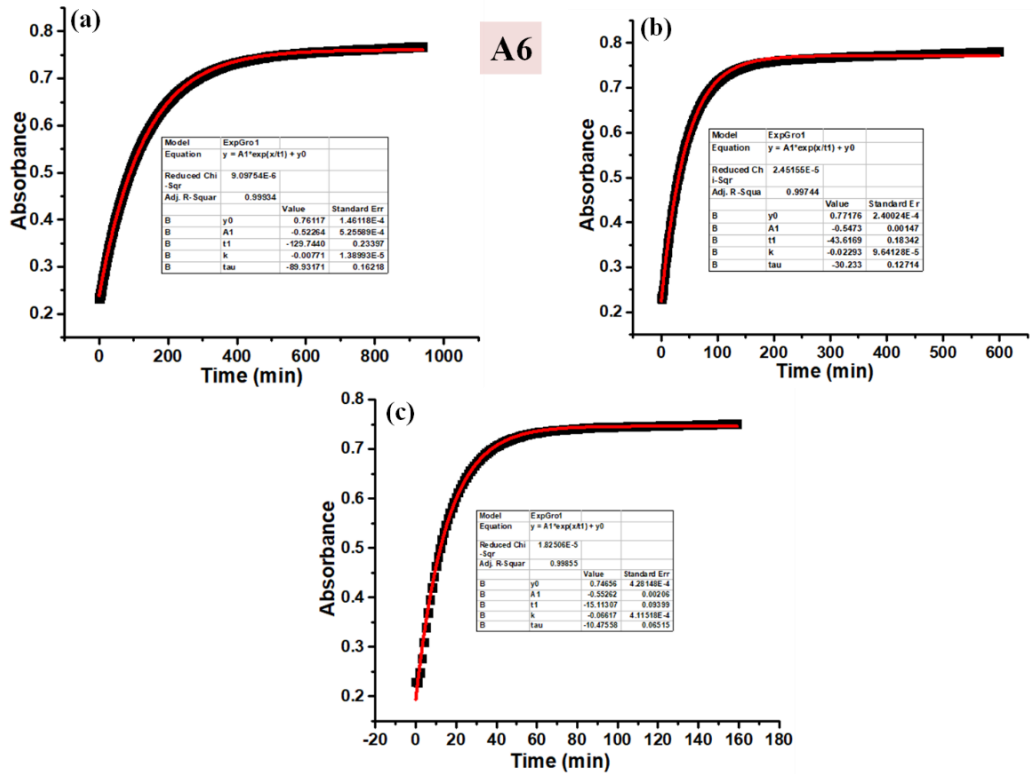

Figure 2C.6 Thermal reverse isomerization kinetics plots of **A6** in DMSO at (a) 60 ^{o}C; (b) 70 ^{o}C; (c) 80 ^{o}C using UV-Vis Spectroscopy

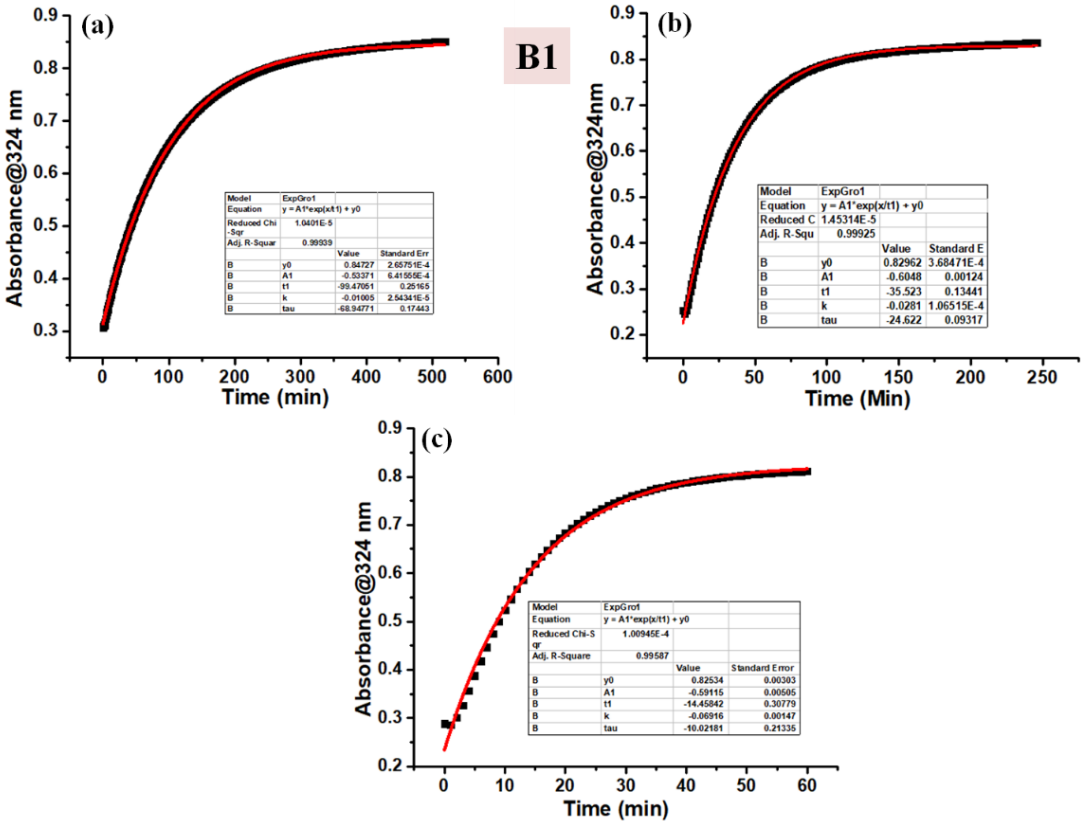

Figure 2C.7 Thermal reverse isomerization kinetics plots of **B1** in DMSO at (a) 70 ^{o}C; (b) 80 ^{o}C; (c) 90 ^{o}C using UV-Vis Spectroscopy.

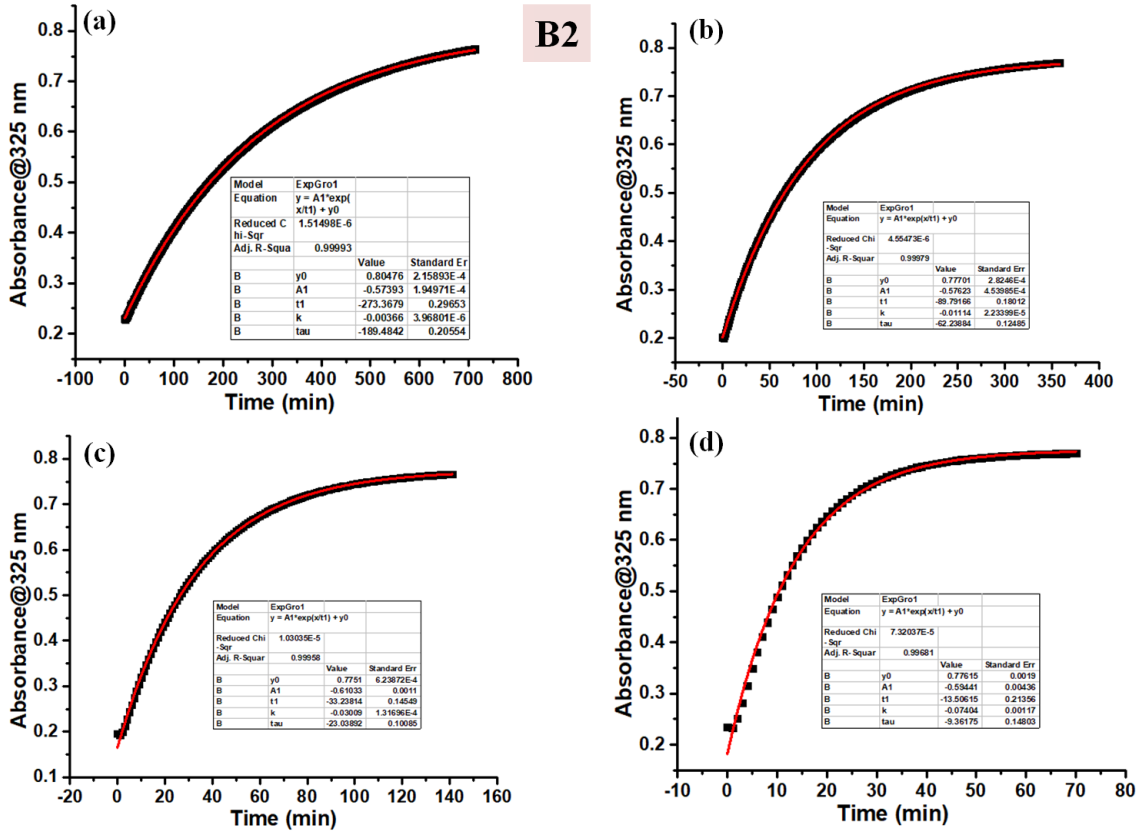

Figure 2C.8 Thermal reverse isomerization kinetics plots of **B2** in DMSO at (a) 60 ^{o}C; (b) 70 ^{o}C; (c) 80 ^{o}C; (d) 90 ^{o}C using UV-Vis Spectroscopy.

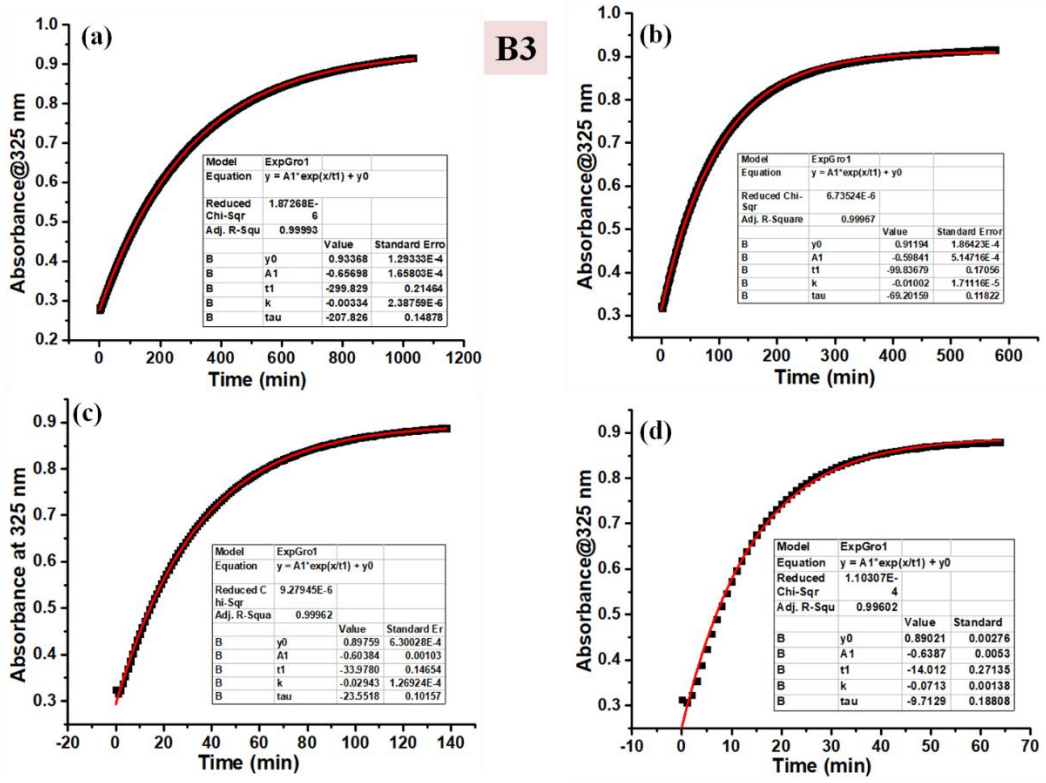

Figure 2C.9 Thermal reverse isomerization kinetics plots of **B3** in DMSO at (a) 60 ^{o}C; (b) 70 ^{o}C; (c) 80 ^{o}C; (d) 90 ^{o}C using UV-Vis Spectroscopy.

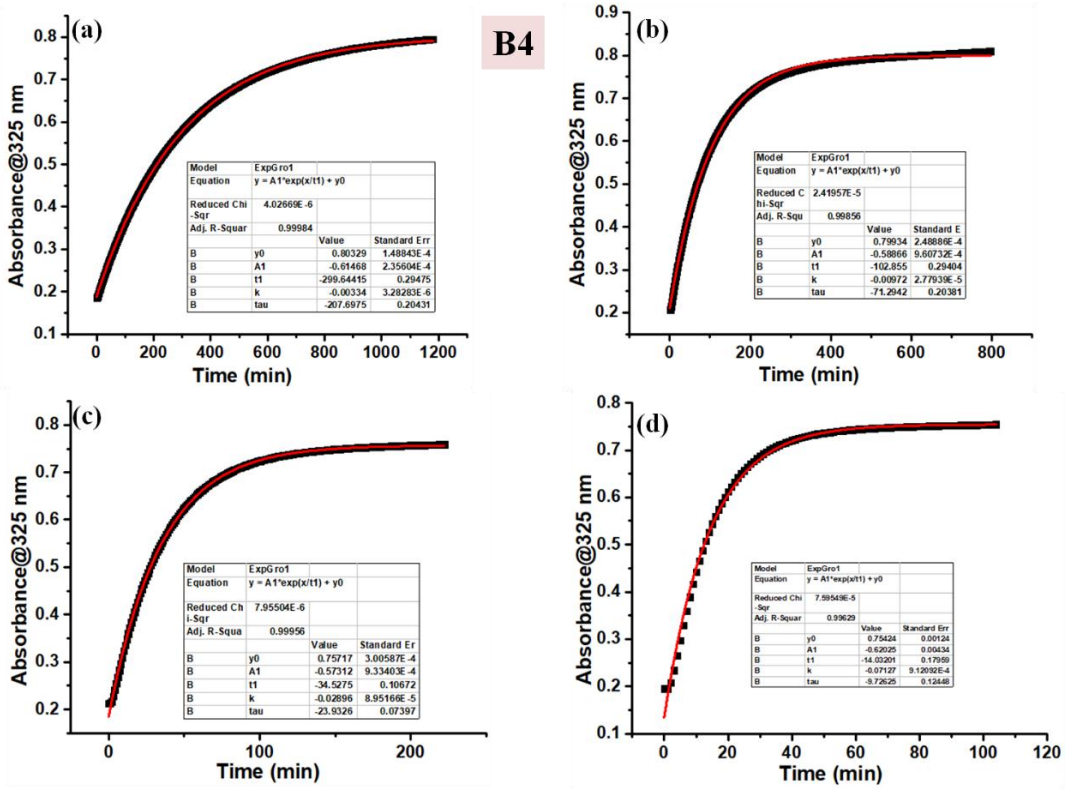

Figure 2C.10 Thermal reverse isomerization kinetics plots of **B4** in DMSO at (a) 60 ^{o}C; (b) 70 ^{o}C; (c) 80 ^{o}C; (d) 90 ^{o}C using UV-Vis Spectroscopy.

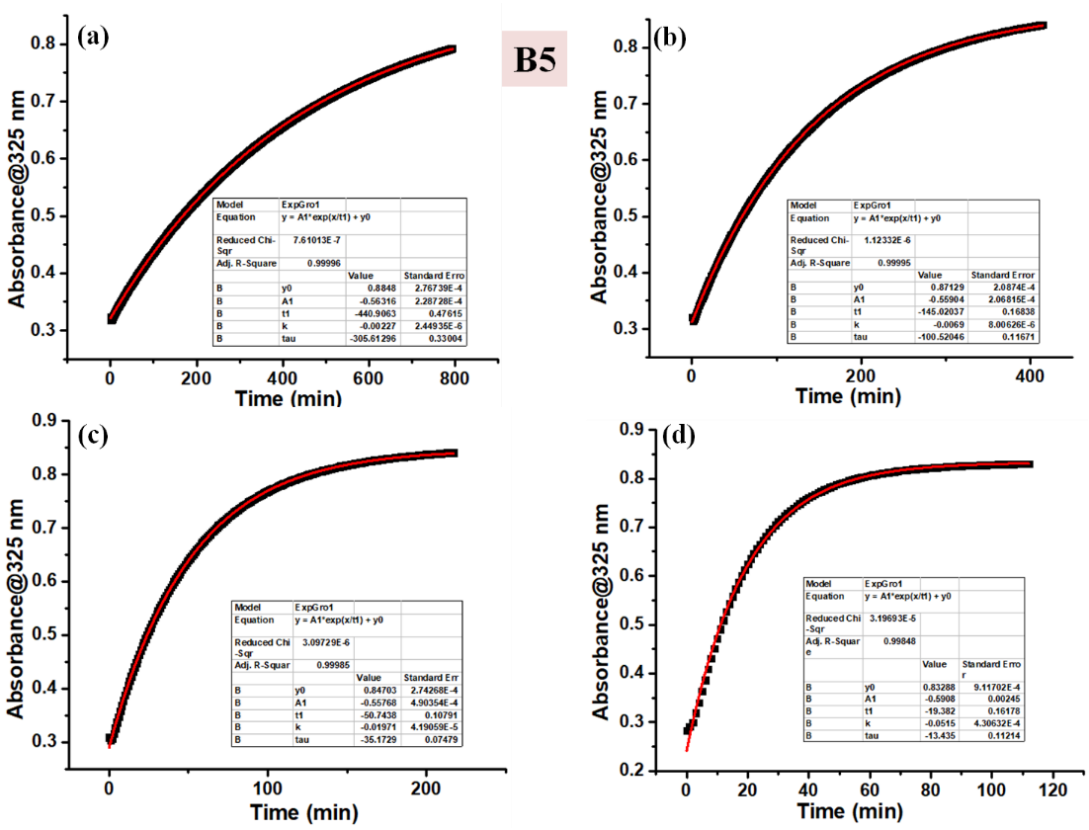

Figure 2C.11 Thermal reverse isomerization kinetics plots of **B5** in DMSO at (a) 60 ^{o}C; (b) 70 ^{o}C; (c) 80 ^{o}C; (d) 90 ^{o}C using UV-Vis Spectroscopy.

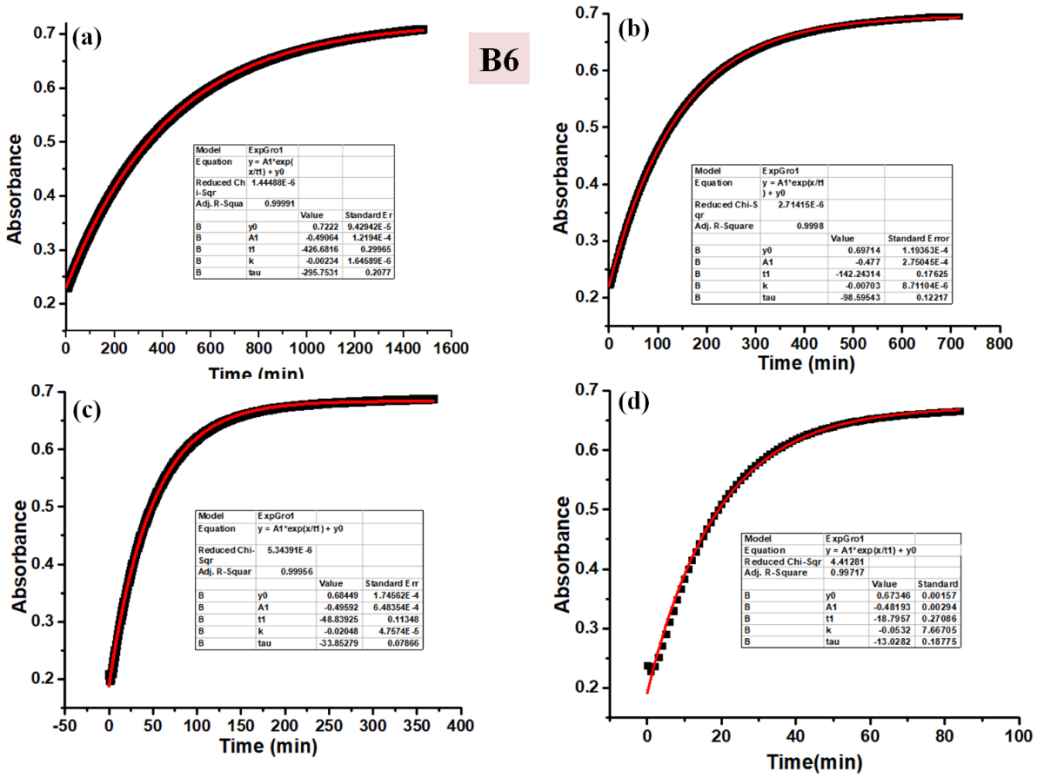

Figure 2C.12 Thermal reverse isomerization kinetics plots of **B6** in DMSO at (a) 60 ^{o}C; (b) 70 ^{o}C; (c) 80 ^{o}C; (d) 90 ^{o}C using UV-Vis Spectroscopy.

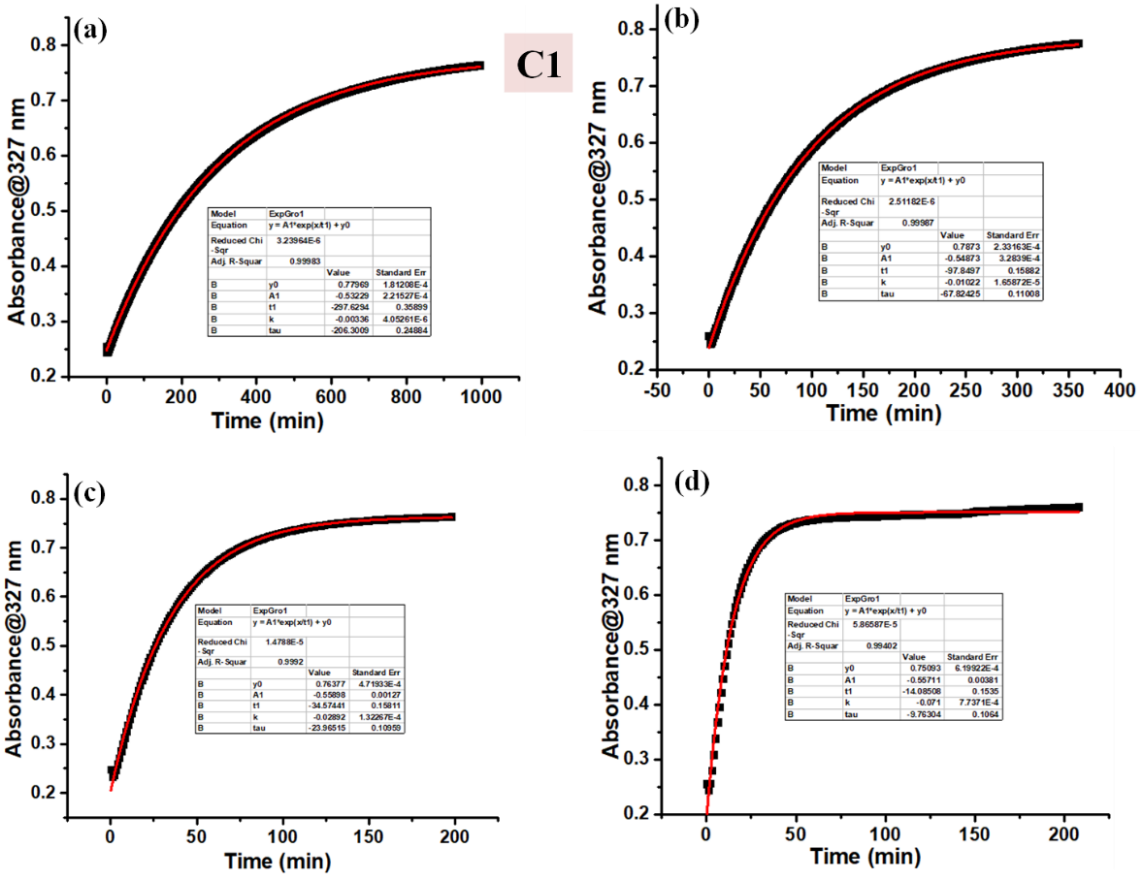

Figure 2C.13 Thermal reverse isomerization kinetics plots of **C1** in DMSO at (a) 60 ^{o}C; (b) 70 ^{o}C; (c) 80 ^{o}C; (d) 90 ^{o}C using UV-Vis Spectroscopy.

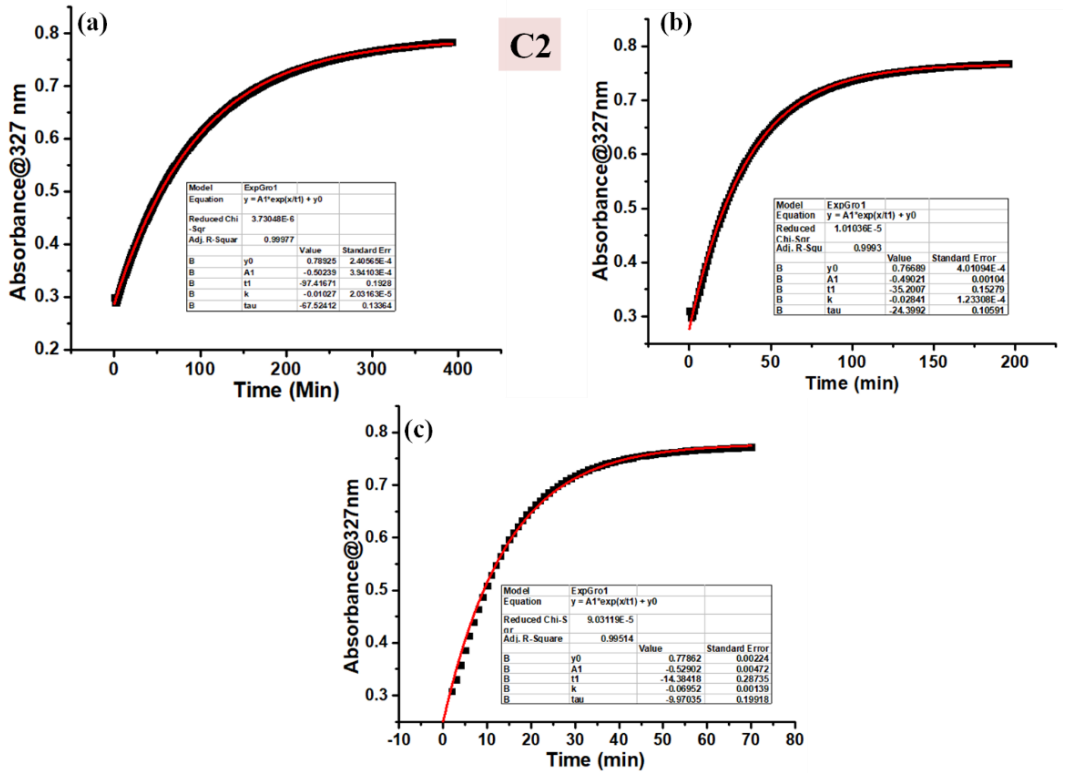

Figure 2C.14 Thermal reverse isomerization kinetics plots of **C2** in DMSO at (a) 70 ^{o}C; (b) 80 ^{o}C; (c) 90 ^{o}C using UV-Vis Spectroscopy.

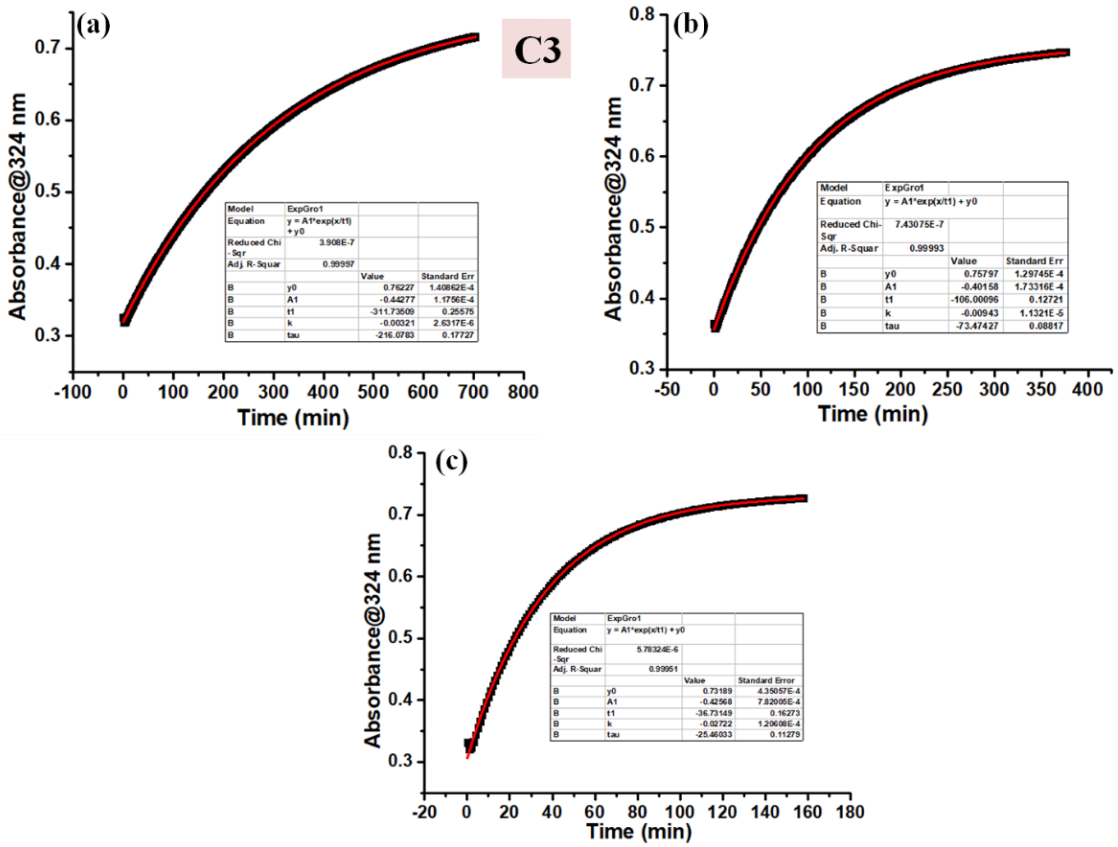

Figure 2C.15 Thermal reverse isomerization kinetics plots of **C3** in DMSO at (a) 60 ^{o}C; (b) 70 ^{o}C; (c) 80 ^{o}C using UV-Vis Spectroscopy.

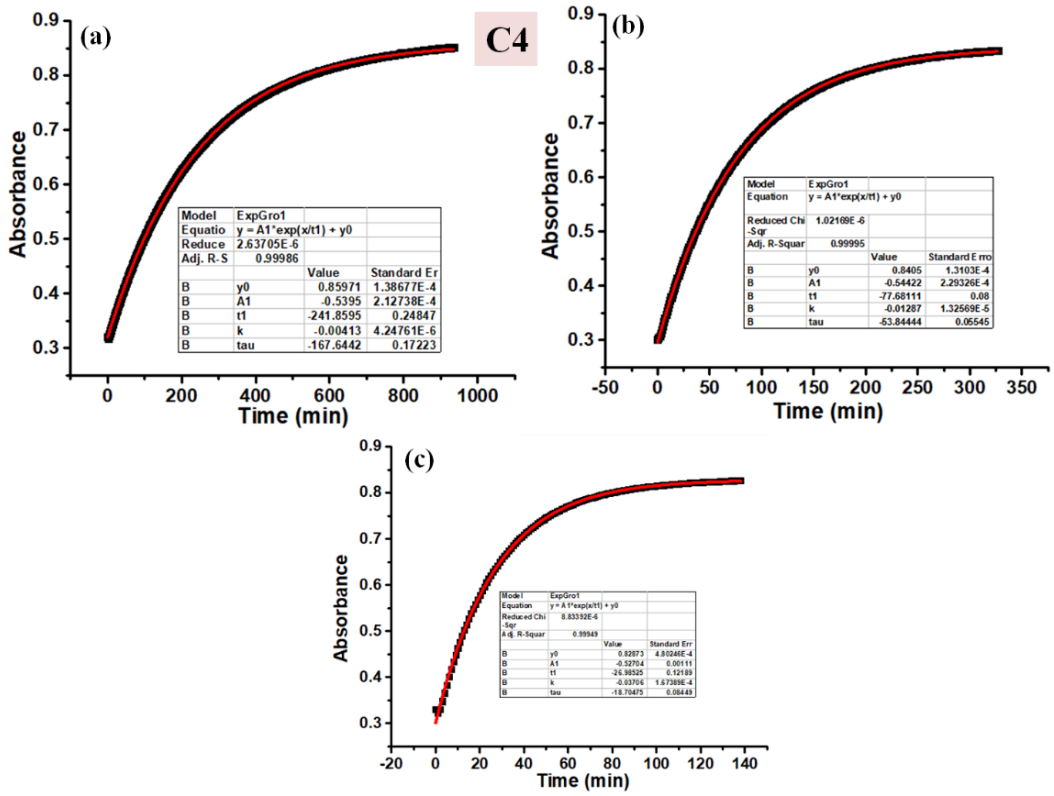

Figure 2C.16 Thermal reverse isomerization kinetics plots of **C4** in DMSO at (a) 60 ^{o}C; (b) 70 ^{o}C; (c)80 ^{o}C using UV-Vis Spectroscopy.

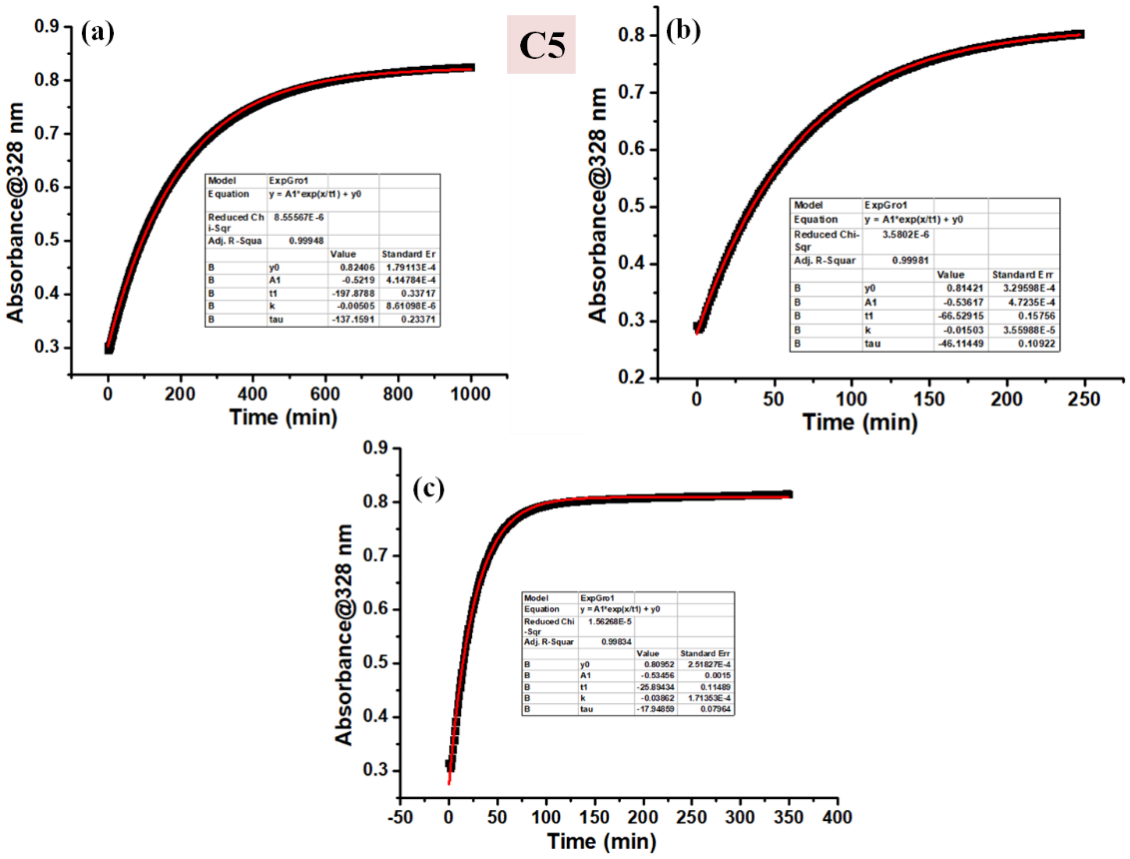

Figure 2C.17 Thermal reverse isomerization kinetics plots of **C5** in DMSO at (a) 70 ^{o}C; (b) 80 ^{o}C; (c) 90 ^{o}C using UV-Vis Spectroscopy.

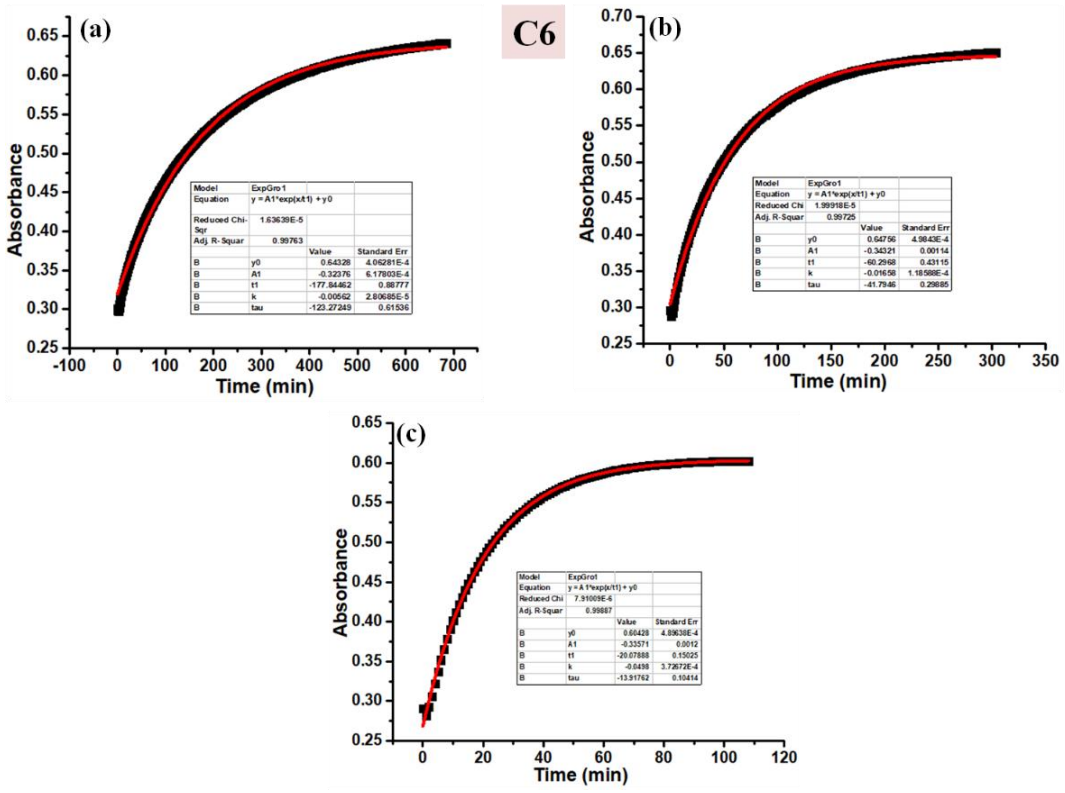

Figure 2C.18 Thermal reverse isomerization kinetics plots of **C6** in DMSO at (a) 70 ^{o}C; (b) 80 ^{o}C; (c) 90 ^{o}C using UV-Vis Spectroscopy.

Appendix 2D

Arrehenius and Eyring plots

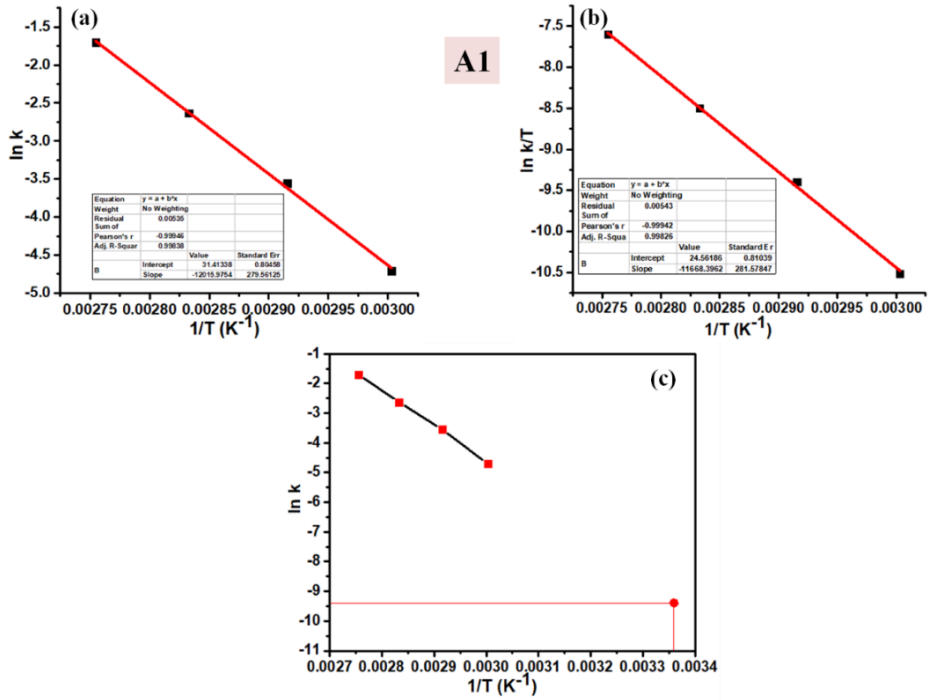

Figure 2D.1 (a) Arrhenius; (b) Eyring Plot; (c) Extrapolation of Arrhenius Plot for **A1** corresponding to thermal reverse isomerization

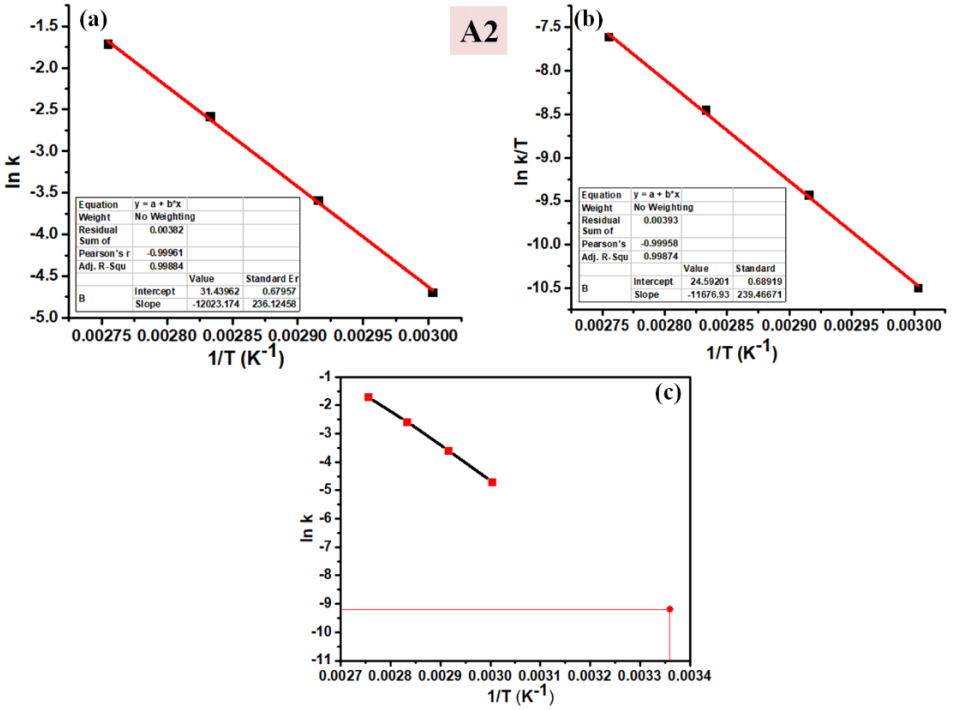

Figure 2D.2 (a) Arrhenius; (b) Eyring Plot; (c) Extrapolation of Arrhenius Plot for **A2** corresponding to thermal reverse isomerization

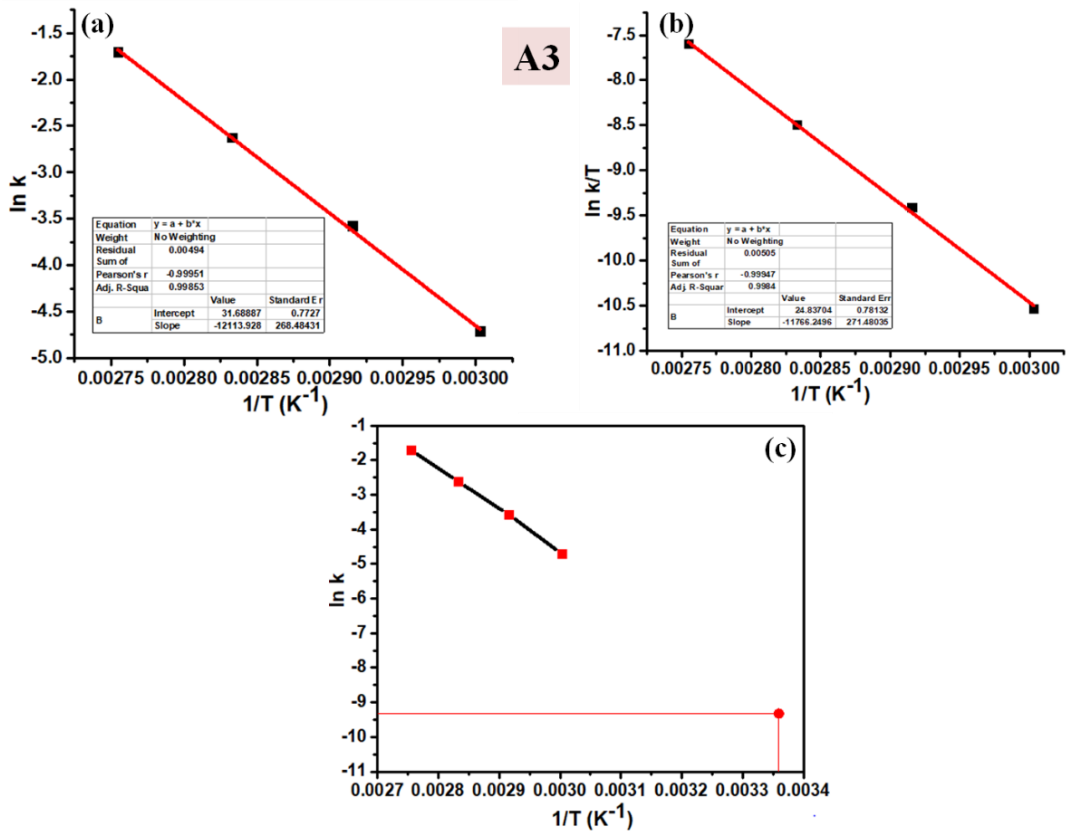

Figure 2D.3 (a) Arrhenius; (b) Eyring Plot; (c) Extrapolation of Arrhenius Plot for **A3** corresponding to thermal reverse isomerization

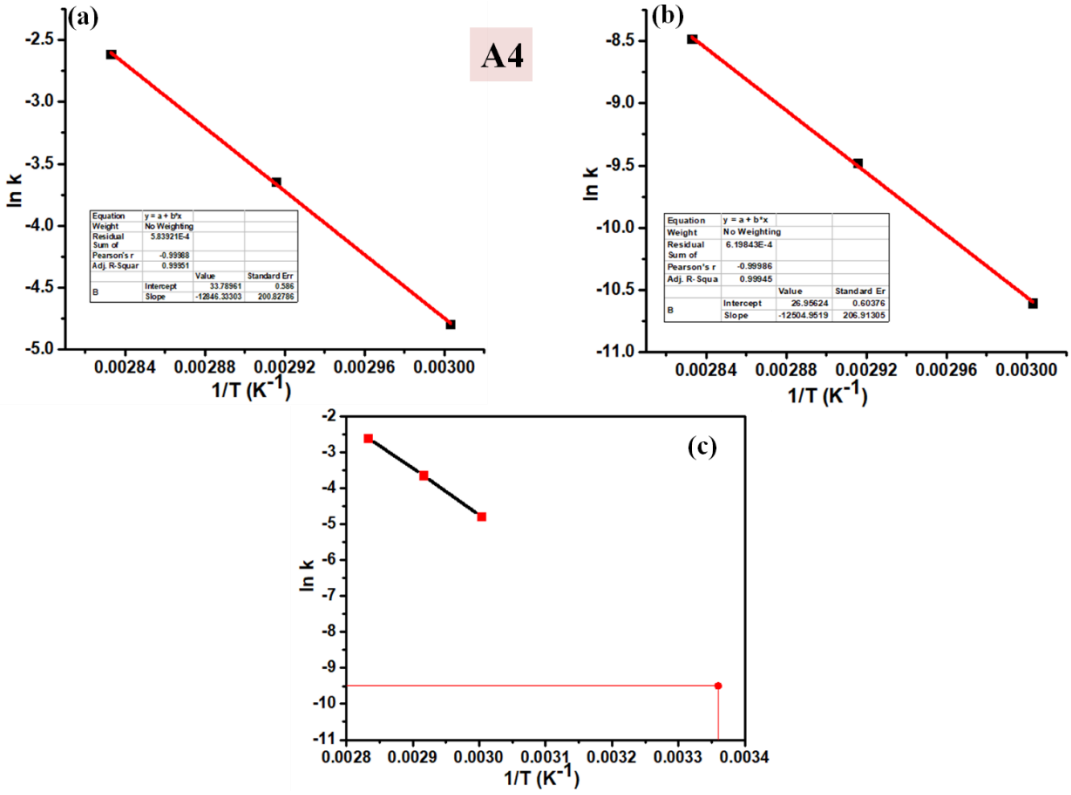

Figure 2D.4 (a) Arrhenius; (b) Eyring Plot; (c) Extrapolation of Arrhenius Plot for **A4** corresponding to thermal reverse isomerization

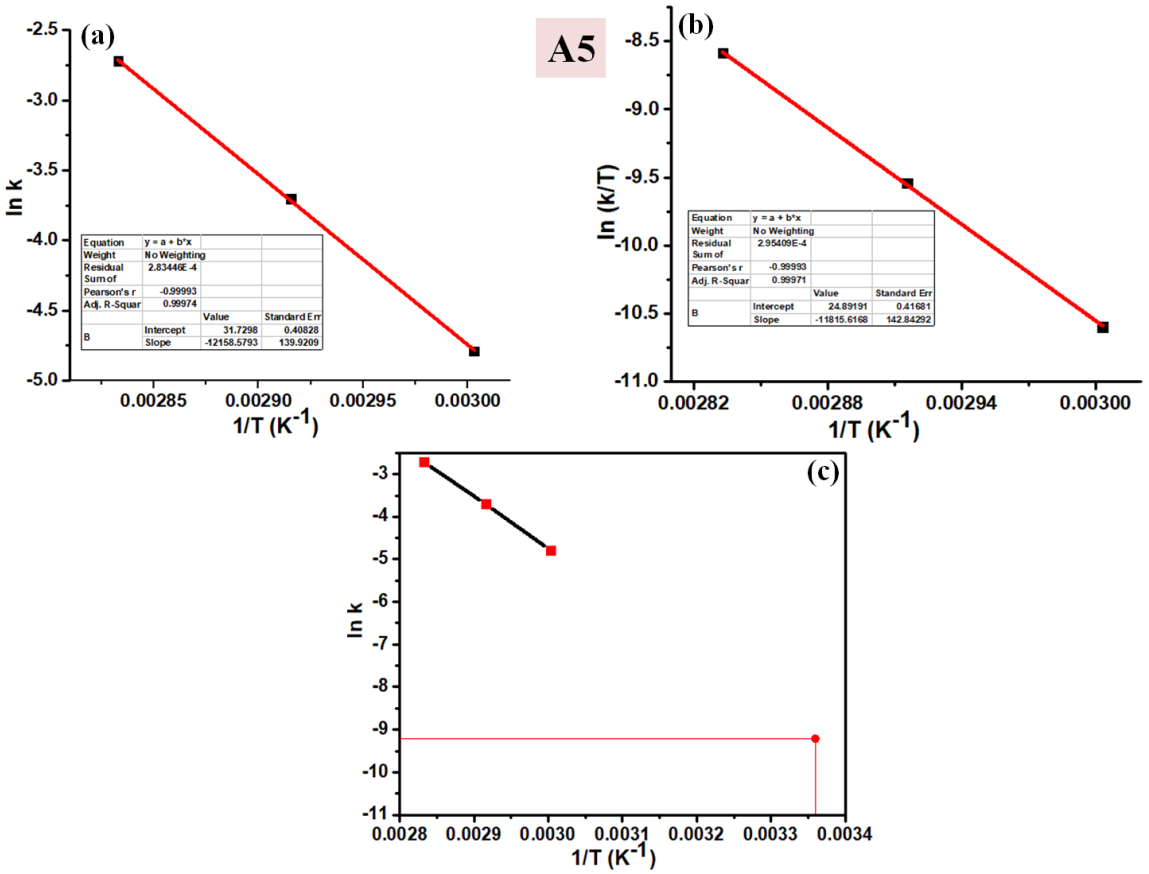

Figure 2D.5 (a) Arrhenius; (b) Eyring Plot; (c) Extrapolation of Arrhenius Plot for **A5** corresponding to thermal reverse isomerization

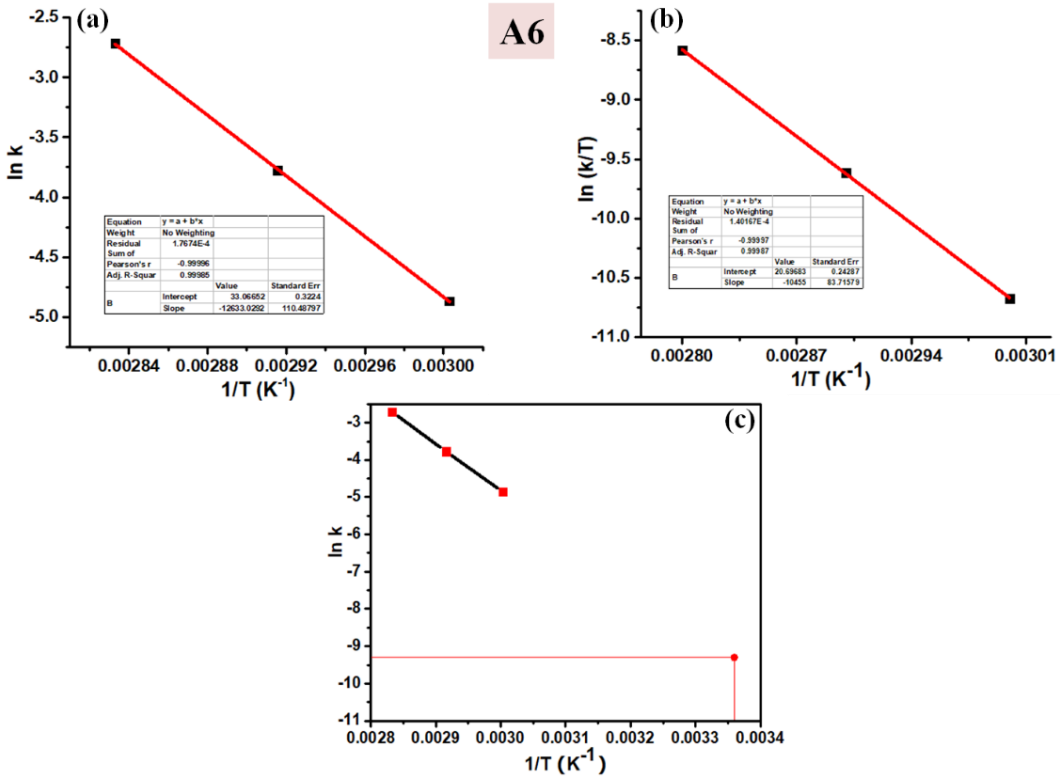

Figure 2D.6 (a) Arrhenius; (b) Eyring Plot; (c) Extrapolation of Arrhenius Plot for **A6** corresponding to thermal reverse isomerization

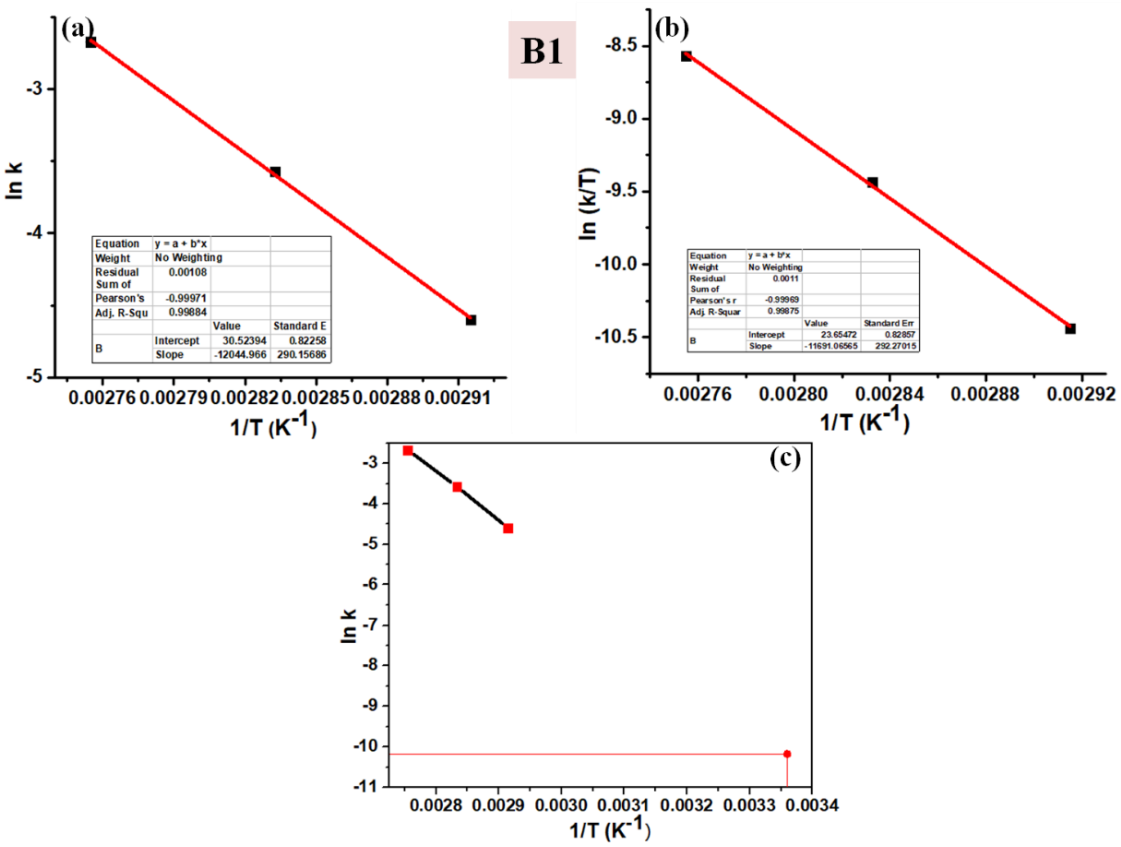

Figure 2D.7 (a) Arrhenius; (b) Eyring Plot; (c) Extrapolation of Arrhenius Plot for **B1** corresponding to thermal reverse isomerization

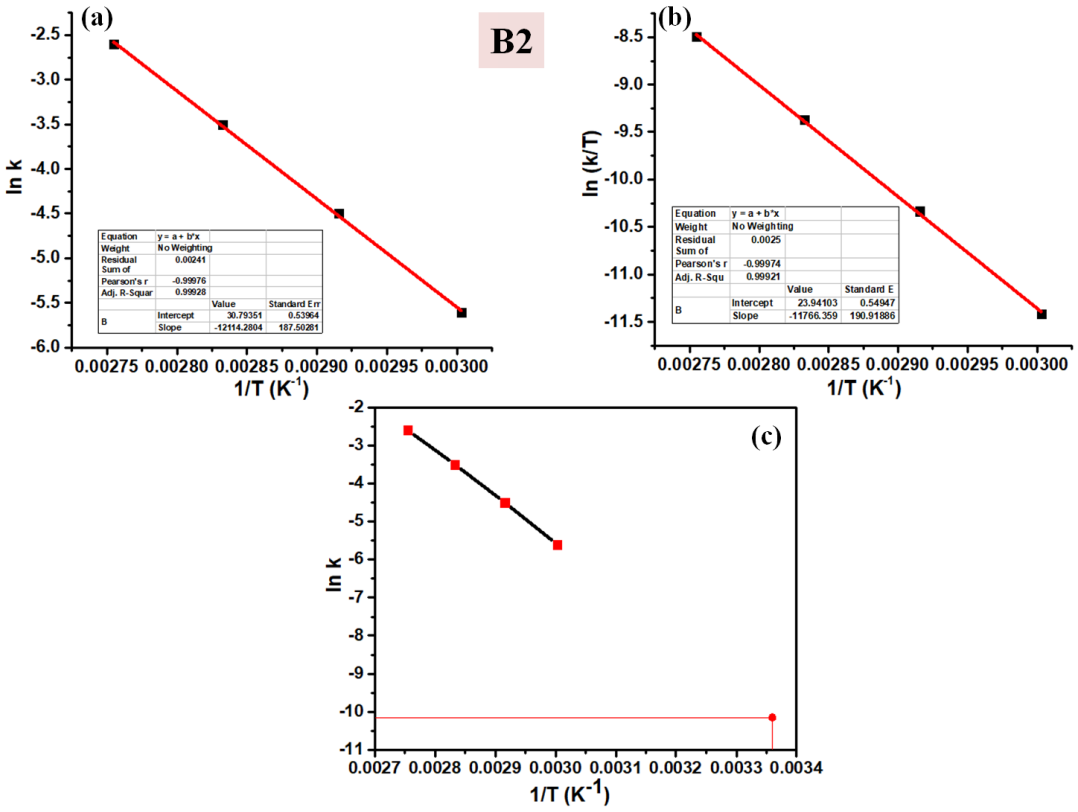

Figure 2D.8 (a) Arrhenius; (b) Eyring Plot; (c) Extrapolation of Arrhenius Plot for **B2** corresponding to thermal reverse isomerization

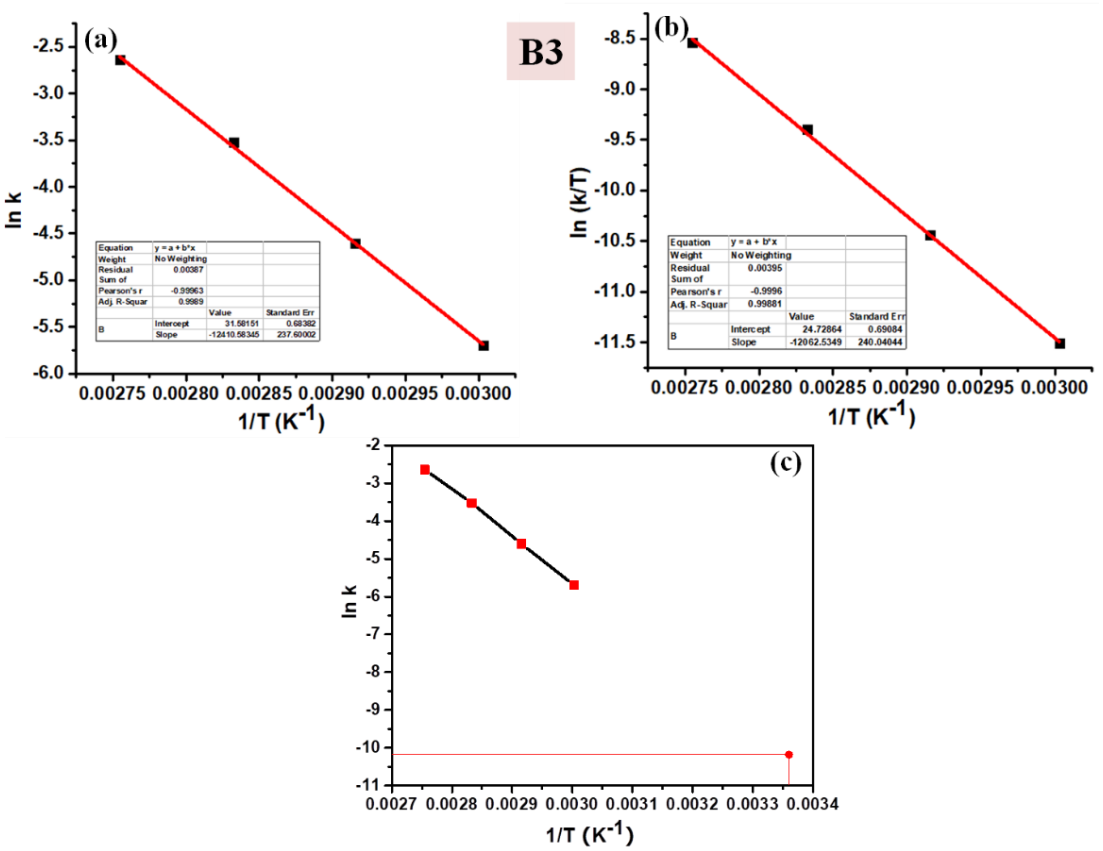

Figure 2D.9 (a) Arrhenius; (b) Eyring Plot; (c) Extrapolation of Arrhenius Plot for **B3** corresponding to thermal reverse isomerization.

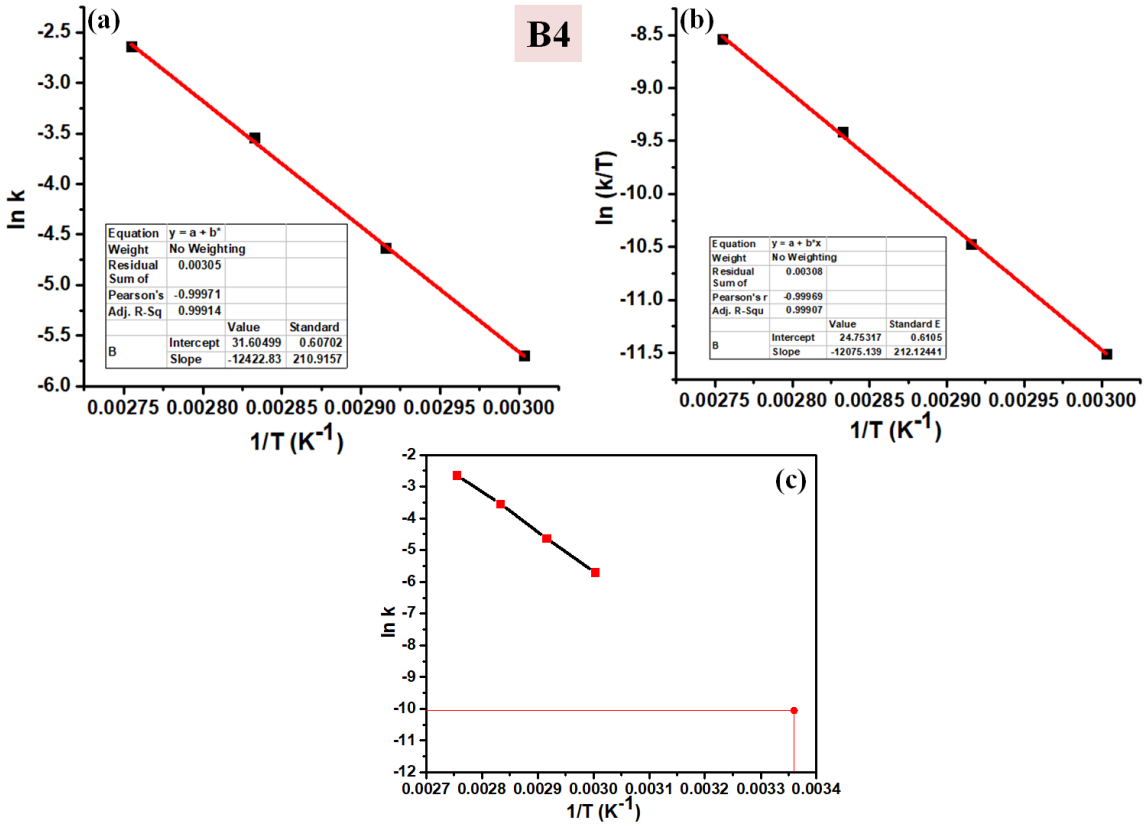

Figure 2D.10 (a) Arrhenius; (b) Eyring Plot; (c) Extrapolation of Arrhenius Plot for **B4** corresponding to thermal reverse isomerization

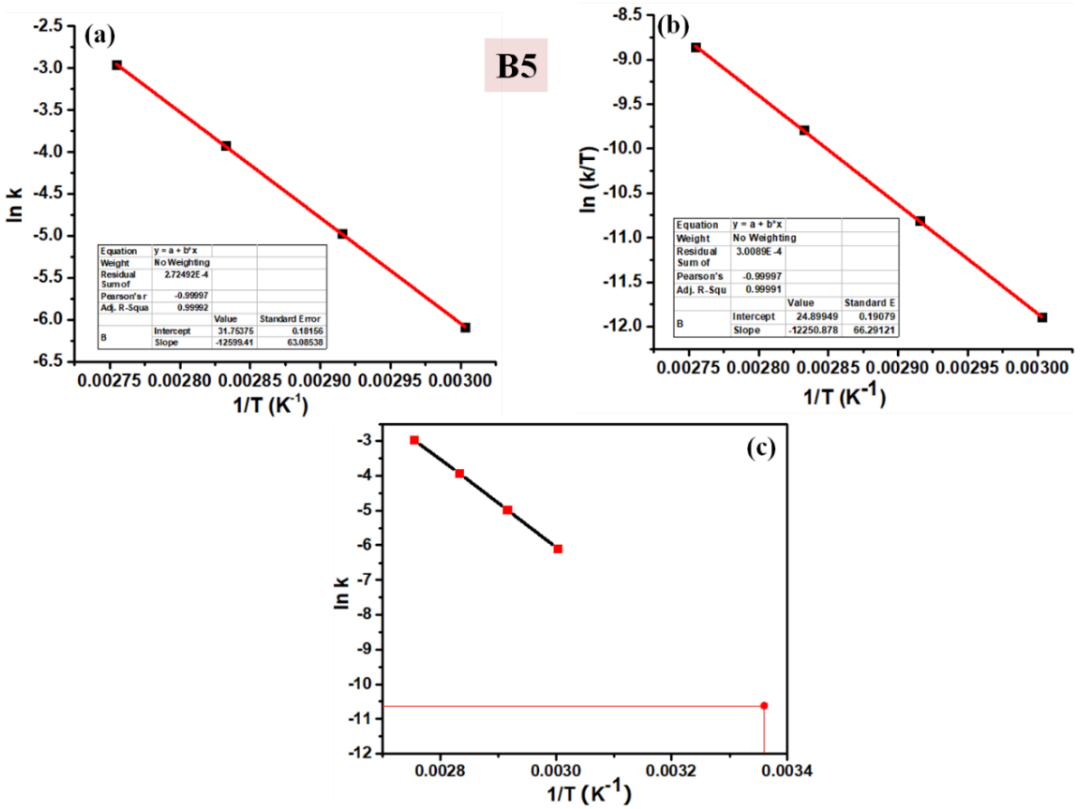

Figure 2D.11 (a) Arrhenius; (b) Eyring Plot; (c) Extrapolation of Arrhenius Plot for **B5** corresponding to thermal reverse isomerization.

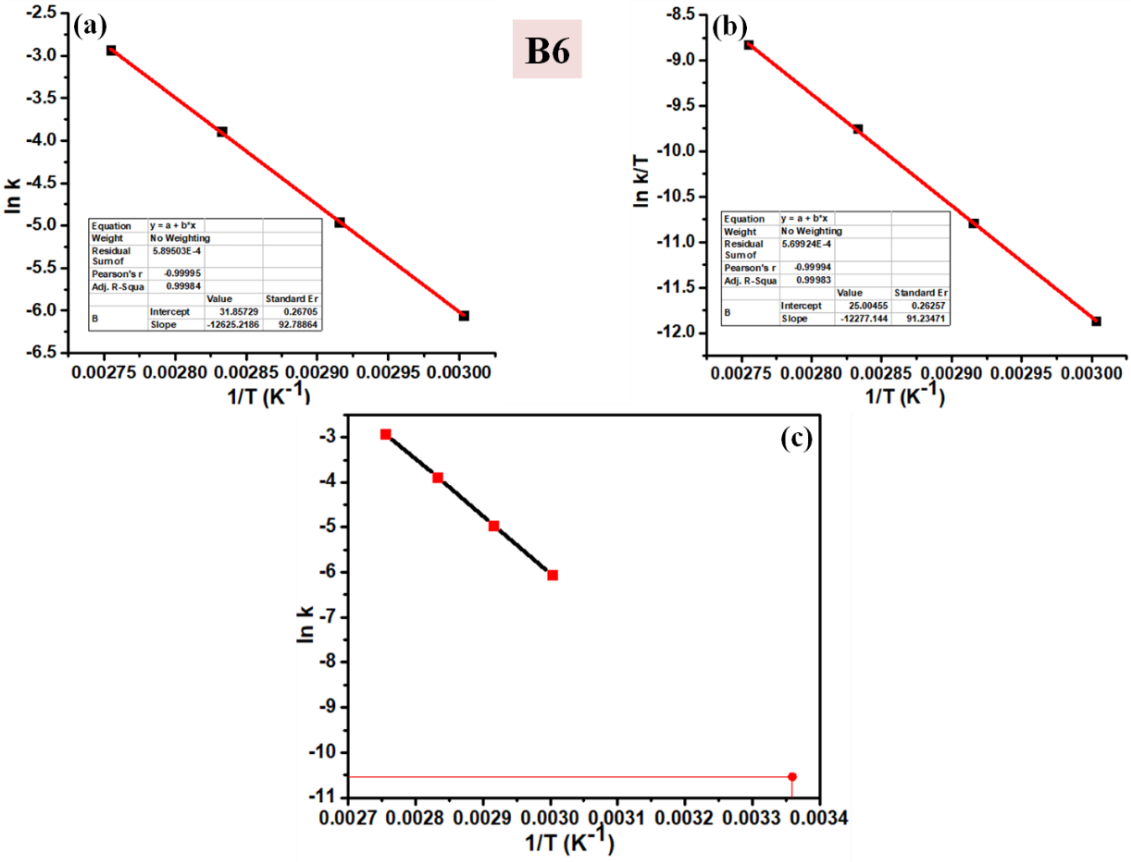

Figure 2D.12 (a) Arrhenius; (b) Eyring Plot; (c) Extrapolation of Arrhenius Plot for **B6** corresponding to thermal reverse isomerization

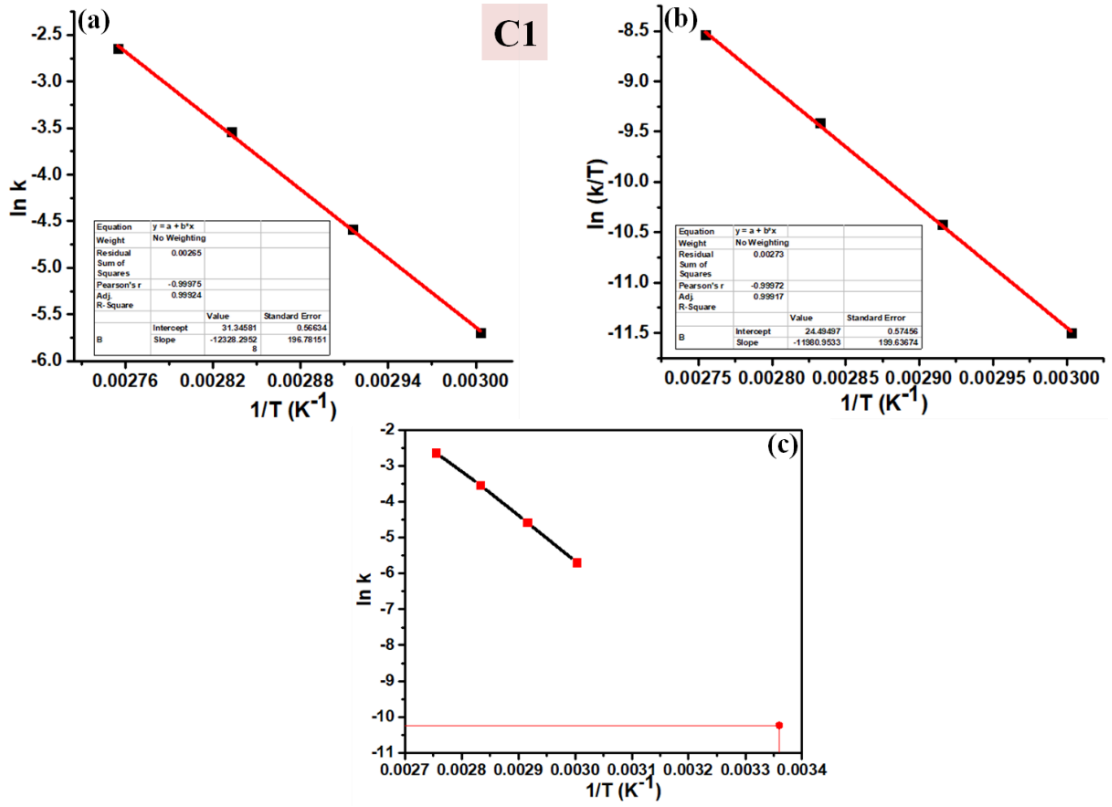

Figure 2D.13 (a) Arrhenius; (b) Eyring Plot; (c) Extrapolation of Arrhenius Plot for **C1** corresponding to thermal reverse isomerization.

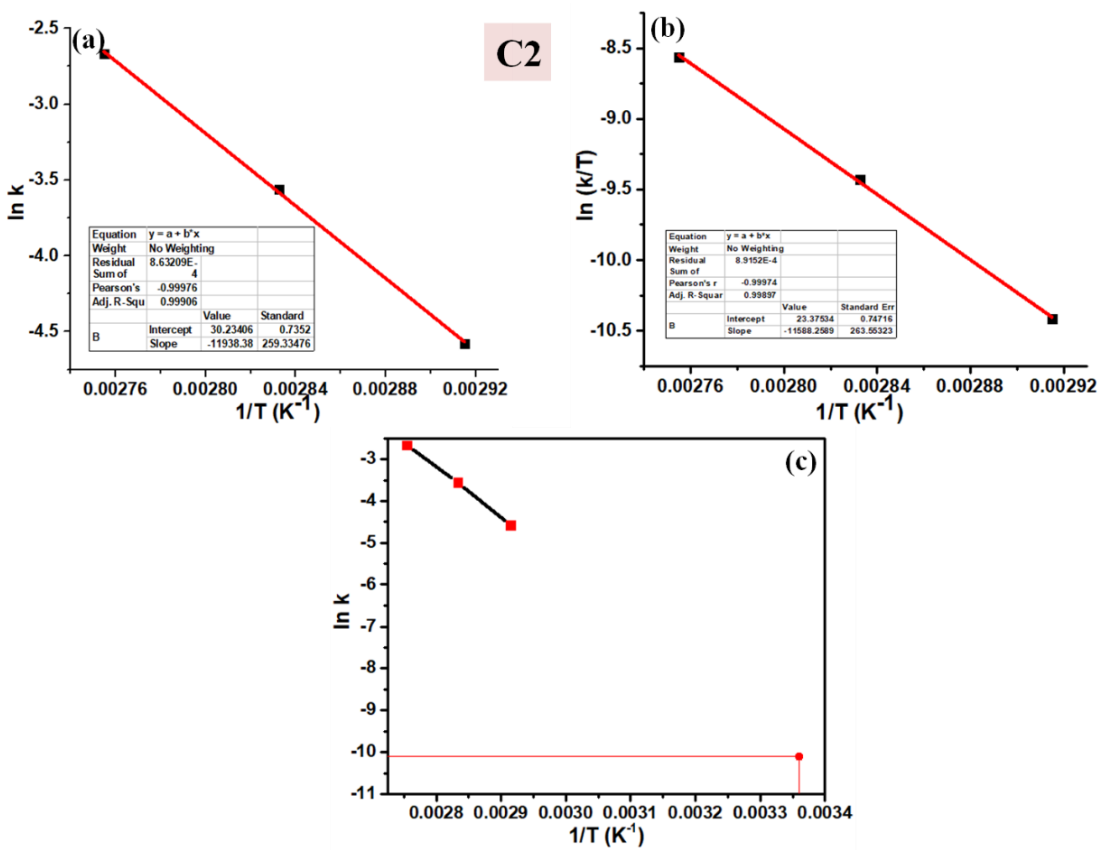

Figure 2D.14 (a) Arrhenius; (b) Eyring Plot; (c) Extrapolation of Arrhenius Plot for **C2** corresponding to thermal reverse isomerization

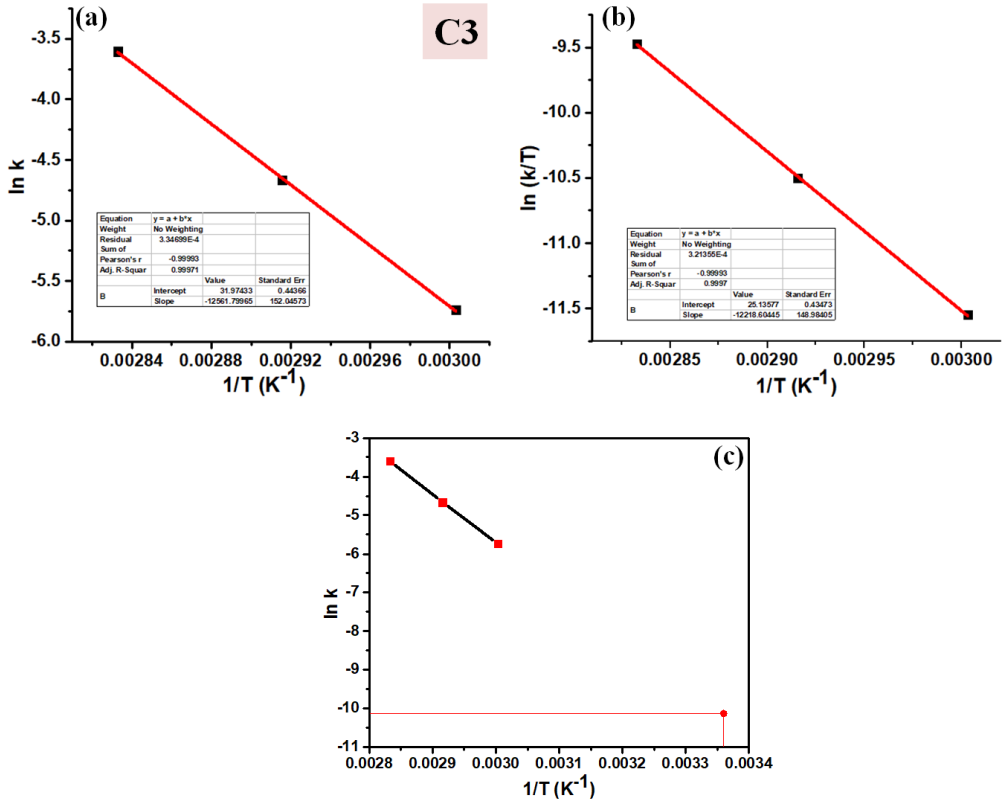

Figure 2D.15 (a) Arrhenius; (b) Eyring Plot; (c) Extrapolation of Arrhenius Plot for **C3** corresponding to thermal reverse isomerization

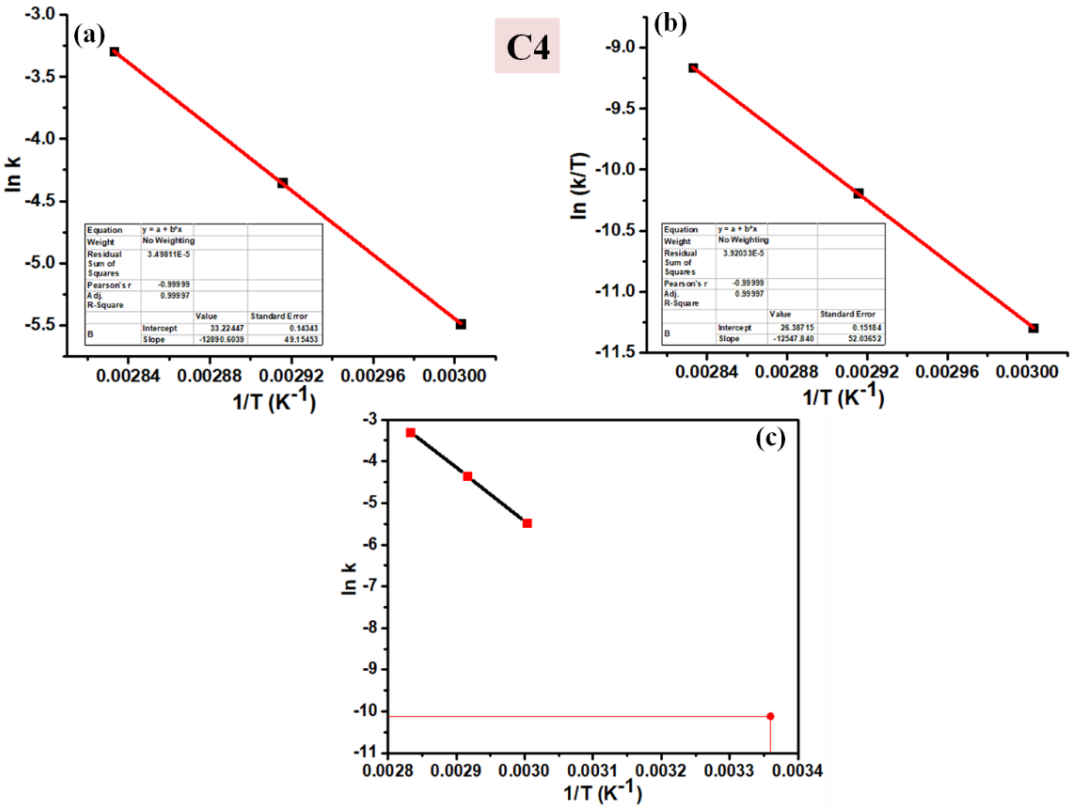

Figure 2D.16 (a) Arrhenius; (b) Eyring Plot; (c) Extrapolation of Arrhenius Plot for **C4** corresponding to thermal reverse isomerization

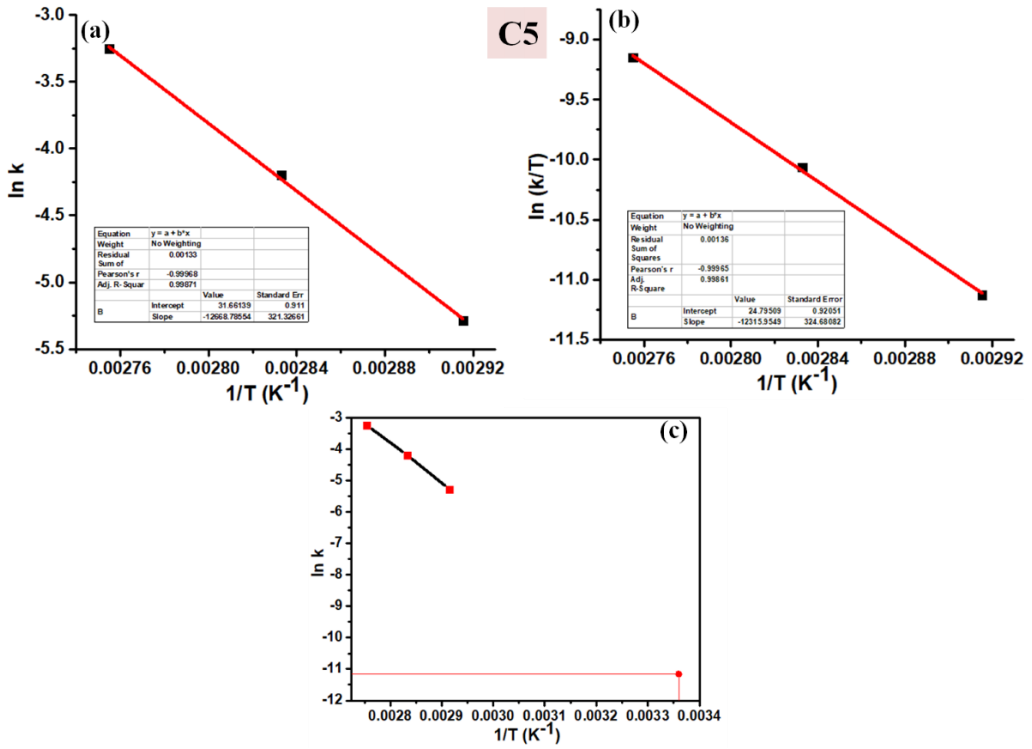

Figure 2D.17 (a) Arrhenius; (b) Eyring Plot; (c) Extrapolation of Arrhenius Plot for **C5** corresponding to thermal reverse isomerization.

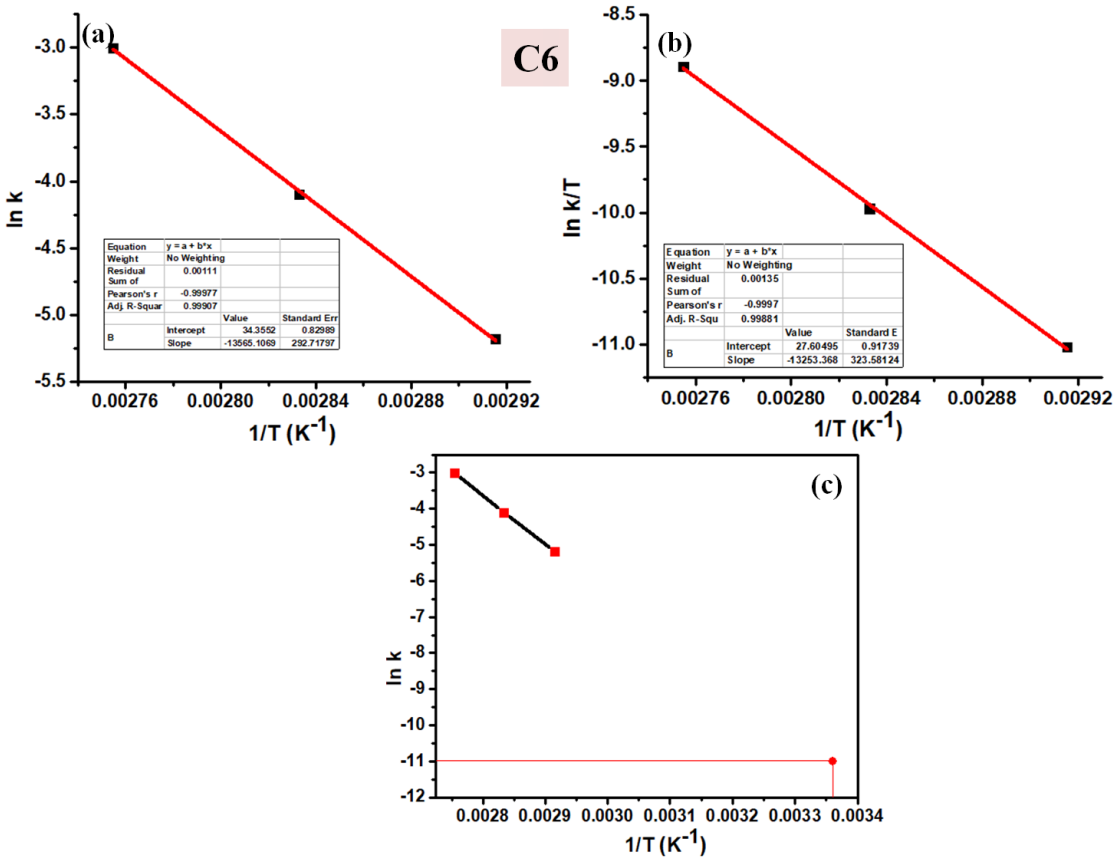

Figure 2D.18 (a) Arrhenius; (b) Eyring Plot; (c) Extrapolation of Arrhenius Plot for **C6** corresponding to thermal reverse isomerization.

Appendix 2E

^{1}H-NMR and ^{13}C-NMR Characterization

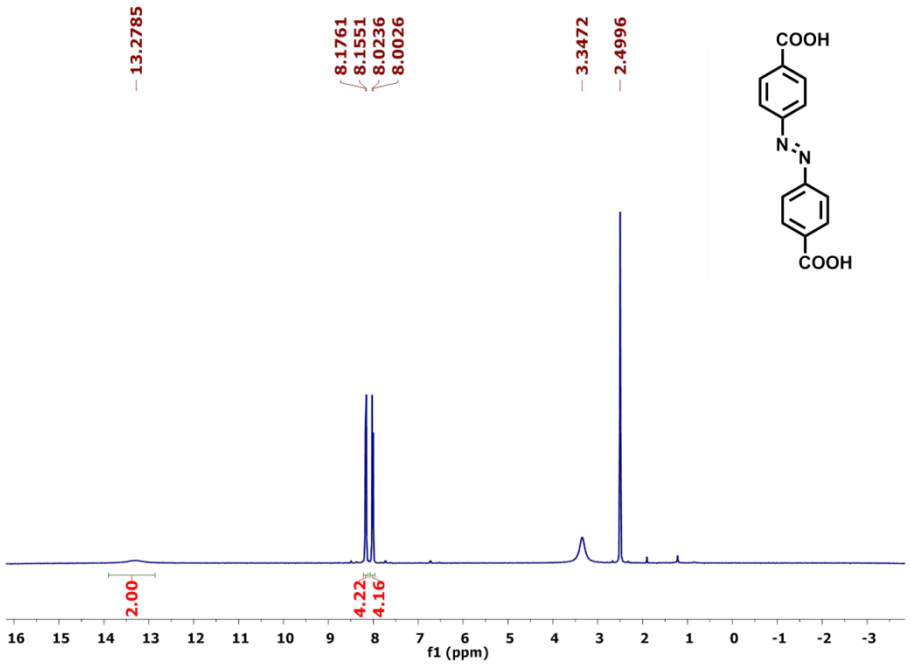

^{1}H-NMR spectrum of (*E*)-4,4'-(diazene-1,2-diyl)dibenzoic acid in [D_6]DMSO.

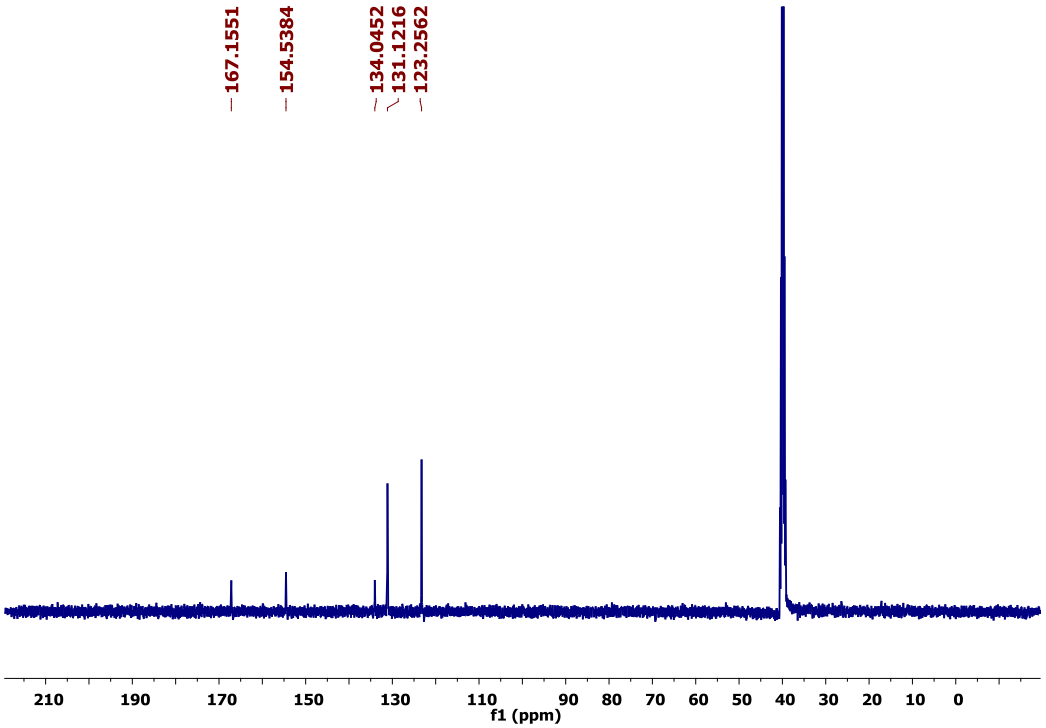

^{13}C-NMR spectrum of (*E*)-4,4'-(diazene-1,2-diyl)dibenzoic acid in [D_6]DMSO.

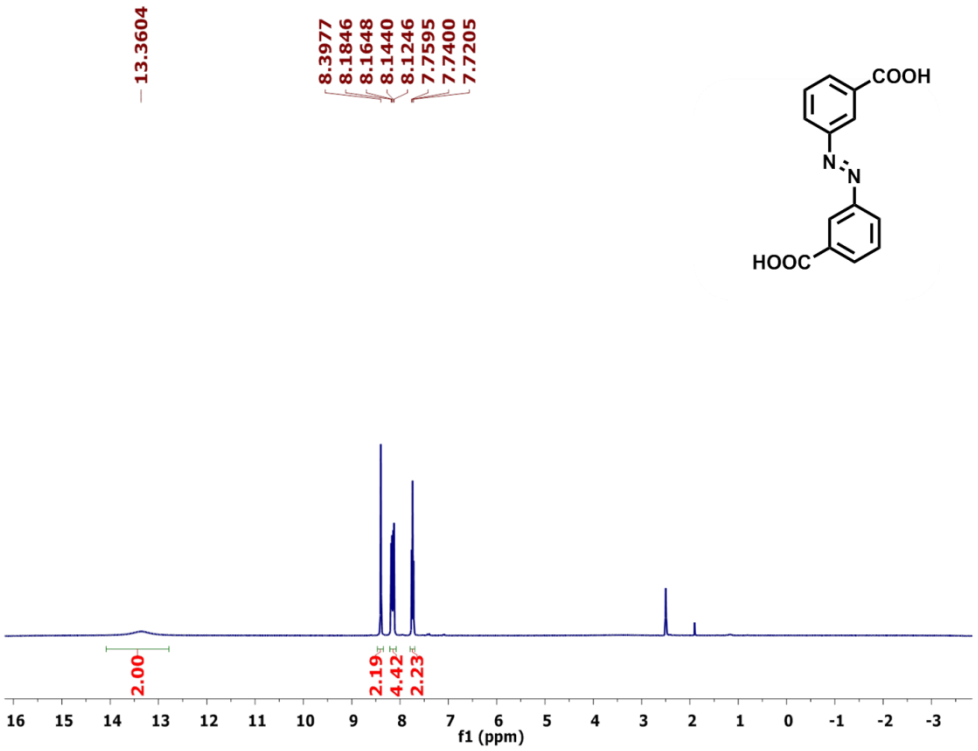

^{1}H-NMR spectrum of (*E*)-3,3'-(diazene-1,2-diyl)dibenzoic acid in [D_6]DMSO.

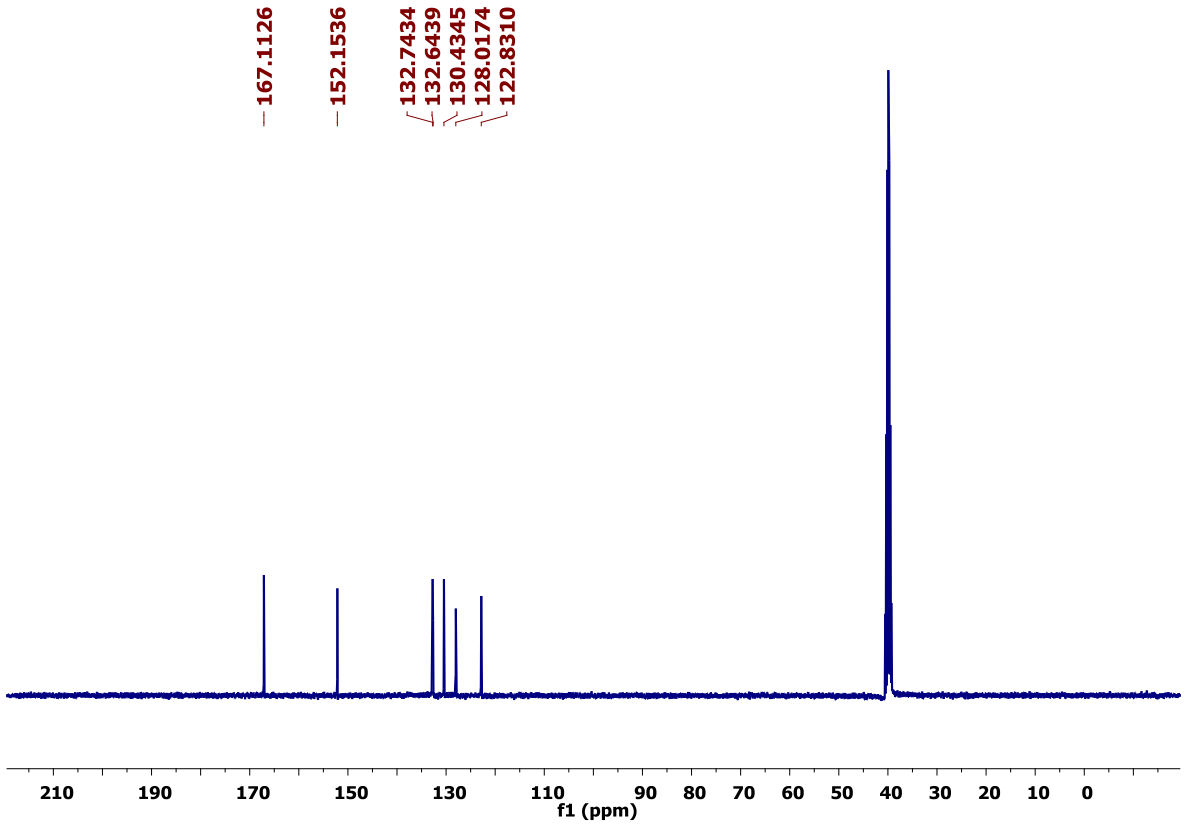

^{13}C-NMR spectrum of (*E*)-3,3'-(diazene-1,2-diyl)dibenzoic acid in [D_6]DMSO.

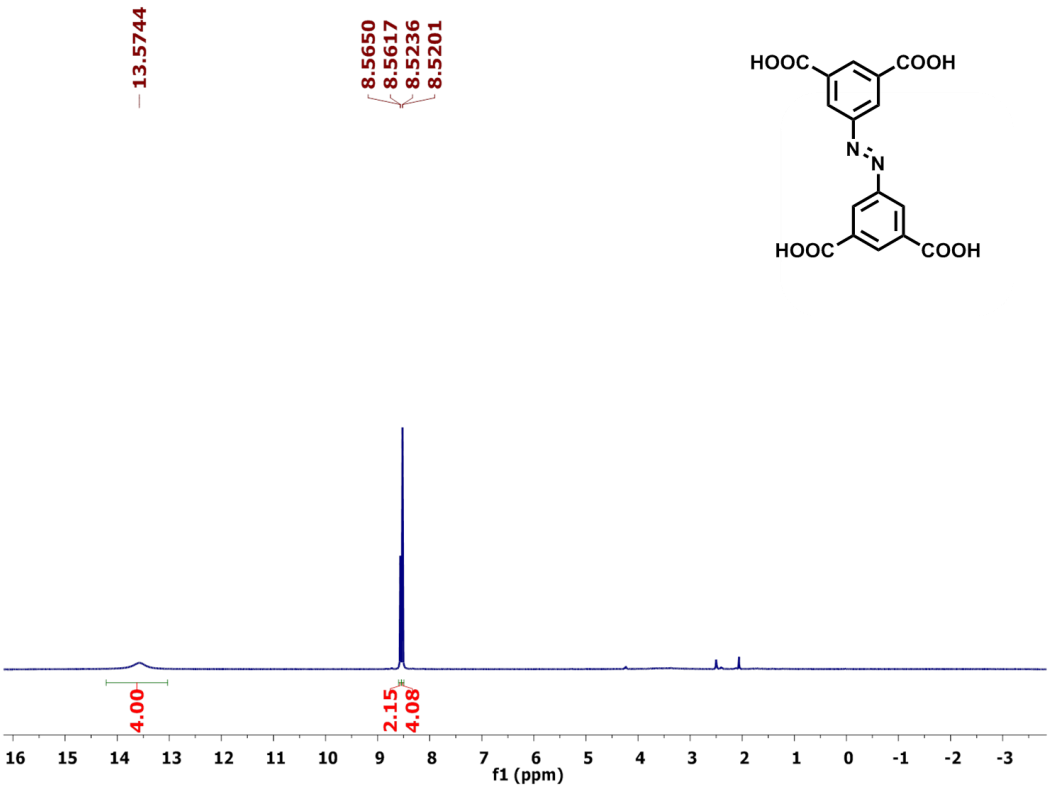

^{1}H-NMR spectrum of (*E*)-5,5'-(diazene-1,2-diyl)diisophthalic acid in [D_6]DMSO.

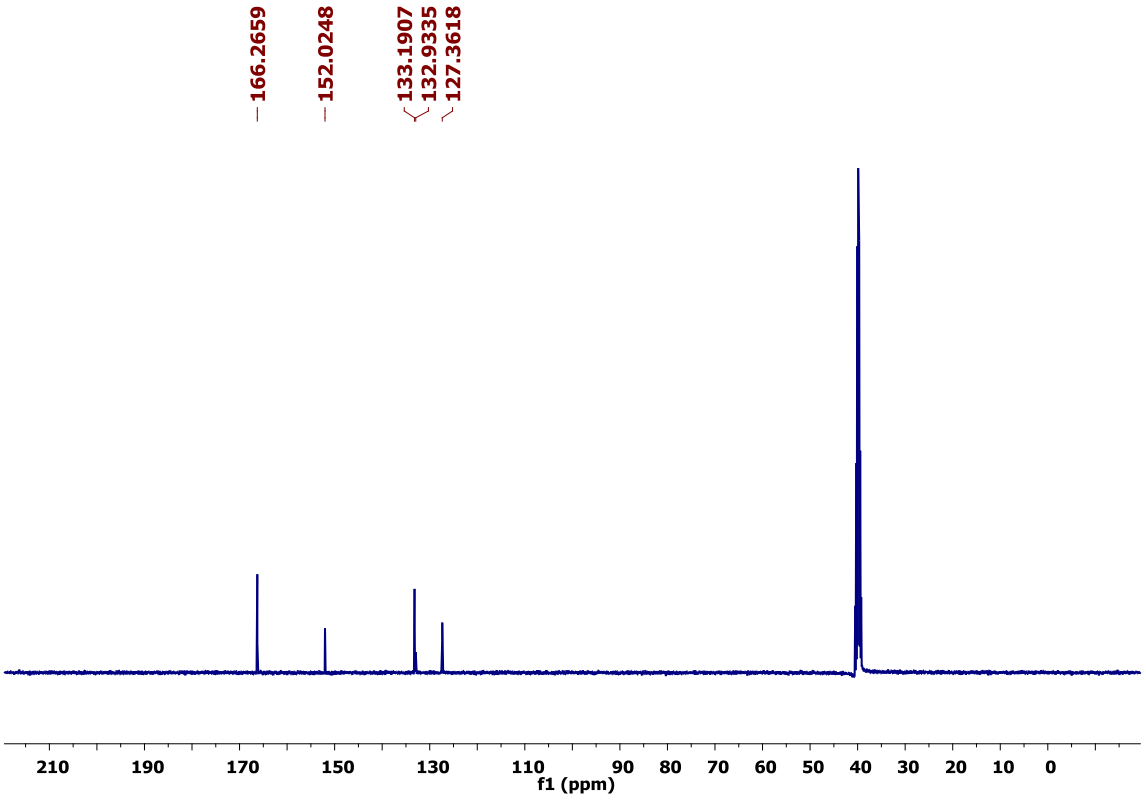

^{13}C-NMR spectrum of (*E*)-5,5'-(diazene-1,2-diyl)diisophthalic acid in [D_6]DMSO.

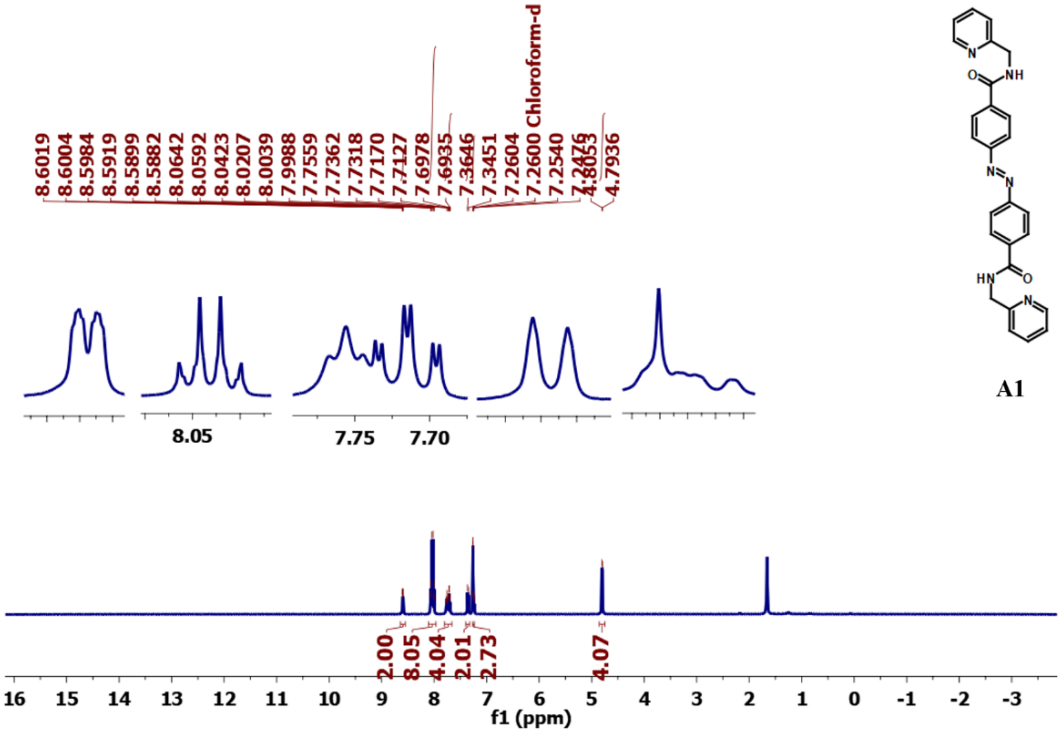

^{1}H-NMR spectrum of (*E*)-4,4'-(diazene-1,2-diyl)bis(N-(pyridin-2-ylmethyl)benzamide) **(A1)** in $CDCl_3$.

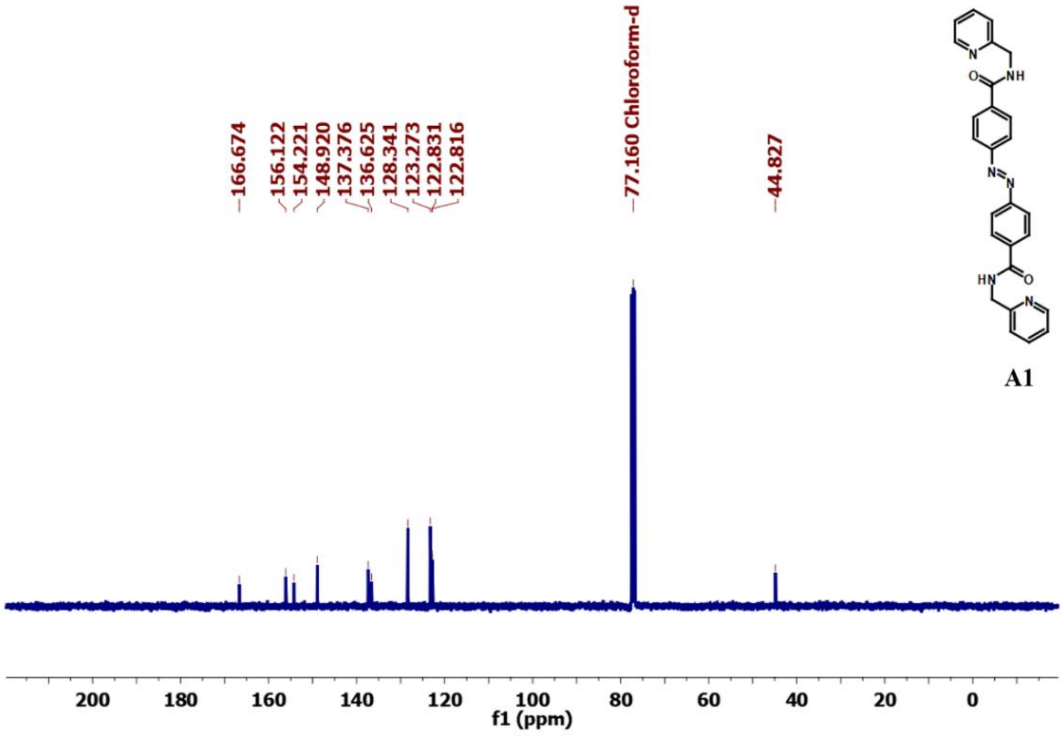

^{13}C-NMR spectrum of (*E*)-4,4'-(diazene-1,2-diyl)bis(N-(pyridin-2-ylmethyl)benzamide) **(A1)** in $CDCl_3$.

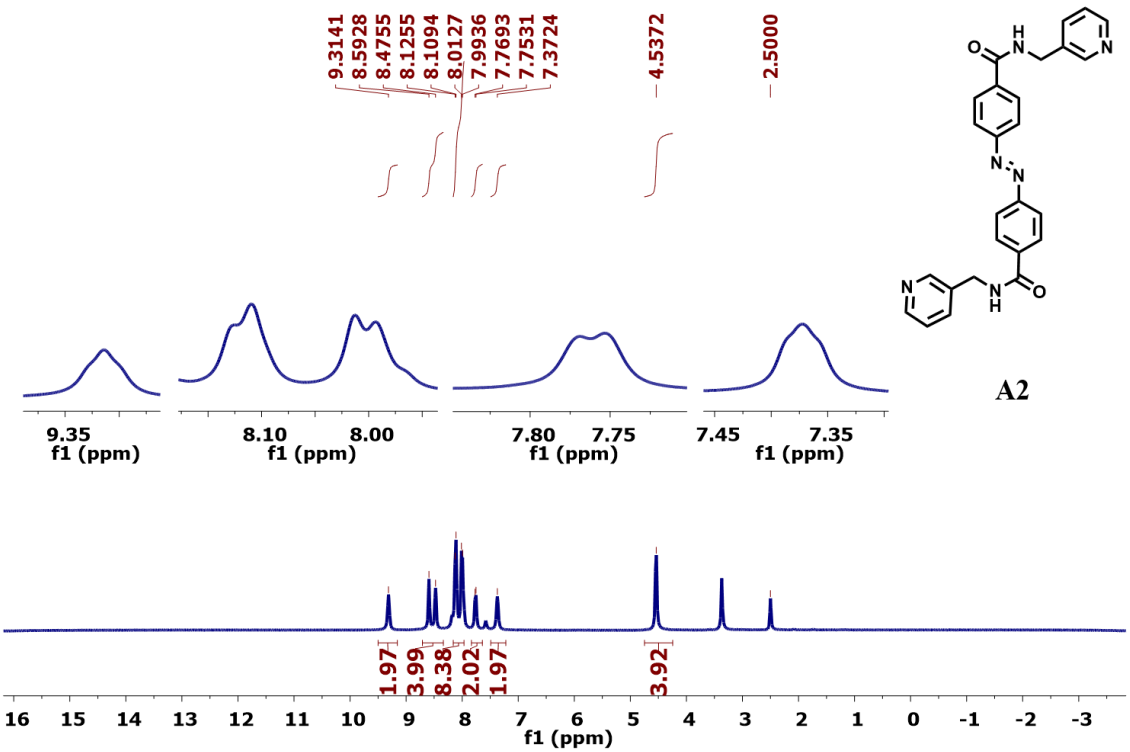

^{1}H-NMR spectrum of (*E*)-4,4'-(diazene-1,2-diyl)bis(N-(pyridin-3-ylmethyl)benzamide) **(A2)** in [D_6]DMSO

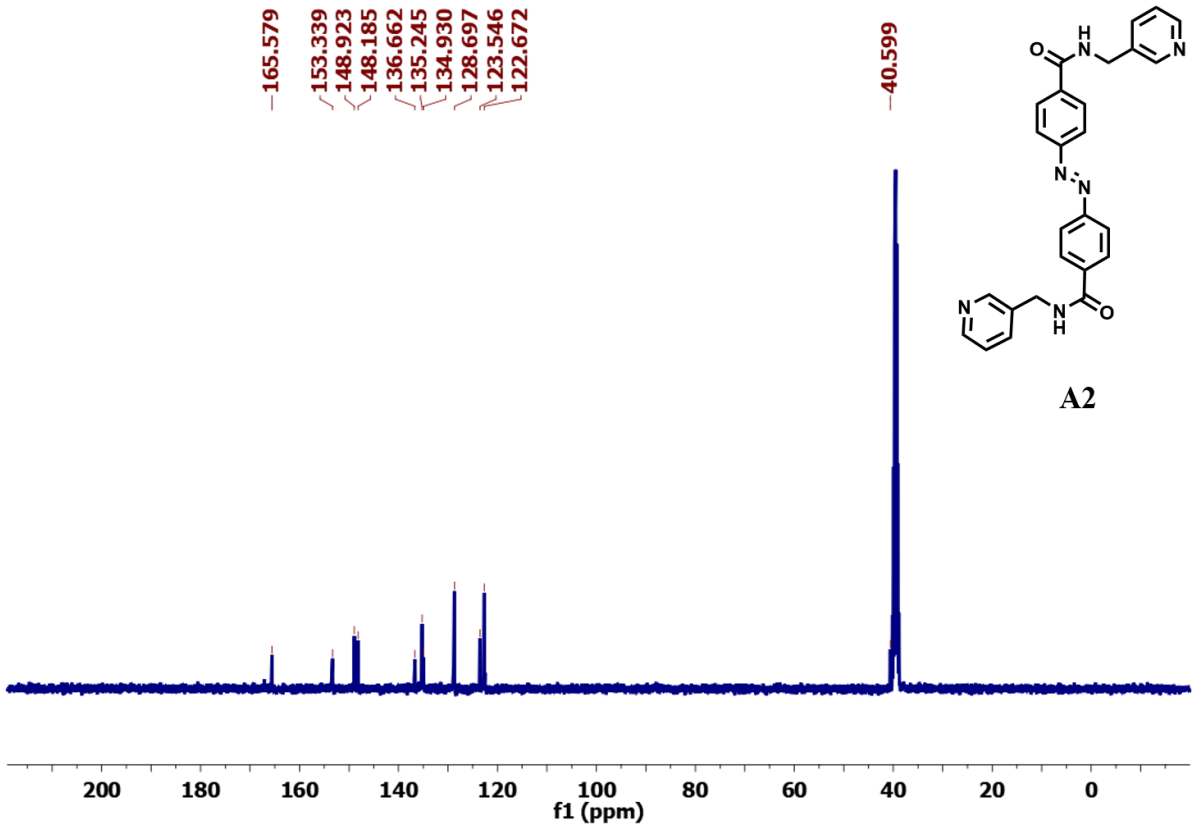

^{13}C-NMR spectrum of (*E*)-4,4'-(diazene-1,2-diyl)bis(N-(pyridin-3-ylmethyl)benzamide) **(A2)** in [D_6]DMSO

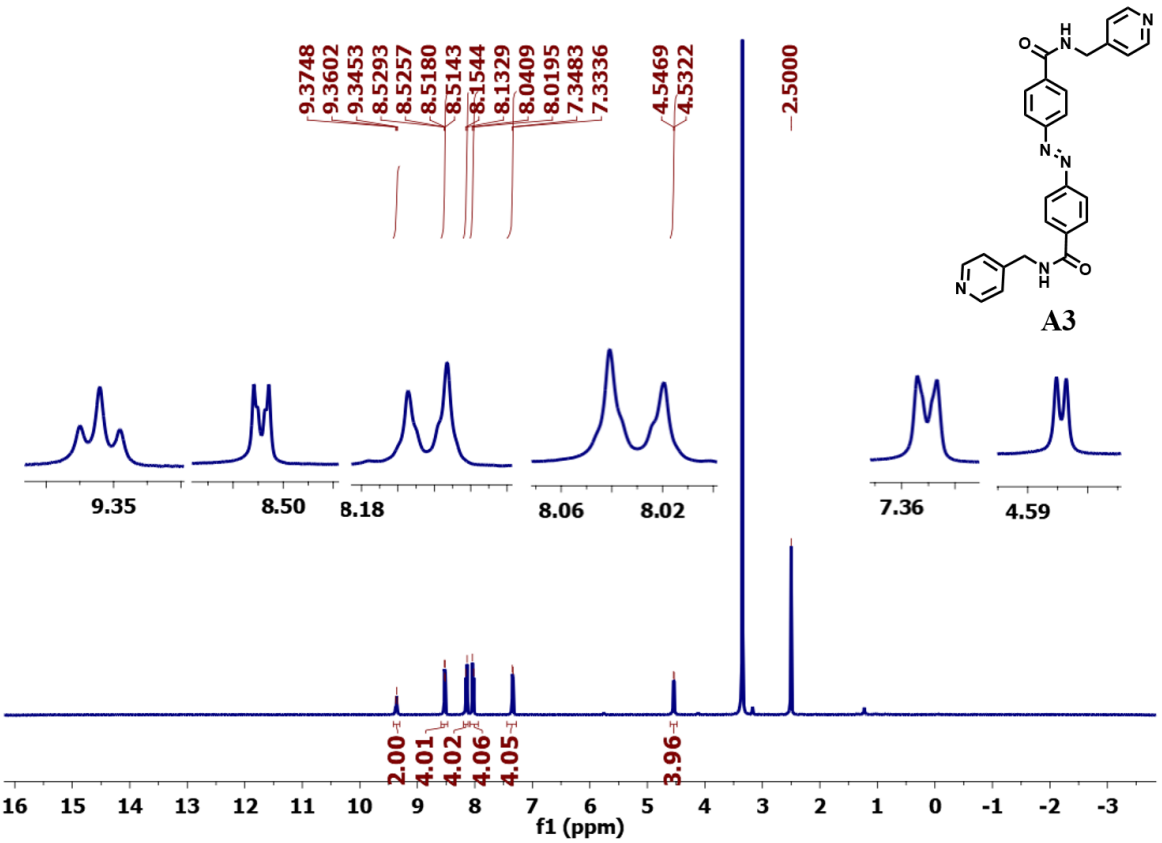

^{1}H-NMR spectrum of (*E*)-4,4'-(diazene-1,2-diyl)bis(N-(pyridin-4-ylmethyl)benzamide) **(A3)** in [D_6]DMSO

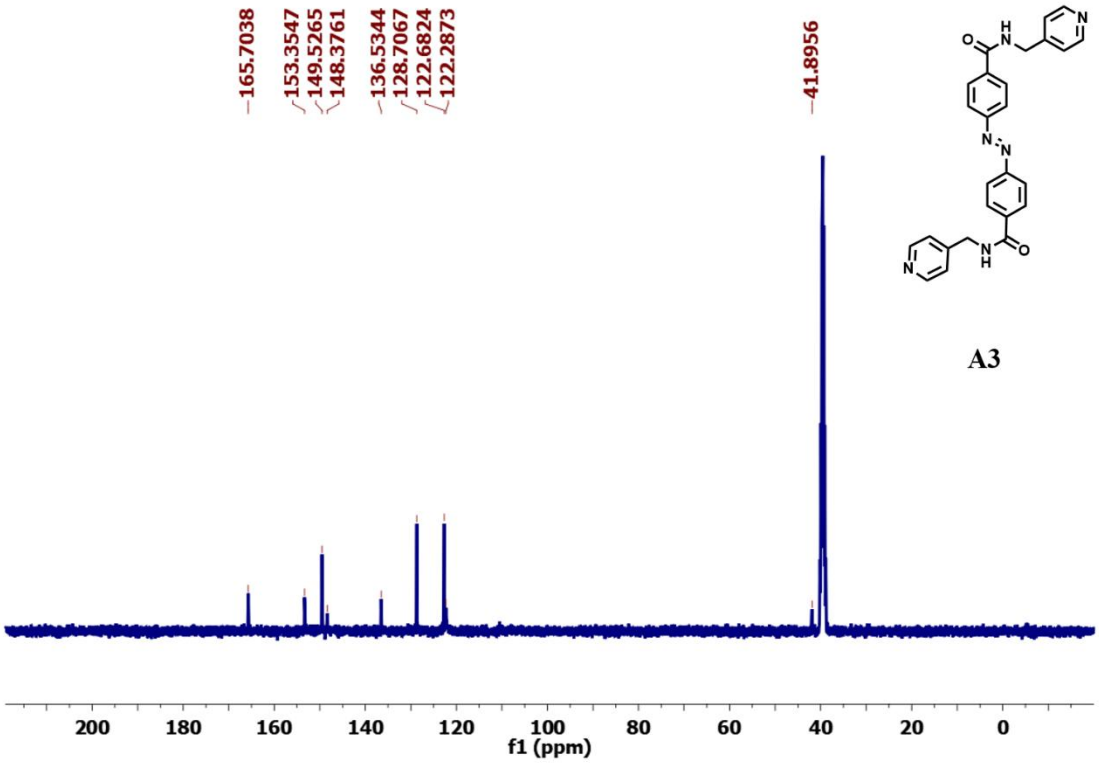

^{13}C-NMR spectrum of (*E*)-4,4'-(diazene-1,2-diyl)bis(N-(pyridin-4-ylmethyl)benzamide) **(A3)** in [D_6]DMSO

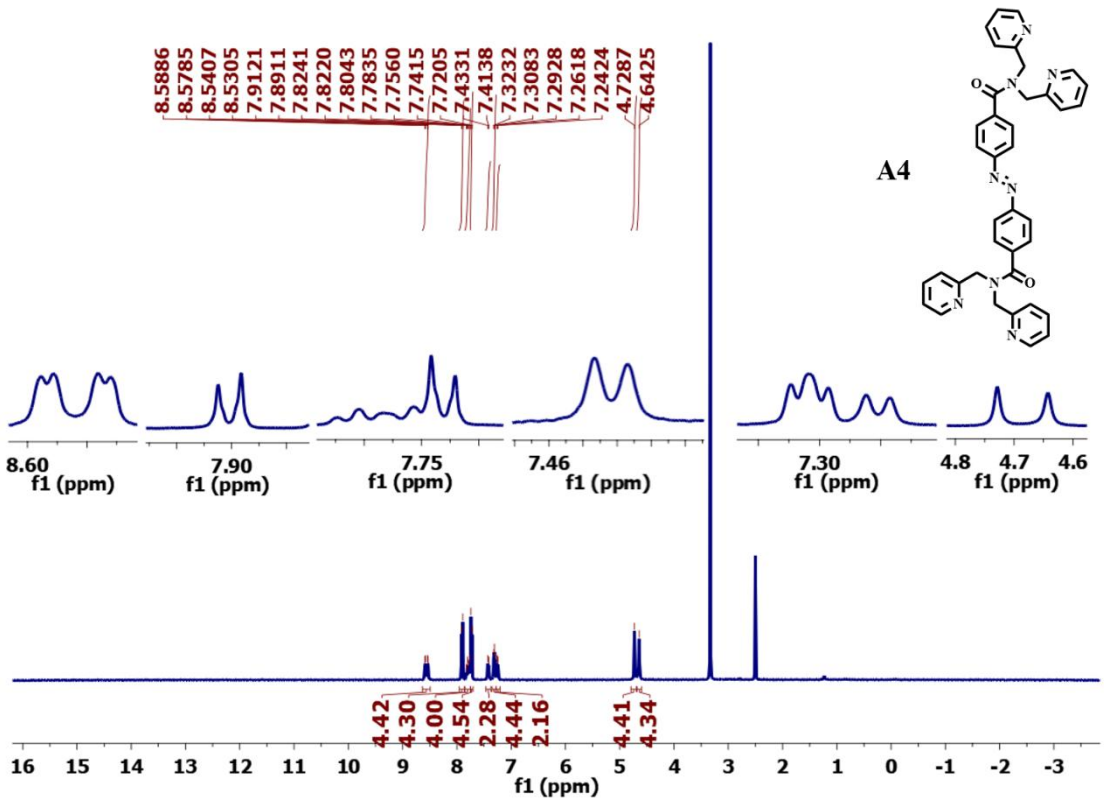

^{1}H-NMR spectrum of (*E*)-4,4'-(diazene-1,2-diyl)bis(N,N-bis(pyridin-2-ylmethyl)benzamide) **(A4)** in [D_6]DMSO.

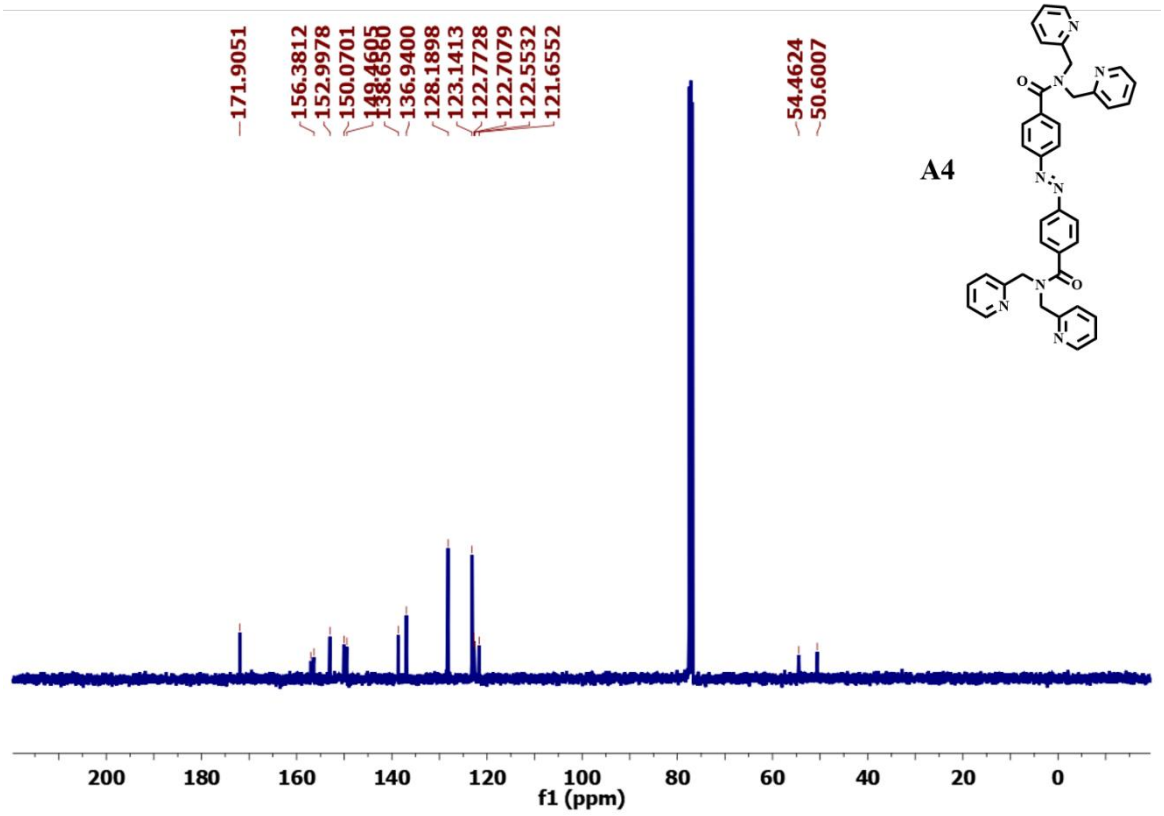

^{13}C-NMR spectrum of (*E*)-4,4'-(diazene-1,2-diyl)bis(N,N-bis(pyridin-2-ylmethyl)benzamide) **(A4)** in $CDCl_3$.

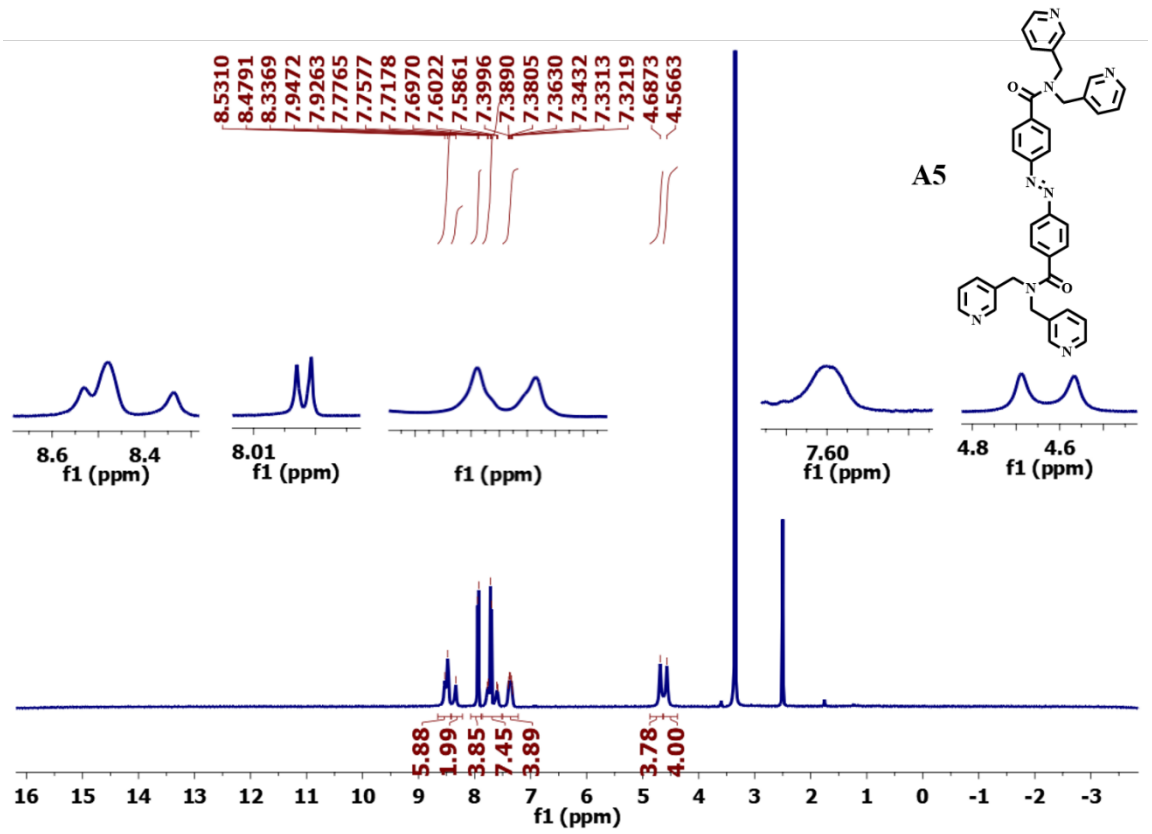

[1]H-NMR spectrum of (*E*)-4,4'-(diazene-1,2-diyl)bis(N,N-bis(pyridin-3-ylmethyl)benzamide) **(A5)** in [D_6]DMSO.

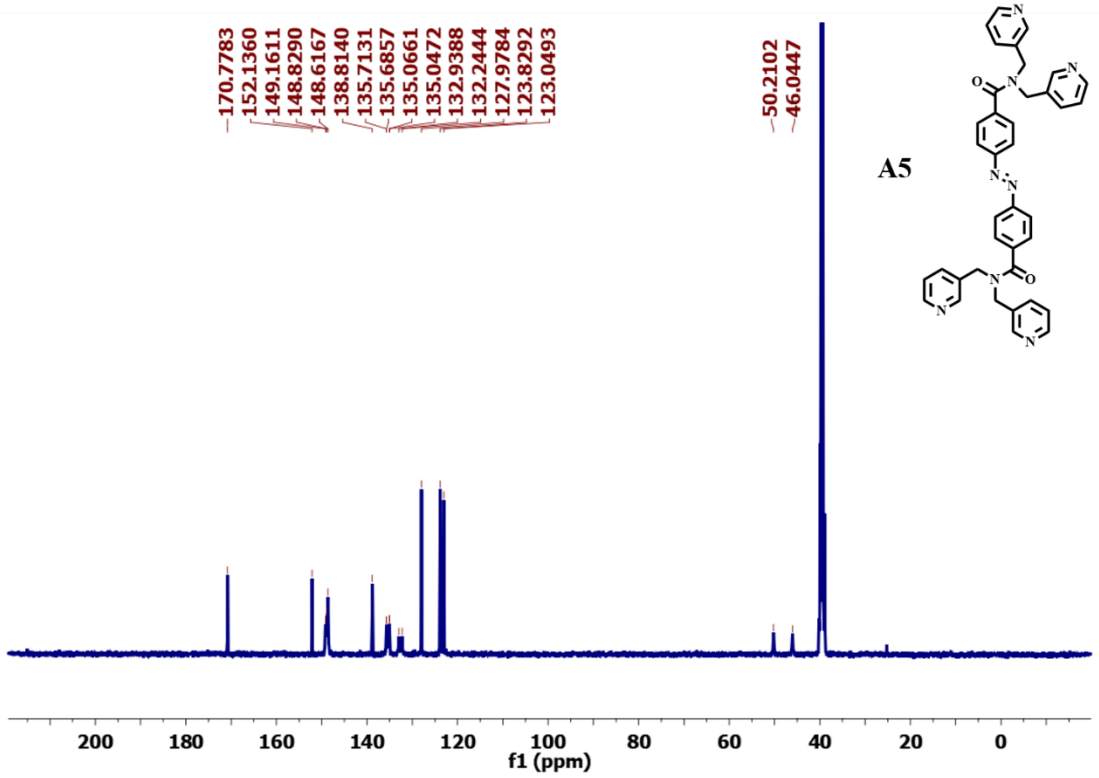

[13]C-NMR spectrum of (*E*)-4,4'-(diazene-1,2-diyl)bis(N,N-bis(pyridin-3-ylmethyl)benzamide) **(A5)** in [D_6]DMSO.

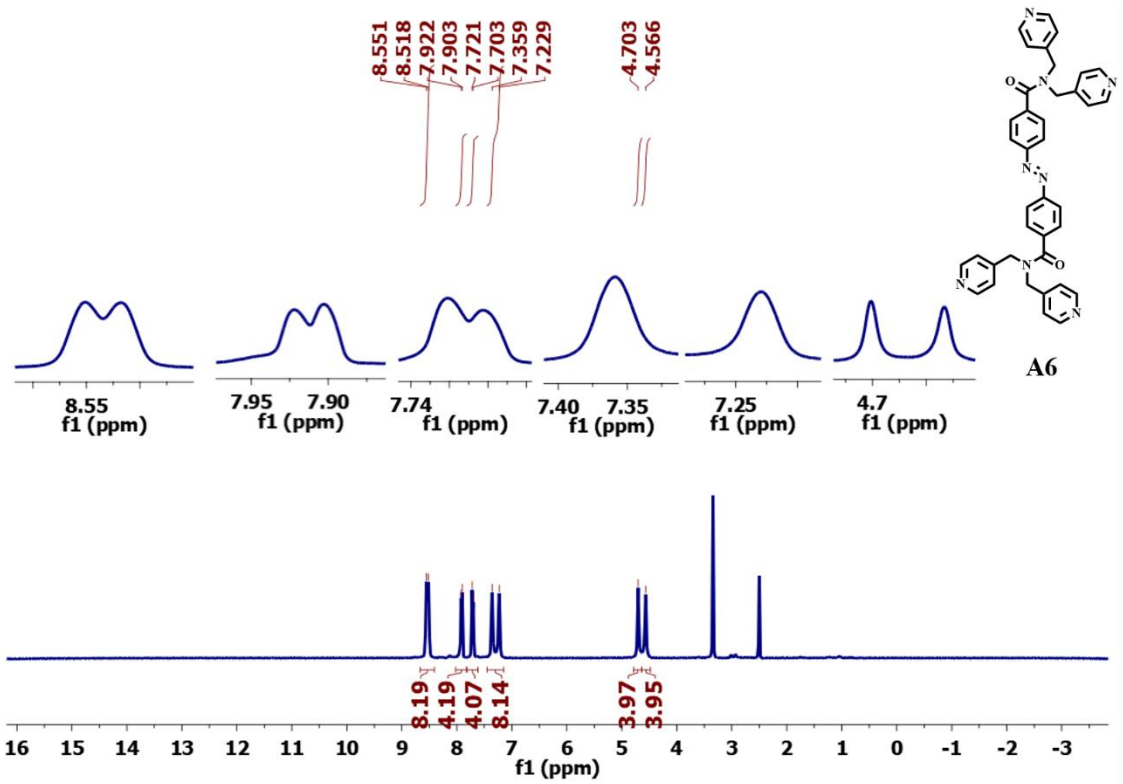

^{1}H-NMR spectrum of (*E*)-4,4'-(diazene-1,2-diyl)bis(N,N-bis(pyridin-4-ylmethyl)benzamide) **(A6)** in [D_6]DMSO.

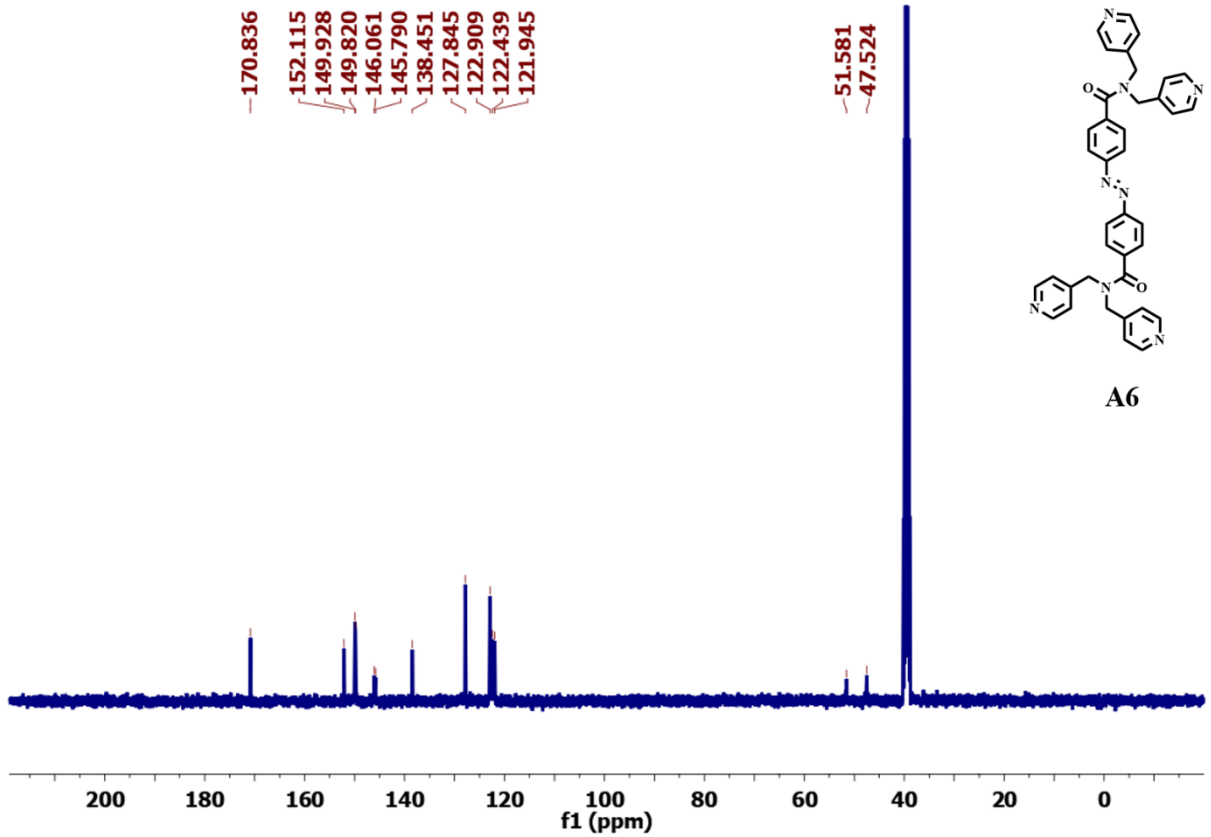

^{13}C-NMR spectrum of (*E*)-4,4'-(diazene-1,2-diyl)bis(N,N-bis(pyridin-4-ylmethyl)benzamide) **(A6)** in [D_6]DMSO.

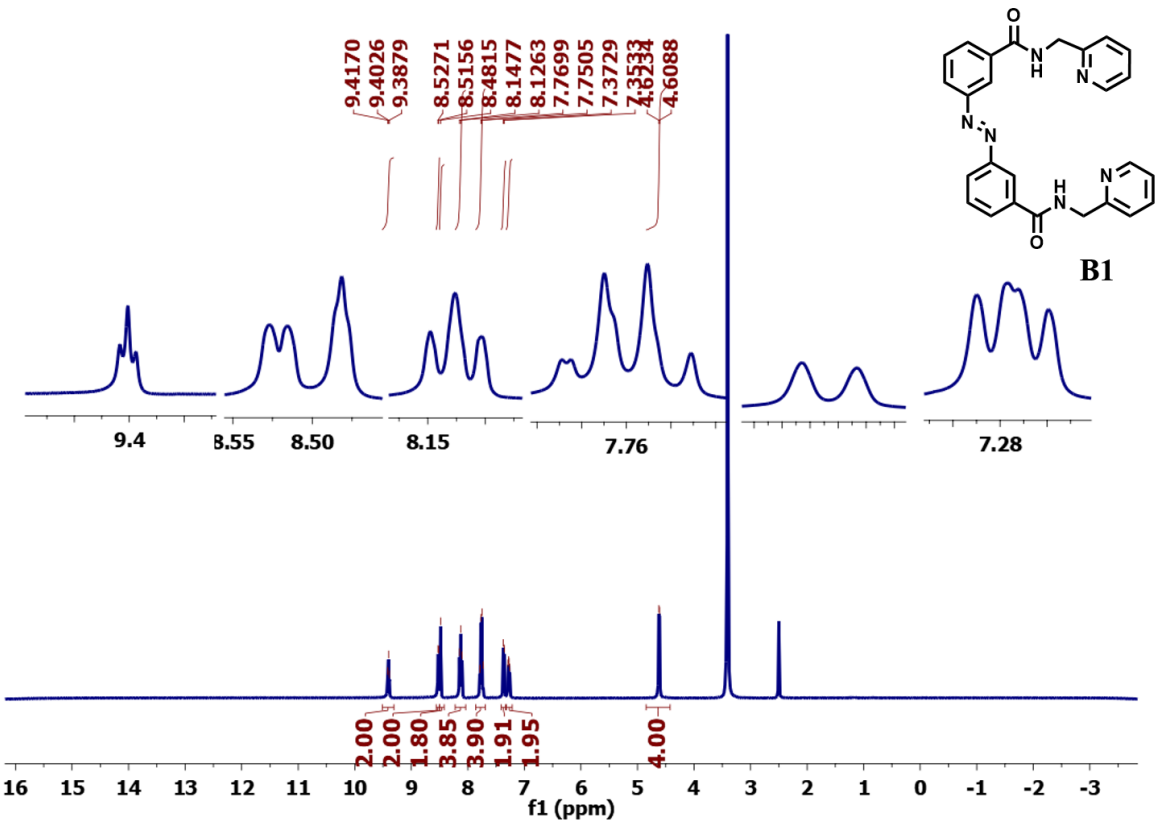

^{1}H-NMR spectrum of (*E*)-3,3'-(diazene-1,2-diyl)bis(N-(pyridin-2-ylmethyl)benzamide) **(B1)** in [D_6]DMSO.

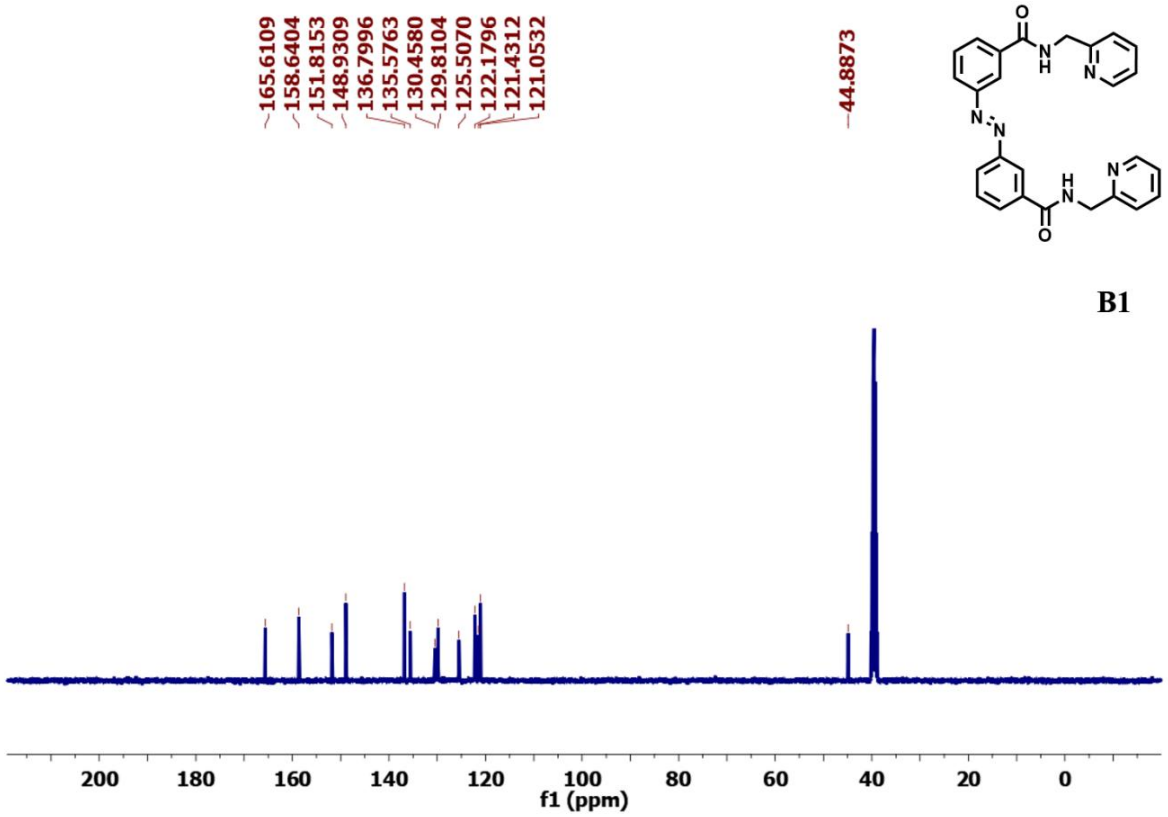

^{13}C-NMR spectrum of (*E*)-3,3'-(diazene-1,2-diyl)bis(N-(pyridin-2-ylmethyl)benzamide) **(B1)** in [D_6]DMSO.

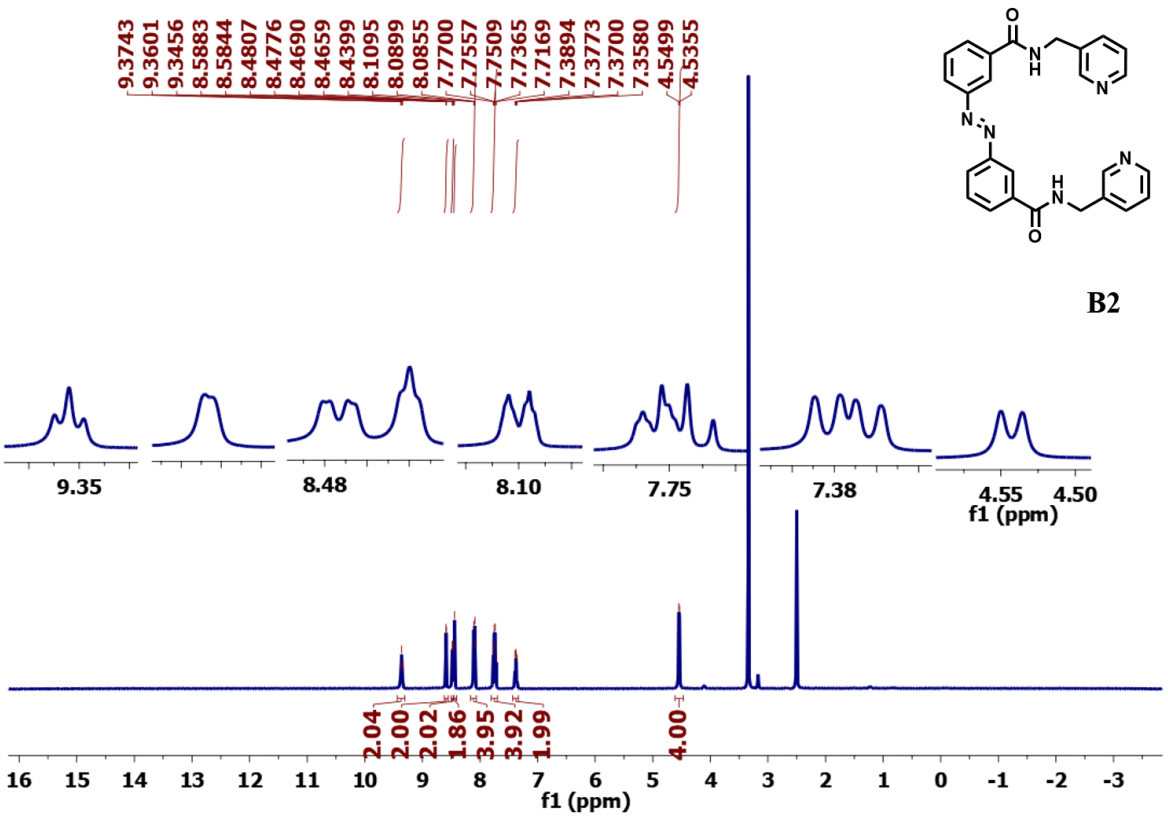

^{1}H-NMR spectrum of (*E*)-3,3'-(diazene-1,2-diyl)bis(N-(pyridin-3-ylmethyl)benzamide) **(B2)** in [D_6]DMSO.

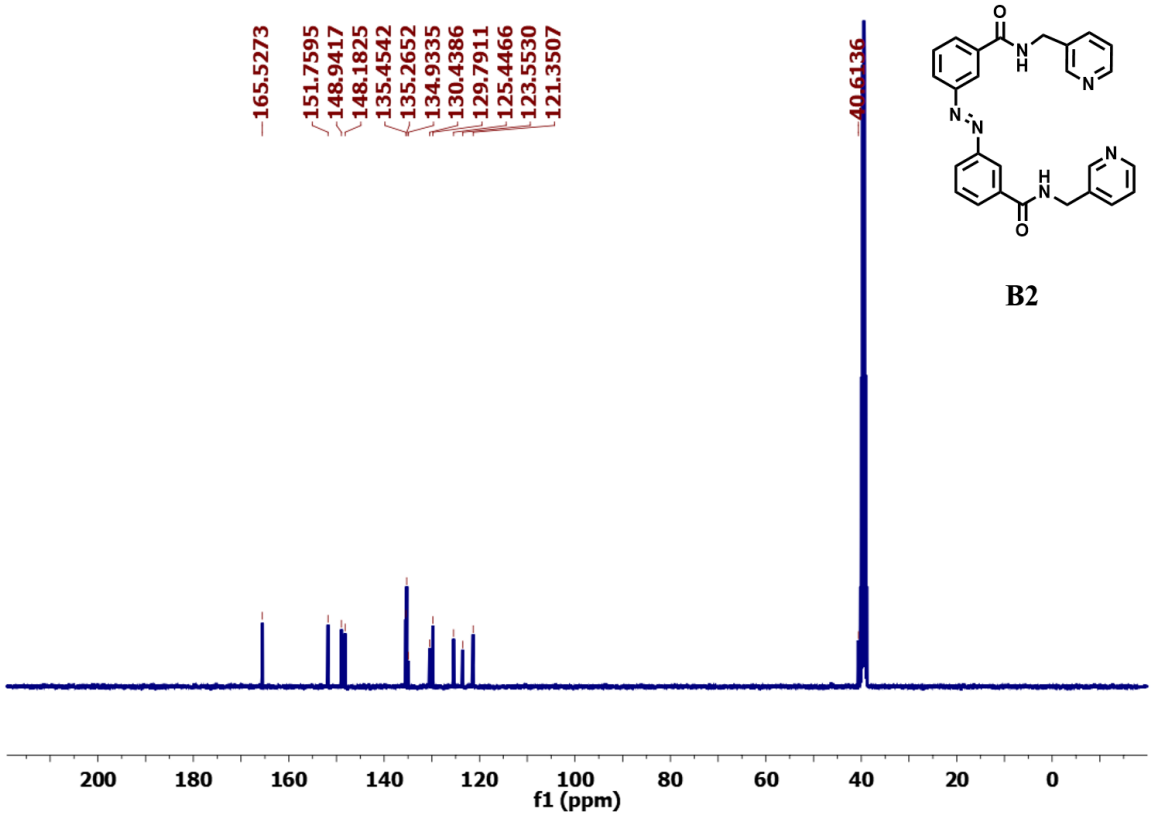

^{13}C-NMR spectrum of (*E*)-3,3'-(diazene-1,2-diyl)bis(N-(pyridin-3-ylmethyl)benzamide) **(B2)** in [D_6]DMSO.

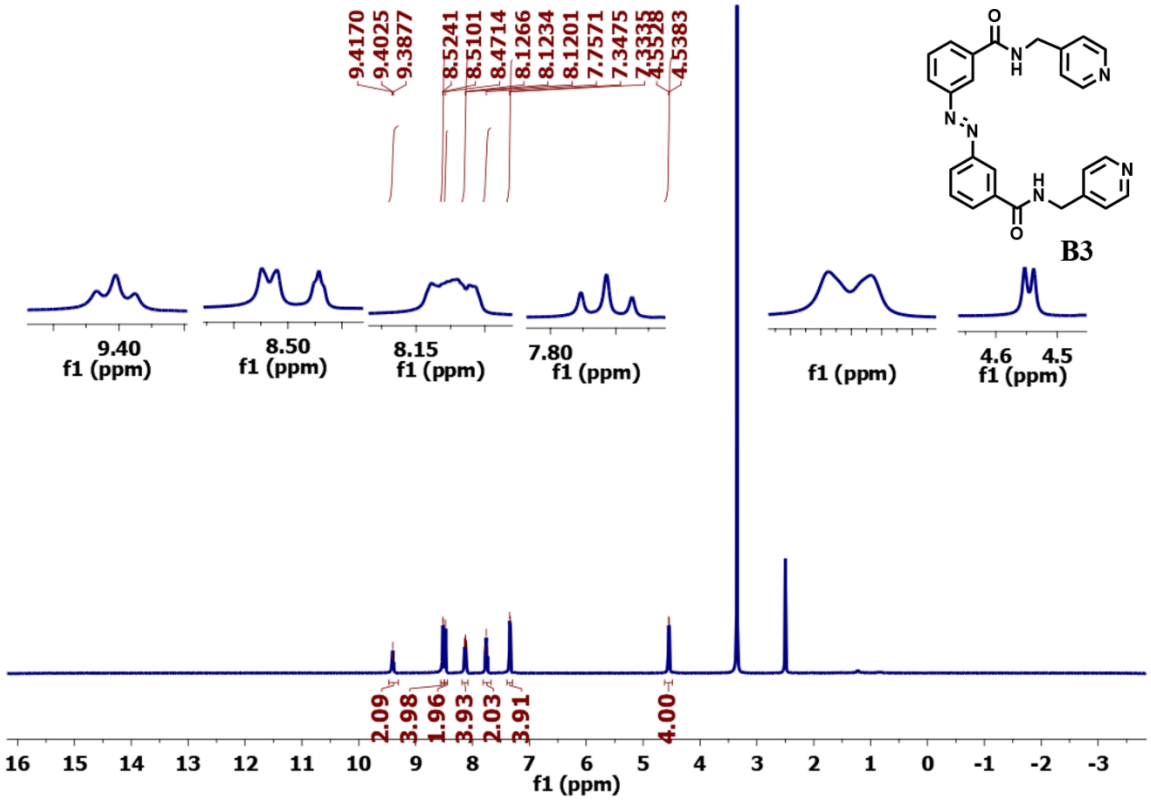

^{1}H-NMR spectrum of (*E*)-3,3'-(diazene-1,2-diyl)bis(N-(pyridin-4-ylmethyl)benzamide) **(B3)** in [D_6]DMSO.

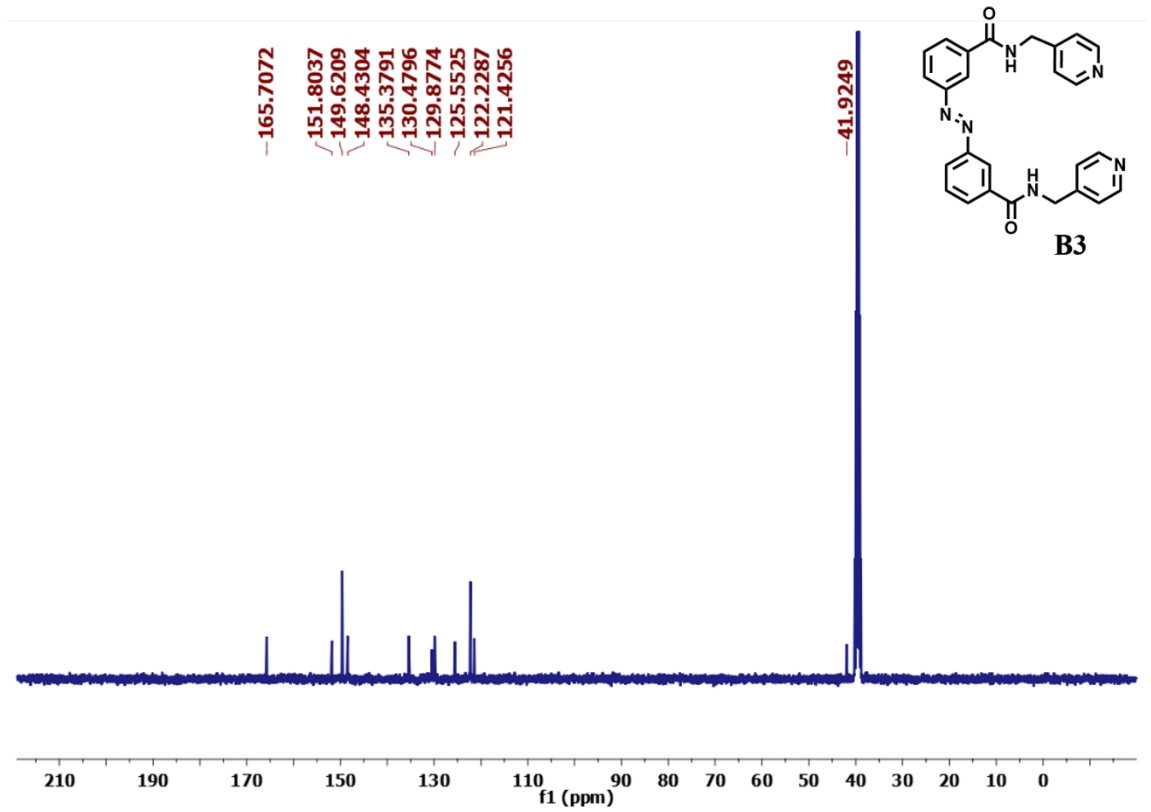

^{13}C-NMR spectrum of (*E*)-3,3'-(diazene-1,2-diyl)bis(N-(pyridin-4-ylmethyl)benzamide) **(B3)** in [D_6]DMSO.

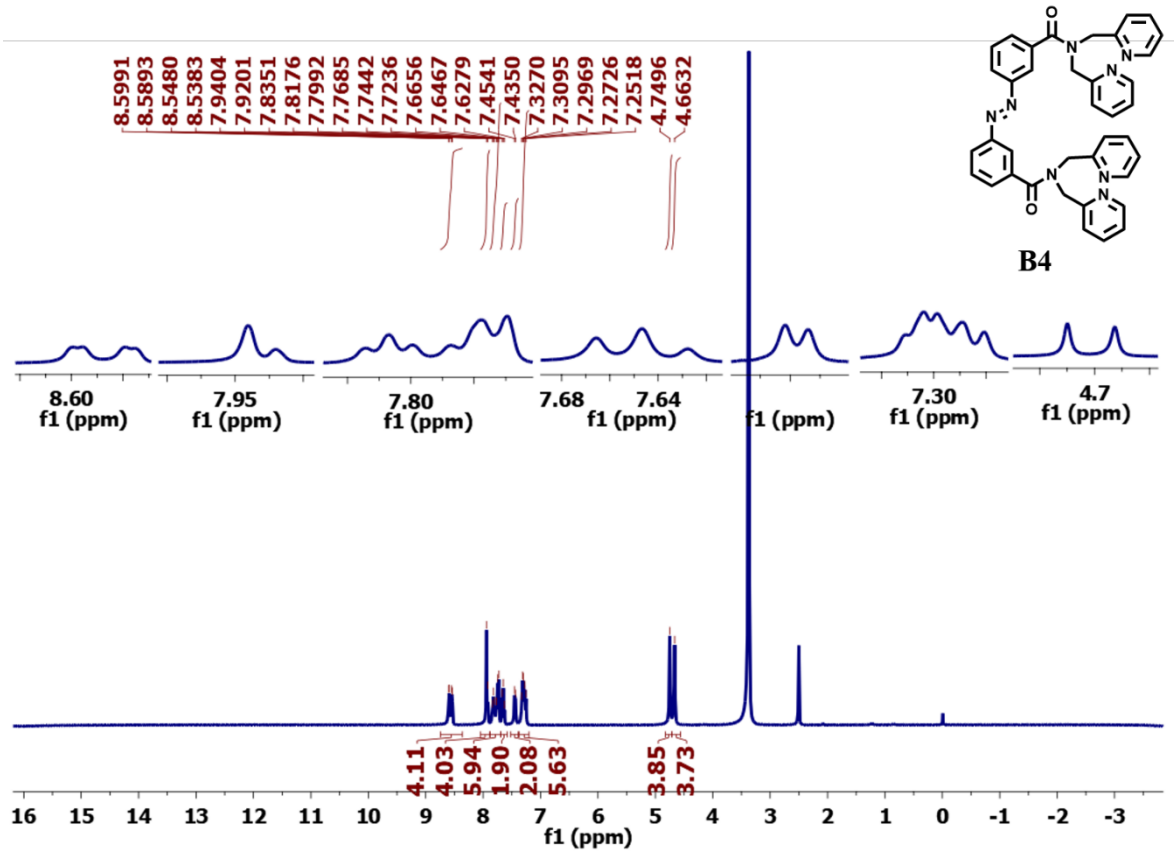

^{1}H-NMR spectrum of (*E*)-3,3'-(diazene-1,2-diyl)bis(N,N-bis(pyridin-2-ylmethyl)benzamide) **(B4)** in [D_6]DMSO.

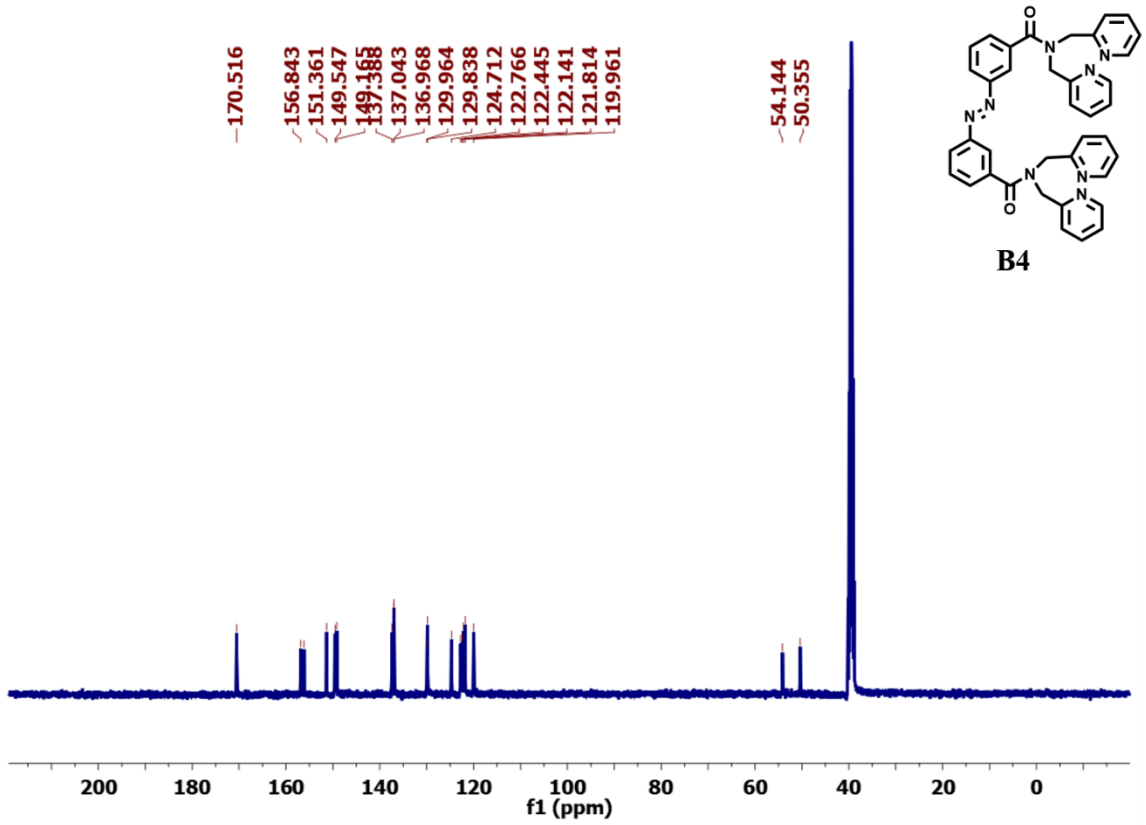

^{13}C-NMR spectrum of (*E*)-3,3'-(diazene-1,2-diyl)bis(N,N-bis(pyridin-2-ylmethyl)benzamide) **(B4)** in [D_6]DMSO.

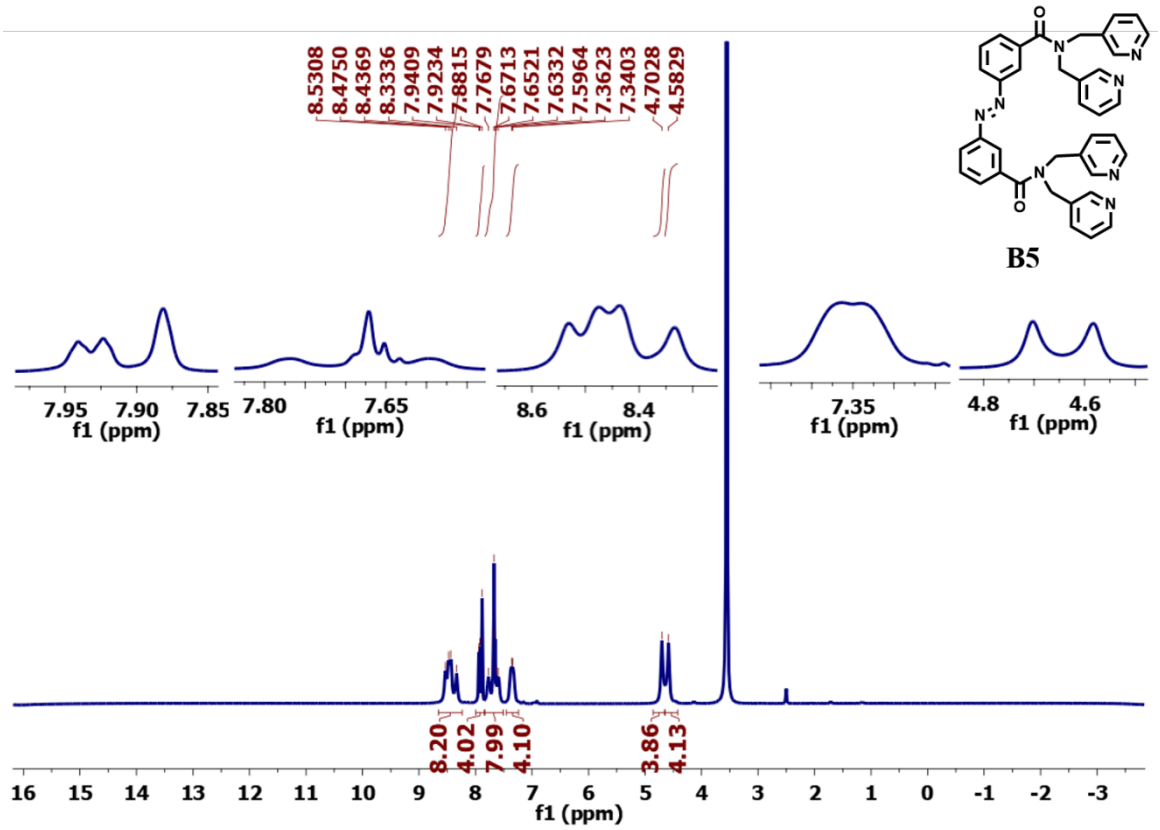

[1]H-NMR spectrum of (*E*)-3,3'-(diazene-1,2-diyl)bis(N,N-bis(pyridin-3-ylmethyl)benzamide) **(B5)** in [D_6]DMSO.

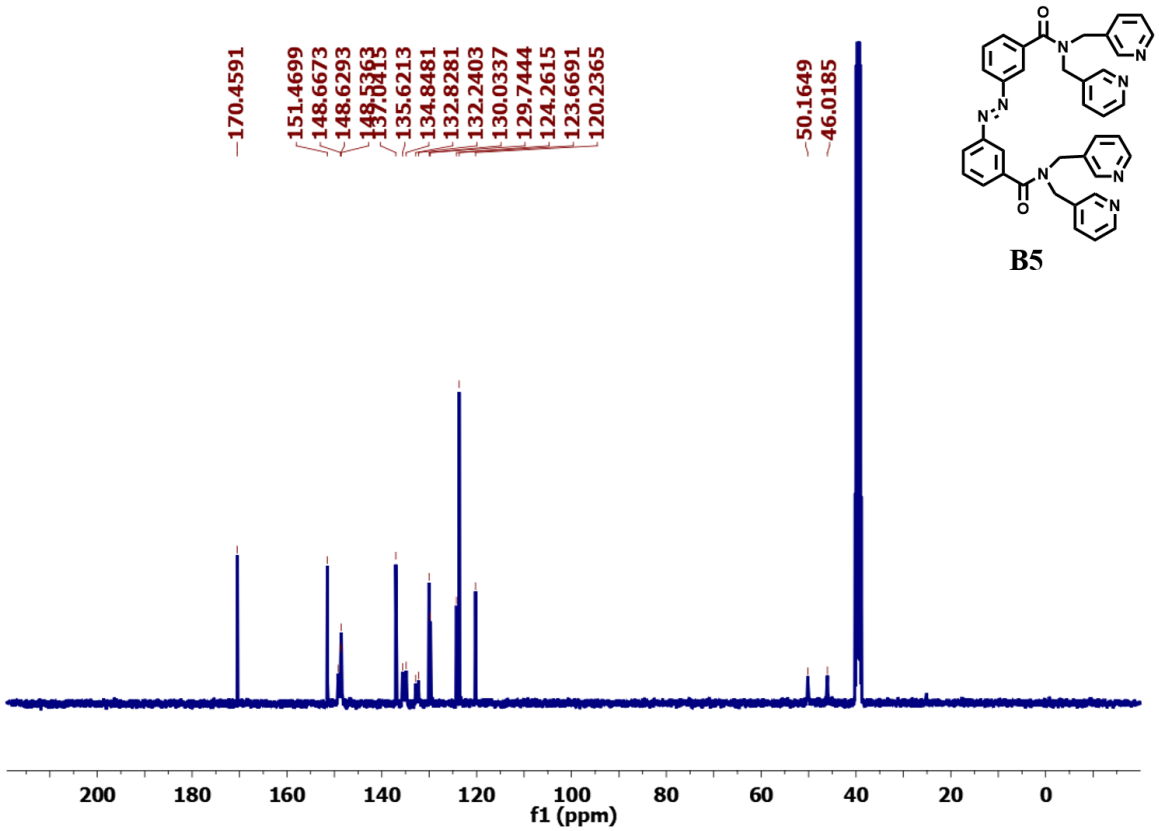

[13]C-NMR spectrum of (*E*)-3,3'-(diazene-1,2-diyl)bis(N,N-bis(pyridin-3-ylmethyl)benzamide) **(B5)** in [D_6]DMSO.

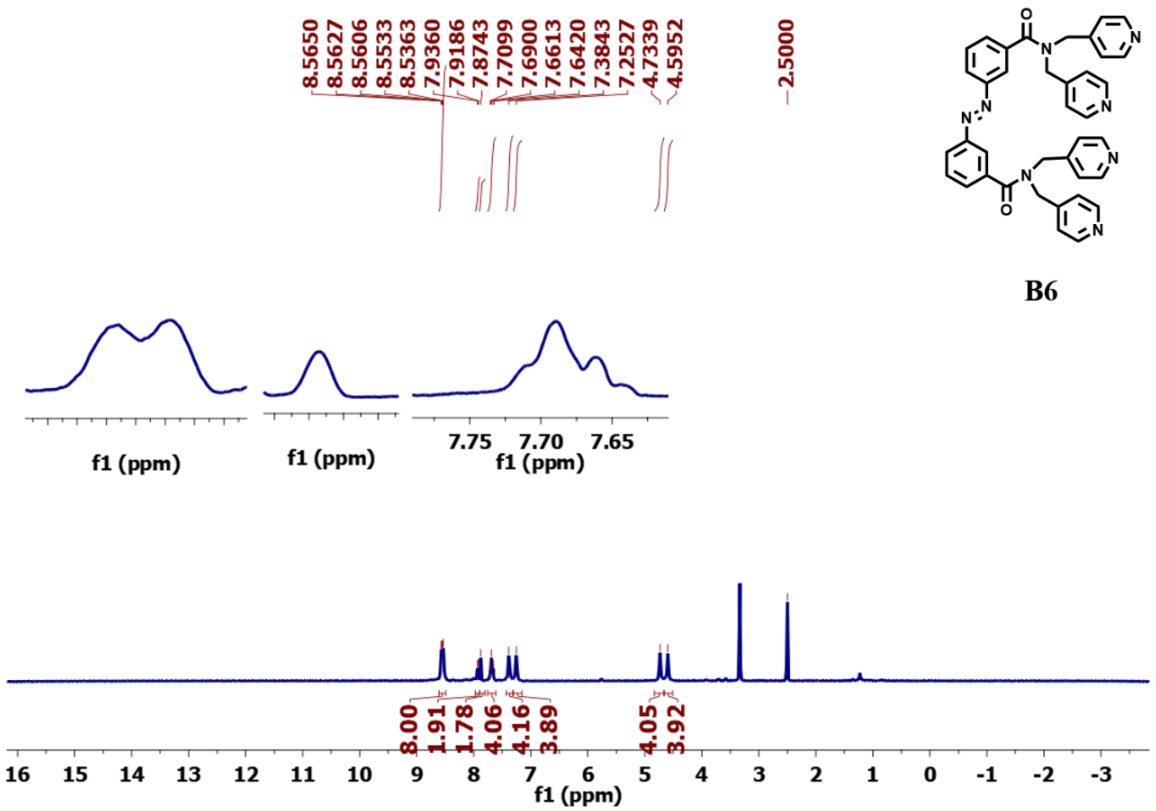

^{1}H-NMR spectrum of (*E*)-3,3'-(diazene-1,2-diyl)bis(N,N-bis(pyridin-4-ylmethyl)benzamide) **(B6)** in [D_6]DMSO.

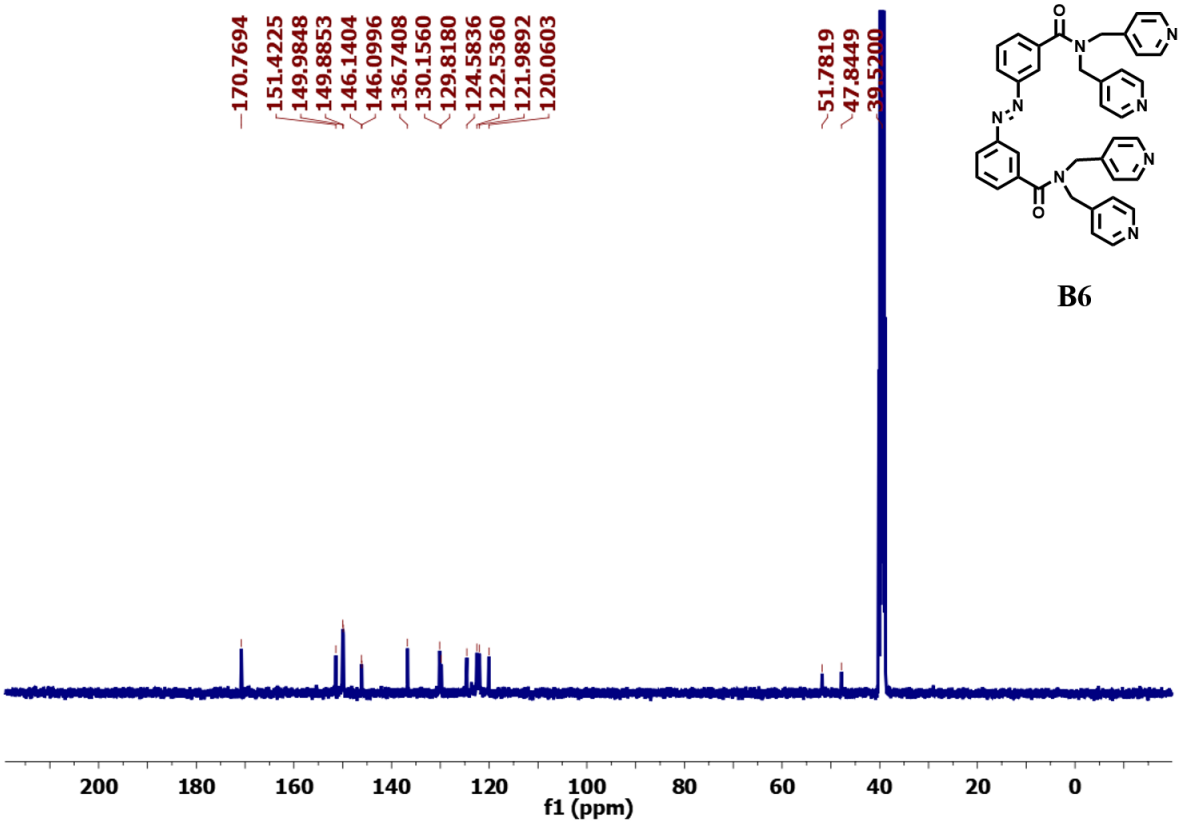

^{13}C-NMR spectrum of (*E*)-3,3'-(diazene-1,2-diyl)bis(N,N-bis(pyridin-4-ylmethyl)benzamide) **(B6)** in [D_6]DMSO.

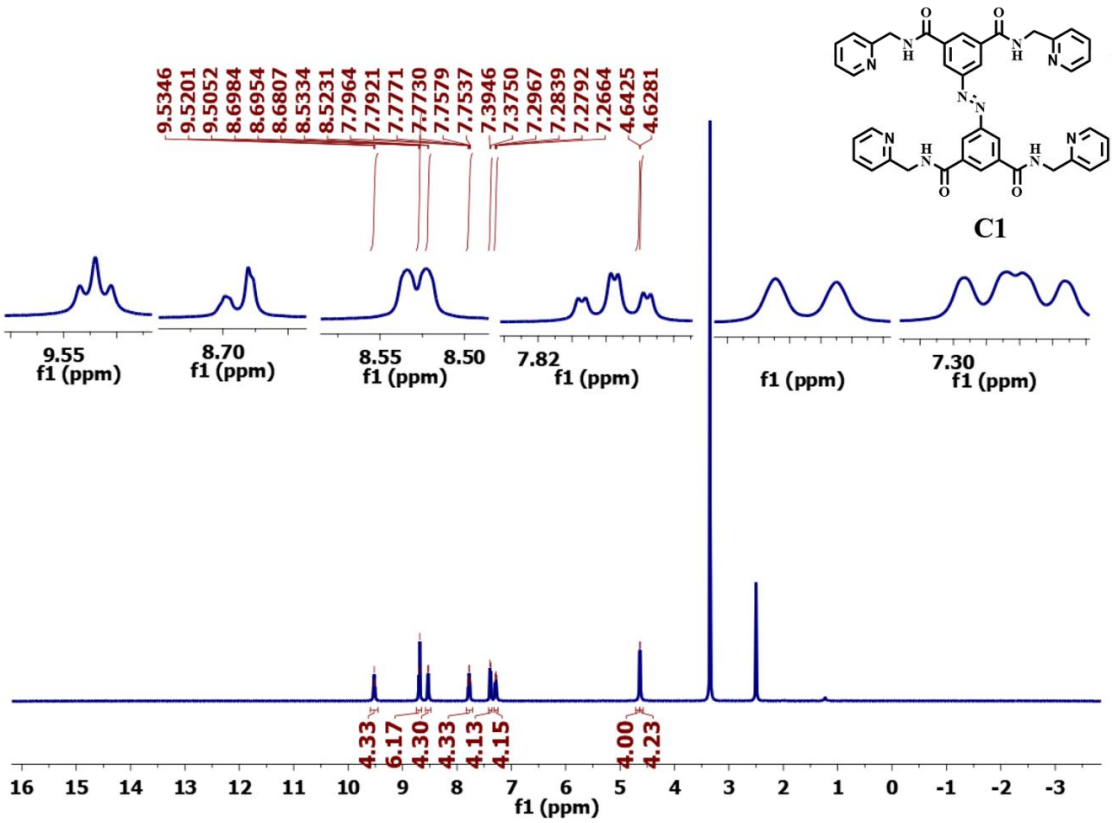

^{1}H-NMR spectrum of (*E*)-5,5'-(diazene-1,2-diyl)bis(N1,N3-bis(pyridin-2-ylmethyl)isophthalamide) **(C1)** in [D_6]DMSO.

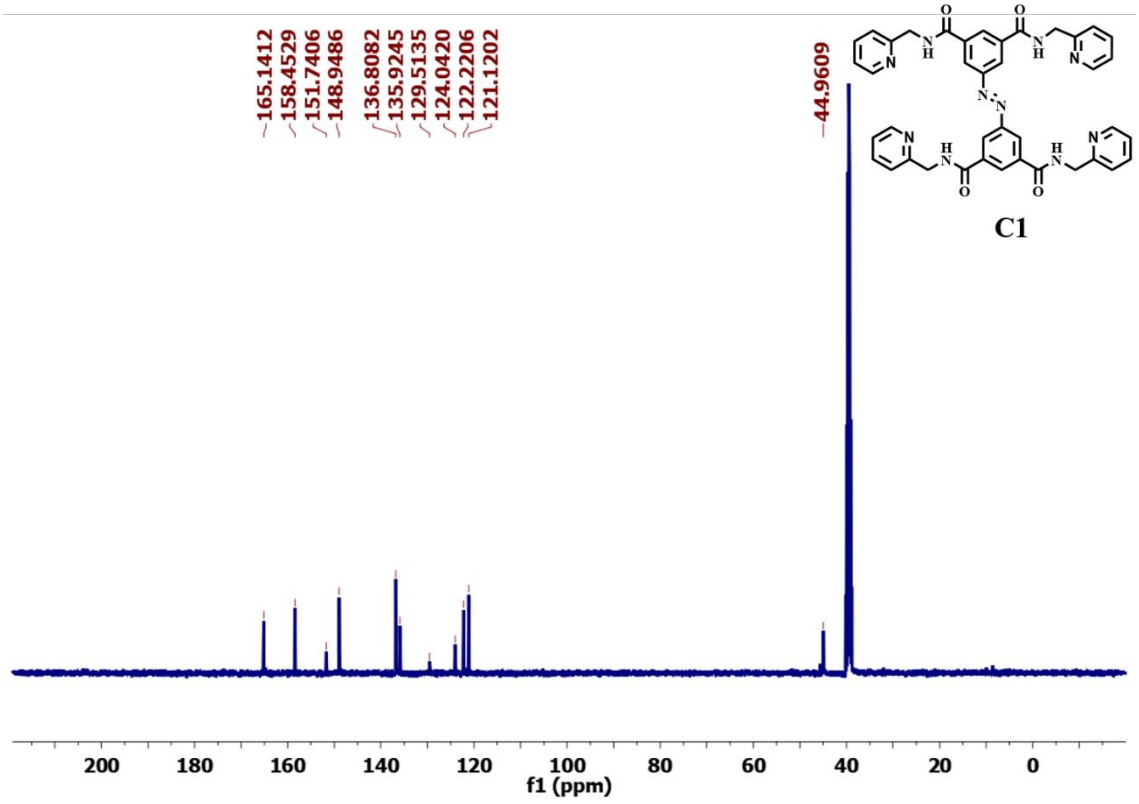

^{13}C-NMR spectrum of (*E*)-5,5'-(diazene-1,2-diyl)bis(N1,N3-bis(pyridin-2-ylmethyl)isophthalamide) **(C1)** in [D_6]DMSO.

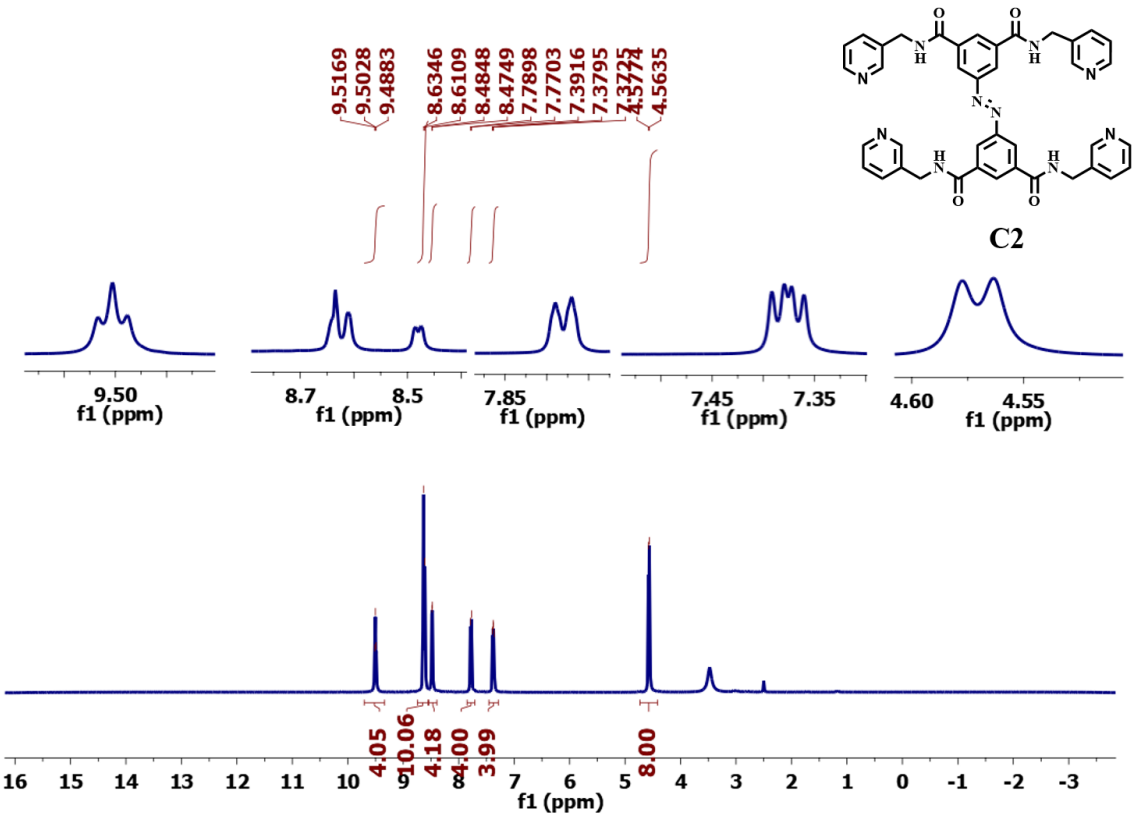

^{1}H-NMR spectrum of (*E*)-5,5'-(diazene-1,2-diyl)bis(N1,N3-bis(pyridin-3-ylmethyl)isophthalamide) **(C2)** in [D_6]DMSO

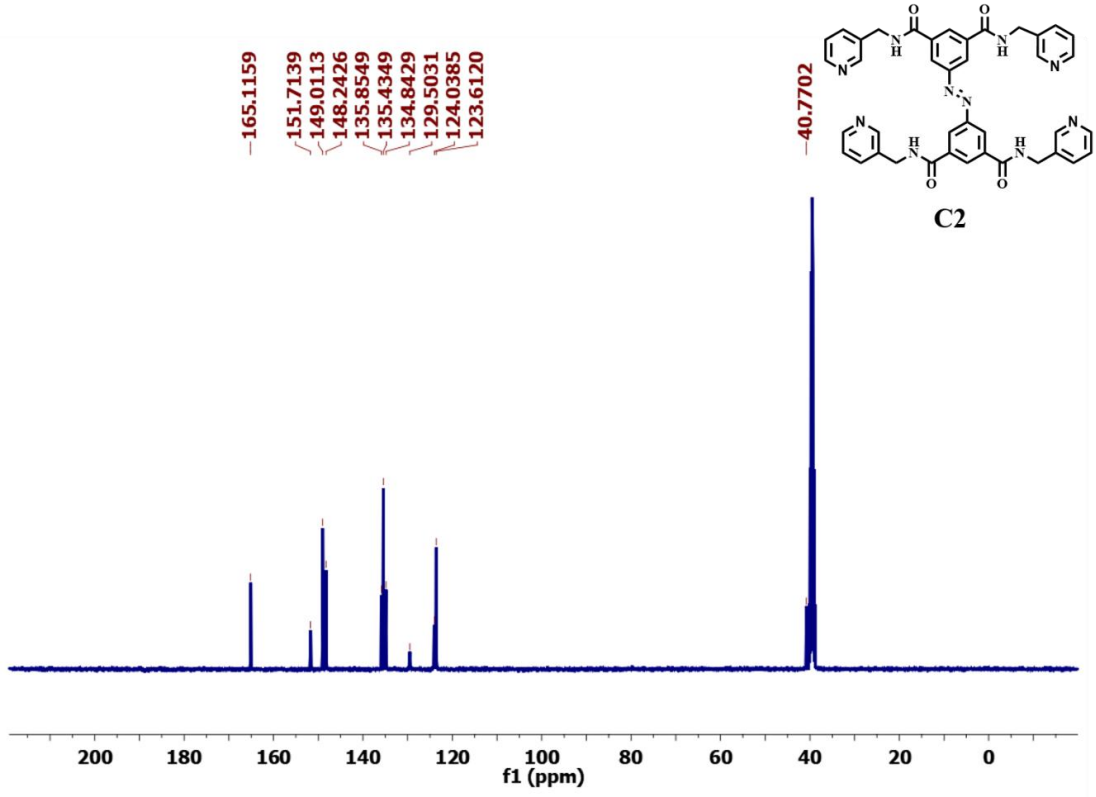

^{13}C-NMR spectrum of (*E*)-5,5'-(diazene-1,2-diyl)bis(N1,N3-bis(pyridin-3-ylmethyl)isophthalamide) **(C2)** in [D_6]DMSO.

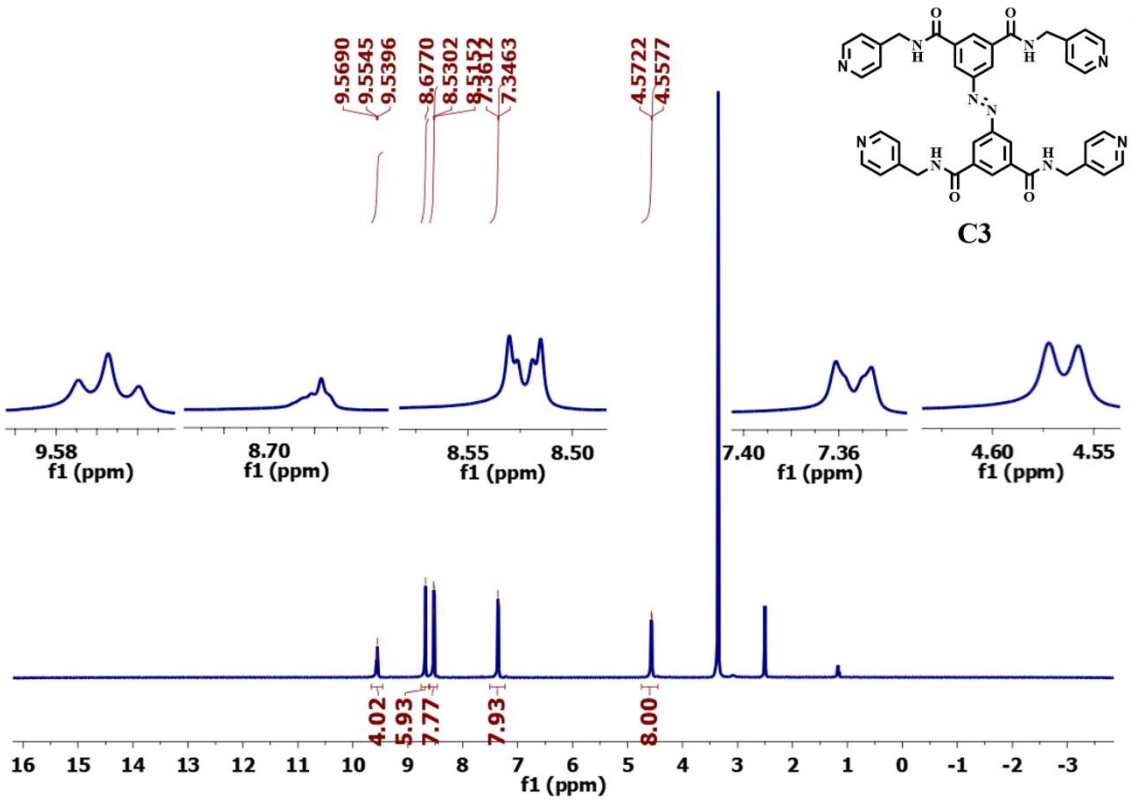

^{1}H-NMR spectrum of (*E*)-5,5'-(diazene-1,2-diyl)bis(N1,N3-bis(pyridin-4-ylmethyl)isophthalamide) **(C3)** in [D_6]DMSO.

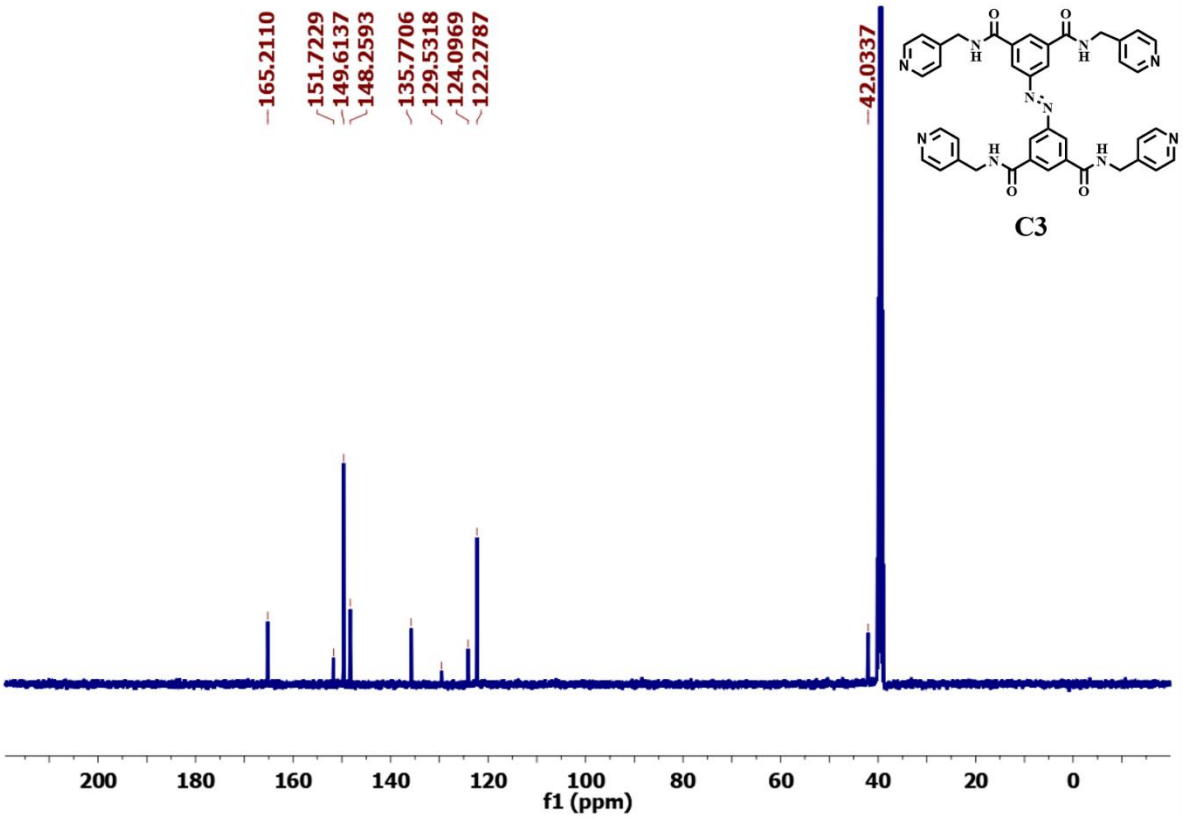

^{13}C-NMR spectrum of (*E*)-5,5'-(diazene-1,2-diyl)bis(N1,N3-bis(pyridin-4-ylmethyl)isophthalamide) **(C3)** in [D_6]DMSO.

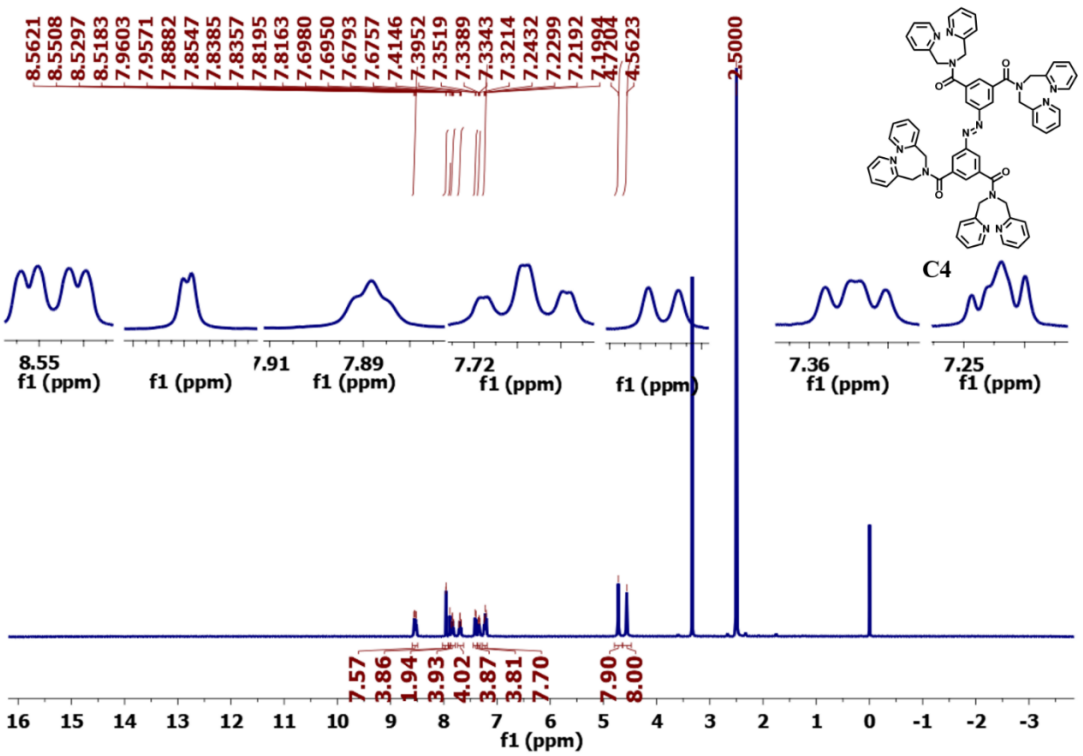

^{1}H-NMR spectrum of (*E*)-3,3'-(diazene-1,2-diyl)bis(N,N-bis(pyridin-2-ylmethyl)benzamide) **(C4)** in [D_6]DMSO.

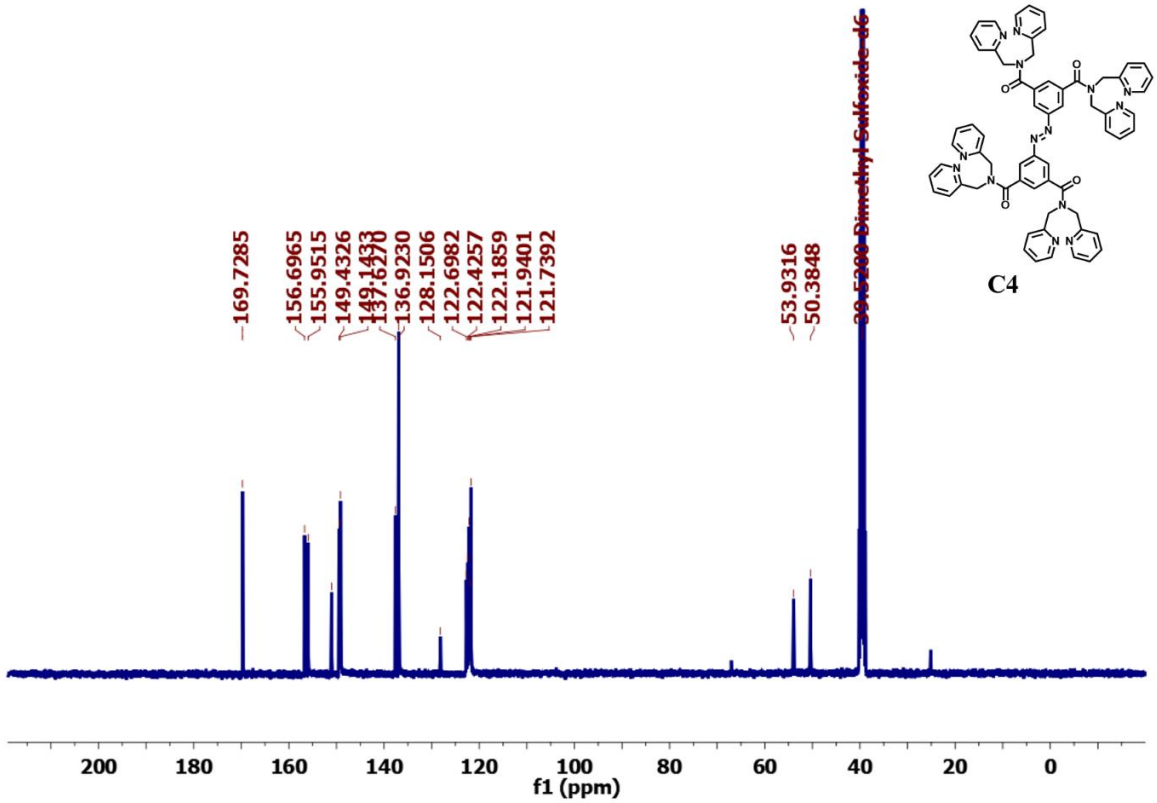

^{13}C-NMR spectrum of (*E*)-3,3'-(diazene-1,2-diyl)bis(N,N-bis(pyridin-2-ylmethyl)benzamide) **(C4)** in [D_6]DMSO.

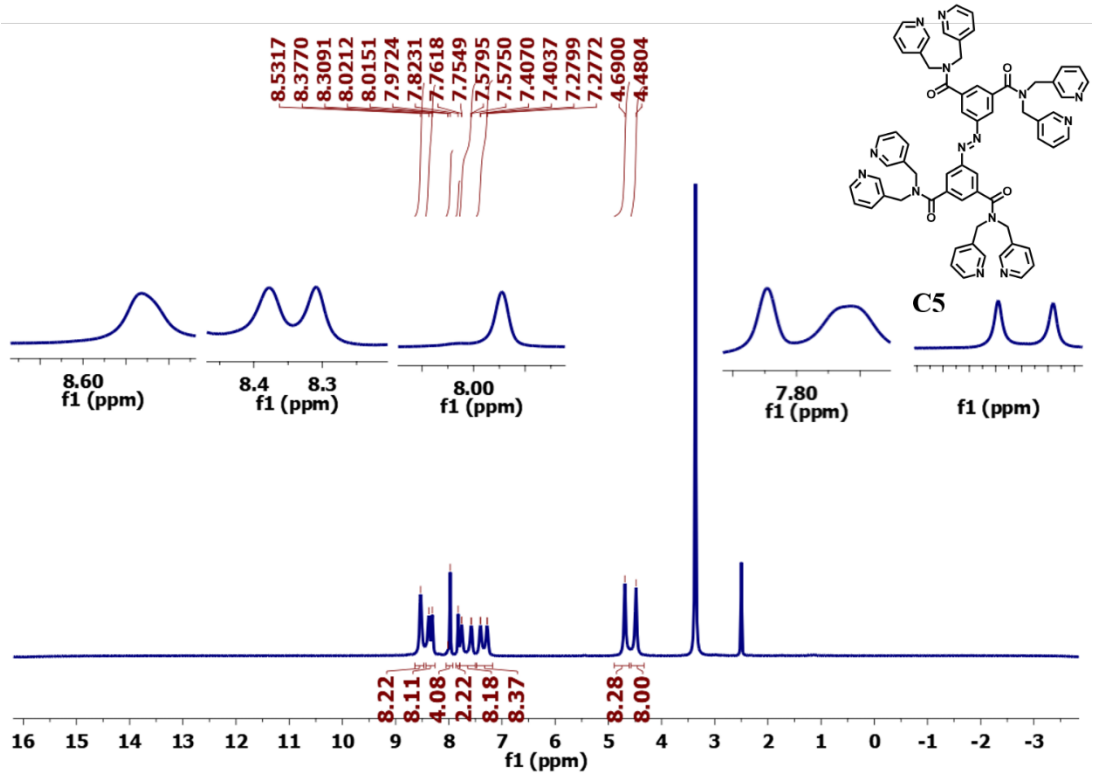

^{1}H-NMR spectrum of (*E*)-3,3'-(diazene-1,2-diyl)bis(N,N-bis(pyridin-3-ylmethyl)benzamide) **(C5)** in [D_6]DMSO.

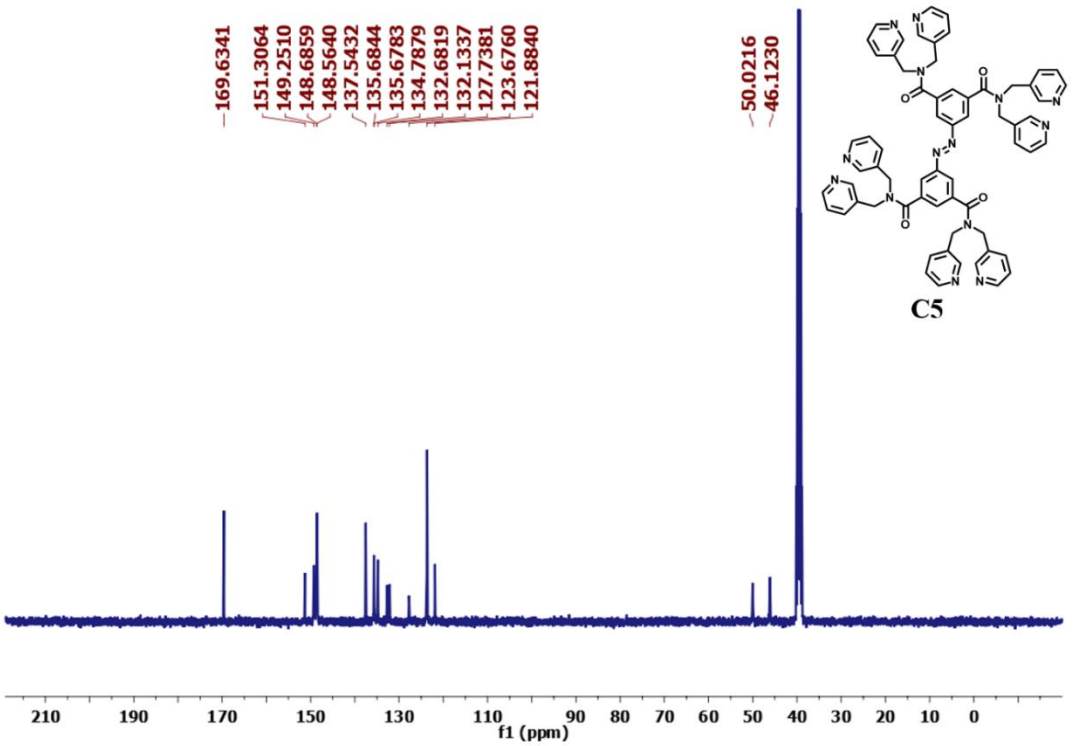

^{13}C-NMR spectrum of (*E*)-3,3'-(diazene-1,2-diyl)bis(N,N-bis(pyridin-3-ylmethyl)benzamide) **(C5)** in [D_6]DMSO.

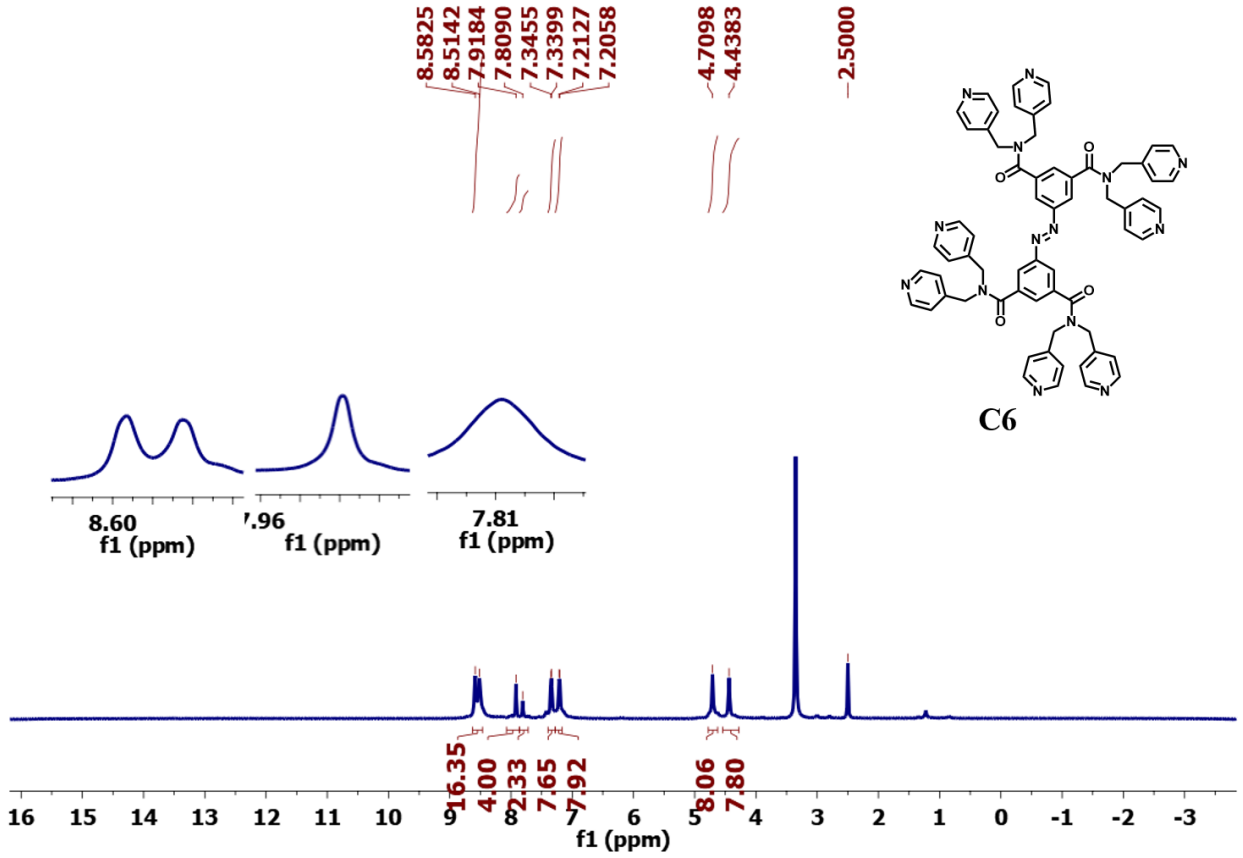

^{1}H-NMR spectrum of (*E*)-3,3'-(diazene-1,2-diyl)bis(N,N-bis(pyridin-4-ylmethyl)benzamide) **(C6)** in [D_6]DMSO.

Chapter 3. Self-assembly in C_3-Symmetric π-Conjugated Azobenzene based Tripodal Systems

3.1 Introduction

Multiple photoswitchable C_3-symmetric systems are attractive scaffolds and have shown a widespread interest in the field of supramolecular chemistry.[1,2] The benzene-1,3,5-tricarboxamide (BTA)[1a-1c] and oligo(phenylenevinylene)s (OPVs)[2] are greatly exemplified as core units in the tripodal C_3-symmetric designs to achieve intriguing supramolecular architectures. The pre-defined hydrogen bonding, π-π stacking and van der Waals forces in such cores strongly influence the hierarchical outcomes of the assemblies. The introduction of azobenzene photoswitches in those superstructures enhances the extension of stacking, and more importantly imparts photoresponsiveness through reversible light-induced changes. The resulting light modulation of self-assemblies in tripodal designs can exhibit a wide range of potential applications such as photoswitchable polymers,[3] liquid crystals,[4] holographic grating element,[5] rewritable actuators,[6] rewritable image printing and erasing,[7] or photoswitchable catalysts.[8]

Typically, the hydrogen bonding in the core part of such tripodal systems can act as a primary driving force for the formation of nanocolumns.[1a] Interestingly, the linkers, spacer units, core part, and orientation of the azo groups strongly determine the photoisomerization ability, thermal relaxation rates of the photoisomeric states, and the organization ability.[9] The assembly of molecules often vary in optical, physical and chemical properties from the constituent.[1b] The reversible photoisomerization of azobenzene incorporated scaffolds, in general, induces phase transitions.[4a] Also, the fabrication can lead to diverse assemblies with morphologies such as fibers, gels, or spheres depending on the conditions employed.[1b] Despite these understandings on the tripodal azobenzene based designs, noteworthy factors such as tunability in the wavelengths for photoisomerization (towards longer wavelengths of light) and architectural diversity are still in demand for futuristic applications.

To modulate the "ON and OFF" functions including assemble-disassemble of the supramolecular systems by light using longer wavelengths, specific functional groups need to be appended in the molecular systems. Various approaches such as introducing push-pull type functions, and *ortho* substitutions (fluorine, methoxy, or thiomethyl groups) are overwhelmingly used to bring bathochromic shifts in the π-π* absorption features or enhancement in the n-π* bands that allow longer wavelengths for photoisomerization in simple azoarenes.[10] However, the major limitations in some of these approaches are the fast thermal relaxations and the attainment of non-planarity due to the substituents that can limit the photoresponsiveness and supramolecular self-

assembly, respectively. At this juncture, our intentions were to enable such longer wavelength photoisomerization without destroying the architectural basis. In this regard, we proposed to extend the π-conjugation, which is so far employed only to simple azo(hetero)arenes.[11] We envisioned that the π-conjugation provide bathochromic shift in the π-π* absorption of the azo group.

Based on these assumptions, we decided to build C_3-symmetric supramolecular systems, which has an elegant combination of reversible noncovalent interactions, such as hydrogen bonding and π–π stacking, which can be profoundly utilized for the previously mentioned applications.

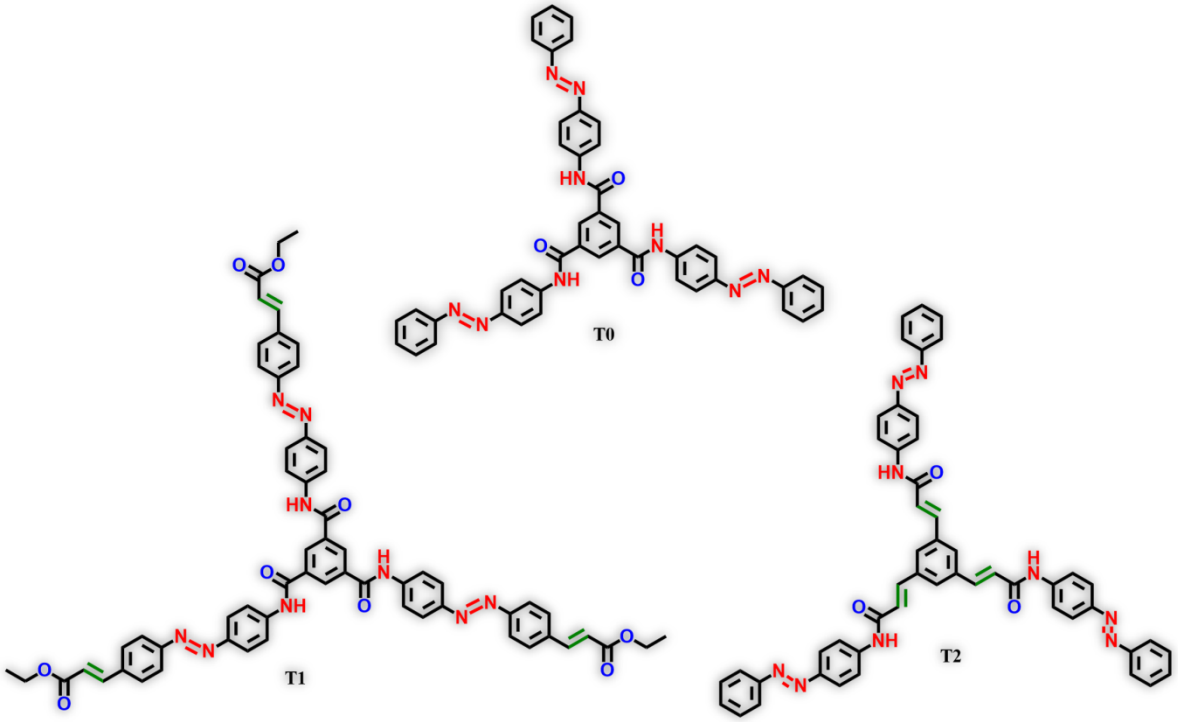

Figure 3.1 The C_3-symmetric targets having benzene-1,3,5-tricarboxamide (BTA) core **(T1)** and oligo(phenylenevinylene)s (OPVs) core **(T2)** for supramolecular assembly. The most commonly studied molecule **T0** is depicted.

Taking cue from the advantages of BTA and OPV based supramolecular synthons, we decided to introduce α,β-unsaturation in such tripodal designs. In this regard, we have designed two targets **T1** (with BTA core and external π-conjugation) and **T2** (with benzene-1,3,5-triacrylamide BTAA core) **(Figure 3.1)**.

The resulting C_3-symmetric designs have been extensively investigated for the photoswitching and supramolecular studies. In order to understand the photoswitching aspects and the thermal stability of the photoswitched states of these targets, extensive spectroscopic studies have been carried out. Furthermore, supramolecular self-assemblies have been characterized using

XRD, AFM, SEM, TEM and POM. Herein, we report the outcomes of those investigations on the two target molecules (**T1, T2**) **(Figure 3.1 and Scheme 3.1)**.

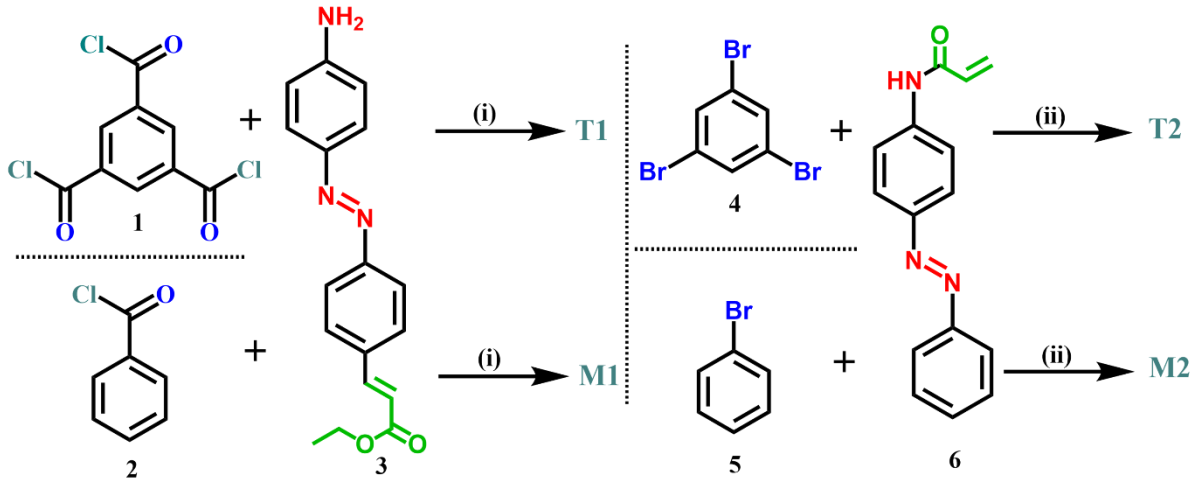

Scheme 3.1 Synthesis of the target molecules **T1, T2, M1** and **M2**. (i) Et_3N, THF, rt-60 °C, overnight, **M1**: 70 % and **T1**: 30 %; (ii) $Pd(OAc)_2$, PPh_3, dry DMF, K_2CO_3, 100 °C, **M2**: 50 % and **T2**: 60 %.

3.2 Design and Synthesis

The two targets were designed to form supramolecular architectures exhibiting light modulated assembly and disassembly. Since benzene-1,3,5-tricarboxamide (BTA) core is well documented as a supramolecular synthon, we used it as one of the cores. The intriguing aspect of BTA core is its C_3-symmetric nature, which can be easily functionalized with three amide groups that are capable of forming strong hydrogen bonding. For bringing photoresponsiveness, we considered azobenzene photoswitches. Inspite of the ubiquity and broad utility of azobenzene based chromophore to trigger the photochemical reaction, they require harmful UV light. Alteration of the HOMO-LUMO gap through extending π-conjugation, in principle, can tune the electronic properties. Moreover, photoisomerization can be achieved with the irradiation of a light of longer wavelength. To the best of our knowledge, no study has been carried out with tripodal C_3-symmetric photoswitches containing extended conjugation till date. In this regard, we have designed a target by incorporating ethyl acrylate groups at the peripheral position of BTA core connected tripodal azobenzene system (**T1**). In yet another design, we incorporated three acrylamide units to a benzene in a tripodal C_3-symmetric fashion, and generated BTAA as a novel core. Once again, the core was decorated with azobenzene photoswitches to generate our second target (**T2**). Such targets with extended conjugation at external and internal positions can provide greater insights on the supramolecular assembly, photoswitching ability, and also the thermal stability of the photoswitched states. For comparison of the results, we have also synthesized their corresponding mono-azobenzene functionalized systems, **M1** and **M2 (Scheme 3.1)**.

All the target molecules **T1**, **T2**, **M1** and **M2** have been synthesized in multiple steps (**Scheme 3.1**). For accessing the target **T1**, we have started with Mill's method to form (*E*)-4-((4-bromophenyl)diazenyl)aniline using 4-bromoaniline and the in situ generated nitroso compound from 4-aminoacetanilide. This azo derivative was then subjected to Heck coupling with ethyl acrylate to form the starting material **3**. Further, acid amine coupling of **3** was performed using trimesoyl chloride **1** and benzoyl chloride **2** to generate the targets **T1** and **M1**, respectively. Similarly, the acid-amine coupling between 4-aminoazobenzene and acryloyl chloride to prepare the starting material (*E*)-*N*-(4-(phenyldiazenyl)phenyl)acrylamide **6**, which on treatment with 1,3,5-tribromobenzene **4** and bromobenzene **5** under Heck coupling conditions led to the targets **T2** and **M2**, respectively. All the molecules were characterized by using ^{1}H, ^{13}C NMR, HRMS, IR, UV-Vis, etc.

3.3 Electronic Spectroscopic and Photoswitching Studies of the Targets

All the four targets **T1**, **T2**, **M1** and **M2** were subjected to UV-Vis spectroscopic studies for unraveling the effects of conjugation on the electronic energy levels. Based on the electronic spectral data, we perceive the effect of extended conjugation at external and internal positions. For comparison, all such studies were performed in a spectroscopic grade DMSO as a solvent (**Figure 3.2 and Appendix 3A**). We observed red-shifted π-π* absorptions for all these four molecules (**T1**: 387 nm, **T2**: 372 nm; **M1**: 385 nm, and **M2**: 371 nm) compared to the previously reported tripodal BTA based azobenzene derivative **T0** (364 nm).[9c] Notably, the n-π* band of all the molecules exhibits overlap with the π-π* absorption feature, as also observed in **T0**. This indicates the effect of conjugation in lowering of energy difference between π and π* orbitals of the azo group. Also, the extended conjugation significantly increases the molar absorption coefficients (66677 and 115389 $M^{-1}cm^{-1}$ for **T2** and **T1**, respectively). Further, photoswitching studies in solution phase have been carried out, and analysed by using UV-vis spectroscopy. Upon isomerization the π-π* bands showed the typical blue-shift, however, a maximum shift of 84 nm was observed in the case of **T1**, whereas **T2** showed only a marginal shift (33 nm). Incidentally, the monoamides **M1** and **M2** exhibit the same λ_{max} for the π-π* bands almost at the same wavelengths as that of **T1** and **T2**, respectively. This signifies the absence of electronic coupling between the azo units in the tripodal design. Indeed, the absorption features have been confirmed by using computed spectral data using TD-DFT methods. Notably, the red-shifted π-π* absorption of the targets allowed us to photoisomerize them in the forward and reverse directions using longer wavelengths of light than the typical UV light (365 nm).

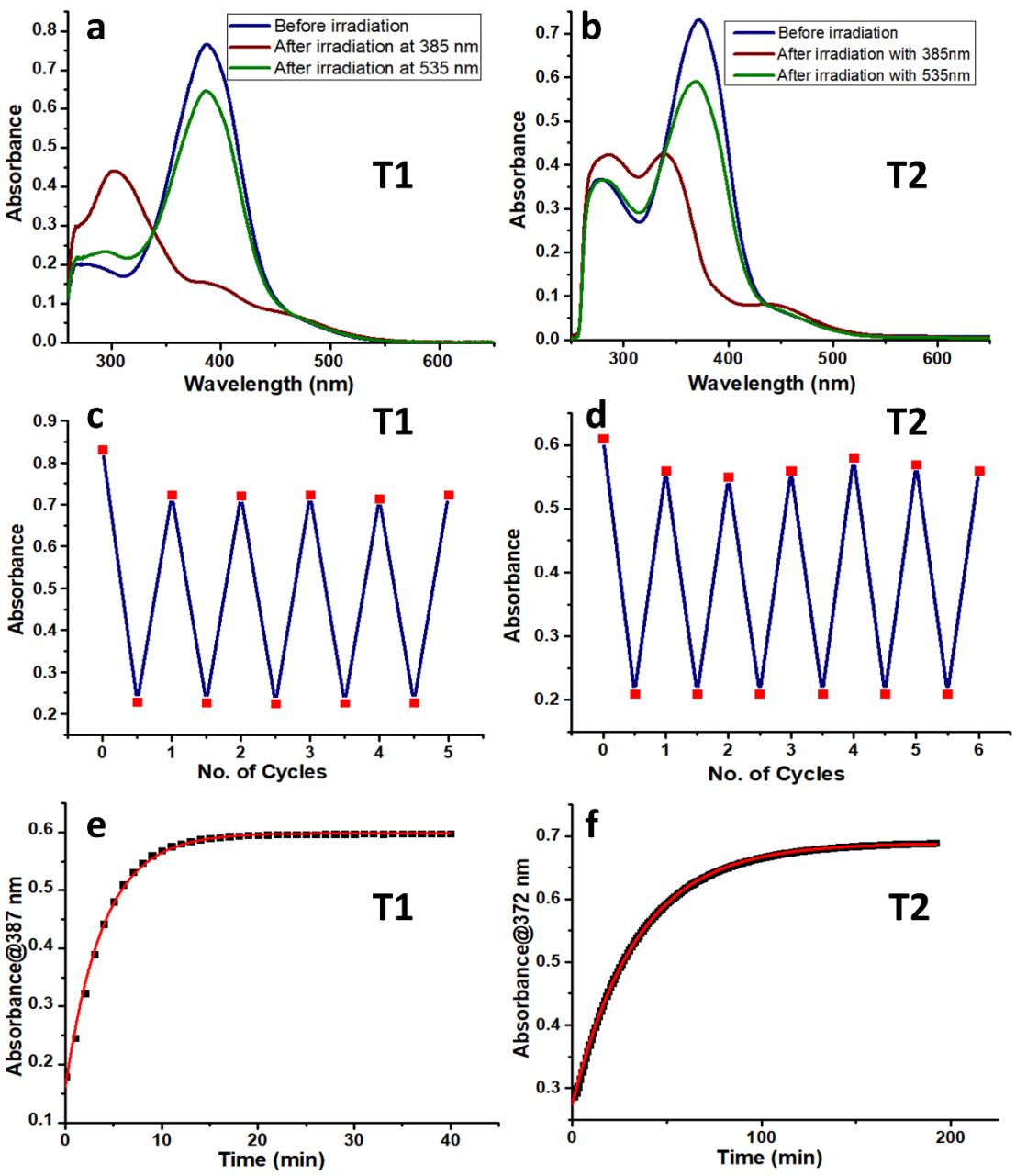

Figure 3.2 Analysis of UV-vis spectroscopic studies of **T1** and **T2**. (a) Photoswitching behaviour of **T1** (5.5 μM, DMSO); (b) Photoswitching behaviour of **T2** (9.7 μM, DMSO); (c) and (d) Photoisomerization stability experiment. (The irradiation at 385 and 535 nm lights have been alternatively used in the forward and reverse isomerization steps, respectively); (e) Kinetics plots of thermal reverse isomerization (5.5 μM, DMSO) at 387 nm of **T1** (R^2=0.99); (f) Kinetics plots of thermal reverse isomerization (9.7 μM, DMSO) at 372 nm of **T2** (R^2=0.99); For the kinetics and photoisomerization stability experiments, the absorptions at λ_{max}=387 and 372 nm were monitored/followed for **T1** and **T2**, respectively.

For instance, 405 nm (blue light), and 535 nm (green light) can be used for the forward and reverse isomerization steps, respectively in all the four targets. However, the maximum forward isomerization was furnished by irradiation at 385 nm. Due to the spectral overlap of π-π* and n-π* absorption bands, the photoswitching efficiency lowered in all the cases, particularly in the reverse

isomerization step. For all the target molecules, the fatigue resistance has also been tested up to five/six cycles.

Unlike the targets **M1** and **M2**, the C_3-symmetric **T1** and **T2** have three photoswitches. To quantify the individual photoisomers namely, *EEE*, *EEZ*, *EZZ*, and *ZZZ*-isomers at the forward and reverse isomerisation steps, we relied on ^{1}H NMR spectroscopy. The photostationary state (PSS) composition of the two targets (**T1** and **T2**) have been obtained by subjecting them to irradiation at appropriate wavelengths of light in [D_6]DMSO [at mM concentrations]. For each system, the N−H proton signal of amide group was chosen for evaluating the amount of conversion from *EEE* to *ZZZ* state **(Figure 3.3)**.[12] The forward isomerisation was done at 385 nm irradiation that led to 47, and 68 % *ZZZ*-isomer at PSS in **T1** and **T2**, respectively. On the other hand, the reverse isomerisation was carried out using 535 nm light, where we estimated 76 and 35 % conversion to *EEE*-isomer at PSS in **T1** and **T2**, respectively. Among the two targets, one with internal extended conjugation exhibits better forward photoswitching compared to the externally conjugated system.

However, the isomerization conversion estimated by ^{1}H NMR spectroscopy seems to be contradicting with the results obtained from UV-vis spectroscopic data. We presume that the drop in the photoisomerization conversion is due to the effect of concentration. To understand this, we performed a series of photoisomerization experiments for both **T1** and **T2** at different concentrations. The details of PSS estimation and the data are given **(Figure 3.4 to Figure 3.6)**.

For target **T1**, we observed a remarkable concentration dependency. For instance, at 0.4 mM concentration, the PSS was found to have 47 % *ZZZ*-isomer, whereas it dropped to 26 % conversion at 2.0 mM. The drop was maximum at 20.0 mM that resulted in 8 % conversion. At identical concentrations, the solutions of **T2** exhibited moderate conversions of 73, 66 and 49 % of *ZZZ*-isomer indicating significantly lower concentration dependency. We presume the possibility of supramolecular assembly through H-bonding and π-π stacking similar to the reports on BTA derivative **T0**.[9c]

Surprisingly, on long standing, the solutions of **T2** derivative also exhibit a strong concentration dependency as in the case of **T1**. The same solutions at 2.0 and 20.0 mM concentrations, after long standing the conversions dropped to 39 and 5 % of *ZZZ*-isomer, respectively **(Figure 3.6)**. To gain further insights, we studied such behaviour using UV-Vis spectroscopy. For illustration, a solution of **T2** in μM concentration was kept standing for 5–6 h, which led to a blue shift in the π-π* band accompanied by a drop in the intensity. However, the initial absorption feature was restored by heating the solution at 60 °C.

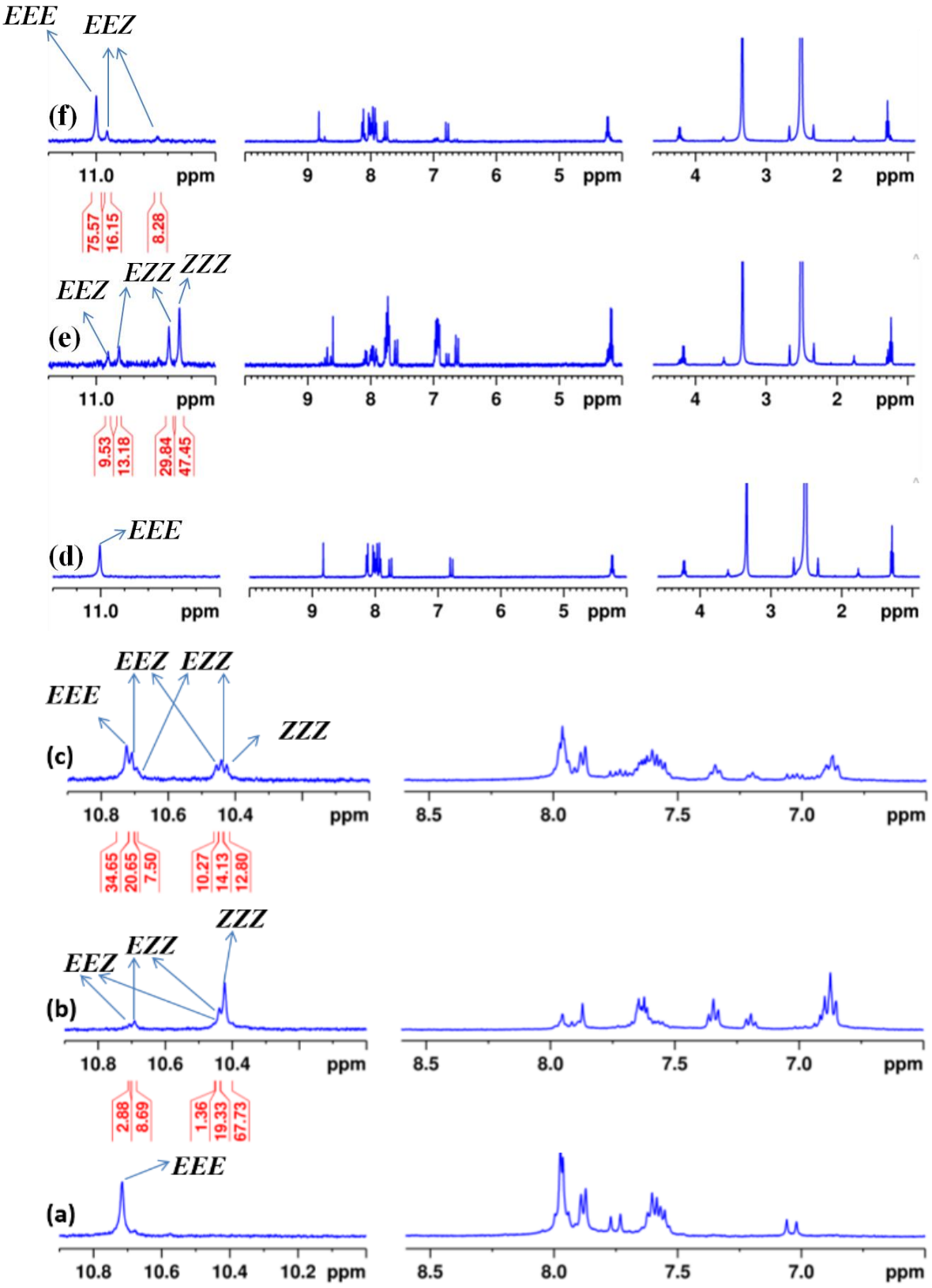

Figure 3.3 Analysis of photoswitching for the targets **T1** (top) and **T2** (bottom) by using ^{1}H-NMR spectroscopy (0.4 mM for **T1**, 1.8 mM for **T2**, [D_6]DMSO): (a) and (d) Before irradiation; (b) and (e) after irradiation at 385 nm, and (c) and (f) after irradiation at 535 nm. (The normalized integral values due to the signals corresponding to amide N-H proton are indicated).

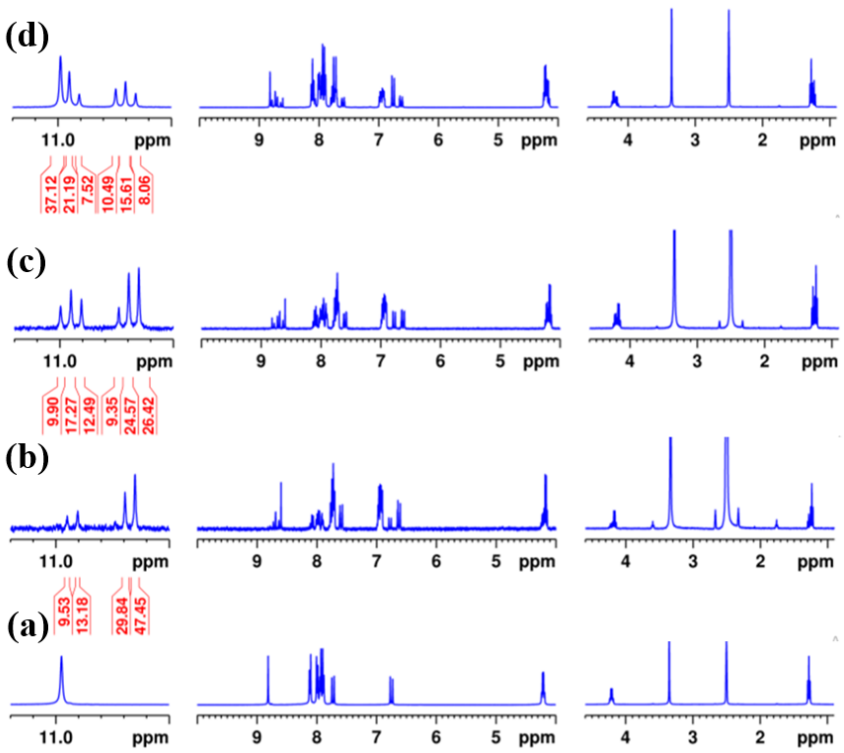

Figure 3.4 Concentration dependency of **T1** in the forward isomerization step (at different concentrations in [D_6]DMSO the samples have been irradiated at 385 nm to attain PSS). Stacking plots depicting (a) before irradiation (20.0 mM); after irradiation at 385 nm (b) 0.4 mM; (c) 2.0 mM; (d) 20.0 mM.

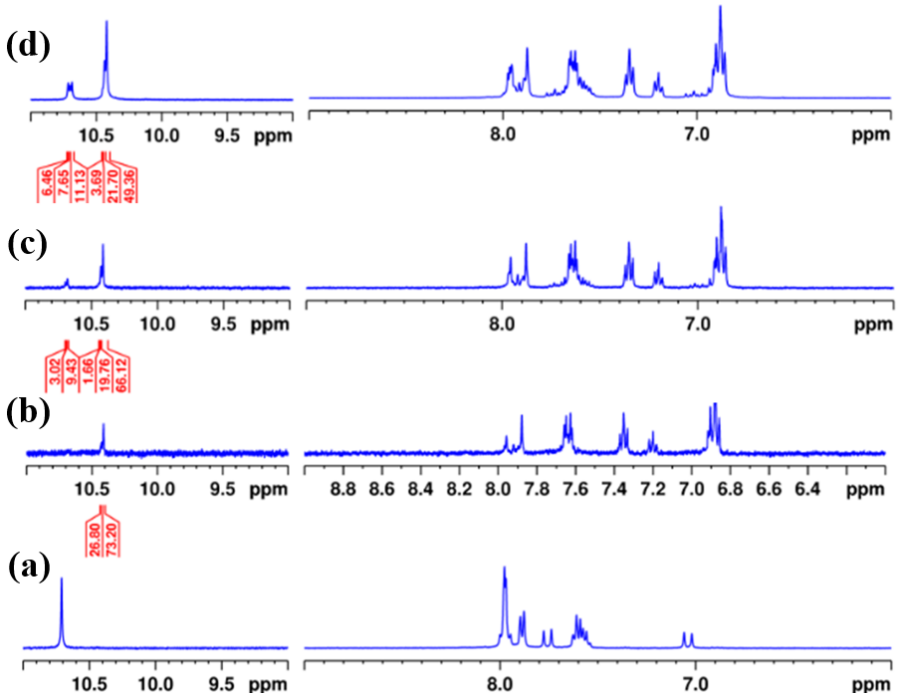

Figure 3.5 Concentration dependency of **T2** in the forward isomerization step (at different concentrations in [D_6]DMSO the samples have been irradiated at 385 nm to attain PSS). Stacking plots depicting (a) before irradiation (20.0 mM); after irradiation at 385 nm (b) 0.4 mM; (c) 2.0 mM; (d) 20.0 mM.

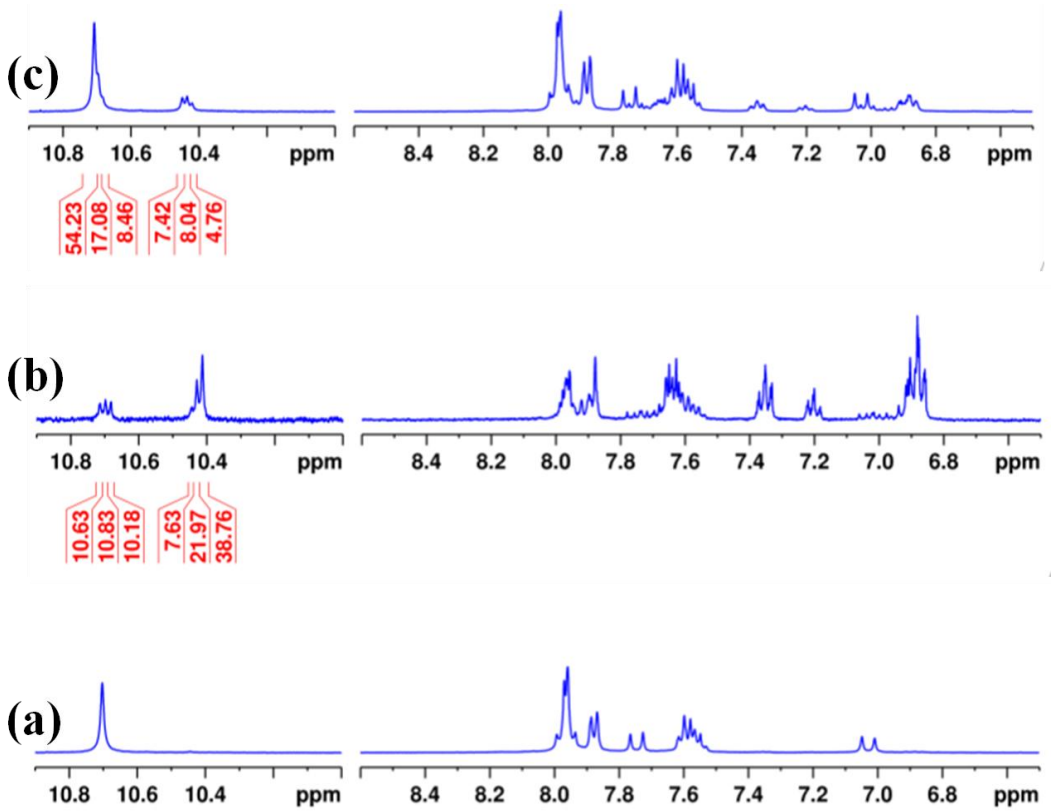

Figure 3.6 Concentration dependency of **T2** (after long standing) in the forward isomerization step (at different concentrations in [D_6]DMSO the samples have been irradiated at 385 nm to attain PSS). Stacking plots depicting (a) before irradiation (20.0 mM); after irradiation at 385 nm; (b) 2.0 mM; (c) 20.0 mM.

For compound **T2**, the core C-H proton signal was merging with other signals due to aromatic protons leading to spectral congestion, which made it difficult in getting the integral values without error. Incidentally, the other aromatic proton signals were also overlapping in nature (either in the all-*trans* or after irradiation). As a result, we were forced to obtain the integral values from the N-H proton signals. On the other hand, for **T1** the core proton signal was non-overlapping, and based on that the normalized integral values were estimated and updated. We observed significant variation in the % of photoisomers depending on the choice of the protons for integration, which is tabulated. Despite this, we used the integral values for **T1** and **T2** based on N-H proton signal as we used them for comparison. **(Table 3.1)**.

Table 3.1 Comparison of individual photoisomers upon integration of N-H and C-H proton signal for **T1**

Proton	***%EEE***	***%EEZ***	***%EZZ***	***%ZZZ***
N-H	0	10	43	47
C-H	10	35	31	24

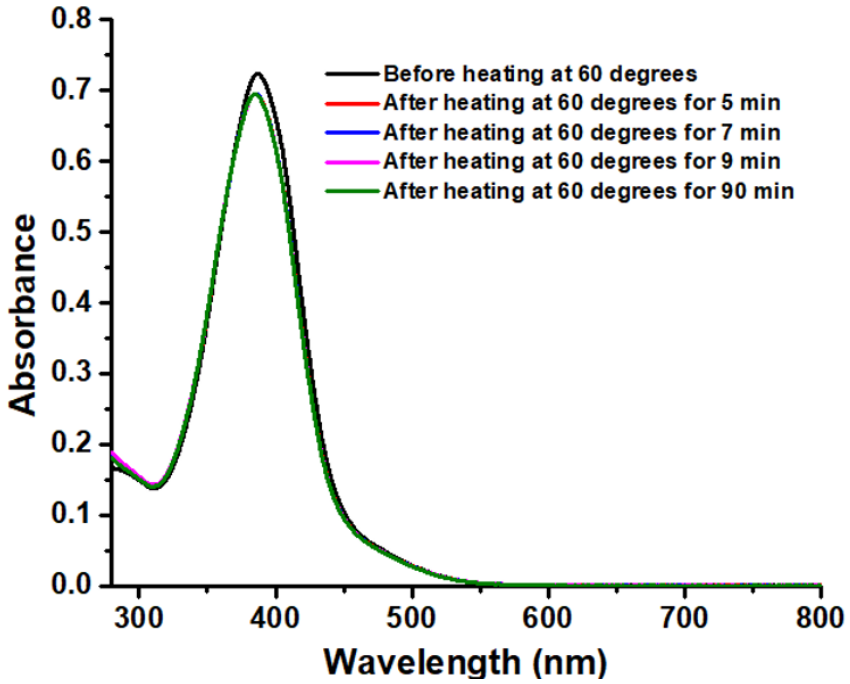

Figure 3.7 Disaggregation of **T1 (**6.3 μM**)** at 60 ^{o}C monitored by UV-Vis Spectroscopy.

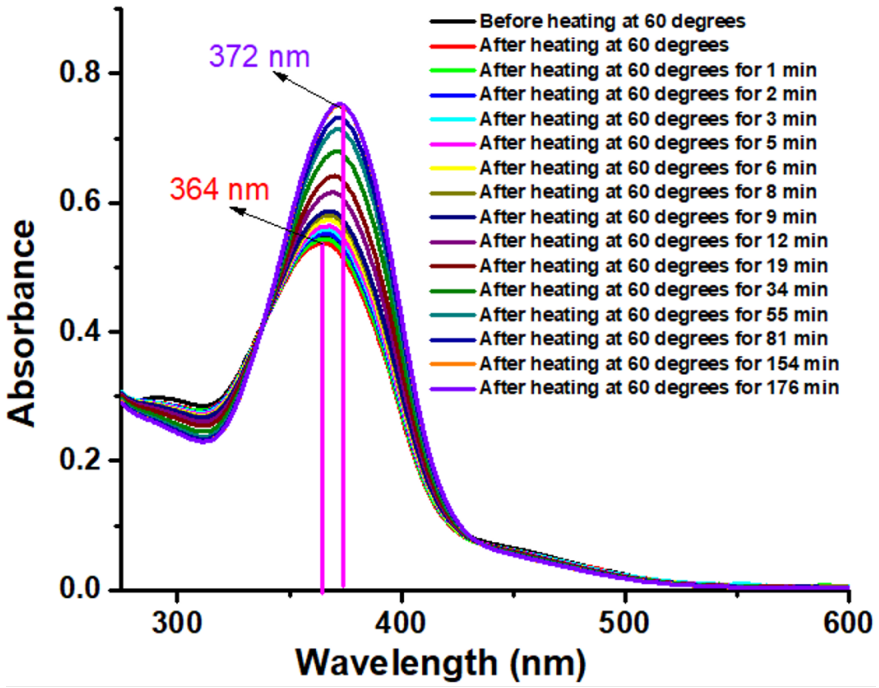

Figure 3.8 Disaggregation of **T2 (**11 μM**)** at 60 ^{o}C monitored by UV-Vis Spectroscopy.

Throughout this process, we observed two isosbestic points indicating the presence of an equilibrium that can be perturbed by means of heating. Based on this, we concluded that the solution of **T2** even at lower concentration tend to aggregate at a relatively slower rate that inhibits the photoisomerization; however, the disaggregation can be thermally induced that can restore the initial state. Indeed, the same trend was also observed in the case of **M2**. In contrast, no remarkable changes were noticed in case of **T1** in μM concentration, albeit keeping the sample standing for

longer period of time **(Figure 3.7 and Figure 3.8)**. At this juncture, we conclude that both **T1** and **T2** are capable of forming aggregation.

3.4 Thermal Stability of the Photoswitched States

Since the photoswitched states of the azobenzene derivatives are thermally activated, we performed reverse isomerization under the influence of temperature. In this regard, kinetics studies have been carried out at variable temperatures for each system **(Table 3.2)**.

Table 3.2 Thermal Kinetics Stability **T1, T2, M1, M2** (in DMSO).

Compound	Temperature [^{o}C]	Rate Constant [min^{-1}]	Half-life [min]	Concentration [μM]
T1	25	$5.4 \times 10^{-3} \pm 5.6 \times 10^{-6}$	129	5.1
	40	$3.0 \times 10^{-2} \pm 4.4 \times 10^{-5}$	23	5.1
	50	$1.0 \times 10^{-1} \pm 8.3 \times 10^{-4}$	7	5.1
	60	$2.6 \times 10^{-1} \pm 4.3 \times 10^{-3}$	3	5.1
T2	25[a]	2.8×10^{-4}	2467[a]	9.7
	40	$2.6 \times 10^{-3} \pm 7.6 \times 10^{-6}$	271	9.7
	50	$8.5 \times 10^{-3} \pm 4.1 \times 10^{-5}$	82	9.7
	60	$2.9 \times 10^{-2} \pm 1.1 \times 10^{-4}$	24	9.7
	70	$8.1 \times 10^{-2} \pm 1.2 \times 10^{-3}$	9	9.7
M1	25	$1.3 \times 10^{-2} \pm 6.7 \times 10^{-6}$	53	26
	40	$7.6 \times 10^{-2} \pm 4.8 \times 10^{-4}$	9	26
	50	$2.0 \times 10^{-1} \pm 4.4 \times 10^{-3}$	3	26
	60	$4.9 \times 10^{-1} \pm 9.8 \times 10^{-3}$	1	26
M2	25[a]	5.1×10^{-4}	1362[a]	44
	40	$3.4 \times 10^{-3} \pm 9.5 \times 10^{-7}$	206	44
	50	$1.1 \times 10^{-2} \pm 7.8 \times 10^{-6}$	65	44
	60	$3.3 \times 10^{-2} \pm 8.1 \times 10^{-5}$	21	44

[a]Extrapolated using the Arrhenius plot to determine the rate constant and half-life at 25 ^{o}C.

The thermal reverse isomerization kinetics experiments of **T1** and **M1** have been monitored at different temperatures (25, 40, 50, and 60 °C in DMSO). Whereas for **T2** and **M2**, such experiments in DMSO have been carried out at slightly elevated temperatures (40, 50, 60, and 70 °C). For all the cases, the formation rate constants and half-lives have been estimated for the *E*-isomer (in **M1** and **M2**), and *EEE*-isomer (in **T1** and **T2**). We have utilized UV-vis spectroscopy to follow the exponential growth of *E*- and *EEE*- isomers **(Appendix 3B)**. Based on the data, we have noticed a remarkable difference in the rate constants and half-lives in comparison with unsubstituted C_3- tripodal system **T0**.[9c] For instance, at 60 °C, **T1** and **T2** showed a half-life of 3

and 24 minutes, respectively, which is lower than that of **T0** (half-life=36 min). Irrespective of the extended conjugation (internal **T2** or external **T1**), the half-life gets dropped on comparison with **T0** (non-conjugated); however, the internally conjugated system **T2** stabilizes the photoswitched states relative to that of the external conjugated **T1**. For further comparison, the target molecules **M1** and **M2** have also been subjected to kinetics experiments. As expected, the monophotoswitches showed slightly lower half-lives compared to their corresponding tripodal targets. The tripodal C_3 connections or *meta* connections have been reported to provide electronic decoupling and enable the photoswitches to act independently.[9b]

The results indicate that the internal conjugation, in particular strongly stabilizes the half-life (At 25 °C, **T2**: 2467 min, **M2**: 1362 min). Whereas for the targets with external conjugation, we observed a substantial lowering in the half-lives (At 25 °C, **T1**: 129 min, **M1**: 53 min). Furthermore, using the variable temperature kinetics measurements, the activation parameters (E_a, $\Delta H^{\neq}$, $\Delta S^{\neq}$, and $\Delta G^{\neq}$) were also estimated utilizing Arrhenius and Eyring plots **(Appendix 3B)**. As expected, the barriers are higher for **T2** in comparison to **T1**. Notably, all the activation parameters including enthalpy and entropy factors are estimated to be higher in **T2** than **T1**. Particularly, the near doubling of entropy of activation in **T2** than in **T1** indicates that the isomerization process is mainly driven by the enthalpy factor, which enhances the photoswitched state in **T2** having internal conjugation.

3.5 Supramolecular Assembly

Primarily, the extended conjugation containing C_3-symmetric tripodal systems with azobenzene units were intended to form supramolecular architectures. Since amide connections and aryl groups are present at the core, both **T1** and **T2** are expected to for such self-assembly through hydrogen bonding and π-π stacking. Besides that, the concentration dependent spectroscopic studies also provided evidences for such aggregation phenomena. To envisage the formation of self-assembly in **T1** and **T2** in the bulk phase, X-ray diffraction (XRD) studies have been carried out at room temperature **(Figure 3.9)**. For compound **T1**, having the acrylate moieties at the peripheral positions exhibit three sharp peaks in the small-angle region with *d*-spacings 34.49 Å, 21.14 Å and 13.77 Å **(Figure 3.9, Table 3.2)**, which can be indexed on the rectangular lattice. The diffuse signal in the wide- angle region (h_a and h_c) represents the intracolumnar distances i. e. flexible side groups correlations and core-core separation, respectively. The broad halo in the wide-angle region excludes the crystalline nature of the compound. Moreover, the compound is not shearable and therefore, the nature of the phase is soft crystalline and can be assigned as Cr_{Colr} (soft crystalline columnar rectangular phase). In contrary to this, for compound **T2** with azobenzene groups at the molecular periphery exhibit different self-assembly behavior. In its XRD pattern, only

one peak in the small-angle region and two broad peaks in the wide-angle region (h_a and h_c) were observed which suggest the possible formation of lamellar (layered) assembly as also reported earlier.[13, 14]

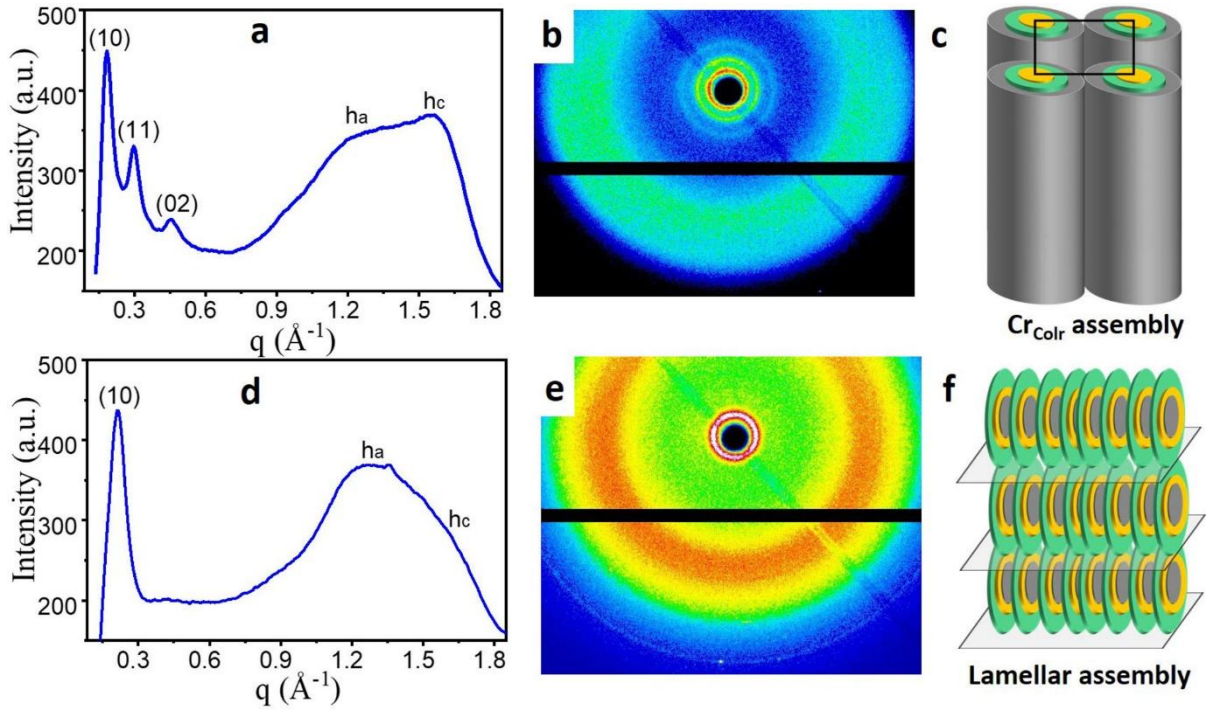

Figure 3.9 1D XRD pattern of compounds (a) **T1** and (d) **T2**. 2D diffraction pattern of compounds (b) **T1** and (e) **T2**. Modelling showing the (c) Soft crystalline columnar rectangular assembly of **T1** and (f) lamellar assembly of **T2**. (Color codes: grey – olefinic part; yellow – amide; green – azobenzene part)

Table 3.3 X-ray diffraction data

Compound	**(*h k*)**	**d_{obs} (Å)[a]**	**d_{cal} (Å)[b]**	**Compound**	**(*h k*)**	**d_{obs} (Å)**
T1 (Cr_{Colr}) *a* = 34.49 Å *b* = 27.15 Å	(1 0)	34.49	34.49	**T2** (Lamellar)	(1 0)	29.44
	(1 1)	21.14	21.33		h_a	4.83
	(0 2)	13.77	13.58		h_c	3.95
	h_a	5.09	-		-	-
	h_c	3.90	-		-	-

[a]d_{obs}: experimental *d*-spacing; [b]d_{cal}: calculated *d*-spacing for Cr_{Colr} by using the relation: $\frac{1}{d^2} = \left[\frac{h^2}{a^2} + \frac{k^2}{b^2}\right]$; h_a and h_c are average separations of the flexible side groups correlations and core-core separations, respectively; (*hk*) is the corresponding Miller indices to the reflecting planes; a,b represent the lattice parameters of the Cr_{Colr} phase.

The validation of layered assembly was further supported from the observed striped patterns in AFM (*vide-infra*), characteristics of lamellar assembly.[15-19] Therefore, small-angle peak with *d*-

spacing 29.44 Å were assigned to lamellar periodicity, whereas peaks representing intracolumnar distances, h_a (4.83 Å) corresponds to the average separations of the flexible side groups correlations and h_c (3.95 Å) be consistent with the core-core separation (**Figure 3.9, Table 3.3**).

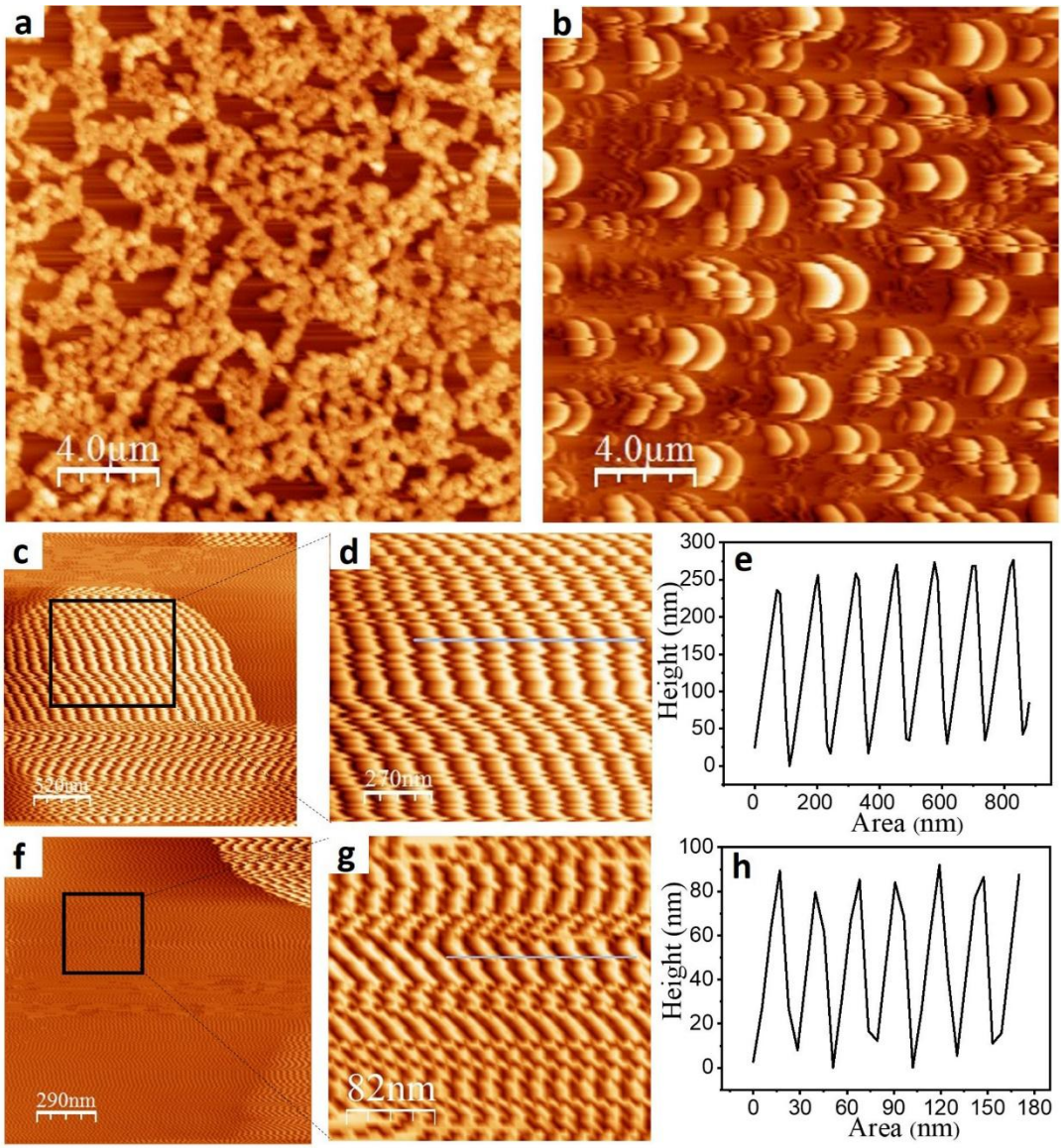

Figure 3.10 AFM surface profiles of (a) **T1**, and (b) **T2** {spin-coated (in THF) onto a silicon wafer showing strikingly different morphology consisting of aggregated structures and striped pattern assembly, respectively}. AFM surface profiles of **T2** depicting (c, d) bright strips, and (f, g) dark strips regions equivalent to lamellae areas covered with thick and thin layer of material, respectively (d and g are corresponding zoomed sections (enclosed by square box)); (e) and (h) shows a cross-section profile along the direction indicated with a blue line in image (d) and (g), respectively.

The 2D diffraction patterns **(Figure 3.9b,e)** and the schematic models **(Figure 3.9c,f)** corresponding to the lamellar and rectangular self-assembly of the C_3-symmetric molecules are depicted in the **Figure 3.9**. XRD studies clearly showed that how the change in the position of the

central acryl groups present in **T2** towards the molecular periphery in **T1**, led to the different self-assembly behaviour. Interestingly, the different self-assembly of both the compounds are further evident from their different morphological behaviour observed through AFM.

The investigation of the self-assembly behaviour by AFM are extremely helpful to provide insights on the molecular arrangements at nanoscopic level. AFM study revealed that the spin-coated solution of **T2** in THF form highly aligned periodic stripes on silicon-wafer surface **(Figure 3.10b)**. On the other hand, **T1** did not form such ordered and layered assembly rather it formed an aggregated structure **(Figure 3.10a)**. The striped patterns observed in case of **T2** are characteristics of lamellar assembly where the molecules are arranged in layered fashion. The similar evidence of layered assembly was obtained from the XRD studies (*vide-supra*).

Further, the question arises, whether the molecules in these layers are face-on or edge-on aligned. The type of arrangement can be investigated by probing the physisorbed molecules with sub-molecular resolution. However, in the present case, the clearly resolved morphology **(Figure 3.10)** was obtained up to several micrometers (far greater than the molecular dimensions) which are inadequate to unravel the type of orientations and dynamics of molecules at surfaces. Interestingly, at a full coverage of the AFM images, the thicker **(Figure 3.10c, d)** and thinner domains **(Figure 3.10f, g)** with discrete and well-defined thickness are observed. It can be noted that the self-assembly obtained by **T2** molecules is very robust. Even thicker domains formed well-ordered striped patterns akin to thinner domains and just differing in the layer thickness and layer periodicity. It has been observed that the distance between the layers is increasing with increase in the thickness of the multilayers. The thicker domains exhibit thickness or height of around 260 nm and the layer periodicity of around 120 nm **(Figure 3.10e)**, whereas the thinner domains are around 90 nm thick and around 30 nm far apart consecutively (**Figure 3.10h**).

The C_3-symmetric molecular design of **T2** consist of BTAA units at the center connected to three azobenzene groups through amide linkages is capable of self-assembly through H-bonding. Recently, Samorì group studied the self-assembly of various C_3-symmetric molecules that are mostly aligned on the highly oriented pyrolitic graphite (HOPG) surface under surface confinement.[9a] However, the spontaneous supramolecular organization of tripodal molecule **T2** takes place simply on silicon surface, indicating the high tendency of molecules to self-assemble, resulting in the formation of supramolecular architecture.

3.6 Sol-gel Properties and Microcrystalline Nature

Interestingly, addition of water to a DMSO solution containing target **T1**, results in gelation; however, no such gelation was observed in the target **T2** under similar or modified conditions. As the target **T1** is appended with three photoswitchable units, we also attempted at the

light induced sol-gel properties change or phase transition under irradiation conditions. The aqueous DMSO gel of **T1** upon subjected to irradiation at 405/385 nm did not show remarkable change. However, a partial melting of gel was observed **(Figure 3.11a)**. On the other hand, heating of the sample led to complete transformation into sol, which reverted back to gel form upon cooling. In order to understand the morphology of the gel formed, we have performed microscopic imaging studies using SEM **(Figure 3.11b)** and TEM **(Figure 3.11c)**, where we observed long fibrous type morphology in case of gel form. Further, the gel form of the sample also exhibited a birefringence pattern in POM (polarized optical microscopy), which collapsed to sol upon heating at 128 °C **(Figure 3.11d)**. To shed further light, we investigated the effect of water in the absorption properties change in DMSO solution of **T1**. We observed a blue shift (387 to 369 nm) upon incremental addition of water to the 6 μM solution of **T1** indicating the formation of aggregate **(Figure 3.12)**. On contrary to the gelation in **T1**, in target **T2**, we have seen the formation of tiny organic microcrystals in DMSO as a solvent. For understanding the morphology of microcrystals, we have performed SEM and POM imaging **(Figure 3.13 and Figure 3.14)**.

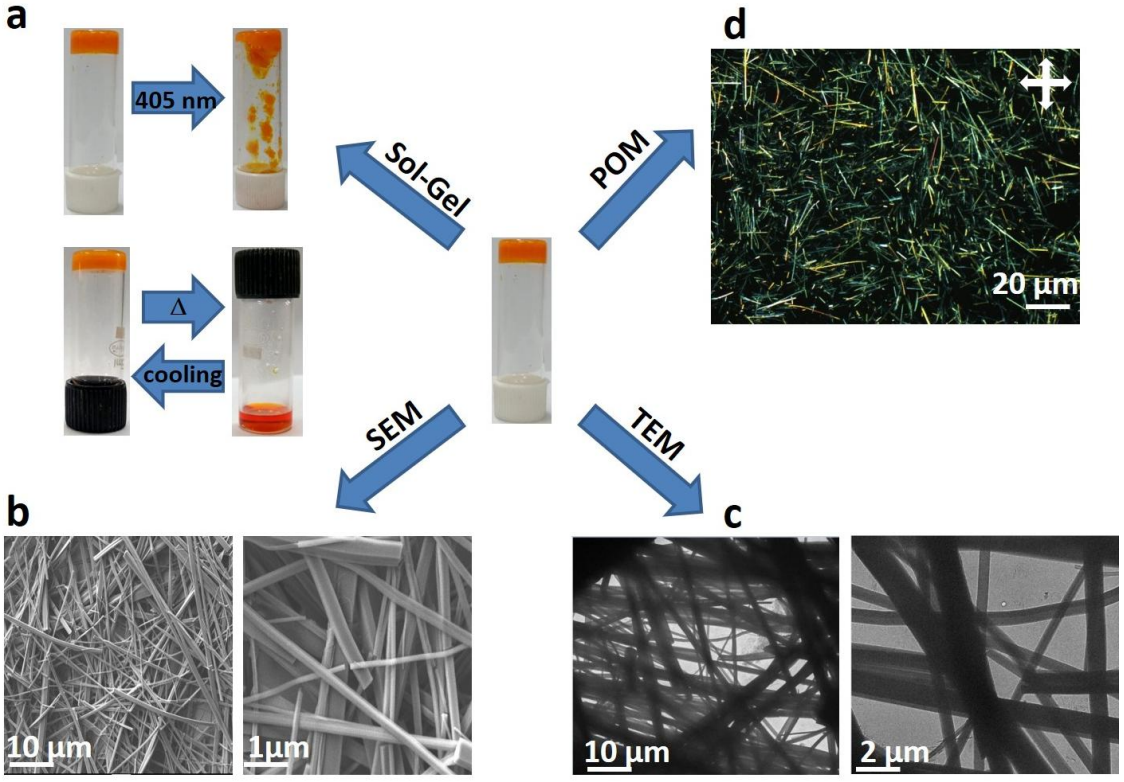

Figure 3.11 Sol-gel properties and morphology of gel form of the compound **T1**: (a) Sol-gel transformation with irradiation at 405 nm (partial melting) and thermoreversible Gel-sol transformation; Morphology of gel form depicted by (b) SEM, (c) TEM (magnification: 10 μm, and 2 μm) and (d) POM technique.

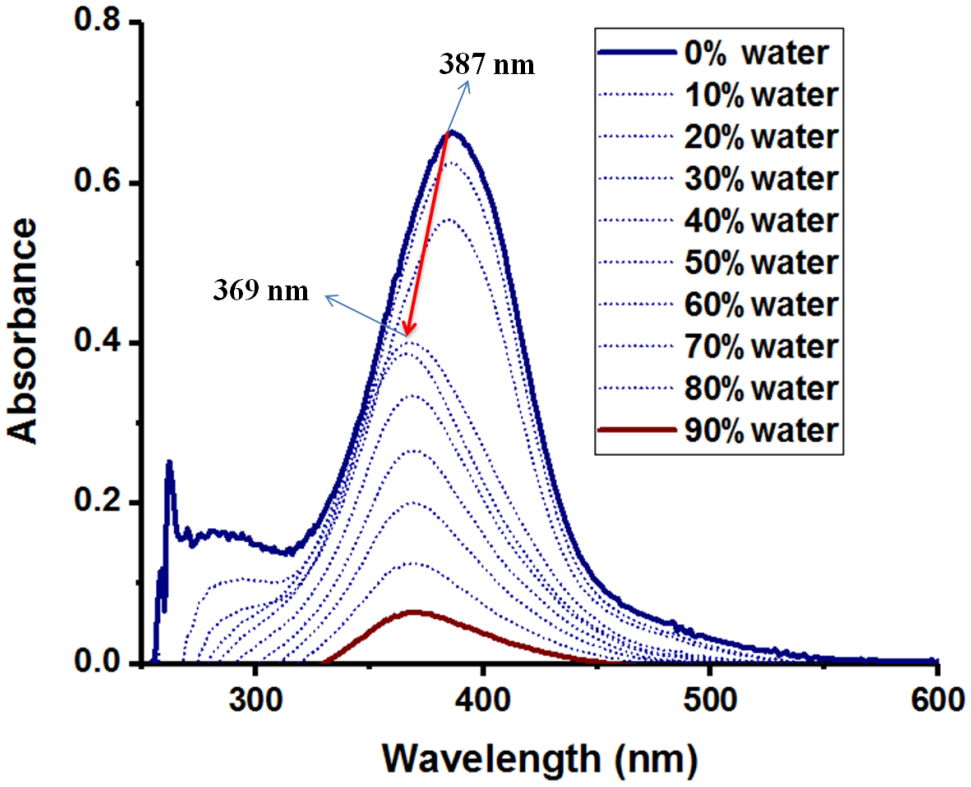

Figure 3.12 Aggregation studies on **T1** in DMSO as a result of varying % of water.

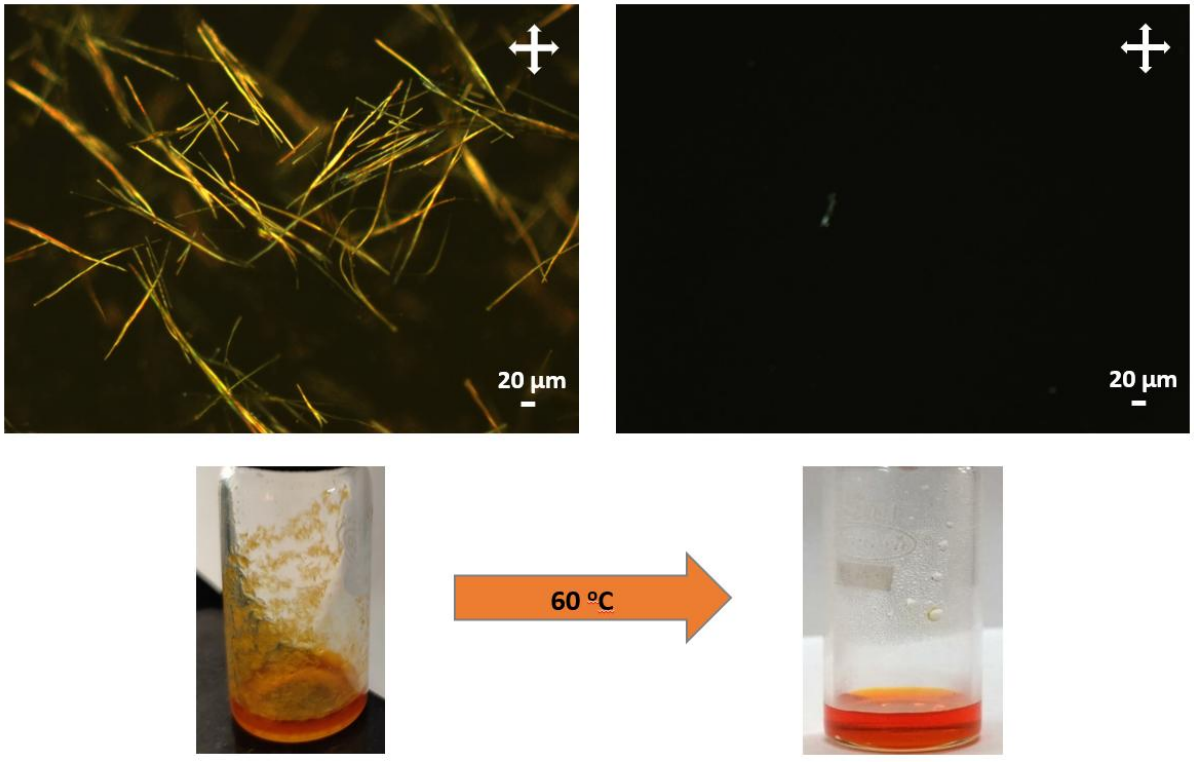

Figure 3.13 POM images of organic microcrystals at 20.0 mM of **T2**.

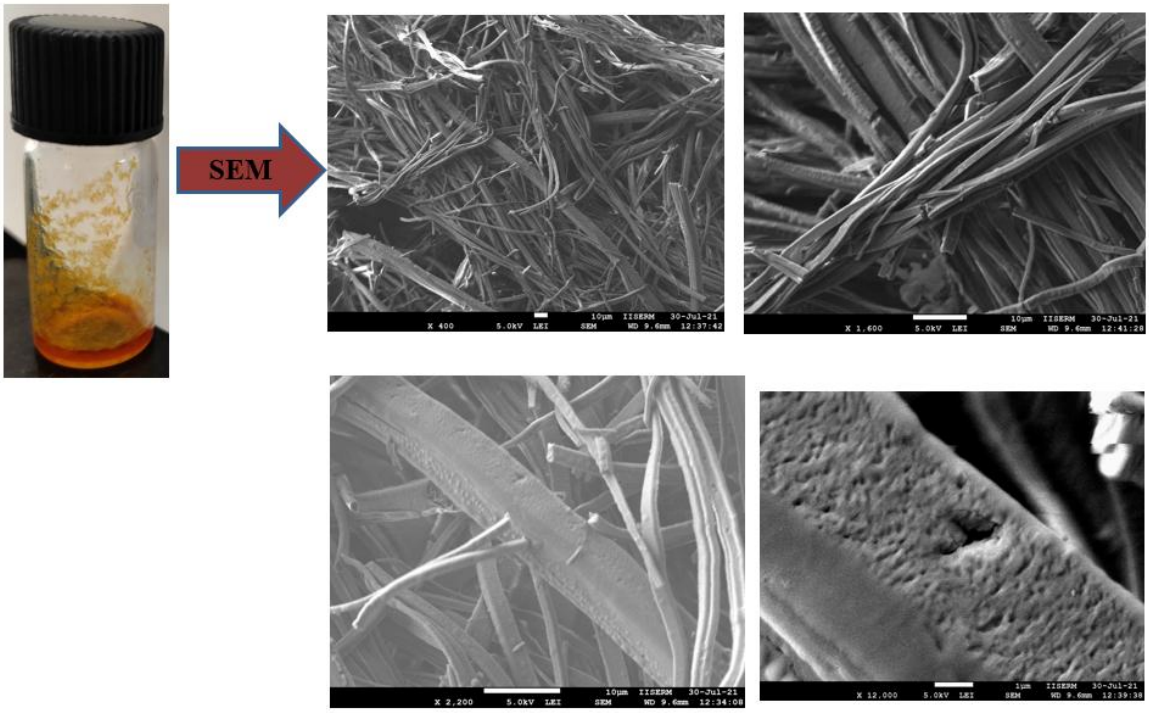

Figure 3.14 SEM images of organic microcrystals at 20.0 mM of **T2**.

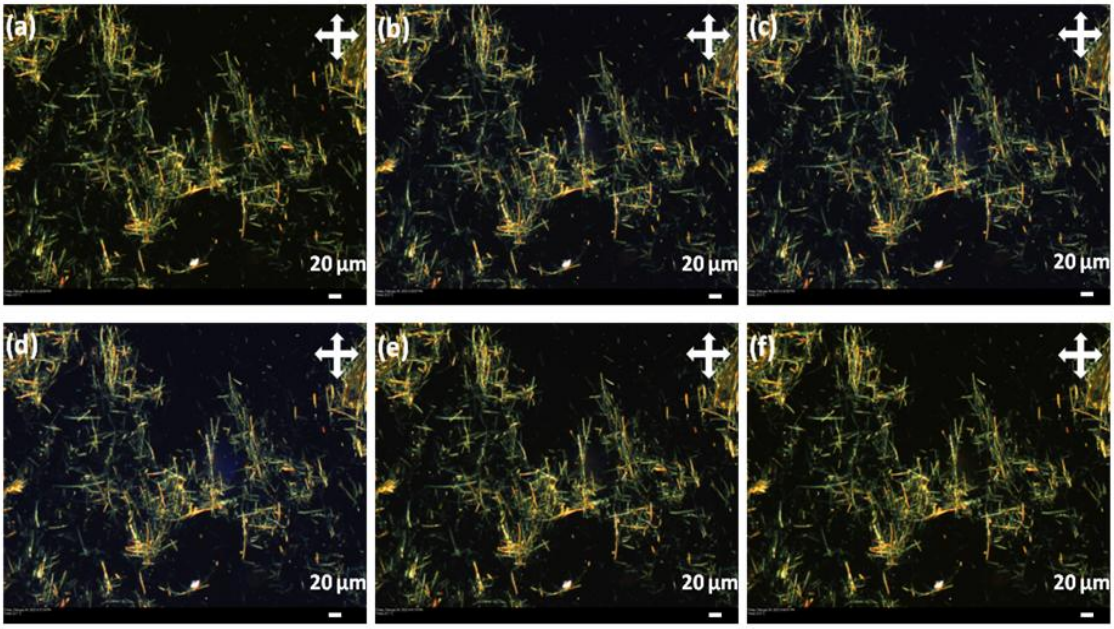

Figure 3.15 POM images of gel (7.0 mM) for **T1** after irradiation with 405 nm at different times (a) before irradiation; after irradiation at 405 nm for (b) 8 min; (c) 12 min; (d) 17 min; (e) 21 min and (f) 24 min.

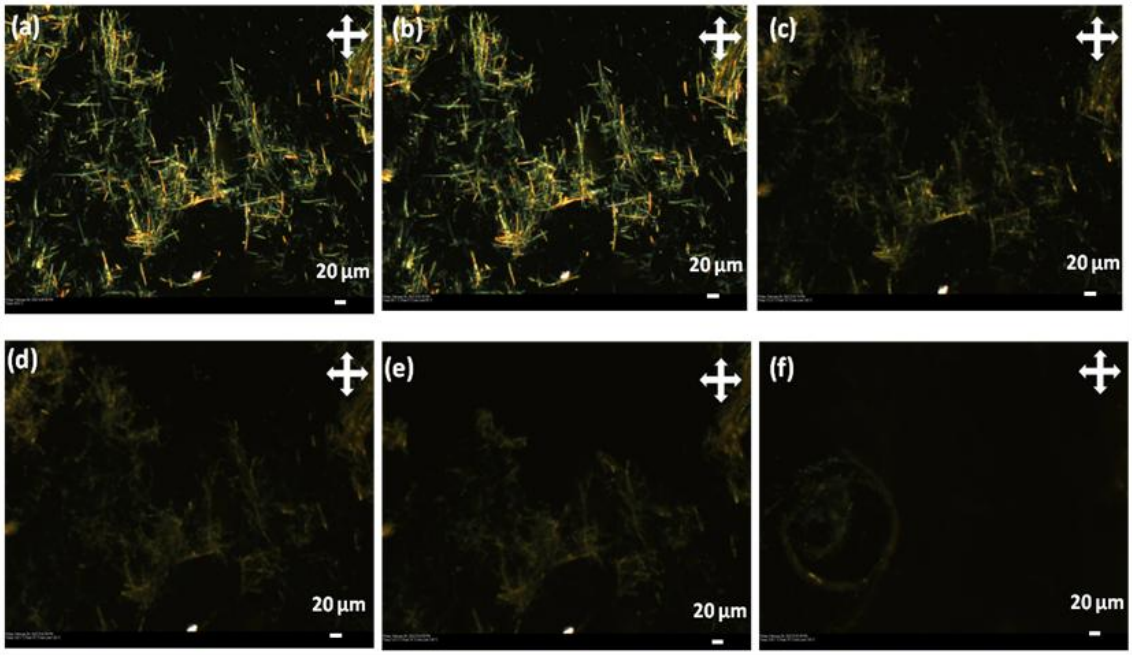

Figure 3.16 POM images of gel (7.0 mM) for **T1** (a) at 30 ^{o}C; after heating at (b) 55 ^{o}C; (c) 112 ^{o}C; (d) 120 ^{o}C; (e) 123 ^{o}C; (e) 128 ^{o}C.

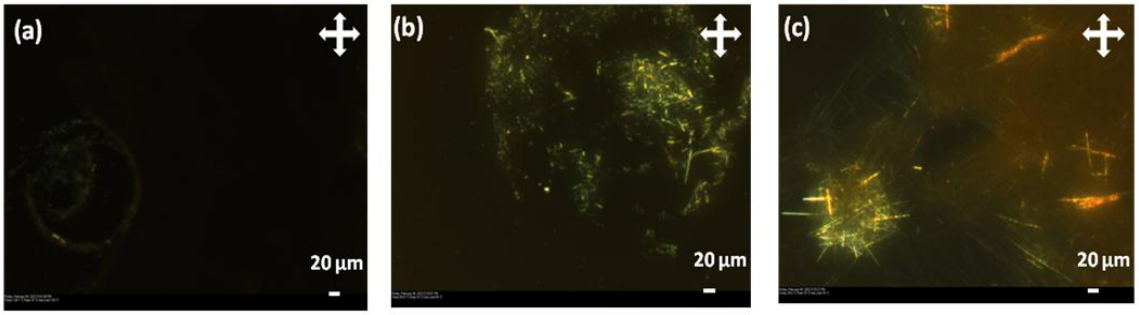

Figure 3.17 POM images of sol on cooling: (a) 128 ^{o}C; (b) 60 ^{o}C; (c) 40 ^{o}C.

All these evidences unambiguously confirmed the supramolecular self-assembly in our designed molecular systems **T1** and **T2**. Based on the XRD studies, the BTA based core part of the target molecule **T1** has higher propensity to form columnar stacks through hydrogen bonding and π-π stacking; whereas the BTAA based target compound **T2** showed the existence of a lamellar stacking. Since the hydrogen bonding is dominant interaction in **T1**, the addition of water induces the gelation. Although both the target molecules are appended with photoswitchable units, the irradiation at relatively longer wavelengths caused only a partial weakening of such interactions in **T1** (in gel form), and completely ineffective in the supramolecular assembly.

3.7 Summary

We have designed and synthesized novel C_3-symmetric tripodal multiple azobenzenes based extended π-conjugated targets **T1** and **T2**. Through these investigations, the effect of extended conjugation at the internal and external positions in the targets **T1** and **T2** have been analyzed. Both the photoswitching characteristics, and the thermal stability of their photoswitched

states showed significant difference. By comparing the results with that of their corresponding mono functionalized systems **M1** and **M2**, we understood that both **T1** and **T2** showed a good solution state photoswitching at the μM concentration range. However, at a higher concentration (mM range), NMR spectroscopic studies predicted a partial isomerization with the coexistence of all four possible photoisomers at their respective photostationary states. All these results corroborate with the higher propensity of these two molecules to form aggregates. XRD studies clearly showed that how the change in the position of the central acryl groups present in **T2** towards the molecular periphery in **T1**, led to the different self-assembly behaviour. The SEM and TEM have shown the long fibrous type of morphology of the gel **T1**, whereas in the case of **T2**, we observed the formation of microcrystals with porous long rod-shaped material. Therefore, these highly ordered materials can be useful in variety of applications through proper functionalization.

3.8 Experimental Section

Synthesis of (*E*)-4-((4-bromophenyl)diazenyl)aniline (S5)

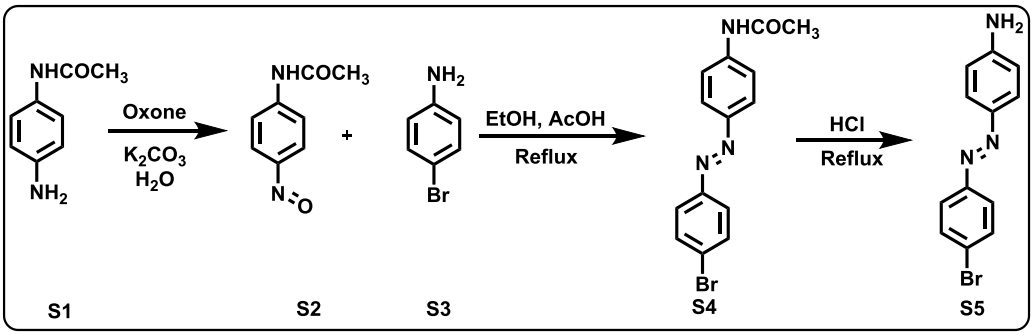

In a round bottom flask, an aqueous solution of oxone (5.7 g, 184.0 mmol) with K_2CO_3 (14.3 g, 104.0 mmol) was taken and stirred at room temperature. To this, an aqueous solution of 4-aminoacetanilide (**S1)** (6.0 g, 40.0 mmol) was quickly added. A green solid product of nitroso compound (**S2)** was obtained, which was filtered off after stirring for half an hour. The wet solid product was directly utilized for the next step. Mill's method was adopted for a condensation reaction between the crude nitroso compound (S**2)** formed in the first step and 4-bromoaniline (**S3)** (6.9 g, 40.0 mmol). This was performed by refluxing these reactants in EtOH (70 ml) and acetic acid (50 ml) for 7 hrs and monitored by TLC. After completion of the reaction, the hydrolysis step was continued by refluxing the *in situ* generated amide product (**S4**) under 6M HCl (20 ml) for 5-6 hrs. After completion of the reaction, the reaction mixture cooled down to room temperature and was neutralized by adding an aqueous sodium bicarbonate solution. The reaction mixture was extracted using ethyl acetate, the organic layer was washed with brine solution, dried on anhydrous sodium sulphate and evaporated to dryness in rotary evaporator. The crude product was then

subjected to purification by column chromatography.

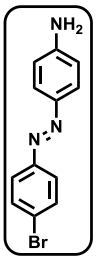

(*E*)-4-((4-bromophenyl)diazenyl)aniline (S5): Orange solid, 97% yield. ^{1}H NMR (400 MHz, $CDCl_3$): δ (ppm) 7.82-7.78 (m, 2H), 7.74-7.71 (m, 2H), 7.62-7.58 (m, 2H), 6.75-6.72 (m, 2H), 4.09 (br, 2H); ^{13}C-NMR (100 MHz, $CDCl_3$): δ (ppm) 151.8, 150.0, 145.4, 132.3, 125.4, 124.0, 123.9, 114.7; IR (ATR): 3450, 3369, 1597, 1283, 1144, 839 cm^{-1}; HRMS (ESI): *m/z* calcd. for $C_{13}H_{10}BrN_3[M+H]^+$: 276.0136; found: 276.0125.

Synthesis of Ethyl (*E*)-3-(4-((*E*)-(4-aminophenyl)diazenyl)phenyl)acrylate (3)

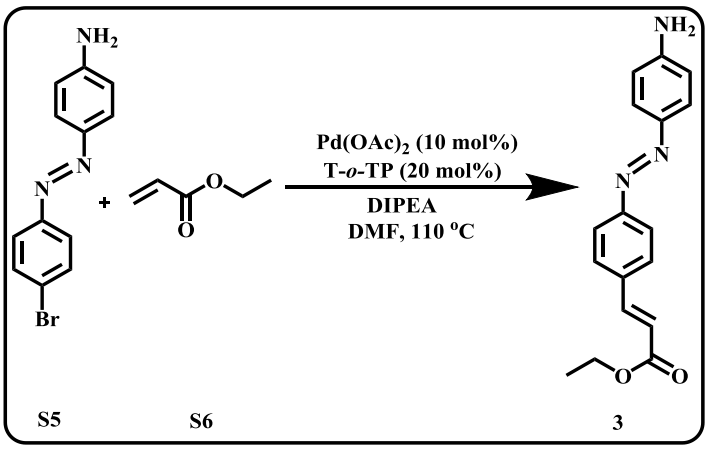

In a round bottom flask, under argon atmosphere, DMF (5 ml) was added and degassed. To this, $Pd(OAc)_2$ (10 mol%) and Tris(*o*-tolyl)phosphine (20 mol%) was added. Then, the mixture was purged with argon for 15 minutes. After purging, (*E*)-4-((4-bromophenyl)diazenyl)aniline (0.1 g, 0.4 mmol) (**S5)** was added, followed by the addition of base DIPEA (0.3 ml, 0.5 mmol) under constant stirring. Then to the mixture, ethyl acrylate (0.1 ml, 1.1 mmol) (**S6)** was added slowly. The reaction mixture was heated at 110 ^{o}C for 24 hrs. The coupling reaction was monitored by TLC. After completion, the reaction mixture was passed through a celite bed, and washed with ethyl acetate. The organic layer was then washed with brine solution, and dried on anhydrous sodium sulphate. Then the organic layer was evaporated to dryness and subjected to purification by column chromatography.

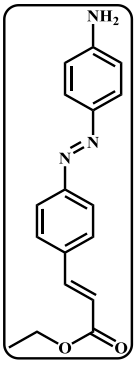

Ethyl (*E*)-3-(4-((*E*)-(4-aminophenyl)diazenyl)phenyl)acrylate (3): Orange solid, mp = 155-156 ^{o}C, 56% yield. ^{1}H NMR (400 MHz, $CDCl_3$): δ (ppm) 7.84 (dd, *J* = 12.1, 8.4 Hz, 4H), 7.72 (d, *J* = 16.0 Hz, 1H), 7.64 (d, *J* = 8.3 Hz, 2H), 6.75 (d, *J* = 8.6, 2H), 6.49 (d, *J* = 16.0 Hz, 1H), 4.28 (q, *J* = 7.1 Hz, 2H), 4.11 (br, 2H), 1.35 (t, *J* = 7.1 Hz, 3H); ^{13}C NMR (100 MHz, $CDCl_3$): δ (ppm) 167.1, 154.0, 150.2, 145.7, 144.0, 135.7, 129.0, 125.6, 123.0, 119.0, 114.7, 60.7, 14.5; IR (ATR): 3360, 3319, 1685, 1591, 1395, 1130, 839 cm^{-1};

HRMS (ESI): *m/z* calcd. for $C_{17}H_{17}N_3O_2[M+H]^+$: 296.1378; found : 296.1386.

Synthesis of ethyl (*E*)-3-(4-((*E*)-(4-benzamidophenyl)diazenyl)phenyl)acrylate (M1)

A mixture of the ethyl (*E*)-3-(4-((*E*)-(4-aminophenyl)diazenyl)phenyl)acrylate (**3**) (4.0 g, 14.0 mmol), triethylamine (4.0 ml, 28.4 mmol) were placed in a 50 mL RB flask and dissolved in dry THF (30 mL). A solution of benzoyl chloride (1.0 g, 7.0 mmol) **(2)** in dry THF (10 mL) was added to it at 0-5 ^oC under a nitrogen atmosphere. After the addition, the resulting mixture was allowed to stir at 60 ^oC temperature. An orange coloured precipitate was formed, which was isolated by filtration, and the product was purified using column chromatography over neutral alumina.

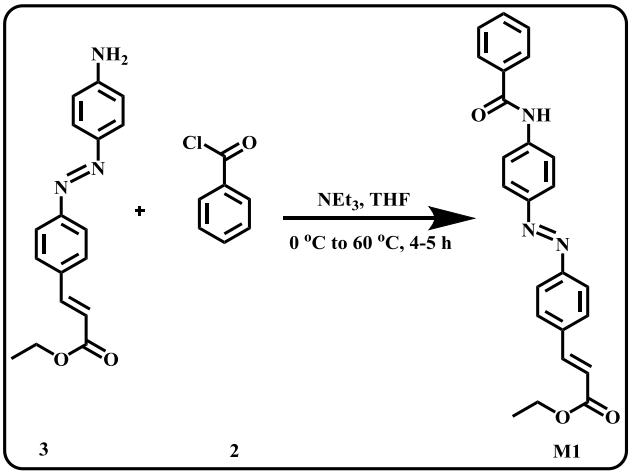

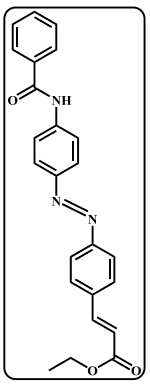

Ethyl (*E*)-3-(4-((*E*)-(4-benzamidophenyl)diazenyl)phenyl)acrylate (M1) Orange solid, mp= 200-203 ^oC, 70% yield. ^1H NMR (400 MHz, $CDCl_3$): δ (ppm) 8.00 (d, J = 8.8 Hz, 2H), 7.92 (t, J = 8.8 Hz, 4H), 7.85 (d, J = 8.8, 2H), 7.74 (d, J = 16.0 Hz, 1H), 7.68 (d, J = 8.4 Hz, 2H), 7.62-7.58 (m, 1H), 7.55-7.51 (m, 2H), 6.52 (d, J = 16.4 Hz, 1H), 4.29 (q, J = 7.2 Hz, 2H), 1.36 (t, J = 7.2 Hz, 3H); ^{13}C NMR (100 MHz, $[D_6]$DMSO): δ (ppm) 166.1, 166.0, 152.8, 147.9, 143.3, 142.8, 136.5, 134.7, 131.9, 129.6, 128.5, 127.9, 123.8, 122.9, 120.4, 119.7, 60.2, 14.2; FT-IR (KBr): 2927, 1687, 1532, 1282, 839 cm^{-1}; HRMS (ESI): *m/z* calcd. for $C_{24}H_{21}N_3O_3[M+H]^+$: 400.1678; found: 400.1660.

Synthesis of triethyl 3,3',3''-(((1*E*,1'*E*,1''*E*)-(((benzene-1,3,5-tricarbonyl)*tris*(azanediyl))*tris*(benzene-4,1-diyl))*tris*(diazene-2,1-diyl))*tris*(benzene-4,1-diyl))(2*E*,2'*E*,2''*E*)-triacrylate (T1)

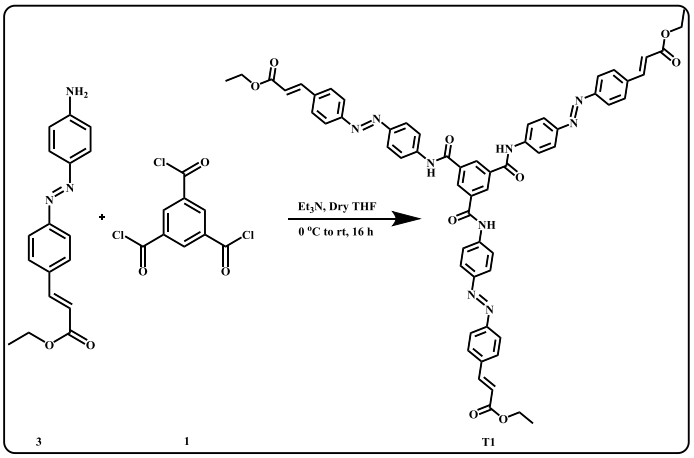

Trimesoyl chloride (**1**) was generated *in situ* from trimesic acid (0.2 g, 1.0 mmol) using $SOCl_2$ (in excess) with a catalytic amount of DMF and refluxed for 4-5 hours. After complete conversion of trimesic acid to trimesoyl chloride (a clear homogeneous solution) (**1**), $SOCl_2$ was evaporated. The *in situ* generated trimesoyl chloride (**1**) was dissolved in dry THF (5 ml) under nitrogen atmosphere, and then transferred dropwise into a mixture containing (**3**) (1.1 g, 3.8 mmol) and Et_3N (1.2 ml, 8.6 mmol) dissolved in THF (30 ml) at 0 ^oC. The reaction mixture was stirred at rt for 16h. Progress of reaction was monitored by TLC. After completion, the reaction mixture was precipitated out by the addition of methanol. The ppt obtained was filtered, washed with methanol and dried in vacuum to get the pure product.

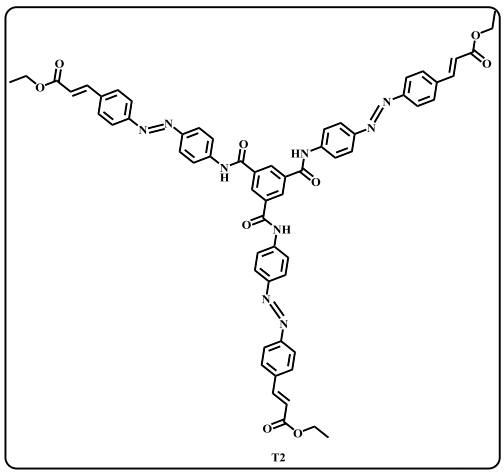

Triethyl 3,3',3''-(((1*E*,1'*E*,1''*E*)-(((benzene-1,3,5-tricarbonyl)*tris*(azanediyl))*tris*(benzene-4,1-diyl))*tris*(diazene-2,1-diyl))*tris*(benzene-4,1 diyl))(2*E*,2'*E*,2''*E*)-triacrylate (T1): Orange solid, mp = Above 300 °C, 30% yield. ^1H NMR (400 MHz, [D_6]DMSO): δ (ppm) 11.00 (s, 3H), 8.82 (s, 3H), 8.12 (d, J = 8.9 Hz, 6H), 8.01 (d, J = 8.8 Hz, 6H), 7.94 (dd, J = 21.8, 8.6 Hz, 12H), 7.74 (d, J = 16.0 Hz, 3H), 6.77 (d, J = 16.0 Hz, 3H), 4.22 (q, J = 7.0 Hz, 6H), 1.28 (t, J = 7.1 Hz, 9H); ^{13}C NMR (100 MHz, [D_6]DMSO): δ (ppm) 166.1, 164.7, 152.8, 148.1, 143.2, 142.4, 136.5, 135.2, 129.6 (2C), 123.9, 122.9, 120.6, 119.6, 60.2, 14.2;

IR(ATR): 2975, 1682, 1520, 1300, 833 cm^{-1}; HRMS (MALDI): *m/z* calcd for $C_{60}H_{51}N_9O_9[M+H]^+$: 1042.888; found: 1042.3894

Synthesis of (*E*)-*N*-(4-(phenyldiazenyl)phenyl)acrylamide (6)

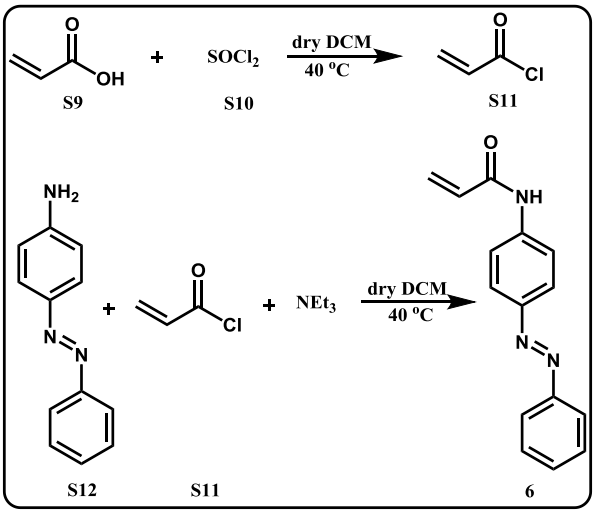

In a two-neck round bottom flask, acrylic acid (**S9)** (0.5 g, 7.0 mmol) was dissolved in 5 mL dry dichloromethane, under nitrogen atmosphere thionyl chloride (0.5 ml, 7.0 mmol) was then added to this solution. The mixture was refluxed at 40 ^oC for 4 h. Afterwards the yellowish solution of acid chloride was utilized directly for the next step i.e. acid amine coupling. In another round bottom flask, to a solution of 4-aminoazobenzene (**S12)** (1.4 g, 7.0 mmol) in dry dichloromethane (10 mL), anhydrous Et_3N (2.0 mL, 14.0 mmol) was added at 0 ^oC under nitrogen atmosphere. Then, acryloyl chloride in dichloromethane was added dropwise at 0 ^oC, and the reaction was continued at 40 ^oC for 24 h. After completion, the reaction mixture was cooled down to room temperature and was poured into water. Then extracted with EtOAc and washed with brine solution. The organic layer was dried on anhydrous sodium sulphate and evaporated under vacuum. The pure product was obtained as an orange shiny solid after purification by column chromatography.

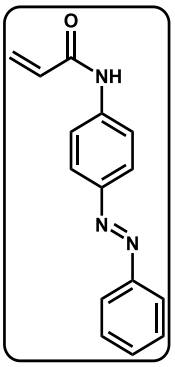

(*E*)-*N*-(4-(phenyldiazenyl)phenyl)acrylamide (6): Orange solid, mp = 169-172 ^oC, 60% yield. ^1H NMR (400 MHz, $CDCl_3$): δ (ppm) 7.96-7.88 (m, 4H), 7.77 (d, *J* = 8.4 Hz, 2H), 7.53-7.44 (m, 4H), 6.50 (dd, *J* = 16.8, 0.8 Hz, 1H), 6.29 (dd, *J* = 16.8, 10.4 Hz, 1H), 5.84 (dd, *J* = 10.4, 0.8 Hz, 1H) ; ^{13}C NMR (100 MHz, $CDCl_3$): δ (ppm) 164.1, 152.7, 149.2, 140.5, 131.1, 130.9, 129.2, 128.6, 124.1, 122.9, 120.3; FT-IR (KBr): 3278, 1666, 1601, 1578, 1407, 1239, 838 cm^{-1}; HRMS (ESI): *m/z* calcd. for $C_{15}H_{13}N_3O[M+H]^+$: 252.1178; found : 252.1128.

Synthesis of *N*-(4-((*E*)-phenyldiazenyl)phenyl)cinnamamide (M2)

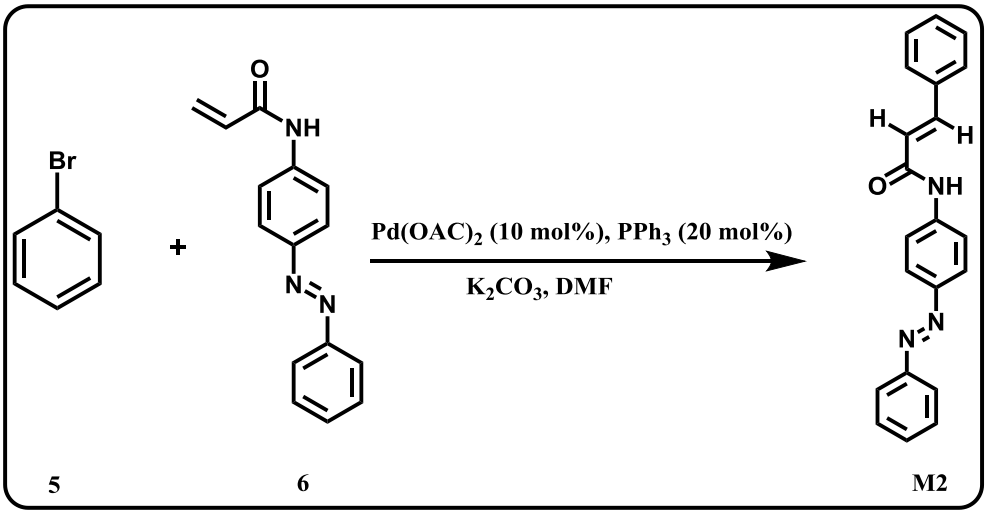

In a round bottom flask, under argon atmosphere, DMF was added and degassed. To this, $Pd(OAc)_2$ (10 mol%) and PPh_3 (20 mol%) were added. Then, the mixture was purged with argon again. With continuous purging, bromobenzene (**5**) (0.1 g, 0.6 mmol) was added and the reaction was allowed to stir at RT for 10 minutes. Then, K_2CO_3 (0.3 g, 2.2 mmol) was added followed by the **6** (0.3 g, 1.3 mmol) and the reaction was refluxed at 100 ^oC. The reaction was monitored by TLC. After completion, the reaction mixture was passed through a celite bed, and washed with ethyl acetate. The combined organic washings were further subjected to a brine wash, dried on anhydrous sodium sulphate, and evaporated to dryness and was subjected to purification by column chromatography.

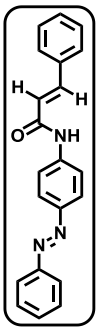

***N*-(4-((*E*)-phenyldiazenyl)phenyl)cinnamamide** (**M2**): Dark orange crystalline solid, mp= 190-193 °C, 50% yield. ^1H NMR (400 MHz, $CDCl_3$): δ (ppm) 7.97 (d, J = 8.8 Hz, 2H), 7.91 (d, J = 7.2 Hz, 2H), 7.83-7.79 (m, 3H), 7.58-7.40 (m, 9H), 6.58 (d, J = 15.2 Hz, 1H); ^{13}C NMR (100 MHz, $[D_6]$DMSO): δ (ppm) 164.1, 152.2, 147.8, 142.5, 141.2, 134.7, 131.3, 130.2, 129.6, 129.2, 128.0, 123.9, 122.5, 121.9, 119.7; FT-IR (KBr): 2927, 1666, 1619, 1535, 1243 cm^{-1}; HRMS (ESI): *m/z* calcd. for $C_{21}H_{17}N_3O[M+H]^+$: 328.1478; found: 328.1456.

Synthesis of (2*E*,2'*E*,2''*E*)-3,3',3''-(benzene-1,3,5-triyl)tris(*N*-(4-((*E*)-phenyldiazenyl)phenyl)acrylamide) (T2)

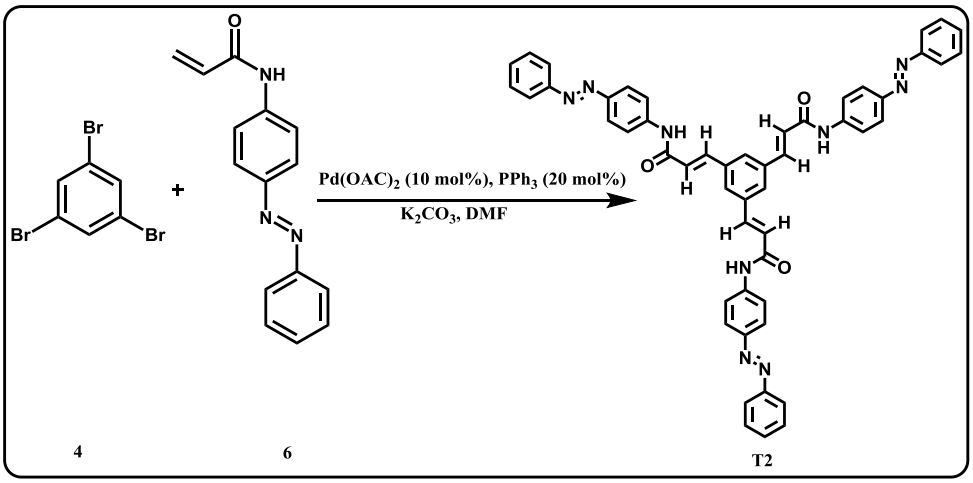

In a round bottom flask, under an argon atmosphere, dry DMF (8 ml) was added and degassed. To this, $Pd(OAc)_2$ (10 mol%) and PPh_3 (20 mol%) were added. Then, the mixture was purged with argon, and 1,3,5-tribromobenzene **4** (0.2 g, 0.6 mmol) was added. The reaction was allowed to stir at rt for 10 minutes under continuous purging of argon. Afterwards, K_2CO_3 (0.3 g, 2.1 mmol) was added followed by **6** (0.8 g, 3.2 mmol) and the reaction mixture was heated to 110 ^oC. The reaction was monitored by TLC. After completion, the reaction mixture was passed through a celite bed and washed with ethyl acetate. The combined organic washings were further subjected to a brine wash, dried on anhydrous sodium sulphate, and evaporated to dryness and was subjected to purification by column chromatography.

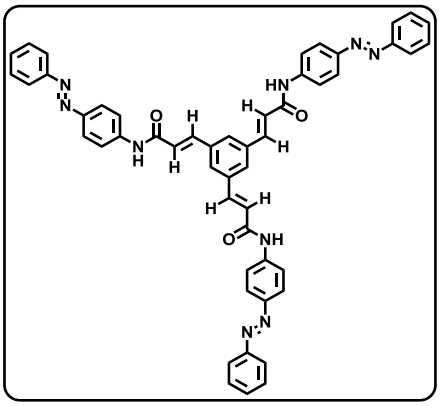

(2*E*,2'*E*,2''*E*)-3,3',3''-(benzene-1,3,5-triyl)tris(*N*-(4-((*E*) phenyldiazenyl)phenyl)acrylamide) (T2): Orange solid, mp = 250-252 °C, 60% yield. ^1H NMR (400 MHz, [D_6]DMSO): δ (ppm) 10.70 (s, 3H), 7.99-7.93 (m, 15H), 7.87 (d, J = 7.2 Hz, 6H), 7.74 (d, J = 15.6 Hz, 3H), 7.61-7.52 (m, 9H), 7.02 (d, J = 15.6 Hz, 3H); ^{13}C NMR (100 MHz, [D_6]DMSO): δ (ppm) 163.7, 152.1, 148.6, 147.8, 142.3, 139.8, 136.2, 129.5, 129.1, 123.9, 122.4, 119.7, 119.6; FT-IR (neat): 3445, 3234, 2957, 1614, 1566, 1486, 1254, 1091, 1023 cm^{-1}; HRMS (ESI): *m/z* calcd for $C_{51}H_{39}N_9O_3[M+H]^+$: 826.3254; found : 826.3271.

3.9 References

[1] Y.-J. Choi, D.-Y. Kim, M. Park, W.-J. Yoon, Y. Lee, J.-K. Hwang, Y.-W. Chiang, S.-W. Kuo, C-H. Hsu, K.-U. Jeong, *ACS Appl. Mater. Interfaces* **2016**, *8*, 9490–9498; b) S. Lee, S. Oh, J. Lee, Y. Malpani, Y.-S. Jung, B. Kang, J. Y. Lee, K. Ozasa, T. Isoshima, S. Y. Lee, M. Hara, D. Hashizume, J. M. Kim, *Langmuir* **2013**, *29*, 5869–5877; c) Y. Huang, D.-H. Kim, *Nanoscale* **2012**, *4*, 6312–6317; d) I. Abe, M. Hara, T. Seki, S. J. Cho, M. Shimizu, K. Matsuura, H-K. Cheong, J. Y. Kim, J. Oh, J. Jung, M. Han, *J. Mater. Chem. C* **2019**, *7*, 2276–2282.

[2] a) V. K. Praveen, C. Ranjith, E. Bandini, A. Ajayaghosh, N. Armaroli *Chem. Soc. Rev.* **2014**, *43*, 4222–4242; b) A. Sandeep, V. K. Praveen, D. S. Shankar Rao, S. K. Prasad, A. Ajayaghosh, *ACS Omega* **2018**, *3*, 4392–4399; c) J. De, S. P. Gupta, S. S. Swayamprabha, D. K. Dubey, I. Bala, I. Sarkar, G. Dey, J.-H. Jou, S. Ghosh, S. K. Pal, *J. Phys. Chem. C* **2018**, *122*, 23659–23674; d) D. W. Chang, L. Dai, *J. Mater. Chem.* **2007**, *17*, 364–371.

[3] a) C. Probst, C. Meichner, H. Audorff, R. Walker, K. Kreger, L. Kador, H.-W. Schmidt, *J. Polym. Sci. Part B* **2016**, *54*, 2110–2117; b) X. Liu, X.-S. Luo, H.-L. Deng, W. Fan, S. Wang, C. Yang, X.-Y. Sun, S.-L. Chen, M.-H. Huang, *Chem. Mater.* **2019**, *31*, 5421–5430; c) X. Cheng, T. Miao, L. Yin, Y. Ji, Y. Li, Z. Zhang, W. Zhang, X. Zhu, *Angew. Chem. Int. Ed.* **2020**, *59*, 9669 –9677; *Angew.Chem.* **2020**, *132*, 9756–9764; d) T. Miao, X. Cheng, H. Ma, Z. He, Z. Zhang, N. Zhou, W. Zhang, X. Zhu, *Angew. Chem. Int. Ed.* **2021**, *60*, 18566 –18571; *Angew. Chem.* **2021**, *133*, 18714–18719; e) L. Yin, M. Liu, H. Ma, X. Cheng, T. Miao, W. Zhang, X. Zhu, *Sci. China Chem.* **2021**, *64*, 2105-2110.

[4] a) M. Pfletscher, C. Wölper, J. S. Gutmann, M. Mezger, M. Giese, *Chem. Commun.* **2016**, *52*, 8549–8552; b) S. Devi, I. Bala, S. P. Gupta, P. Kumar, S. K. Pal, S. Venkataramani, *Org. Biomol. Chem.* **2019**, *17*, 1947–1954.

[5] a) K. Kreger, P. Wolfer, H. Audorff, L. Kador, N. Stingelin-Stutzmann, P. Smith, H.-W. Schmidt, *J. Am. Chem. Soc.* **2010**, *132*, 509–516; b) P. Wolfer, H. Audorff, K. Kreger, L. Kador, H.-W. Schmidt, N. Stingelinae, P. Smith, *J. Mater. Chem.* **2011**, *21*, 4339–4345; c) L. M. Goldenberg, L. Kulikovsky, O. Kulikovska, J. Tomczyk, J. Stumpe, *Langmuir* **2010**, *26*, 2214–2217.

[6] J. Lee, S. Oh, J. Pyo, J.-M. Kim, J. H. Je, *Nanoscale* **2015**, *7*, 6457– 6461.

[7] S. Devi, A. K. Gaur, D. Gupta, M. Saraswat, S. Venkataramani, *Chem PhotoChem* **2018**, *2*, 806–810.

[8] S. Grewal, S. Roy, H. Kumar, M. Saraswat, N. K. Bari , S. Sinha, S. Venkataramani, *Catal. Sci. Technol.* **2020**, *10*, 7027–7033.

[9] a) A. Galanti, V. Diez-Cabanes, J. Santoro, M. Valášek, A. Minoia, M. Mayor, J. Cornil, P. Samorì, *J. Am. Chem. Soc.* **2018**, *140*, 16062–16070; b) F. Cisnetti, R. Ballardini, A. Credi, M. T. Gandolfi, S. Masiero, F. Negri, S. Pieraccini, G. P. Spada, *Chem. Eur. J.* **2004**, *10*, 2011–2021; c) D. Gupta, A. K. Gaur, P. Kumar, H. Kumar, A. Mahadevan, S. Devi , S. Roy, S. Venkataramani, *Chem. Eur. J.* **2021**, *27*, 3463–3472.

[10] a) D. Bléger, S. Hecht, *Angew. Chem. Int. Ed.* **2015**, *54*, 11338–11349; *Angew.Chem* .**2015**, *127*, 11494–11506; b) M. Dong, A. Babalhavaeji, C. V. Collins, K. Jarrah, O. Sadovski, Q. Dai, G. A. Woolley, *J. Am. Chem. Soc.* **2017**, *139*, 13483–13486; c) S. Samanta, T. M. McCormick, S. K. Schmidt, D. S. Seferos, G. A. Woolley, *Chem. Commun.* **2013**, *49*, 10314–10316; d) O. Sadovski, A. A. Beharry, F. Zhang, G. A. Woolley, *Angew. Chem. Int. Ed.* **2009**, *48*, 1484–1486; e) C. Poloni, W. Szymański, L. Hou, W. R. Browne, B. L. Feringa, *Chem. Eur. J.* **2014**, *20*, 946–951; f) Y. Ouyang, Z. Yuan, J. Wang, *New J. Chem.*, **2018**, *42*, 5660–5663; g) S.-W. Oh, S.-M. Nam, S.-H. Kim, T.-H. Yoon, W. S. Kim, *ACS Appl. Mater. Interfaces* **2021**, *13*, 5028–5033.

[11] a) L. Muñoz-Rugeles, D. Gallardo-Rosas, J. Durán-Hernández, R. López-Arteaga, R. A. Toscano, N. Esturau-Escofet, J. G. López-Cortés, J. Peón, M. C. Ortega-Alfaro, *ChemPhotoChem* **2019**, *3*, 1–12; b) J. A. Balam-Villarreal, B. J. López-Mayorga, D. Gallardo-Rosas, R. A. Toscano, M. P. Carreón-Castro, V. A. Basiuk, F. Cortés-Guzmán, J. G. López-Cortés, M. C. Ortega-Alfaro, *Org. Biomol. Chem.* **2020**, *18*, 1657–1670; c) E. Villatoro, L. Muñoz-Rugeles, J. Durán-Hernández, B. Salcido-Santacruz, N. Esturau-Escofet, J. G. López-Cortés, M. C. Ortega-Alfaro, J. Peón, *Chem. Commun.* **2021**, *57*, 3123–3126; d) S. Özkınalı, M. Gür, N. Şener, S. Alkın, M. S. Çavuş, *J. Mol. Struct.* **2018**, *1174*, 74–83; e) E. Rezaei-Seresht, E. Mireskandari, M. Kheirabadi, H. Cheshomi, H. Rezaei-Seresht, L. S. Aldaghi, *Chem. Pap.* **2017**, *71*, 1463–1469; f) A. C. Razus, L. Birzan, M. Cristea, V. Tecuceanu, C. Enache, *Dye. Pigment.* **2012**, *92*, 1166–1176; g) Z. Yan, B. Sun, C. Guo, Y. Li, *J. Mater. Chem. C* **2014**, *2*, 7096–7103; h) B. A. Trofimov, E. Y. Schmidt, A. I. Mikhaleva, A. M. Vasil'tsov, A. B. Zaitsev, N. S. Smolyanina, E. Y. Senotrusova, A. V. Afonin, I. A. Ushakov, K. B. Petrushenko, O. N. Kazheva, O. A. Dyachenko, V. V. Smirnov, A. F. Schmidt, M. V. Markova, L. V. Morozova, *Eur. J. Org. Chem.* **2006**, 4021–4033.

[12] The PSS composition for the forward reverse isomerization steps have been estimated using the non-overlapping protons of the native and photoisomers in **T1** and **T2**. In this regard, we utilized the amide N-H proton signals for the quantification.

[13] I. Bala, H. Singh, V. R. Battula, S. P. Gupta, J. De, S. Kumar, K. Kailasam, S. K. Pal, *Chem. Eur. J.* **2017**, *23*, 14718–14722.

[14] Y. Hashimoto, T. Sato, R. Goto, Y. Nagao, M. Mitsuishi, S. Nagano, J. Matsui, *RSC adv.* **2017**, *7*, 6631–6635.

[15] S. N. Magonov, N. A. Yerina, G. Ungar, D. H. Reneker, D. A. Ivanov, *Macromolecules* **2003**, *36*, 5637–5649.

[16] S. N. Magonov, N. A. Yerina, *Langmuir* **2003**, *19*, 500–504.

[17] A. Temiryazev, A. Frolov, M. Temiryazeva, *Carbon* **2019**, *143*, 30–37.

[18] R. Zhang, W. S. Fall, K. W. Hall, G. A. Gehring, X. Zeng, G. Ungar, *Nat. commun.* **2021**, *12*, 1–7

[19] J. G. Murphy, J. G. Raybin, S. J. Sibener, *J Polym Sci.* **2021**, 1–17.

Appendix 3A

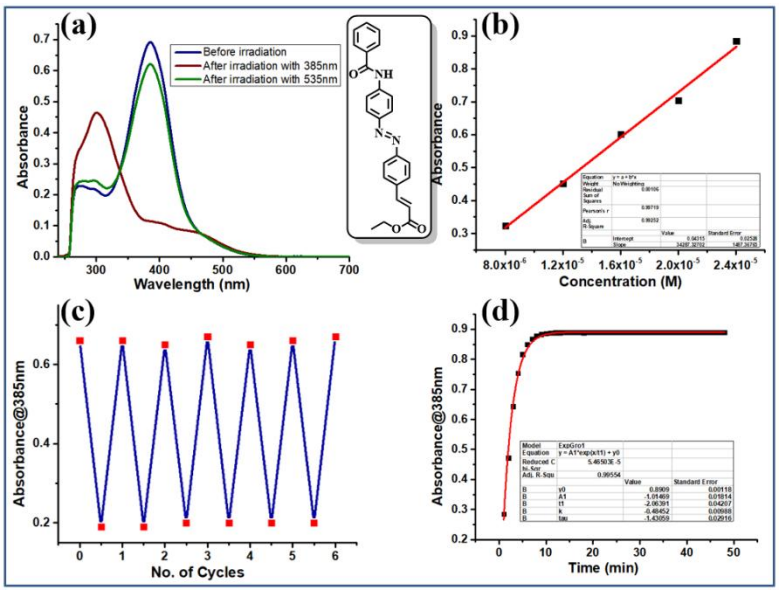

Figure 3A.1 UV-Vis spectroscopic data of **M1**: (a) Photoswitching studies performed in DMSO (26.0 μM); (b) Estimation of the molar absorption coefficient for π–π* absorption maxima; (c) Photoswitching stability test upto five cycles in DMSO (forward isomerization step: 385 nm; reverse isomerization step: 535 nm) and (d) first order thermal reverse isomerization kinetics plot and exponential fit (26.0 μM solution at 60 ^{o}C).

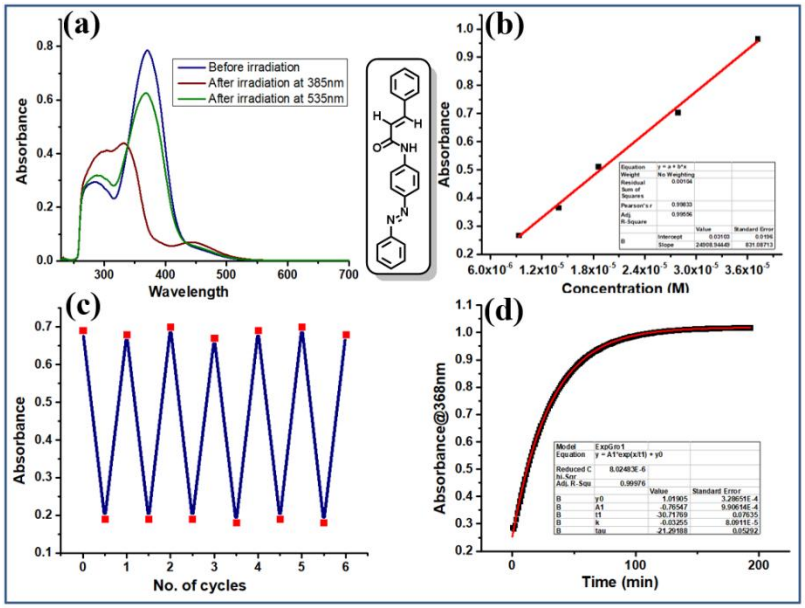

Figure 3A.2 UV-Vis spectroscopic data of **M2**: (a) Photoswitching studies performed in DMSO (44.0 μM); (b) Estimation of the molar absorption coefficient for π–π* absorption maxima; (c) Photoswitching stability test upto five cycles in DMSO (forward isomerization step: 385 nm; reverse isomerization step: 535 nm) and (d) First order thermal reverse isomerization kinetics plot and exponential fit (44.0 μM solution at 60 ^{o}C).

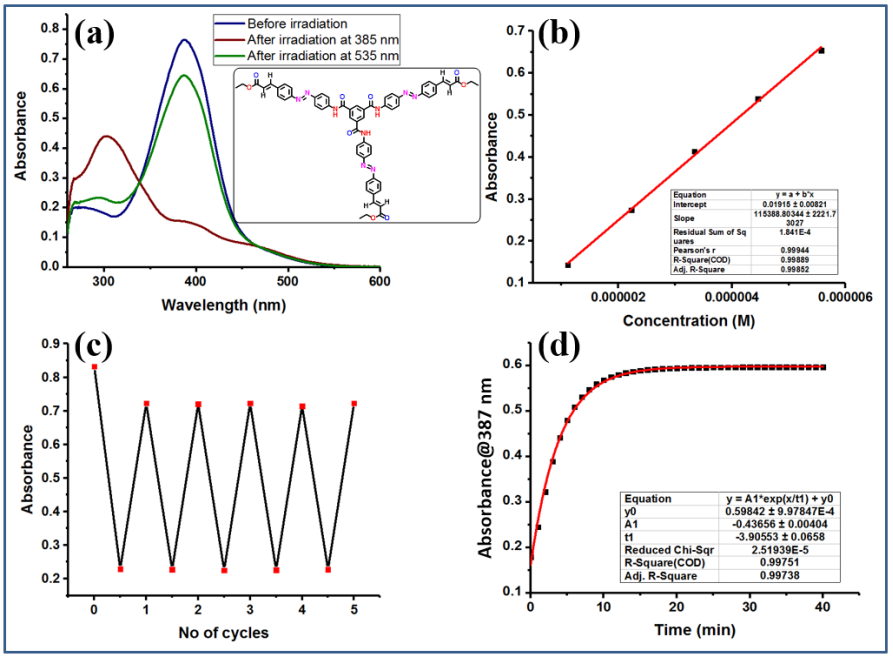

Figure 3A.3 UV-Vis spectroscopic data of **T1**: (a) Photoswitching studies performed in DMSO (5.1 μM); (b) Estimation of the molar absorption coefficient for π–π* absorption maxima; (c) Photoswitching stability test upto five cycles in DMSO (forward isomerization step: 385 nm; reverse isomerization step: 535 nm) and (d) First order thermal reverse isomerization kinetics plot and exponential fit (5.1 μM solution at 60 ^{o}C).

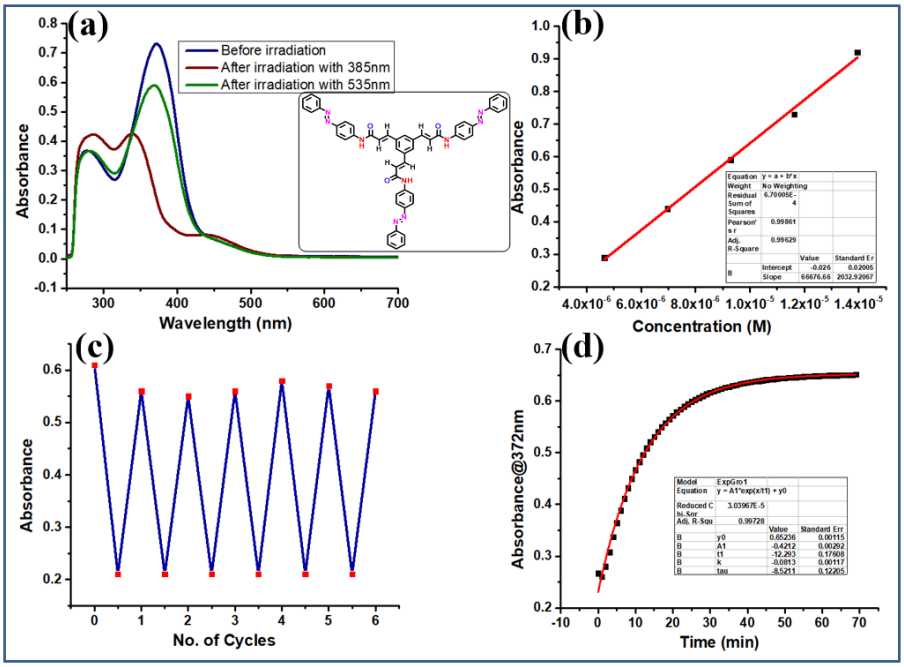

Figure 3A.4 UV-Vis spectroscopic data of **T2**: (a) Photoswitching studies performed in DMSO (9.7 μM); (b) Estimation of the molar absorption coefficient for π–π* absorption maxima; (c) Photoswitching stability test upto five cycles in DMSO (forward isomerization step: 385 nm; reverse isomerization step: 535 nm) and (d) First order thermal reverse isomerization kinetics plot and exponential fit (9.7 μM solution at 70 ^{o}C).

Table 3A.1 Electronic spectroscopic data and analysis of photoswitching properties using UV- Vis spectroscopic data:

S. No.	Target	UV-Vis spectroscopic data[a]			
		Native isomer		After 365 nm irradiation	
		π-π^* ($\lambda_{max}/\varepsilon$)	n–π^* (λ_{max})	π-π^* (λ_{max})	n–π^* (λ_{max})
1.	**M1**	385 (34287±1487)	[b]	300	[b]
2.	**M2**	368 (24909±831)	[b]	332	443
3.	**T1**	387 (115389±2222)	[b]	303	[b]
4.	**T2**	372 (66677±2033)	[b]	339	437

[a]The λ_{max} and ε values are expressed in nm and L.mol^{-1}.cm^{-1}, respectively; [b]Note that n-π^* bands are overlapping.

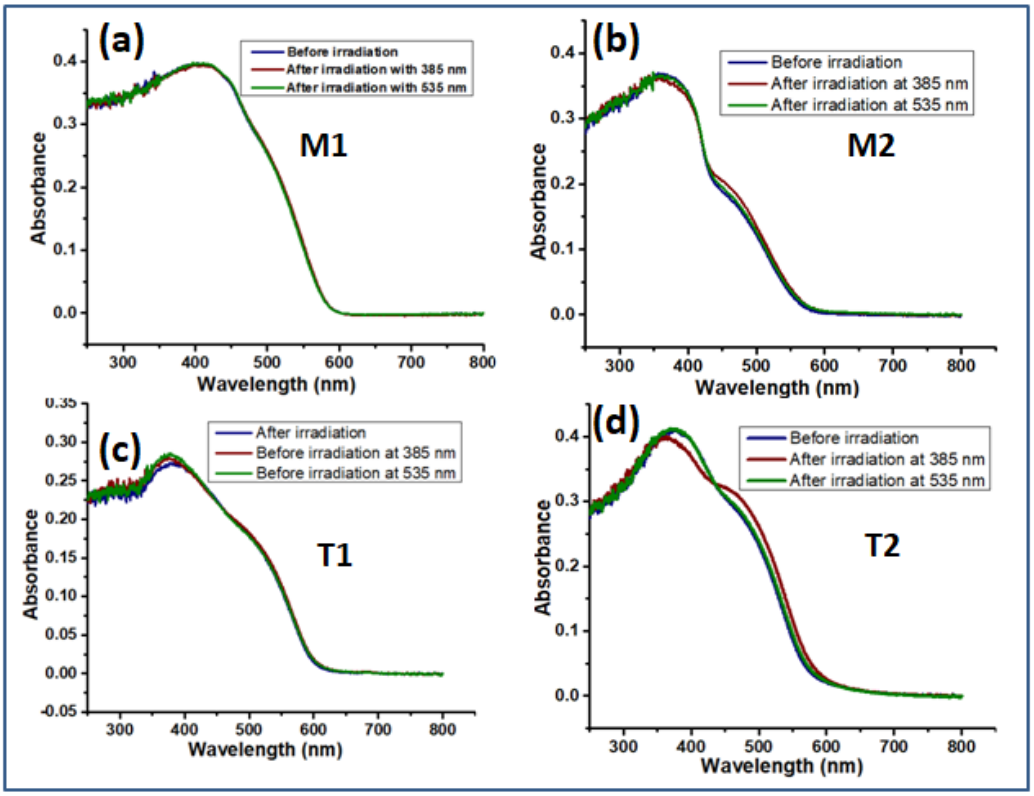

Figure 3A.5 Analysis of photoswitching in solid-state (in KBr medium) using UV-Vis spectroscopy of (a) **M1**; (b) **M2**; (c) **T1**; (d) **T2**.

Appendix 3B
Thermal reverse isomerization kinetics data

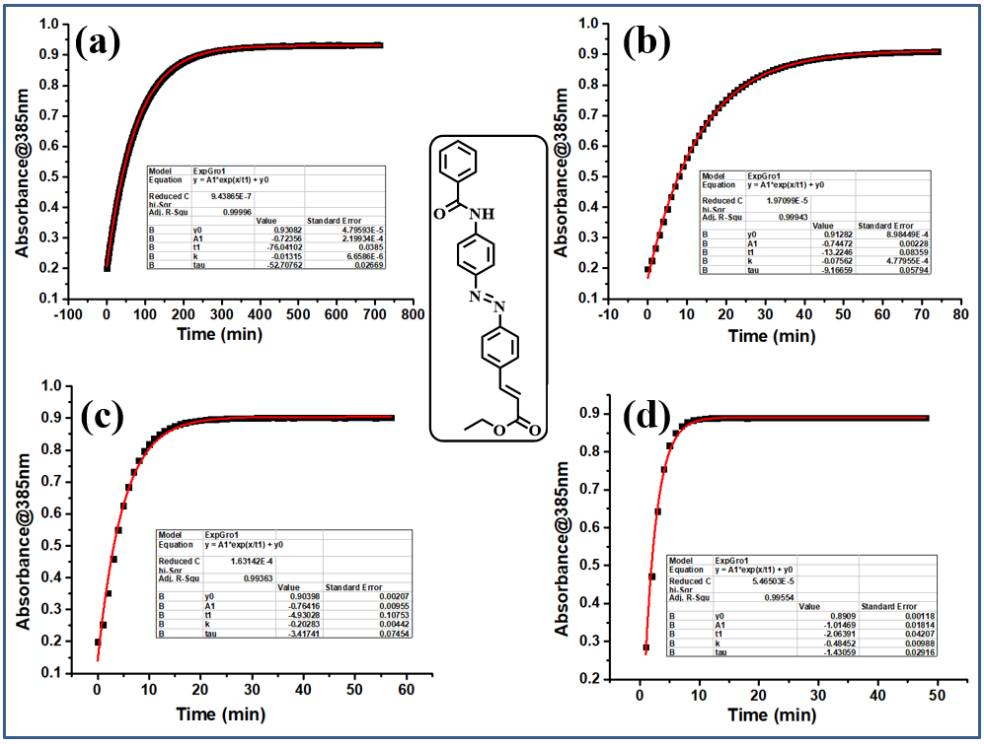

Figure 3B.1 Thermal reverse isomerization kinetics plots of **M1** in DMSO (26.0 μM) at (a) 25 ^{o}C; (b) 40 ^{o}C; (c) 50 ^{o}C and (d) 60 ^{o}C using UV-Vis spectroscopy.

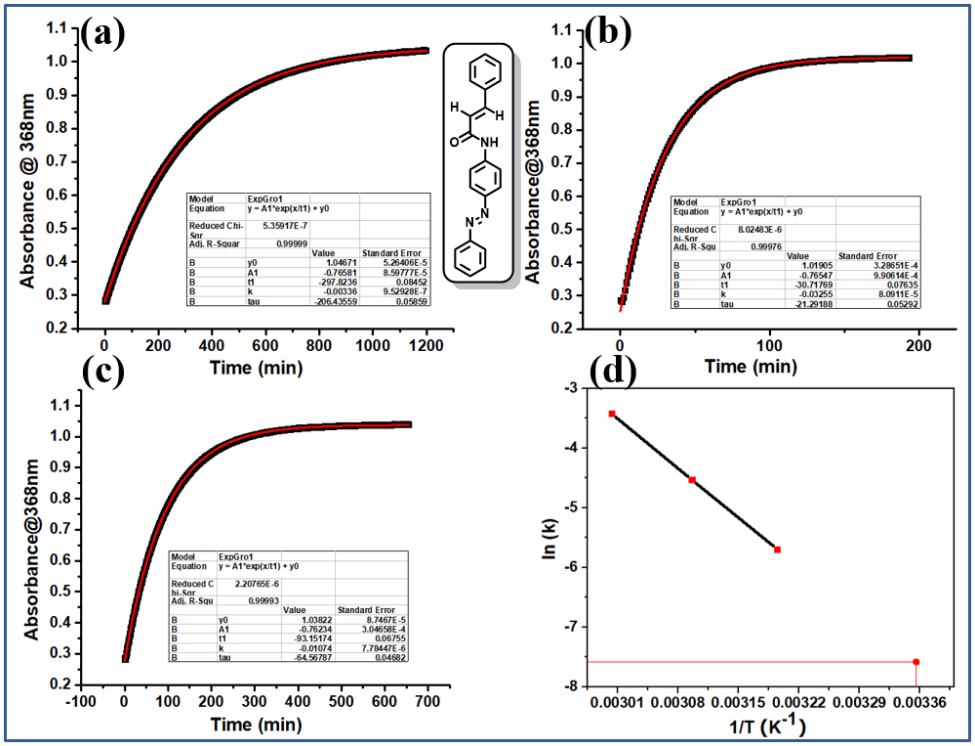

Figure 3B.2 Thermal reverse isomerization kinetics plots of **M2** in DMSO (44.0 μM) at (a) 40 ^{o}C; (b) 50 ^{o}C; (c) 60 ^{o}C and (d) Arrhenius plot with extrapolation to determine the rate constant at 25 ^{o}C.

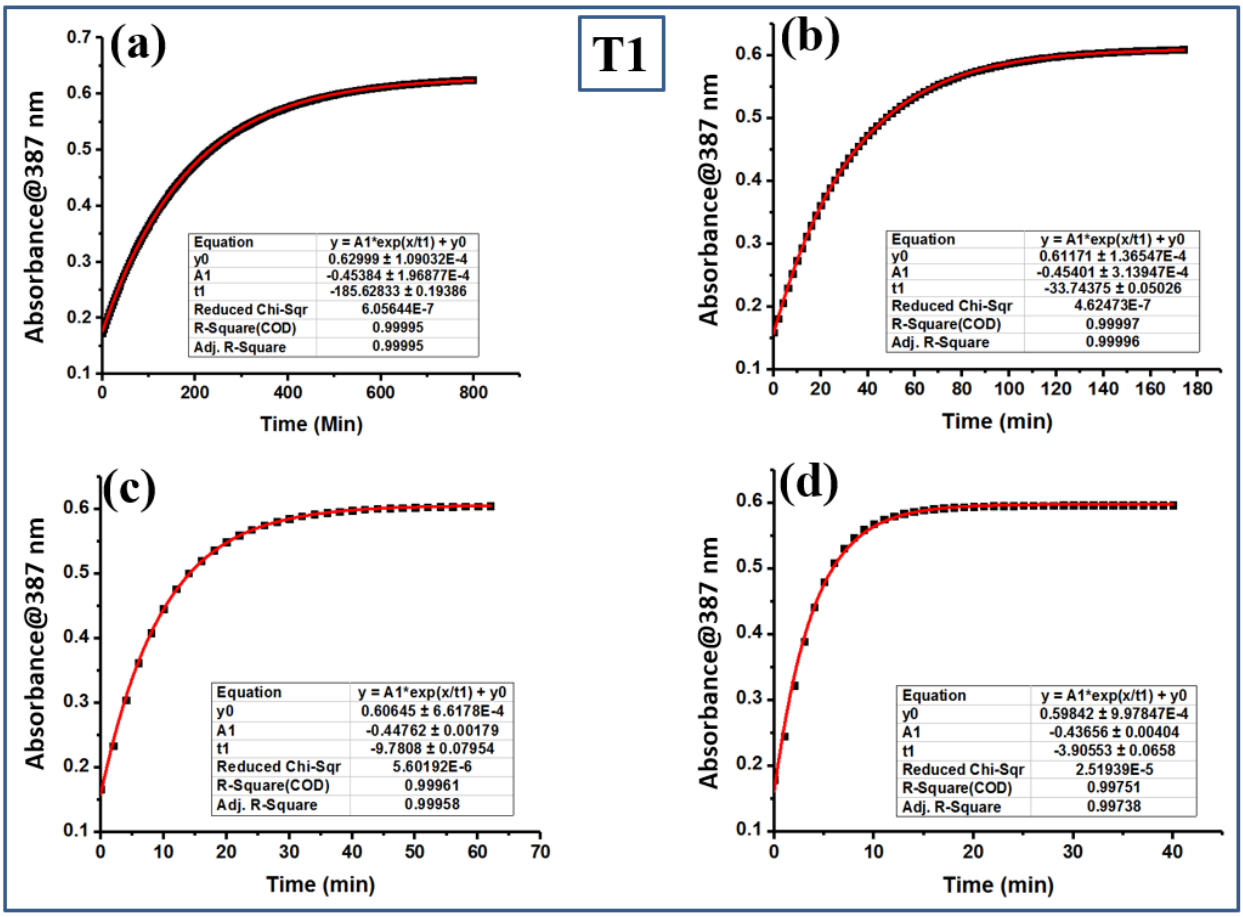

Figure 3B.3 Thermal reverse isomerization kinetics plots of **T1** in DMSO (5.1 μM) at (a) 25 ^{o}C; (b) 40 ^{o}C; (c) 50 ^{o}C and (d) 60 ^{o}C using UV-Vis spectroscopy.

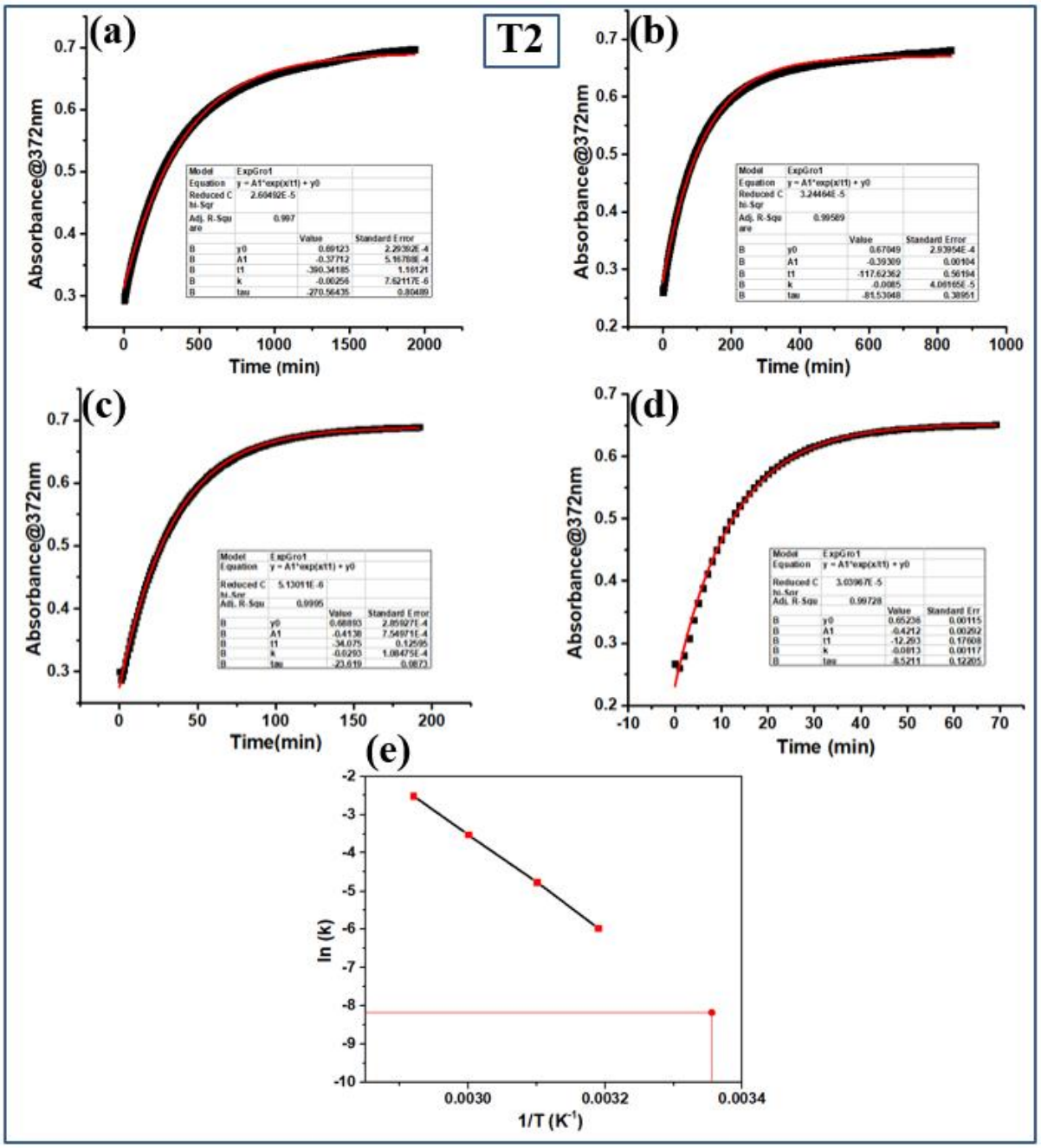

Figure 3B.4 Thermal reverse isomerization kinetics plots of **T2** in DMSO (9.7 μM) at (a) 40 ^{o}C; (b) 50 ^{o}C; (c) 60 ^{o}C, (d) 70 ^{o}C using UV-Vis spectroscopy and (e) Arrhenius plot with extrapolation to determine the rate constant at 25 ^{o}C.

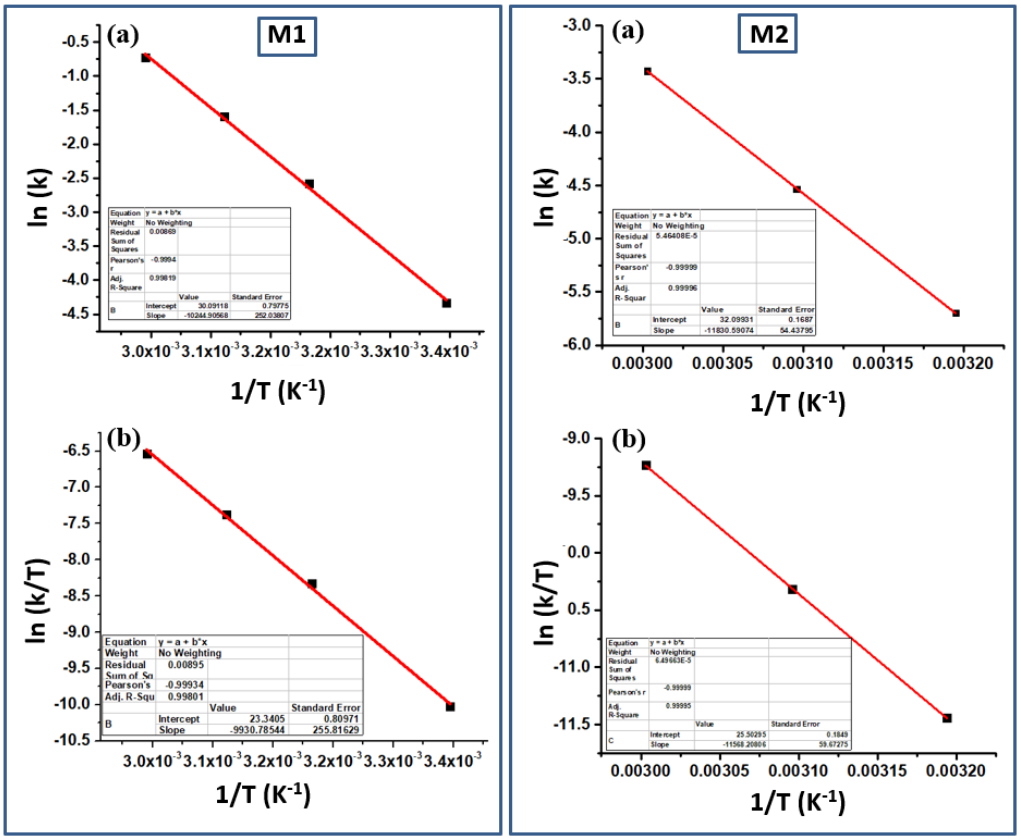

Figure 3B.5 Arrhenius (top) and Eyring (bottom) plots for **M1** and **M2** corresponding to the thermal reverse isomerization.

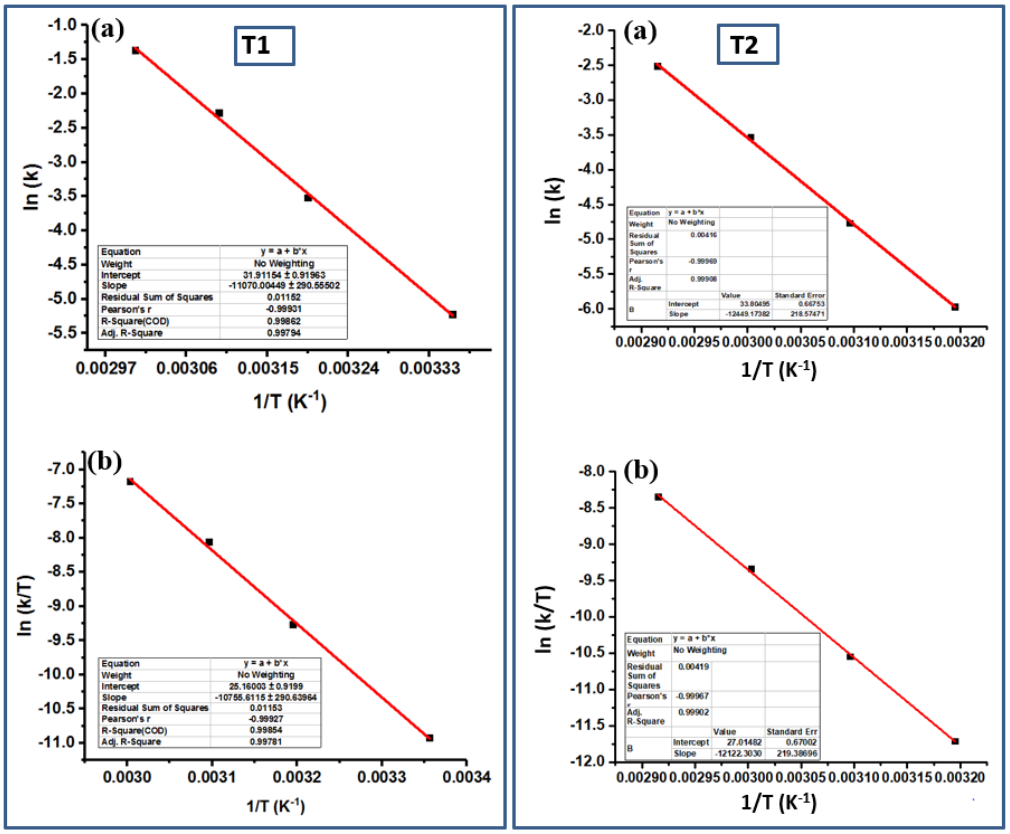

Figure 3B.6 Arrhenius (top) and Eyring (bottom) plots for **T1** and **T2** corresponding to the thermal reverse isomerization.

Table 3B.1 Activation parameters associated with the thermal reverse isomerization step in **T1, T2, M1, M2** (in DMSO).

Compound	E_a	$\Delta G^{\ddagger}$ **(298 K)**	$\Delta H^{\ddagger}$	$\Delta S^{\ddagger}$
T1	92.0 ± 2.4[a]	85.9 ± 3.3[a]	89.4 ± 2.4[a]	11.6 ± 7.6[c]
	22.0 ± 0.6[b]	20.5 ± 0.8[b]	21.4 ± 0.6[b]	2.8 ± 1.8[d]
T2	106.1 ± 1.1[a]	92.7 ± 3.4[a]	100.0 ± 2.5[a]	24.5 ± 7.6[c]
	25.37 ± 0.3[b]	22.2 ± 0.8[b]	23.9 ± 0.6[b]	5.9 ± 1.8[d]
M1	85.2 ± 2.1[a]	83.6 ± 2.9[a]	82.6 ± 2.1[a]	-3.49 ± 6.7[c]
	20.4 ± 0.5[b]	19.9 ± 0.7[b]	19.7 ± 0.5[b]	0.83 ± 1.6[d]
M2	98.4 ± 0.4[a]	91.9 ± 0.7[a]	96.2 ± 0.5[a]	14.5 ± 1.5[c]
	23.5 ± 0.1[b]	21.9 ± 0.2[b]	22.9 ± 0.1[b]	3.5 ± 0.4[d]

[a]kJ mol^{-1}; [b]kcal mol^{-1}; [c]J K^{-1}; [d]cal K^{-1}.

Appendix 3C

Spectral characterization data (^{1}H- and ^{13}C- data)

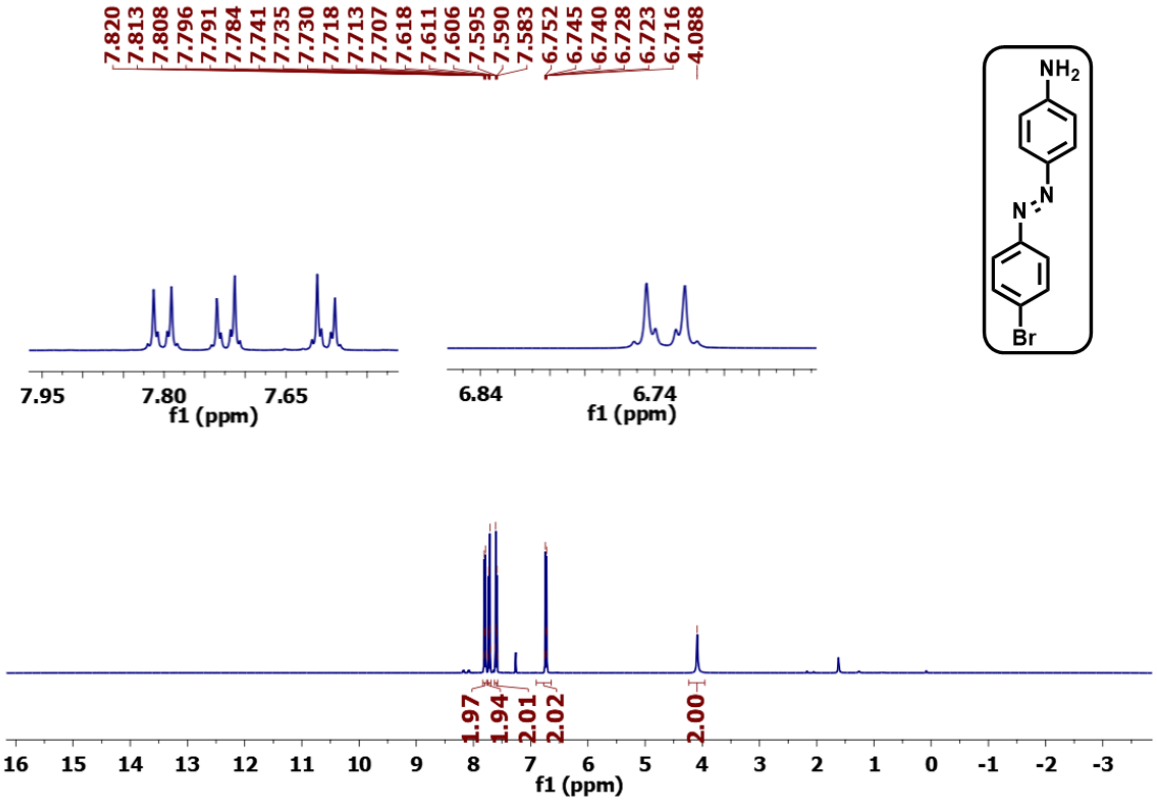

^{1}H-NMR spectrum of (*E*)-4-((4-bromophenyl)diazenyl)aniline (**S5**) in $CDCl_3$.

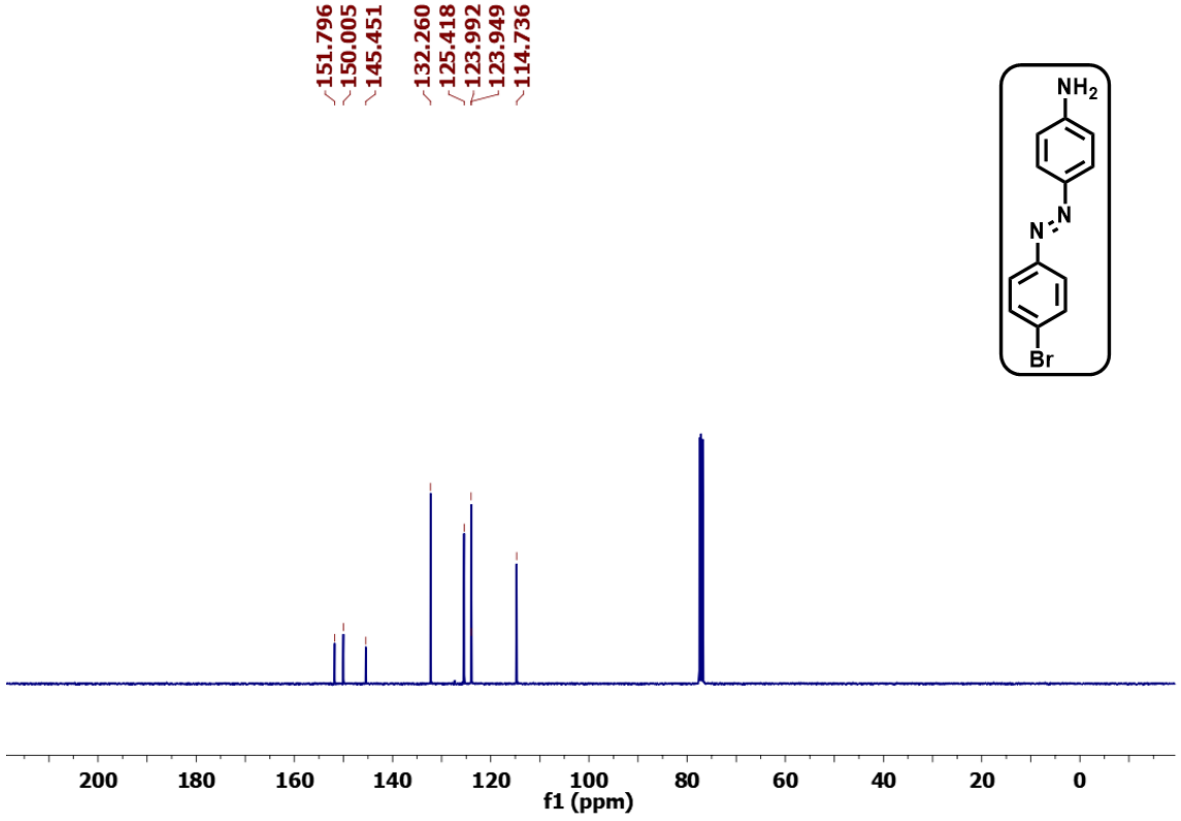

^{13}C-NMR spectrum of (*E*)-4-((4-bromophenyl)diazenyl)aniline (**S5**) in $CDCl_3$.

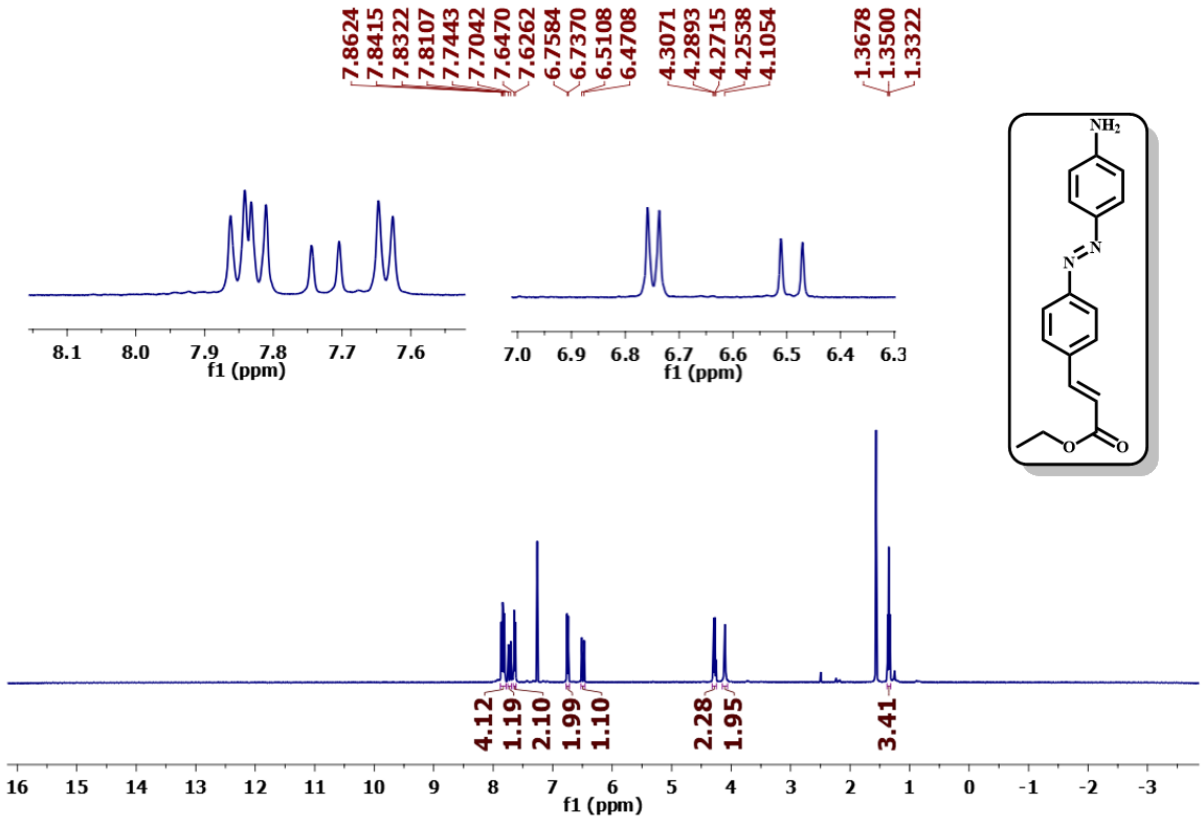

^{1}H-NMR spectrum of Ethyl (*E*)-3-(4-((*E*)-(4-aminophenyl)diazenyl)phenyl)acrylate **(3)** in $CDCl_3$.

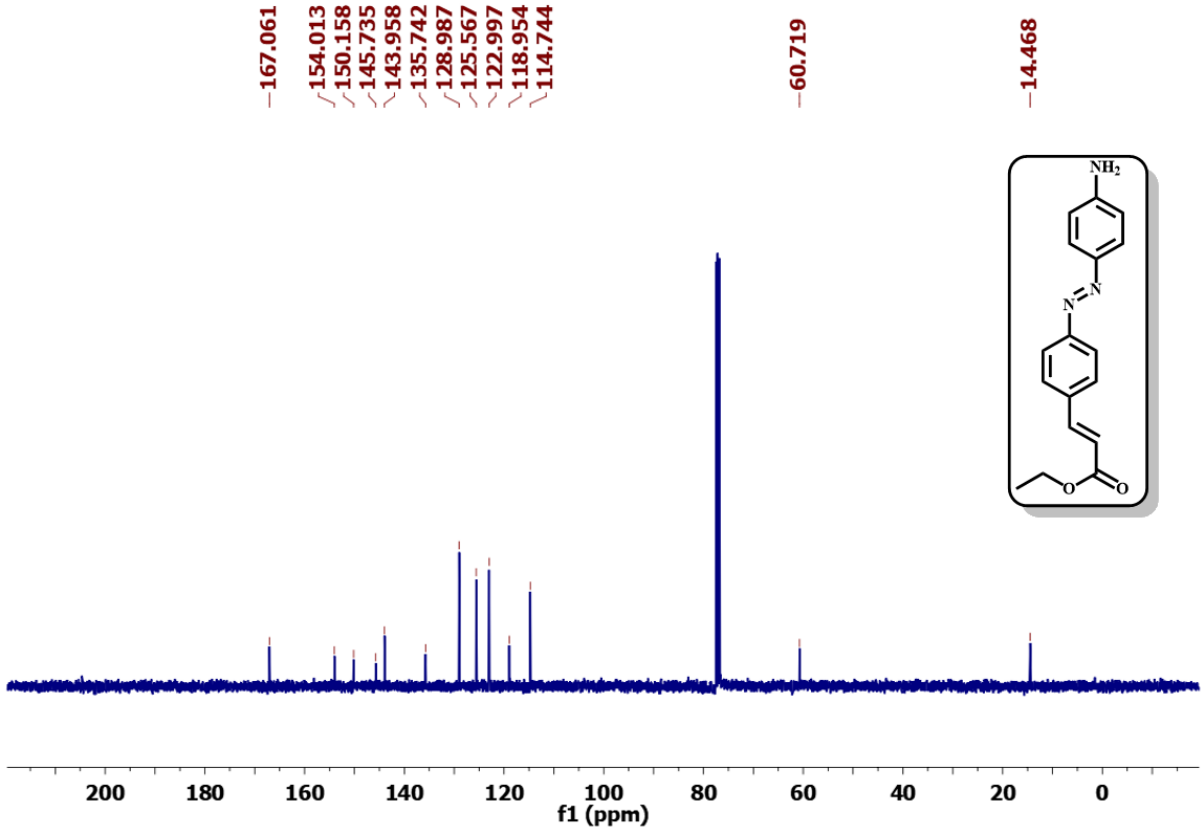

^{13}C-NMR spectrum of Ethyl (*E*)-3-(4-((*E*)-(4-aminophenyl)diazenyl)phenyl)acrylate **(3)** in $CDCl_3$.

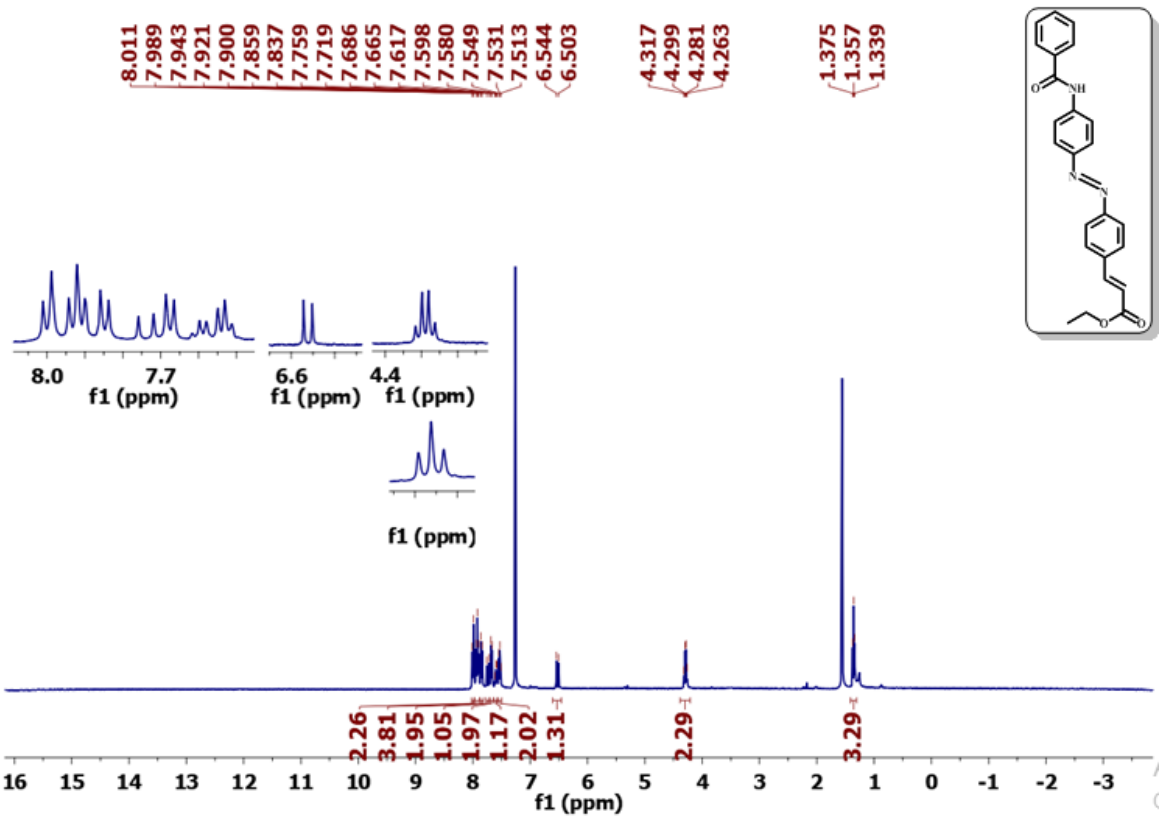

^{1}H-NMR spectrum of Ethyl (*E*)-3-(4-((*E*)-(4-benzamidophenyl)diazenyl)phenyl)acrylate **(M1)** in $CDCl_3$.

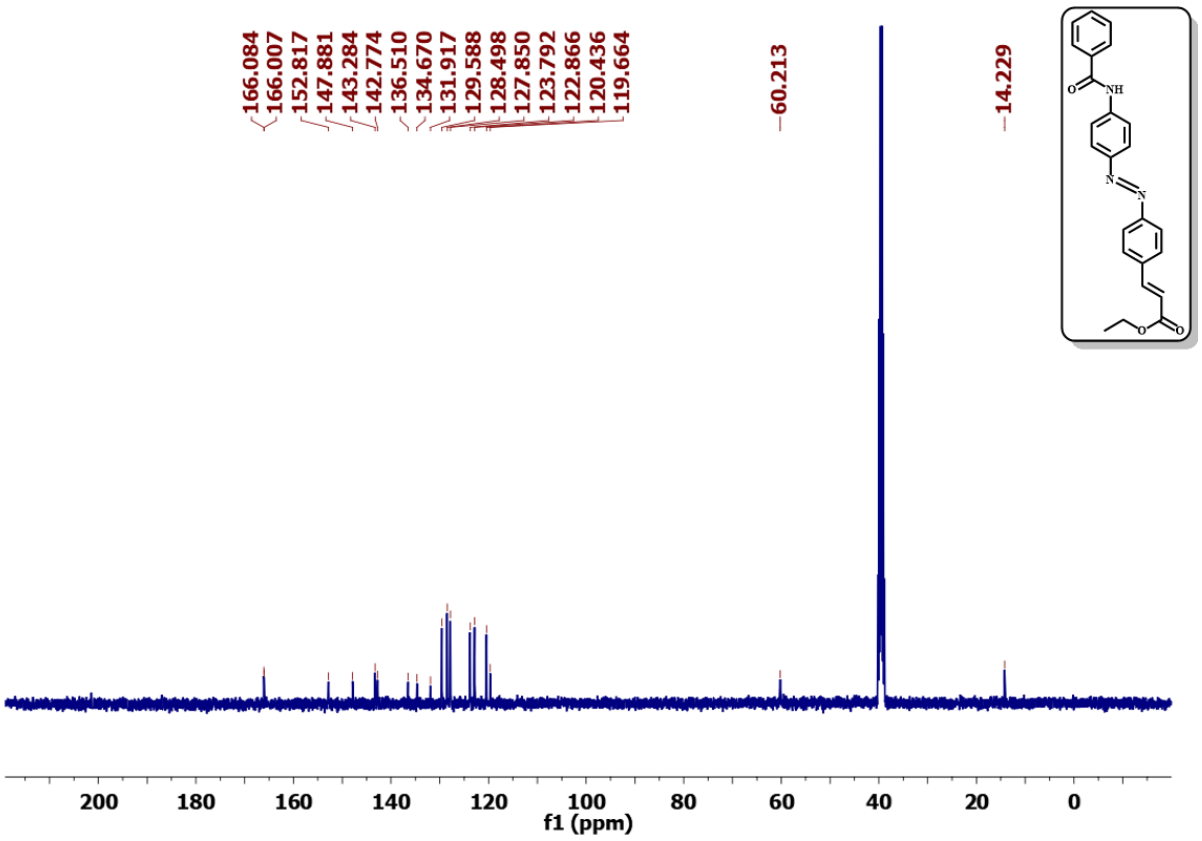

^{13}C-NMR spectrum of Ethyl (*E*)-3-(4-((*E*)-(4-benzamidophenyl)diazenyl)phenyl)acrylate **(M1)** in [D_6]DMSO.

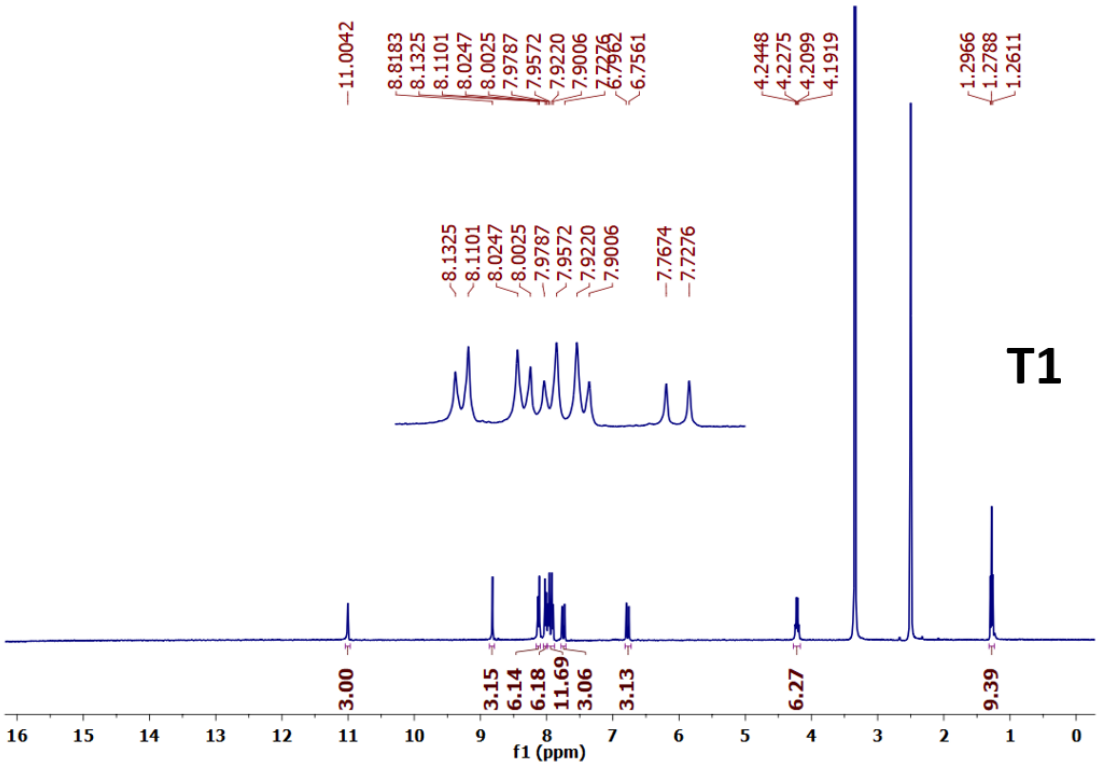

^{1}H-NMR spectrum of Triethyl 3,3',3"-(((1*E*,1'*E*,1"*E*)-(((benzene-1,3,5-tricarbonyl)*tris*(azanediyl))*tris*(benzene-4,1-diyl))*tris*(diazene-2,1-diyl))*tris*(benzene-4,1 diyl))(2*E*,2'*E*,2"*E*)-triacrylate (**T1**) in [D_6]DMSO

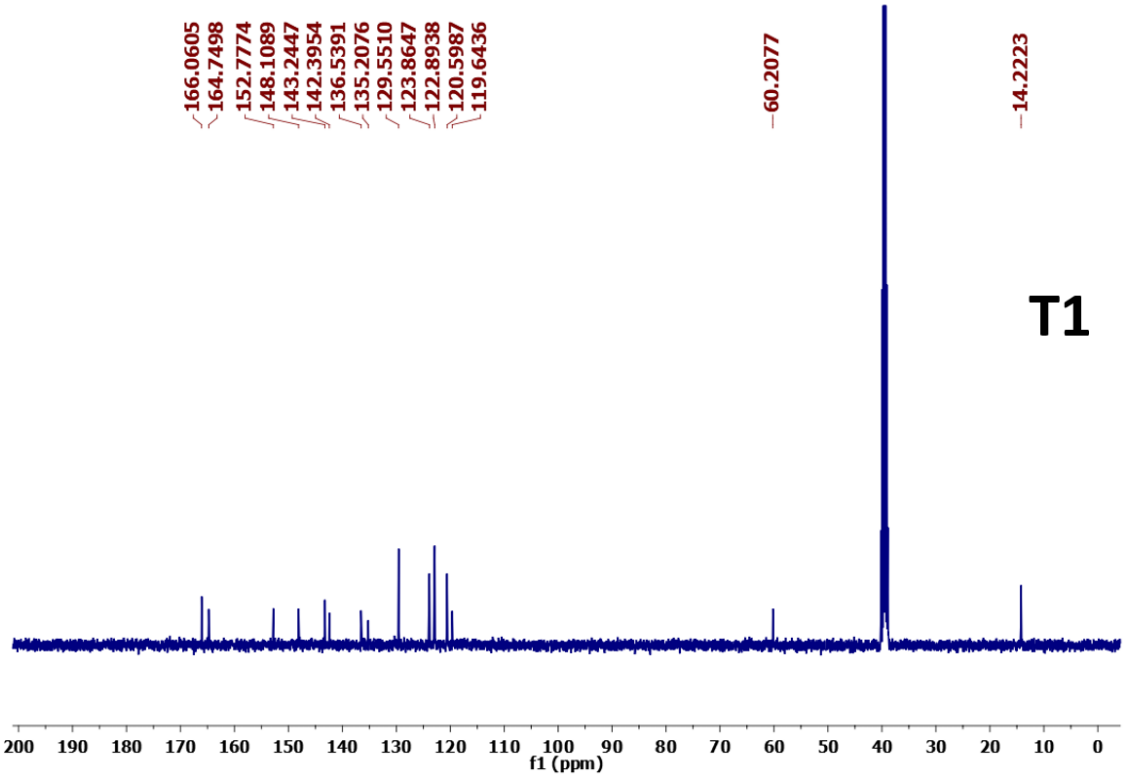

^{13}C-NMR spectrum of Triethyl 3,3',3"-(((1*E*,1'*E*,1"*E*)-(((benzene-1,3,5-tricarbonyl)*tris*(azanediyl))*tris*(benzene-4,1-diyl))*tris*(diazene-2,1-diyl))*tris*(benzene-4,1 diyl))(2*E*,2'*E*,2"*E*)-triacrylate (**T1**) in [D_6]DMSO.

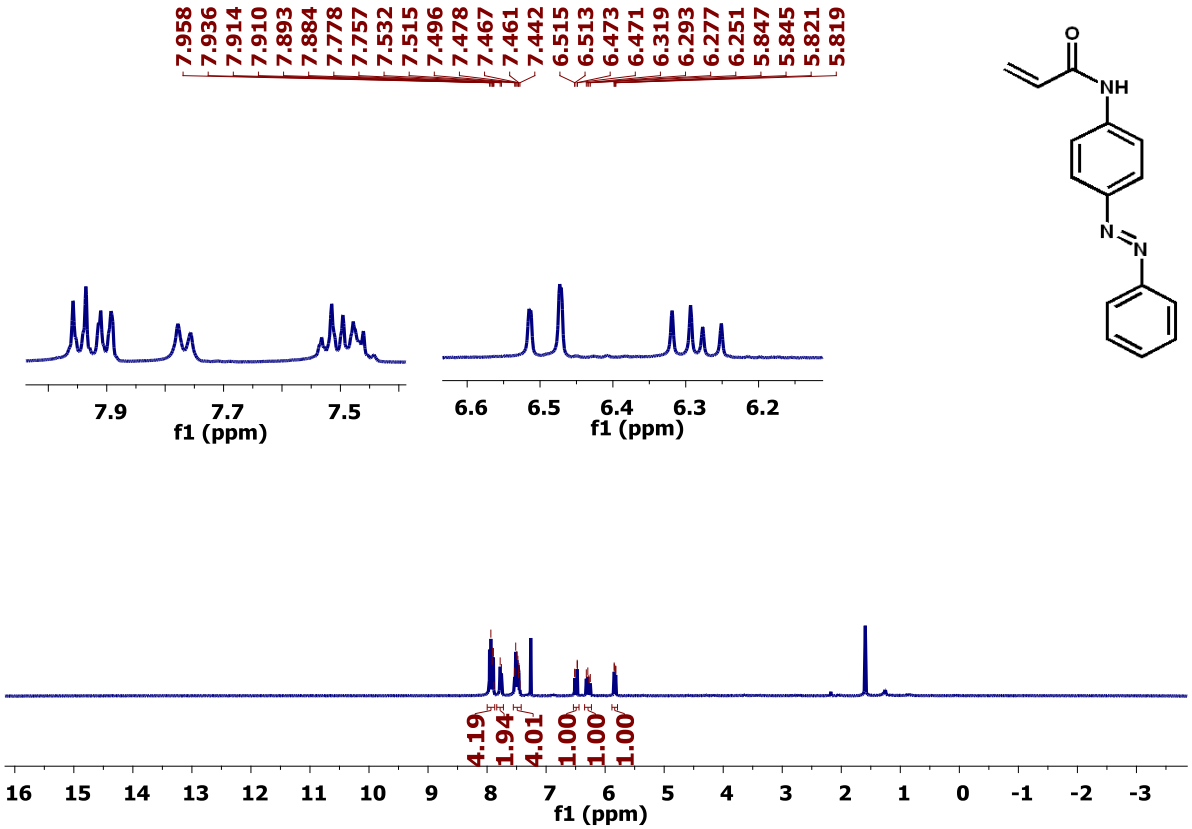

^{1}H-NMR spectrum of (*E*)-*N*-(4-(phenyldiazenyl)phenyl)acrylamide **(6)** in $CDCl_3$.

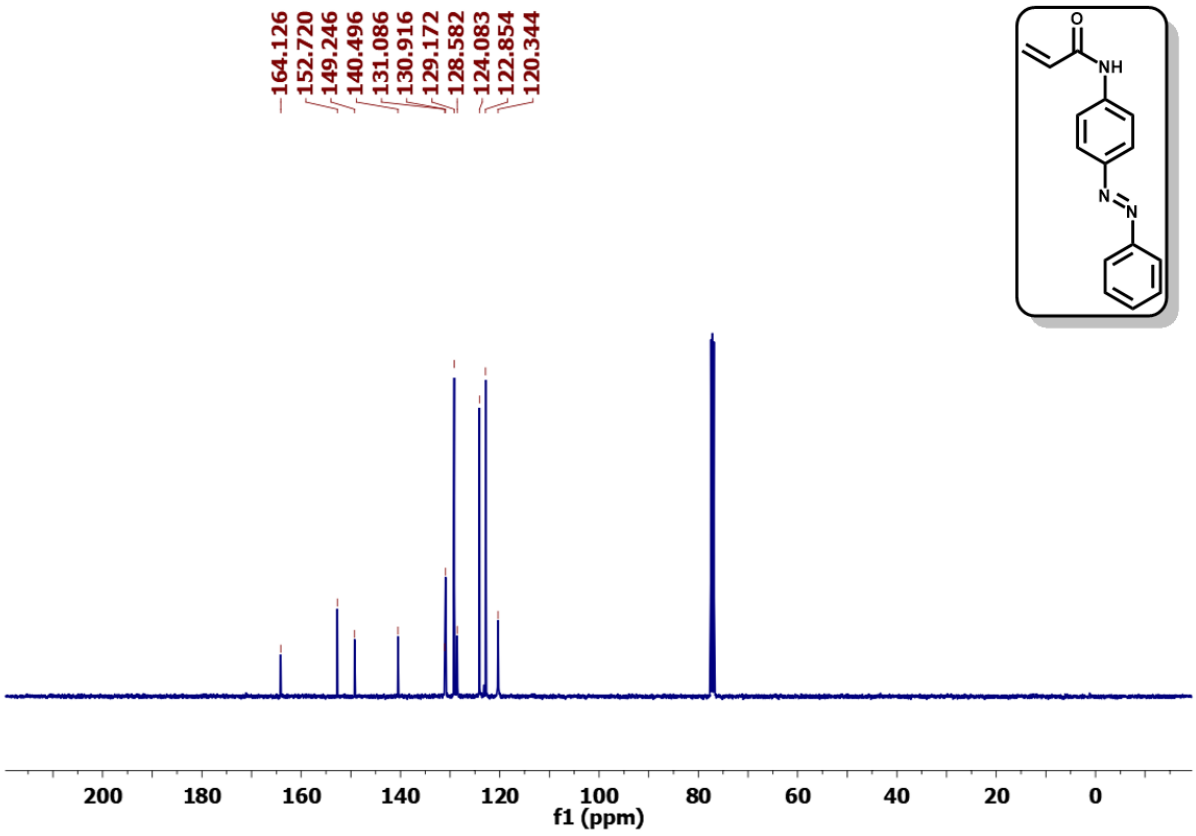

^{13}C-NMR spectrum of (*E*)-*N*-(4-(phenyldiazenyl)phenyl)acrylamide **(6)** in $CDCl_3$.

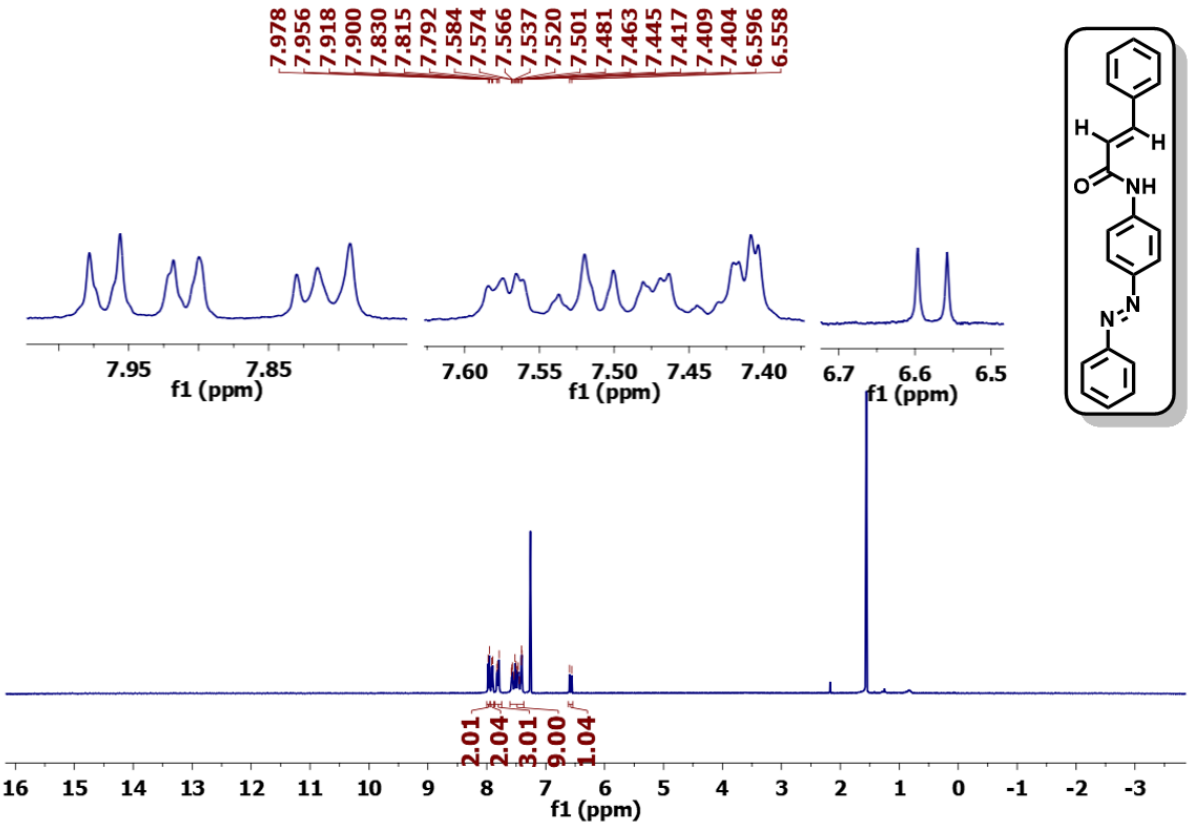

[1]H-NMR spectrum of *N*-(4-((*E*)-phenyldiazenyl)phenyl)cinnamamide (**M2**) in $CDCl_3$.

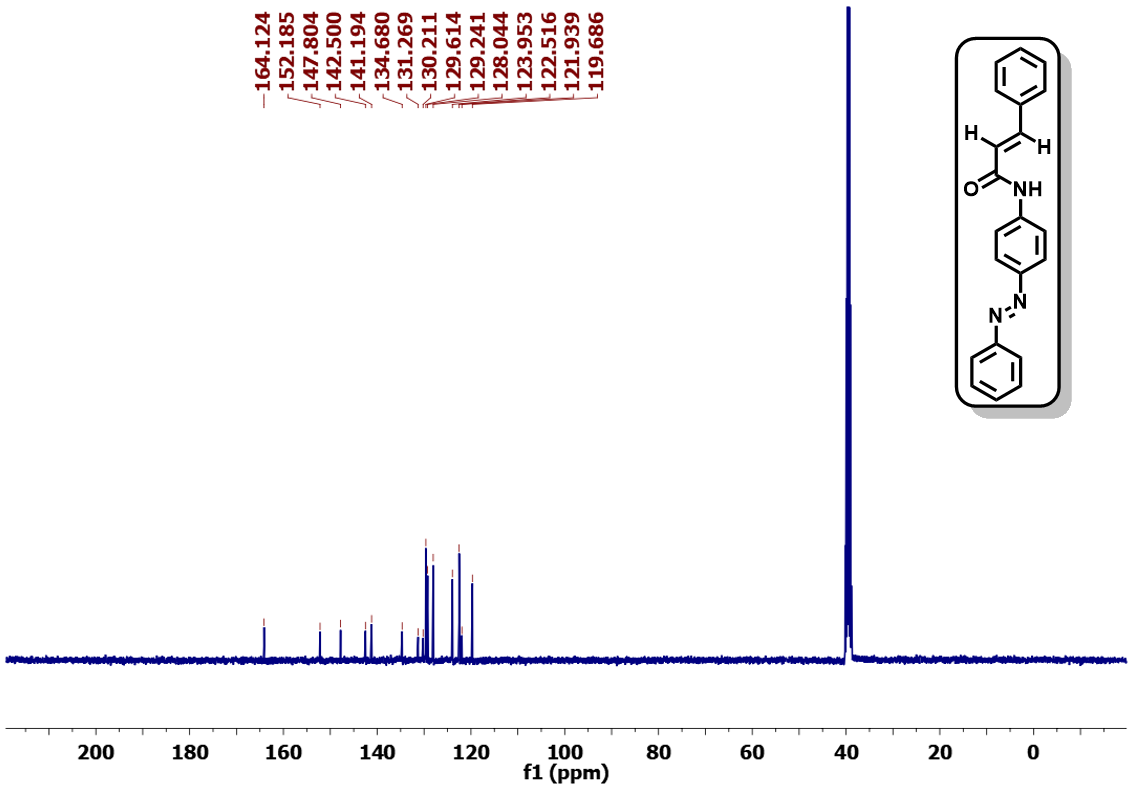

[13]C-NMR spectrum of *N*-(4-((*E*)-phenyldiazenyl)phenyl)cinnamamide (**M2**) in $[D_6]$DMSO.

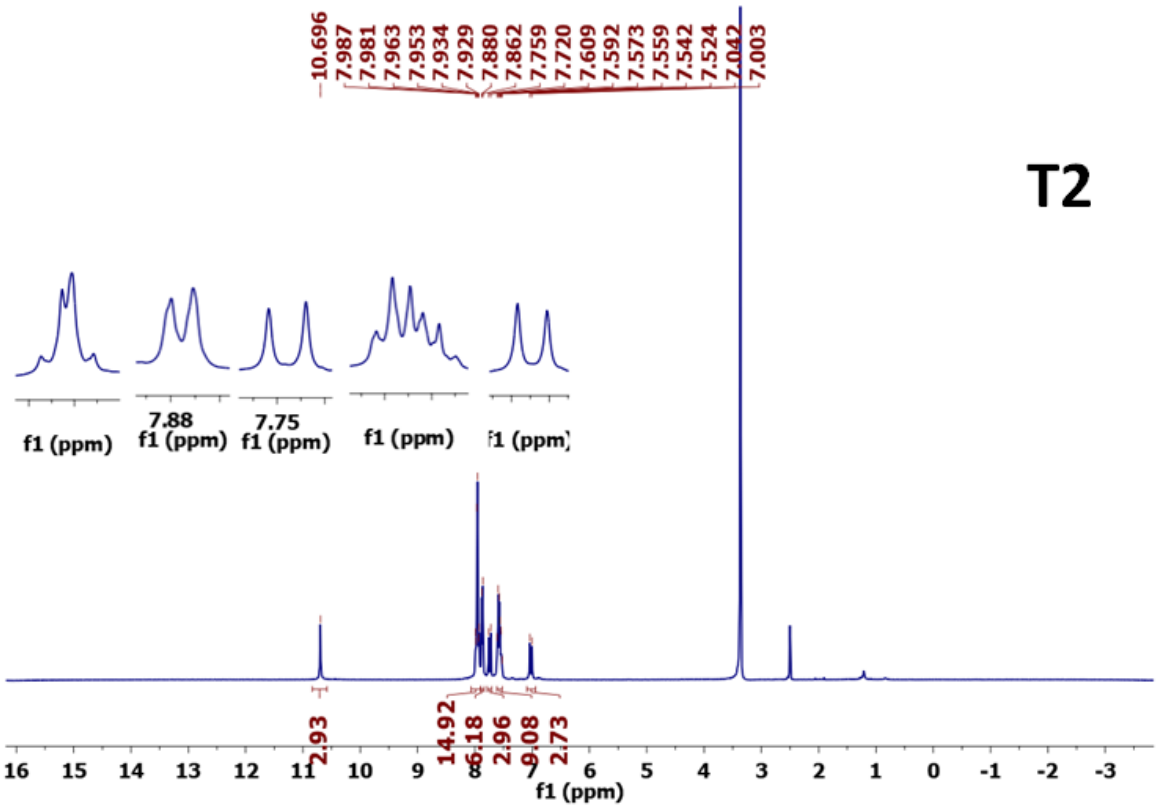

^{1}H-NMR spectrum of (2*E*,2'*E*,2"*E*)-3,3',3"-(benzene-1,3,5-triyl)tris(*N*-(4-((*E*)-phenyldiazenyl)phenyl)acrylamide) **(T2)** in [D_6]DMSO.

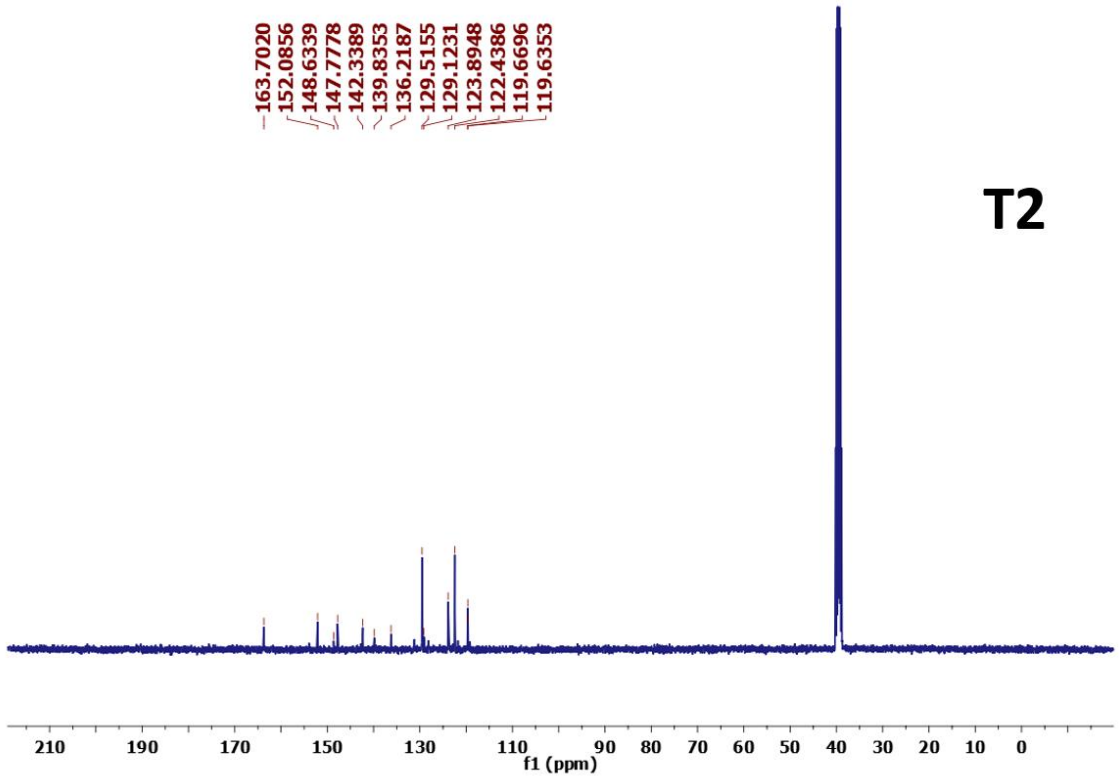

^{13}C-NMR spectrum of (2*E*,2'*E*,2"*E*)-3,3',3"-(benzene-1,3,5-triyl)tris(*N*-(4-((*E*)-phenyldiazenyl)phenyl)acrylamide) **(T2)** in [D_6]DMSO.

Appendix 3D

Computational Data (done by Chitranjan Sah)

For comparing the experimental data and for the further understanding of the molecular properties, the target molecules (i. e. **M1**, **M2**, **T1**, and **T2**) were subjected to the DFT computations at B3LYP/6-311G(d,p) level of theory (**Figure 3D.1.**). The monoamides (**M1** and **M2**) and the tripodal systems (**T1** and **T2**) were optimized to minima in *E, Z* and *EEE, EEZ, EZZ* and *ZZZ* isomeric states and the thermochemical data are provided (**Figure 3D.1.a and Table 3D.1.**). In order to gain insights, we inspected the HOMO-1, HOMO and LUMO orbitals for each one of the optimized isomeric states. The molecular orbital analysis revealed that HOMO-1 and HOMO orbitals of the *EEE*-isomer of **T1** and **T2** are degenerate. Whereas, in the cases of **M1** and **M2**, HOMO-1 and HOMO orbitals of the *E*-isomers are non-degenerate. In case of monoamides (**M1** and **M2**), HOMO-1, HOMO and LUMO for the *E*-isomers corresponds to n, π, and π* orbitals, respectively. For the tripodal systems (**T1** and **T2**), HOMO and HOMO-1 for the *EEE*-isomers corresponds to π orbital and LUMO being a π* orbital. The HOMO-LUMO energy gap of the *E* and *EEE* isomeric states for **M1** and **T1** was found to be lower than **M2** and **T2** as shown in **Figure 3D.1.b**.

On the other hand, the *Z*-isomers of **M1** and **M2**, and *ZZZ*-isomers of **T1** and **T2** showed a mix of n and π character in the HOMO and LUMO orbitals. In cases of **M1** and **M2**, HOMO-1 and HOMO orbitals of the *Z*- isomers are non-degenerate. Whereas, for **T1** and **T2** those orbitals were found to be degenerate. The HOMO-LUMO energy gap for *Z* and *ZZZ*-isomers was relatively higher in **M2** and **T1** as compared to **M1** and **T2** as depicted in **Figure 3D.1.b**. In all the cases except **M1**, HOMO-LUMO gap for the photoswitched state was lower than the native state. To understand the UV-Vis spectral data and the electronic transitions involving in the photoisomers, we performed TD-DFT computations for **M1**, **M2**, **T1** and **T2**. We witnessed a blue shift in the λ_{max} corresponding to π-π* transition involving HOMO and LUMO orbitals upon isomerization, which is in line with the experimental data. For the triamides **T1** and **T2**, TD-DFT computations predicted a blue shift of π-π* transitions involving the azo group for each progressive *Z*-isomerization step from their corresponding *EEE*-isomers (**Figure 3D.1.c**). Besides that, we observed a decrease in the molar absorptivity (ϵ) as a result of breaking of the three-fold symmetry, and progressively lowered in each consecutive photoisomerization step from *EEE* to *ZZZ*-isomer. A similar trend was observed for the *E*-*Z* isomerization step in **M1** and **M2**.

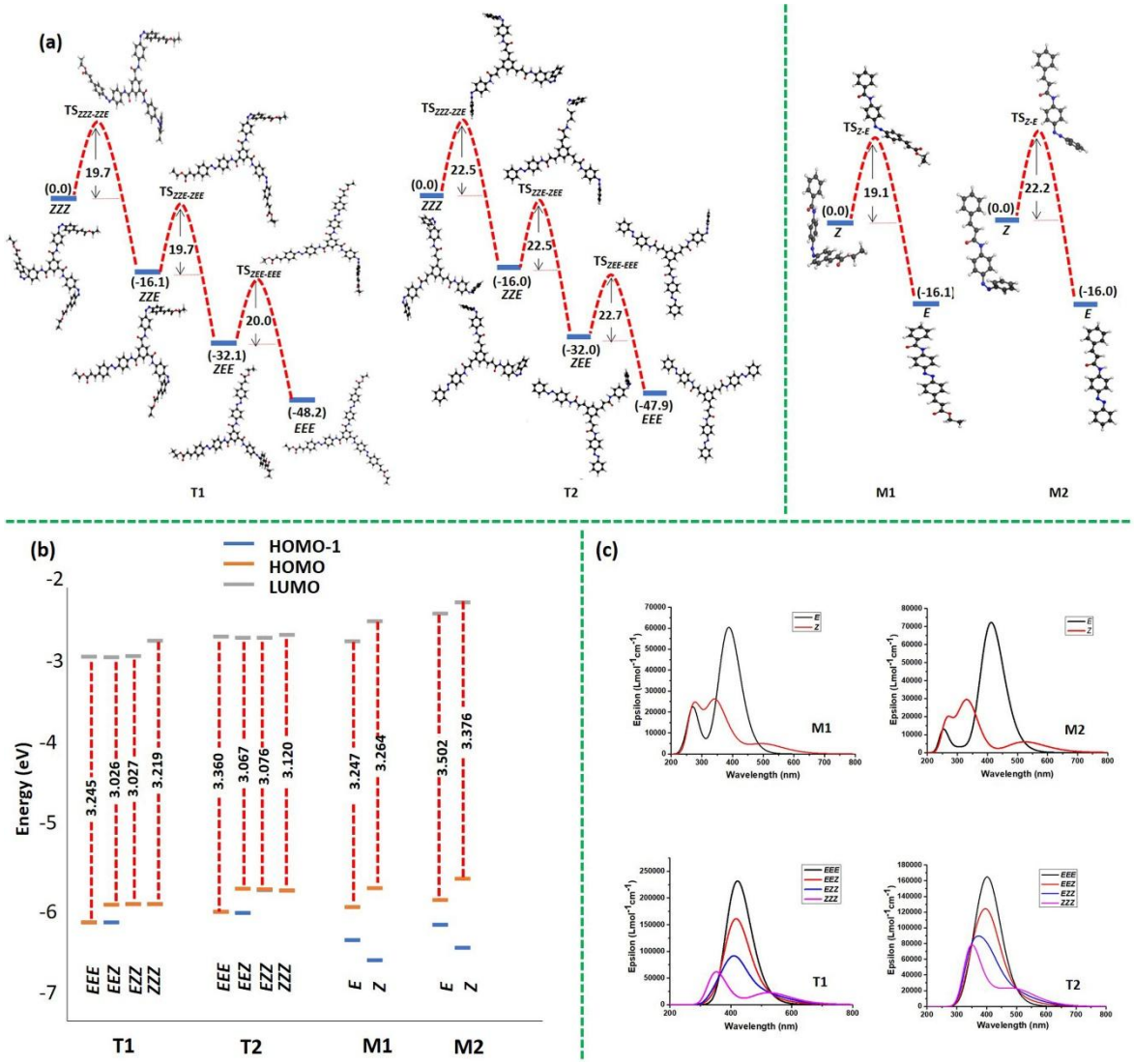

Figure 3D.1. Computational data (B3LYP/6-311G(d,p) level of theory): (a) Thermal barriers for the individual reverse isomerization steps of **T1**, **T2**, **M1** and **M2**. The optimized structures of the individual isomers and their corresponding transition states, and also their relative energies (in kcal/mol) are indicated; (b) HOMO–LUMO gaps (in eV) in the photoisomers of **T1**, **T2**, **M1** and **M2**; (c) computed electronic absorption spectral data (TD-DFT/6-311G(d,p) level of theory) depicting the changes in the spectral shifts and intensities of the photoisomers in **T1**, **T2**, **M1** and **M2**.

To shed light on the effect of extended conjugation on the isomerization kinetics, inversion mechanism has been considered and computed at the B3LYP/6-311G(d,p) level of theory. The transition state barriers, corresponding to thermal isomerization steps, *ZZZ* to *ZZE*, *ZZE* to *ZEE*, and *ZEE* to *EEE* in (**T1** and **T2**) and *Z-E* isomerization in (**M1** and **M2**) is shown in **Figure 3D.1.a**. The computed activation energy barrier for **T1** was found to be lower than **T2**. Likewise, similar

correlation was observed in their corresponding monoamides **M1** and **M2**. The computed barriers for these species ranges from 19.1-22.7 kcal/mol. All these computational data show consistency with the experimental results discussed earlier.

Chapter 4. Light Controlled Catalysis in Tritylation Reactions through Reversible Encapsulation of Chloride Ions

4.1 Introduction

Artificial control of functions such as catalysis, molecular recognition, supramolecular assembly, etc. demands variations in the environment or changes in selected parameters that can act as a stimulus.[1,2] Apart from the possibility of switching "on and off", stimuli responsive systems have also been reported to offer spatial (selectivity) and/or temporal (kinetic) control.[3] Light, pH, coordination, redox properties and supramolecular interactions have been considered to be popular choices for external stimuli.[4] Controlling reactions through light, and in particular, light-driven and/or photoswitchable catalysis have been of considerable interest in recent times.[5] Reversible control, the utility of ambient conditions, subtle changes, and also the viability of visible light as a stimulus in the biomolecular reactions offer great advantages but pose key challenges in light induced catalysis.

Several photo-controlled catalyst designs have been reported, which offer catalytic modulation predominantly through covalent and hydrogen bonding interactions.[3a,4b,6] Steric effects, electronic factors and the concepts of aggregation/dissociation have also been reversibly tuned in this regard.[7] In spite of the recent surge in light-driven covalent catalysis in synthetic organic chemistry,[8] the development of photoswitchable catalysis based on other weak interactions have been less explored.[9]

Among the recent strategies in non-covalent catalysis, activation of ion-pairs through anion binding has started gaining importance.[10] Particularly, the utility of dual hydrogen donor ability of thiourea and bis-triazole moieties has shown remarkable results.[11] Recently, Mancheño and co-workers have utilized the concept of chloride ion binding as a catalysis strategy in the tritylation of various nucleophiles and dearomatization of heterocycles.[12] Leigh and co-workers constructed a rotaxane based dual-function catalyst that can remarkably switch (pH driven) from anion-binding catalysis to aminocatalysis.[13a] Apparently, these catalysts demand reasonably higher temperature and/or long reaction times for catalysis, presumably due to the structural rigidity and restricted rotations. Indeed, such arguments have been validated by Flood and co-workers.[13b] Using smartly designed triazole-based molecular cages, they demonstrated chloride ion capture with exceptional affinity in the attomolar range.

Taking advantages of such studies, we intended to design a molecule with a tunable affinity toward chloride ions, which can be utilized for light-controllable catalysts. We hypothesized that

catalytic activity (tritylation reaction rates) can be modulated by varying the anion binding ability of the catalyst in its native and photoswitched states with light **(Figure 4.1)**.

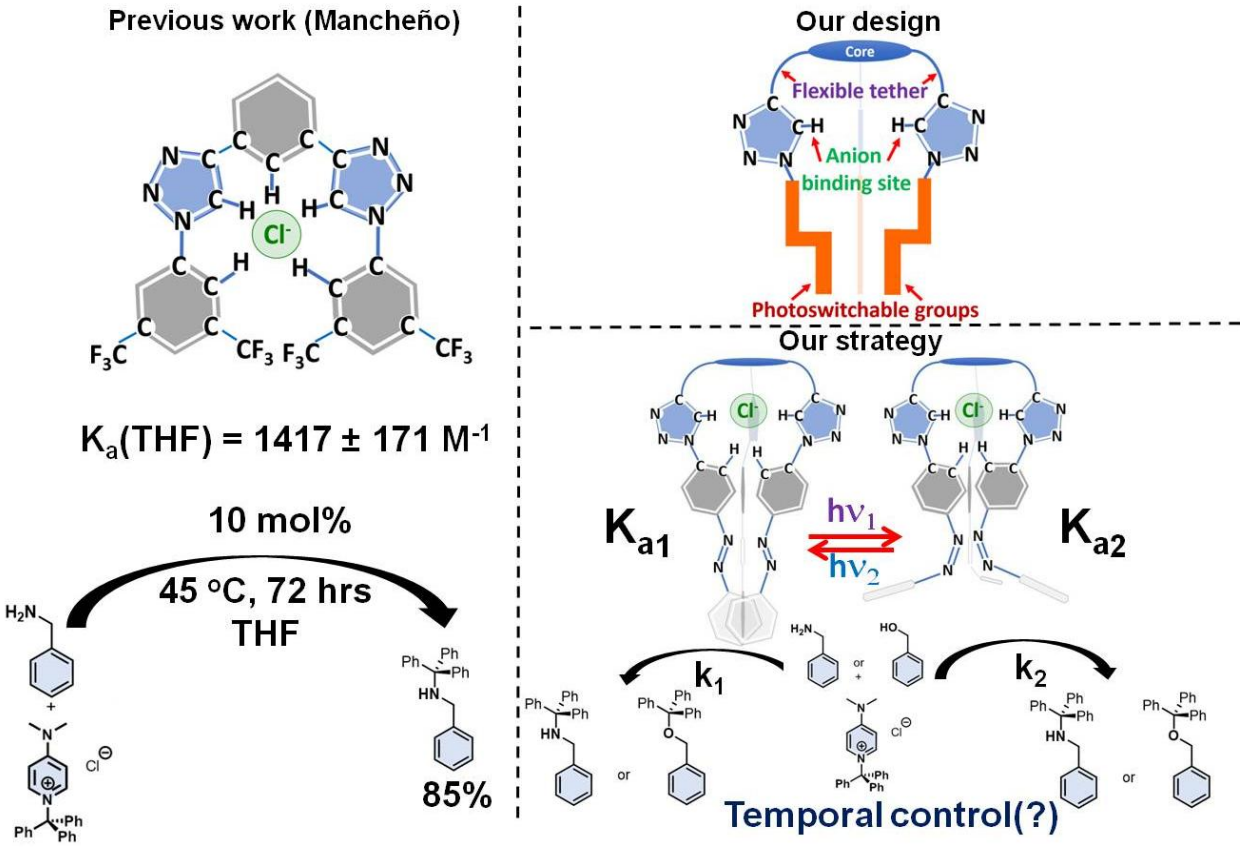

Figure 4.1 Design and possible temporal control of photoswitchable catalysts for tritylation reactions based on chloride ion binding.

Hence, as a proof of concept, we have combined photoswitchable units and anion binding sites to alter the reaction rates of the tritylation reactions with light. Considering the thermal stability of the photoswitched states, and also for efficiently utilizing the concept of photoswitching in catalysis, it is necessary to perform the reactions at ambient temperature so, reasonably, a weak binding and flexibility are necessary. In this regard, we considered utilizing tripodal 1,3,5-tris-functionalized benzene (core unit) decorated with azobenzenes (photoswitches) bearing triazole moieties (anion binding sites) through a flexible tether. Although our initial aim is to enable "fully activate or completely deactivate" the catalyst with light, we observed a residual catalytic activity upon photoisomerization of the catalyst. These residual activities are in line with the inhibition of catalytic activity through photoirradiation step, and reversible activation is known in the hydrogen bonding based catalysis and photocontrol of protein function.[6d,e] Herein, we report the design, synthesis, utility of the catalyst, spectroscopic, isothermal titration calorimetric and computational investigations in understanding the anion binding strategy in photoswitchable

catalysis in tritylation reactions.

4.2 Design and Synthesis

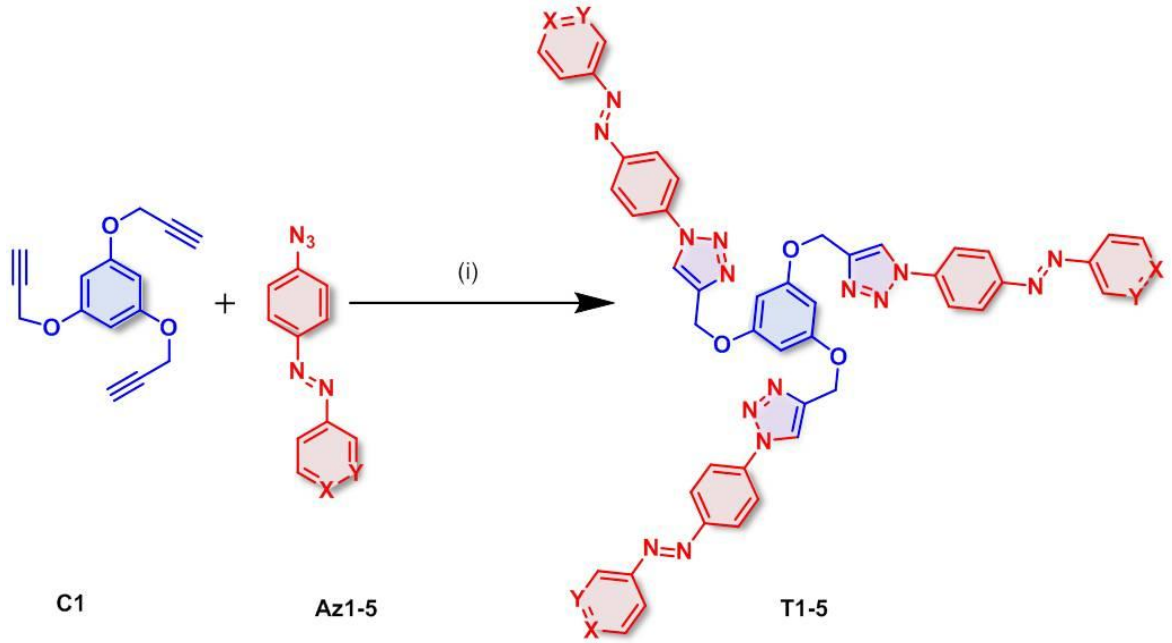

Scheme 4.1 Synthesis of the target photoswitchable catalysts **T1-5**. Conditions: (i) **C1** (1.0 eq.), Az1-5 (3.3 eq.), $CuSO_4.5H_2O$ (0.6 eq.), sodium (L)-ascorbate (1.2 eq.), 1:1 ^{t}BuOH-H_2O, and RT.

Table 4.1 Derivative and yields of the target catalysts:

Compound	X	Y	%Yield
T1	CH	CH	70
T2	C-OH	CH	80
T3	N	CH	70
T4	CH	N	75
T5	C-$CONH_2$	CH	70

The tripodal photoswitchable catalysts are designed utilizing covalent connections of photoswitches and triazole units with a core moiety in the 1,3,5-*tris*-functionalization mode. The choice of triazoles is made due to their exceptionally high binding affinity towards chloride ions through C-$H_{triazole}$...Cl^- interactions, and their reported use in catalysis.[11c,12,13] Azobenzenes have been chosen as photoswitches due to the light-induced changes in their molecular shape and size, and also the ease of functionalization.[14] Apparently, the direct 1,3-*bis* functionalization of triazole moieties to a benzene ring led to rigidity and restricted rotations, and so reasonably higher temperature ($T \geq 40\ ^oC$) has been reported for catalysis.[12d] In contrast, in our design, we have attached the triazole moieties through the -OCH_2- group to render flexibility and cooperativity to enable room temperature catalysis. The target catalysts **T1-5** were synthesized by click chemistry using a core unit **C1** and the azidoazoarenes **Az1-5 (Scheme 4.1)**.[15] To synthesize the core unit **C1**, phloroglucinol was tris-propargylated.[12d] In order to bring additional characteristics to the

catalyst, apart from parent **Am1**, four different amine functionalized photoswitches **Am2-5** with different solubility, hydrogen bonding prospects and heterocycles have been considered. 4-Aminoazoarenes and 4-aminoazopyridines have been synthesized using standard procedures.[14b] Subsequently all the amines **Am1-5** were converted into their corresponding azides **Az1-5** by using the diazotization procedure. Using Cu(I) mediated 1,3-dipolar cycloaddition strategies, all the five catalysts **T1-5** have been successfully synthesized in excellent yields.

4.3 Photoswitching Studies

Photoswitching studies for all the catalysts **T1-5** are performed in DMSO or $[D_6]$DMSO, and probed by UV-vis and ^{1}H-NMR spectroscopic techniques, respectively. At 365 nm, except the 4-hydroxy derivative **T2**, all the other catalysts showed excellent photoswitching **(Figure 4.2a, Table 4.2 and Appendix 4A)**.

Upon irradiation at 405 nm, the reverse isomerization led to regeneration of the native state in an excellent conversion.[16] Interestingly, all the derivatives except **T2** showed reasonable photoswitching even in the solid state (KBr medium). Also, the photoswitching stability of **T1** was studied by alternately irradiating in the forward and reverse directions at 365 and 405 nm, respectively. The alternating irradiation steps were conducted up to five cycles and no fatigue was observed **(Figure 4.2b)**. The photoswitching experiments have also been followed by NMR spectroscopy. For identification and quantification of the individual isomers, the shifts and signal patterns of the triazole protons have been utilized **(Figures 4.2c-f)**.

^{1}H-NMR spectroscopic studies showed that 365 nm irradiation led to a maximum of 83% *ZZZ* isomer of **T1** in the photostationary state (PSS).[14a] Also, a small amount (17%) of the *EZZ* isomer was identified based on the two additional singlet signals at a 1:2 ratio, and their chemical shifts. Upon 405 nm irradiation, nearly 84% *EEE*-isomer has been formed back. This clearly indicates that **T1** can reversibly be converted between the *EEE*- and *ZZZ*- isomers under 365 (forward direction) and 405 nm (reverse direction) irradiation conditions, respectively, with excellent yields.

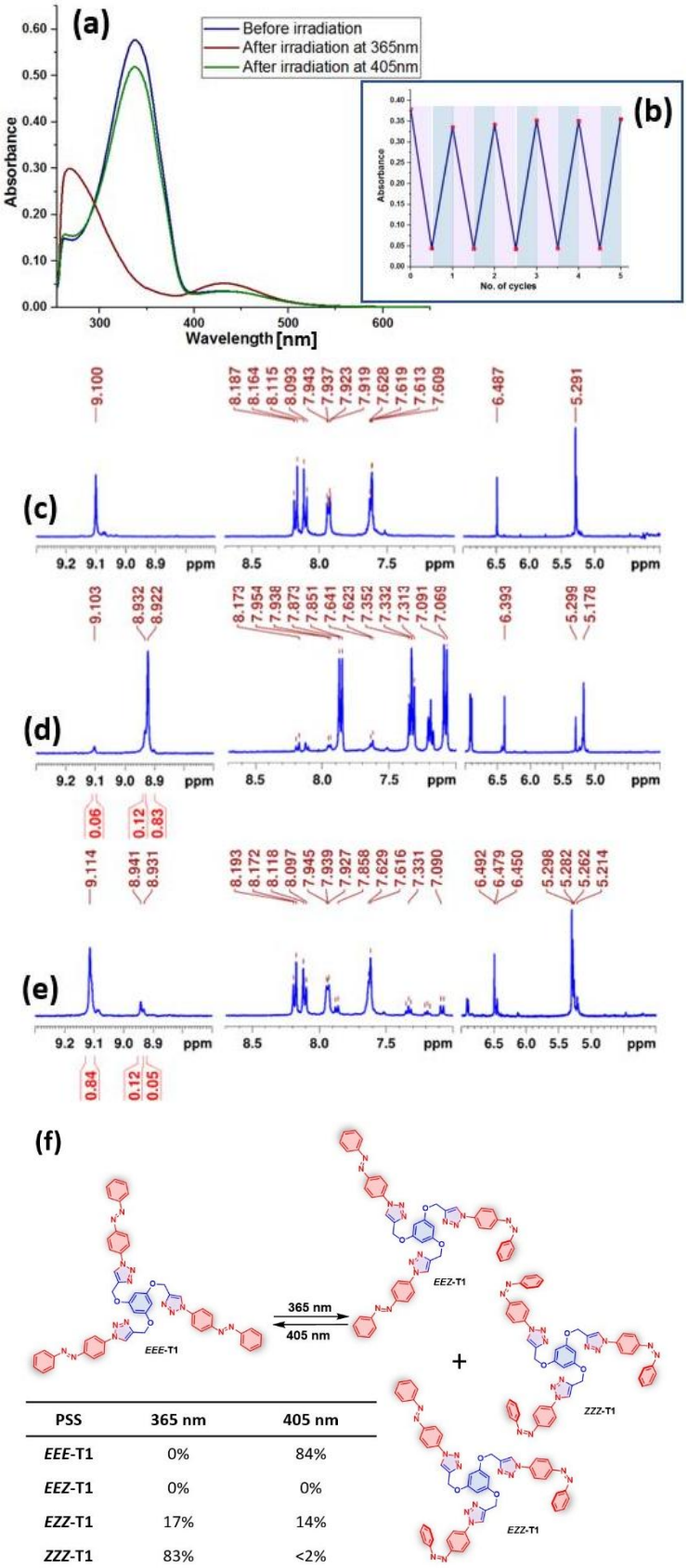

PSS	365 nm	405 nm
EEE-T1	0%	84%
EEZ-T1	0%	0%
EZZ-T1	17%	14%
ZZZ-T1	83%	<2%

Figure 4.2 Photoswitching in catalyst **T1**. (a) Analysis using UV-vis spectroscopy (DMSO, 9 μM); (b) photoswitching stability (alternating irradiation at 365 and 405 nm); NMR spectral data ([D_6]DMSO, 11 mM): (c) before irradiation; (d) after irradiation at 365 nm for 40 min, and (e) after

irradiation at 405 nm for 20 min; the PSS compositions have been estimated using the normalized integral values corresponding to the triazole-CH signal(s) and are tabulated (bottom); (f) possible photoisomers of **T1**, and the composition of individual isomers in the PSS.

Table 4.2 Electronic spectroscopic data and analysis of photoswitching properties of the catalysts **T1-5** and **B1** using UV-Vis and NMR spectroscopic data:

S. No.	Catalyst	UV-Vis spectroscopic data[a]				^{1}H-NMR spectroscopic data[b]				
		Native isomer		After 365 nm irradiation		PSS composition				C [mM]
		π-π^* (λ_{max}/ε)	n–π^* (λ_{max}/ε)	π-π^* (λ_{max})	n–π^* (λ_{max})	%*EEE*	%*EEZ*	%*EZZ*	%*ZZZ*	
1.	**T1**	338 (77237±2047)	442 (4148±75)	269	432	0 **84**	0 **0**	16 **14**	84 **<2**	11
2.	**T2**	368 (83957±4325)	-	-	-	-	-	-	-	-
3.	**T3**	335 (77680±808)	441 (3107±408)	267	431	14 **77**	- **10**	17 **13**	69 -	11
4.	**T4**	339 (63632±1281)	440 (3140±116)	274	439	-	-	-	-	-
5.	**T5**	342 (66825±2917)	441 (3654±135)	268	437	-	-	-	-	-
6	**B1**	338 (87222±2455)	448 (4186±205)	275	435	5 **61**	- **21**	- **18**	95 -	16

[a]The λ_{max} and ε values are expressed in nm and L.mol^{-1}.cm^{-1}, respectively. [b]The PSS composition for forward (at 365 nm, normal font) and reverse isomerization (at 405 nm, bold font) were estimated using the normalized integral values of triazole C-H signals from the ^{1}H-NMR spectral data.

4.4 Reaction Optimization

All the targets **T1-5** have been utilized as a catalyst in the tritylation reaction of benzylamine **R1**. In this regard, we have adopted a procedure from the literature using DMAP-TrCl adduct **A1** as a tritylating agent.[12d] In order to optimize the reaction conditions, 1.0 eq. of salt **A1** was used along with 2.0 eq. of $BzNH_2$ and stirred with catalyst **T1** at room temperature. The formation of the product was monitored by TLC, and was isolated and purified using column chromatography. We have carried out all the reactions at room temperature in duplicate (with and without irradiation of the catalyst) in order to observe the effect of photoswitching on the catalyst **(Table 4.3)**.

Although various solvents have been screened, we were restricted mainly to CH_2Cl_2 and DMSO for the optimization based on the factors, such as solubility, and spectroscopic investigations.[17] Apart from the screening of solvents, the other parameters such as catalyst loading, time, etc. of catalysts **T2-5** have also been screened. The complete screening for the optimization and corresponding results are tabulated in **Table 4.3.**

Table 4.3 Optimization of the reaction conditions*:

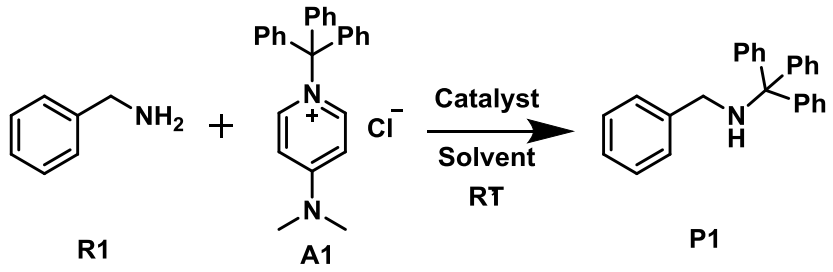

Entry	Catalyst	Catalyst loading (mol%)	Solvent	Time(hrs)	Yield[#](%)
1	***EEE*-T1**	10.0	DCM	9	85
2	***EEE*-T1**	5.0	DCM	9	82
3	**none**	none	DCM	9	52
4	***EEE*-T1**	10.0	DMSO	9	80
5	***EEE*-T1**	5.0	DMSO	9	80
6	**none**	none	DMSO	9	45
7	***EEE*-T1**	10.0	THF[**]	9	20
8	***EEE*-T1**	5.0	THF[**]	9	20
9	**none**	none	THF[**]	9	0
10	***EEE*-T1**	3.0	DCM	9	72
11	***EEE*-T1**	2.0	DCM	9	68
12	***EEE*-T1**	5.0	DCM	7	72
13	***EEE*-T2**	5.0	DCM	9	70
14	***EEE*-T2**	5.0	DMSO	9	40
15	***EEE*-T3**	5.0	DMSO	9	60
16	***EEE*-T4**	5.0	DMSO	9	68
17	***EEE*-T5**	5.0	DMSO	9	34
18	***ZZZ*-T1[a]**	5.0	DMSO	9	78
19	***ZZZ*-T1[b]**	5.0	DMSO	9	72
20	***ZZZ*-T1[c]**	5.0	DMSO	9	68
21	***ZZZ*-T1[d]**	5.0	DMSO	9	55
22	***ZZZ*-T1[e]**	5.0	DMSO	9	38
23	**ZZZ-T1[f]**	5.0	DCM	9	38
24	**ZZZ-T1[g]**	5.0	DMSO	9	33

*Conditions: **R1** (22.9 μL, 0.21 mM), **A1** (50 mg, 0.10 mM), 0.5 mL solvent; [#]Isolated yields; **In THF, the catalyst was insoluble; The catalyst was irradiated at 365 nm [a]in DMSO for 1 min; [b]in DMSO for 3 min; [c]in DMSO for 5 min; [d]in DMSO for 30 min; [e]in DMSO for 40 min; [f]in DCM for 40 min; [g]in DMSO with continuous irradiation up to 9 h; Irradiation was done in the presence of DMAP-TrCl salt in each case.

Based on these optimization procedures, we have finalized our standard conditions as follows: DMSO or CH_2Cl_2 as a solvent, 5 mol% catalyst **T1**, room temperature, and 9 hours. After optimization of the conditions, we next tested the effect of photoswitching of catalyst **T1** on the reaction yield. Interestingly, with the photoswitched catalyst **T1** (upon irradiation at 365 nm in DMSO for 40 minutes), the yield has been decreased to 38%. Furthermore, we evaluated the time-dependent photoswitching of the catalyst **T1** to understand the effect of irradiation times on the yield. The catalyst solution is subjected to 1, 3, 5, and 30 min irradiation times at 365 nm. Correspondingly, the yields are found to be 78, 72, 68 and 55%, respectively.

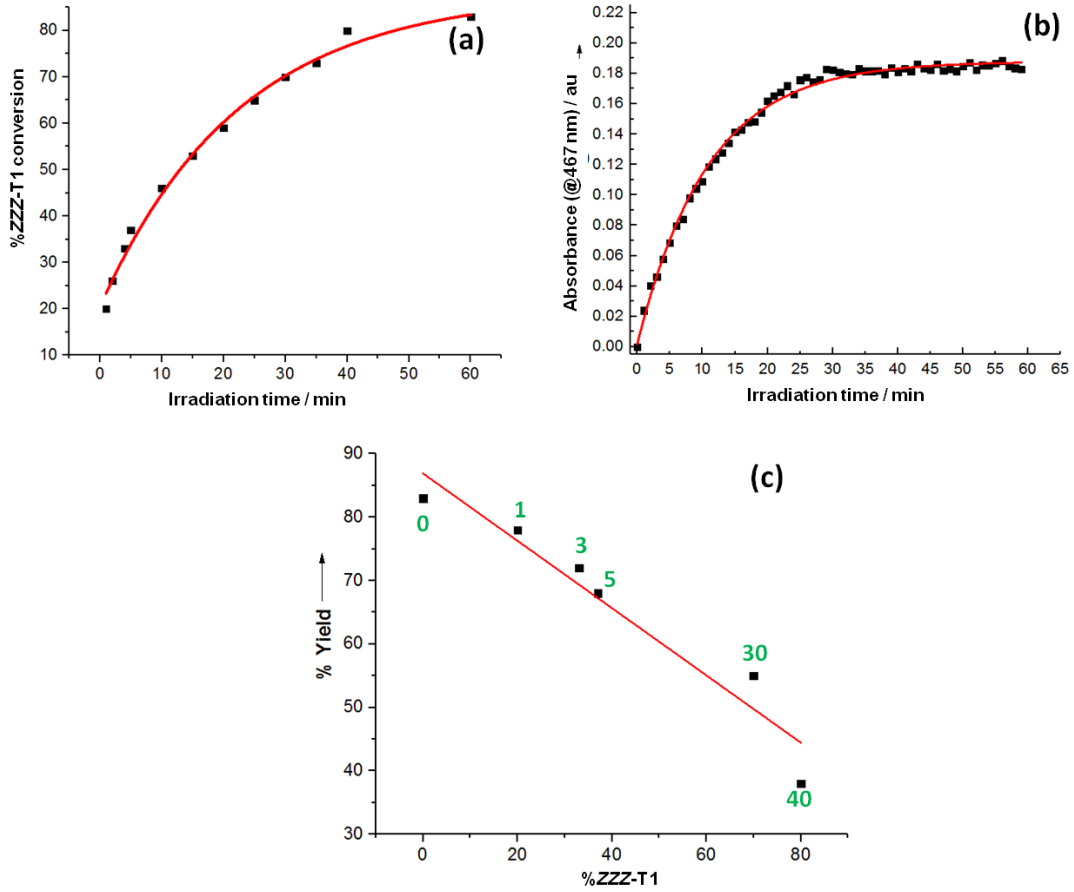

Figure 4.3 Forward isomerization rate plots for the conversion of ***EEE*-T1** to ***ZZZ*-T1** up to the attainment of PSS using (a) ^{1}H-NMR (Solvent: [D_6]DMSO; 11 mM; Forward isomerization rate constant, k_f = 4.43 x 10^{-2} ± 5.5 x 10^{-3} min^{-1}) and (b) UV-Vis spectroscopy (Solvent: DMSO; 11 mM; Forward isomerization rate constant, k_f = 9.14 x 10^{-2} ± 2.0 x 10^{-3} min^{-1}) (Both samples were irradiated with 365 nm LED light source of intensity 7 mW at a fixed distance of 4 cm); (c) Plot depicting a linear correlation between the %yield in the tritylation reaction of $BzNH_2$ and %***ZZZ*-T1** conversion (catalyst); The corresponding 365 nm irradiation times for obtaining the respective %***ZZZ*-T1** conversion are indicated.

To shed further light into this phenomenon, a separate experiment has been performed with *in situ* irradiation at 365 nm, which resulted in 33% yield. This clearly confirmed the influence of

the *ZZZ*-isomer enriched catalyst in decreasing the rate of the reaction despite the observation of residual catalytic activity. Remarkably, the rates for the forward isomerisation step, and a linear correlation between irradiation times (or %***ZZZ*-T1**) vs yields showed excellent consistency **(Figures 4.3 a-c)**.

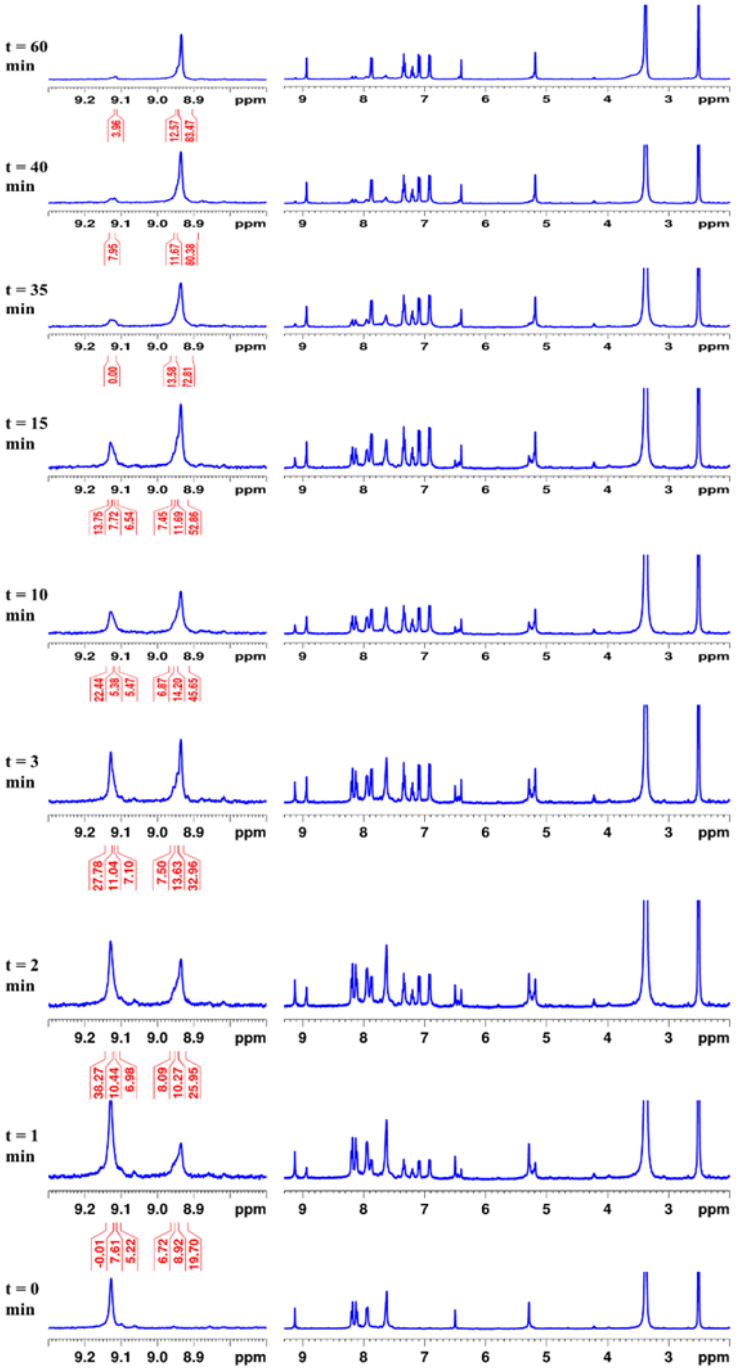

Figure 4.4 Photoswitching in catalyst **T1** ^{1}H-NMR spectral data ([D_6]DMSO, 11 mM) for the estimation of forward isomerisation rate constant at different irradiation times (365 nm LED light source of intensity 7 mW at a fixed distance of 4 cm was used for irradiation).

Photoswitchable catalyst **T1** upon irradiation using 365 nm light gives a mixture of different photoisomers, namely ***ZZZ*-**, ***ZZE*-**, and ***ZEE*-** along with the residual native isomer ***EEE*-**

T1 have been formed. The Forward isomerisation kinetics have been followed using a 400 MHz NMR and UV-Vis spectrophotometer at 298 K. For following the kinetics, the sample (as a solution either in a quartz NMR tube (for NMR experiments) or in a quartz cuvette (for UV-Vis spectroscopic experiments)) has been kept at a distance of 4 cm from the light source.

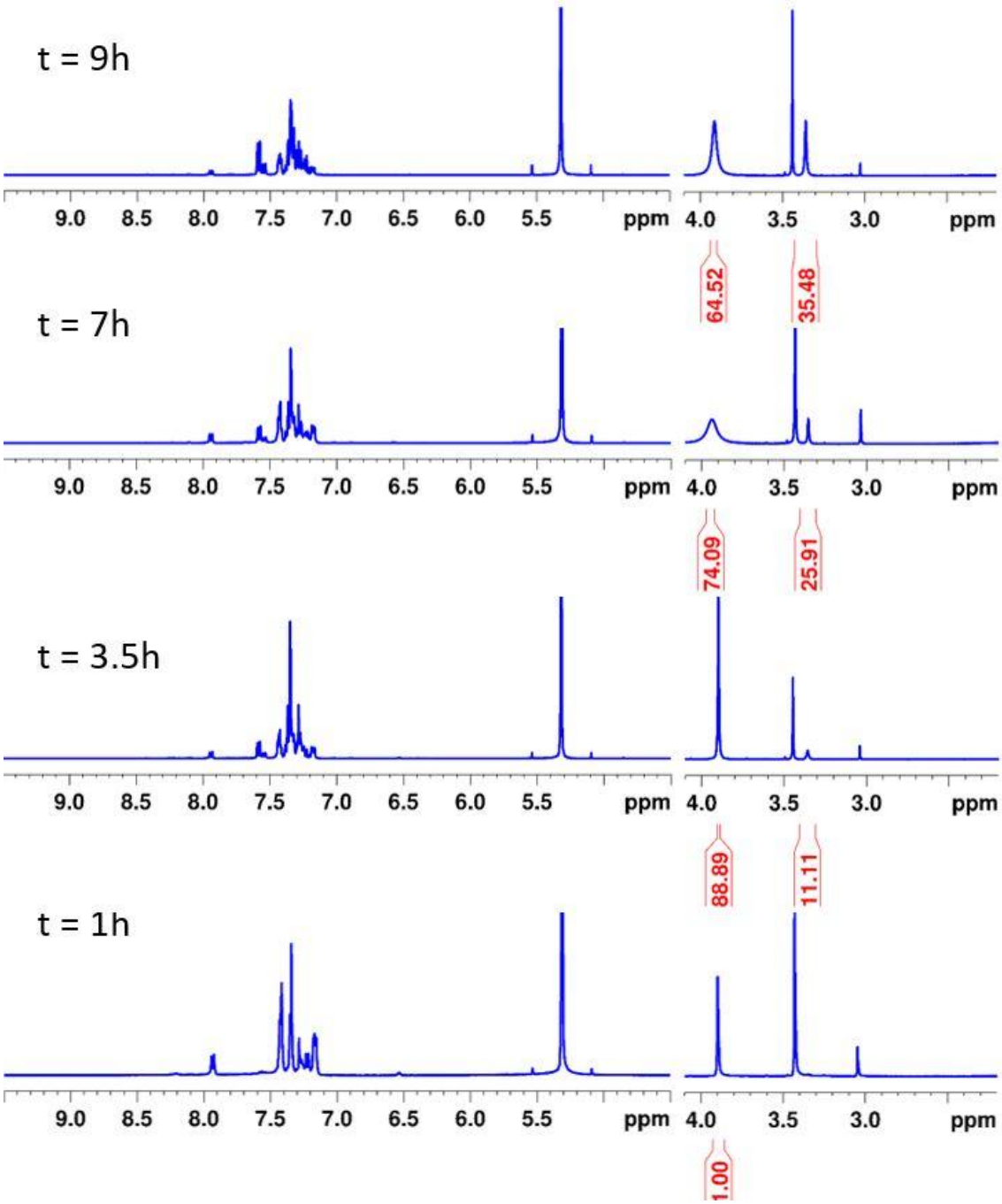

Figure 4.5 ^{1}H-NMR experiment depicting the conversion of tritylated benzylamine using **(*ZZZ*)-T1** as a catalyst. (The reaction was conducted with the following conditions: $BzNH_2$ **R1**(22.91 μL, 2.0 eq.), DMAP-TrCl adduct **A1**(50 mg, 1.0 eq.), **(*ZZZ*)-T1** (5 mol%) in 0.5 mL DCM).

The observed rate of forward isomerization kinetics experiments performed by using NMR and UV-Vis spectroscopy are found to be 4.43 x 10^{-2} and 9.14 x 10^{-2}, respectively. The

corresponding data for the estimation of rate constant through NMR spectroscopy and changes in the composition of ***ZZZ*-T1** over a period of 60 minutes have been shown as stacking plot in **Figure 4.4**.

Next, two additional reactions (conversion of $BzNH_2$ **R1** into BzNHTr **P1**) catalysed by ***EEE*-T1** and ***ZZZ*-T1**, respectively, in CH_2Cl_2 under identical conditions have been executed in parallel, and the reactions were followed by ^{1}H-NMR.

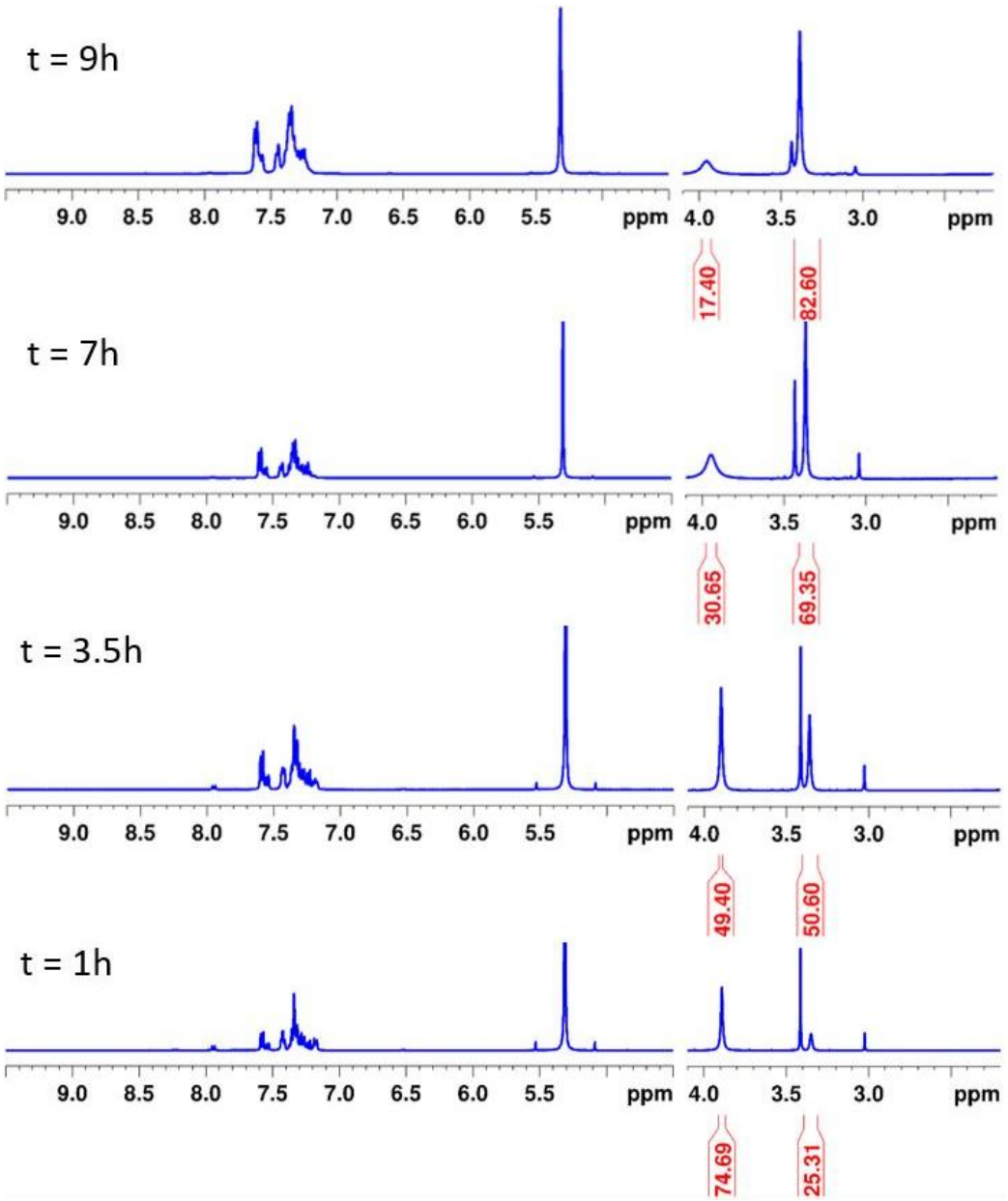

Figure 4.6 ^{1}H-NMR experiment depicting the conversion of tritylated benzylamine using **(*EEE*)-T1** as a catalyst. The reaction was conducted with the following conditions: $BzNH_2$ **R1** (22.91 μL, 2.0 eq.), DMAP-TrCl adduct **A1** (50 mg, 1.0 eq.), **(*EEE*)-T1** (5 mol%) in 0.5 mL DCM).

All the NMR spectra have been recorded in $CDCl_3$ for the crude reaction mixture collected at different intervals of time as indicated in the spectra; The normalized integral values corresponding to CH_2 protons of the reactant and the product have been used for the estimation of

conversion **(Figure 4.5-4.6)**. The reaction profile clearly proved that the reaction rates under the influence of the native and photoswitched catalysts are quite different. More importantly, the conversions were found to be comparable to the isolated yields in both the cases.

We have also extended this concept of photoswitchable catalysis in tritylation reaction to additional substrates **(Table 4.4)**. Remarkably, the presence of 5 mol% of catalyst **T1** in the native state led to the tritylation reaction of benzyl alcohol with a 65% yield.

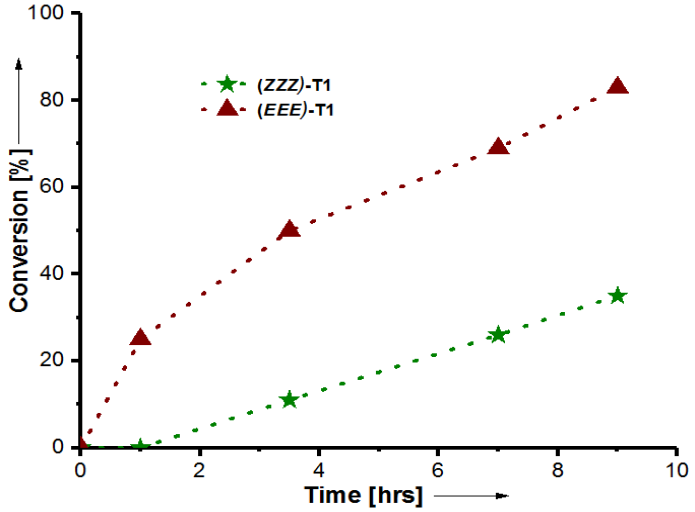

Figure 4.7 Reaction profiles for the by ***EEE*-T1** and ***ZZZ*-T1**. (The %conversion was obtained from the crude ^{1}H-NMR using the normalized integral values of CH_2 protons corresponding to **R1** and **P1**).

On the other hand, the photoisomerized catalyst ***ZZZ*-T1**, lowered the yield by three times (20%). As expected, the aliphatic cyclohexylamine, and secondary amines such as, morpholine and pyrrolidine under identical conditions led to moderate yields in the presence of ***EEE*-T1**.

We observed that the irradiation of the catalyst **T1** in the presence of the adduct **A1** reduced the yields further. All these yields were estimated based on the isolation after 9 h. On extending the reaction time up to 36 h, the yields were getting better, however, due to a slow thermal reverse isomerization of the photoswitched state of **T1**, it is quite unlikely to predict the reaction rate solely by ***ZZZ*-T1**. Based on these studies, the temporal control of the catalyst by light has been successfully demonstrated. Besides the light modulation, our current catalyst **T1** showed excellent catalytic activity in comparison to the previously reported catalysts for the similar reactions involving anion binding **(Table 4.5)**.

Table 4.4 Additional illustrations for photoswitchable catalysis[a]:

S. No.	Catalyst	Substrate	Product	Yield (%)[c]
1	***EEE*-T1**	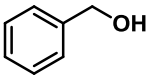	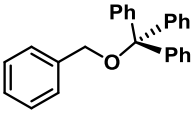	65 (**80**)
2	***ZZZ*-T1**[b]			20 (**38**)
		R2	**P2**	
3	***EEE*-T1**	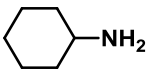	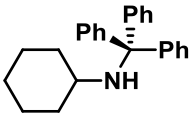	55 (**65**)
4	***ZZZ*-T1**[b]			35 (**48**)
		R3	**P3**	
5	***EEE*-T1**	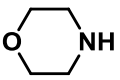	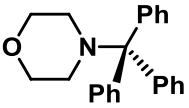	35
6	***ZZZ*-T1**[b]			15
		R4	**P4**	
7	***EEE*-T1**		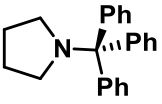	54 (**68**)
8	**ZZZ-T1**[b]			35 (**46**)
		R5	**P5**	

[a]For each substrate, both the reactions have been executed in parallel; (Conditions: substrates **R2-5** (0.21 mM), **A1** (0.10 mM), 0.5 ml CH_2Cl_2); [b]The catalyst was irradiated at 365 nm in CH_2Cl_2 in the presence of **A1**. [c]Isolated yields: Normal font – after 9 h; Bold – after 36 h.

Table 4.5 Comparison of catalytic activity of the present catalyst **T1** with the previously reported anion binding catalysts:

S. No.	Catalyst	Tunability/ Controlling factor	Catalyst loading (mol%)	Time (hrs)	T (^{o}C)
1	*Bis*-triazole[12d]	No	10.0	72	45
2	Rotaxane bases triazolium[13a]	Yes (pH)	20.0	120	40
3	Dipyrrolyldik-etone boron complex[10b]	No	2.5	24	RT
4	**T1** (This work)	Yes (Light)	5.0	9	RT

4.5. Mechanistic Studies

For a mechanistic understanding of the underlying catalytic process, we have performed several control experiments and additional studies.

Control experiments:

(a) In order to verify the influence of column condition or work up procedure in controlling the yields, we have also performed the purification using alumina column and also a work up using a base wash, before evaporation of solvent and column purification. However, we did not observe any changes in the yields with respect to the photoswitching of the catalysts.

(b) Under higher catalytic loading, we observed solubility issues and so the understanding the effects of photoswitching was unsuccessful. Interestingly, the parent catalyst was showing a partial photoswitching in solid state, however to a limited extent.

(c) In many solvents, the presence of moisture influences the reaction rates. Upon using dry solvents, the yields were found to be lower than the indicated values. For instance, when dry DMSO was used as a solvent, the yields were found to be 15%, 42% and 10% for the uncatalyzed, ***EEE*-T1** and ***ZZZ*-T1** catalysed reactions, respectively. As reported by Hirata et al., we also observed moderate yields in certain solvents even without the catalyst.[10b] However, under identical conditions, the native and photoswitched catalyst showed remarkable difference in the yields, indicating rate changes by the catalyst.

The preliminary evidence for the **T1**-Cl^- binding was obtained from the HRMS data of the solution containing **T1** and TBAC that confirmed the mass corresponding to the [M+Cl^-] in both native as well as photoswitched states of the catalyst **T1 (Table 4.6)**

Table 4.6 HRMS data of the catalyst **T1** binding with various Cl^- ions:

S. No.	Guest	Host	Exact mass	Observed mass	Description	Mass error (ppm)
1.	TBAC	***EEE*-T1**	944.3049 946.3051	944.3008 946.2984	[M + $^{35}Cl^-$] [M + $^{37}Cl^-$]	4 5.3
2.	TBAC	***ZZZ*-T1**	944.3049 946.3051	944.3013 946.3007	[M + $^{35}Cl^-$] [M + $^{37}Cl^-$]	4 4.5

In order to confirm the cooperativity effect of the three triazole units, we have also synthesized a *bis*-triazole based catalyst **B1**, and utilized for the catalysis. We have observed a variation in the yields for the tritylation reaction in benzylamine using the native (50%) and photoswitched (36%) catalysts **B1** under the optimized conditions in CH_2Cl_2. However, the relative yields were considerably lower than that of the reactions catalysed by **T1**. Such

evidence confirmed the existence of binding as well as cooperativity of the catalyst with chloride ions, which is necessary for the effectiveness in the catalysis.

In order to understand the binding sites and the binding constants for the catalyst with chloride ions, we have performed titrations between TBAC in [D_6]DMSO. In this regard, both the native and photoswitched states of **T1** have been utilized **(Figure 4.8)**.

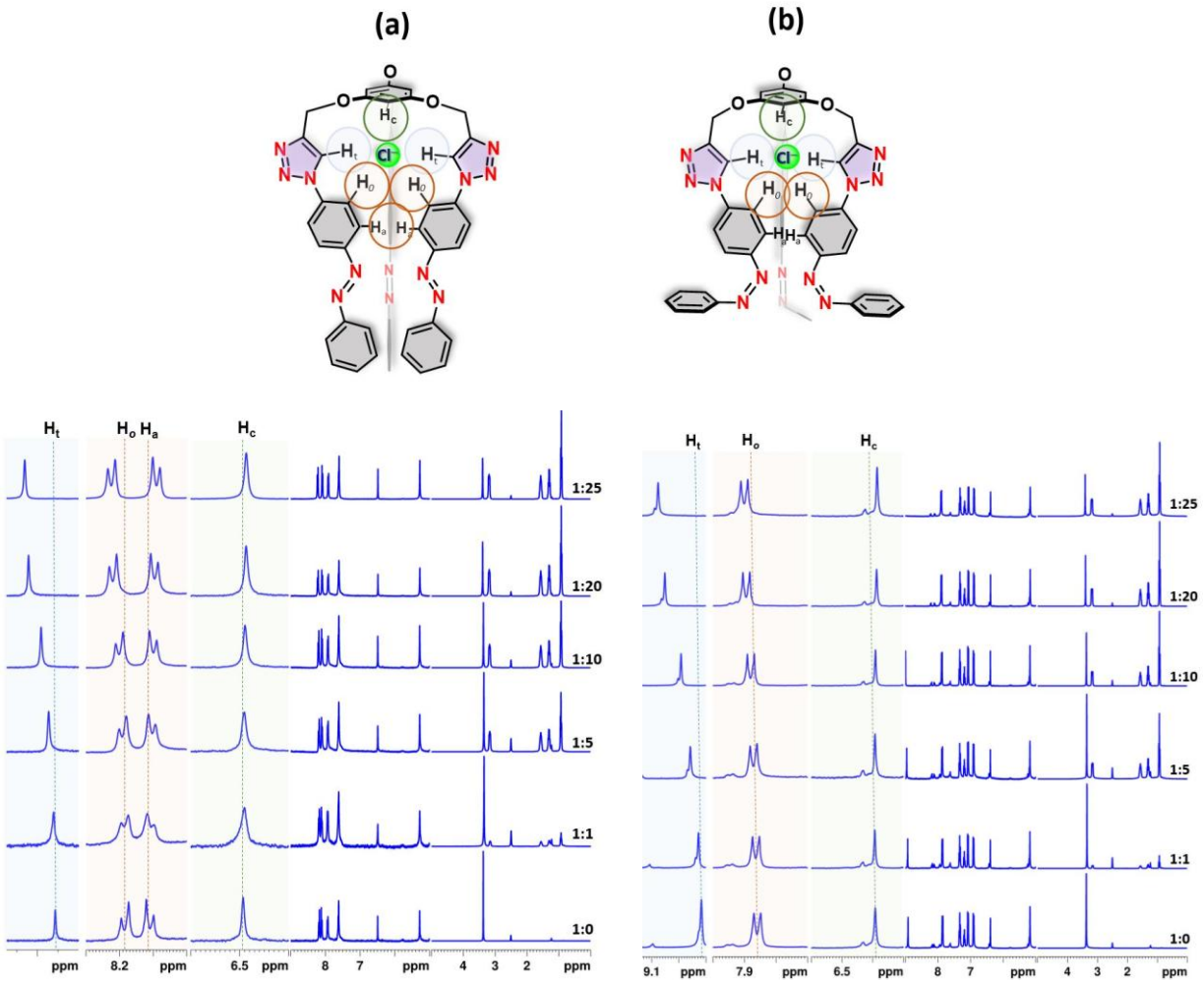

Figure 4.8 ^{1}H-NMR experiment depicting the shifts in the catalyst **T1** upon titration with TBAC with a stoichiometric ratios (**T1**:TBAC): (a) 1:0; (b) 1:1; (c) 1:5; (d) 1:10; (e) 1:20 and (f) 1:25. (left: for the native state of ***EEE*-T1** and right: after photoswitching at 365 nm) [Concentrations: **T1** – 11 mM] (The protons exhibiting major shifts upon addition of chloride ions are depicted separately. The position of the respective proton signals without chloride ion is indicated through a dotted line. Although methylene protons of the linker part showed upfield shifts, we observed broadness in the signals upon increasing the concentration of chloride ions.)

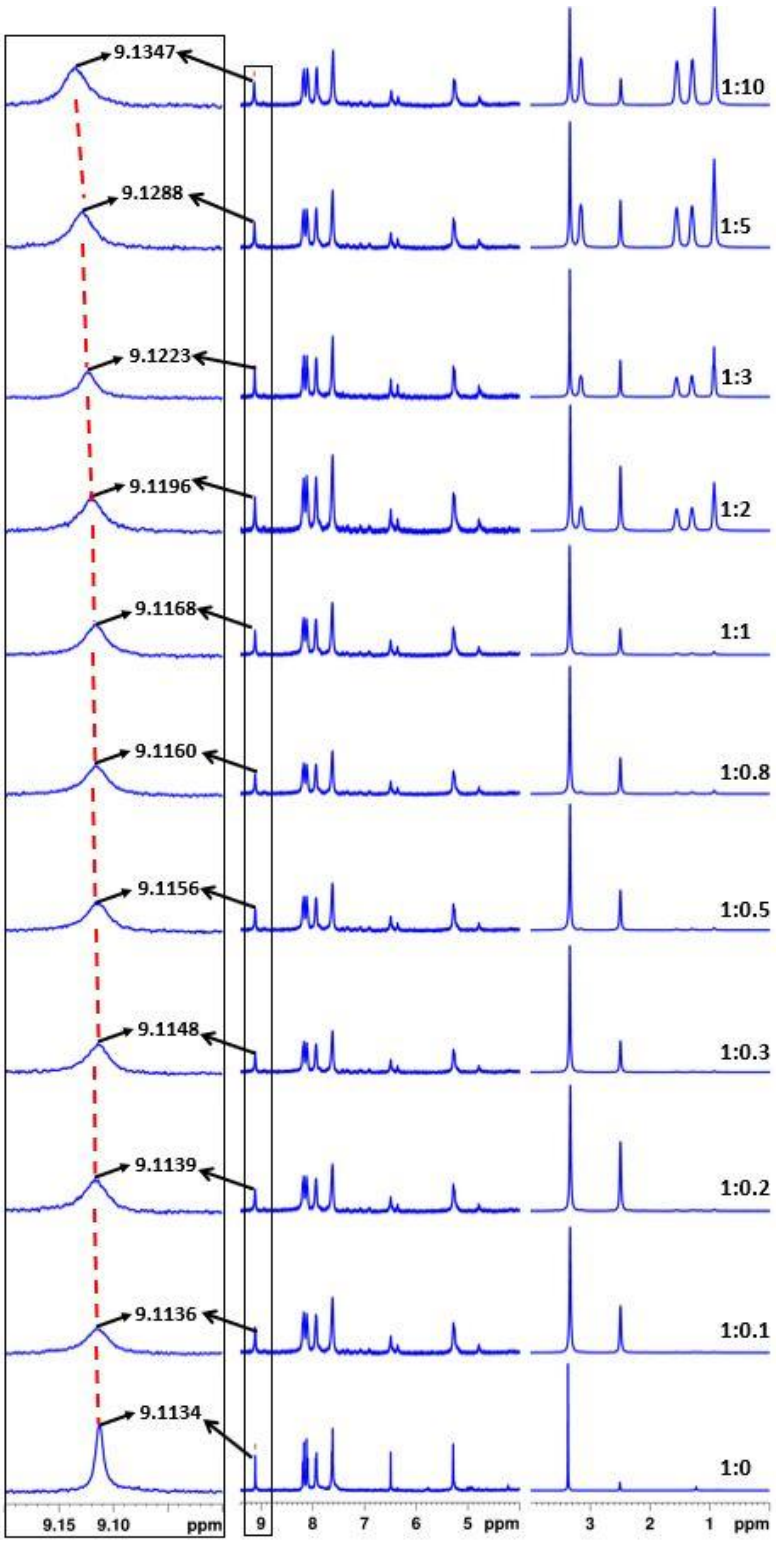

Figure 4.9 ^{1}H-NMR experiment depicting the shifts in the catalyst **T1** upon titration with TBAC with stoichiometric ratios (**T1**:TBAC) as follows (bottom to top): 1:0; 1:0.1; 1:0.2; 1:0.3; 1:0.5 1:0.8; 1:1; 1:2; 1:3; 1:5 and 1:10. (for the native state of ***EEE*-T1**) [Concentrations: **T1** – 5.4 mM in [D_6]DMSO].

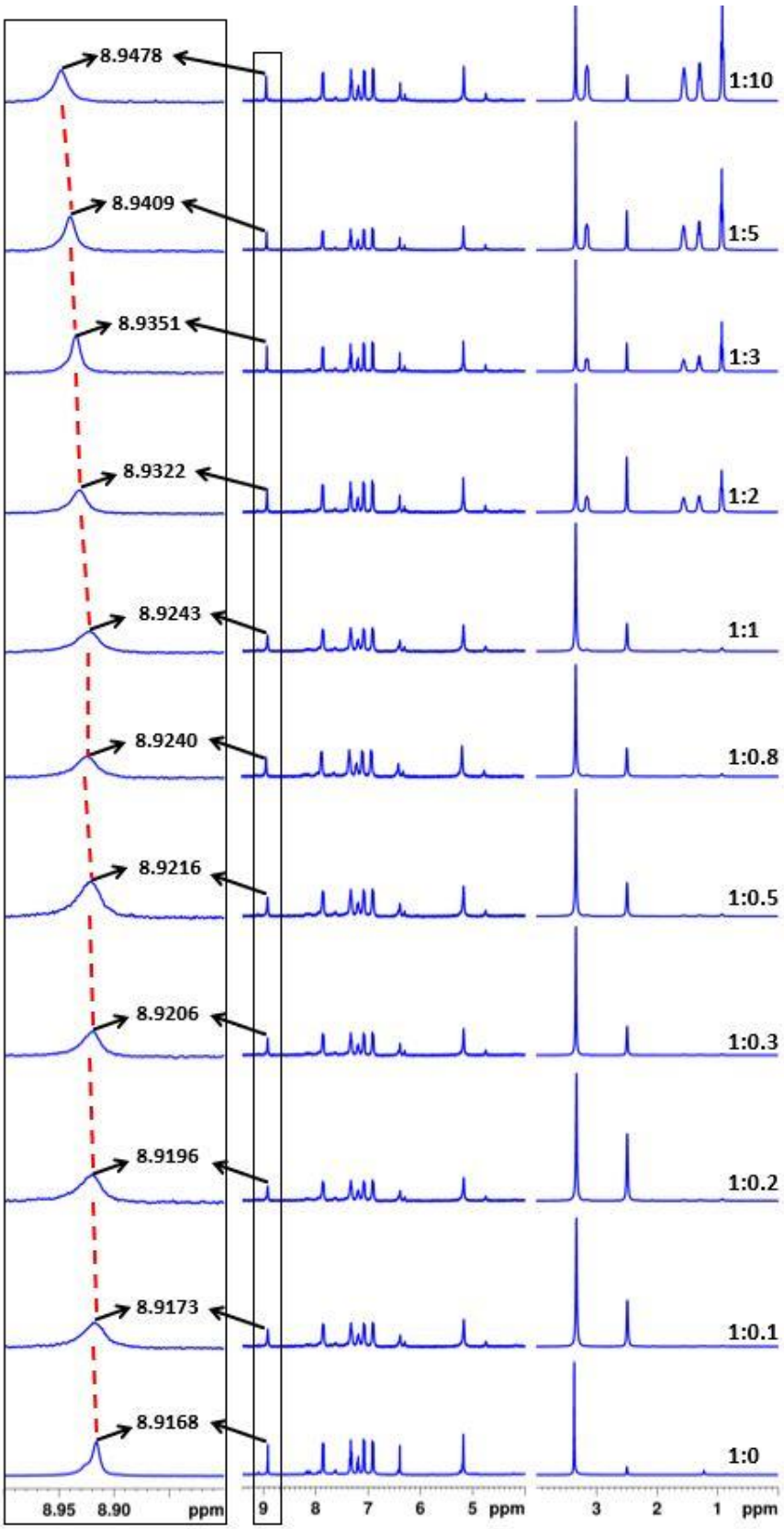

Figure 4.10 ^{1}H-NMR experiment depicting the shifts in the catalyst **T1** upon titration with TBAC with stoichiometric ratios (**T1**:TBAC) as follows (bottom to top): 1:0; 1:0.1; 1:0.2; 1:0.3; 1:0.5 1:0.8; 1:1; 1:2; 1:3; 1:5 and 1:10. (after photoswitching at 365 nm) [Concentrations: **T1** – 5.4 mM in [D_6]DMSO].

Based on the ^{1}H-NMR data for **T1** vs TBAC titrations, we observed downfield shifts in the protons of triazole, and phenyl group (*ortho* protons of the phenyl with respect to the triazole moiety) in both *EEE* and *ZZZ* isomeric states of T1 indicating a plausible interaction sites with the chloride ions. Whereas minor upfield shifts were observed for the protons of the benzene core and methylene group **(Figure 4.9 and Figure 4.10)**. Although the effect of ionic strengths of the medium (at higher concentration of TBAC) cannot be ruled out, only a restricted number of protons exhibiting the downfield shifts could be an indicative of the binding sites. Among the protons exhibiting shifts, only triazole protons showed maximum chemical shift indicating it as a major binding site. Interestingly, the binding sites did not change even after isomerization of the catalyst that can be realized once again by the signals exhibiting shifts and their magnitude.

Since the changes associated with chemical shifts in NMR titration experiments were found to be too little, we have estimated the binding constant using the standard isothermal calorimetry (ITC) technique.[18] Binding affinity of the chloride ions with tripodal triazole linked azoarene **T1** was measured using Isothermal Titration Calorimetry (ITC). This is the gold standard approach for the determination of binding constant (K), and the thermodynamic parameters associated with binding interactions (ΔH, ΔS, ΔG).

The experiment was carried out by MicroCal PEAQ-ITC200 (Malvern) at 293.15 K, by titrating the ligand (TBAC) and the substrate (**T1**, Catalyst), wherein the ligand (55.49 mM) was kept in the syringe (Volume = 40 µl) and the substrate (native as well as in photoswitched state) was filled in the cell (Volume = 280 µl) (**T1**, 0.733 mM). Two-µl of the ligand was injected for 4 s through an automated injector into the cell at an interval of 300 s. The contents inside the cell were stirred at 750 rpm to assure proper mixing of the contents. Appropriate blanks experiments were conducted for data analysis.

In order to check the biding affinity of the chloride ion with the photoswitched state, the native catalyst is exposed to UV light (λ = 365 nm) for a duration of 30 min, prior to start of the experiment. The binding curves are fitted to a one site binding model to determine the $K_{d,}$ for the interaction, ΔH, ΔS and ΔG for the interactions. At 20 ^{O}C, the bindings are associated with negative ΔG values indicating a spontaneous interaction of the TBAC and the catalyst in both the native (***EEE*-T1**) and photoswitched (***ZZZ*-T1**) states.

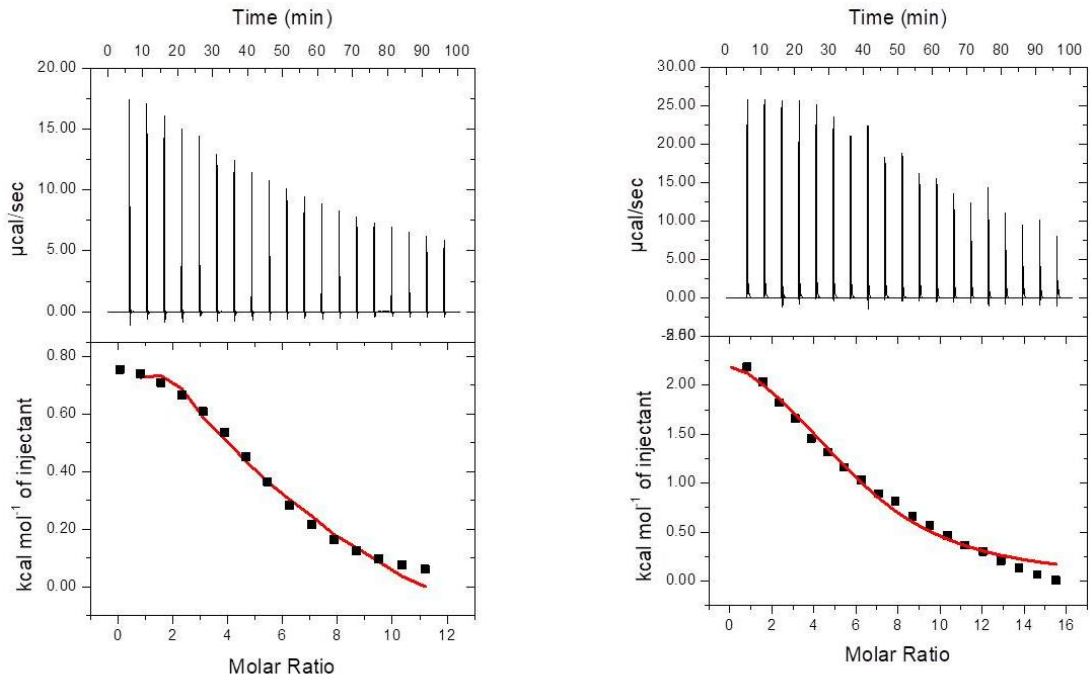

Figure 4.11 Estimation of binding constants using isothermal calorimetry: Experimental data and sigmoidal fittings for the binding constant of (a & b) ***ZZZ*-T1** with chloride ions (TBAC); (c & d) ***EEE*-T1** with chloride ions, respectively. (TBAC: 55.49 mM; ***EEE*-T1** and ***ZZZ*-T1**: 0.733 mM; Addition rate: 2 µL/4 Sec; Temperature: 20 ^{o}C)

A positive enthalpy indicates an endothermic reaction in both the cases. The positive entropy value suggests an entropically driven desolvation binding mechanism. While the entropy values are similar in both the cases, the binding of TBAC to the native state of **T1** is associated with higher enthalpy changes compared to the photoswitched state. Our results indicate that the dissociation constant, K_d for the binding of TBAC with the photoswitched catalyst is 2070 ± 431 M, which is two-fold greater than that of the native state catalyst, which is estimated to be 877 ± 157 M **(Table 4.7 and Figure 4.11).**

Table 4.7 Thermodynamic parameters[a] for the binding of catalyst **T1** with chloride ion before and after photoswitching:

Catalyst	***EEE*-T1**	***ZZZ*-T1**
K_d	877 ± 157	2070 ± 431
ΔH	2763.0 ± 185.1	851.2 ± 42.5
ΔS	22.9	18.1
ΔG	-3946.7	-4452.3

[a]ITC studies were performed in DMSO at 20 ^{O}C, and the dissociation constant K_d, ΔH, ΔS and ΔG are expressed in M, cal.M^{-1}, cal.M^{-1}.K^{-1}, and cal.M^{-1}, respectively.

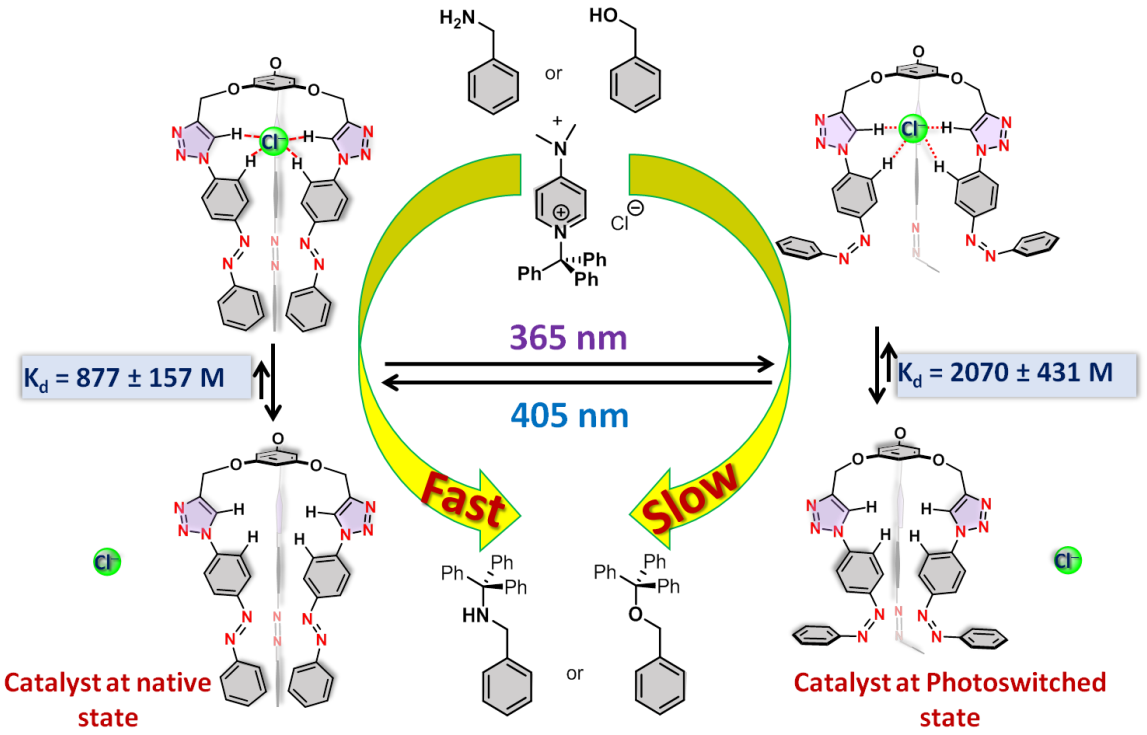

Figure 4.12 Overall summary depicting photoswitchable catalysis in tritylation reactions by light-driven variation in binding of chloride Ions.

Based on these observations, it is apparent that the higher enthalpy change for the native state catalyst upon binding to the ligand leads to efficient catalysis in contrast to the photoswitched state. More importantly, the difference in the dissociation constants between native and photoswitched states is corroborating with the variation in the yields (or the difference in the reaction rates) suggesting a crucial role of the photoisomerization of **T1** in determining the reaction yields. The overall summary based on the results has been portrayed as figure 4.12.

4.6. Summary

In summary, we have designed and developed *tris*(triazole) based photoswitchable catalysts that can exhibit light-controlled catalysis through chloride ion binding. Based on careful optimization of various parameters, and also the isolated yields, we inferred that the catalyst **T1** can control the tritylation reaction rates by light – through photoswitching of the catalyst. The native state of the catalyst **T1** exhibited fast catalysis, whereas upon photoisomerization of it inhibited the reaction rates. Based on the isolated yields, we observed a maximum of two times variation in the rates by controlling photoisomerization in the catalyst. Such temporal control was extended to additional substrates too. Through HRMS data, NMR titrations, control experiments, and DFT computations, we confirmed the mode of binding and the importance of cooperative binding. Isothermal calorimetric measurements revealed a two-fold difference in the dissociation constant between chloride

ion and the catalyst **T1** in its native (*EEE*) and photoswitched (*ZZZ*) states that is very well corroborated with the differences in the isolated yields. Overall, the influence of chloride ion binding in the light-controlled catalysis and temporal control by light have been demonstrated.

4.7 Experimental Section:

Synthesis of core unit C1:

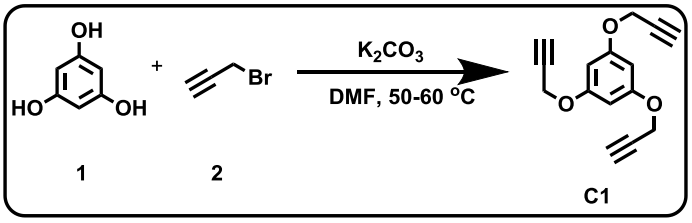

To a solution of phloroglucinol **1** (1.26 g, 10 mmol) in dry DMF (30 mL), anhydrous potassium carbonate (5.52 g, 40 mmol) was added and heated to 50 ^{o}C for 1 h under nitrogen atmosphere. Propargyl bromide **2** (4.76 g, 40 mmol) was then dropwise added and the reaction was continued at 65 ^{o}C for 36 h. After completion, the reaction mixture was cooled down to room temperature, and was poured into water. The crude solid product was collected by filtration. The pure product was obtained as fine white needle crystals after purification by column chromatography.

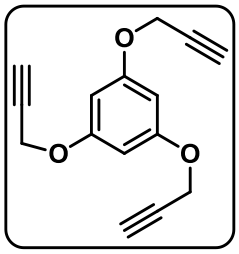

1,3,5-*tris*(prop-2-yn-1-yloxy)benzene (**C1**): White solid, mp= 82-84 ^{o}C, 57% yield. ^{1}H NMR (400 MHz, [D$_6$]DMSO): δ (ppm) 6.25 (s, 3H), 4.75 (d, J = 2.4 Hz, 6H), 3.57 (t, J = 2.3 Hz, 3H); ^{13}C NMR (100 MHz, [D$_6$]DMSO): δ (ppm) 158.9, 95.1, 79.1, 78.4, 55.6; FT-IR (KBr): 3279, 3269, 3259, 2908, 2134, 2115, 1617 cm^{-1}.

Synthesis of *(E)*-N-(4-((4-hydroxyphenyl)diazenyl)phenyl)acetamide(5):

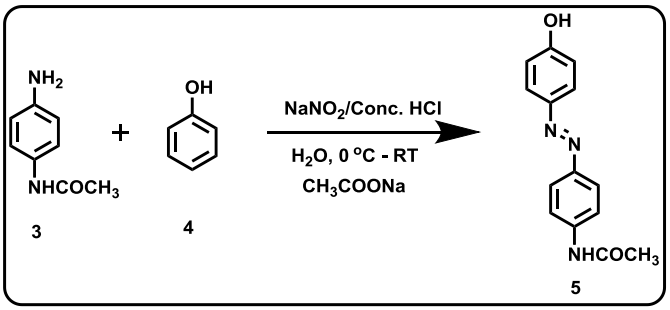

In a round bottom flask, 4-aminoacetanilide **3** (3.3 g, 22 mM) was dissolved in deionized water and the flask was cooled to 0 ^{o}C. To this mixture, 37% conc. HCl (6.5 mL) was added. Then a cold aqueous solution of sodium nitrite (1.52 g, 22 mM) in 20 mL of water was dropwise added into the reaction mixture. After the addition, the reaction

mixture was allowed to stir for half an hour. Afterwards, cold aqueous solutions of sodium acetate (5.9 g, 70 mM) and phenol **4** (2.16 g, 23 mM) in 100 mL of water were sequentially added at 0 ^{o}C. After the addition, the reaction was allowed to stir at RT and was monitored by TLC. After completion of the reaction, the reaction mixture was filtered off and water washings were given to obtain the pure orange solid product, which was dried under vacuum.

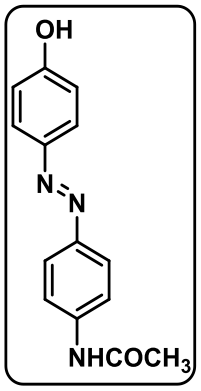

***(E)*-N-(4-((4-hydroxyphenyl)diazenyl)phenyl)acetamide(5)**: Dark orange solid, mp= 157-160°C, 91% yield. ^{1}H NMR (400 MHz, [D$_6$]DMSO): δ (ppm) 10.29 (s, 1H), 7.77-7.73 (m, 6H), 6.92 (d, J = 8.4 Hz, 2H), 2.09 (s, 3H); ^{13}C NMR (100 MHz, [D$_6$]DMSO): δ (ppm) 168.8, 161.1, 147.7, 145.2, 141.5, 124.6, 123.1, 119.2, 116.1, 24.2; FT-IR (ATR): 3341, 3043, 2998, 2920, 2789, 2660, 2586, 1651, 1587, 1529, 1500, 1401,1369, 1322, 1264,1226, 1142, 965, 834, 675, 640cm^{-1}; HRMS (ESI): *m/z* calcd. for $C_{14}H_{13}N_3O_2[M+H]^+$: 256.1088; found : 256.1086.

Synthesis of (*E*)-N-(4-((4-hydroxyphenyl)diazenyl)phenyl)acetamide(Am2):

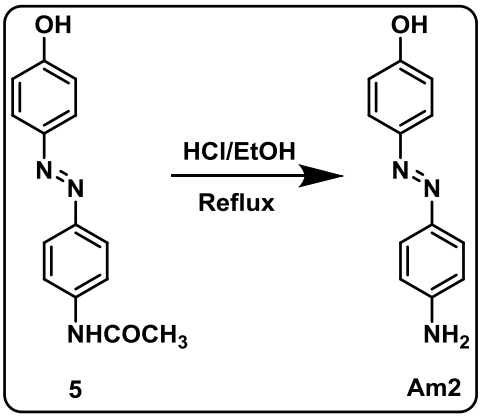

To the (*E*)-N-(4-((4-hydroxyphenyl)diazenyl)phenyl)acetamide **5** (1.75 g, 5.16 mM) in ethanol (150 mL), 37% con. HCl (4 mL) was added and refluxed. The hydrolysis reaction was monitored by TLC. After completion of the reaction, the reaction mixture was neutralised by adding aqueous sodium bicarbonate solution. The extraction of the reaction mixture was done using ethyl acetate. The extracted organic layer was washed with brine solution and evaporated to dryness and was subjected to purification by column chromatography.

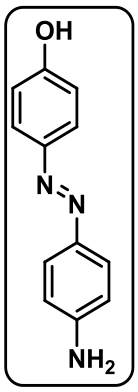

(*E*)-4-((4-aminophenyl)diazenyl)phenol (**Am2**): Orange solid, mp= 185-190 °C, 88% yield. ^{1}HNMR (400 MHz, [D$_6$]DMSO): δ (ppm) 9.98 (d, J = 6.9 Hz, 1H), 7.66-7.56 (m, 4H), 6.87 (t, J = 8.0 Hz, 2H), 6.64 (t, J = 7.7 Hz, 2H), 5.89 (br, 2H); ^{13}C NMR (100 MHz, [D$_6$]DMSO): δ (ppm) 159.2, 151.9, 145.6, 142.9, 124.5, 123.7, 115.8, 113.5; FT-IR (ATR): 3359, 3286, 3004, 2672, 1589, 1493, 1470, 1448, 1385, 1238, 1150, 1143, 1099, 1095, 1088, 1007, 948, 883, 836, 804, 762, 728, 710 cm^{-1}; HRMS (ESI): *m/z* calcd. for $C_{12}H_{11}N_3O[M+H]^+$: 214.0980; found : 214.0971.

Synthesis of sodium (phenylamino)methanesulfonate (6):

To a solution of formaldehyde (0.1 mol) and distilled water (40 mL), sodium bisulfite (0.1 mol) was added with stirring. The mixture was heated to 65 ^{o}C for 1 h. To this mixture, aniline (0.08 mol) was dropwise added over 15 min and stirred for 2 h at 65 ^{o}C. The reaction mixture was cooled to about 0 ^{o}C, which resulted in a dull-white crystalline solid that was filtered off, which was dried and used directly for next step.

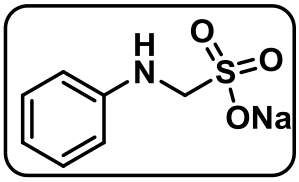

Synthesis of (*E*)-4-(pyridin-4-yldiazenyl)aniline Am3:

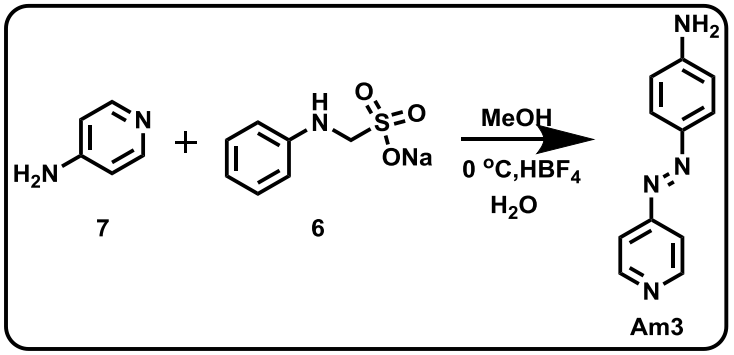

4-Aminopyridine **7** (0.500 g, 5.3 mmol) was dissolved in 20 ml of 85% aqueous fluoroboric acid solution and cooled to 0 °C. To this, 0.296 g of sodium nitrite was slowly added while maintaining the temperature below 5 °C. After stirring for about one hour, 2.208 g of sodium (phenylamino)methanesulfonate**6** as a suspension in 30 ml cold methanol was dropwise added, while maintaining the internal temperature below 5 °C. After the addition, the reaction mixture was warmed to room temperature, and 20 ml of isopropanol was dropwise added to it. The product as a precipitate filtered off to give wet crystals. This product was dissolved in 0.269 g of sodium hydroxide in 32ml of water and refluxed for 1-2 hours. After cooling down to room temperature, an orange solid product was filtered off, washed with acetonitrile and dried.

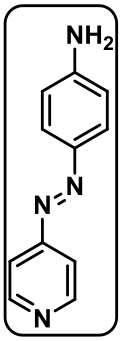

(*E*)-4-(pyridin-4-yldiazenyl)aniline (**Am3**): Orange solid, 90% yield. ^{1}H-NMR (400 MHz, $CDCl_3$): δ (ppm) 8.74-8.73 (dd, J = 4.6, 1.6 Hz, 2H), 7.85 (d, J = 8.8 Hz, 2H), 7.64 (dd, J = 4.6, 1.6Hz, 2H), 6.75 (d, J = 8.8 Hz, 2H), 4.22 (s, 2H) ; ^{13}C NMR (100 MHz, $CDCl_3$): δ (ppm) 151.2, 151.1, 146.5, 145.5, 126.2, 116.2, 114.7; FT-IR (ATR): 3435, 3301, 3139, 1639, 1600, 1587, 1504, 1456, 1416, 1400, 1320, 1136, 839 cm^{-1}; HRMS (ESI): *m/z* calcd. for $C_{11}H_{10}N_4$ $[M+H]^+$: 199.0983; found : 199.0981.

Synthesis of (*E*)-4-(pyridin-3-yldiazenyl)aniline (Am4):

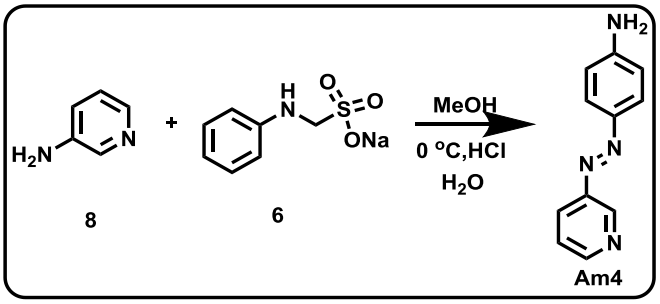

3-Aminopyridine **8** (0.500 g, 5.3 mmol) was dissolved in 5 ml of 37% hydrochloric acid, and cooled to 0 °C. To this, 0.296 g of sodium nitrite as aqueous solution (5 mL) was dropwise added slowly while maintaining the temperature below 5 °C. The reaction mixture was stirred for about one hour. Afterwards, 2.208 g of sodium (phenylamino)methanesulfonate**6**as a suspension in 30 ml cold methanol was dropwise added slowly, while maintaining the internal temperature below 5 °C. After the addition, the reaction mixture was warmed to room temperature, and 20 ml of isopropanol was

dropwise added in to it. The product as a precipitate was filtered off to give wet crystals. This product was dissolved in aq. sodium hydroxide solution (0.269 g of sodium hydroxide in 32ml of water), and refluxed for 1-2 hours. After cooling to room temperature, the product was filtered off, washed with acetonitrile and dried.

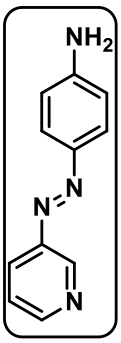

(*E*)-4-(pyridin-3-yldiazenyl)aniline (**Am4**): Orange solid, 92% yield. ^{1}H NMR (400 MHz, $CDCl_3$): δ (ppm)9.104-9.098 (m, 1H), 8.62-8.61 (dd, J = 4.7, 1.6 Hz, 1H), 8.09-8.06 (ddd, J = 8.2, 2.3, 1.6 Hz, 1H), 7.84-7.81 (m, 2H), 7.41-7.38 (ddd, J = 8.2, 4.8, 0.6 Hz, 1H), 6.76-6.72 (m, 2H), 4.17 (s, 2H); ^{13}C NMR (100 MHz, [D_6]DMSO): δ (ppm)150.6, 150.4, 148.4, 146.9, 145.6, 126.7, 125.7, 123.9, 114.7;FT-IR (ATR): 3368, 3328, 3151, 1660, 1601, 1571, 1384, 1332, 1138, 824, 703 cm^{-1}; HRMS (ESI): *m/z* calcd. for $C_{11}H_{10}N_4[M+H]^+$: 199.0983; found : 199.0982.

Synthesis of (*E*)-4-((4-aminophenyl)diazenyl)benzamide (Am5):

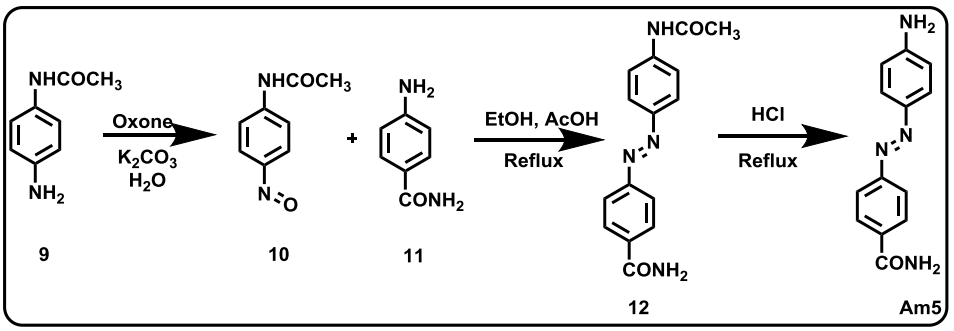

In a round bottom flask, aqueous solution of oxone (4.6 eq., 9.4 g) with K_2CO_3 (2.6 eq., 2.4 g) was taken and stirred at room temperature. To this, an aqueous solution of 4-aminoacetanilide **9** (1 eq., 1 g) was quickly added. A green solid product of nitroso compound **10** was obtained, which was filtered off after half an hour. The wet solid product was directly utilised for the next step. Mill's method was adopted for a condensation reaction between the crude nitroso compound **10** formed in first step (1 eq, 1.068 g) and 4-aminobenzamide **11** (1 eq, 0.976 g). This was performed by refluxing these reactants in EtOH (10 ml) and acetic acid (5 ml) for 7 hrs and monitored by TLC. After completion of the reaction, the hydrolysis step was continued by refluxing the *in situ* generated amide product **11** under conc. HCl condition for 3 hrs. After completion of the reaction, the reaction mixture cooled down to room temperature and was neutralised by adding aqueous sodium bicarbonate solution. The product was extracted using ethyl acetate, the organic layer was washed with brine solution, and evaporated to dryness. The crude product was then subjected to purification by column chromatography.

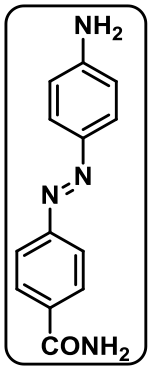

(*E*)-4-((4-aminophenyl)diazenyl)benzamide (**Am5**): Orange solid, 97% yield. ^{1}H NMR (400 MHz, [D$_6$]DMSO): δ (ppm) 8.08 (s, 1H), 7.99 (d, J = 8.4 Hz, 2H), 7.77 (d, J = 8.4 Hz, 2H), 7.69 (d, J = 8.7 Hz, 2H), 7.45 (s, 1H), 6.68 (d, J = 8.7 Hz, 2H), 6.25 (s, 2H); ^{13}C-NMR (100 MHz, [D$_6$]DMSO): δ (ppm) 167.6, 154.2, 153.5, 143.0, 134.4, 128.7, 125.8, 121.5, 113.6; FT-IR (neat): 3392, 3327, 3233, 2919, 1697, 1593, 1422, 1269, 1136, 1094 cm^{-1}; HRMS (ESI): *m/z* calcd. for $C_{13}H_{12}N_4O[M+H]^+$: 241.1089; found : 241.1079

Synthesis of 4-azido azoarene and azoheteroarene derivatives

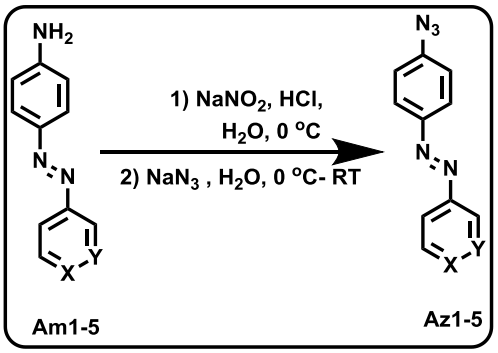

General Procedure: In a round-bottom flask, amines **Am1-5** (10 mmol) was dissolved in HCl (6 N, 10 mL) in an ice bath. $NaNO_2$ (15 mmol) dissolved in 25 mL water was dropwise added. The reaction mixture was stirred for 30 min. Sodium azide (40 mmol) dissolved in 50 mL water was dropwise added. Afterwards, the reaction mixture was stirred for another 2–4 hours at room temperature and followed by TLC. Then, the mixture was extracted with ethyl acetate and the combined organic extracts were washed with H_2O, dried over anhydrous Na_2SO_4, filtered, and concentrated in vacuo and then subjected to purification by column chromatography using neutral alumina.

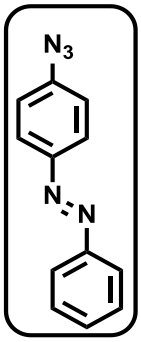

(*E*)-1-(4-azidophenyl)-2-phenyldiazene (**Az1**): Orange solid, 98% yield. ^{1}H NMR (400 MHz, $CDCl_3$): δ (ppm) 7.95 (d, J = 8.3 Hz, 2H), 7.90 (d, J = 7.9 Hz, 2H), 7.54-7.46 (m, 3H), 7.16 (d, J = 8.3 Hz, 2H); ^{13}C NMR (100 MHz, $CDCl_3$): δ (ppm)152.7, 149.9, 142.7, 131.2, 129.3, 124.7, 122.9, 119.7; FT-IR (ATR): 2922, 2115, 1593, 1579, 1494, 1287, 1129, 838, 764, 687,543 cm^{-1}.

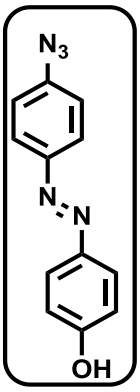

(*E*)-4-((4-azidophenyl)diazenyl)phenol (**Az2**): Orange solid, 97% yield. ^{1}H NMR (400 MHz, $CDCl_3$): δ (ppm)7.89 (d, J = 8.3, 2H), 7.86 (d, J = 8.4 Hz, 2 H), 7.14 (d, J = 8.3 Hz, 2H), 6.95 (d, J = 8.3 Hz, 2H), 5.63 (s, 1H); ^{13}C-NMR (100 MHz, $CDCl_3$): δ(ppm)159.1, 150.0, 146.9, 142.0, 125.1, 124.4, 119.7, 116.0; FT-IR (ATR): 3424, 2403, 2252, 2115, 1587, 1579, 1471, 1442, 1413, 1386, 1299, 1286, 1223, 1152, 1143, 1129, 1107, 1005, 944, 839, 813, 808, 773, 726, 709, 670 cm^{-}1; HRMS (ESI): *m/z* calcd. for $C_{12}H_9N_5ONa[M+Na]^+$: 262.0705; found : 262.0703.

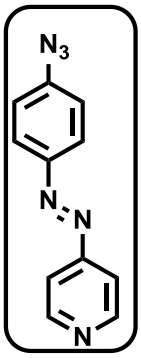

(*E*)-4-((4-azidophenyl)diazenyl)pyridine (**Az3**): Orange solid, 97% yield. ^{1}H NMR (400 MHz, [D_6]DMSO): δ (ppm) 8.81-8.80 (dd, J = 4.6, 1.6 Hz, 2H), 8.01-7.98 (m, 2H), 7.71-7.69 (dd, J = 4.6, 1.6, 2H), 7.20-7.16 (m, 2H); ^{13}C-NMR (100 MHz, [D_6]DMSO): δ (ppm) 157.2, 151.5, 149.6, 144.3, 125.4, 119.9, 116.4; FT-IR (ATR): 2975, 2935, 2134, 2110, 1617, 1471, 1450, 1369, 1272, 1157, 1062, 1015, 975, 956, 950, 909, 814. cm^{-1};HRMS (ESI): *m/z* calcd. for $C_{11}H_8N_6$ $[M+Na]^+$: 247.0708; found : 247.0710.

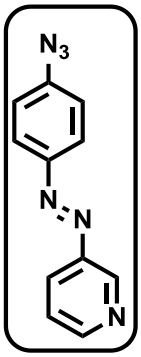

(*E*)-3-((4-azidophenyl)diazenyl)pyridine (**Az4**): Orange solid, 95% yield.^{1}H NMR (400 MHz, [D_6]DMSO): δ (ppm) 9.17 (d, J = 2.1 Hz, 1H), 8.70-8.68 (dd, J = 4.7, 1.5 Hz, 1H), 8.14-8.11 (ddd, J = 8.2, 2.2, 1.6 Hz, 1H), 7.99-7.95 (m, 2H), 7.46-7.42 (ddd, J = 8.2, 4.8, 0.6 Hz, 1H), 7.18-7.15 (m, 2H); ^{13}C NMR (100 MHz, [D_6]DMSO): δ (ppm) 151.8, 149.7, 147.9, 147.5, 143.6, 126.9, 125.0, 124.1, 119.8; FT-IR (ATR): 2920, 2115, 1566, 1486, 1254, 1091, 1023, 834 cm^{-1}; HRMS (ESI): *m/z* calcd. for $C_{11}H_8N_6Na$ $[M+Na]^+$: 247.0708; found : 247.0710.

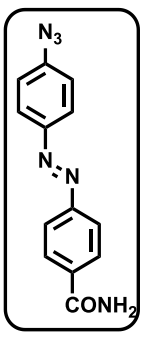

(*E*)-4-((4-azidophenyl)diazenyl)benzamide (**Az5**): Orange solid, 90% yield.^{1}H NMR (400 MHz, [D_6]DMSO): δ (ppm) 8.21-8.18 (m, 2H), 8.00-7.96 (m, 2H), 7.95-7.92 (m, 2H), 7.19-7.15 (m, 2H);^{13}C NMR (100 MHz, [D_6]DMSO): δ (ppm) 166.1, 155.0, 149.7, 143.4, 132.1, 130.6, 125.0, 122.6, 119.7; FT-IR (ATR): 3451, 3185, 2924, 2132,1660, 1596, 1396, 1278, 1123, 863 cm^{-1}; HRMS (ESI): *m/z* calcd for $C_{11}H_8N_6Na$ $[M+Na]^+$: 247.0708; found : 247.0710.

Synthesis of core unit C2:

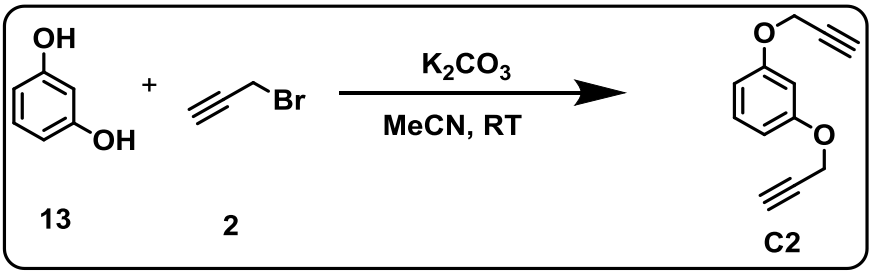

A mixture of resorcinol **13** (1 g, 9.09 mmol) and anhydrous potassium carbonate (5.01 g, 36.4 mmol) in dry acetonitrile (30 mL), was refluxed for 1h and then propargyl bromide **2** (4.37 g, 36.4 mmol) was added to it. The reaction mixture was further refluxed for 4h. After completion of the reaction, the organic solvent was evaporated off under reduced pressure and water was added to it. The reaction mixture was then extracted with $CHCl_3$, washed with water and dried over anhydrous Na_2SO_4. Evaporation of the solvent gave the crude product, which was purified by column chromatography using hexane and ethylacetate as the eluent.

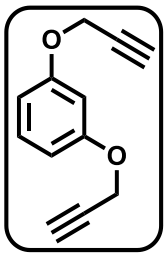

1,3-*bis*(prop-2-yn-1-yloxy)benzene (**C2**): Colourless liquid, 88% yield. ^{1}H NMR (400 MHz, $CDCl_3$): δ (ppm) 7.24-7.19 (m, 1H), 6.62 (d, J = 6.3 Hz, 3H), 4.66 (s, 4H), 2.54 (s, 2H); ^{13}C NMR (100 MHz, $CDCl_3$): δ (ppm) 158.7, 130.0, 107.9, 102.4, 78.5, 75.7, 55.9.

Synthesis of catalysts T1-5 and B1:

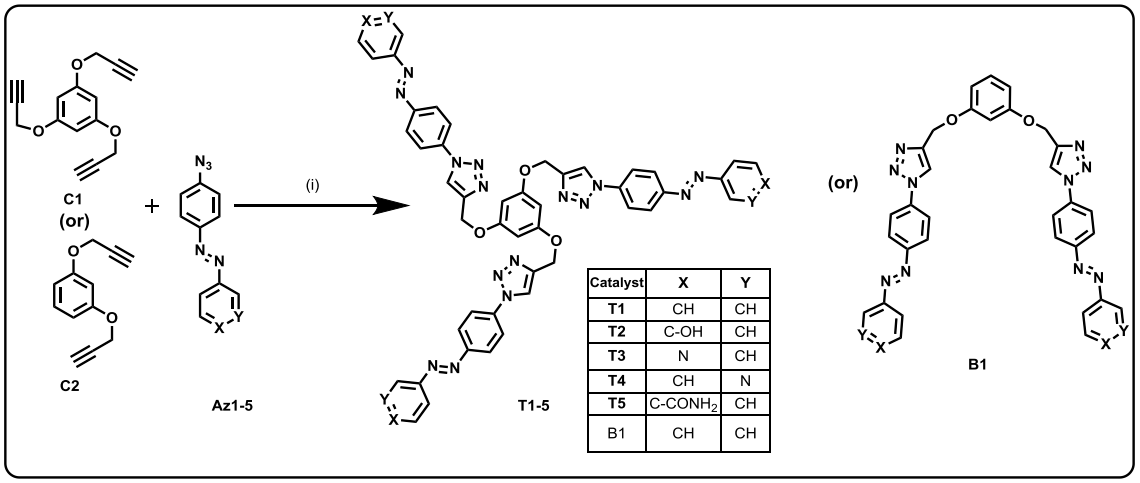

Catalyst	X	Y
T1	CH	CH
T2	C-OH	CH
T3	N	CH
T4	CH	N
T5	C-$CONH_2$	CH
B1	CH	CH

General Procedure: For click chemistry,1,3,5-*tris*(prop-2-yn-1-yloxy)benzene **C1**(1.0 eq for **T1-5**) or 1,3-*bis*(prop-2-yn-1-yloxy)benzene **C2**(1.0 eq for **B1**) was added with the corresponding azides**Az1-5** (3.3 eq for **T1-5** and 2.2 eq. for **B1**) in 5 ml of 1:1 ^{t}BuOH/H_2O mixture. Followed by, the $CuSO_4.5H_2O$ (0.6 eq) and sodium ascorbate (1.2 eq) were added

as an aqueous solution. The reaction was stirred for 3 days at room temperature and followed by TLC. The resulting yellow coloured precipitate was filtered off and was washed three times with H_2O and acetone. The yellow solid product was further purified by column chromatography using DCM:MeOH (95:5) as an eluent. After removing the solvent through rotary evaporator, the final product was dried under vacuum to yield the desired product.

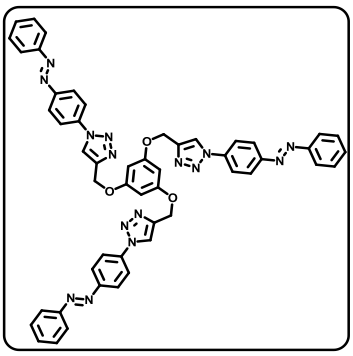

4,4'-(((5-((2-(4-((*E*)-phenyldiazenyl)phenyl)-2*H*-1,2,3-triazol-4-yl)methoxy)-1,3-phenylene)bis(oxy))bis(methylene))bis(1-(4-((*E*)-phenyldiazenyl)phenyl)-1*H*-1,2,3-triazole) (**T1**): Yellow solid, mp= 250-253 °C, 70% yield. ^{1}H NMR (400 MHz, [D_6]DMSO): δ (ppm) 9.10 (s, 3H), 8.17 (d, J = 8.8 Hz, 6H), 8.09 (d, J = 8.8 Hz, 6H), 7.94-7.92 (m, 6H), 7.62-7.60 (m, 9H), 6.49 (s, 3H), 5.28 (s, 6H); ^{13}C NMR (100 MHz, [D_6]DMSO): δ(ppm) 159.9, 151.9, 151.3, 144.1, 138.2, 132.0, 129.6, 124.2, 123.0, 122.8, 120.9, 94.9, 52.0; FT-IR (ATR): 2923, 2852, 1597, 1502, 1384, 1138, 863, 617 cm^{-1}; HRMS (MALDI): *m/z* calcd. for $C_{51}H_{39}N_{15}O_3$ Na[M+Na]$^+$: 932.3258; found : 932.3243.

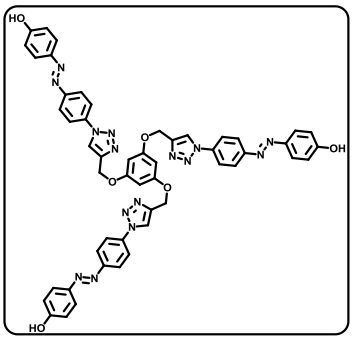

4,4'-((1*E*,1'*E*)-(((((5-((2-(4-((*E*)-(4-hydroxyphenyl)diazenyl)phenyl)-2*H*-1,2,3-triazol-4-yl)methoxy)-1,3-phenylene)bis(oxy))bis(methylene))bis(1*H*-1,2,3-triazole-4,1-diyl))bis(4,1-phenylene))bis(diazene-2,1-diyl))diphenol (**T2**): Orange solid, mp= 260-262°C, 80 %yield. ^{1}H NMR (400 MHz, [D_6]DMSO):δ (ppm) 10.42 (s, 3H), 9.08 (s, 3H), 8.12 (d, J = 8.4 Hz, 6H), 8.00 (d, J = 8.3 Hz, 6H), 7.84 (d, J = 8.3 Hz, 6H), 6.96 (d, J = 8.5, 6H), 6.49 (s, 3H), 5.27 (s, 6H); ^{13}C NMR (100 MHz, [D_6]DMSO): δ(ppm) 161.4, 159.9, 151.6, 145.2, 144.0, 137.4, 125.2, 123.6, 122.9, 120.9, 116.1, 94.9, 61.1; FT-IR (ATR): 3424, 2922, 2856, 1596, 1508,1386, 1150, 842, 617 cm^{-1}; HRMS (MALDI): *m/z* calcd. for $C_{51}H_{39}N_{15}O_6$ Na[M+Na]$^+$: 980.3106; found : 980.3137.

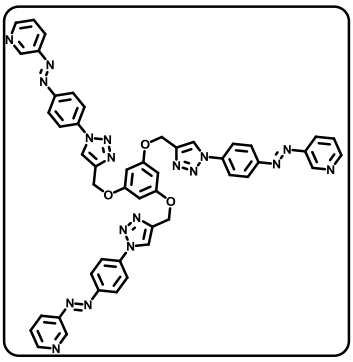

4,4'-((1*E*,1'*E*)-(((((5-((2-(4-((*E*)-pyridin-4-yldiazenyl)phenyl)-2*H*-1,2,3-triazol-4-yl)methoxy)-1,3-phenylene)bis(oxy))bis(methylene))bis(1*H*-1,2,3-triazole-4,1-diyl))bis(4,1-phenylene))bis(diazene-2,1-diyl))dipyridine (**T3**): Orange solid, mp= 254-255°C, 70 %yield.^{1}H NMR (400 MHz, [D_6]DMSO): δ (ppm)9.13 (s, 3H), 8.23-8.16 (m, 14H), 7.93 (br, 10H), 6.49 (s, 3H), 5.28 (s, 6H); FT-IR (ATR): 2922, 2851, 1600, 1583, 1509, 1194, 849, 705 cm^{-1};HRMS (ESI): *m/z* calcd. for $C_{48}H_{36}N_{18}O_3$ $[M+Na]^+$: 935.3116; found : 935.4329.

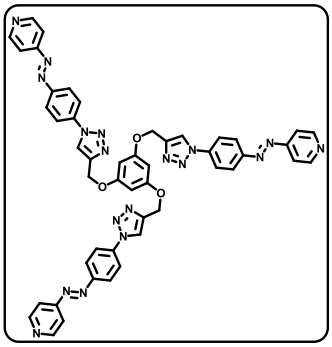

3,3'-((1*E*,1'*E*)-(((((5-((2-(4-((*E*)-pyridin-3-yldiazenyl)phenyl)-2*H*-1,2,3-triazol-4-yl)methoxy)-1,3-phenylene)bis(oxy))bis(methylene))bis(1*H*-1,2,3-triazole-4,1-diyl))bis(4,1-phenylene))bis(diazene-2,1-diyl))dipyridine (**T4**): Orange solid, mp= 258-259°C, 75 %yield.^{1}H NMR (400 MHz, [D_6]DMSO):δ (ppm) 9.12 (s, 3H), 8.22-8.11 (m, 21H), 7.67 (s, 3H), 6.49 (s, 3H), 5.28 (s, 6H); FT-IR (ATR): 2921, 2851, 1600, 1583, 1509, 1194, 848, 704 cm^{-1};HRMS (ESI): *m/z* calcd. for $C_{48}H_{36}N_{18}O_3$ $[M+Na]^+$: 935.3116; found : 935.4329.

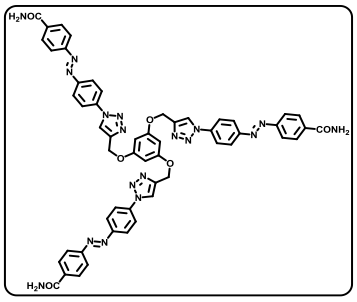

4,4'-((1*E*,1'*E*)-(((((5-((2-(4-((*E*)-(4-carbamoylphenyl)diazenyl)phenyl)-2*H*-1,2,3-triazol-4-yl)methoxy)-1,3-phenylene)bis(oxy))bis(methylene))bis(1*H*-1,2,3-triazole-4,1-diyl))bis(4,1-phenylene))bis(diazene-2,1-diyl))dibenzamide (**T5**): Orange solid, mp= 278-280°C, 70% yield.^{1}HNMR (400 MHz, [D_6]DMSO): δ (ppm)9.56 (s, 6H), 9.09 (s, 3H), 8.21-8.01 (dd, J = 61.8, 9.7 Hz,24H), 6.12 (s, 3H), 5.21 (s, 6H);^{13}C NMR (100 MHz, [D_6]DMSO): δ (ppm) 167.6, 153.7, 149.5, 143.5, 136.8, 129.3, 129.2, 125.1, 124.8, 123.0, 122.7, 121.4, 120.6, 31.7;FT-IR (ATR): 3451, 3185, 2923, 1658, 1596, 1410, 1302, 1194, 848, 704 cm^{-1};HRMS

(ESI): *m/z* calcd. for $C_{54}H_{42}N_{18}O_6$ $[M+Na]^+$: 1061.3433; found : 1061.4735.

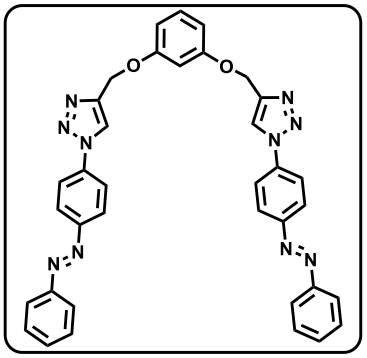

1,3-bis((1-(4-((*E*)-phenyldiazenyl)phenyl)-1*H*-1,2,3-triazol-4-yl)methoxy)benzene (**B1**): Orange solid, 95% yield.^{1}H NMR (400 MHz, [D_6]DMSO): δ (ppm) 9.11 (s, 2H), 8.19 (d, *J* = 8.9 Hz, 4H), 8.11 (d, *J* = 8.8 Hz, 1H), 7.95-7.93 (m, 4H), 7.65-7.62 (m, 6H), 7.26 (t, 1H), 6.84 (s, 1H), 6.74-6.71 (dd, , *J* = 8.2, 2.12 Hz), 5.28 (s, 4H) ; ^{13}C NMR (100 MHz, [D_6]DMSO): δ (ppm) 159.7, 152.3, 151.8, 150.4, 144.7, 138.7, 136.3, 130.0,124.6, 123.5, 123.2, 121.4, 108.0, 61.5, 61.49; FT-IR (ATR): 2923, 1675, 1585, 1483, 1362, 1135, 1019 cm^{-1}; HRMS (ESI): *m/z* calcd. for $C_{36}H_{28}N_{10}O_2[M+H]^+$: 633.2475; found : 633.2454.

Synthesis of DMAP-TrCl adduct (A1):

DMAP **14** (1.0 equiv.) and tritylchloride **15** (1.1 equiv.) were mixed in a flame dried Schlenk flask. Dichloromethane (40mL) was dropwise added over 30 minutes. The resulting solution was stirred for 3h at rt. Ethylacetate (200mL) was then added dropwise over 1h. The inhomogeneous reaction mixture was kept in a refrigerator for 10 minutes to obtain maximum precipitation of the salt. The products were filtered off, washed with dry ethylacetate (30mL) and dried at high vacuum to obtain the desired product trityl-DAMP-salt as a white semi-crystalline solid (It was found to be a DCM-adduct with 0.75 eq. of dichloromethane).

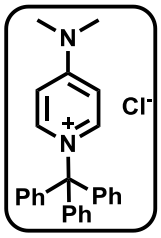

4-(Dimethylamino)-1-tritylpyridin-1-ium chloride (**A1**): White solid, mp= 116-118 °C, 98% yield. ^{1}H NMR (400 MHz, $CDCl_3$): δ (ppm) 7.91-7.87 (m, 2H), 7.40-7.35 (m, 9H), 7.21-7.18 (m, 2H), 7.14-7.10 (m, 6H), 3.38 (s, 6H)

General procedure for the reactions:

DMAP-TrCl·0.75CH_2Cl_2 adduct **A1** (1.0equiv.) and catalyst **T1-5** or **B1** (0.05 equiv.) were suspended in DCM (0.5mL) in a 10mL screw cap vial. The corresponding amine or alcohol (**R1-4**) (2.0equiv.) was added. The resulting mixture was stirred for 9 h at rt. Purification of the crude mixture by column chromatography on deactivated silica provided the desired *N*- or *O*-tritylated product. (The catalyst may be used either as a native solid or photoswitched with 365 nm irradiation after dissolved in any of the solvents; For uncatalyzed reactions, the reaction procedures were the same except the addition of the catalyst).

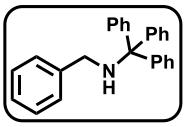

***N*-Benzyl-1,1,1-triphenylmethanamine** (**P1**): White solid, mp= 103-106 °C, 85% yield. ^{1}H NMR (400 MHz, $CDCl_3$): δ (ppm) 7.59-7.57 (d, *J*= 8 Hz, 6H), 7.43-7.20 (m, 14H), 3.35 (s, 2H); ^{13}C NMR (100 MHz, [D_6]DMSO): δ(ppm) 146.1, 141.0, 128.4, 128.2, 127.8, 127.6, 126.5, 126.2, 70.6, 47.4.

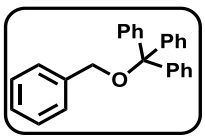

((Benzyloxy)methanetriyl)tribenzene (**P2**): White solid, 65% yield. ^{1}H NMR (400 MHz, $CDCl_3$): δ (ppm) 7.55-7.53 (d, *J*= 7.5 Hz, 6H), 7.43-7.24 (m, 14H), 4.20 (s, 2H); ^{13}C NMR (100 MHz, [D_6]DMSO): δ(ppm) 144.2, 139.3, 128.9, 128.4, 128.0, 127.21, 127.15, 127.1, 87.1, 66.0.

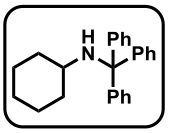

***N*-Tritylcyclohexanamine** (**P3**): White solid, mp= 126-128 °C, 55% yield. ^{1}H NMR (400 MHz, $CDCl_3$): δ (ppm) 7.61-7.59 (m, 6H), 7.30-7.26 (m, 6H), 7.21-7.17 (m, 3H), 2.32-2.26 (m, 1H), 1.60 (s, 1H), 1.52-1.42 (m, 4H), 1.24-1.21(m, 2H), 1.0-0.85 (m, 4H); ^{13}C NMR (100 MHz, [D_6]DMSO): δ(ppm) 147.6, 128.9, 127.8, 126.2,71.4, 52.2, 35.9, 26.1, 25.8.

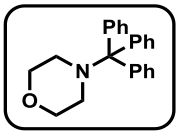

***N*-Tritylmorpholine** (**P4**): White solid, mp= 185-187 °C, 35% yield. ^{1}H NMR (400 MHz, $CDCl_3$): δ (ppm) 7.40 (brs, 6H), 7.33-7.29(m, 6H), 7.20-7.17 (m, 3H), 3.73 (s, 4H), 2.67 (brs, 1H), 1.49-1.23 (m, 3H); ^{13}C NMR (100 MHz, [D_6]DMSO): δ(ppm) 129.0, 128.9, 127.7, 126.1,76.5, 66.6, 48.4.

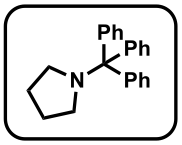

***N*-Tritylpyrrolidine** (**P5**): White solid, mp= 124-126 °C, 54% yield. ^{1}H NMR (400 MHz, [D_6]DMSO): δ (ppm) 7.41-7.39 (m, 6H), 7.31-7.27 (m, 6H), 7.20-7.15 (m, 3H), 2.21 (s, 4H), 1.57 (s, 4H); ^{13}C NMR (100 MHz, [D_6]DMSO): δ(ppm) 142.5, 128.9, 127.4, 126.0,73.9,

45.8, 21.9.

4.8 References

[1] K. Kinbara and T. Aida, *Chem. Rev.,* 2005, **105**, 1377−1400.

[2] a) V. Balzani, M. Venturi, A. Credi, *Molecular Devices and Machines*, Wiley-VCH: Weinheim, Germany, **2003**; b) S. Erbas-Cakmak, D. A. Leigh, C. T. McTernan, A. L. Nussbaumer, *Chem. Rev.* **2015**, *115*, 10081–10206.

[3] a) R. Dorel, B. L. Feringa, *Chem. Commun.* **2019**, *55*, 6477−6486; b) R. S. Stoll, S. Hecht, *Angew. Chem., Int. Ed.* **2010**, *49*, 5054−5075; c) R. Göstl, A. Senf, S. Hecht, *Chem. Soc. Rev.* **2014**, *43*, 1982−1996; d) B. M. Nielson, C. W. Bielawski, *ACS Catal.* **2013**, *3*, 8, 1874−1885; e) E. M. Broderick, N. Guo, C. S. Vogel, C. Xu, J. Sutter, J. T. Miller, K. Meyer, P. Mehrkhodavandi, P. L. Diaconescu, *J. Am. Chem. Soc.* **2011**, *133*, 9278–9281.

[4] a) R. Cacciapaglia, S. Di Stefano, L. Mandolini, *J. Am. Chem. Soc.* **2003**, *125*, 2224–2227; b) V. Blanco, D. A. Leigh, V. Marcos, *Chem. Soc. Rev.* **2015**, *44*, 5341−5370; c) V. Blanco, A. Carlone, K. D. Hänni, D. A. Leigh, B. Lewandowski, *Angew. Chem., Int. Ed.* **2012**, *51*, 5166–5169; d) M. Schmittel, *Chem. Commun.* **2015**, *51*, 14956−14968; e) H. J. Yoon, J. Heo, C. A. Mirkin, *J. Am. Chem. Soc.* **2007**, *129*, 14182–14183; f) C. K. A. Gregson, V. C. Gibson, N. J. Long, E. L. Marshall, P. J. Oxford, A. J. P. White, *J. Am. Chem. Soc.* **2006**, *128*, 7410–7411; g) V. Blanco, D. A. Leigh, U. Lewandowska, B. Lewandowski, V. Marcos, *J. Am. Chem. Soc.* **2014**, *136*, 15775–15780.

[5] a) S. P. Ihrig, F. Eisenreich, S. Hecht, *Chem. Commun.* **2019**, *55*, 4290−4298; b) M. Szewczyk, G. Sobczak, V. Sashuk, *ACS Catal.* **2018**, *8*, 2810−2814; c) Y. Liu, T. Pan, Y. Fang, N. Ma, S. Qiao, L. Zhao, R. Wang, T. Wang, X. Li, X. Jiang, F. Shen, Q. Luo, J. Liu, *ACS Catal.* **2017**, *7*, 6979−6983; d) S. Neri, S. G. Martin, C. Pezzato, L. J. Prins, *J. Am. Chem. Soc.* **2017**, *139*, 1794−1797; e) S. F. Pizzolato, B. S. L. Collins, T. van Leeuwen, B. L. Feringa, *Chem. –Eur. J.* **2017**, *23*, 6174−6184.

[6] a) F. Würthner, J. Rebek, *J. Chem. Soc., Perkin Trans*. 2 **1995**, 1727–1734; b) F. Eisenreich, M. Kathan, A. Dallmann, S. P. Ihrig, T. Schwaar, B. M. Schmidt, S. Hecht, *Nat. Catal.* **2018**, *1*, 516-522; c) R. S. Stoll, M. V. Peters, A. Kühn, S. Heiles, R. Goddard, M. Bühl, C. M. Thiele, S. Hecht, *J. Am. Chem. Soc.* **2009**, *131*, 357–367; d) L. O-. Planes, C. R-. Escrich, M. A. Pericàs, *Org. Lett.* **2014**, *16*, 1704–1707; e) J. Luo, S. Samanta, M. Convertino, N. V. Dokholyan, A. Deiters, *ChemBioChem* **2018**, *19*, 2178-2185.

[7] a) M. D. Visco, J. Attard, Y. Guan, A. E. Mattson, *Tett. Lett.* **2017**, *58*, 2623−2628; b) W.-S. Lee, A. Ueno, *Macromol. Rapid Commun.* **2001**, *22*, 448–450; c) M. V. Peters, R. S. Stoll, A.

Kühn, S. Hecht, *Angew. Chem., Int. Ed.* **2008**, *47*, 5968–5972; d) D. Wilson, N. R. Branda, *Angew. Chem., Int. Ed.* **2012**, *51*, 5431–5434; e) Y. Wei, S. Han, J. Kim, S. Soh, B. A. Grzybowski, *J. Am. Chem. Soc.* **2010**, *132*, 11018–11020.

[8] a) B. M. Neilson, C. W. Bielawski, *J. Am. Chem. Soc.* **2012**, *134*, 12693–12699; b) B. M. Neilson, C.W. Bielawski, *Chem. Commun.* **2013**, *49*, 5453–5455; c) A. Nojiri, N. Kumagai, M. Shibasaki, *Chem. Commun.* **2013**, *49*, 4628–4630.

[9] a) J. Wang, B. L. Feringa, *Science* **2011**, 331, 1429–1432; b) R. S. Stoll, S. Hecht, *Org. Lett.* **2009**, *11*, 4790–4793; c) L. Osorio-Planes, C. Rodríguez-Escrich, M. A. Pericàs, *Org. Lett.* **2014**, *16*, 1704–1707.

[10] a) Y. Nishikawa, *Tet. Lett.* **2018**, *59*, 216–233; b) G. Hirata, H. Maeda, *Org. Lett*. **2018**, *20*, 2853–2856; c) C. Zhao, C. A. Sojdak, W. Myint, D. Seidal, *J. Am. Chem. Soc.* **2017**, *139*, 10224–10227; d) A. Bosmani, S. A. Pujari, C. Besnard, L. Guenee, A. I. Poblador-Bahamonde, J. Lacour, *Chem. -Eur. J.* **2017**, *23*, 8678–8684; e) S. Benz, J. Lopez-Andarias, J. Mareda, N. Sakai, S. Matile, *Angew. Chem., Int. Ed.* **2017**, *56*, 812–815; f) O. G. Mancheño, S. Asmus, M. Zurro, T. Fischer, *Angew. Chem., Int. Ed.* **2015**, *54*, 8823–8827.

[11] a) D. D. Ford, D. Lehnherr, C. R. Kennedy, E. N. Jacobsen, *J. Am. Chem. Soc.* **2016**, *138*, 7860–7863; b) M. Wasa, R. Y. Liu, S. P. Roche, E. N. Jacobsen, *J. Am. Chem. Soc.* **2014**, *136*, 12872–12875; c) S. Asmus, S. Beckendorf, M. Zurro, C. Mueck-Lichtenfeld, R. Froehlich, O. G. Mancheño, *Chem. Asian J.* **2014**, *9*, 2178–2186.

[12] a) M. Zurro, S. Asmus, J. Bamberger, S. Beckendorf, O. G. Mancheño, *Chem. -Eur. J.* **2016**, *22*, 3785–3793; b) Q-N. Duong, L. Schifferer, O. G. Mancheño, *Eur. J. Org. Chem.* **2019**, *31*, 5452–5461; c) T. Fischer, J. Bamberger, O. G. Mancheno, *Org. Biomol. Chem.* **2016**, *14*, 5794-5802; d) S. Beckendorf, S. Asmus, C. Mueck-Lichtenfeld, O. G. Mancheño, *Chem. – Eur. J.* **2013**, *19*, 1581-1585.

[13] a) K. Eichstaedt, J. Jaramillo-Garcia, D. A. Leigh, V. Marcos, S. Pisano, T. A. Singleton, *J. Am. Chem. Soc.* **2017**, *139*, 9376–9381; b) Y. Liu, W. Zhao, C-H. Chen, A. H. Flood, *Science* **2019**, *365*, 159–161.

[14] a) S. Devi, A. K. Gaur, D. Gupta, M. Saraswat, S. Venkataramani, *ChemPhotoChem* **2018**, *2*, 806–810; b) S. Devi, I. Bala, S. P. Gupta, P. Kumar, S. K. Pal, S. Venkataramani, *Org. Biomol. Chem.* **2019**, *17*, 1947–1954.

[15] V. V. Rostovtsev, L. G. Green, V. V. Fokin, K. B. Sharpless, *Angew. Chem., Int. Ed.* **2002**, *41*, 2596–2599.

[16] Different wavelengths have been tried for the reverse isomerization steps for all the catalysts **T1-5**. However, at 405 nm irradiation, we obtained a maximum conversion in the reverse photoisomerization step. Indeed, the conversion has limits due to attainment of a photostationary equilibrium.

[17] Surprisingly the uncatalyzed tritylation of $BzNH_2$ reactions in DCM and DMSO led to moderate product formation. Indeed, similar observation was also reported in ref. 10b in THF as a solvent. However, under identical conditions if two reactions have been executed in parallel, we observed two times higher yields for the reaction catalysed by native state compared to that of photoswitched state of **T1**.

[18] a) S. M. Taimoory, K. Twum, M. Dashti, F. Pan, M. Lahtinen, K. Rissanen, R. Puttreddy, J. F. Trant, N. K. Beyeh, *J. Org. Chem.* **2020**, *9*, 5884–5894; b) N. A. Tcyrulnikov, R. Varadharajan, A. A. Tikhomirova, M. Pattabiraman, V. Ramamurthy, R. M. Wilson, *J. Org. Chem.* **2019**, *84*, 8759−8765; c) R. Dutta, S. Samala, H. Jo, K. M. Ok, C.- H. Lee, *J. Org. Chem.* **2019**, *84*, 6851−6857.

Appendix 4A

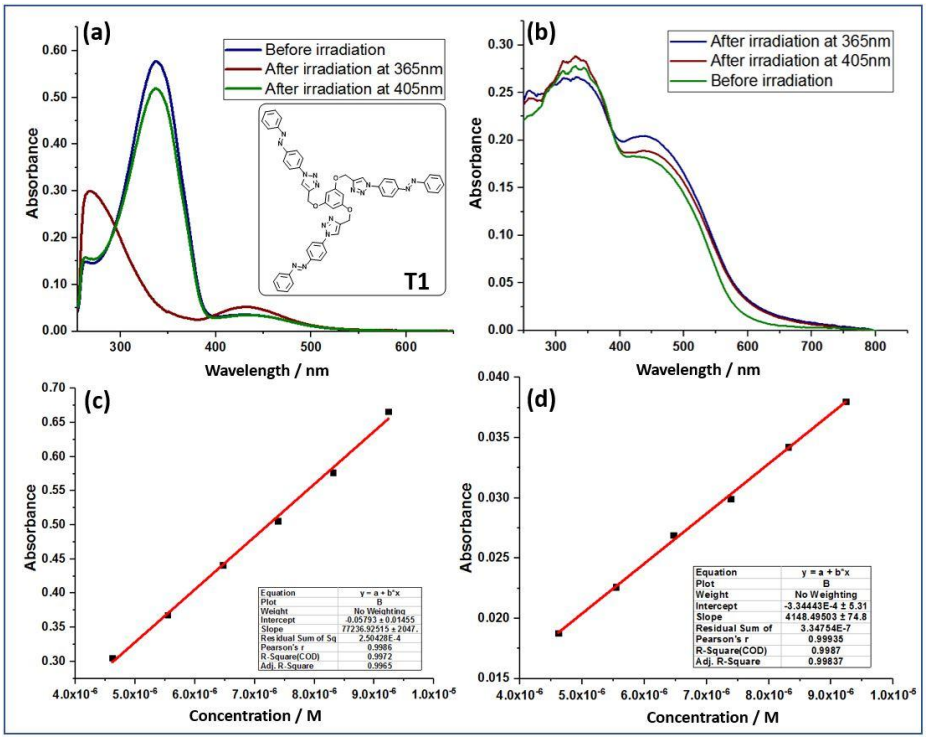

Figure 4A.1 UV-Vis spectroscopic data of **T1**: (a) Photoswitching studies performed in DMSO (9 μM); (b) Photoswitching studies performed in KBr medium; Estimation of molar absorption coefficient for (c) π–π* absorption maxima and (d) n–π* absorption maxima.

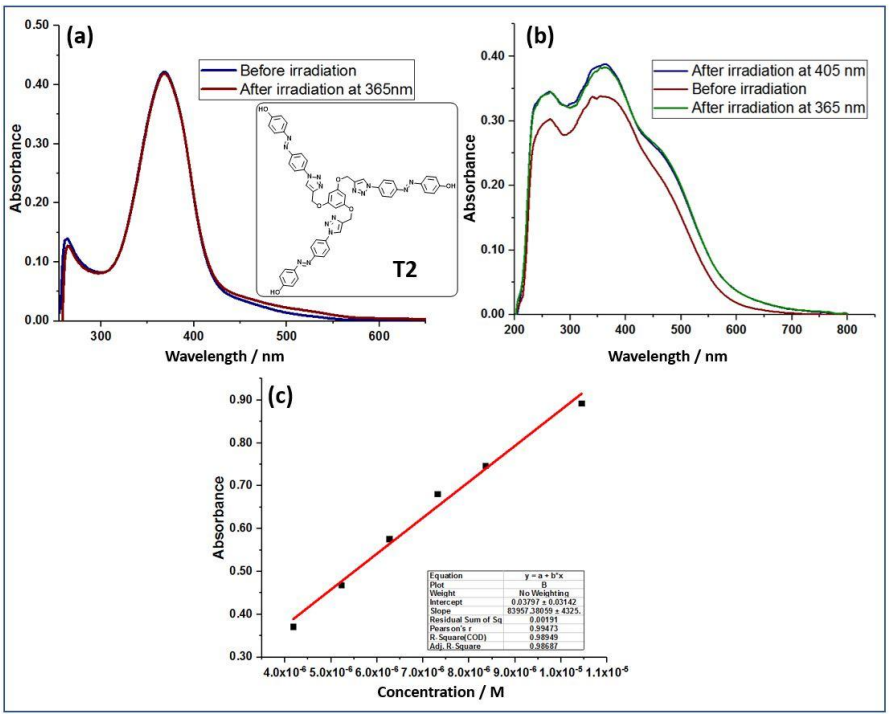

Figure 4A.2 UV-Vis spectroscopic data of **T2**: (a) Photoswitching studies performed in DMSO (10 μM); (b) Photoswitching studies performed in KBr medium; Estimation of molar absorption coefficient for (c) π–π* absorption maxima and (d) n–π* absorption maxima.

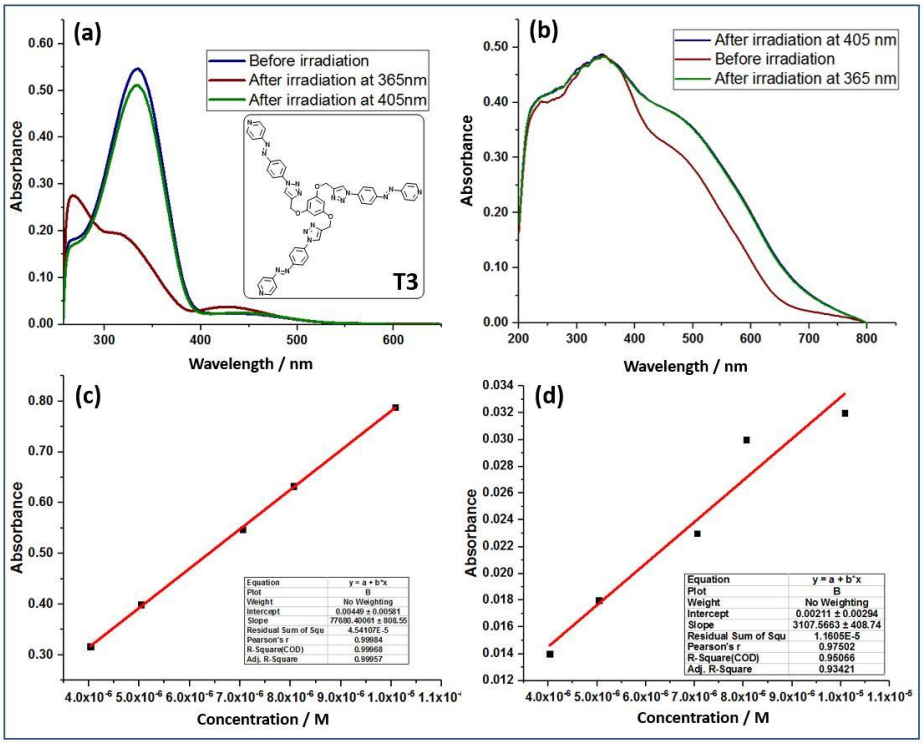

Figure 4A.3 UV-Vis spectroscopic data of **T3**: (a) Photoswitching studies performed in DMSO (10 μM); (b) Photoswitching studies performed in KBr medium; Estimation of molar absorption coefficient for (c) π–π* absorption maxima and (d) n–π* absorption maxima.

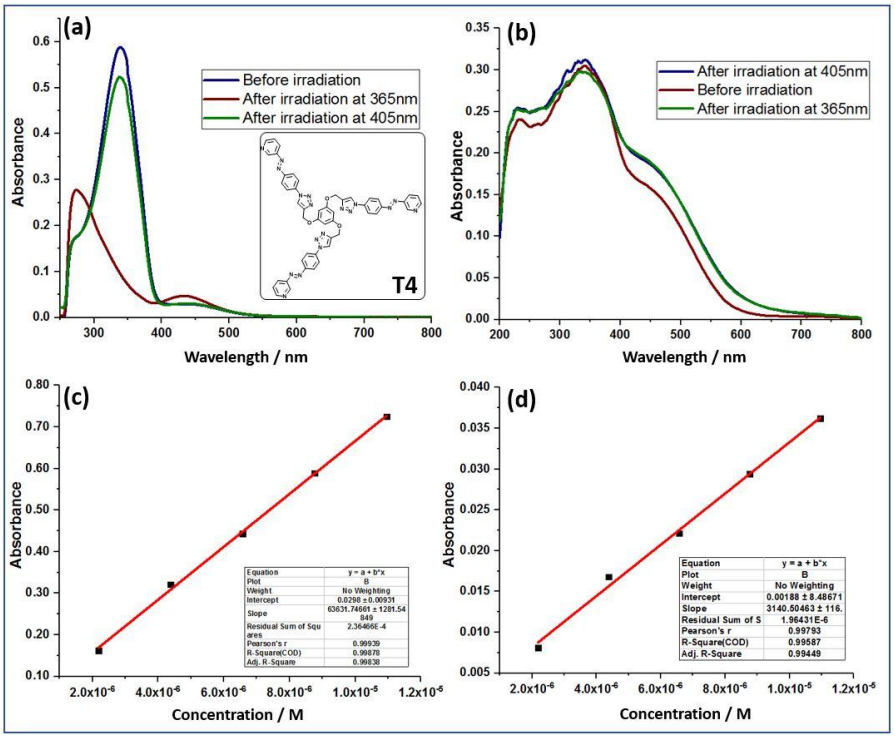

Figure 4A.4 UV-Vis spectroscopic data of **T4**: (a) Photoswitching studies performed in DMSO (11 μM); (b) Photoswitching studies performed in KBr medium; Estimation of molar absorption coefficient for (c) π–π* absorption maxima and (d) n–π* absorption maxima.

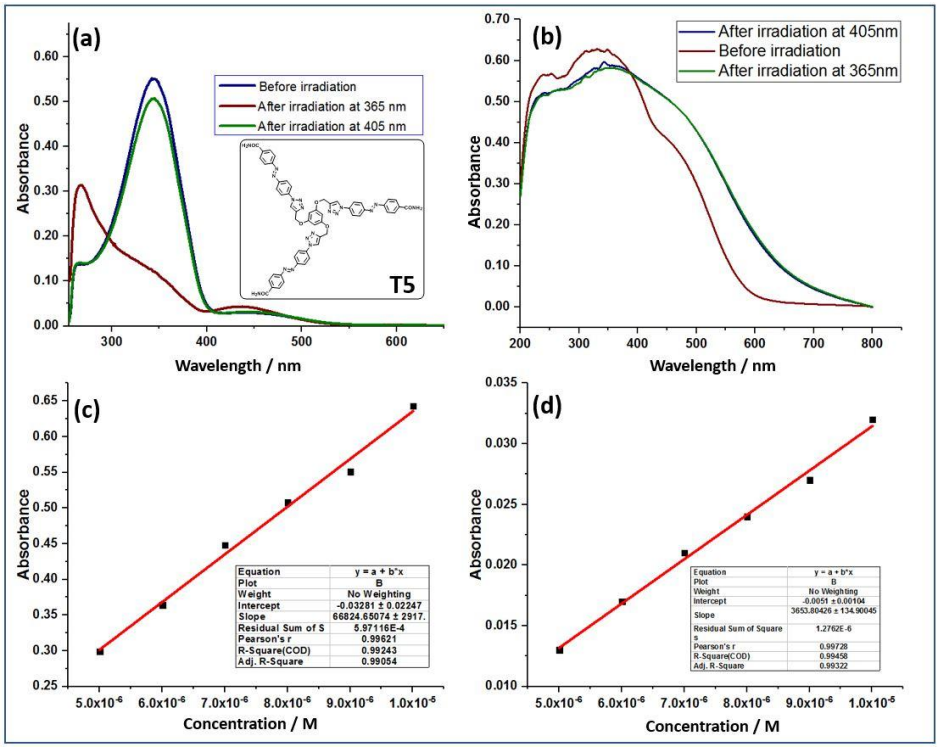

Figure 4A.5 UV-Vis spectroscopic data of **T5**: (a) Photoswitching studies performed in DMSO (10 μM); (b) Photoswitching studies performed in KBr medium; Estimation of molar absorption coefficient for (c) π–π* absorption maxima and (d) n–π* absorption maxima.

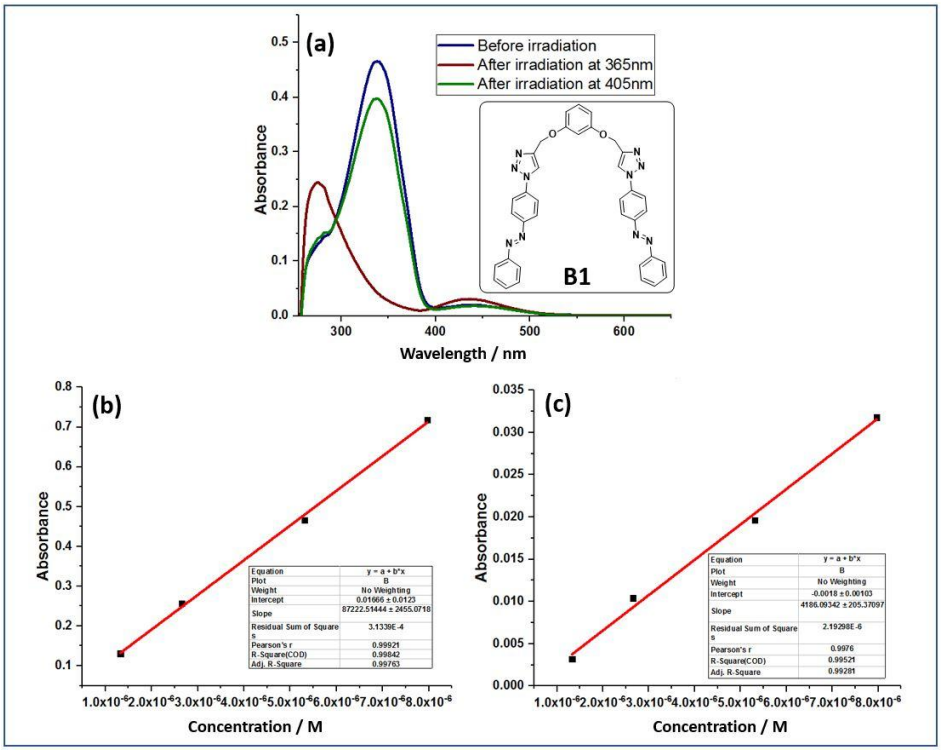

Figure 4A.6 UV-Vis spectroscopic data of **B1**: (a) Photoswitching studies performed in DMSO (13 μM); Estimation of molar absorption coefficient for (b) π–π* absorption maxima and (c) n–π* absorption maxima.

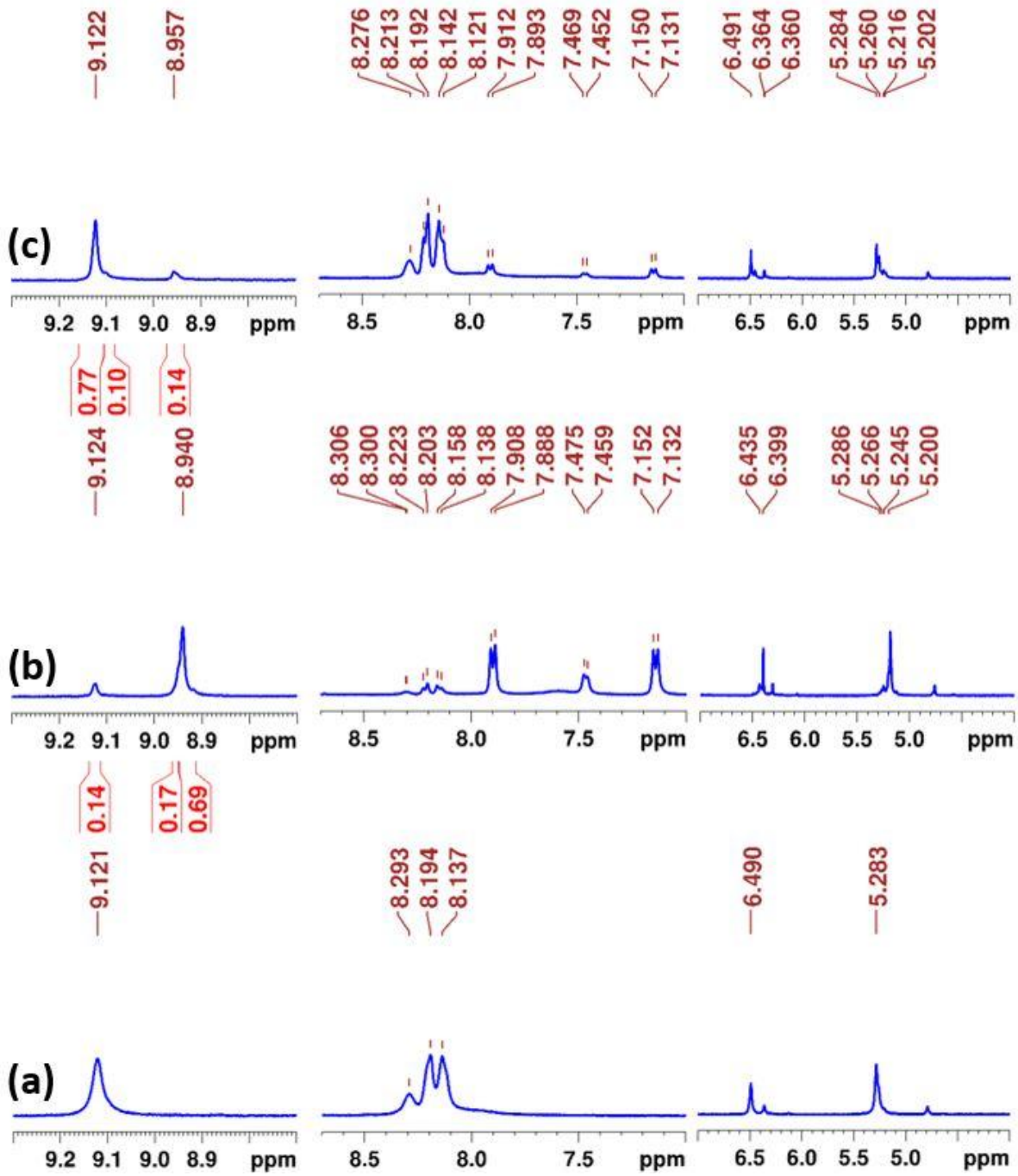

Figure 4A.7 Photoswitching in catalyst **T4**. ^{1}H-NMR spectral data ([D_6]DMSO, 11 mM): (a) Before irradiation; (b) After irradiation at 365 nm; (c) After irradiation at 405 nm. (The PSS compositions have been estimated using the normalized integral values corresponding to triazole-CH signals).

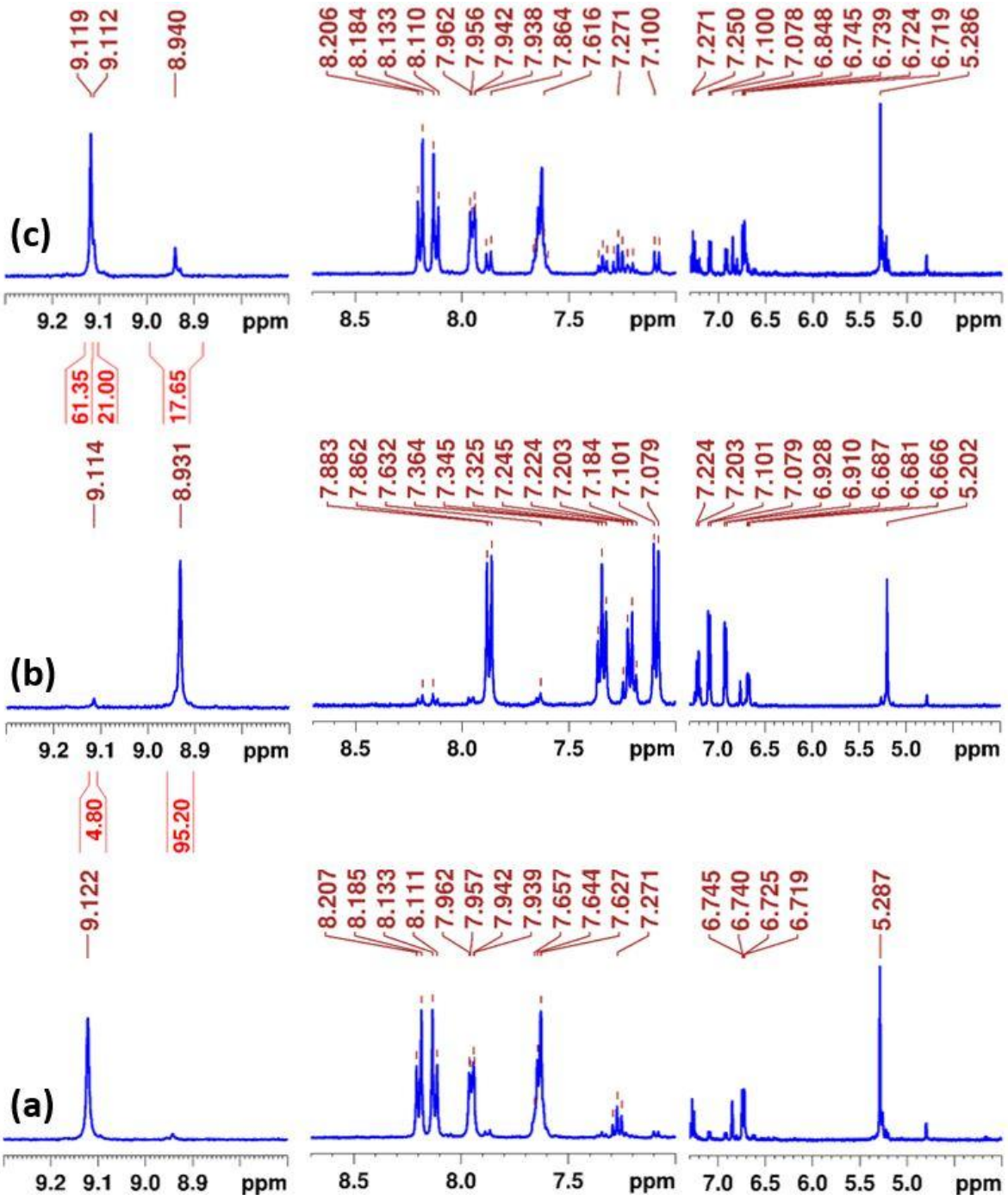

Figure 4A.8 Photoswitching in catalyst **B1**. ^{1}H-NMR spectral data ([D_6]DMSO, 13 mM): (a) Before irradiation; (b) After irradiation at 365 nm; (c) After irradiation at 405 nm. (The PSS compositions have been estimated using the normalized integral values corresponding to triazole-CH signals).

Appendix 4B

Reverse thermal isomerization kinetics data

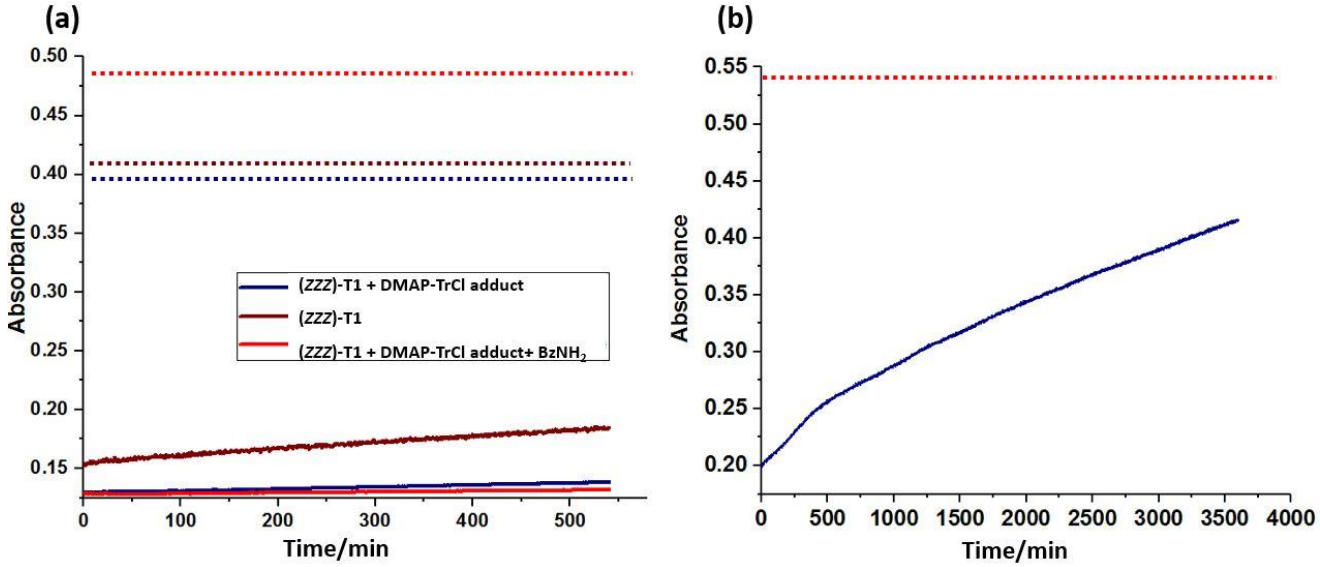

Figure 4B.1 Kinetics profiles depicting the thermal stability of photoisomerized state (*ZZZ*) of the catalyst **T1** (a) up to 9 h (the optimized reaction time) using UV-Vis spectroscopy in DMSO; The dotted lines indicate the absorption maxima due to the ***EEE*-T1** under the respective conditions (prior to irradiation at 365 nm); (b) up to 60 h (The dotted lines indicate the absorption maxima due to the ***EEE*-T1**).

The stability of ***ZZZ*-T1**was measured by estimating the % of the catalyst ***ZZZ*-T1** undergoing thermal reverse isomerization after 9 hours using the following expression:

$$\%\ \text{conversion of } ZZZ\text{-isomer} = \frac{\text{A}(\pi-\pi^*)\ \text{after 9h} - \text{A}(\pi-\pi^*)\ \text{at initial time}}{\text{A}(\pi-\pi^*)\ \text{before irradiation}} \text{ x } 100$$

$$= \frac{A_{9h}(\pi-\pi^*) - A_0(\pi-\pi^*)}{A_\infty(\pi-\pi^*)} \text{ x } 100$$

Table 4B.1 Kinetic stability of ***ZZZ*-T1**

S. No.	System	Conditions	% conversion after 9 h
1	***ZZZ*-T1**	DMSO,7 µm, 25±1 ^{o}C	<8
2	***ZZZ*-T1** + DMAP-TrCl adduct	DMSO, 1:0.05, 25±1 ^{o}C	<2
3	***ZZZ*-T1** + DMAP-TrCl adduct + $BzNH_2$	DMSO, 1:0.05:2, 25±1 ^{o}C	<2

Appendix 4C

Titration with different anions (TBAC, TBAB, TBAF, TBAI)

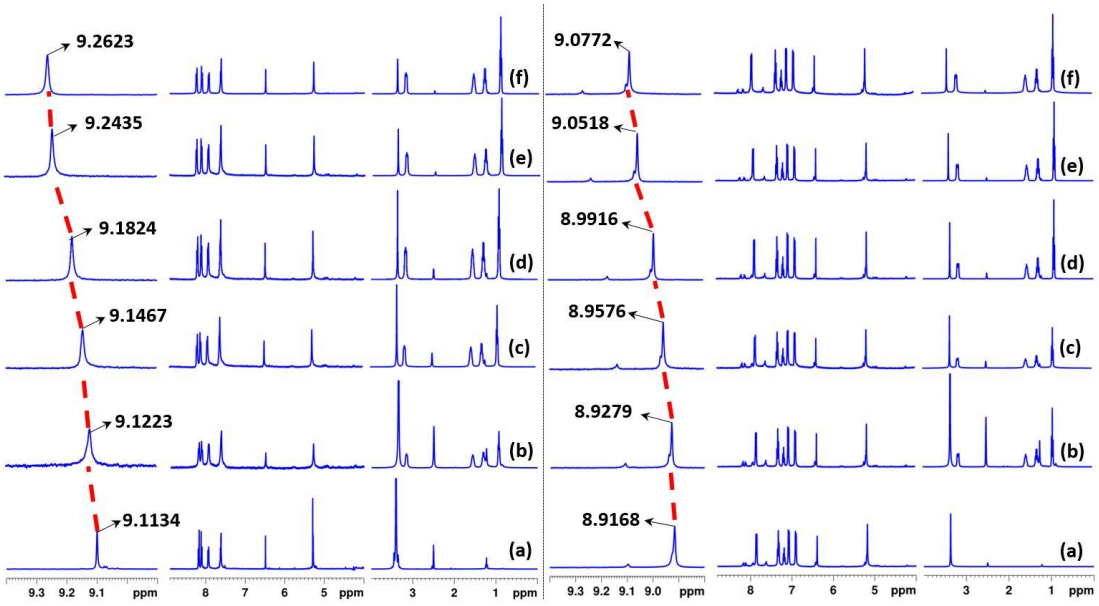

Figure 4C.1 ^{1}H-NMR experiment depicting the shifts in the catalyst **T1** upon titration with TBAC with a stoichiometric ratios (**T1**:TBAC): (a) 1:0; (b) 1:1; (c) 1:5; (d) 1:10; (e) 1:20 and (f) 1:25. (left: for the native state of ***EEE*-T1** and right: after photoswitching at 365 nm) [Concentrations: **T1** – 11 mM].

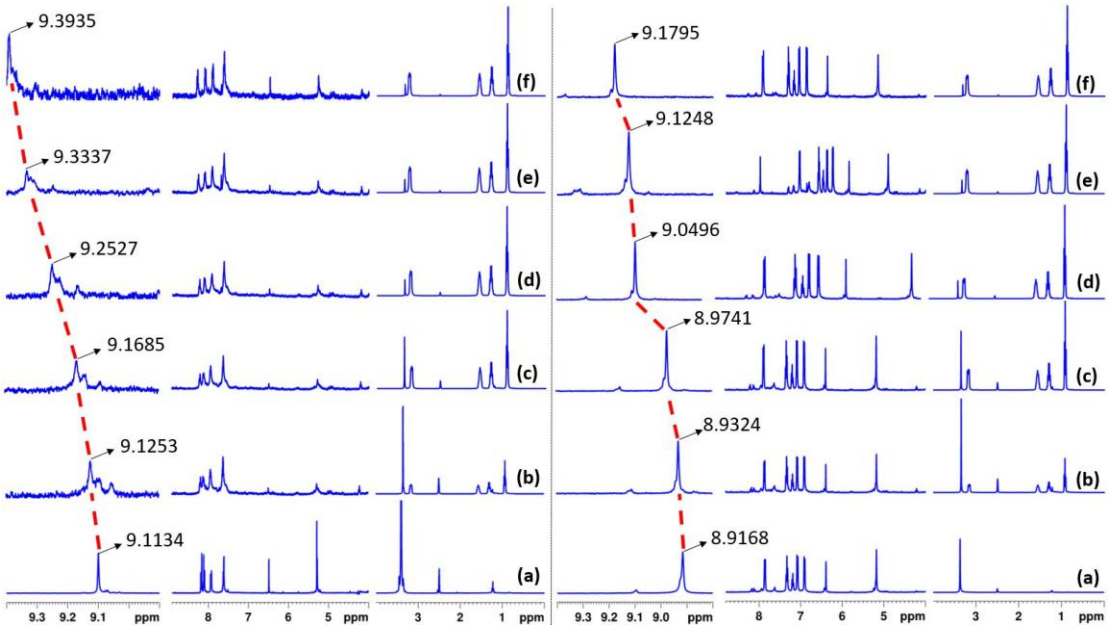

Figure 4C.2 ^{1}H-NMR experiment depicting the shifts in the catalyst **T1** upon titration with TBAB with a stoichiometric ratios (**T1**:TBAB): (a) 1:0; (b) 1:1; (c) 1:5; (d) 1:10; (e) 1:20 and (f) 1:25. (left: for the native state of ***EEE*-T1** and right: after photoswitching at 365 nm) [Concentrations: **T1** – 11 mM].

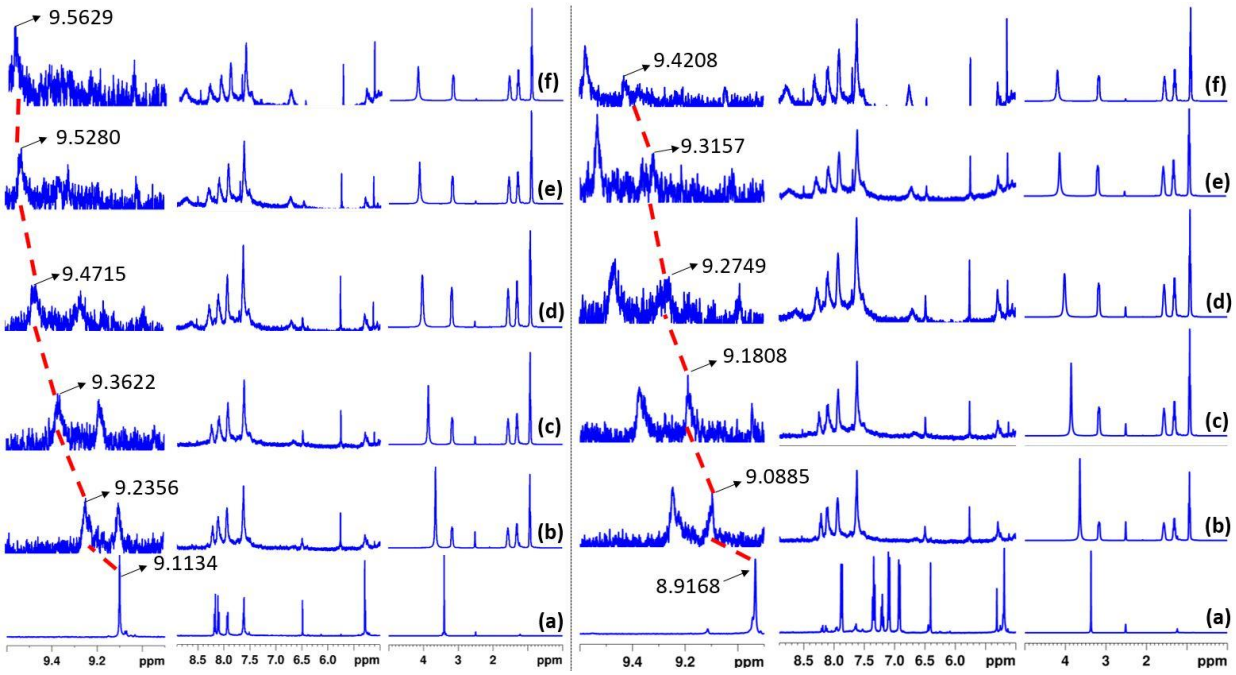

Figure 4C.3 ^{1}H-NMR experiment depicting the shifts in the catalyst **T1** upon titration with TBAF with a stoichiometric ratios (**T1**:TBAF): (a) 1:0; (b) 1:1; (c) 1:5; (d) 1:10; (e) 1:20 and (f) 1:25. (left: for the native state of ***EEE*-T1** and right: after photoswitching at 365 nm) [Concentrations: **T1** – 11 mM].

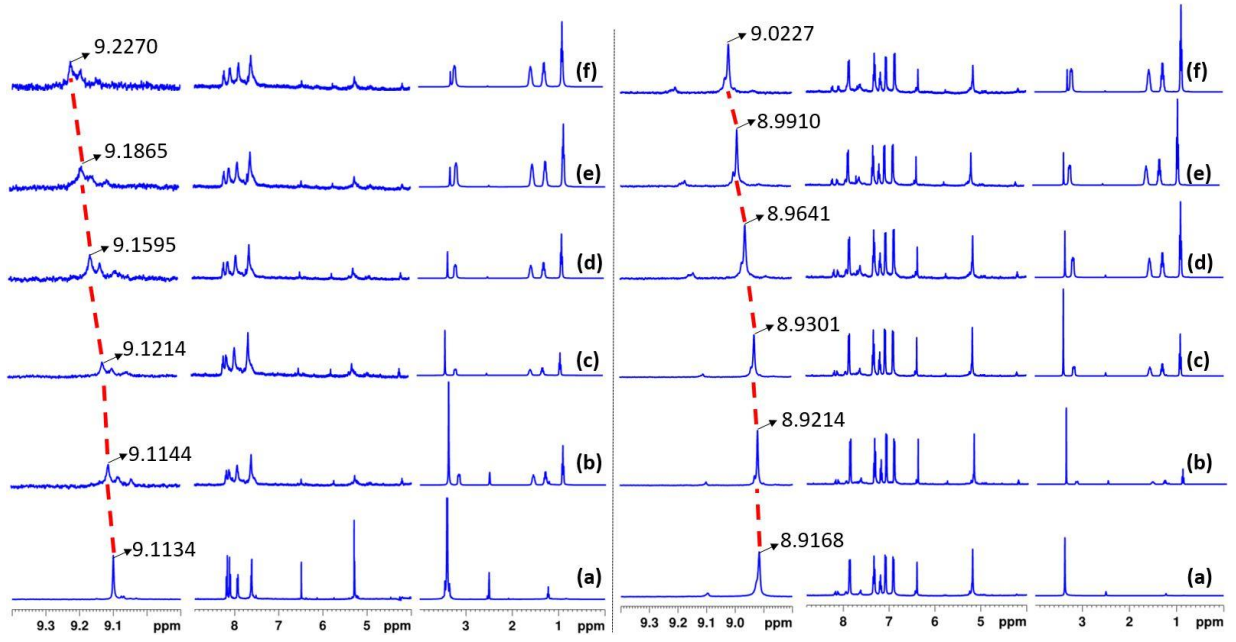

Figure 4C.4 ^{1}H-NMR experiment depicting the shifts in the catalyst **T1** upon titration with TBAI with a stoichiometric ratios (**T1**:TBAI): (a) 1:0; (b) 1:1; (c) 1:5; (d) 1:10; (e) 1:20 and (f) 1:25. (left: for the native state of ***EEE*-T1** and right: after photoswitching at 365 nm) [Concentrations: **T1** – 11 mM].

Appendix 4D

Spectral characterization data (^{1}H- and ^{13}C-NMR data)

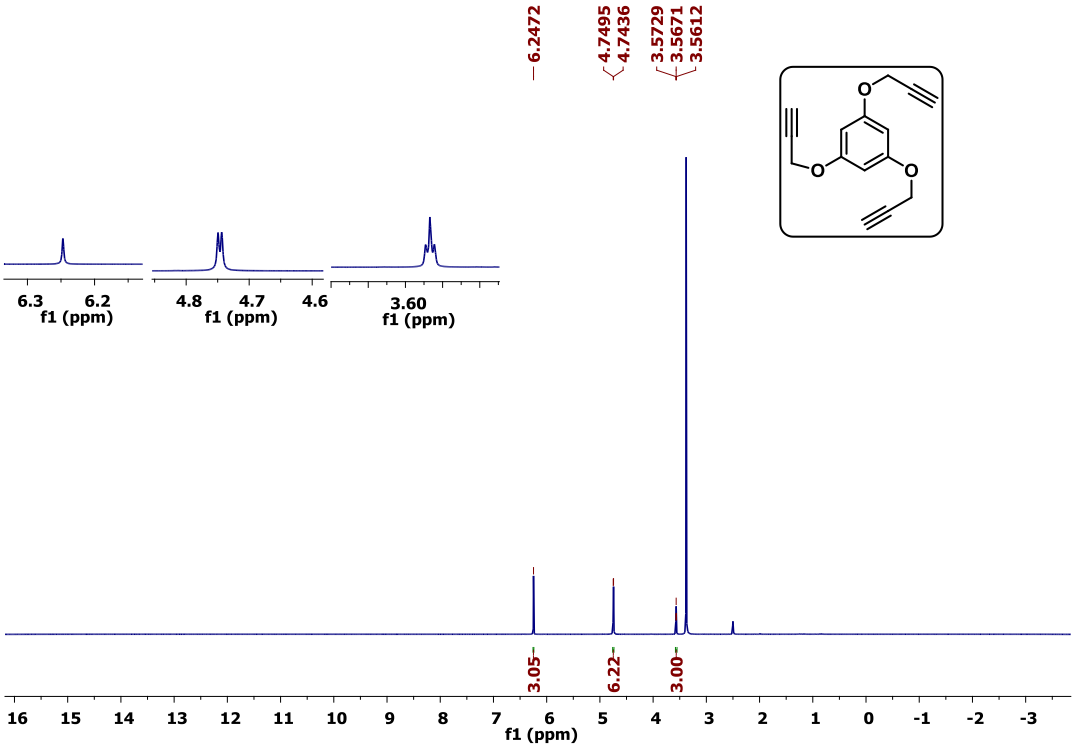

^{1}H-NMR spectrum of 1,3,5-*tris*(prop-2-yn-1-yloxy)benzene (**C1**) in [D_6]DMSO.

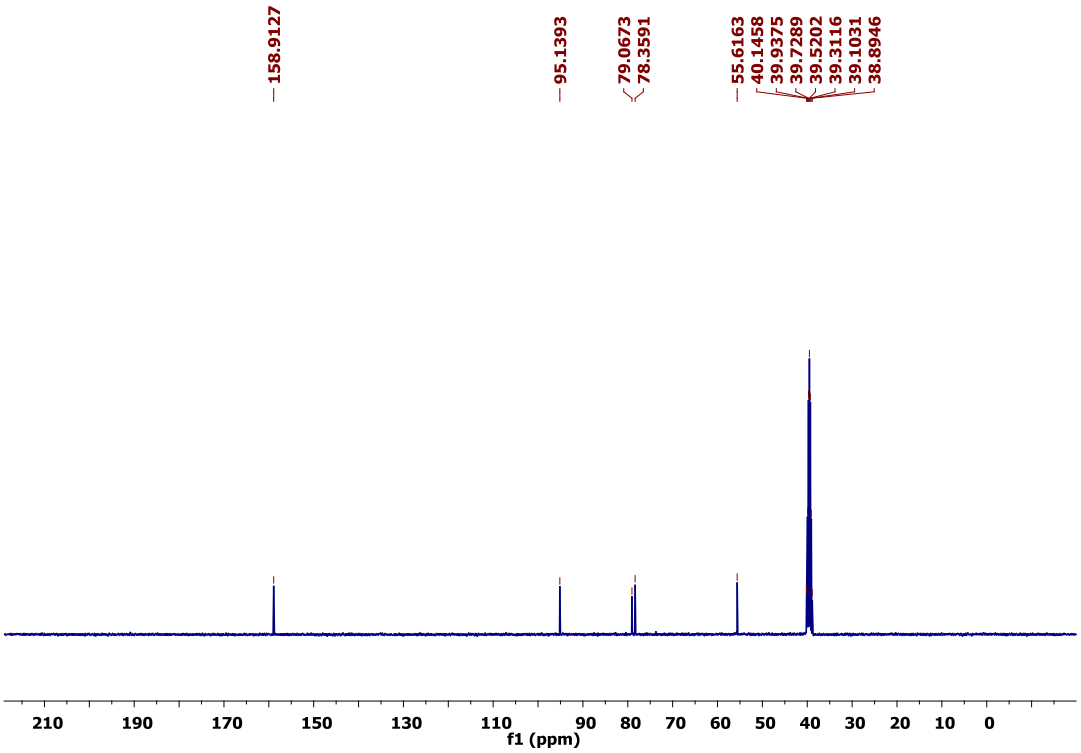

^{13}C-NMR spectrum of 1,3,5-*tris*(prop-2-yn-1-yloxy)benzene (**C1**) in [D_6]DMSO.

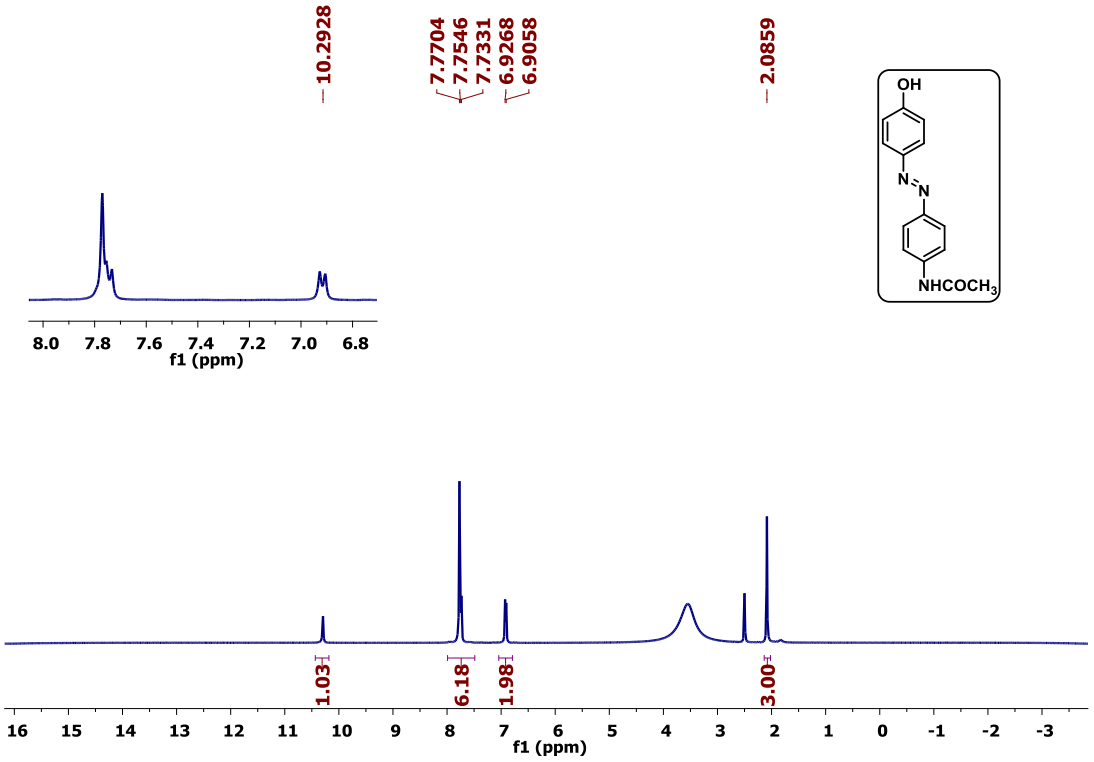

[1]H-NMR spectrum of *(E)*-N-(4-((4-hydroxyphenyl)diazenyl)phenyl)acetamide(**3**) in [D_6]DMSO.

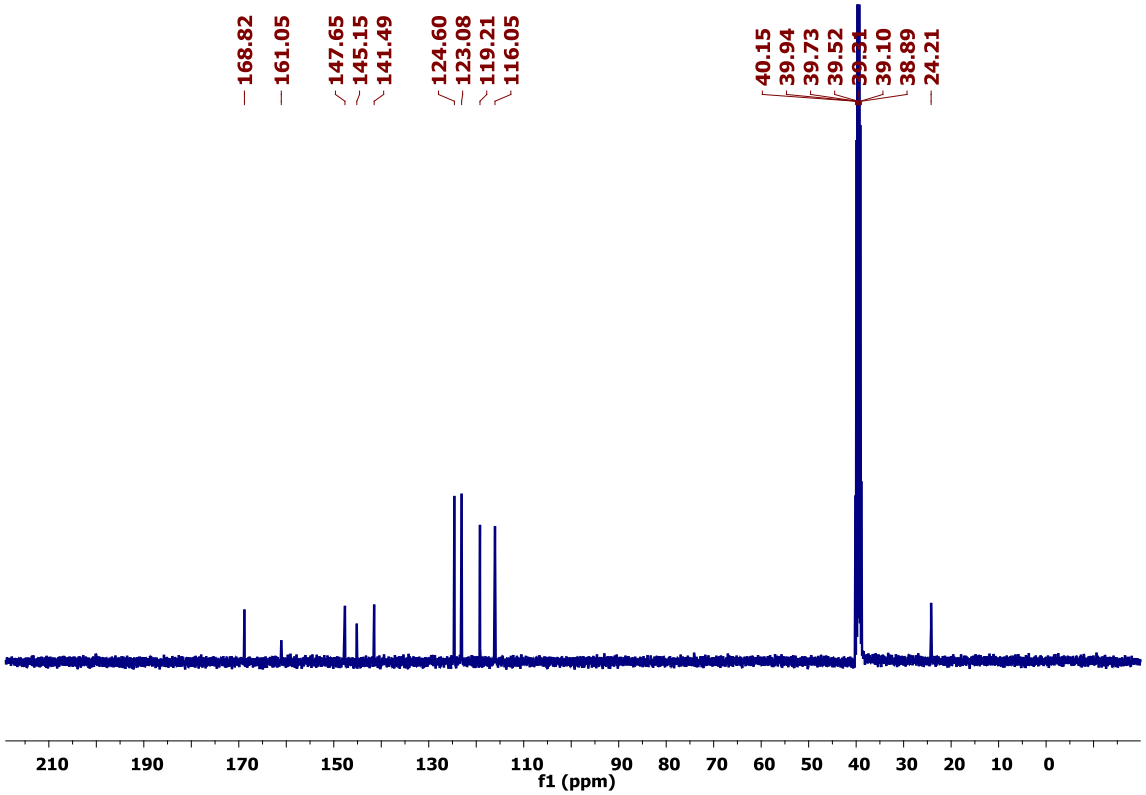

[13]C-NMR spectrum of *(E)*-N-(4-((4hydroxyphenyl)diazenyl)phenyl)acetamide(**3**) in [D_6]DMSO.

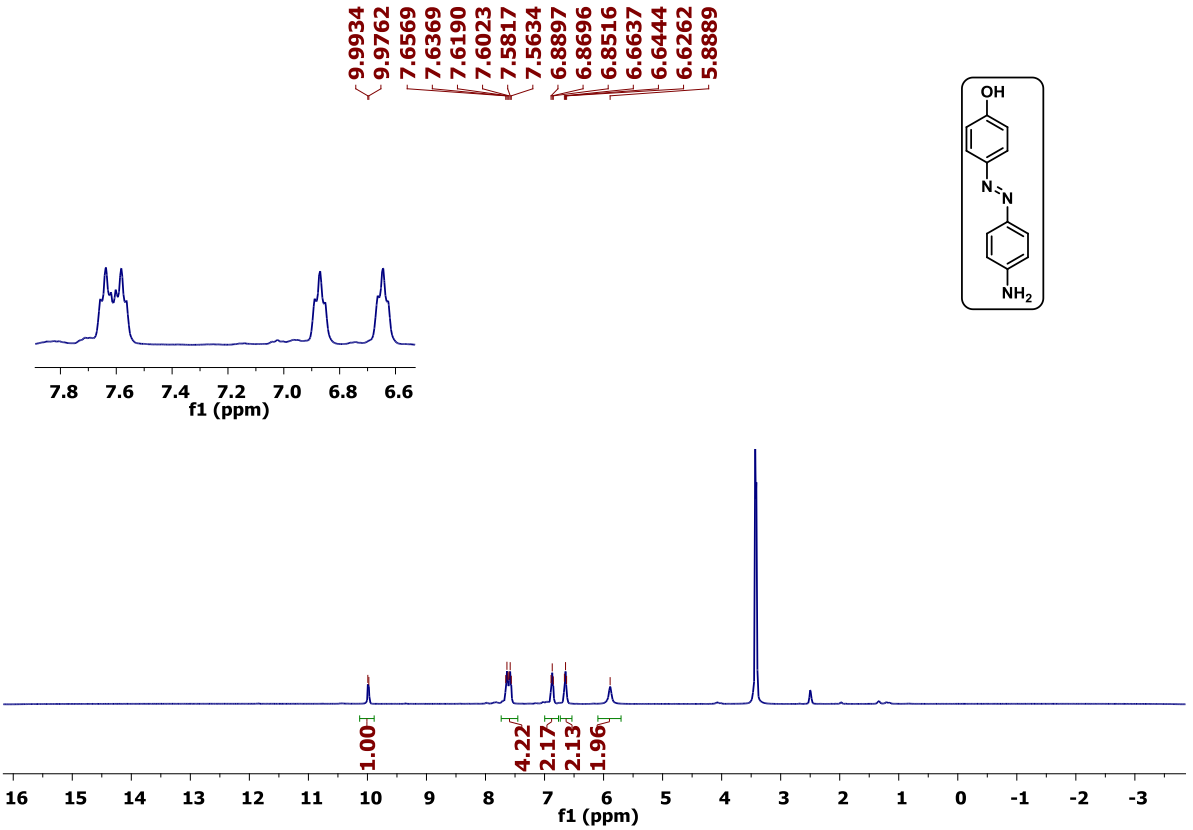

^{1}H-NMR spectrum of (*E*)-4-((4-aminophenyl)diazenyl)phenol(**Am2**) in [D_6]DMSO.

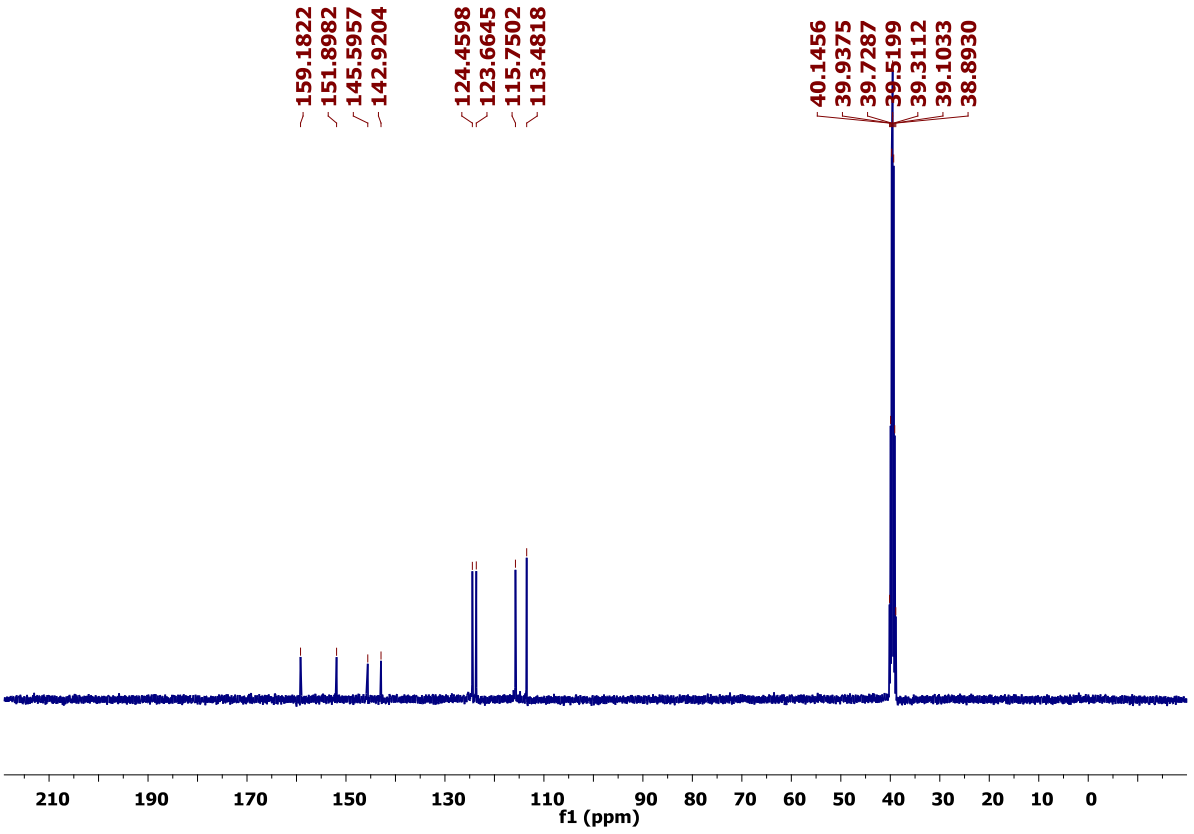

^{13}C-NMR spectrum of (*E*)-4-((4-aminophenyl)diazenyl)phenol (**Am2**) in [D_6]DMSO.

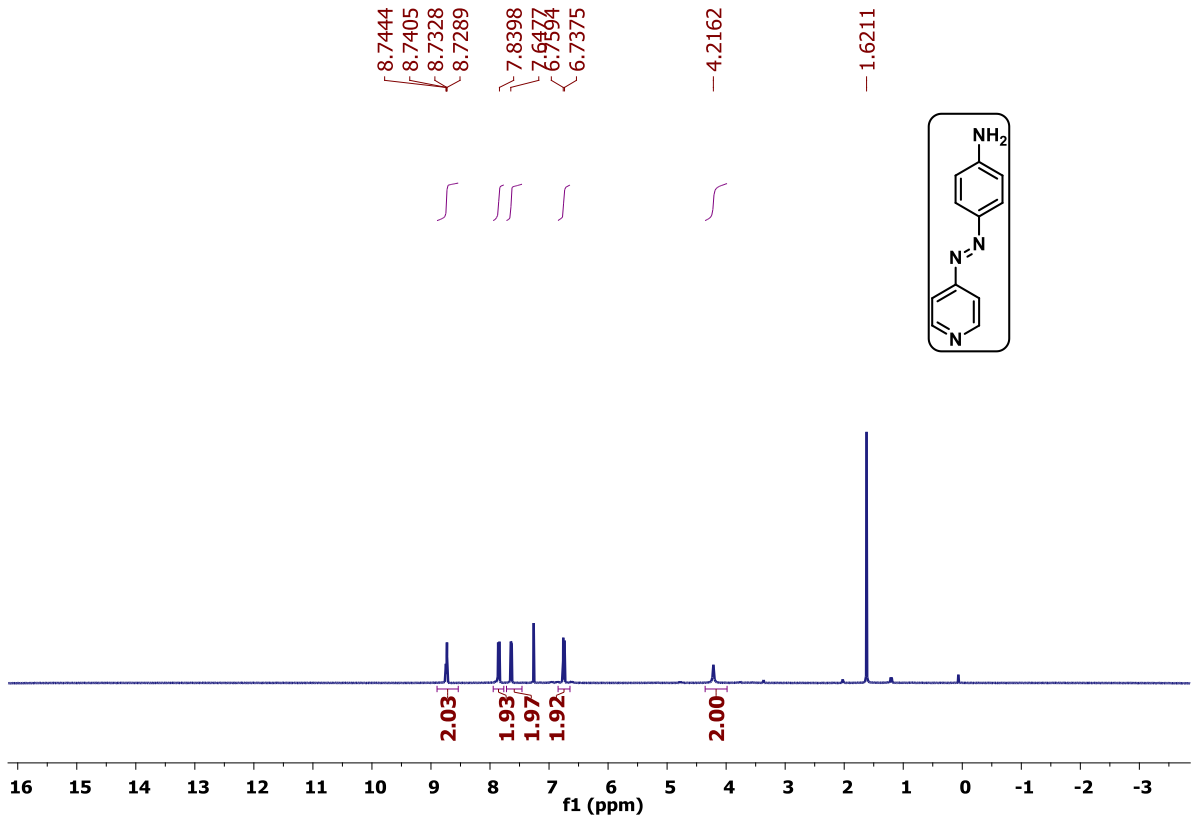

^{1}H-NMR spectrum of (*E*)-4-(pyridin-4-yldiazenyl)aniline (**Am3**) in $CDCl_3$.

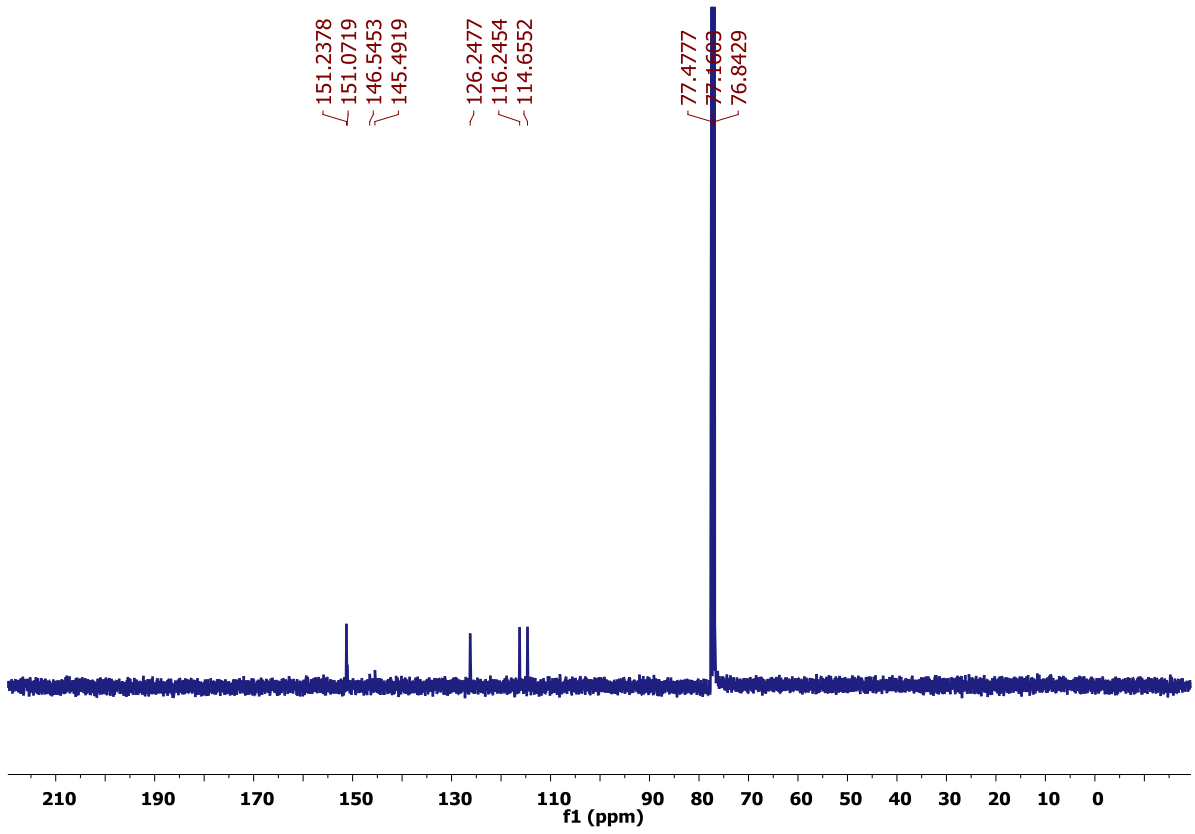

^{13}C-NMR spectrum of (*E*)-4-(pyridin-4-yldiazenyl)aniline (**Am3**) in $CDCl_3$.

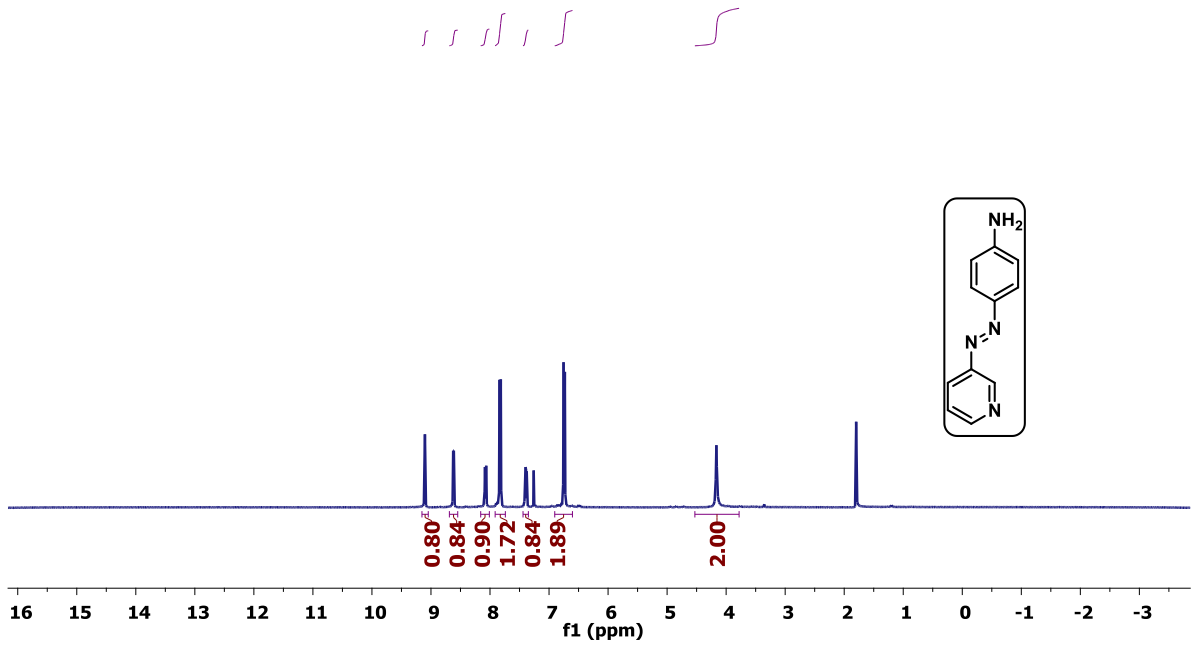

^{1}H-NMR spectrum of (*E*)-4-(pyridin-3-yldiazenyl)aniline (**Am4**) in $CDCl_3$.

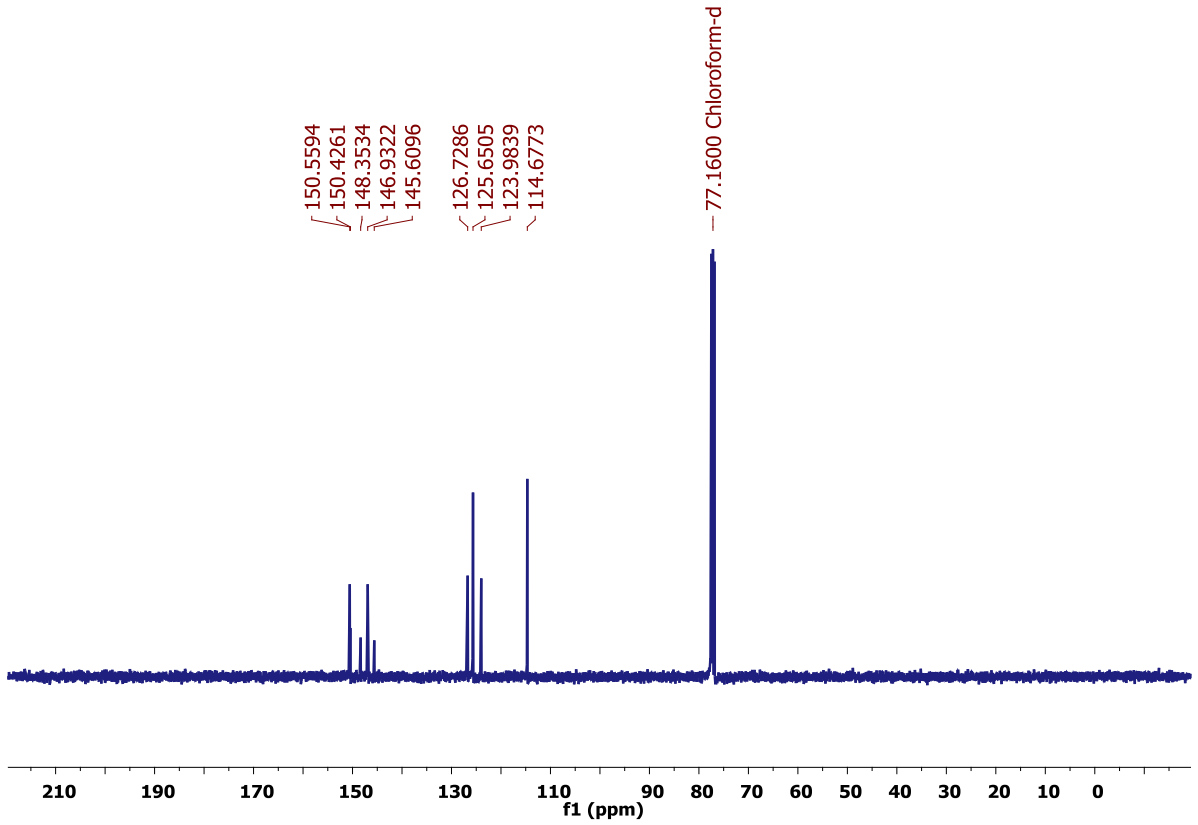

^{13}C-NMR spectrum of (*E*)-4-(pyridin-3-yldiazenyl)aniline (**Am4**) in $CDCl_3$.

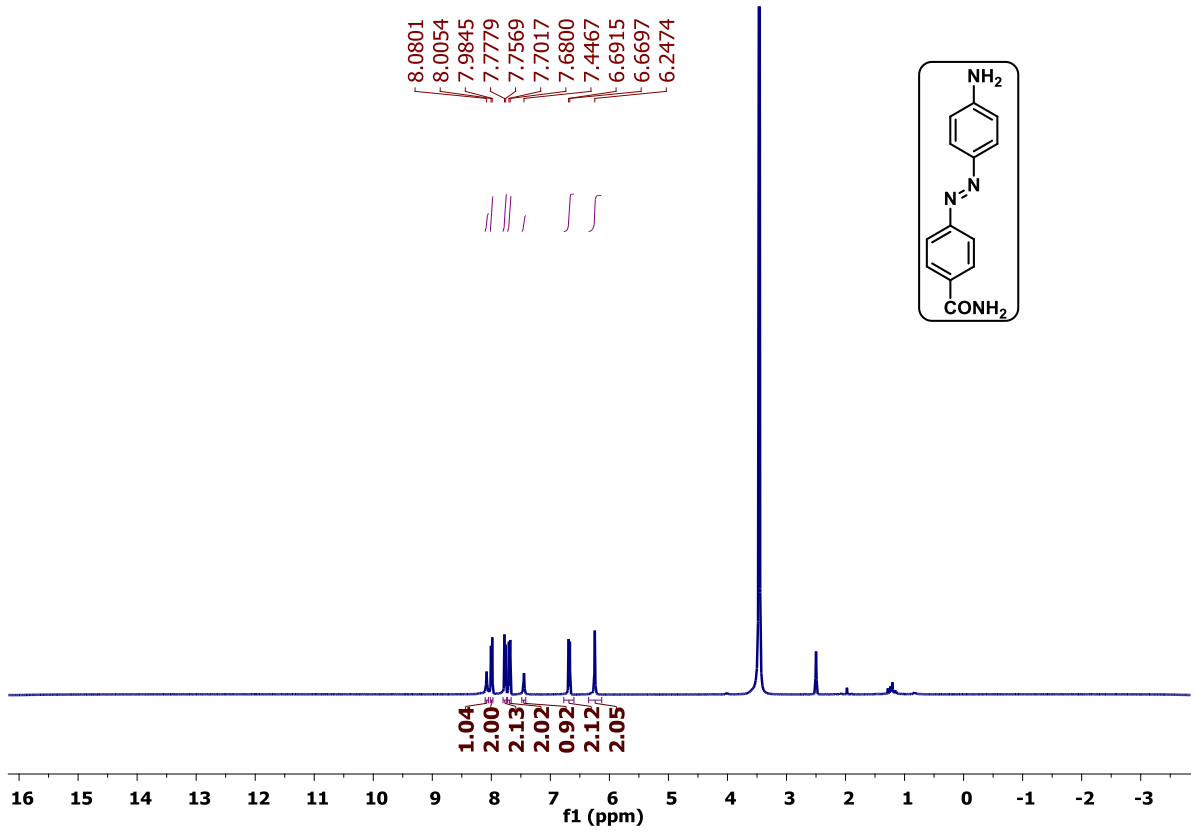

^{1}H-NMR spectrum of (*E*)-4-((4-aminophenyl)diazenyl)benzamide (**Am5**) in [D_6]DMSO.

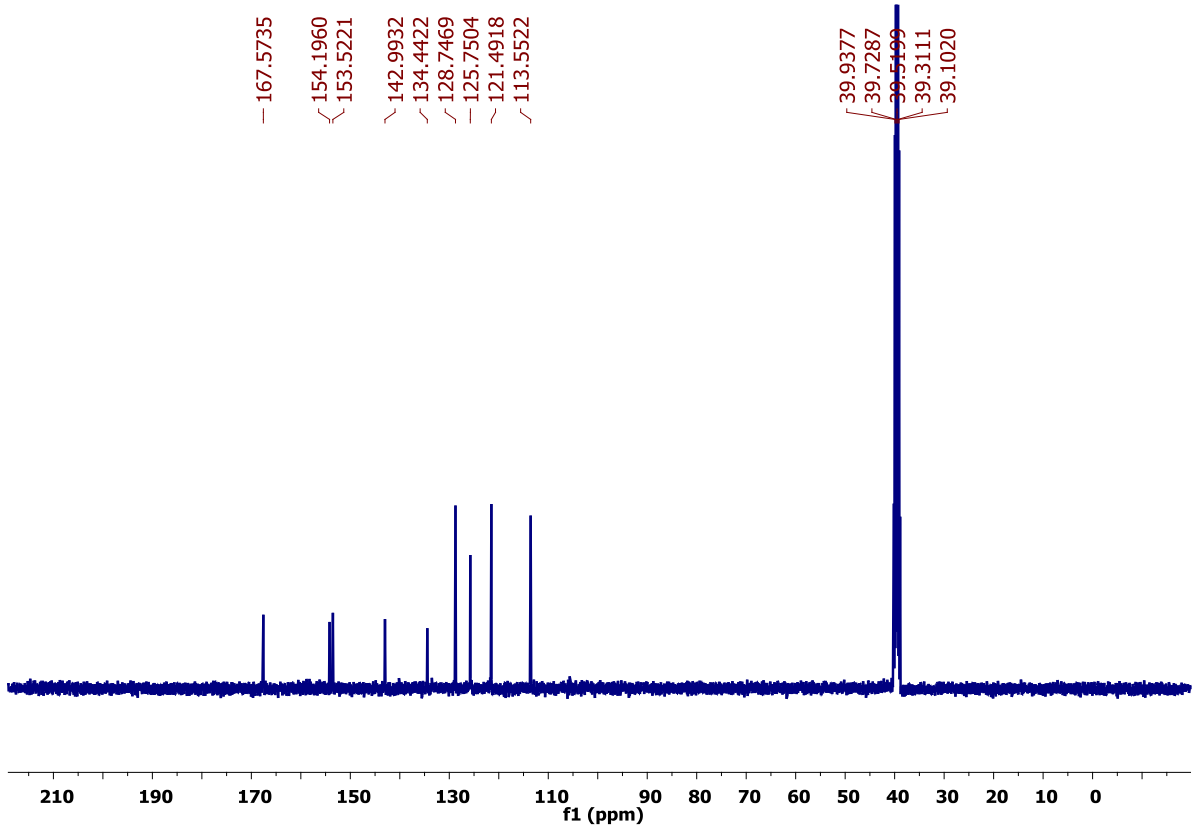

^{13}C-NMR spectrum of (*E*)-4-((4-aminophenyl)diazenyl)benzamide (**Am5**) in [D_6]DMSO.

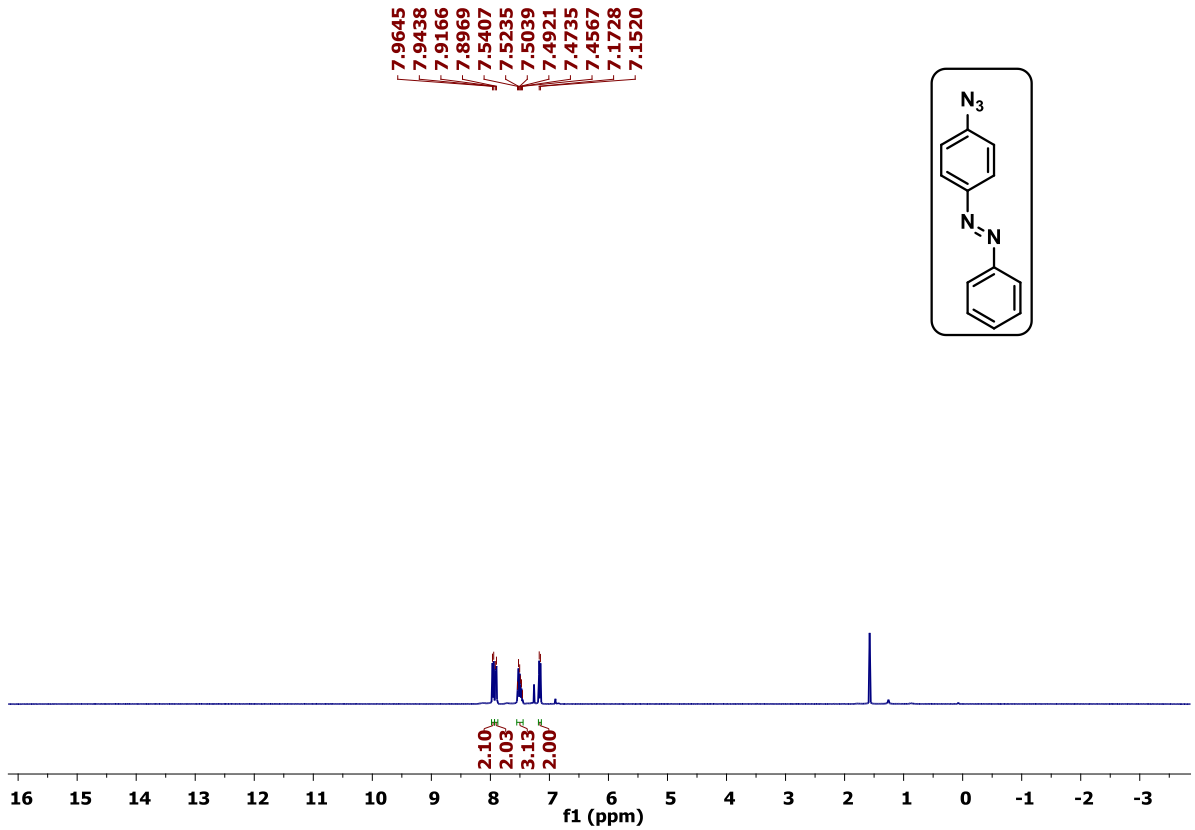

^{1}H-NMR spectrum of (*E*)-1-(4-azidophenyl)-2-phenyldiazene (**Az1**) in $CDCl_3$.

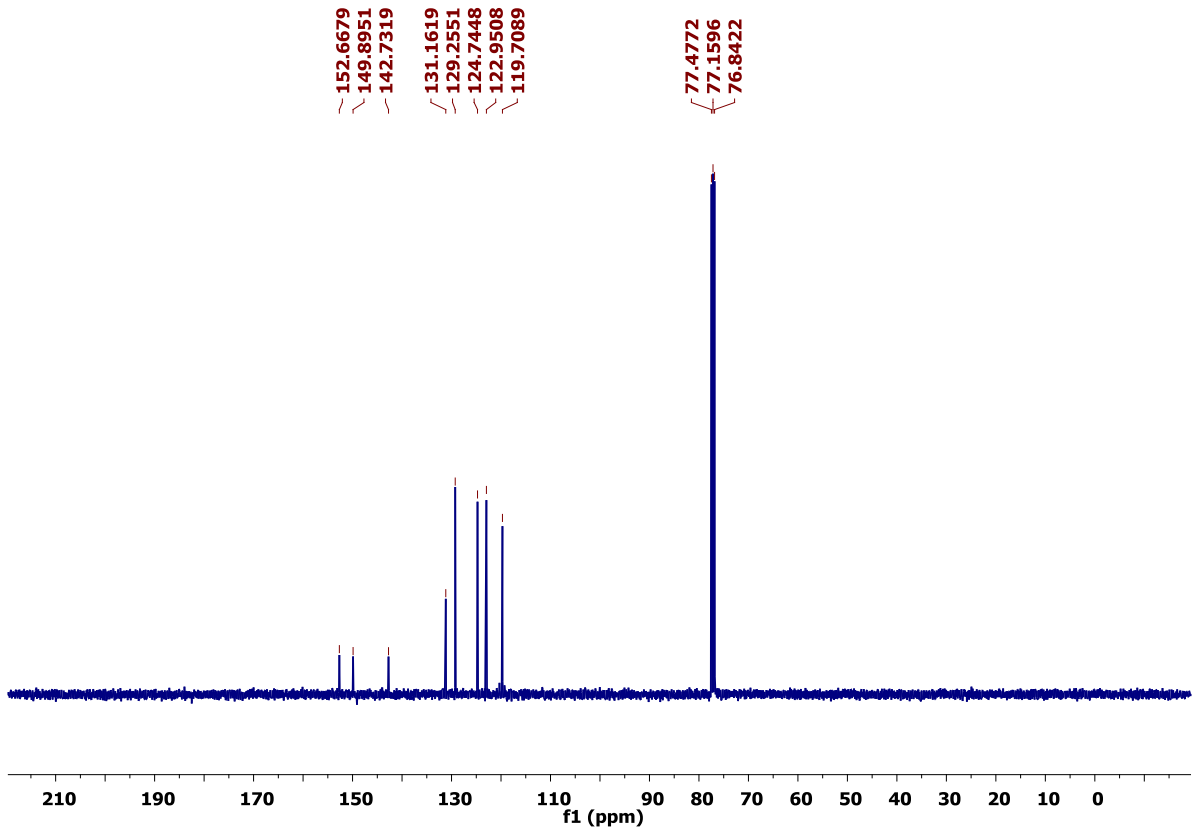

^{13}C-NMR spectrum of (*E*)-1-(4-azidophenyl)-2-phenyldiazene (**Az1**) in $CDCl_3$.

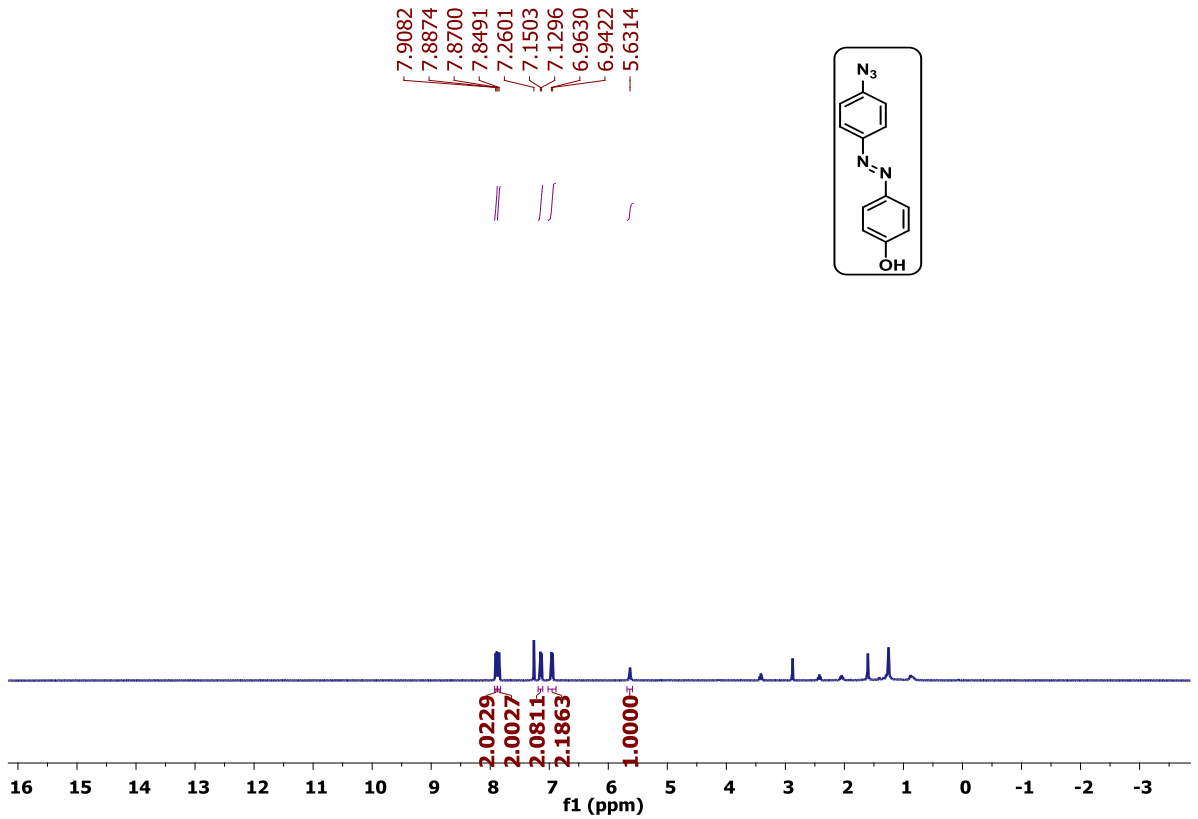

^{1}H-NMR spectrum of (*E*)-4-((4-azidophenyl)diazenyl)phenol (**Az2**) in $CDCl_3$.

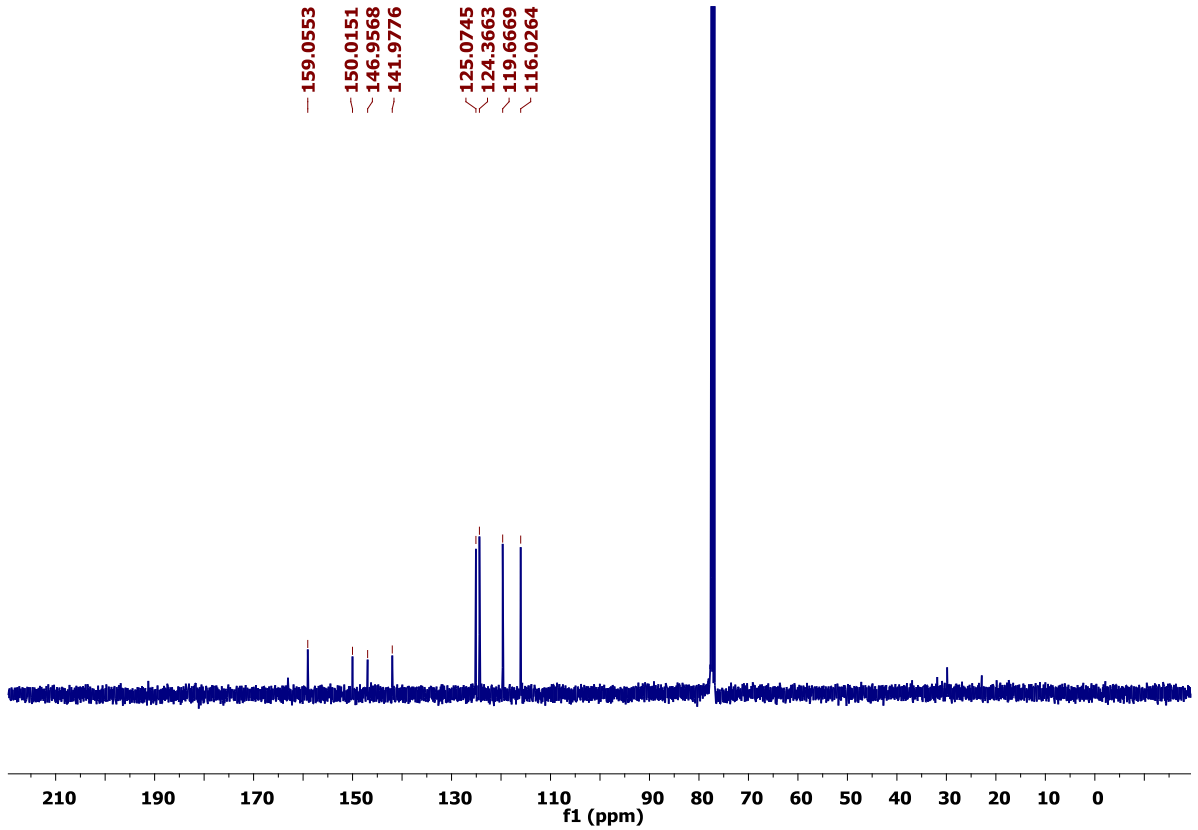

^{13}C-NMR spectrum of (*E*)-4-((4-azidophenyl)diazenyl)phenol (**Az2**) in $CDCl_3$.

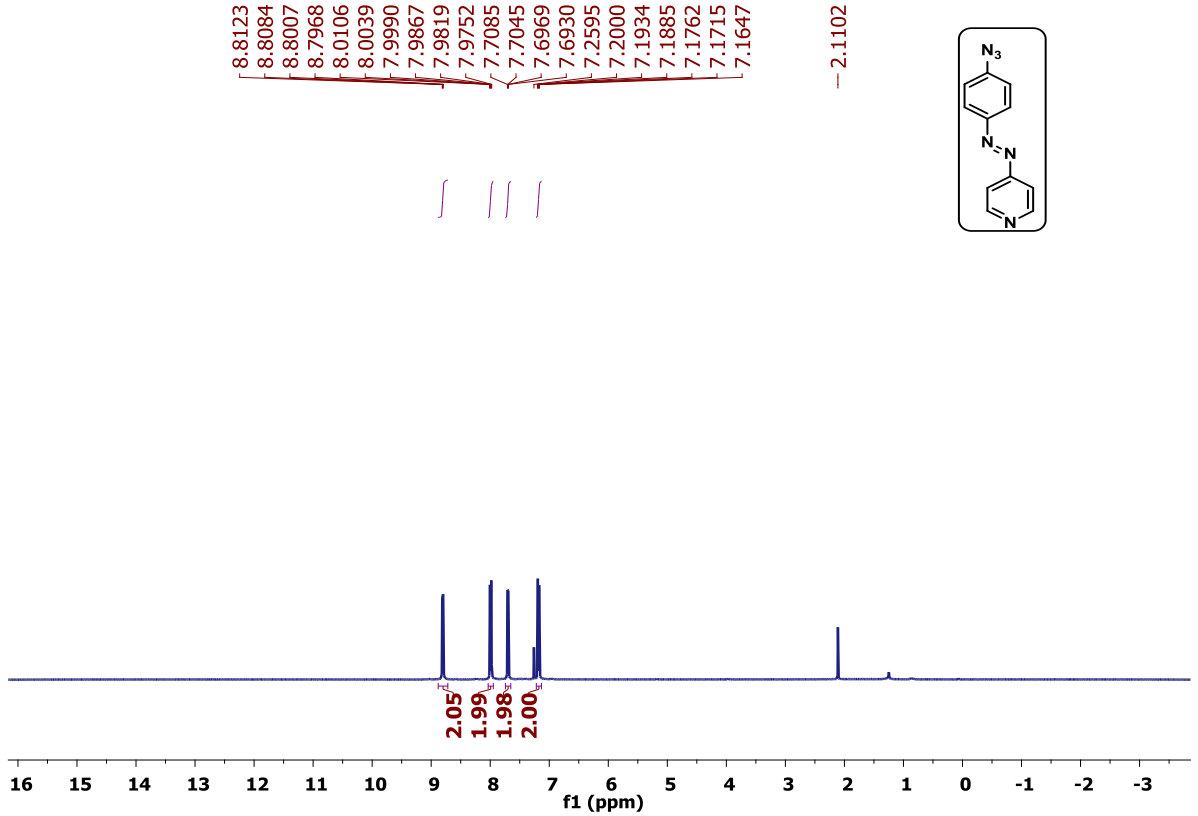

^{1}H-NMR spectrum of (*E*)-4-((4-azidophenyl)diazenyl)pyridine (**Az3**) in $CDCl_3$.

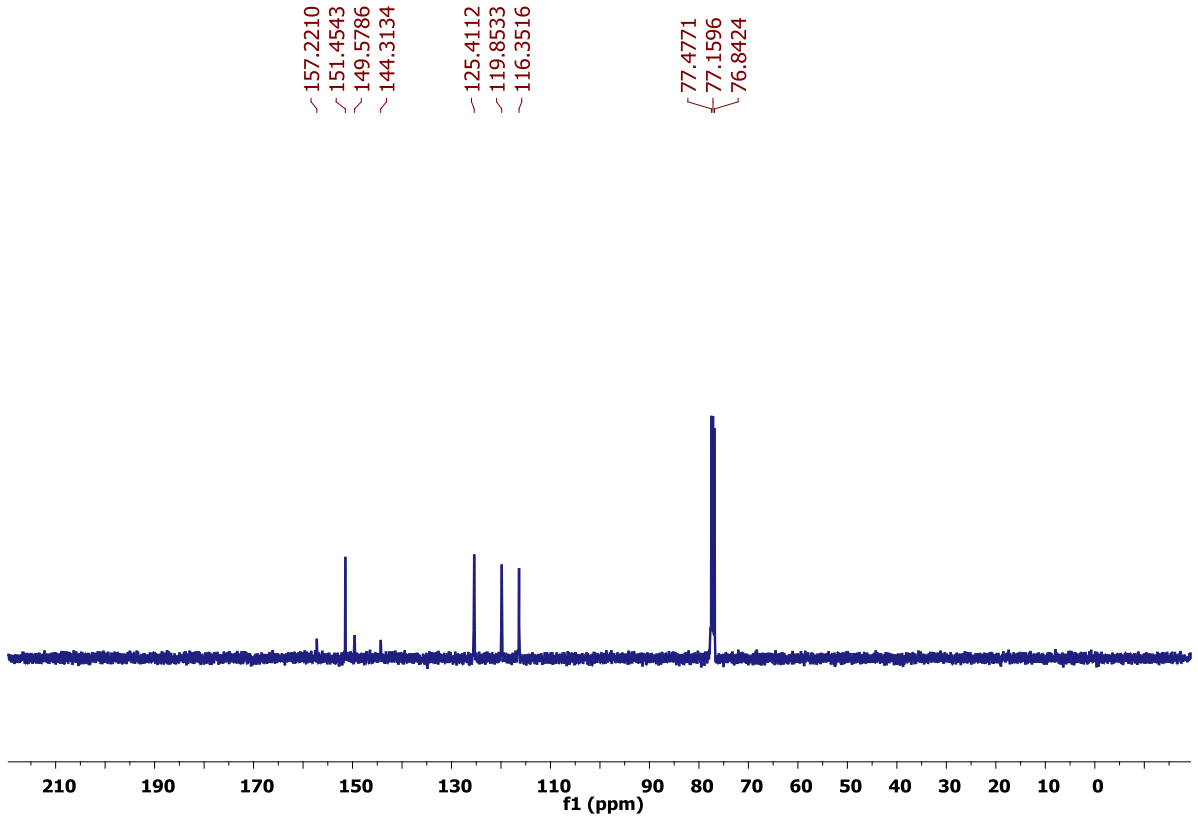

^{13}C-NMR spectrum of (*E*)-4-((4-azidophenyl)diazenyl)pyridine (**Az3**) in $CDCl_3$.

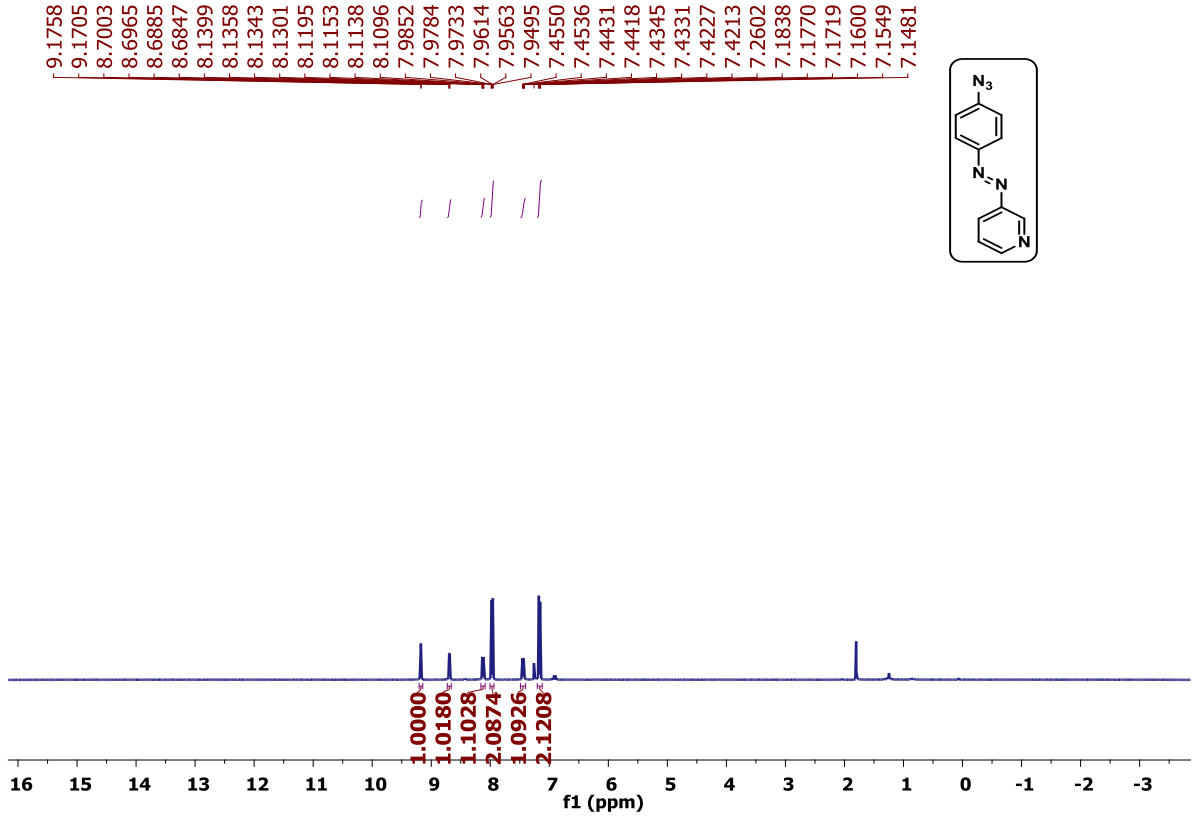

^{1}H-NMR spectrum of (*E*)-3-((4-azidophenyl)diazenyl)pyridine (**Az4**) in $CDCl_3$.

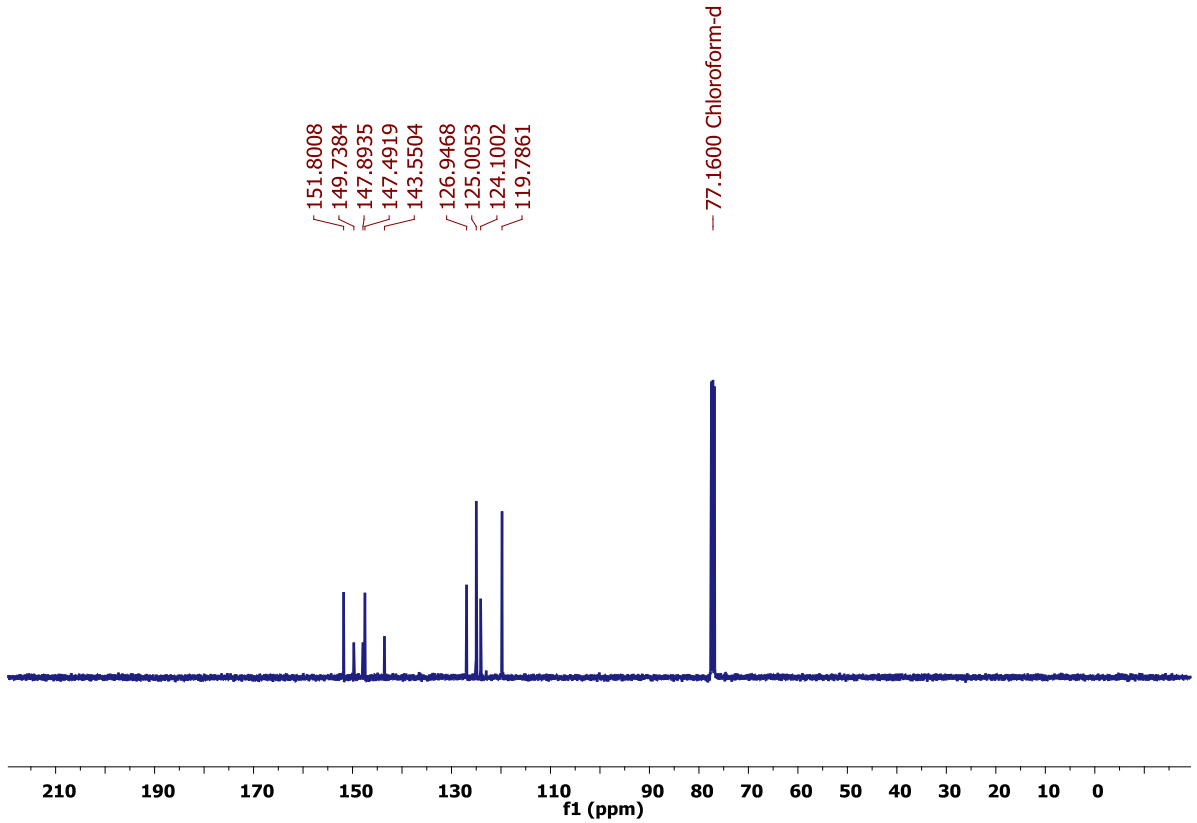

^{13}C-NMR spectrum of (*E*)-3-((4-azidophenyl)diazenyl)pyridine (**Az4**) in $CDCl_3$.

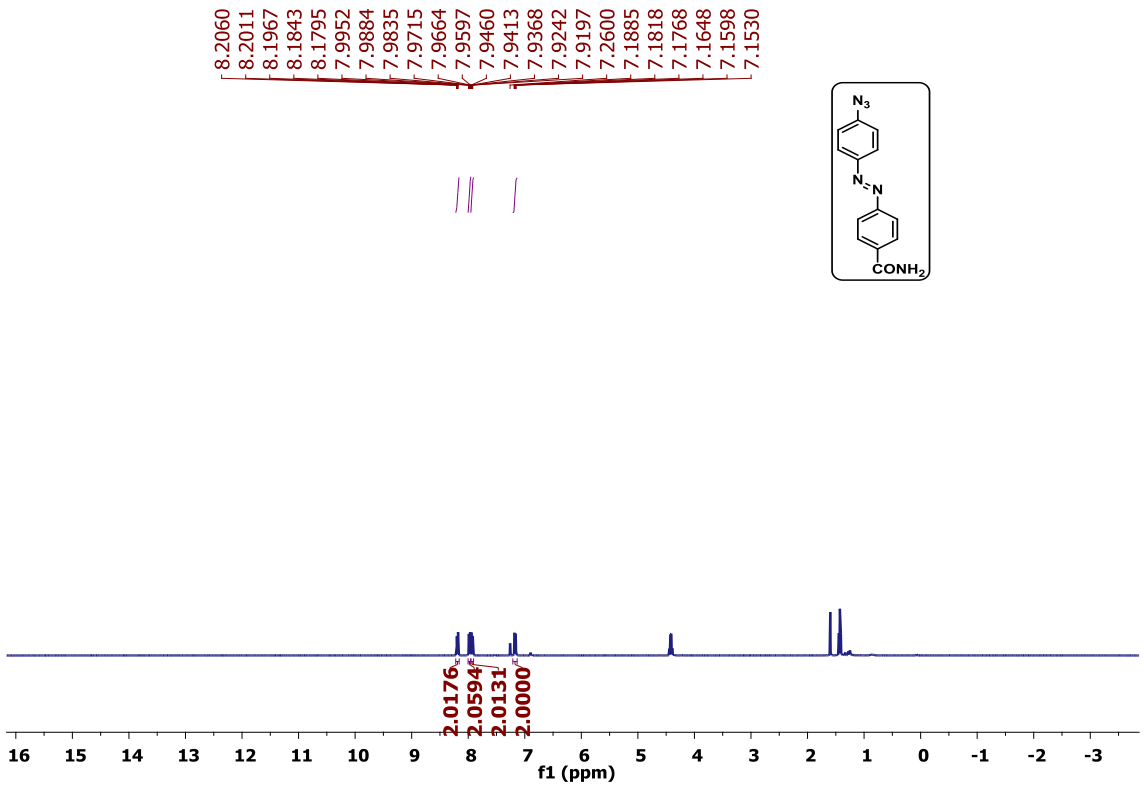

^{1}H-NMR spectrum of (*E*)-4-((4-azidophenyl)diazenyl)benzamide (**Az5**) in $CDCl_3$.

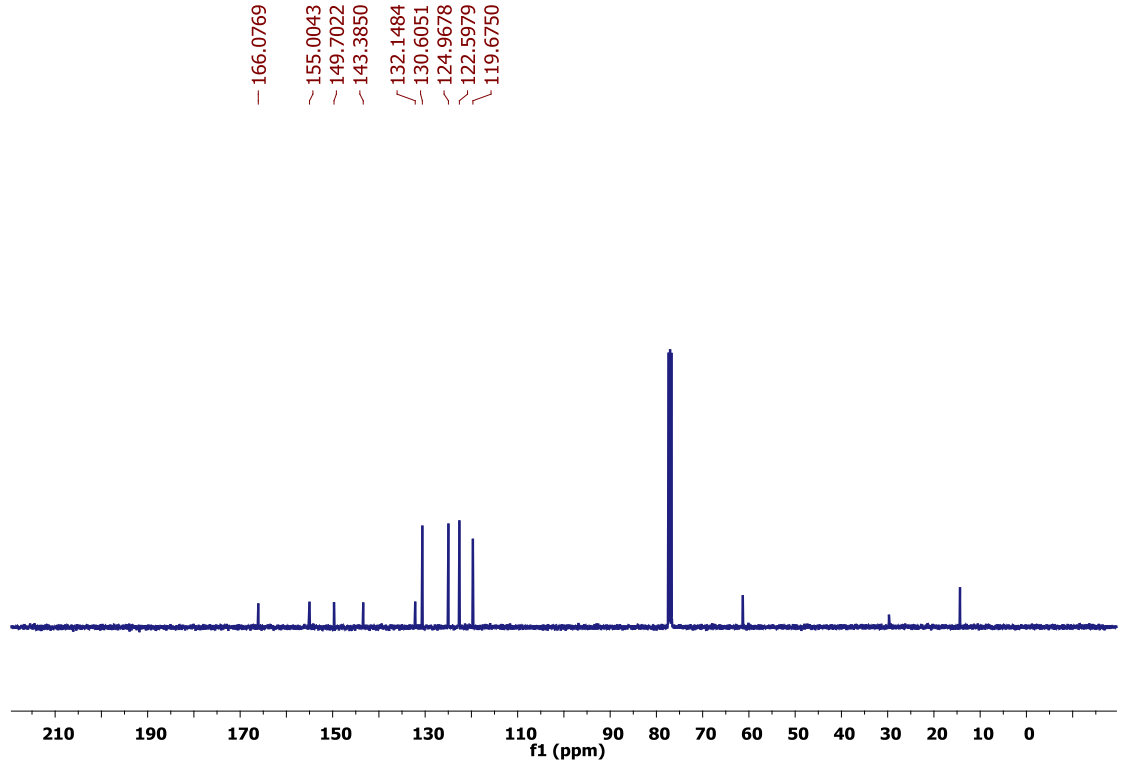

^{13}C-NMR spectrum of (*E*)-4-((4-azidophenyl)diazenyl)benzamide (**Az5**) in $CDCl_3$.

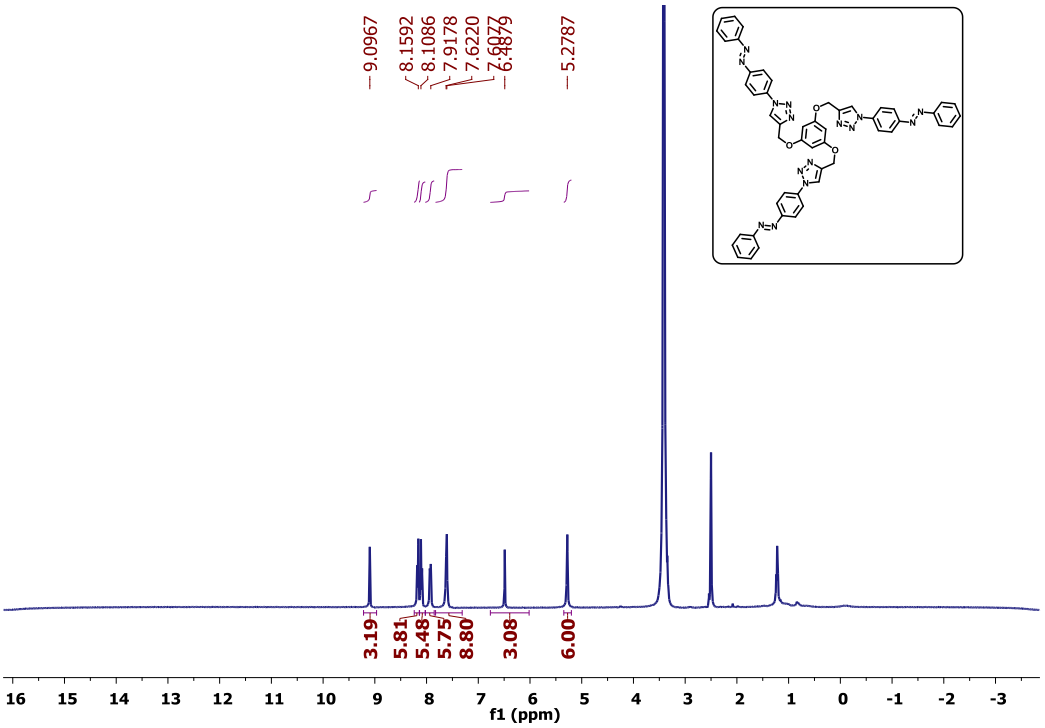

^{1}H-NMR spectrum of 4,4'-(((5-((2-(4-((*E*)-phenyldiazenyl)phenyl)-2*H*-1,2,3-triazol-4-yl)methoxy)-1,3-phenylene)bis(oxy))bis(methylene))bis(1-(4-((*E*)-phenyldiazenyl)phenyl)-1*H*-1,2,3-triazole) (**T1**) in [D_6]DMSO.

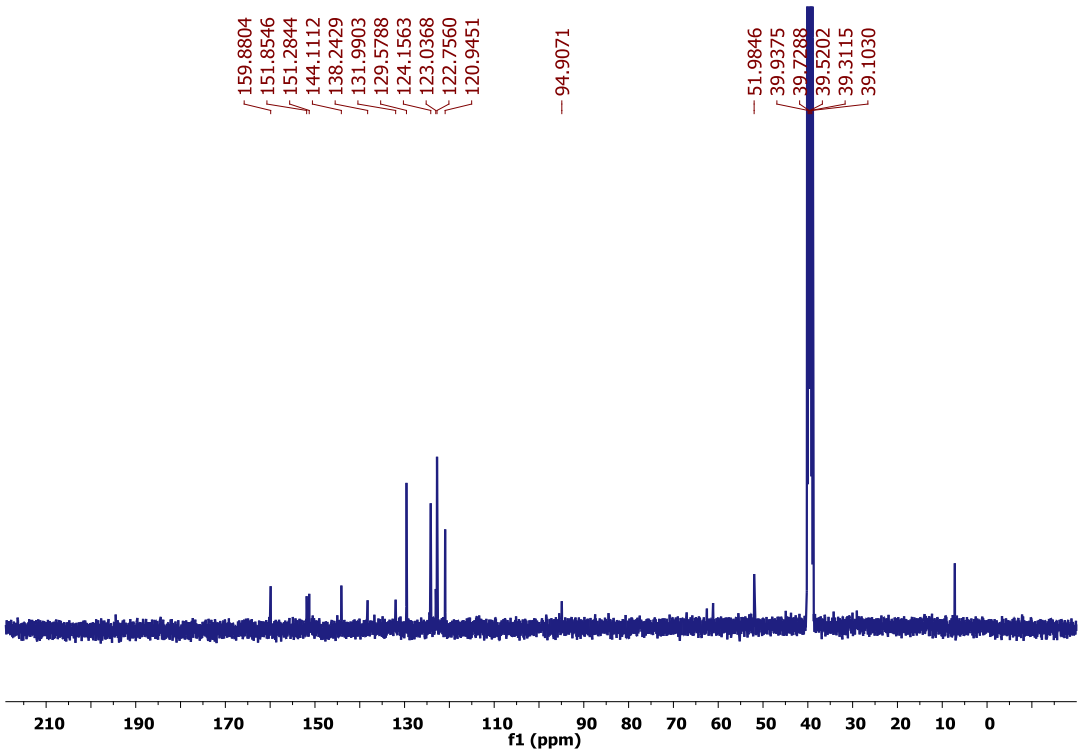

^{13}C-NMR spectrum of 4,4'-(((5-((2-(4-((*E*)-phenyldiazenyl)phenyl)-2*H*-1,2,3-triazol-4-yl)methoxy)-1,3-phenylene)bis(oxy))bis(methylene))bis(1-(4-((*E*)-phenyldiazenyl)phenyl)-1*H*-1,2,3-triazole) (**T1**) in [D_6]DMSO.

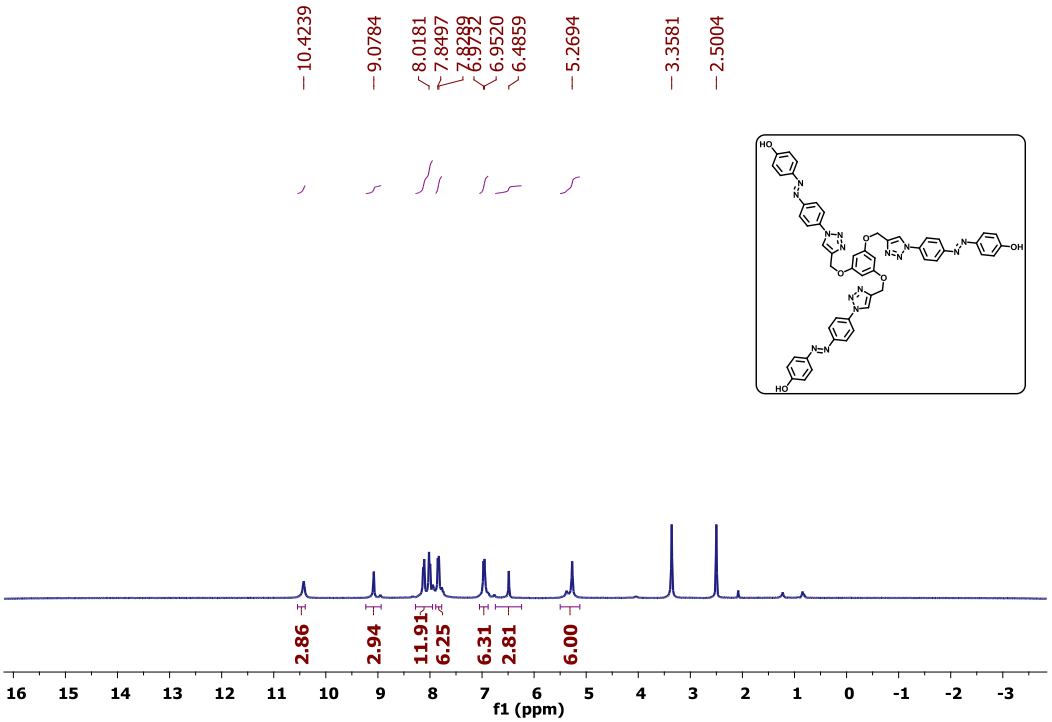

^{1}H-NMR spectrum of 4,4'-((1*E*,1'*E*)-(((((5-((2-(4-((*E*)-(4-hydroxyphenyl)diazenyl)phenyl)-2*H*-1,2,3-triazol-4-yl)methoxy)-1,3-phenylene)bis(oxy))bis(methylene))bis(1*H*-1,2,3-triazole-4,1-diyl))bis(4,1-phenylene))bis(diazene-2,1-diyl))diphenol (**T2**) in [D_6]DMSO.

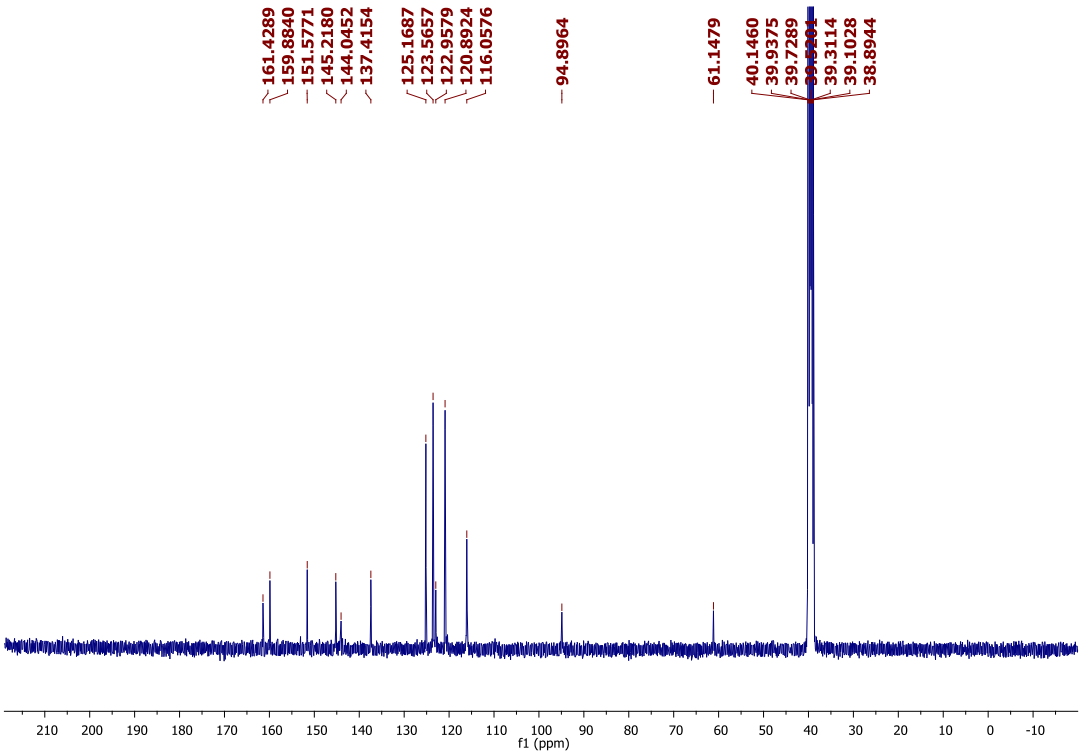

^{13}C-NMR spectrum of 4,4'-((1*E*,1'*E*)-(((((5-((2-(4-((*E*)-(4-hydroxyphenyl)diazenyl)phenyl)-2*H*-1,2,3-triazol-4-yl)methoxy)-1,3-phenylene)bis(oxy))bis(methylene))bis(1*H*-1,2,3-triazole-4,1-diyl))bis(4,1-phenylene))bis(diazene-2,1-diyl))diphenol (**T2**) in [D_6]DMSO.

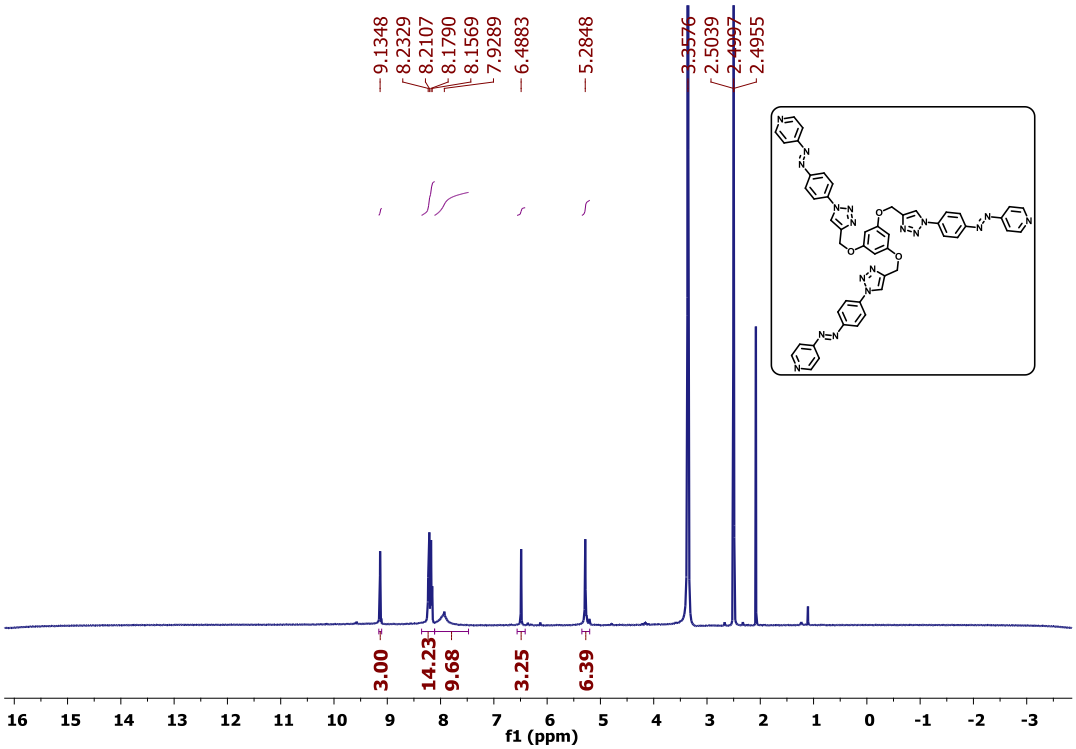

^{1}H-NMR spectrum of 4,4'-((1*E*,1'*E*)-(((((5-((2-(4-((*E*)-pyridin-4-yldiazenyl)phenyl)-2*H*-1,2,3-triazol-4-yl)methoxy)-1,3-phenylene)bis(oxy))bis(methylene))bis(1*H*-1,2,3-triazole-4,1-diyl))bis(4,1-phenylene))bis(diazene-2,1-diyl))dipyridine (**T3**) in [D_6]DMSO.

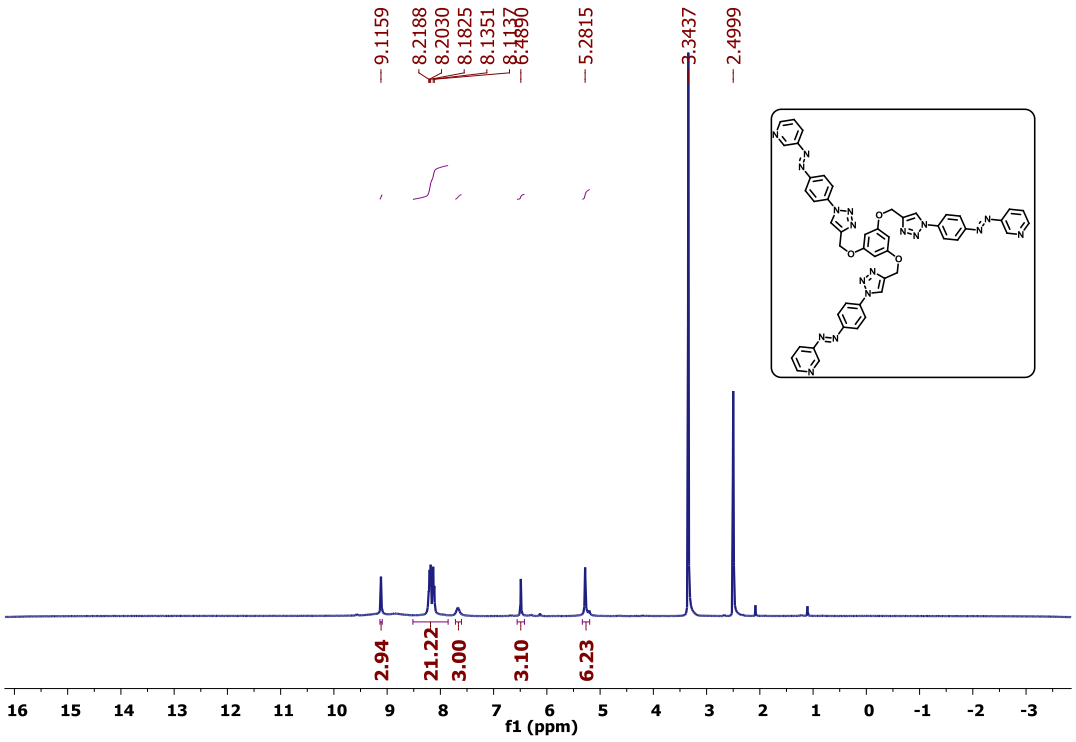

^{1}H-NMR spectrum of 3,3'-((1*E*,1'*E*)-(((((5-((2-(4-((*E*)-pyridin-3-yldiazenyl)phenyl)-2*H*-1,2,3-triazol-4-yl)methoxy)-1,3-phenylene)bis(oxy))bis(methylene))bis(1*H*-1,2,3-triazole-4,1-diyl))bis(4,1-phenylene))bis(diazene-2,1-diyl))dipyridine (**T4**) in [D_6]DMSO.

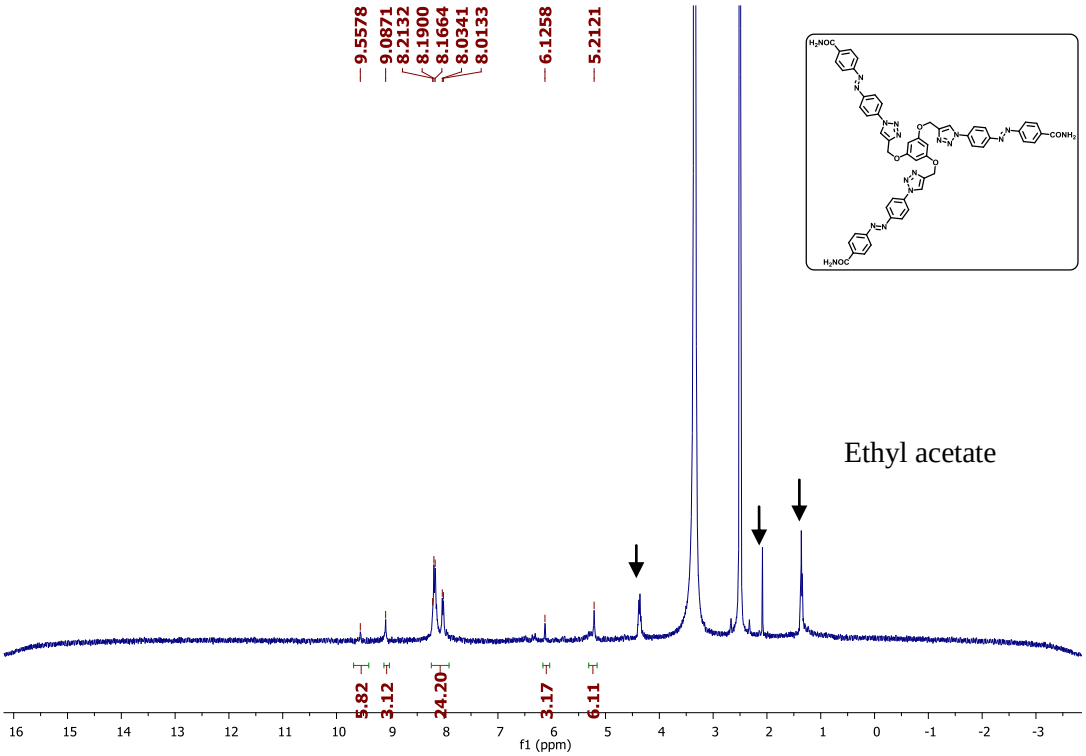

^{1}H-NMR spectrum of 4,4'-((1*E*,1'*E*)-(((((5-((2-(4-((*E*)-(4-carbamoylphenyl)diazenyl)phenyl)-2*H*-1,2,3-triazol-4-yl)methoxy)-1,3-phenylene)bis(oxy))bis(methylene))bis(1*H*-1,2,3-triazole-4,1-diyl))bis(4,1-phenylene))bis(diazene-2,1-diyl))dibenzamide (**T5**) in [D_6]DMSO.

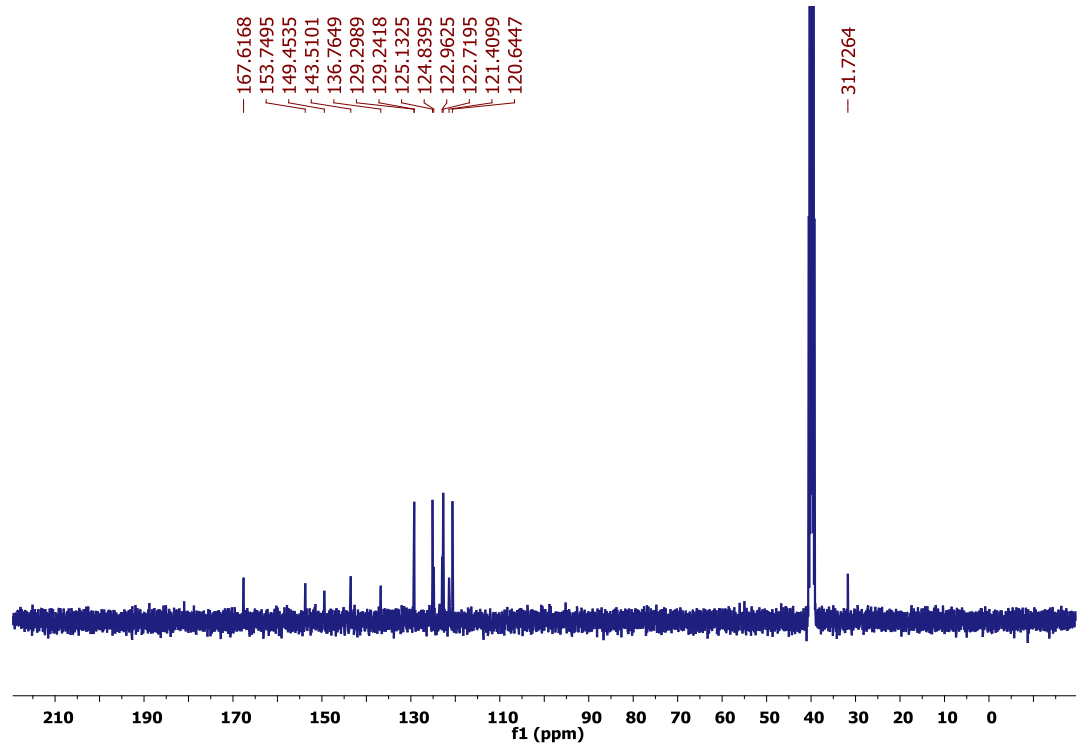

^{13}C-NMR spectrum of 4,4'-((1*E*,1'*E*)-(((((5-((2-(4-((*E*)-(4-carbamoylphenyl)diazenyl)phenyl)-2*H*-1,2,3-triazol-4-yl)methoxy)-1,3-phenylene)bis(oxy))bis(methylene))bis(1*H*-1,2,3-triazole-4,1-diyl))bis(4,1-phenylene))bis(diazene-2,1-diyl))dibenzamide (**T5**) in [D_6]DMSO.

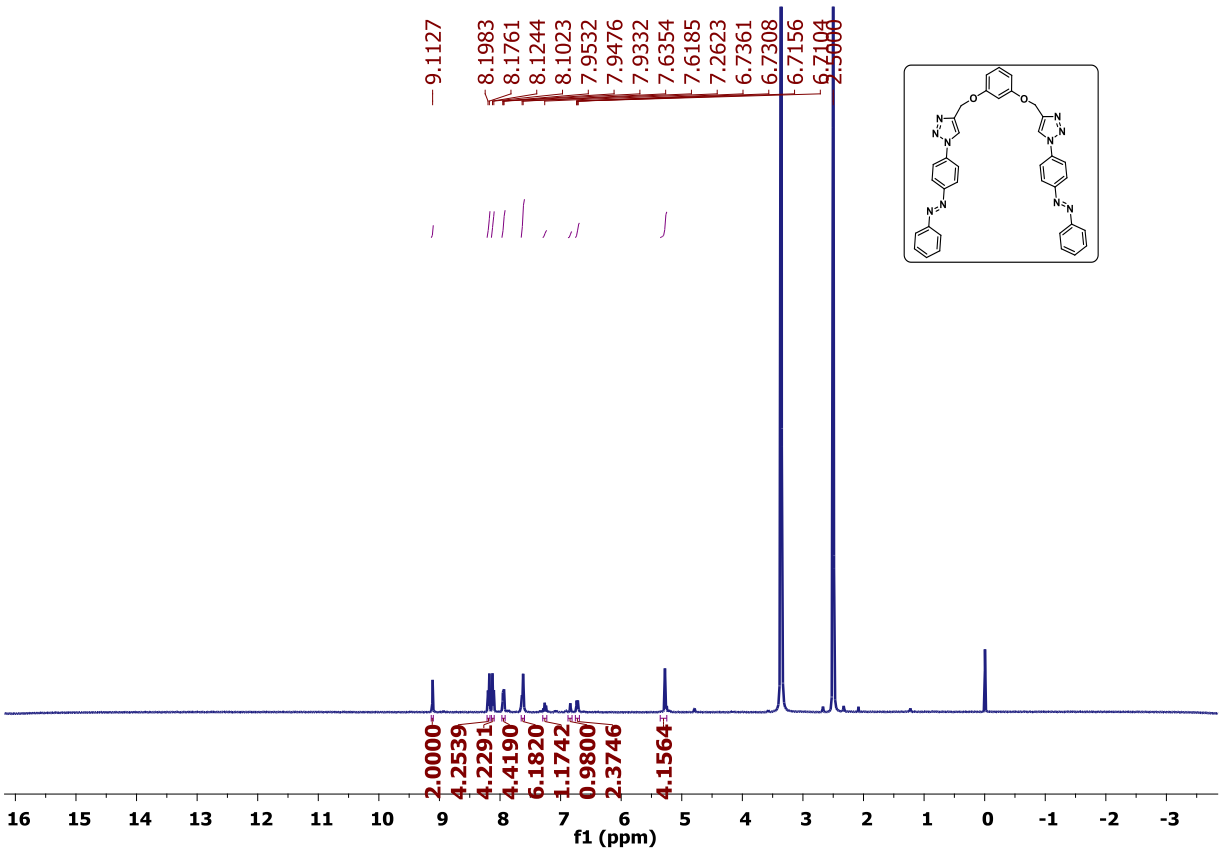

^{1}H-NMR spectrum of 1,3-bis((1-(4-((*E*)-phenyldiazenyl)phenyl)-1*H*-1,2,3-triazol-4-yl)methoxy)benzene (**B1**) in [D_6]DMSO.

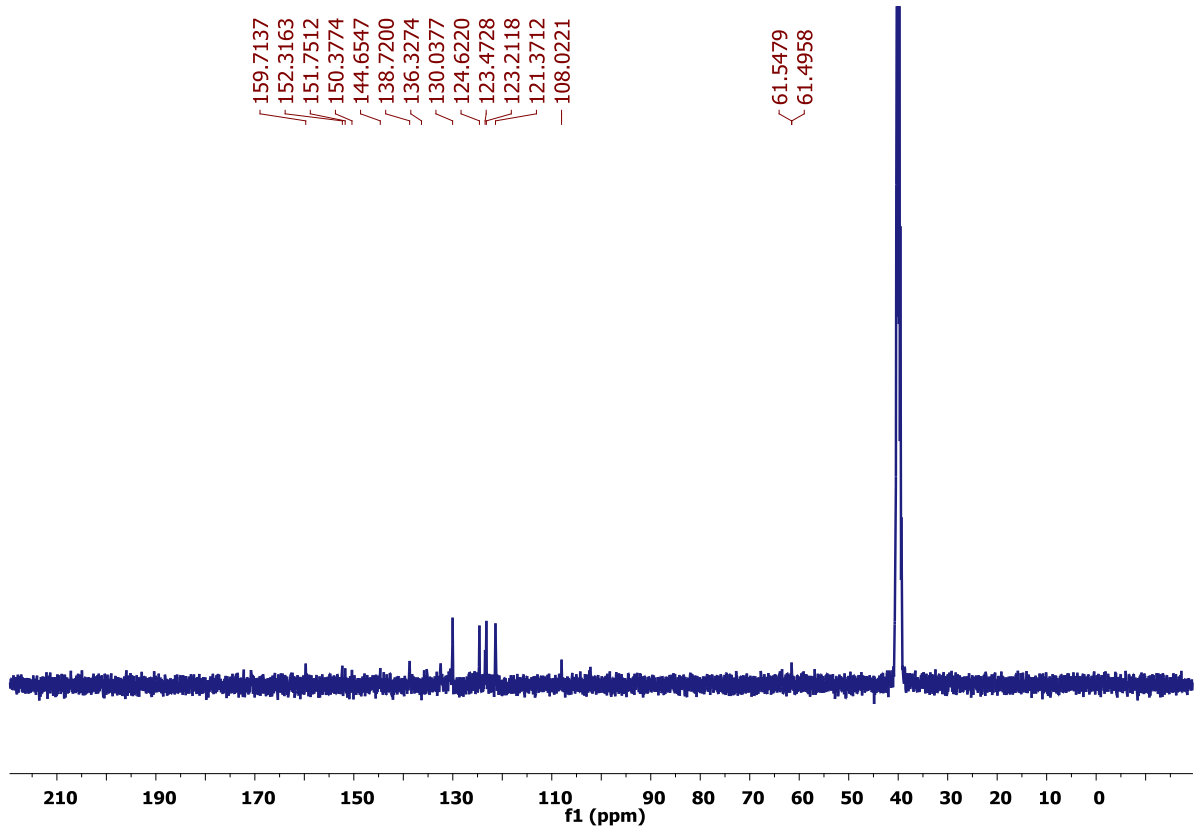

^{13}C-NMR spectrum of 1,3-bis((1-(4-((*E*)-phenyldiazenyl)phenyl)-1*H*-1,2,3-triazol-4-yl)methoxy)benzene (**B1**) in [D_6]DMSO.

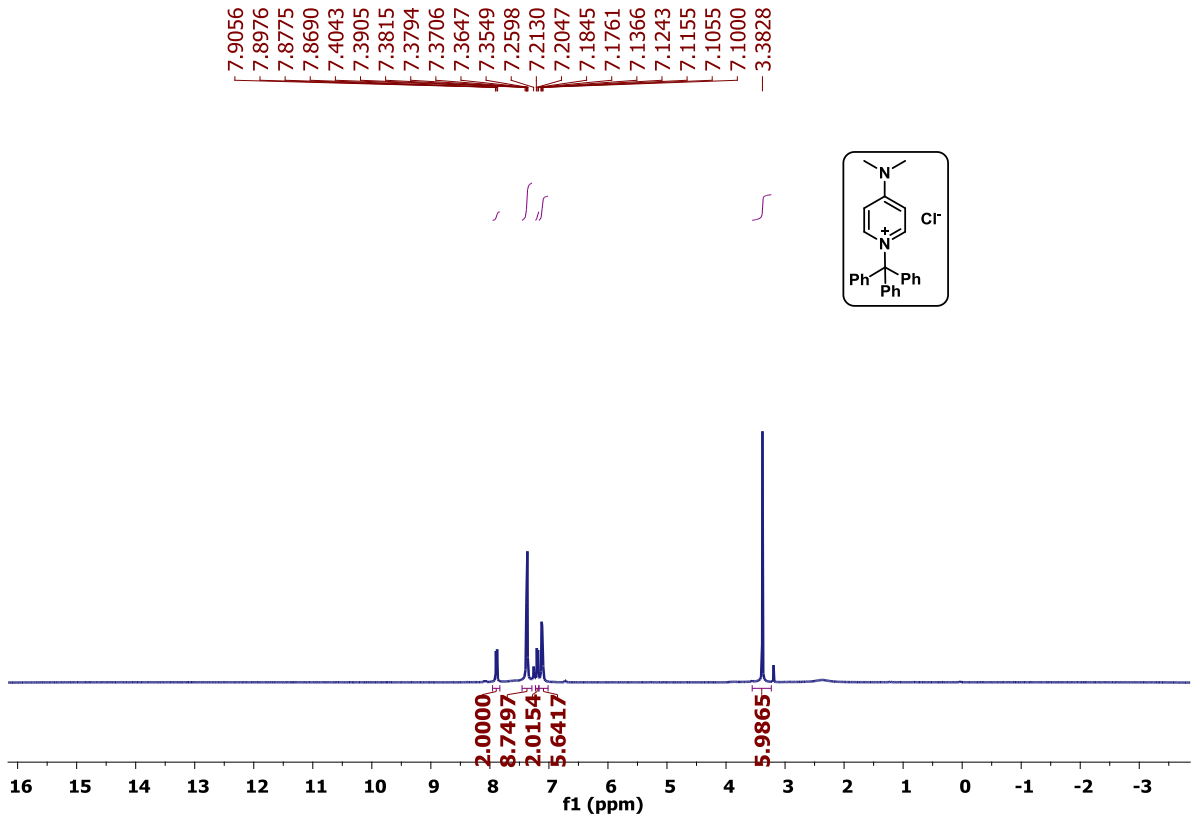

^{1}H-NMR spectrum of 4-(dimethylamino)-1-tritylpyridin-1-ium chloride (**A1**) in $CDCl_3$.

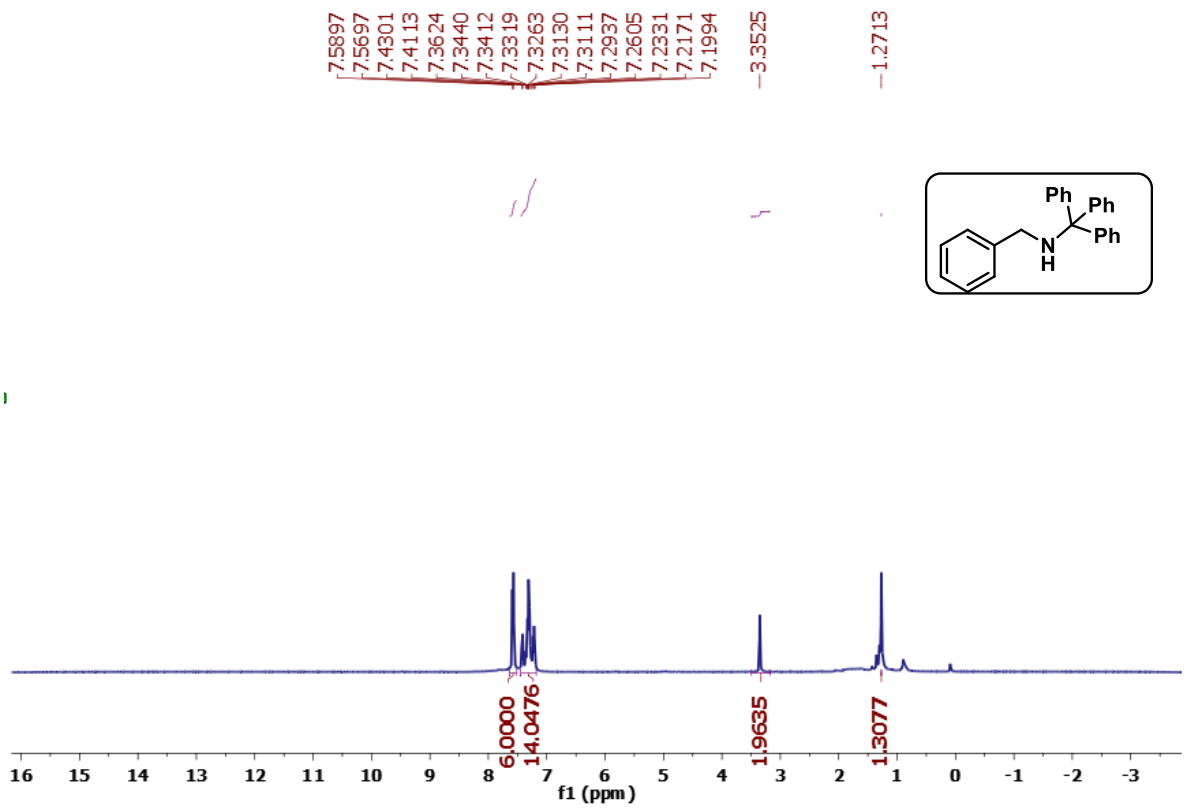

^{1}H-NMR spectrum of *N*-benzyl-1,1,1-triphenylmethanamine (**P1**) in $CDCl_3$.

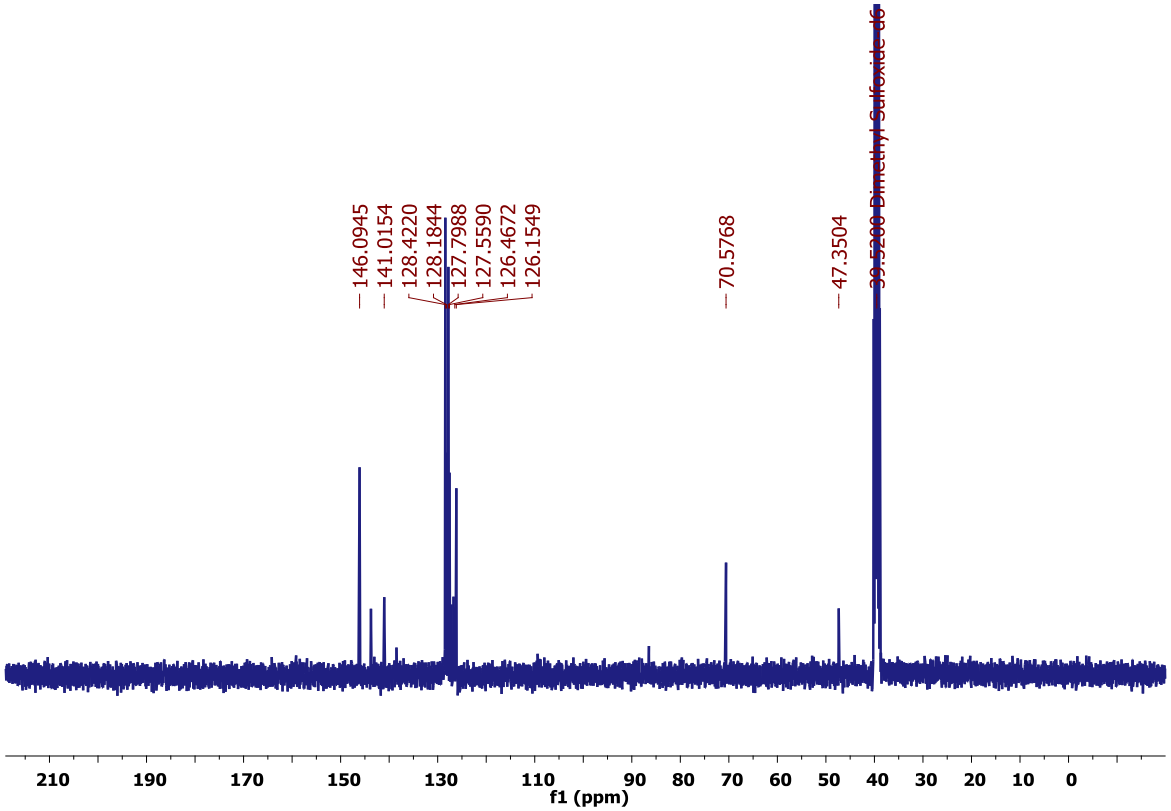

^{13}C-NMR spectrum of *N*-benzyl-1,1,1-triphenylmethanamine (**P1**) in $[D_6]$DMSO.

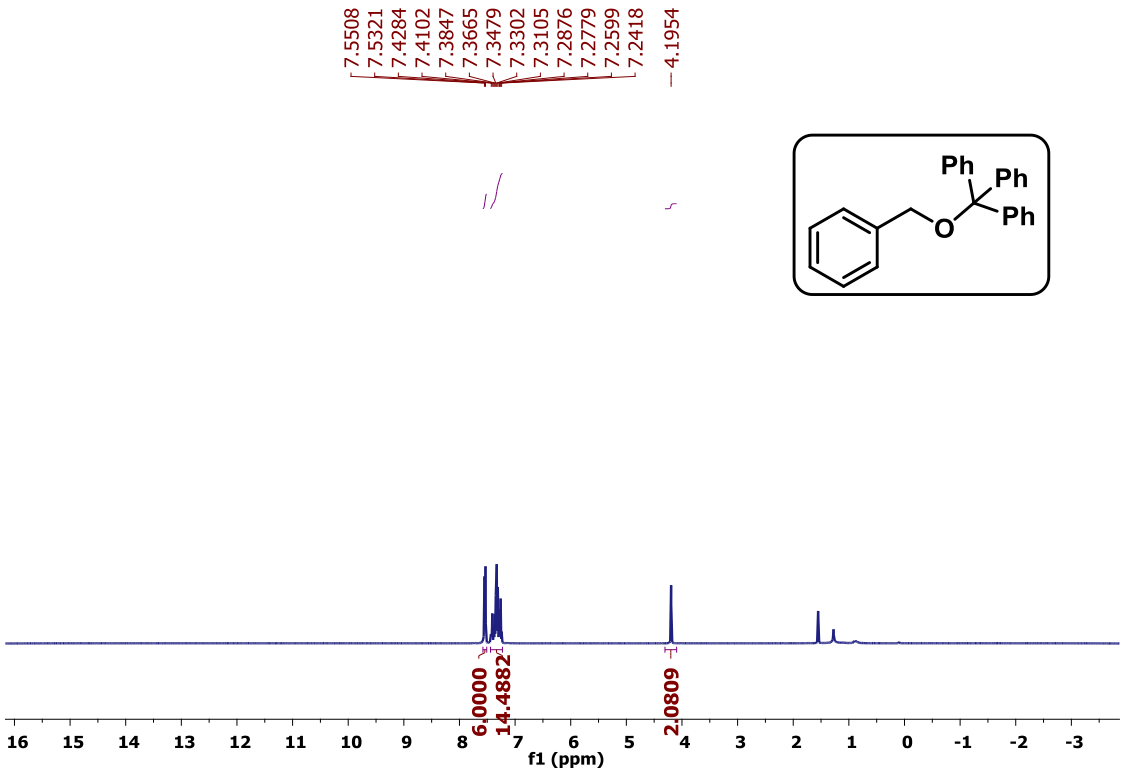

^{1}H-NMR spectrum of ((benzyloxy)methanetriyl)tribenzene (**P2**) in $CDCl_3$.

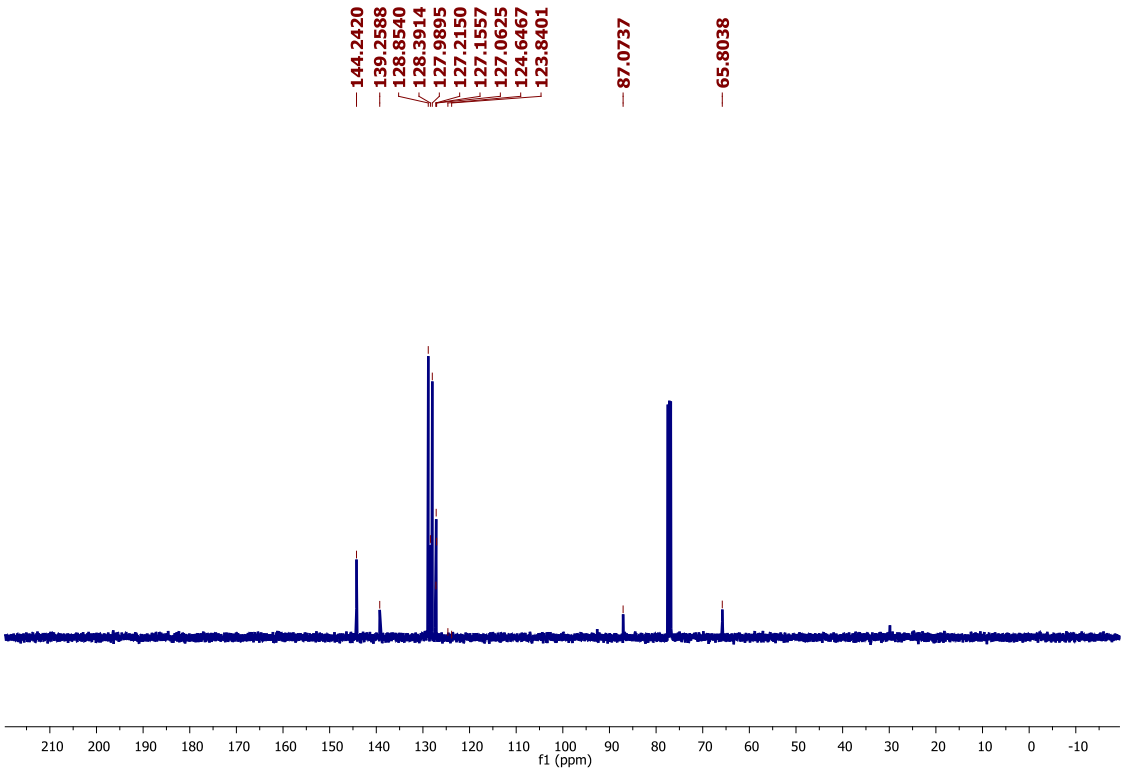

^{13}C-NMR spectrum of ((benzyloxy)methanetriyl)tribenzene (**P2**) in $CDCl_3$.

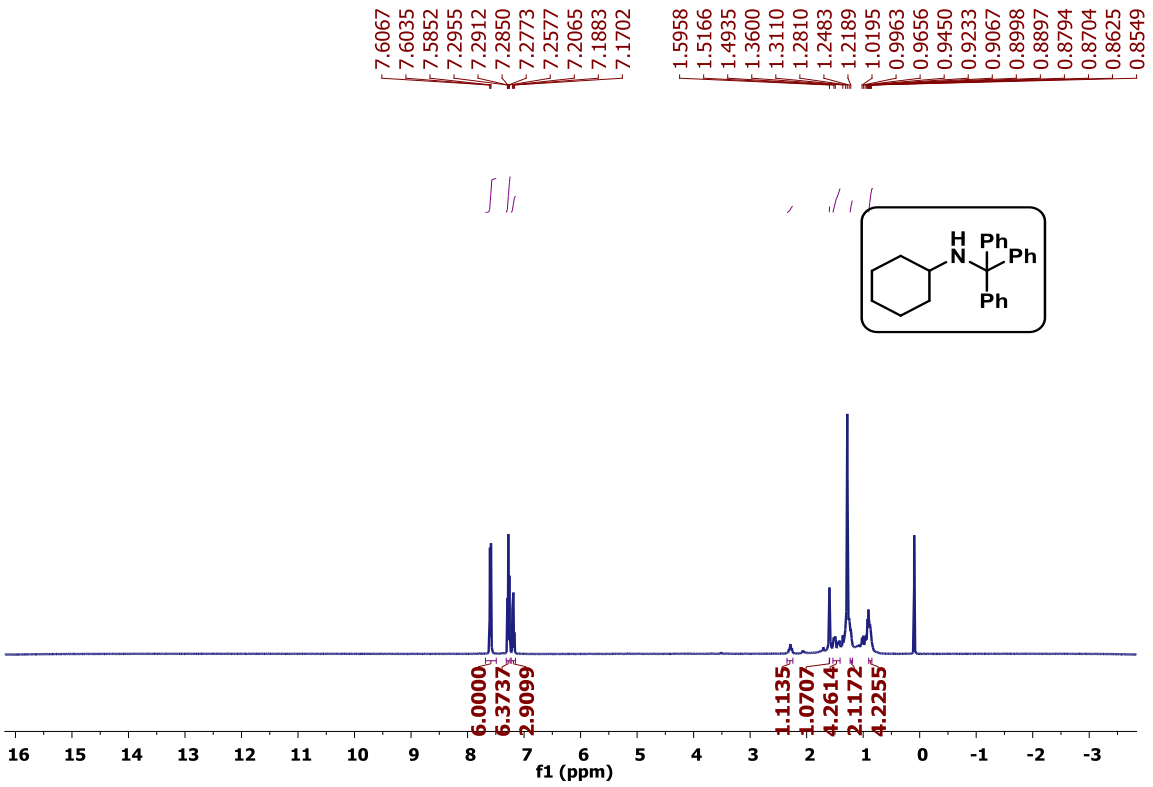

^{1}H-NMR spectrum of *N*-Tritylcyclohexanamine (**P3**) in $CDCl_3$.

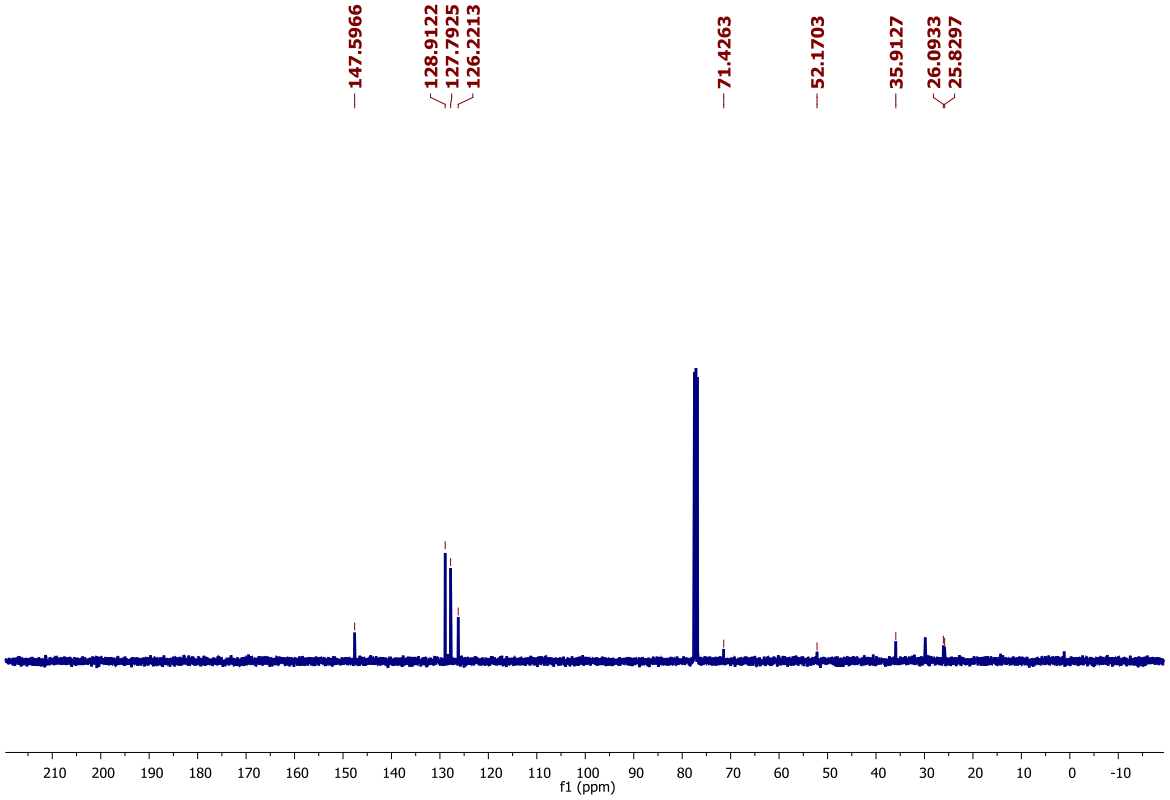

^{13}C-NMR spectrum of *N*-Tritylcyclohexanamine (**P3**) in $CDCl_3$.

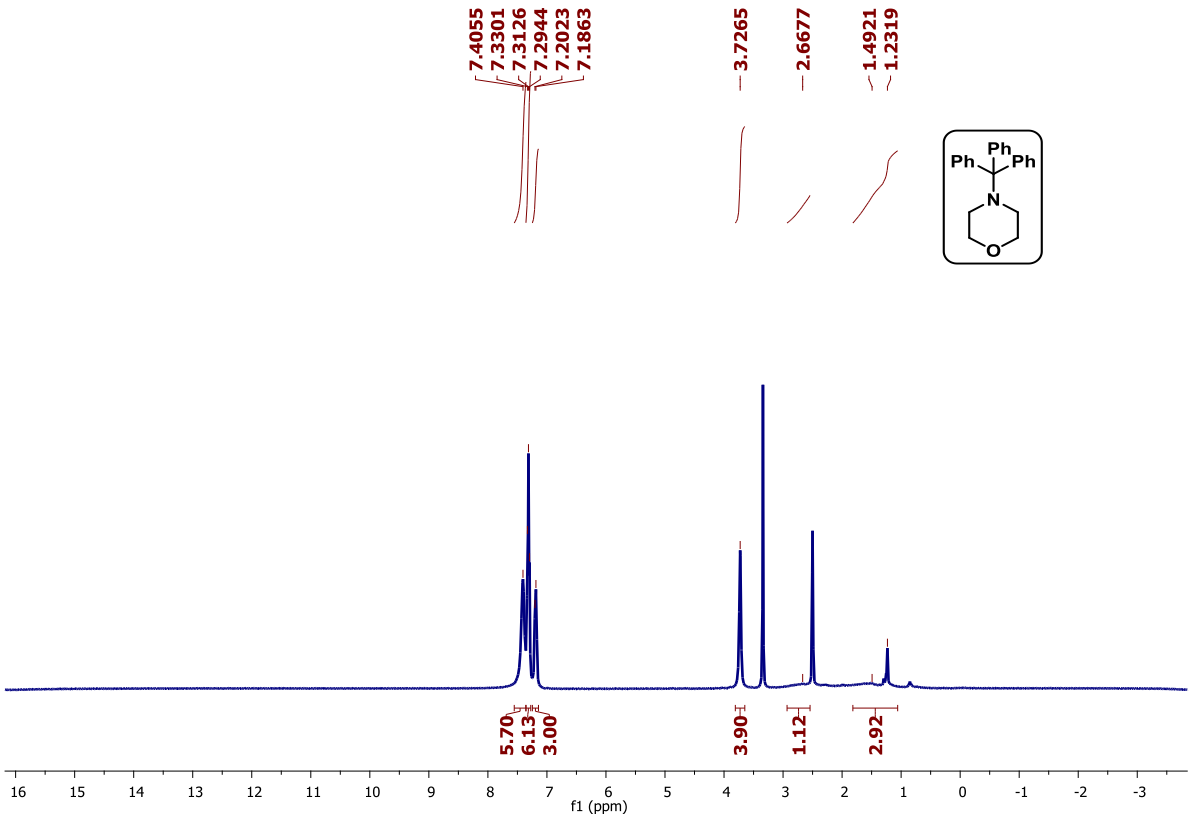

^{1}H-NMR spectrum of *N*-Tritylmorpholine (**P4**) in [D_6]DMSO.

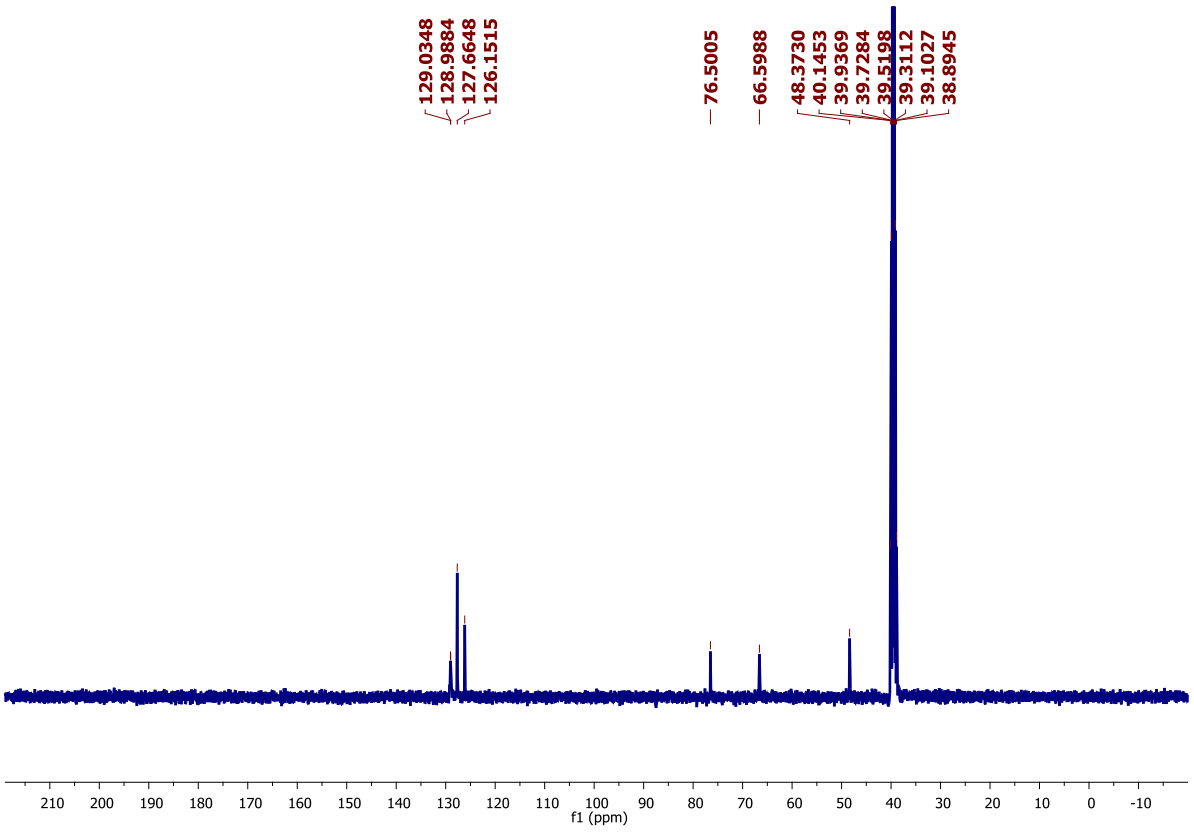

^{13}C-NMR spectrum of *N*-Tritylmorpholine (**P4**) in [D_6]DMSO.

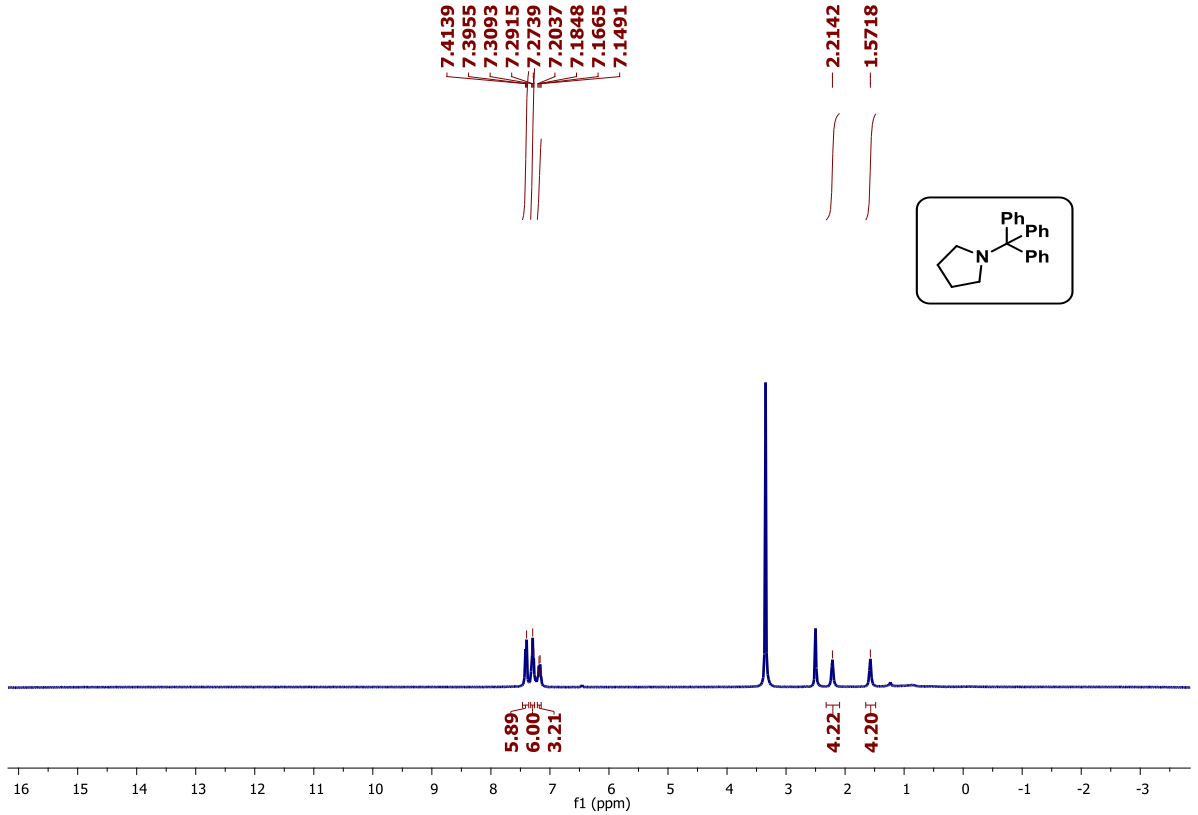

^{1}H-NMR spectrum of *N*-Tritylpyrrolidine (**P5**) in [D_6]DMSO.

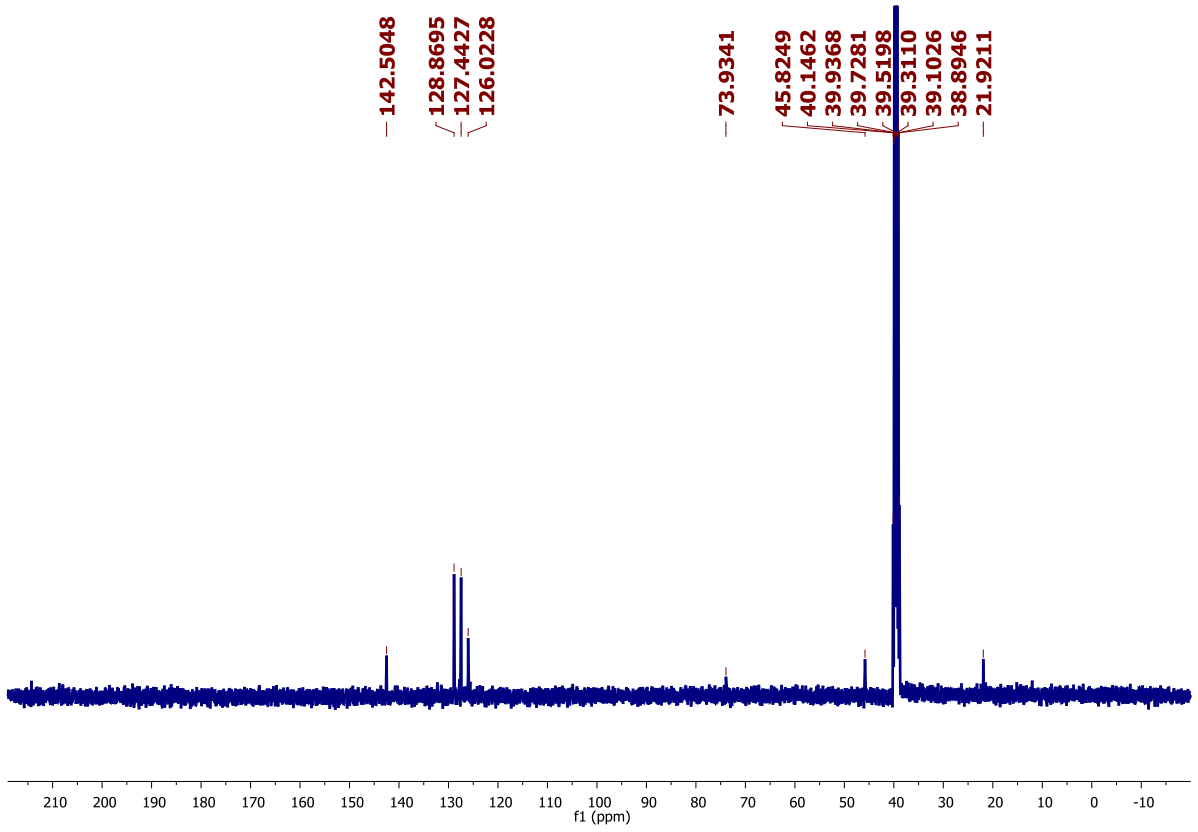

^{13}C-NMR spectrum of *N*-Tritylpyrrolidine (**P5**) in [D_6]DMSO.

Appendix 4E

Computational Data (Done by Mayank Saraswat)

In order to confirm the experimentally predicted binding modes as well as to understand the difference upon photoswitching, computations have also been performed at density functional theory. Geometries have been optimized for *EEE*-, *EEZ*-, *EZZ*- and *ZZZ*-photoisomers of the catalyst **T1** and their respective complexes with Cl^- ions at B3LYP/6-311G(d,p) level of theory. The relative energies of all these isomers with and without the binding of chloride ions were also calculated (**Figures 4E.1 and Figures 4E.2**). In addition to that, relative energies and Mulliken charges analysis have been performed for all four *EEE*-, *EEZ*-, *EZZ*- and *ZZZ* isomers with the Cl^- ion. Natural bond orbital (NBO) analysis has been performed to quantify the interaction energies at M06-2X/6-311G(d,p) level of theory. All these calculations were performed using Gaussian09 suite of program. Based on the computations, the native state of the catalyst is found to be more stable. The progressive *Z*-isomerization increases the destabilization up to a maximum of 45.6 kcal/mol.

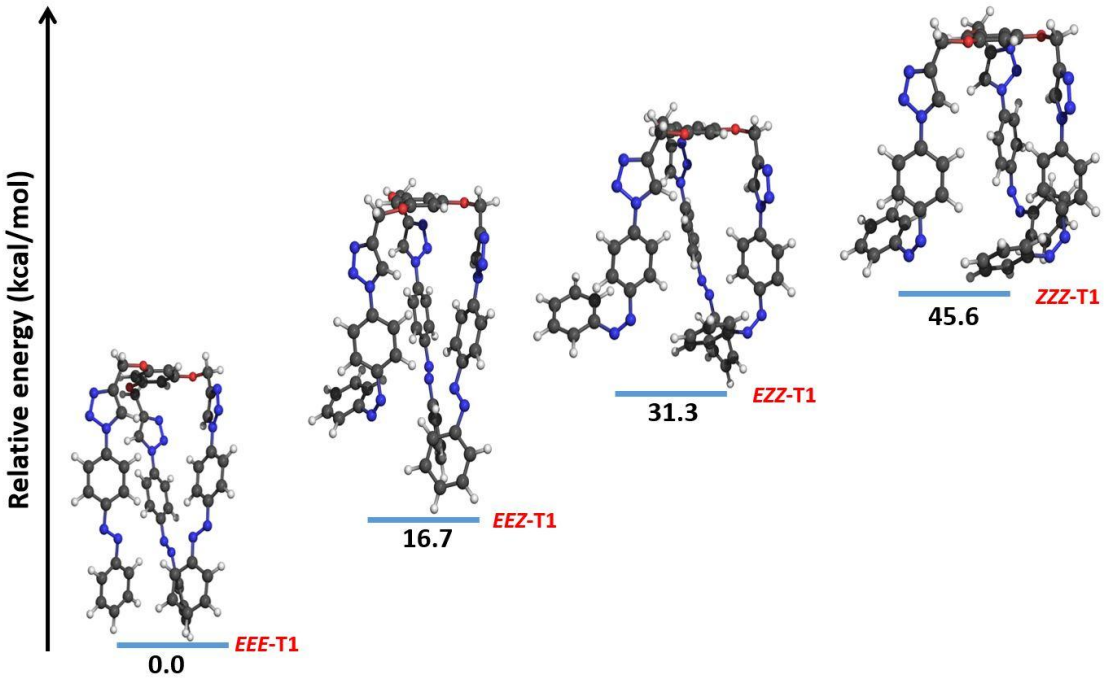

Figure 4E.1 Optimized geometries of ***EEE*-T1**, ***EEZ*-T1**, ***EZZ*-T1** and ***ZZZ*-T1**and their relative energies (kcal/mol) at B3LYP/6-311G(d,p) level of theory.

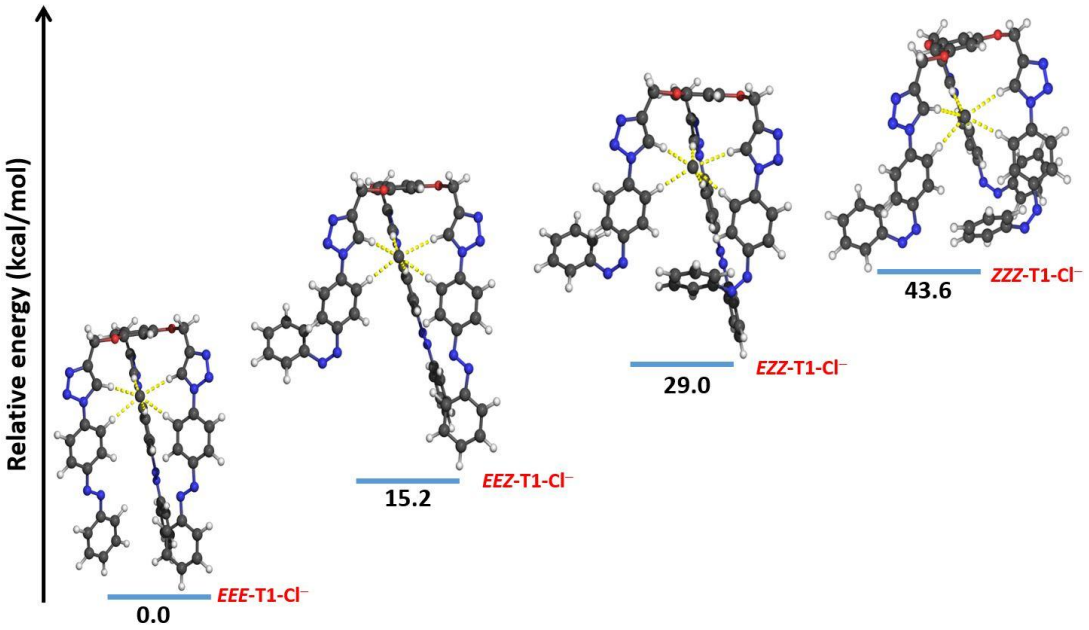

Figure 4E.2 Optimized geometries of complexes ***EEE*-T1-Cl**$^-$, ***EEZ*-T1-Cl**$^-$, ***EZZ*-T1-Cl**$^-$ and ***ZZZ*-T1-Cl**$^-$ and their relative energies (kcal/mol) at B3LYP/6-311G(d,p) level of theory.

However, the chloride ion binding increases the stability of the *Z*-component containing photoisomers. It revealed that the anion binding enhances the stability ranging between 1.5 and 2.3 kcals/mol. Furthermore, the inspection of Mulliken charges revealed the involvement of various atoms in the interactions with chloride ion (**Table 4E.1.**). Incidentally, the triazole C-H, the *ortho* proton of the phenyl relative to the triazole were found to gain maximum positive charge upon interacting with the chloride ion. Apparently, the same protons of the photoswitched states exhibited only a marginal difference in the charges. However, the chloride ion became more negative in the photoswitched states compared to the native state. Furthermore, natural bond orbital (NBO) analysis has been performed to quantify the interaction energies at M06-2X/6-311G(d,p) level of theory. In this regard, the interaction energies of chloride ion with all the binding sites in native and the photoswitched states of the catalyst have been estimated (**Table 4E.2.**). Based on the analysis, we inferred that the triazole C-H is strongly binding compared to the *ortho* proton of the phenyl attached to the triazole in both the cases. However, the interaction energies of all the binding sites showed a decrease in the photoswitched state. All these results are consistent with the experimentally observed NMR shifts. The difference in the binding strength is attributed to the changes in the electronic effects arising due to the photoswitching (*E* to *Z* isomerization), and in turn, the lowering of electron withdrawing character of azo group.

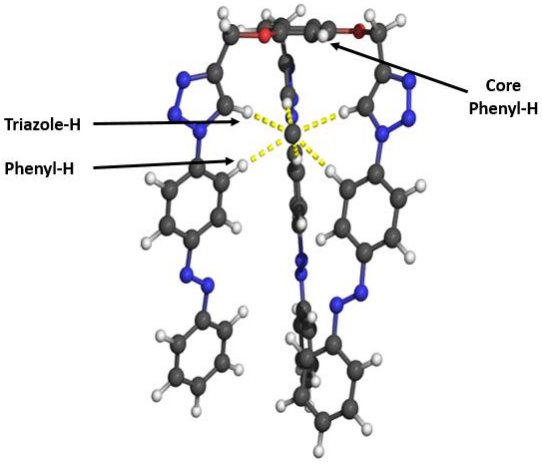

Table 4E.1 Computed Mulliken charges forthe selected hydrogen's in ***EEE*-T1**, ***EEZ*-T1**, ***EZZ*-T1** and ***ZZZ*-T1** and their complexes with Cl^-using B3LYP/6-311G(d,p)) calculations

S.No	Species	Mulliken Charges (atomic units)			
		Triazole-H	Phenyl-H	Core Phenyl-H	Cl^-ion
1	***EEE*-T1**	0.134, 0.132, 0.132	0.118, 0.118, 0.118	0.125, 0.125, 0.128	–
2	***EEE*-T1**–Cl^-	0.218, 0.212, 0.211	0.198, 0.191, 0.200	0.101, 0.100, 0.104	–0.886
3	***EEZ*-T1**	0.138, 0.134, 0.132	0.125, 0.120, 0.118	0.126, 0.121, 0.123	
4	***EEZ*-T1**–Cl^-	0.220, 0.215, 0.210	0.202, 0.199, 0.192	0.105, 0.104, 0.100	–0.890
5	***EZZ*-T1**	0.133, 0.131, 0.130	0.115, 0.115, 0.114	0.126, 0.124, 0.123	–
6	***EZZ*-T1**–Cl^-	0.223, 0.213, 0.207	0.203, 0.189, 0.197	0.105, 0.103, 0.098	–0.890
7	***ZZZ*-T1**	0.133, 0.131, 0.129	0.116, 0.116, 0.112	0.130, 0.124, 0.117	–
8	***ZZZ*-T1**–Cl^-	0.216, 0.211, 0.211	0.199, 0.199, 0.196	0.105, 0.103, 0.105	–0.892

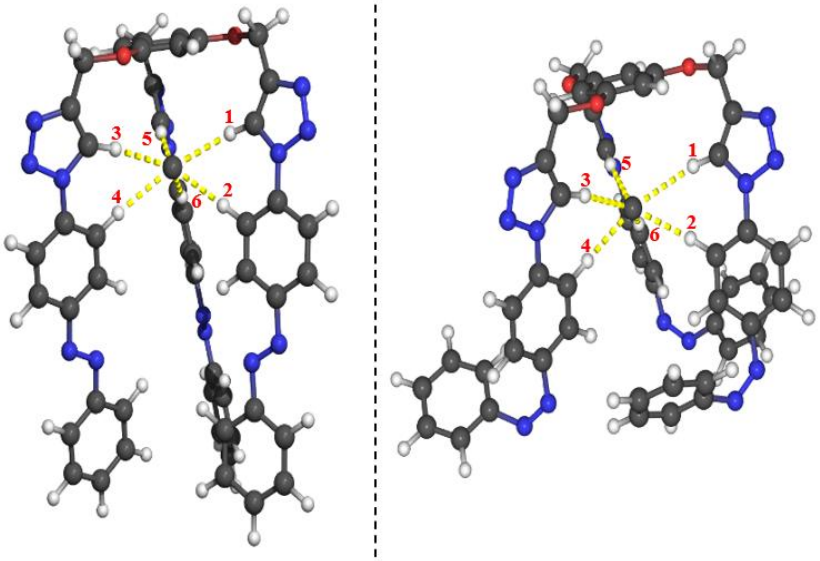

***EEE*-Cl^-** ***ZZZ*-Cl^-**

Table 4E.2 The second order perturbation orbital interaction energies (in kcal/mol) from the natural bond orbital (NBO) analysis in ***EEE*-Cl$^-$** and **ZZZ-Cl$^-$** isomers at M06-2X/6-311G(d,p) level of theory

Species	Donor	Acceptor	E (kcal/mol)	Species	Donor	Acceptor	E (kcal/mol)
***EEE*-Cl$^-$**	n_{Cl-}	$\sigma^*_{(1H-C)}$	10.2	***ZZZ*-Cl$^-$**	n_{Cl-}	$\sigma^*_{(1H-C)}$	6.9
	n_{Cl-}	$\sigma^*_{(2H-C)}$	6.1		n_{Cl-}	$\sigma^*_{(2H-C)}$	3.0
	n_{Cl-}	$\sigma^*_{(3H-C)}$	8.5		n_{Cl-}	$\sigma^*_{(3H-C)}$	7.5
	n_{Cl-}	$\sigma^*_{(4H-C)}$	6.0		n_{Cl-}	$\sigma^*_{(4H-C)}$	5.3
	n_{Cl-}	$\sigma^*_{(5H-C)}$	9.6		n_{Cl-}	$\sigma^*_{(5H-C)}$	7.6
	n_{Cl-}	$\sigma^*_{(6H-C)}$	4.3		n_{Cl-}	$\sigma^*_{(6H-C)}$	5.4

Chapter 5 Conclusions and perspectives

5.1 Introduction

Photoresponsive materials refer to those materials that can reversibly toggle between two isomeric forms and can undergo physical and chemical changes upon irradiation of light at appropriate wavelengths. Therefore, various properties such as planarity, geometrical structure, absorption spectra, dipole moment, dielectric constant, color, solubility, chemical reactivity, refractive index, magnetic properties, π-conjugation, fluorescence emission, covalent bonding, non-covalent interaction, electrochemical properties, electron conductivity, coordination properties, etc. can be modulated with the help of suitable light.[1] Among the various classes of photoswitchable molecules, azobenzenes are one of the robust molecules with excellent efficiency of photoisomerization between *trans* (thermodynamically stable) and *cis*-isomers, and also can easily be synthesized and functionalized. Due to the geometrical changes, both *E* and *Z*-isomers show distinct absorptions in UV-Vis spectroscopy.[2] Typically these molecules can undergo *E*-*Z* isomerization by irradiating at 365 nm, whereas the reverse isomerization can happen either through visible light irradiation or under thermal conditions. Photoresponsive materials have widespread applications in numerous fields, for instance, molecular recognition, molecular machines, photopharmacological applications, supramolecular assembly, liquid crystals, catalysis, sensors, logic operations, data storage, optical memory devices, and molecular devices, etc.[3],[4] For various applications, tuning and controlling the factors influencing the photoswitching behavior and *cis*-isomer stability of azoarenes are crucial. In order to achieve this, the mechanistic aspects in the the forward-reverse isomerization and the influencing factors need to be understood.[5]

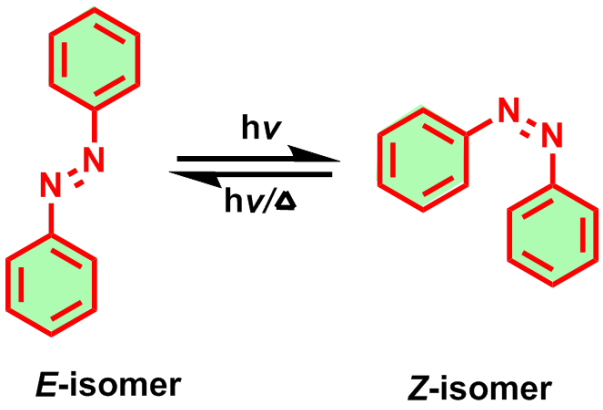

Scheme 5.1 Reversible isomerization in azobenzene.

As functionalization of azobenzene opens the door for a variety of applications as aforementioned, in this context, we have functionalized the azobenzene moiety and utilized them for catalysis application and supramolecular properties.

5.2 Structure-property Relationship in Azobenzene Photoswitches Appended with Picolinyl Amides and their Supramolecular Assemblies

Herein, we have synthesized 18 photoresponsive molecular systems in high yields through modular synthesis, having amide linkages for envisaging their aggregation and supramolecular behavior. All the designed targets have subtle variation at the connections to the azobenzene units, position and orientations of pyridyl groups and the incorporation of 2^{o} vs 3^{o} amide groups. Through systematic variations in the designs, we have evaluated the structure-property relationships.

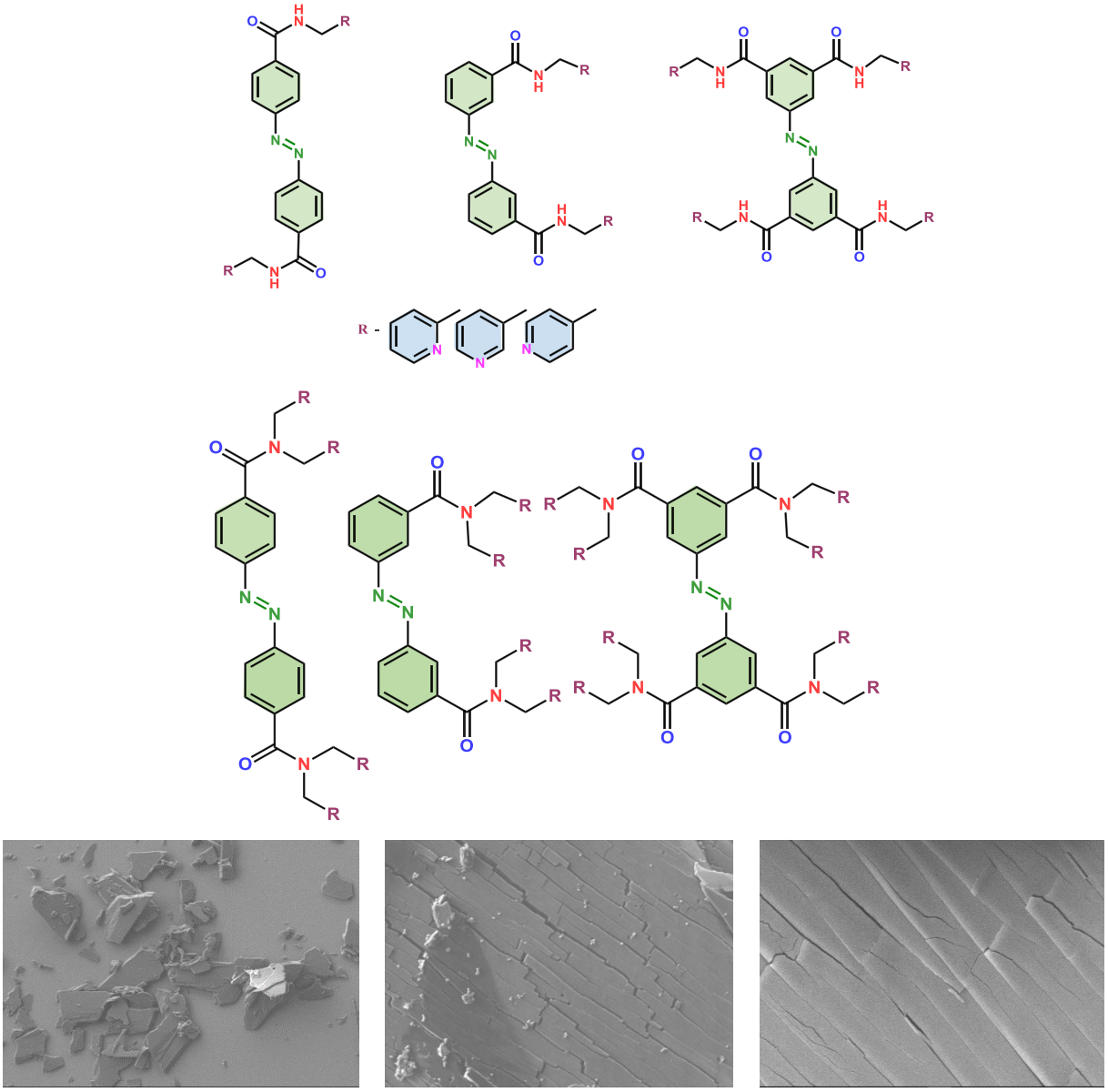

Figure 5.1 Summary of target photoswitchable molecular systems and representative SEM morphology of their supramolecular assemblies.

Furthermore, we have also investigated the effect of structural modification on *Z*-isomeric thermal stability. Among the 4,4′ and 3,3′ substitution on azobenzene, 4,4′ derivatives exhibit fast thermal relaxation in all the cases irrespective of the 2^{o} amide and 3^{o} amide connections compared with 3,3′ substitution. However, when the substitution is extended to 3,3′,5,5′, then the half-life is

increased in the case of 3° amides, whereas minimal increment was observed in the case of 2° amides. Further, the formation of microcrystals was observed in few derivatives, revealed their tendency of forming aggregation. The changes in the morphology of supramolecular assembly/microcrystals have been studied using polarized optical microscopy (POM), Scanning electron microscopy (SEM), and the effect of photo-isomerization on their morphology is also examined.

5.3 Self-assembly in C_3-Symmetric π-Conjugated Azobenzene based Tripodal Systems

As mentioned previously, azobenzene-based molecular systems are also capable of forming supramolecular assembly through appropriate functionalization. In this regard, we have designed and synthesized the tripodal C_3-symmetric molecular systems **T1** and **T2** containing external and internal extended π-conjugation, which are appended with amide linkages having azobenzenes as a photoswitchable units. We have investigated the impact of the design on the supramolecular self-assembly and also, demonstrated the morphological changes in the self-assembly behavior by atomic force microscopy (AFM). Further, organic hydrogels and organic microcrystals have been obtained, and morphological studies were performed using various imaging techniques such as scanning electron microscope (SEM), transmission electron microscopy (TEM), and polarized optical microscopy (POM).

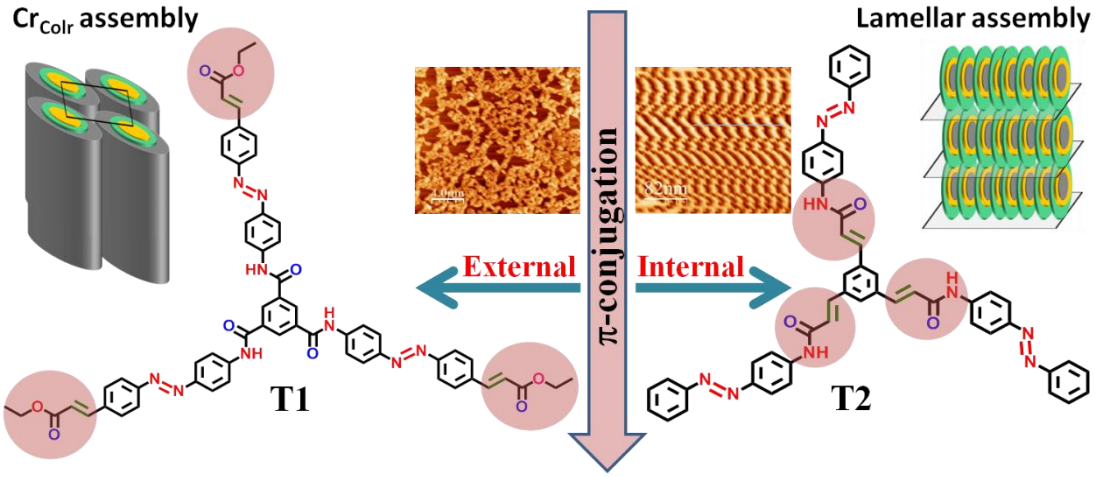

Figure 5.2 Summary of C_3-symmetric π-conjugated molecular systems for supramolecular assembly.

Remarkably, X-ray diffraction studies (XRD) and atomic force microscopy (AFM) imaging helped in giving more insights about how the change in the position of the central acrylic groups present in one target towards the molecular periphery in another molecule, led to the different self-assembly behavior. The SEM and TEM have shown the long fibrous type of morphology of the gel **T1**, whereas in the case of **T2**, we observed the formation of microcrystals with long porous rod-

shaped material. Therefore, these highly ordered materials can be useful in a variety of applications through proper functionalization.

5.4 Light Controlled Catalysis in Tritylation Reactions through Reversible Encapsulation of Chloride Ions

Molecular machines with well-defined functions such as catalysis, molecular recognition, supramolecular assembly, etc. are very important in biology and biochemical processes. Inspired by nature, designing molecular systems that can mimic such functions can be a smart molecular machine for the next generation. Artificial control of functions such as catalysis demands variation in the environment or changes in selected parameters that can act as stimuli. Thus, the stimuli-responsive systems, in principle, can act in "on and off" modes. Furthermore, the external stimuli can control such functions either spatially (selectivity) or temporally (kinetics) of a molecular system. In this regard, light, pH, coordination, redox properties, and supramolecular interaction have been profoundly utilized as external stimuli. Designs incorporating photoswitches in the catalyst part render modulation of catalysis by light. Several photoswitches in general have been exploited for bringing catalysis. In spite of several designs, weak interaction-based photoswitchable catalysis are largely unknown. In this regard, we present the design, synthesis and functionalization of azobenzene derivatives towards developing molecular systems that can reversibly encapsulate chloride ions through which it can exhibit catalysis through triazole moieties. Through this strategy, we have successfully synthesized five different catalysts and utilized in the catalysis of tritylation of the benzylamine. After careful optimization of the conditions, the results showed that the catalyst in *EEE* state showed an increase, whereas the *ZZZ* state decreases the rate of the reaction that had been established based on isolated yields. This concept of controlling the tritylation reaction rates by light has also been extended to additional substrates. Through HRMS data, NMR titrations, control experiments, and DFT computations, we confirmed the mode of binding and the importance of cooperative binding. Isothermal titration calorimetric (ITC) measurements revealed a two-fold difference in the dissociation constant between chloride ion and the catalyst in its native (*EEE*) and photoswitched (*ZZZ*) states that is very well corroborated with the differences in the isolated yields. In summary, a detailed spectroscopic, calorimetric and computational studies have been utilized to confirm the critical role of the triazole C-H…Cl interactions. Through this investigation, the effect of variation in the binding affinities between the native and photoswitched states of the catalyst at room temperature in the temporal control of the catalysis has been demonstrated.

S. No.	Parameters	Methods	Technique/ Spectroscopy	Native (*E*-isomer) + TBAC	Photoswitched state (*Z*-isomer) + TBAC
1	Catalyst Binding with chloride ion	Catalyst and TBAC solution mixture	HRMS	Binding (Mass M + Cl^-]	Binding (Mass M + Cl^-]
2	Binding sites	Titration of **T1** with TBAC	NMR	Binding (Chemical Shifts in signals)	Binding (Chemical Shifts in signals)
3	Dissociation constant, K_d	Titration of **T1** with TBAC	ITC	877 ± 157	2070 ± 431
4	Cooperativity	Control experiment (reactions catalysed by a bis-triazole photoswitch)	Isolated Yields	Higher yields compared to **B1**	-

Dissociation constant K_d are expressed in M

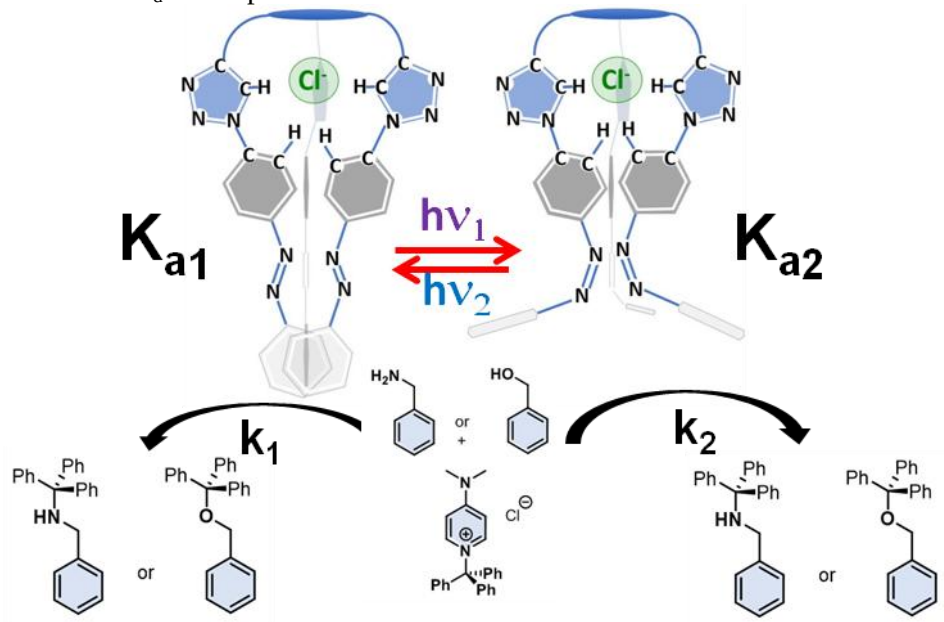

Figure 5.3 Summary of light modulated catalysis through encapsulation of chloride ions

5.5 Perspectives

In this thesis, we have exploited various azobenzene containing molecular systems for supramolecular properties and catalysis application. Functionalization of azobenzenes and their effect on photoswitching ability, thermal *cis*-isomer stability were considered as the main objectives. Despite a correlation has been reached for the designed targets, the solubility issues prevented us to explore the corresponding *ortho* derivatives. Additional incorporation of groups enhancing solubility may be needed. In addition, the binding with metal ions through intermolecular chelation in *trans* isomeric state and intramolecular chelation in *cis* state can be explored. A preliminary exploration using Zn salts showed shielding effects after binding. However, a systematic search and binding studies are needed, which could be helpful in reversible binding and release of the metal ions. Also, the studies on tripodal C_3-symmetric benzene-1,3,5-

tricaboxamide (BTA) core based systems with extended π-conjugation revealed exceptional ordered self-assemblies, which can be useful to design discotic liquid crystals with proper functionalization. However, the decrease in the photoswitching characteristics in columnar assembly needs to be overcome by providing proper room for photoswitching without compromising the columnar assemblies. Then, the catalytic effects of novel C_3-symmetric *tris*-triazole based photoswitchable catalyst provides a lot of conceptual designs to make them useful in selectivity and "ON and OFF" control of the reactions. However, a lot of designs need to be screened for achieving them. Furthermore, these molecules can be further utilized for reversible metal ion binding and metal based catalytic activation with light control properties.

5.6 References

[1] a) Y. Ru, Z. Shi, J. Zhang, J. Wang, B. Chen, R. Huang, G. Liu, T. Yu, *Mater. Chem. Front.* **2021**, *5*, 7737–7758; b) J. Cui, A. D. Campo, *Photoresponsive polymers: properties, synthesis and applications*. In Smart Polymers and Their Applications, *Elsevier*, **2014**, pp. 93–13; c) H. Tian, S. Yang, *Chem. Soc. Rev.* **2004**, *33*, 85–97; d) Szacilowski, K. *Chem. Rev.* **2008**, *108*, 3481-3548.

[2] a) H. M. D. Bandara, Shawn C. Burdette, *Chem. Soc. Rev.* **2012**, *41*, 1809-1825; b) S. Grewal, D. Gupta, A. K. Gaur, M. Saraswat, S. Venkataramani, *Azoheteroarene photoswitches – Synthesis, Photoswitching and Utility*. In Photoisomerization: Causes, Behavior and Effects; Sampedro, D., Ed.; Nova Publishers, USA, **2019**; pp 111-188; c) F. A. Jerca, V. V. Jerca, R. Hoogenboom, *Nat. Rev. Chem.* **2022**, *6*, 51–69.

[3] a) J. Zhang, Q. Zou, H. Tian, *Adv. Mater.* **2013**, *25*, 378–399; b) A. Goulet-Hanssens, F. Eisenreich, S. Hecht, *Adv. Mater.* **2020**, *32*, 1905966; c) Y. Wakayama, R. Hayakawa, K. Higashiguchi, K. Matsuda, *J. Mater. Chem. C* **2020**, *8*, 10956-10974; d) I. M. Welleman, M. W. H. Hoorens, B. L. Feringa, H. H. Boersma, W. Szymański, *Chem. Sci.* **2020**, *11*, 11672–11691; e) X. Huang, T. Li, *J. Mater. Chem. C* **2020**, *8*, 821-848; f) H.-B. Cheng, S. Zhang, J. Qi, X.-J. Liang, J. Yoon, *Adv. Mater.* **2021**, *33*, 2007290; g) Z. Yang, Z. Liu, L. Yuan, *Asian J. Org. Chem.* **2021**, *10*, 74– 90.

[4] a) V. Blanco, D. A. Leigh, V. Marcos, *Chem. Soc. Rev.* **2015**, *44*, 5341–5370; b) R. Dorel, B. L. Feringa, *Chem. Commun.* **2019**, *55*, 6477-6486.

[5] J. Garcia–Amoros, D. Velasco, *Beilstein J. Org. Chem.* **2012**, *8*, 1003–1017.

Chapter 6. Materials and Methods

Reagents and solvents: All the reagents (AR or LR grade) and solvents were purchased from commercially available sources such as Sigma Aldrich, Avra, Rankem, CDH, Alfa Aesar, Spectrochem, and TCI, etc., and used without further purification. Dry solvents such as toluene, THF, and DCE were obtained from MBraun-SPS solvent purification system. UV spectroscopic grade solvents have been used for UV-vis photoswitching and kinetics studies. For column chromatography, pre-distilled solvents have been utilized.

Chromatography: Thin layer chromatography was performed on Merck Silica gel 60 F_{254} TLC plates and visualized using a UV chamber (λ = 254 nm). Column chromatography was performed over (100-200 mesh) silica gel EtOAc/hexane and DCM/MeOH as an eluent

NMR spectroscopy: ^{1}H and ^{13}C NMR spectra were recorded in $CDCl_3$ or [D_6]DMSO deuterated solvents on a Bruker Avance-III 400 MHz spectrometer with operational frequencies of 400 and 100 MHz, respectively. Chemical shift (δ) values are reported in parts per million (ppm), and coupling constants (*J*) are reported in Hz. The signals of residual solvents from $CDCl_3$ (7.26 ppm) and [D_6]DMSO (2.50 ppm) have been used for internal calibration in ^{1}H NMR, whereas in ^{13}C NMR signals of $CDCl_3$ (77.16 ppm) and [D_6]DMSO (39.52 ppm) have been used for calibration. The signal multiplicities are abbreviated as singlet (s), doublet (d), triplet (t), quartet (q), pentet (p), doublet of doublets (dd), doublet of triplets (dt), triplet of doublets (td), doublet of doublet of doublets (ddd), multiplet (m), and broad (br).

HRMS: High-resolution mass spectra (HRMS) have been recorded using Waters Synapt G2-Si Q-TOF mass spectrometer. The ionization for those samples was done using the electrospray ionization (ESI) or Matrix-assisted laser desorption/ionization (MALDI) methods, and the detections were done in both positive and negative modes.

Melting Points (MPs): Melting points were recorded on the SMP20 melting point apparatus and are uncorrected.

FT-IR studies: FT-IR spectra were recorded as a neat solid or neat liquid on a Bruker Alpha ZnSe ATR spectrometer or a KBr pellet on a Perkin Elmer Spectrum in a transmittance mode.

Photoswitching studies and light sources: The analysis of photoswitching and kinetics measurements has been carried out using a Bruker Avance-III 400 MHz ^{1}H NMR spectrometer and Cary 5000 or Cary 60 UV-Vis spectrophotometer from Agilent technology attached with a temperature controller Peltier assembly. For forward (*E*-Z) isomerization, either a light of

wavelengths 365 nm, 385 nm, or 405 nm has been used, and for the reverse (*Z*-*E*) photoisomerization steps, either light of wavelength 405 nm or 535 nm (LED light SX-20 from Applied Photophysics) has been used. The samples were irradiated in a quartz cuvette of 1 cm path length or a quartz NMR tube. The photostationary states (PSS) have been established by irradiating the sample for a prolonged time such that no further spectral change is observed.

X-ray diffraction studies: X-ray diffraction (XRD) was carried out using Cu Kα (λ=1.54 Å) radiation from a source (GeniX 3D, Xenocs) operating at 50 kV and 0.6 mA. The diffraction patterns were collected on a two module Pilatus detector.

Atomic Force Microscopy (AFM): Atomic force microscopy (AFM) was performed using Nano wizard 3, JPK Instruments, Germany. The images were acquired by Olympus, OMCLTR400PSA-1. All AFM output files were analyzed in WSxM data processing software.

Transmission electron microscopy (TEM): Transmission electron microscopy was performed using JEOL JEM-F200.

Scanning electron microscopy (SEM): Field emission-scanning electron microscopy (FE-SEM) was done using the JEOL JSM-7600F instrument.

Polarised optical microscopy (POM): Polarised optical microscopy has been conducted using Nikon Eclipse LV100POL polarising microscope provided with a Linkam heating stage (LTS 420). All images were captured using a Q-imaging camera.

Isothermal titration calorimetry (ITC): Isothermal titration calorimetry experiments were executed using Malvern MicroCal PEAQ-ITC200 at 293.15 K.

Copyrights

Chapter 3

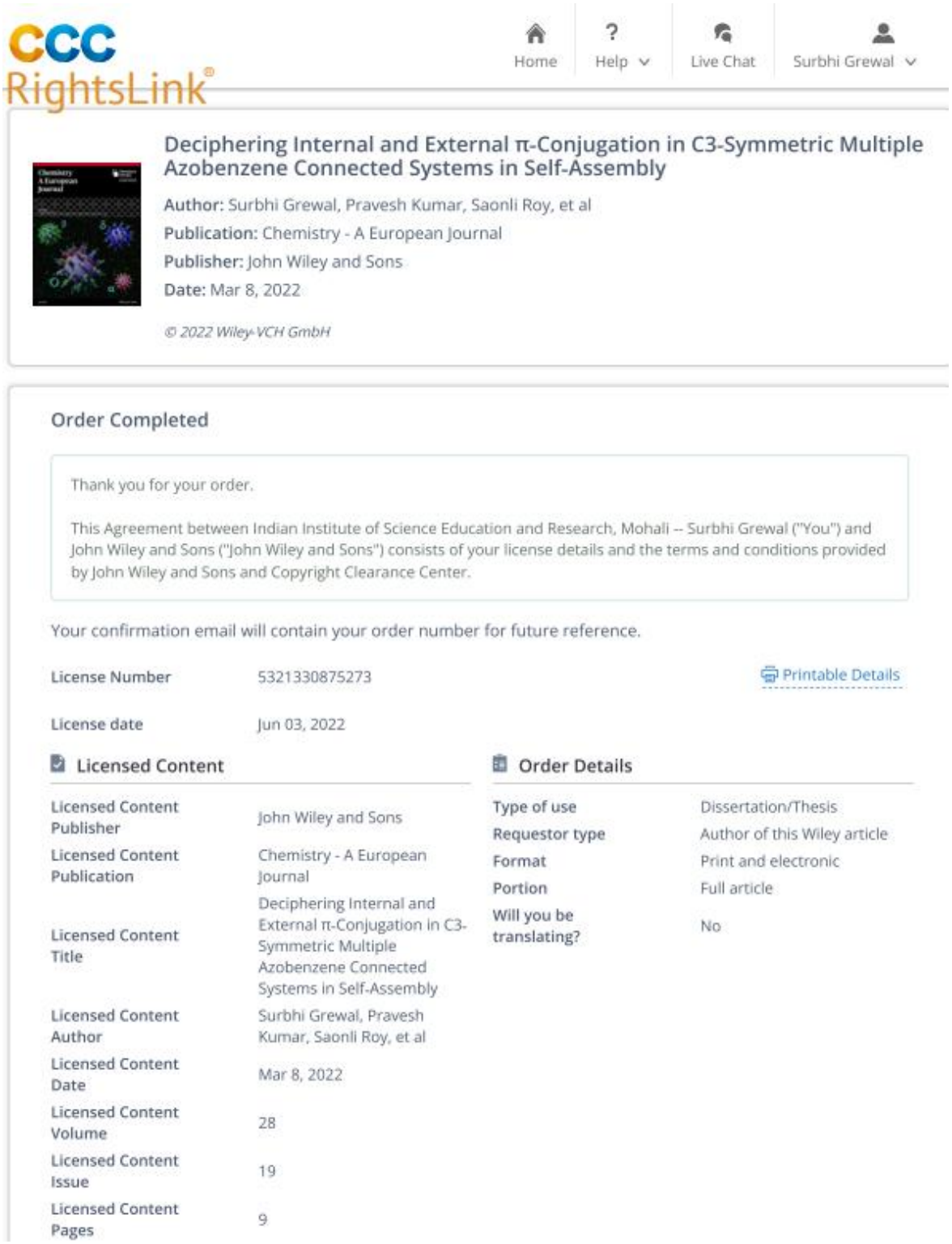

CCC RightsLink®

Home | Help | Live Chat | Surbhi Grewal

Deciphering Internal and External π-Conjugation in C3-Symmetric Multiple Azobenzene Connected Systems in Self-Assembly

Author: Surbhi Grewal, Pravesh Kumar, Saonli Roy, et al

Publication: Chemistry - A European Journal

Publisher: John Wiley and Sons

Date: Mar 8, 2022

© 2022 Wiley-VCH GmbH

Order Completed

Thank you for your order.

This Agreement between Indian Institute of Science Education and Research, Mohali -- Surbhi Grewal ("You") and John Wiley and Sons ("John Wiley and Sons") consists of your license details and the terms and conditions provided by John Wiley and Sons and Copyright Clearance Center.

Your confirmation email will contain your order number for future reference.

License Number	5321330875273
License date	Jun 03, 2022

Printable Details

Licensed Content

Licensed Content Publisher	John Wiley and Sons
Licensed Content Publication	Chemistry - A European Journal
Licensed Content Title	Deciphering Internal and External π-Conjugation in C3-Symmetric Multiple Azobenzene Connected Systems in Self-Assembly
Licensed Content Author	Surbhi Grewal, Pravesh Kumar, Saonli Roy, et al
Licensed Content Date	Mar 8, 2022
Licensed Content Volume	28
Licensed Content Issue	19
Licensed Content Pages	9

Order Details

Type of use	Dissertation/Thesis
Requestor type	Author of this Wiley article
Format	Print and electronic
Portion	Full article
Will you be translating?	No

Chapter 4

Temporal control in tritylation reactions through light-driven variation in chloride ion binding catalysis – a proof of concept

S. Grewal, S. Roy, H. Kumar, M. Saraswat, N. K. Bari, S. Sinha and S. Venkataramani, *Catal. Sci. Technol.*, 2020, **10**, 7027 **DOI:** 10.1039/D0CY01090A

Surbhi Grewal

Email: ph16021@iisermohali.ac.in
Department of Chemical Sciences
Indian Institute of Science Education and Research (IISER) Mohali

PhD Chemistry

07/2018–09/2022 **Senior Research Fellow**
Indian Institute of Science Education and Research (IISER) Mohali

07/2016–07/2018 **Junior Research Fellow**
Indian Institute of Science Education and Research (IISER) Mohali

Education

07/2013–06/2015 Master's of Science (Chemistry), DAV College (affiliated to Panjab University)

05/2010–05/2013 Bachelor's of Science, MCM DAV College (affiliated to Panjab University)

Awards & Honors

07/2016–09/2022 Junior Research Fellowship and Senior Research Fellowship for Doctoral Studies, Ministry of Human Resource Development, Government of India

02/2016–06/2016 Junior Research Fellowship (Project), Science and Engineering Research Board, Government of India

2015 & 2019 Qualified GATE (Graduate Aptitude Test in Engineering)

Teaching

Indian Institute of Science Education and Research (IISER) Mohali (Teaching Assistant)

1. CHM211-lab course, Introduction to spectroscopy and spectrometers (for 2nd year undergraduate students); **August 2017, August 2018**
2. CHM212-lab course, Synthesis of organic compounds and their purification using chromatographic techniques (for 2nd year undergraduate students); **January 2018**
3. Co-guided master thesis students, and mentored undergraduate students during summer internships and mentored junior colleagues.

Technical Skills

- Expertise in ChemDraw, Topspin, Origin, Scifinder Softwares.
- Hands on experience in Ultravoilet-visible spectroscopy (UV-vis), Fluorescence spectroscopy, Fourier-transform infrared spectroscopy (FT-IR), Fourier transform infrared spectroscopy-Attenuated total reflection (FTIR-ATR) and Nuclear magnetic resonance spectroscopy (NMR).

- Proficiency in handling Atomic force microscopy (AFM), Time-correlated single photon counting (TCS-PC) and Isothermal titration calorimetry (ITC) instruments.
- Can effectively devise and perform multi−step syntheses to prepare complex products.
- Capable of using distillation, recrystallization, column chromatography and thin layer chromatography to purify products.
- Excellent practical skills in handling air/moisture sensitive reagents/reactions and milligram/gram scale reactions.
- Experience in carrying out heck coupling, acid-amine coupling, reductive-amination, sonogashira coupling, acid-alcohol coupling etc.
- Good communication skill, self-motivated, creative, well organized and a good team worker with leadership qualities.